



HAL
open science

Croissance epitaxiale et recuit laser nanosecondes d'hétérostructures GeSn/SiGeSn

Marvin Frauenrath

► **To cite this version:**

Marvin Frauenrath. Croissance epitaxiale et recuit laser nanosecondes d'hétérostructures GeSn/SiGeSn. Physique [physics]. Université Grenoble Alpes [2020-..], 2022. Français. NNT : 2022GRALY092 . tel-04086845

HAL Id: tel-04086845

<https://theses.hal.science/tel-04086845v1>

Submitted on 2 May 2023

HAL is a multi-disciplinary open access archive for the deposit and dissemination of scientific research documents, whether they are published or not. The documents may come from teaching and research institutions in France or abroad, or from public or private research centers.

L'archive ouverte pluridisciplinaire **HAL**, est destinée au dépôt et à la diffusion de documents scientifiques de niveau recherche, publiés ou non, émanant des établissements d'enseignement et de recherche français ou étrangers, des laboratoires publics ou privés.

THÈSE

Pour obtenir le grade de

DOCTEUR DE L'UNIVERSITÉ GRENOBLE ALPES

École doctorale : PHYS - Physique

Spécialité : Physique des matériaux

Unité de recherche : Laboratoire d'Electronique et de Technologie de l'Information (LETI - CEA)

**Croissance epitaxiale et recuit laser nanosecondes
d'hétérostructures GeSn/SiGeSn**

**Epitaxial growth and nanosecond laser annealing of GeSn/SiGeSn
heterostructures**

Présentée par :

Marvin FRAUENRATH

Direction de thèse :

Jean-Michel HARTMANN

Directeur de recherche, CEA Centre de Grenoble

Directeur de thèse

Pablo ACOSTA ALBA

Ingénieur - Chercheur, CEA

Co-encadrant de thèse

Rapporteurs :

ISABELLE BERBEZIER

Directeur de recherche, CNRS DELEGATION PROVENCE ET CORSE

CAROLINE BONAFOS

Directeur de recherche, CNRS DELEGATION OCCITANIE OUEST

Thèse soutenue publiquement le **13 décembre 2022**, devant le jury composé de :

MICKAEL GROS-JEAN

Ingénieur HDR, ST MICROELECTRONICS

Examineur

ISABELLE BERBEZIER

Directeur de recherche, CNRS DELEGATION PROVENCE ET CORSE

Rapporteuse

CAROLINE BONAFOS

Directeur de recherche, CNRS DELEGATION OCCITANIE OUEST

Rapporteuse

AHMAD BSIESY

Professeur des Universités, UNIVERSITE GRENOBLE ALPES

Président

Invités :

DAN BUCA

Directeur de recherche, Forschungszentrum Jülich



Table of Contents

Introduction..... 2

Chapter I : Challenges of Growing and Doping GeSn and SiGeSn Layers . 8

I.1 Epitaxy.....	Error! Bookmark not defined.
I.1.1 The concept of Epitaxy	Error! Bookmark not defined.
I.1.2 The concept of plastic strain relaxation	Error! Bookmark not defined.
I.1.3 Critical thickness for plastic strain relaxation	Error! Bookmark not defined.
I.1.4 Lattice defects	Error! Bookmark not defined.
I.2 The (Si)GeSn material system	Error! Bookmark not defined.
I.2.1 (Si)GeSn: a direct band-gap group IV semiconductor	Error! Bookmark not defined.
I.2.2 Doping of (Si)GeSn	Error! Bookmark not defined.
I.2.3 Strain Relaxation in (Si)GeSn.....	Error! Bookmark not defined.
I.3 Thermal Treatment	Error! Bookmark not defined.
I.3.1 Thermal stability of (Si)GeSn.....	Error! Bookmark not defined.
I.3.2 Heat Transfer Mechanism.....	Error! Bookmark not defined.
I.3.3 Atomic diffusion	Error! Bookmark not defined.
I.3.4 Annealing Methods	Error! Bookmark not defined.
I.4 Laser-Matter Interaction	Error! Bookmark not defined.
I.4.1 Liquid phase recrystallization.....	Error! Bookmark not defined.
I.4.2 Segregation	Error! Bookmark not defined.
I.4.3 Dopant Activation	Error! Bookmark not defined.
I.5 Conclusion	Error! Bookmark not defined.

Chapter II : Experimental Techniques.....26

II.1 Reduced Pressure Chemical Vapour Deposition (RP-CVD) ..	Error! Bookmark not defined.
II.1.1 Chemical Vapour Deposition.....	Error! Bookmark not defined.
II.1.2 The Epi Centura 5200 cluster tool.....	Error! Bookmark not defined.
II.1.3 Growth Mechanisms	Error! Bookmark not defined.
II.2 Nanosecond Laser Annealing (NLA)	Error! Bookmark not defined.
II.2.1 The Nanosecond Laser Annealing tool.....	Error! Bookmark not defined.
II.2.2 In-situ Time Resolved Reflectivity Measurements.....	Error! Bookmark not defined.
II.3 X-Ray Diffraction	Error! Bookmark not defined.
II.3.1 Introduction	Error! Bookmark not defined.
II.3.2 Measurement Modes.....	Error! Bookmark not defined.
II.4 Surface Characterization Techniques	Error! Bookmark not defined.
II.4.1 Atomic Force Microscope (AFM).....	Error! Bookmark not defined.
II.4.2 Scanning Electron Microscopy (SEM).....	Error! Bookmark not defined.
II.5 Transmission Electron Microscope (TEM)	Error! Bookmark not defined.
II.6 Composition Characterization Techniques	Error! Bookmark not defined.
II.6.1 Secondary Ion Mass Spectrometry (SIMS).....	Error! Bookmark not defined.
II.6.2 Wavelength Dispersive X-ray Fluorescence (WDXRF).....	Error! Bookmark not defined.
II.6.3 Energy Dispersive X-ray Spectroscopy (EDX)	Error! Bookmark not defined.

II.6.4 X-ray Photoelectron Spectroscopy (XPS)	Error! Bookmark not defined.
II.7 Electrical Characterization Techniques.....	Error! Bookmark not defined.
II.7.1 Transmission Line Method (TLM).....	Error! Bookmark not defined.
II.7.2 Four Point Probe measurements (4PP).....	Error! Bookmark not defined.
II.7.3 Electrochemical Capacitance Voltage (ECV) profiling.....	Error! Bookmark not defined.
II.8 Conclusion	Error! Bookmark not defined.

Chapter III : In-Situ B and P Doping of GeSn54

III.1 Intoduction	Error! Bookmark not defined.
III.2 Confirmation of new growth parameters.....	Error! Bookmark not defined.
III.3 Layer thickness and Sn content determination	Error! Bookmark not defined.
III.4 Incorporation of Sn and dopants into the GeSn lattice	Error! Bookmark not defined.
III.5 Catalytic impact of dopants on growth rate	Error! Bookmark not defined.
III.6 Surface morphology and roughness.....	Error! Bookmark not defined.
III.7 Conclusions.....	Error! Bookmark not defined.

Chapter IV : In-Situ B and P Doping of SiGeSn56

IV.1 Introduction	73
IV.2 Impact of dopant precursors on crystalline quality and layer thickness.....	73
IV.3 Impact of dopant precursors on composition	74
IV.4 Catalytic impact of dopants on growth rate.....	76
IV.5 Surface morphology and roughness	79
IV.6 Incorporation and activation of dopants in the SiGeSn lattice.....	81
IV.7 Conclusions.....	83

Chapter V : Nanosecond Laser Annealing of In-Situ B Doped Ge.....88

V.1 Introduction	90
V.2 Impact of the substitutional B concentration on the melt threshold	90
V.3 Single pulse nanosecond laser annealing: Dopant activation	91
V.4 Single pulse nanosecond laser annealing: Surface morphology evolution.....	92
V.5 Single pulses nanosecond laser annealing on Ge:B: Crystalline structure	96
V.6 Multipulse nanosecond laser annealing: Surface morphology evolution	97
V.7 Multipulse nanosecond laser annealing: Crystalline structure evolution	99
V.8 Multipulse nanosecond laser annealing: Dopant activation	100
V.9 Conclusions.....	100

Chapter VI : Single Pulse Nanosecond Laser Annealing of GeSn.....104

VI.1 Introduction	106
VI.2 Wafer uniformity	106
VI.3 Impact of different Sn contents on Time Resolved Reflectivity Response	107
VI.4 Effect of Nanosecond Laser Annealing on Surface Morphology.....	110
VI.5 Effect of Nanosecond Laser Annealing on Crystalline Structure.....	115
VI.6 Effect of Nanosecond Laser Annealing on Sn redistribution	120
VI.7 Conclusions.....	122

Chapter VII : Multi Pulse Nanosecond Laser Annealing of GeSn 128

VII.1 Introduction130
VII.2 Multi Pulse NLA - Evolution of Time Resolved Reflectivity130
VII.3 Multi Pulse NLA - Evolution of surface structure at the melt threshold136
VII.4 Multi Pulse NLA - Evolution of surface morphology at the full melt threshold139
VII.5 Multi Pulse NLA - Evolution of crystalline structure at the melt threshold146
VII.6 Multi Pulse NLA – Sn redistribution147
VII.7 Conclusions.....150

Chapter VIII : Nanosecond Laser Annealing of Phosphorus Implanted GeSn..... 154

VIII.1 Introduction.....156
VIII.2 Time Resolved Reflectivity evolution.....156
VIII.3 P implanted GeSn NLA – Surface Morphology Evolution157
VIII.4 P implanted GeSn NLA – Crystalline Structure159
VIII.5 P implanted GeSn NLA – Tin and phosphorus redistribution162
VIII.6 P implanted GeSn NLA – Solid Phase Epitaxial Regrowth164
VIII.7 Conclusions.....167

Conclusions and Perspectives 170

Appendix A : Résumé Français Etendu..... 178

Appendix B : NLA of Pseudomorphic GeSn Layers : Impact of Sn Content 208

Appendix C : Multi Pulse Nanosecond Laser Annealing of GeSn.....220

Appendix D : GeSnOI Mid-Infrared Laser Technology

Appendix E : Room Temperature Optically Pumped GeSn Microdisk Lasers

Appendix F : Up to 300 K Lasing with GeSn-On-Insulator Microdisk Resonators

Appendix G : Valorization

Introduction

Introduction

Environmental sensing in the Mid Infra-Red (MIR) is a growing sector with a market value of 1.40 billion US dollars in 2020, which is expected to grow by 9.25% per year to reach 2.17 billion US dollars in 2026. Main driving forces of this growth are Industry 4.0, which requires environmental sensing for advanced automation, smart city initiatives, the Internet of Things (IoT), with sensing needed to adapt to environmental changes, and the global climate crises calling for emission reductions of greenhouse gases among others.

Short range optical data communications are mainly driven by silicon photonics in the Near Infra-Red (NIR), which ranges up to wavelengths of 1.6 μm . MIR, with wavelengths ranging from 2 up to 5 μm , is however interesting for many types of applications [1]–[3] such as environmental sensing, life sensing, medical diagnostics [4] and security. Indeed, it permits the detection of molecular vibrations in carbon monoxide (CO) or greenhouse gases like carbon dioxide (CO₂) and methane (CH₄). [5], [6]

CMOS-photonics compatibility (e.g. the avoidance of thermal and chemical incompatibilities with processes commonly used in CMOS device fabrication) and possibly an all-group-IV semiconductor solution would yield low cost, efficient MIR integrated photonic devices. So far, light sources on group IV templates have, indeed, been obtained by bonding III-V lasers on Si [7]–[10] or growing III-V stacks on Si [11], [12], with then some chemical incompatibility and thermal mismatch.

In order to benefit from an indirect-to-direct bandgap transition in a group IV semiconductor and therefore, have efficient light emission properties, tensile strained Ge (biaxial tensile strain above 1.7% [13], [14]) and/or Ge alloyed with at least 7.5% of Sn (unstrained) are used according to k.p. simulation [15], [16]. The first demonstration of optically pumped lasing in GeSn up to 90 K was reported in 2015. [17] Since then, remarkable progresses were made, with near unity wall plug efficiency lasing in 2019 [21], ultra-low threshold power density lasing in 2020 [20], and optically pumped room temperature lasing in 2022 [18], [19]. Electrically pumped lasing in GeSn at temperatures up to 100 K [22], [23] was the most recent step towards a fully group-IV integrated photonic platform.

The maximum lasing temperature requires, however, to be further increased. The lasing threshold of electrically pumped GeSn lasers and the dark current of GeSn photo-detectors should as well be reduced. To achieve this, carrier confinement should be high and contact resistance low. The former can be achieved by alloying GeSn with higher bandgap, lower lattice parameter Si, with then additional degrees of freedom in terms of strain and band gap engineering. [24] Meanwhile, the contact resistance can be reduced by introducing high amounts of active dopants in the lattice. (Si)GeSn is, however, impacted by Sn segregation and precipitation. [25] Ion implantation would require high thermal budgets to heal implantation damages and have dopants in electrically active lattice sites, which is not compatible with the poor thermal stability of (Si)GeSn.

Dopants can be incorporated during the epitaxial growth of stacks. When in-situ doping (Si)GeSn, dopant precursors are supplied and dissociate during the growth. This results in dopant incorporation directly into substitutional lattice sites, where they are electrically active.

No defects are created during the growth process that would, later, require annealing to remove them, at variance with ion implantation. Therefore, in-situ doping does not contribute to Sn segregation and precipitation.

Another alternative to dope (Si)GeSn would be to combine ion implantation with an ultrafast annealing process such as Nanosecond Laser Annealing (NLA), which utilizes laser pulses with Full Widths at Half Maximum of a few tens of nanoseconds and a short absorption depth. The energy of the applied laser pulses is absorbed by the material and light/matter interaction transform that energy into heat. Thanks to ultra-short pulse durations, ultra-shallow temperature gradients are formed, resulting in a precise control of the melt depth and the possibility to form defect-free monocrystalline layers. In addition, the short pulse duration yields a limited diffusion of dopants in the solid, at variance with a significant diffusion in the liquid phase, resulting in dopant concentrations well above the solid solubility and low contact resistances. [26]

In this PhD thesis, the feasibility of in-situ doping GeSn and SiGeSn with Boron and Phosphorous is thoroughly explored. Various characterization methods are used to understand how in-situ doping affects growth mechanisms, crystalline quality and dopant activation. The Nanosecond Laser Annealing of various types of GeSn layers is another topic covered in this manuscript. Our aim is to understand the interaction of laser annealing with the (Si)GeSn material system and see how it is impacted by the system's metastability.

In **Chapter I**, the specificities of (Si)GeSn are presented. The huge lattice parameter mismatch between Sn and Ge (14.7%) results, in (Si)GeSn layers grown on Ge Strain-relaxed Buffers, in large amounts of compressive strain that might relax if the layer thickness or the thermal budget used are too high, with then the formation of large amounts of large misfit dislocations. Sn atoms in (Si)GeSn layers are also prone to surface segregation/precipitation if the Sn concentration is significantly higher than the equilibrium Sn concentration in Ge (less than 1%), which is always the case in the metastable layers probed here. Nanosecond laser annealing requires only small thermal budgets thanks to ultra-short pulses, which might reduce such Sn redistribution. The light/matter interaction is introduced and mechanisms governing recrystallization are presented.

In **Chapter II**, the Reduced Pressure Chemical Vapor Deposition and the Ultraviolet Excimer Nanosecond Laser Annealing tools used are described. These tools allow the incorporation of high active dopant concentrations thanks to dopant incorporation during the epitaxial growth or the ultrafast liquefaction and re-solidification of the ion implanted thin layer. The introduction of comparatively small amounts of dopants had a definite impact on growth mechanisms and resulted in composition, crystalline quality and surface morphology changes. The dopant incorporation efficiency was assessed by measuring the ion concentration with Four Point Probe and Electrochemical Capacitance-Voltage measurements. Atomic dopant concentrations were also assessed by Secondary Ion Mass Spectrometry. Wavelength Dispersive X-Ray Fluorescence, Raman and Energy-Dispersive X-ray spectroscopy enabled us to track changes in the chemical composition of intrinsic and doped (Si)GeSn layers, while X-Ray Diffraction and Transmission Electron Microscopy gave us clues about the crystalline structure of such layers. Finally, the surface morphology was assessed thanks to Atomic Force and Secondary Electron Microscopy.

When diborane and phosphine are added to the gaseous mixture, growth mechanism changes happen. This is investigated in details in **Chapter III**. It is shown that the incorporation of boron and phosphorus impacts differently the incorporation of Ge and Sn, resulting in composition changes. Comprehensive studies of the various elemental growth rates unveiled reactions happening during growth. It was found that the ion dopant concentration was limited to a few 10^{19} cm^{-3} in boron and phosphorus doped GeSn compared to pure Ge.

Switching over to in-situ B and P doped SiGeSn with boron and phosphorous, as discussed in **Chapter IV**, enabled to reach much higher ion concentrations (at most, a few 10^{20} cm^{-3}) than in doped GeSn. Intrinsic SiGeSn was found in the literature to have a grainy surface. The introduction of dopants had a beneficial impact on the surface morphology, as outlined in this chapter. As for GeSn, the introduction of dopants resulted in SiGeSn growth mechanisms and chemical composition changes. Very high Si over Sn ratios were notably obtained in SiGeSn:B layers, which might be useful in devices.

The capability to enhance dopant activation by Nanosecond Laser Annealing is investigated in **Chapter V** for in-situ B doped Ge. Sheet resistance changes were evidenced, most likely due to the formation of clusters. The impact of clusters on strain was investigated and surface structures similar to those found for SiGe on Si were observed.

Laser annealing of intrinsic, pseudomorphic GeSn layers grown with 6, 10 and 14% of Sn on Ge Strain-Relaxed Buffers is discussed in **Chapter VI**. The melt threshold was identified and the formation of surface structures investigated. The surface structure's shape and size were compared to that on Ge and SiGe and trends on how chemical composition impacted the formation of surface structures revealed. When the entire GeSn layers melted without melting the Ge Strain Relaxed Buffers underneath, rather smooth, high crystalline layers with Sn contents well above the solid solubility were obtained.

Multipulse laser annealing was also conducted on the same GeSn layers on Ge SRBs. Data provided in **Chapter VII** showed that the roughness of the liquid/solid interface influenced the surface morphology. Energy Dispersive X-ray spectrometry gave us access to the composition of surface structures. There was also some oxygen incorporation in those annealed films although NLA was conducted in a nominally oxygen-free chamber.

The knowledge gained in the previous chapters on NLA was used to obtain high active dopant concentrations when laser annealing pseudomorphic, P implanted GeSn. Resulting data are provided in **Chapter VIII**. The chapter ends with a discussion about Solid Phase Epitaxial Regrowth, an alternative which might help obtaining high dopant concentrations in GeSn without Sn redistribution.

References

- [1] D. Stange *et al.*, “Optically Pumped GeSn Microdisk Lasers on Si,” *ACS Photonics*, vol. 3, no. 7, pp. 1279–1285, Jul. 2016, doi: 10.1021/acsp Photonics.6b00258.
- [2] S. Al-Kabi *et al.*, “An optically pumped 2.5 μ m GeSn laser on Si operating at 110 K,” *Appl. Phys. Lett.*, vol. 109, no. 17, p. 171105, Oct. 2016, doi: 10.1063/1.4966141.
- [3] V. Reboud *et al.*, “Optically pumped GeSn micro-disks with 16% Sn lasing at 3.1 μ m up to 180 K,” *Appl Phys Lett*, p. 5, 2017.
- [4] J. Juan-Colás, A. Parkin, K. E. Dunn, M. G. Scullion, T. F. Krauss, and S. D. Johnson, “The electrophotonic silicon biosensor,” *Nat. Commun.*, vol. 7, no. 1, p. 12769, Nov. 2016, doi: 10.1038/ncomms12769.
- [5] M. Sieger and B. Mizaikoff, “Toward On-Chip Mid-Infrared Sensors,” *Anal. Chem.*, vol. 88, no. 11, pp. 5562–5573, Jun. 2016, doi: 10.1021/acs.analchem.5b04143.
- [6] R. Wang *et al.*, “III–V-on-Silicon Photonic Integrated Circuits for Spectroscopic Sensing in the 2–4 μ m Wavelength Range,” *Sensors*, vol. 17, no. 8, p. 1788, Aug. 2017, doi: 10.3390/s17081788.
- [7] T. Spuesens, D. Van Thourhout, P. Rojo-Romeo, P. Regreny, and J.-M. Fedeli, “CW operation of III-V microdisk lasers on SOI fabricated in a 200 mm CMOS pilot line,” in *8th IEEE International Conference on Group IV Photonics*, London, United Kingdom, Sep. 2011, pp. 199–201. doi: 10.1109/GROUP4.2011.6053762.
- [8] G. Roelkens *et al.*, “III-V-on-Silicon Photonic Devices for Optical Communication and Sensing,” *Photonics*, vol. 2, no. 3, pp. 969–1004, Sep. 2015, doi: 10.3390/photonics2030969.
- [9] G. Crosnier *et al.*, “Hybrid indium phosphide-on-silicon nanolaser diode,” *Nat. Photonics*, vol. 11, no. 5, pp. 297–300, May 2017, doi: 10.1038/nphoton.2017.56.
- [10] H. Guan *et al.*, “Widely-tunable, narrow-linewidth III-V/silicon hybrid external-cavity laser for coherent communication,” *Opt. Express*, vol. 26, no. 7, p. 7920, Apr. 2018, doi: 10.1364/OE.26.007920.
- [11] R. Chen *et al.*, “Material characterization of high Sn-content, compressively-strained GeSn epitaxial films after rapid thermal processing,” *J. Cryst. Growth*, vol. 365, pp. 29–34, Feb. 2013, doi: 10.1016/j.jcrysgr.2012.12.014.
- [12] T. Stettner *et al.*, “Direct Coupling of Coherent Emission from Site-Selectively Grown III–V Nanowire Lasers into Proximal Silicon Waveguides,” *ACS Photonics*, vol. 4, no. 10, pp. 2537–2543, Oct. 2017, doi: 10.1021/acsp Photonics.7b00805.
- [13] P. Vogl, M. M. Rieger, J. A. Majewski, and G. Abstreiter, “How to convert group-IV semiconductors into light emitters,” *Phys. Scr.*, vol. T49B, pp. 476–482, Jan. 1993, doi: 10.1088/0031-8949/1993/T49B/017.
- [14] Y. M. Niquet, D. Rideau, C. Tavernier, H. Jaouen, and X. Blase, “Onsite matrix elements of the tight-binding Hamiltonian of a strained crystal: Application to silicon, germanium, and their alloys,” *Phys. Rev. B*, vol. 79, no. 24, p. 245201, Jun. 2009, doi: 10.1103/PhysRevB.79.245201.
- [15] M. Bertrand *et al.*, “Experimental Calibration of Sn-Related Varshni Parameters for High Sn Content GeSn Layers,” *Ann. Phys.*, vol. 531, no. 6, p. 1800396, Jun. 2019, doi: 10.1002/andp.201800396.
- [16] D. Sukhdeo, Y. Kim, S. Gupta, K. Saraswat, B. Dutt, and D. Nam, “Theoretical Modeling for the Interaction of Tin Alloying With N-Type Doping and Tensile Strain for GeSn Lasers,” *IEEE Electron Device Lett.*, vol. 37, no. 10, pp. 1307–1310, Oct. 2016, doi: 10.1109/LED.2016.2603162.

- [17] S. Wirths *et al.*, “Lasing in direct-bandgap GeSn alloy grown on Si,” *Nat. Photonics*, vol. 9, no. 2, pp. 88–92, Feb. 2015, doi: 10.1038/nphoton.2014.321.
- [18] J. Chrétien *et al.*, “Room temperature optically pumped GeSn microdisk lasers,” *Appl. Phys. Lett.*, vol. 120, no. 5, p. 051107, Jan. 2022, doi: 10.1063/5.0074478.
- [19] A. Bjelajac *et al.*, “Up to 300 K lasing with GeSn-On-Insulator microdisk resonators,” *Opt. Express*, vol. 30, no. 3, p. 3954, Jan. 2022, doi: 10.1364/OE.449895.
- [20] A. Elbaz *et al.*, “Ultra-low-threshold continuous-wave and pulsed lasing in tensile-strained GeSn alloys,” *Nat. Photonics*, vol. 14, no. 6, pp. 375–382, Jun. 2020, doi: 10.1038/s41566-020-0601-5.
- [21] F. T. Armand Pilon *et al.*, “Lasing in strained germanium microbridges,” *Nat. Commun.*, vol. 10, no. 1, p. 2724, Dec. 2019, doi: 10.1038/s41467-019-10655-6.
- [22] Y. Zhou *et al.*, “Electrically injected GeSn lasers on Si operating up to 100 K,” *Optica*, vol. 7, no. 8, p. 924, Aug. 2020, doi: 10.1364/OPTICA.395687.
- [23] Y. Zhou *et al.*, “Electrically injected GeSn lasers with peak wavelength up to 2.7 μm ,” *Photonics Res.*, vol. 10, no. 1, p. 222, Jan. 2022, doi: 10.1364/PRJ.443144.
- [24] P. Moontragoon, R. A. Soref, and Z. Ikonc, “The direct and indirect bandgaps of unstrained $\text{Si}_x\text{Ge}_{1-x-y}\text{Sn}_y$ and their photonic device applications,” *J. Appl. Phys.*, vol. 112, no. 7, p. 073106, Oct. 2012, doi: 10.1063/1.4757414.
- [25] S. Takeuchi, A. Sakai, O. Nakatsuka, M. Ogawa, and S. Zaima, “Tensile strained Ge layers on strain-relaxed $\text{Ge}_{1-x}\text{Sn}_x$ /virtual Ge substrates,” *Thin Solid Films*, vol. 517, no. 1, pp. 159–162, Nov. 2008, doi: 10.1016/j.tsf.2008.08.068.
- [26] E. Rosseel *et al.*, “Characterization of Epitaxial Si:C:P and Si:P Layers for Source/Drain Formation in Advanced Bulk FinFETs,” *ECS Trans.*, vol. 64, no. 6, pp. 977–987, Aug. 2014, doi: 10.1149/06406.0977ecst.

Chapter I : Challenges of Growing and Doping GeSn and SiGeSn Layers

Chapter I: Challenges of growing and doping GeSn and SiGeSn layers

Chapter I: Challenges of growing and doping GeSn and SiGeSn layers..... 1

I.1 Epitaxy	Error! Bookmark not defined.
I.1.1 The concept of Epitaxy	Error! Bookmark not defined.
I.1.2 The concept of plastic strain relaxation	Error! Bookmark not defined.
I.1.3 Critical thickness for plastic strain relaxation	Error! Bookmark not defined.
I.1.4 Lattice defects	Error! Bookmark not defined.
I.2 The (Si)GeSn material system	Error! Bookmark not defined.
I.2.1 (Si)GeSn: a direct band-gap group IV semiconductor	Error! Bookmark not defined.
I.2.2 Doping of (Si)GeSn	Error! Bookmark not defined.
I.2.3 Strain Relaxation in (Si)GeSn.....	Error! Bookmark not defined.
I.3 Thermal Treatmentment	Error! Bookmark not defined.
I.3.1 Thermal stability of (Si)GeSn.....	Error! Bookmark not defined.
I.3.2 Heat Transfer Mechanism.....	Error! Bookmark not defined.
I.3.3 Atomic diffusion	Error! Bookmark not defined.
I.3.4 Annealing Methods.....	Error! Bookmark not defined.
I.4 Laser-Matter Interaction	Error! Bookmark not defined.
I.4.1 Liquid phase recrystallization.....	Error! Bookmark not defined.
I.4.2 Segregation	Error! Bookmark not defined.
I.4.3 Dopant Activation	Error! Bookmark not defined.
I.5 Conclusion	Error! Bookmark not defined.

Chapter I: Challenges of growing and doping GeSn and SiGeSn layers

I.1 Epitaxy

I.1.1 The concept of Epitaxy

In 1951 Gordon Teal and Howard Christensen from the Bell Labs [1] pioneered epitaxy, which consists in the deposition of a *single-crystalline* layer on top a *single-crystalline* substrate. The word epitaxy comes from the two Greek words “Epi” meaning upon and “Taxis” meaning in an ordered manner. Epitaxy is performed upon a substrate (“Epi”) and the goal is to extend the atomic columns of the substrate into the grown layer (“Taxis”).

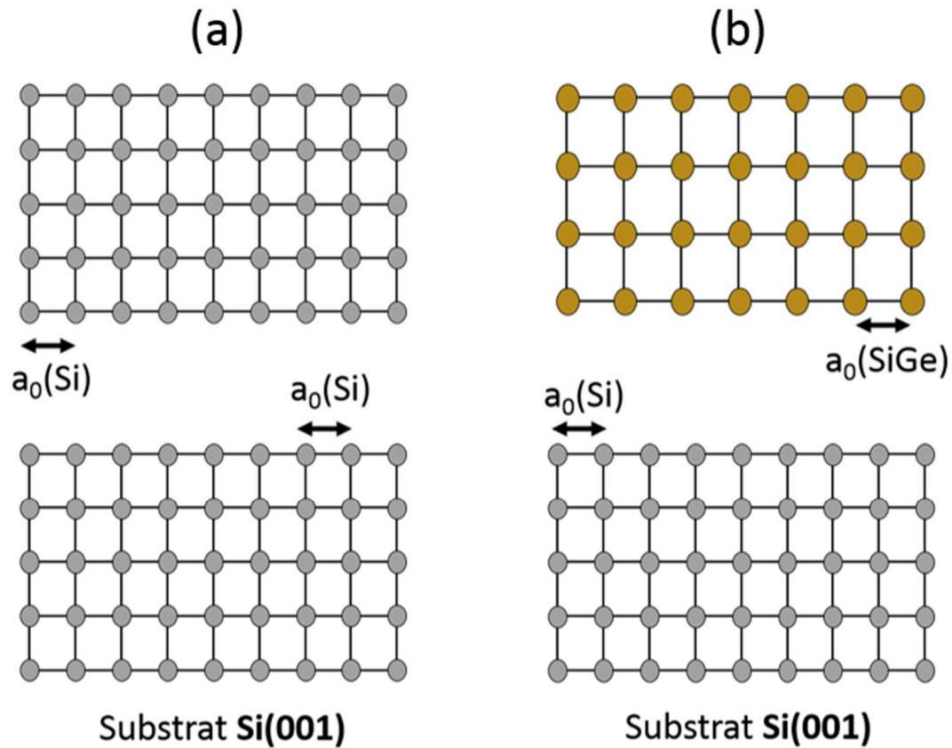


Figure I.1: Schematics of homoepitaxy (a) and heteroepitaxy (b). [2]

In general, epitaxy is split into two types: *homoepitaxy*, shown in **Figure I.1 (a)**, i.e. the growth of a layer of the same nature than the substrate, and *heteroepitaxy*, shown in **Figure I.1 (b)**, the growth of a layer of material, which is different from the substrate. When different materials are deposited on each other, they usually have different lattice parameters resulting in some mismatch.

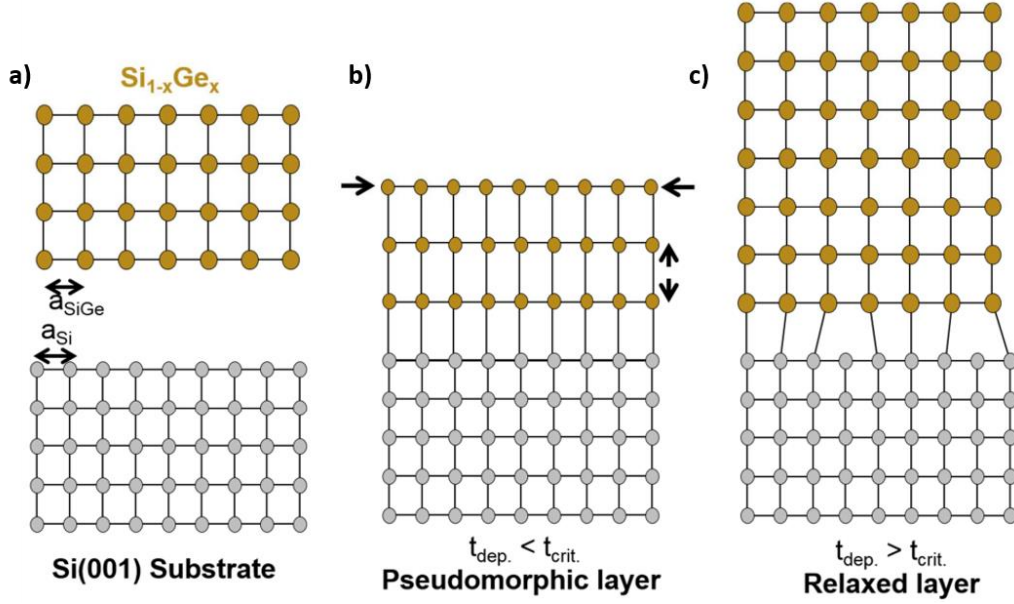
I.1.2 The concept of plastic strain relaxation


Figure I.2: Schematic of plastic strain relaxation. [2] (a) Si substrate (grey) and SiGe layer (yellow) with $a_{SiGe} > a_{Si}$. SiGe layer grown on top of a Si substrate with (b) a layer thickness below the critical thickness for plastic strain relaxation t_c , resulting in pseudomorphic growth. (c) Above the critical thickness, defects like misfit dislocations are nucleated to release the accumulated strain energy.

When the layer lattice parameter a_L is smaller than the substrate lattice parameter a_S ($a_L < a_S$) the layer's lattice is under tensile strain. Compressive strain occurs when a_L is larger than a_S ($a_L > a_S$), as shown in **Figure I.2 (a)**. The lattice mismatch results in an accumulation of elastic energy. For thin layers deposited on a substrate, the substrate's atomic columns directly extend into the epitaxial layer. The growth is then said to be *Pseudomorphic*. In this case, the in-plane lattice parameter of the layer a_L^{\parallel} and substrate a_S^{\parallel} are equal ($a_L^{\parallel} = a_S^{\parallel}$), as shown in **Figure I.2.(b)** The out-of-plane layer lattice parameter a_L^{\perp} is either compressively strained when the substrate's lattice parameter is smaller ($a_L^{\perp} > a_L > a_L^{\parallel} = a_S^{\parallel}$) or tensile strained when the substrate lattice parameter is larger ($a_L^{\perp} < a_L < a_L^{\parallel} = a_S^{\parallel}$), as shown in **Figure I.2.(c)** The out-of-plane lattice parameter is calculated according to **Equation (I.1.1)**, assuming tetragonal distortion.

$$a_L^{\perp} = a_L + \frac{2C_{12}}{C_{11}}(a_L - a_S) \quad (\text{I.1.1})$$

Where C_{ii} are the cubic elastic coefficients with $\frac{2C_{12}}{C_{11}}$ ratios of 0.77 [3], 0.74 [4] and 1.02 [5] for Si, Ge and α -Sn.

I.1.3 Critical thickness for plastic strain relaxation

Accumulated strain energy increases when the layer thickness increases. At a critical thickness h_c , it becomes energetically favorable to plastically relax some strain by forming misfit dislocations. The critical thickness h_c is calculated using models proposed by People and Bean [7], Matthews and Blakeslee [8], and Maree *et al.* [9]. The critical thickness h_c of GeSn grown on Ge for various Sn contents and models are shown in **Figure I.3**. Various defects are introduced when strain is plastically relaxed in materials consisting of elements of various size.

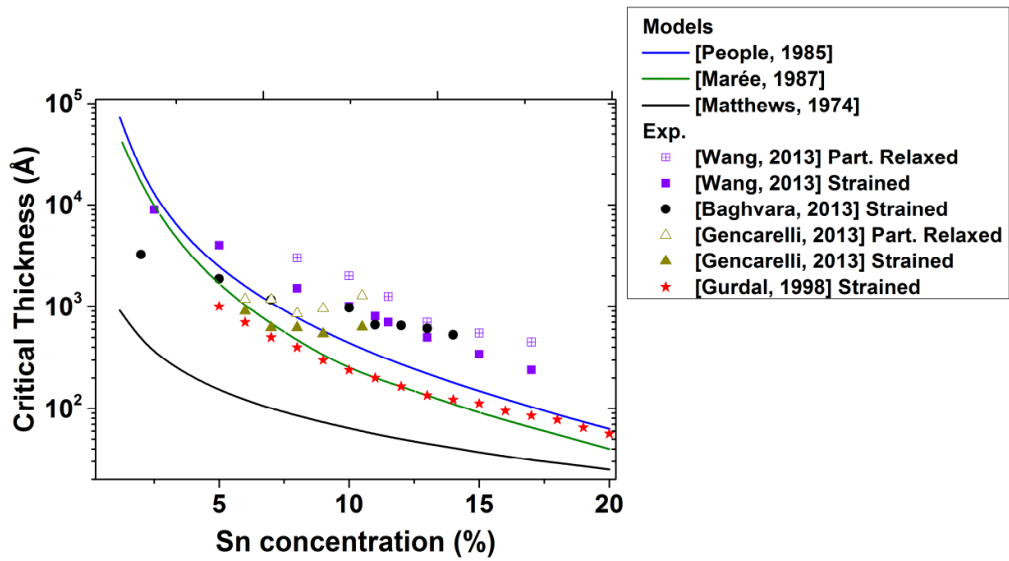


Figure I.3: Critical thickness h_c of GeSn on Ge for various Sn contents. Various experimental data from Wang *et al.* [10], Baghvara *et al.* [11], Gencarelli *et al.* [12] and Gurdal *et al.* [13] are compared to models.

I.1.4 Lattice defects

Various types of defects can be present in epitaxial layers. Point defects are 0D defects. Dislocations are 1D defects referred to as line defects. Anti-phase boundaries and stacking faults are typical 2D defects, while precipitates are 3D defects.

Point defects can be vacancies, e.g. vacant lattice sites, foreign or self-interstitials, a different or the same atom occupying a position not defined by the lattice, or a foreign substitutional atom, a different atom occupying a lattice site. Depending on the size and the position of the point defect, it locally applies a tensile or compressive strain to the lattice, which might result in the formation of half-loop dislocations.

Abrupt changes in the arrangement of the lattice occur when enough strain energy accumulates to form linear defects, called dislocations. The vector along the dislocation line is the line vector \vec{L} . A closed loop encircling a dislocation's core deviates from a close loop in an

ideal crystal. The difference is defined as the *Burger's vector* \vec{b} , which describes the direction and magnitude of the lattice distortion resulting from the presence of a dislocation. [14] Two types of dislocations can typically be found in crystals: (i) edge dislocations, where the Burger's vector \vec{b} is perpendicular to the line vector \vec{L} , and (ii) screw dislocations, where \vec{b} is parallel to the line vector \vec{L} . Dislocations usually nucleate as half-loops on the surface and are unstable. [15] The half-loops glide along $\{111\}$ planes in a conservative motion, that readjusts atom positions near the dislocation, towards the layer-substrate-interface to minimize strain. At the interface, half-loops split in three segments, part of which penetrate the substrate. Dislocation segments extending from the interface towards the surface are called *Threading Dislocations*.

The energy required to form a dislocation E_{disloc} is proportional to the square absolute value of the Burger's vector $E_{\text{disloc}} \propto |\vec{b}|^2$. A stable dislocation is formed when the associated energy is minimized. This is the case for 60° dislocations with a Burger's vector $\vec{b} = \frac{a}{2} \langle 101 \rangle$. When the strain energy becomes too high, 60° dislocations split in 30° and 90° Shockley partial dislocations. [9] In the case of even higher strain, the 30° and 90° Shockley partial dislocations are bound by a stacking fault [16]. When glide occurs, the 30° Shockley partial dislocations leads and the 90° Shockley partial dislocations follows. [17]

In GeSn divacancies formation is dominant because the low growth temperature does not favor the formation of cluster defects. [18] Clusters that form typically consist in five or more vacancies. [19] As the Sn content x_{Sn} increases, the amount of vacancy clusters reduces because there might be some attraction of vacancies by Sn. [20], [21]

I.2 The (Si)GeSn material system

I.2.1 (Si)GeSn: a direct band-gap group IV semiconductor

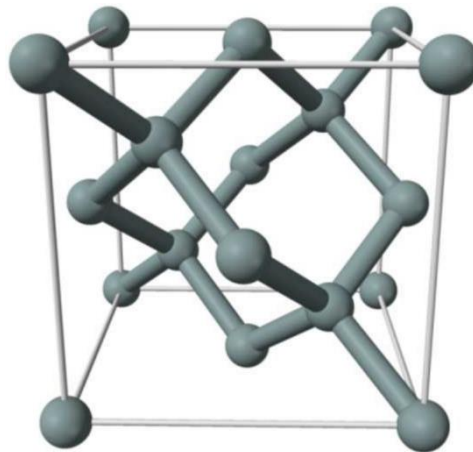


Figure I.4: Diamond crystalline structure. [2]

The material system (Si)GeSn consists of three group IV elements. All three of them crystallize in a diamond crystalline structure, which consists of two overlapping sphalerite

structures shifted by a quarter of the large diagonal, as shown in **Figure I.4**. Si and Ge are indirect bandgap semiconductor, with for Ge a minimum at the L symmetry point. α -Sn, on the other hand, is a semimetal with a negative band gap of -0.41 eV at the Γ symmetry point. In addition, the lattice parameter of α -Sn, 6.489 Å, is significantly larger than that of Ge (5.658 Å) and Si (5.431 Å). The lattice mismatch between Sn and Ge or Si is huge, 14.7% and 19.8%, respectively. [22] To accommodate the large lattice mismatch between GeSn, with a few percent of Sn, and Si substrates, 2.5 μm thick Ge Strain Relaxed Buffers (SRB) are typically grown on Si (0 0 1) substrates (with a miscut of $\pm 0.25^\circ$). [23] The growth of Ge SRBs is performed in a regular epitaxy chamber. Prior to growth, a H_2 bake for 2 minutes at 1100 °C is performed inside the epitaxy chamber to prepare the surface for epitaxy. The Ge SRB growth itself is based on a low growth temperature/high growth temperature approach. First, a ~ 120 nm thick Ge “seed” layer is grown at 400 °C, 100 Torr thanks to GeH_4 with a Growth Rate (GR) typically around 15 nm/min. The growth temperature is then ramped up from 400 °C to 750 °C and the growth pressure is reduced from 100 Torr down to 20 Torr. During the active ramping, growth continues as GeH_4 flows into the epitaxy chamber, resulting in the deposition of another 80 nm of Ge. 2.3 μm of Ge are then grown on top, at 750 °C, 20 Torr with a GR around 60 nm/min. To reduce the threading dislocation density (TDD) to values around 10^7 cm^{-2} , thermal cycling is performed in the epitaxy chamber just after growth. It consists of three cycles of annealing under H_2 , at 875 °C for 10 s and at 750 °C for 10 s. When doped (Si)GeSn layers were deposited, the top 1.2 μm of the Ge SRB were p-type (with an ions concentration of $9 \times 10^{18} \text{ cm}^{-3}$) or n-type doped (with an ions concentration of $4 \times 10^{18} \text{ cm}^{-3}$) to form pn or np junctions. Thermal cycling was then performed prior to the deposition of the doped layer to prevent dopant diffusion/loss.

Table 1 Melting temperature, band gap (high symmetry point) and lattice parameter of Si, Ge and Sn.

	Melting temperature [°C]	Band gap [eV]	Lattice parameter [Å]
Si	1414	1.11 (X)	5.431
Ge	938	0.66 (L)	5.658
α-Sn	232	-0.41 (Γ) [24]	6.489

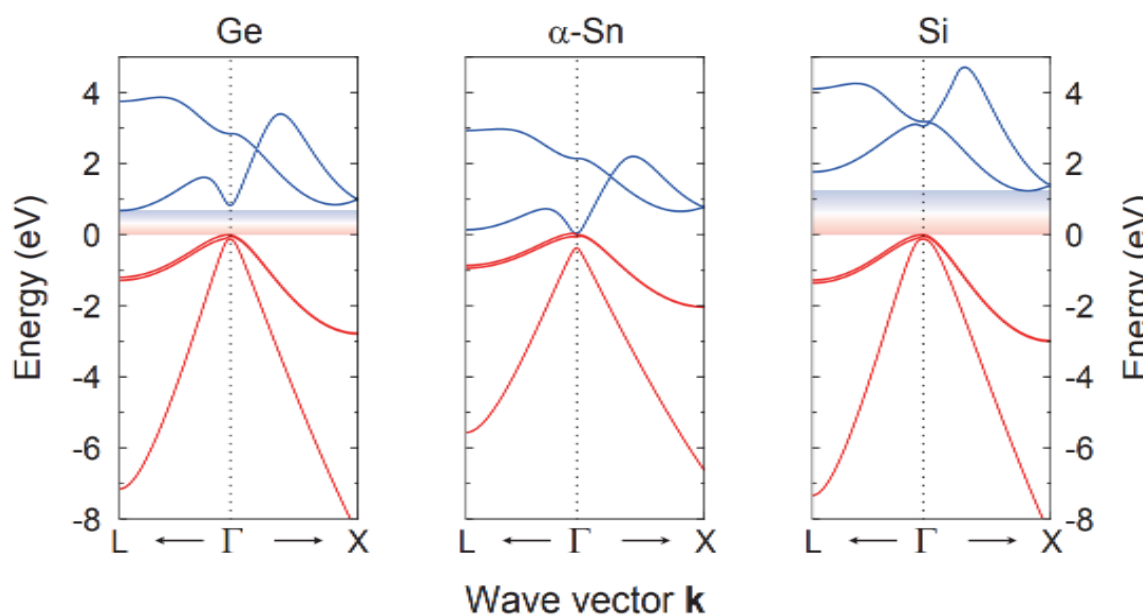


Figure I.5: Band structure of Ge, α -Sn and Si. [25]

By tensile straining and/or alloying Ge with Sn, an indirect-to-direct band gap transition occurs. As shown in **Figure I.5**, the band gap at the L point is only slightly smaller than the band gap at the Γ point with a band offset around -140 meV ($\Delta E = E_L - E_\Gamma$). [26] Tensile strain or alloying with Sn shifts down E_Γ faster than E_L . At a biaxial tensile strain above 1.7% along the (100) crystallographic plane [27], [28] or a Sn content of 7.5% (unstrained), a transition to a direct band gap group IV semiconductor occurs. In 2015, Wirths *et al.* [22] showed the first GeSn optically pumped lasing at 90 K. Since then, room temperature optically pumped lasing [29], [30], low power lasing [31], near unity wall plug efficiency [26] and electrically pumped lasing [32], [33] were shown in (Si)GeSn. By alloying GeSn with Si the band offset decreases and the semiconductor becomes more indirect. [34] This enables an independent tailoring of the band gap and lattice parameter. SiGeSn was used as barrier material in complex heterostructures. [32], [33], [35], [36]

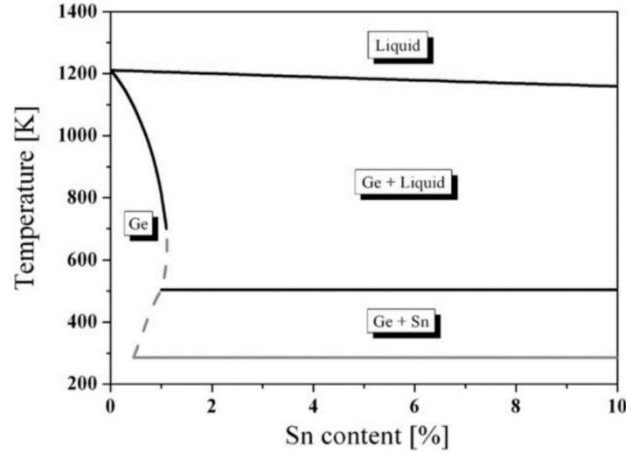


Figure I.6: GeSn phase diagram [37]

To achieve Sn contents required for an indirect-to-direct bandgap transitions, the solid solubility limit needs to be overcome by growing at out-of-equilibrium conditions. The solid solubility limit of Sn in Ge is indeed below 1% [37]. The GeSn phase diagram is shown in **Figure I.6**. Meanwhile, the solid solubility of Ge in Sn is below 0.6%. [38] The solid solubility limit of Sn in Si is even lower than in Ge, with a limit below 0.1%. [2] This might be the way to be one reason as to why the Sn content in SiGeSn ternary alloys decreases when the Si content increases.

During epitaxial growth, phase separation due to surface segregation occurs. [39]–[42] When growing GeSn, it is energetically favorable for Ge atoms to switch their position with subsurface Sn atoms. [43], [44] This process is governed by a characteristic segregation length Δs [37], [45], which is calculated according to **Equation (I.2.1)**.

$$\Delta s \propto \frac{1}{\sqrt{GR}} \exp\left(\frac{E_s}{k_B T}\right) \quad (\text{I.2.1})$$

Where E_s is the characteristic energy linked to surface diffusion, T the temperature, k_B the Boltzmann factor and GR the growth rate. **Equation (I.2.1)** outlines two parameters that do have an impact on Sn surface segregation. It is reduced for low growth temperatures T and high growth rates GR . Higher order hydrides like Ge_2H_6 and Si_2H_6 and an adequate Sn precursor like SnCl_4 should therefore be used. [46]

In addition to the growth challenges encountered with GeSn, SiGeSn faces some additional growth challenges. Khazaka *et al.* previously reported rough surfaces with a grainy $\langle 110 \rangle$ cross-hatch [47] and maximum Si contents of 17% [48], while the crystalline quality of the film was good.

The lattice parameter increases when alloying Ge with Sn. Gencarelli *et al.* [12] proposed a modified Vegard's law with a bowing parameter $b_{\text{GeSn}}=0.041$ to account for such an increase. **Equation (I.2.2)** quantifies it:

$$a_{\text{GeSn}}(x) = 5.65785 + 0.87215x - 0.041x^2 \quad (\text{I.2.2})$$

A modified Vegard's law was used to compute the SiGeSn lattice constant from WDXRF contents, shown in **Equation (I.2.3)**.

$$a_{\text{SiGeSn}} = a_{\text{Ge}}x_{\text{Ge}} + a_{\text{Si}}x_{\text{Si}} + a_{\text{Sn}}x_{\text{Sn}} - b_{\text{GeSn}}x_{\text{Sn}}(1 - x_{\text{Sn}}) - b_{\text{SiGe}}x_{\text{Si}}(1 - x_{\text{Si}}) \quad (\text{I.2.3})$$

With $x_{\text{Ge}} = 1 - x_{\text{Si}} - x_{\text{Sn}}$. It was opted to use the bowing parameters found by Gencarelli *et al.* for GeSn ($b_{\text{GeSn}} = -0.041$) [12] and by Dismukes *et al.* for SiGe ($b_{\text{SiGe}} = 0.028$). [49]

I.2.2 Doping of (Si)GeSn

A big step towards the co-integration of group IV photonics with CMOS circuits was recently made by research teams in the US, with electrically pumped lasing in GeSn up to 100 K. [32], [33] In CEA-LETI, we have so far used in-situ doped Ge in our pin Light Emitting Devices (LEDs) and Photo-Detectors (PDs). [50] Such Ge:P or Ge:B layers were grown at somewhat elevated temperatures (350°C) compared to the optically active, high Sn content GeSn layers (313°C). Growth at such an elevated temperature might have resulted in Sn segregation and precipitation, deteriorating the performance of the pin structures in our previous investigations. [51] To reproduce electrically pumped lasing [32], [33] and, beyond that, achieve electrically pumped lasing at high temperatures, it is necessary to investigate the low temperature doping of GeSn. Ion implantation together with mainstream anneals are not really suitable for doping GeSn. The high thermal budget of typical post-implantation annealing that is mandatory to heal defects and incorporate dopants into electrically active lattice sites would indeed result in Sn surface segregation and precipitation. [52] Another possibility is to in-situ dope GeSn during the epitaxial growth itself. This way, dopants are incorporated into the lattice as the layer grows, without any annealing requirement, afterwards. Sn segregation and precipitation are thus avoided, as shown in the literature for GeSn:B [46] and GeSn:P [53].

Doping relies on the incorporation of foreign elements into substitutional lattice sites. These foreign elements have one electron more (n-type) or less (p-type) than the matrix element, shown in **Figure I.7**, resulting in the supply of free electrons (n-type) or holes (p-type) for electrical conduction.

The in-situ doping of GeSn has not thoroughly been investigated. Vincent *et al.* [46] studied the in-situ boron doping of GeSn with Sn contents of around 7%. They found that the introduction of B₂H₆ in the gas mixture and, therefore, the incorporation of boron (B) into the GeSn lattice, resulted in a reduction of the Sn content, which was explained by a competition between Sn and B for incorporation into the lattice. Rutherford backscattering (RBS) and micro-Hall measurements were used to unambiguously determine the Sn and B contents in the studied layers. Margetis *et al.* [54] investigated this phenomenon in more details. They found from RBS and Secondary Ion Mass Spectrometry (SIMS) measurements that Sn content reductions were due to a GeSn:B growth rate increase, reducing the amount of time Sn atoms had to incorporate and, hence, the amount of Sn.

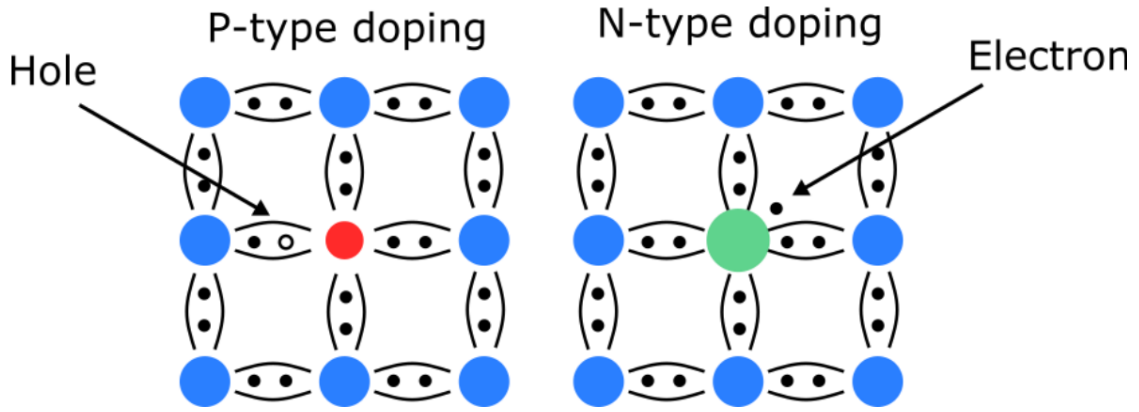


Figure I.7: Schematics of the incorporation of p- and n-type dopants. [55]

In-situ phosphorus doping of GeSn was studied even less. Margetis *et al.* [53] reported increased Sn contents for GeSn:P compared to intrinsic GeSn. It was attributed to the presence of P atoms on the surface, catalyzing the reduction of SnCl_x^* (where * denotes an open surface site) with the formation of PCl_x (g). Margetis *et al.* did not evidence any dependence of the Sn content or GeSn growth rate on the PH_3 flow supplied, however.

Fang *et al.* were, to our knowledge, the first to study SiGeSn in-situ doping in Chemical Vapor Deposition (CVD). [56] Ge_2H_6 , B_2H_6 and SnD_4 , the Sn precursor used before SnCl_4 , were then selected as precursors. More specific precursors like Si_3H_8 , SiGeH_6 , and some designer hydrides, e.g. $\text{P}(\text{GeH}_3)_3$ and $\text{P}(\text{SiH}_3)_3$, were also evaluated. Growth temperatures between 320 °C and 345 °C were used and Sn contents ranging from 2% to 8% probed. Growth rates were two to three times higher when dopant precursors were added to the gaseous mixture. SiGeSn layers lattice matched to the Ge buffer underneath were grown. B doping levels between $5 \times 10^{19} \text{ cm}^{-3}$ and $2 \times 10^{20} \text{ cm}^{-3}$ were obtained, together with P doping levels around 10^{19} cm^{-3} (from Hall measurements and contactless Infra-Red spectroscopic ellipsometry). Wirths *et al.* explored the growth of in-situ doped SiGeSn with Ge_2H_6 , Si_2H_6 , and SnCl_4 [57], i.e. the precursors used in the present studies. The growth temperature was 425 °C, then. B_2H_6 diluted at 100 ppm in H_2 and undiluted PH_3 were adopted as dopant sources. Wirths *et al.* used an AIXTRON TRICENT Reduced Pressure-CVD system with N_2 as a carrier gas, a showerhead for vertical gas injection, and a thermocouple in close proximity with the wafer to monitor the temperature. Such a hardware is quite different from ours, with a horizontal laminar flow of H_2 over the wafer surface supplying precursors to it and a dedicated pyrometer monitoring the wafer plate's backside temperature. This seemed to result in growth temperature differences between setups around 75 °C. More precisely, a growth temperature of 425 °C in the AIXTRON tool is comparable to 350 °C in our Epi Centura tool. Wirths *et al.* found reduced layer resistivities at high B_2H_6 partial pressures and increased layer resistivity at high PH_3 partial pressures due to the reduced layer quality because of the high, undiluted flow of PH_3 . The introduction of dopant precursors did not significantly change the growth rates in their case. They achieved electrically active carrier concentrations (determined by electrochemical capacitance voltage (ECV) measurements) of $2 \times 10^{19} \text{ cm}^{-3}$ (p-type) and $8 \times 10^{19} \text{ cm}^{-3}$ (n-type), with a good SiGeSn:B or SiGeSn:P crystalline quality.

I.2.3 Strain Relaxation in (Si)GeSn

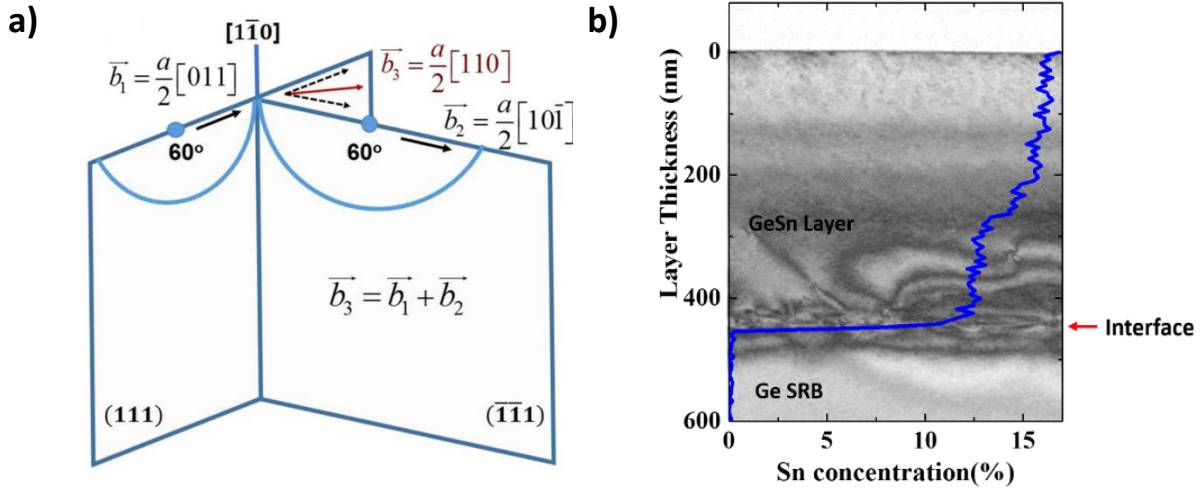


Figure I.8: Schematic of the formation of a Lomer dislocation \vec{b}_3 when two 60° dislocations on $(1\ 1\ 1)$ (\vec{b}_1) and $(\bar{1}\ \bar{1}\ \bar{1})$ (\vec{b}_2) planes intersect. [58] (b) Scanning transmission electron microscopy (STEM) images of nominally constant composition, thick GeSn and superimposed the corresponding Energy Dispersive X-ray (EDX) profile. [59]

Thick, relaxed and high Sn content (Si)GeSn layers are required to fabricate performant devices. Al-Kabi *et al.* and Aubin *et al.* [51], [59], [60] found, when growing relaxed, constant composition GeSn, a lower Sn content GeSn layer with a high misfit dislocation density close to the Ge SRB. Above the critical thickness [61], the Sn content spontaneously increased when the compressive strain started to plastically relax. Dou *et al.* and Assali *et al.* [58], [61] reported a spontaneous Sn content enhancement resulting in Hagen-Strunk misfit dislocation multiplication. [62], [63] The generation of additional 60° dislocations with complementary Burger's vector \vec{b} resulted in the interaction of 60° dislocations gliding along different $\{1\ 1\ 1\}$ planes. When meeting each other, they intersected thanks to a cross-slipping mechanism and formed sessile Lomer dislocations, as shown in **Figure I.9 (a)**. The formed Lomer dislocations were prohibited from gliding and the threading arms of the 60° mixed dislocations annihilated. This resulted in the formation of a self-assembled dislocation network, with almost defect free layers grown on top, as shown in **Figure I.8 (b)**. In addition, strain relaxation resulted in higher Sn incorporation. [58], [59], [61], [64], outlining that strain was the main force driving the incorporation of Sn.

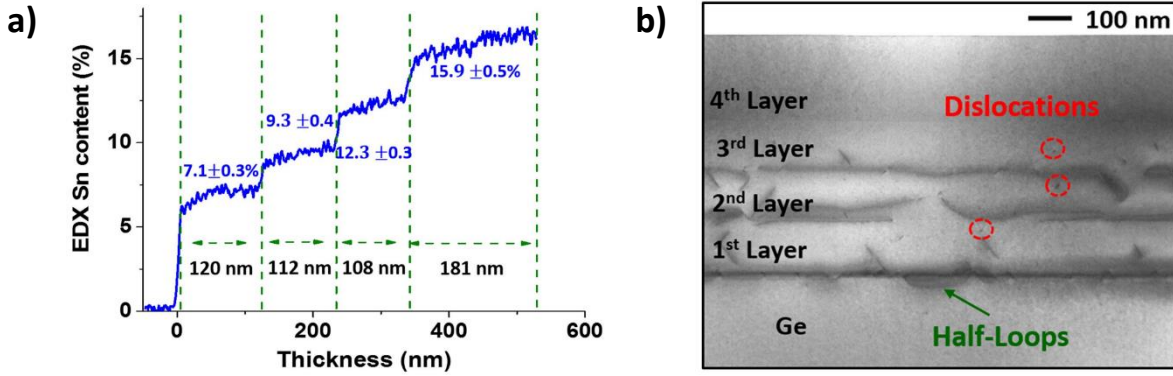


Figure I.9: (a) Scanning transmission electron microscopy (STEM) images of step-graded GeSn and (b) the corresponding Energy Dispersive X-ray (EDX) profile. [59]

Aubin *et al.* evidenced that some Sn surface segregation could happen when high Sn content GeSn layers spontaneously relaxed. [51], [59] To solve this Sn surface segregation phenomenon, Aubin *et al.* proposed to control the plastic strain relaxation process thanks to a step-wise increase of the Sn content, as shown in **Figure I.9 (a)**. [59] No Sn segregation occurred and the GeSn stack gradually relaxed. Moreover, half-loops misfit dislocations were mostly confined at the GeSn/Ge SRB interface. The first 300 nm of the layer stack were less defective with a step-graded structure and almost no defects were found in the top, high Sn content GeSn layer of **Figure I.9 (b)**, enabling the fabrication of high quality optical devices. [29], [65] Following studies, showed the importance of the bottom GeSn buffers for the relaxation of the top, high Sn content GeSn layer. [61]

I.3 Thermal Treatment

With the demonstration of room temperature optically pumped lasing in GeSn [29], [30], the focus of research teams is currently shifting to electrically pumped lasing. Zhou *et al.* showed electrically pumped lasing for the first time in 2020. [32], [33] GeSn lasing capabilities were then limited to temperatures below 100 K. To further improve performances, better electrical confinement and lower contact resistance are required. To reduce the contact resistance, it is mandatory to reach high active dopant concentrations. Due to the metastable nature of GeSn, ion implantation and conventional anneal strategies are not suitable, as they would lead to Sn segregation and precipitation. [66]–[68]

One way to overcome this challenge is in-situ doped GeSn, as discussed in the previous section. Nanosecond laser annealing (NLA) is another ultrafast, non-equilibrium option with an extremely short thermal budget thanks to its pulse duration that allows liquid phase recrystallization resulting in dopant activation at concentrations above the solid solubility limit. [69] Crystal recovery can be achieved by NLA and pulses faster than atom diffusion might enable to freeze atoms like Sn in place. Such a technique might be crucial if the use of ion implantation is mandatory to locally dope GeSn-based devices.

I.3.1 Thermal stability of (Si)GeSn

In addition to Sn segregation, precipitation is another challenge one faces when working with (Si)GeSn. Sn precipitation formation typically occurs during post-epitaxial thermal annealing. [37], [52], [70]

Von den Driesch *et al.* [68] investigated the impact of annealing on pseudomorphic (Si)GeSn. They found that, when the annealing temperature increased, Sn gradually segregated on the surface, through the formation of a GeSn layer with a Sn concentration of 1%, corresponding to the Sn solid solubility in Ge. Sn diffusion mainly occurred along dislocations [71], [72] and it seemed that Sn diffused more easily in SiGeSn than in GeSn. [68] Sn diffusion was likely driven by the chemical potential gradient, while Si diffusion was affected by its interaction with Sn. [73] No plastic strain relaxation after annealing was otherwise observed. It was instead elastic relaxation thanks to Sn and Si redistribution.

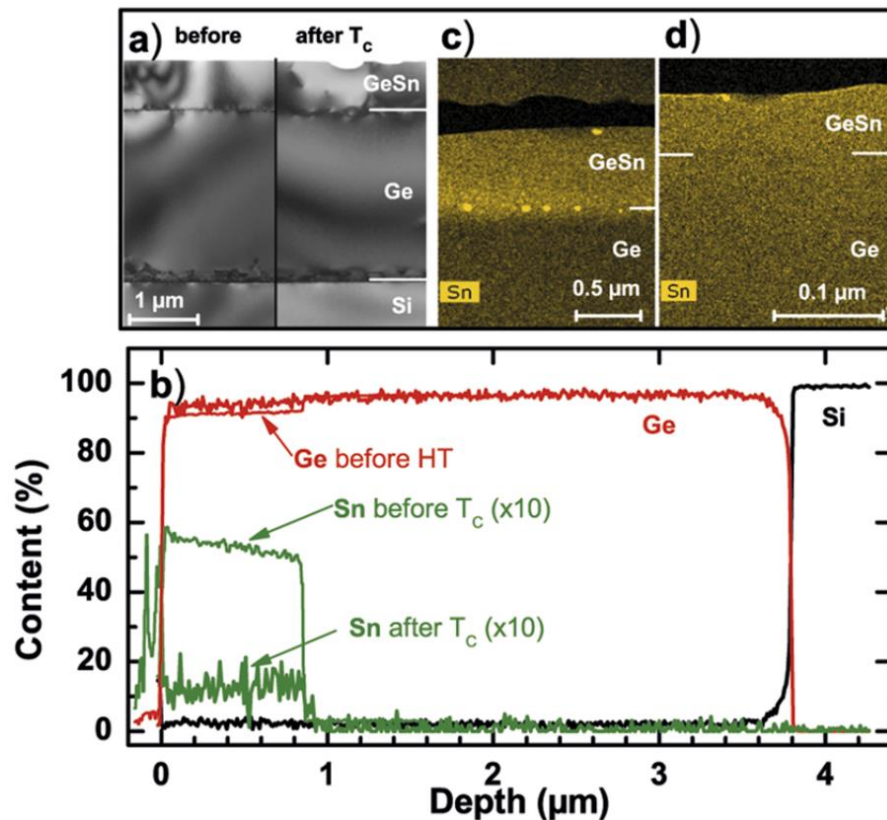


Figure I.10: (a) Cross sectional TEM micrographs of a 770 nm thick GeSn 5% layer before and after high-temperature treatment and (b) corresponding EDX line scan of partially relaxed GeSn 6%. EDX profile of (c) partially relaxed and (d) pseudomorphic GeSn 5% after annealing. [66]

Zaumseil *et al.* extended such findings by investigating the impact of annealing on pseudomorphic, fully compressively strained and on partially relaxed GeSn layers. [66] It was found that above a critical temperature, which decreased as the as-grown Sn content increased, pseudomorphic and partially relaxed GeSn layers started to segregate, forming GeSn 1% layers.

The excess Sn formed Sn clusters at the surface for pseudomorphic and partially relaxed GeSn layers and at the GeSn/Ge SRB interface for partially relaxed GeSn layers, shown in **Figure I.10**. Those Sn segregation clusters at the GeSn/Ge SRB interface likely formed around Misfit Dislocation cores because Sn accumulated around misfit dislocations due to loose covalent bonds, resulting in the formation of β -Sn defects. [74] This explained why there were no Sn clusters at the GeSn/Ge SRB interface for pseudomorphic GeSn layers. Annealing at intermediate temperature below the critical temperature (~ 350 °C) resulted in plastic strain relaxation thanks to the extension of Misfit Dislocation segments for partially relaxed GeSn 5% and 9%. For higher Sn contents, the critical temperature was too low to observe this behavior. No plastic relaxation was observed in pseudomorphic layers. Rather, a smooth, gradual segregation occurred as the annealing temperature was increased. The strain relaxation observed in partially relaxed GeSn gave rise to increased photoluminescence peak intensity.

GeSn's surface evolution during thermal annealing was investigated by Fournier-Lupien *et al.* [67] For $\text{Ge}_{0.84}\text{Si}_{0.04}\text{Sn}_{0.12}$, Sn rich surface clusters formed at an annealing temperature of 418 °C. Meanwhile, no such clusters appeared for $\text{Ge}_{0.88}\text{Sn}_{0.12}$. Phase separation for binary GeSn indeed occurred at 460 °C. For GeSn, surface structures were ordered along $\langle 1\ 1\ 0 \rangle$ directions, while they were randomly distributed for SiGeSn. When the annealing temperature increased, the surface structure density increased, too. At higher temperatures, Ostwald ripening, e.g. the merging of adjacent clusters, occurred. Tails behind the Sn rich surface clusters were also observed. They were due to the propagation of Sn-rich clusters on the surface. In addition, material was exchanged between neighboring islands by first forming Sn rich tails and then, by Sn diffusing away, completely wetting terraces.

I.3.2 Heat Transfer Mechanism

Heat is transferred by three mechanisms. (i) It either flows through a body or in-between bodies from a hotter region to a colder region by collision of atoms and electron movement when regions are in physical contact. This is called heat transfer by conduction. (ii) In a fluid or gas, heat is transferred by convection. The motion of molecules or atoms is driven by a thermal gradient if no accelerating electrical or pressure gradients are present. (iii) Without any physical contact, radiation transfers heat without any medium. [75] Thermal emission of excited photons arises thanks to the black body principle. When thermal radiation interacts with matter, it is (a) absorbed, (b) reflected or (c) transmitted. All three sum up to unity. Reflection occurs either in diffuse (omnidirectional) or specular (direction dependent) manner. Absorption is governed by Beer's law, shown in **Equation (I.3.1)**.

$$I(z) = I_0 e^{-\alpha z} \qquad \alpha = \frac{4\pi k}{\lambda} \qquad (\text{I.3.1})$$

Where α is the absorption coefficient, k the extinction coefficient and λ the wavelength.

I.3.3 Atomic diffusion

When a specimen is heated, the heat is transferred to the lattice and impurities move (with an activation energy E_a). This movement is called diffusion, which is driven by concentration gradients when no electrical or thermal forces act on atoms. The diffusion process is described

by the heat flux J defined by Fick's first law and the transport equation, shown in **Equations (I.3.2)** and **(I.3.3)**.

$$J(x, t) = -D(T) \frac{\partial C(x, t)}{\partial x} \quad (\text{I.3.2})$$

$$\frac{\partial C(x, t)}{\partial t} = \frac{\partial}{\partial x} \left(D(T) \frac{\partial C(x, t)}{\partial x} \right) \quad (\text{I.3.3})$$

Where $D(T)$ is the temperature dependent diffusivity and $C(x, t)$ the time and position dependent concentration. By combining Fick's first law and the transport equation, Fick's second law, shown in **Equation (I.3.4)**, is obtained, which yields a simple Arrhenius law for $D(T)$, shown in **Equation (I.3.5)**.

$$\frac{\partial C(x, t)}{\partial t} = D(T) \frac{\partial^2 C(x, t)}{\partial x^2} \quad (\text{I.3.4})$$

$$D(T) = D_0 e^{-\frac{E_a}{kT}} \quad (\text{I.3.5})$$

Where k is the Boltzman constant. The activation energy E_a varies with impurity species (described in **Section Lattice defects**). The distance at which diffusion can occur in a time t is described by the diffusion length L , shown in **Equation (I.3.6)**.

$$L(T, t) = 2\sqrt{D(T) \cdot t} \quad (\text{I.3.6})$$

I.3.4 Annealing Methods

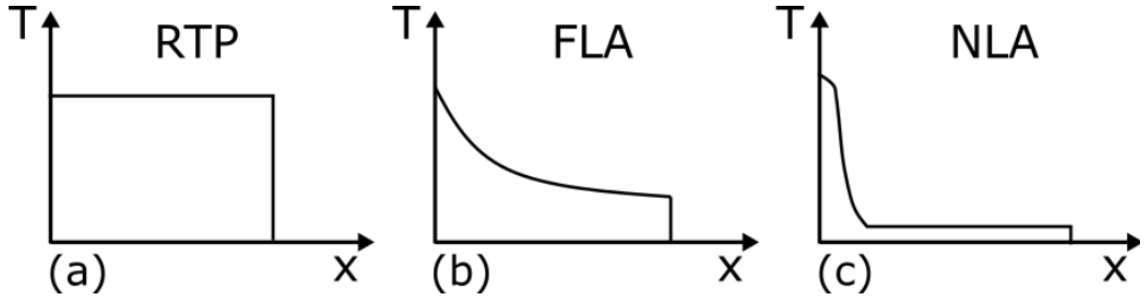


Figure I.11: Temperature profile inside a sample for Rapid Thermal Processing (RTP, (a)), Flash-Lamp Annealing (FLA, (b)) and Nanosecond Laser Annealing (NLA, (c)). [76]

In, general dopant activation is limited by the solid solubility, which increases with the sample temperature. As shown in **Equation (I.3.5)**, diffusion and therefore, the diffusion length given in **Equation (I.3.6)**, increase at high temperatures, too. For thermally metastable materials like GeSn, high temperatures will also result in some material degradation. The thermal budget (e.g. the amount of time spent at high temperatures) should therefore be limited, especially for (Si)GeSn, to obtain high material quality, as discussed in **Section Thermal stability of (Si)GeSn**. Similar dopant activation can, indeed, be achieved at higher temperatures and much shorter durations (1×10^{-1} s to 1×10^{-4} s), while preventing diffusion and material

degradation. [75] Various annealing methods can be used to reduce the thermal budget. Rapid Thermal Processing (RTP) typically occurs at 1100 °C for a few seconds, as shown in **Figure I.11 (a)**. [77] RTP results in heating of the entire specimen. [78] Flash lamp annealing (FLA) overcomes this limitation by creating a temperature gradient inside the sample irradiating it with Infra-Red (IR) lamps for a few milliseconds [79], shown in **Figure I.11 (b)**.

To obtain even steeper temperature gradients, annealing steps lasting a few tens to hundreds of nanoseconds are required. These are achieved by Nanosecond Laser Annealing (NLA), shown in **Figure I.11 (c)**. NLA uses laser pulses with a Full Width at Half Maximum (FWHM) around a few tens of nanoseconds. The resulting process is quasi adiabatic with surface temperatures close to the sample's melt temperature. Meanwhile, the temperature drops abruptly within the sample, which largely suppresses diffusion in the solid. Diffusion, therefore, only occurs in the liquid part of the sample, resulting in box like profiles.

I.1 Laser-Matter Interaction

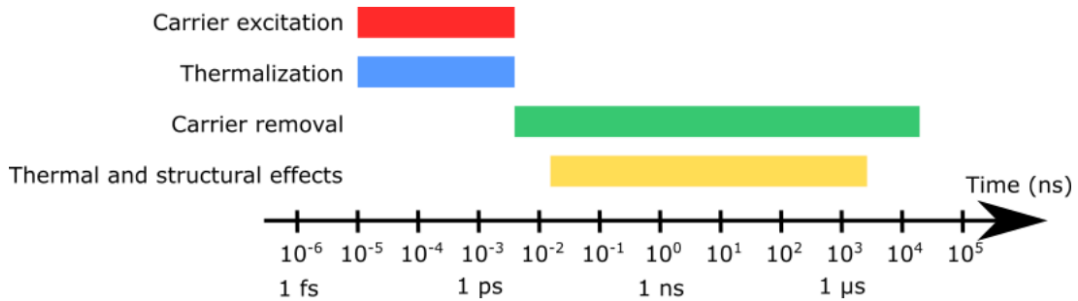


Figure I.12: Timescale of laser-matter-interaction. [80]

The various processes happening when irradiating a sample with a laser light were described by Sundaram *et al.* They are shown schematically in **Figure I.11**. [80]

(i) Carrier excitation takes place when a single photon is absorbed, resulting in the excitation of a valence electron to the conduction band and possibly the emission of a phonon in indirect bandgap materials. This process takes a few picoseconds

(ii) Carrier-carrier or carrier-phonon scattering results in the transfer of a small amount of energy to the lattice and, hence, thermalization in less than a picosecond. As the temperature increases, more scattering occurs.

(iii) During a few milliseconds, excess free carriers diffuse and recombine resulting in carrier loss.

(iv) If nucleation takes place due to cooling thanks to deeper regions, phase changes result in thermal and structural effects on the millisecond timescale.

Because (i) carrier excitation and (ii) thermalization are faster than the laser pulse (ps vs. ns) lattice heating can be assumed as being immediate. This assumption needs to fulfill three requirements. (i) Carrier diffusion must be smaller than light penetration and/or heat diffusion,

(ii) free carrier absorption is negligible and (iii) the carrier lifetime (recombination time) is shorter than the pulse width. This applies for NLA of Si. [81]

I.3.5 Liquid phase recrystallization

During solidification, the growing crystal adopts the adjacent crystal's structure. For instance, an adjacent crystal with a (0 0 1) surface will result in the growth of a highly crystalline sample, while a (1 1 1) surface might result in defective growth because of different solidification velocities. Short pulses (2-3 ns) result in strong undercooling, which results in high crystallization velocities. In such a case, amorphization takes place. [82]–[84]

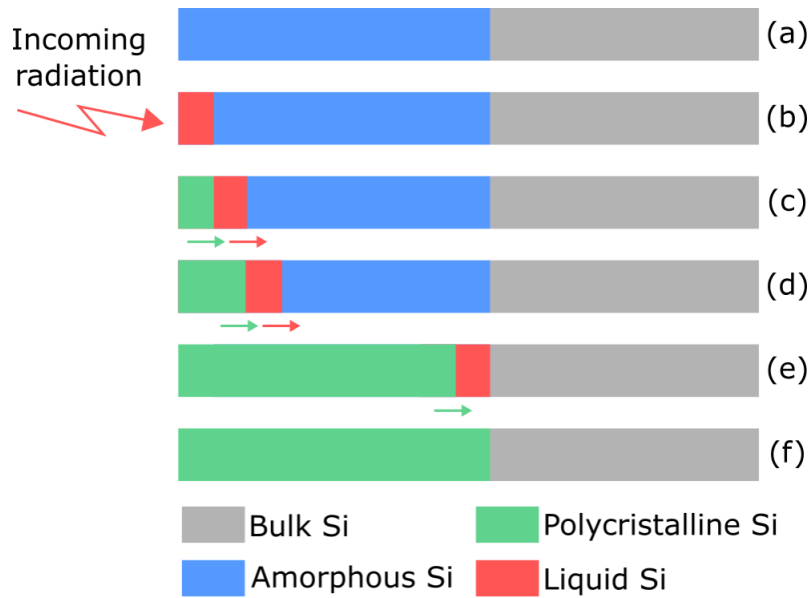


Figure I.13: Schematic outlining the various steps involved in the explosive recrystallization in amorphous materials. [85]

A unique feature of NLA is explosive recrystallization (**Figure I.13**). It occurs when an amorphous layer first crystallizes into a polycrystalline material. The melt temperature of the amorphous layer is significantly lower than that of the polycrystalline layer [86], resulting in undercooling and therefore, rapid solidification. The phase transition releases heat, which is absorbed by the underlying amorphous layer, which in turn melts. This process repeats with a high velocity of around $10 \frac{\text{m}}{\text{s}}$ until the entire amorphous layer is polycrystalline.

A second melt occurs when the melt temperatures of the (poly)crystalline material is reached.

I.3.6 Segregation

One main driving force during solidification is segregation. The equilibrium segregation coefficient k_e is given by the ratio of the liquid c_l and solid c_s impurity concentration determined from phase diagrams, shown in **Equation (I.1.1)**.

$$k_e = \frac{c_s}{c_l} \quad (\text{I.1.1})$$

Because NLA is an out-of-equilibrium process, **Equation (I.1.1)** is not enough to accurately describe segregation. The Continuous Growth Model and Aperiodic Stepwise Growth Model give a more accurate description of segregation in out-of-equilibrium conditions. [87]–[89]

I.3.7 Dopant Activation

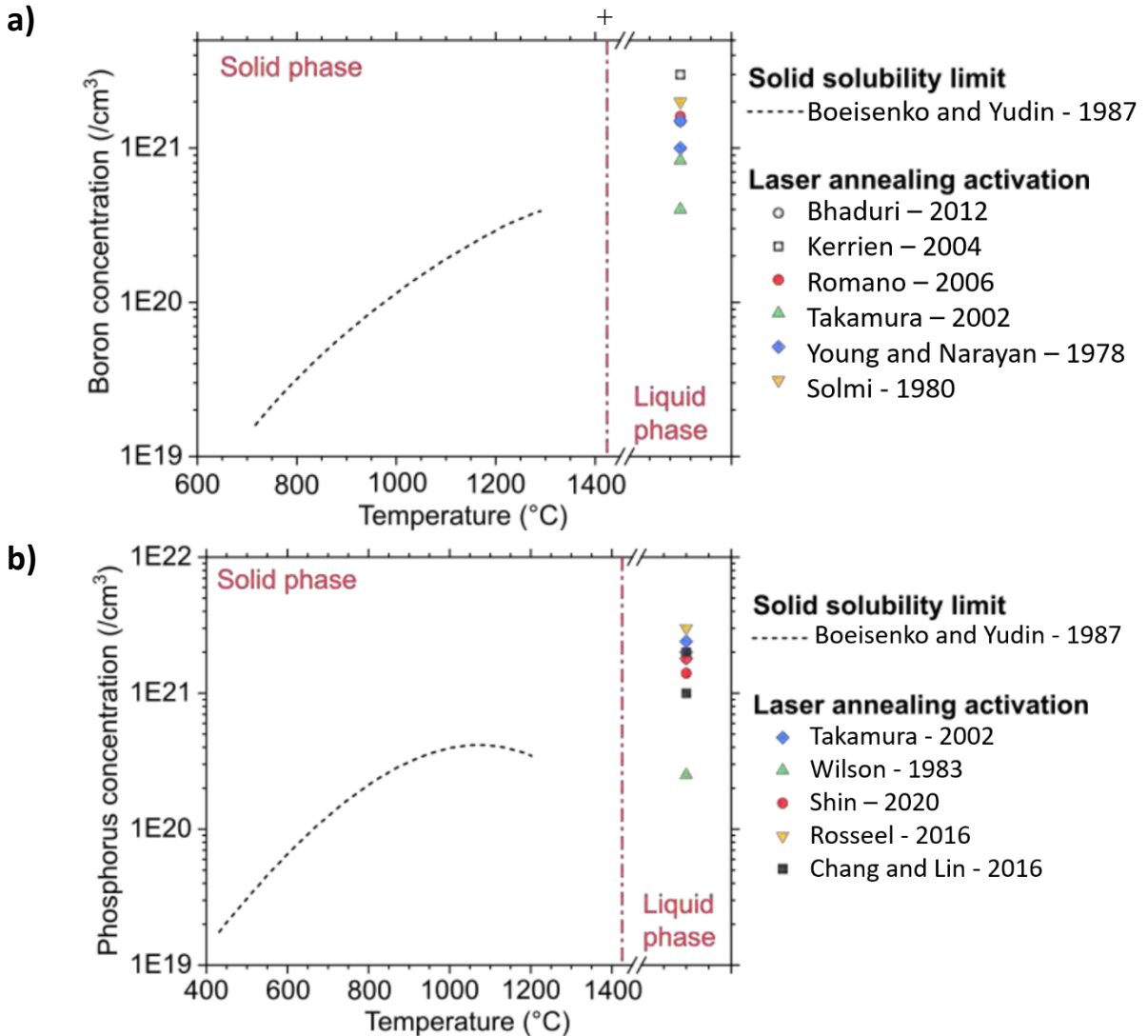


Figure I.14: Estimated solid solubility limit of (a) boron or (b) phosphorus [90], [91] and active (a) boron [92]–[97] or (b) phosphorus [98]–[102] concentrations in Si with nanosecond annealing. Dopants were supplied by ion implantation prior to annealing (full data points) or by gas source during annealing (empty data points, Gas Immersion Laser Doping (GILD)).

The bombardment of the sample during ion implantation causes significant lattice disorder resulting in amorphization. To reorganize the lattice, atom diffusion thanks to thermal annealing

is required. 200 ns NLA results in the melting of the top layer of the sample, the remainder staying solid. Diffusion is suppressed in the solid, while diffusion lengths of tens of nanometers are obtained in the liquid, resulting in box like shapes for melt depths up to 200 nm. [103]–[105] For thicker melt depths, the pulse duration is not long enough.

NLA enables to obtain higher dopant activation because only a thin layer is molten. During the solidification process, dopants are quenched into place resulting in active dopant levels above the solid solubility limit [69], [92]–[102], as shown in **Figure I.14**. Dopant concentration limits are metastable with NLA (dopants are frozen in place). Successive annealing might deactivate dopants.

NLA on B doped Si [106]–[112] and Ge [113]–[115] resulted in boron pile-ups at the maximum melt depth and depletion near the surface. The boron concentration at intermediate depth, meanwhile, remained stable. The pile-up was dependent on the time given for diffusion. A model was proposed that attributed such a profile, with the pile-up at maximum melt depth, to dopant absorption near the melt depth. In this model, two bonding states are present within the liquid phase, which result in two segregation coefficients causing the pile-up. [110], [116] Diffusivity is low for covalent bonds and high for metallic bonds. Boron pile-ups are electrically inactive in Ge [100] and active in Si. [117] In addition, B doping suffers from partial activation due to oxygen incorporation and B-B complex formation. [113]–[115]

I.4 Conclusion

The concept of epitaxy was introduced in the **first part of Chapter I**, with a focus on the interaction of substrate and layer. Strain will accumulate in the layer when lattice parameters are different. If the layer is thick enough, strain will plastically relax through the formation of point or extended defects.

We thus discuss the specifics of (Si)GeSn, with a focus on the indirect-to-direct bandgap transition happening with that class of group IV semiconductors. The challenges of growing and doping (Si)GeSn, which is prone to Sn segregation/precipitation, were outlined and a detailed summary of the strain relaxation mechanisms in (Si)GeSn given.

Annealing is required to suppress the lattice disorder introduced by ion implantation and activate dopants. The metastable nature of (Si)GeSn that limits the thermal budget usable during such anneals was described in the **second part of Chapter I**. The various heat transfer and diffusion processes happening when performing anneals were introduced. Various annealing methods were compared and the advantages of Nanosecond Laser Annealing were highlighted. Various features like explosive recrystallization, segregation and dopant activation involved in the solidification process (after melting with the laser light) were discussed. Nanosecond Laser Annealing should yield active dopant concentrations well above the solid solubility limit in (Si)GeSn, which would improve contact and therefore, device performances.

References

- [1] C. Howard and G. Teal, "Method of fabricating germanium bodies," 2,692,839
- [2] J. Aubin, "Low temperature epitaxy of Si, Ge, and Sn based alloys," Université Grenoble Alpes, Grenoble, 2017. [Online]. Available: <https://tel.archives-ouvertes.fr/tel-01759244>
- [3] R. Beeler, R. Roucka, A. V. G. Chizmeshya, J. Kouvetakis, and J. Menéndez, "Nonlinear structure-composition relationships in the Ge_{1-y}Sn_y/Si(100) ($y < 0.15$) system," *Phys. Rev. B*, vol. 84, no. 3, p. 035204, Jul. 2011, doi: 10.1103/PhysRevB.84.035204.
- [4] W. P. Mason, *Physical acoustics and the properties of solids*. 1958.
- [5] H. J. McSkimin, "Measurement of Elastic Constants at Low Temperatures by Means of Ultrasonic Waves—Data for Silicon and Germanium Single Crystals, and for Fused Silica," *J. Appl. Phys.*, vol. 24, no. 8, pp. 988–997, Aug. 1953, doi: 10.1063/1.1721449.
- [6] J. Kouvetakis, J. Menendez, and A. V. G. Chizmeshya, "TIN-BASED GROUP IV SEMICONDUCTORS: New Platforms for Opto- and Microelectronics on Silicon," *Annu. Rev. Mater. Res.*, vol. 36, no. 1, pp. 497–554, Aug. 2006, doi: 10.1146/annurev.matsci.36.090804.095159.
- [7] R. People and J. C. Bean, "Calculation of critical layer thickness versus lattice mismatch for Ge_xSi_{1-x}/Si strained-layer heterostructures," *Appl. Phys. Lett.*, vol. 47, no. 3, pp. 322–324, Aug. 1985, doi: 10.1063/1.96206.
- [8] J. W. Matthews and A. E. Blakeslee, "Defects in epitaxial multilayers," *J. Cryst. Growth*, vol. 27, pp. 118–125, Dec. 1974, doi: 10.1016/S0022-0248(74)80055-2.
- [9] P. M. J. Marée, J. C. Barbour, J. F. van der Veen, K. L. Kavanagh, C. W. T. Bulle-Lieuwma, and M. P. A. Vieggers, "Generation of misfit dislocations in semiconductors," *J. Appl. Phys.*, vol. 62, no. 11, pp. 4413–4420, Dec. 1987, doi: 10.1063/1.339078.
- [10] W. Wang, Q. Zhou, Y. Dong, E. S. Tok, and Y.-C. Yeo, "Critical thickness for strain relaxation of Ge_{1-x}Sn_x ($x \leq 0.17$) grown by molecular beam epitaxy on Ge(001)," *Appl. Phys. Lett.*, vol. 106, no. 23, p. 232106, Jun. 2015, doi: 10.1063/1.4922529.
- [11] N. Bhargava, M. Coppinger, J. Prakash Gupta, L. Wielunski, and J. Kolodzey, "Lattice constant and substitutional composition of GeSn alloys grown by molecular beam epitaxy," *Appl. Phys. Lett.*, vol. 103, no. 4, p. 041908, Jul. 2013, doi: 10.1063/1.4816660.
- [12] F. Gencarelli *et al.*, "Crystalline Properties and Strain Relaxation Mechanism of CVD Grown GeSn," *ECS J. Solid State Sci. Technol.*, vol. 2, no. 4, pp. P134–P137, 2013, doi: 10.1149/2.011304jss.
- [13] O. Gurdal *et al.*, "Low-temperature growth and critical epitaxial thicknesses of fully strained metastable Ge_{1-x}Sn_x ($x \leq 0.26$) alloys on Ge(001)2×1," *J. Appl. Phys.*, vol. 83, no. 1, pp. 162–170, Jan. 1998, doi: 10.1063/1.366690.
- [14] W. D. Callister and D. G. Rethwisch, *Fundamentals of materials science and engineering: an integrated approach*, 3rd ed. Hoboken, NJ: John Wiley & Sons, 2008.
- [15] R. Hull, J. C. Bean, L. Peticolas, Y. H. Xie, and Y. F. Hsieh, "Growth of Ge_xSi_{1-x}/Si Alloys on Si (100), (110) and (111) Surfaces," *MRS Proc.*, vol. 220, p. 153, 1991, doi: 10.1557/PROC-220-153.
- [16] J. Narayan, "Recent progress in thin film epitaxy across the misfit scale (2011 Acta Gold Medal Paper)," *Acta Mater.*, vol. 61, no. 8, pp. 2703–2724, May 2013, doi: 10.1016/j.actamat.2012.09.070.
- [17] P. J. Simmonds and M. Larry Lee, "Tensile-strained growth on low-index GaAs," *J. Appl. Phys.*, vol. 112, no. 5, p. 054313, Sep. 2012, doi: 10.1063/1.4749407.
- [18] S. Assali *et al.*, "Vacancy complexes in nonequilibrium germanium-tin semiconductors," *Appl. Phys. Lett.*, vol. 114, no. 25, p. 251907, Jun. 2019, doi: 10.1063/1.5108878.
- [19] M. Elsayed, N. Yu. Arutyunov, R. Krause-Rehberg, G. A. Oganessian, and V. V. Kozlovski, "Formation and annealing of vacancy-P complexes in proton-irradiated

- germanium,” *Acta Mater.*, vol. 100, pp. 1–10, Nov. 2015, doi: 10.1016/j.actamat.2015.08.039.
- [20] I. Riihimäki *et al.*, “Elastic interactions and diffusion of Sn in Si_{1-x}Ge_x systems,” *Appl. Phys. Lett.*, vol. 90, no. 18, p. 181922, Apr. 2007, doi: 10.1063/1.2736279.
- [21] S. Decoster, S. Cottenier, U. Wahl, J. G. Correia, and A. Vantomme, “Lattice location study of ion implanted Sn and Sn-related defects in Ge,” *Phys. Rev. B*, vol. 81, no. 15, p. 155204, Apr. 2010, doi: 10.1103/PhysRevB.81.155204.
- [22] S. Wirths, D. Buca, and S. Mantl, “Si–Ge–Sn alloys: From growth to applications,” *Prog. Cryst. Growth Charact. Mater.*, vol. 62, no. 1, pp. 1–39, Mar. 2016, doi: 10.1016/j.pcrysgrow.2015.11.001.
- [23] J. M. Hartmann and J. Aubin, “Assessment of the growth/etch back technique for the production of Ge strain-relaxed buffers on Si,” *J. Cryst. Growth*, vol. 488, pp. 43–50, Apr. 2018, doi: 10.1016/j.jcrysgro.2018.02.036.
- [24] S. Groves and W. Paul, “Band Structure of Gray Tin,” *Phys. Rev. Lett.*, vol. 11, no. 5, pp. 194–196, Sep. 1963, doi: 10.1103/PhysRevLett.11.194.
- [25] P. Moontragoon, Z. Ikonić, and P. Harrison, “Band structure calculations of Si–Ge–Sn alloys: achieving direct band gap materials,” *Semicond. Sci. Technol.*, vol. 22, no. 7, pp. 742–748, Jul. 2007, doi: 10.1088/0268-1242/22/7/012.
- [26] F. T. Armand Pilon *et al.*, “Lasing in strained germanium microbridges,” *Nat. Commun.*, vol. 10, no. 1, p. 2724, Dec. 2019, doi: 10.1038/s41467-019-10655-6.
- [27] P. Vogl, M. M. Rieger, J. A. Majewski, and G. Abstreiter, “How to convert group-IV semiconductors into light emitters,” *Phys. Scr.*, vol. T49B, pp. 476–482, Jan. 1993, doi: 10.1088/0031-8949/1993/T49B/017.
- [28] Y. M. Niquet, D. Rideau, C. Tavernier, H. Jaouen, and X. Blase, “Onsite matrix elements of the tight-binding Hamiltonian of a strained crystal: Application to silicon, germanium, and their alloys,” *Phys. Rev. B*, vol. 79, no. 24, p. 245201, Jun. 2009, doi: 10.1103/PhysRevB.79.245201.
- [29] J. Chrétien *et al.*, “Room temperature optically pumped GeSn microdisk lasers,” *Appl. Phys. Lett.*, vol. 120, no. 5, p. 051107, Jan. 2022, doi: 10.1063/5.0074478.
- [30] A. Bjelajac *et al.*, “Up to 300 K lasing with GeSn-On-Insulator microdisk resonators,” *Opt. Express*, vol. 30, no. 3, p. 3954, Jan. 2022, doi: 10.1364/OE.449895.
- [31] A. Elbaz *et al.*, “Ultra-low threshold cw and pulsed lasing in tensile strained GeSn alloys,” p. 12.
- [32] Y. Zhou *et al.*, “Electrically injected GeSn lasers on Si operating up to 100 K,” *Optica*, vol. 7, no. 8, p. 924, Aug. 2020, doi: 10.1364/OPTICA.395687.
- [33] Y. Zhou *et al.*, “Electrically injected GeSn lasers with peak wavelength up to 2.7 μm ,” *Photonics Res.*, vol. 10, no. 1, p. 222, Jan. 2022, doi: 10.1364/PRJ.443144.
- [34] P. Moontragoon, R. A. Soref, and Z. Ikonik, “The direct and indirect bandgaps of unstrained Si_xGe_{1-x-y}Sn_y and their photonic device applications,” *J. Appl. Phys.*, vol. 112, no. 7, p. 073106, Oct. 2012, doi: 10.1063/1.4757414.
- [35] G. Sun, R. A. Soref, and H. H. Cheng, “Design of a Si-based lattice-matched room-temperature GeSn/GeSiSn multi-quantum-well mid-infrared laser diode,” *Opt. Express*, vol. 18, no. 19, p. 19957, Sep. 2010, doi: 10.1364/OE.18.019957.
- [36] G.-E. Chang, S.-W. Chang, and S. L. Chuang, “Strain-Balanced Ge_zSn_{1-z}--Si_xGe_ySn_{1-x-y} Multiple-Quantum-Well Lasers,” *IEEE J. Quantum Electron.*, vol. 46, no. 12, pp. 1813–1820, Dec. 2010, doi: 10.1109/JQE.2010.2059000.
- [37] E. Kasper, J. Werner, M. Oehme, S. Escoubas, N. Burle, and J. Schulze, “Growth of silicon based germanium tin alloys,” *Thin Solid Films*, vol. 520, no. 8, pp. 3195–3200, Feb. 2012, doi: 10.1016/j.tsf.2011.10.114.

- [38] R. W. Olesinski and G. J. Abbaschian, "The Ge–Sn (Germanium–Tin) system," *Bull. Alloy Phase Diagr.*, vol. 5, no. 3, pp. 265–271, Jun. 1984, doi: 10.1007/BF02868550.
- [39] T. Tsukamoto, N. Hirose, A. Kasamatsu, T. Mimura, T. Matsui, and Y. Suda, "Investigation of Sn surface segregation during GeSn epitaxial growth by Auger electron spectroscopy and energy dispersive x-ray spectroscopy," *Appl. Phys. Lett.*, vol. 106, no. 5, p. 052103, Feb. 2015, doi: 10.1063/1.4907863.
- [40] N. Taoka *et al.*, "Non-uniform depth distributions of Sn concentration induced by Sn migration and desorption during GeSnSi layer formation," *Appl. Phys. Lett.*, vol. 106, no. 6, p. 061107, Feb. 2015, doi: 10.1063/1.4908121.
- [41] N. Taoka *et al.*, "Sn migration control at high temperature due to high deposition speed for forming high-quality GeSn layer," *Appl. Phys. Express*, vol. 9, no. 3, p. 031201, Mar. 2016, doi: 10.7567/APEX.9.031201.
- [42] H. Li, C. Chang, T. P. Chen, H. H. Cheng, Z. W. Shi, and H. Chen, "Characteristics of Sn segregation in Ge/GeSn heterostructures," *Appl. Phys. Lett.*, vol. 105, no. 15, p. 151906, Oct. 2014, doi: 10.1063/1.4898583.
- [43] K. A. Bratland, Y. L. Foo, P. Desjardins, and J. E. Greene, "Sn-enhanced epitaxial thickness during low-temperature Ge(001) molecular-beam epitaxy," *Appl. Phys. Lett.*, vol. 82, no. 24, pp. 4247–4249, Jun. 2003, doi: 10.1063/1.1578712.
- [44] W. Dondl, G. Lütjering, W. Wegscheider, J. Wilhelm, R. Schorer, and G. Abstreiter, "Sn and Sb segregation and their possible use as surfactant for short-period Si/Ge superlattices," *J. Cryst. Growth*, vol. 127, no. 1–4, pp. 440–442, Feb. 1993, doi: 10.1016/0022-0248(93)90656-H.
- [45] J. F. Nützel and G. Abstreiter, "Segregation and diffusion on semiconductor surfaces," *Phys. Rev. B*, vol. 53, no. 20, pp. 13551–13558, May 1996, doi: 10.1103/PhysRevB.53.13551.
- [46] B. Vincent *et al.*, "Undoped and *in-situ* B doped GeSn epitaxial growth on Ge by atmospheric pressure-chemical vapor deposition," *Appl. Phys. Lett.*, vol. 99, no. 15, p. 152103, Oct. 2011, doi: 10.1063/1.3645620.
- [47] R. Khazaka, J. Aubin, E. Nolot, and J.-M. Hartmann, "Investigation of the Growth of Si-Ge-Sn Pseudomorphic Layers on 200 mm Ge Virtual Substrates: Impact of Growth Pressure, HCl and Si₂H₆ Flows," *ECS Trans.*, vol. 86, no. 7, pp. 207–218, Jul. 2018, doi: 10.1149/08607.0207ecst.
- [48] R. Khazaka, E. Nolot, J. Aubin, and J.-M. Hartmann, "Growth and characterization of SiGeSn pseudomorphic layers on 200 mm Ge virtual substrates," *Semicond. Sci. Technol.*, vol. 33, no. 12, p. 124011, Dec. 2018, doi: 10.1088/1361-6641/aaea32.
- [49] J. P. Dismukes, L. Ekstrom, and R. J. Paff, "Lattice Parameter and Density in Germanium-Silicon Alloys¹," *J. Phys. Chem.*, vol. 68, no. 10, pp. 3021–3027, Oct. 1964, doi: 10.1021/j100792a049.
- [50] M. Bouschet *et al.*, "Photoelectron spectroscopy study of GeSn epitaxial layers for photonic applications," *Microelectron. Eng.*, vol. 253, p. 111663, Jan. 2022, doi: 10.1016/j.mee.2021.111663.
- [51] J. Aubin *et al.*, "Impact of thickness on the structural properties of high tin content GeSn layers," *J. Cryst. Growth*, vol. 473, pp. 20–27, Sep. 2017, doi: 10.1016/j.jcrysgro.2017.05.006.
- [52] S. Takeuchi, A. Sakai, O. Nakatsuka, M. Ogawa, and S. Zaima, "Tensile strained Ge layers on strain-relaxed Ge_{1-x}Sn_x/virtual Ge substrates," *Thin Solid Films*, vol. 517, no. 1, pp. 159–162, Nov. 2008, doi: 10.1016/j.tsf.2008.08.068.
- [53] J. Margetis *et al.*, "Growth and Characterization of Epitaxial Ge_{1-x}Sn_x Alloys and Heterostructures Using a Commercial CVD System," *ECS Trans.*, vol. 64, no. 6, pp. 711–720, Aug. 2014, doi: 10.1149/06406.0711ecst.

- [54] J. Margetis *et al.*, “Fundamentals of Ge_{1-x}Sn_x and Si_yGe_{1-x-y}Sn_x RPCVD epitaxy,” *Mater. Sci. Semicond. Process.*, vol. 70, pp. 38–43, Nov. 2017, doi: 10.1016/j.mssp.2016.12.024.
- [55] L. Dagault, “Investigation of Si_{1-x}Ge_x epilayers behavior upon Ultraviolet Nanosecond Laser Annealing,” Université Toulouse 3 Paul Sabatier, 2021. [Online]. Available: hal.laas.fr/tel-03356506
- [56] Y.-Y. Fang, J. Tolle, A. V. G. Chizmeshya, J. Kouvetakis, V. R. D’Costa, and J. Menendez, “Practical B and P doping via SixSnyGe_{1-x-y-z}Mz quaternaries lattice matched to Ge: Structural, electrical, and strain behavior,” *Appl. Phys. Lett.*, vol. 95, no. 8, p. 081113, Aug. 2009, doi: 10.1063/1.3204456.
- [57] S. Wirths *et al.*, “Growth Studies of Doped SiGeSn/Strained Ge(Sn) Heterostructures,” *ECS Trans.*, vol. 64, no. 6, pp. 689–696, Aug. 2014, doi: 10.1149/06406.0689ecst.
- [58] W. Dou *et al.*, “Investigation of GeSn Strain Relaxation and Spontaneous Composition Gradient for Low-Defect and High-Sn Alloy Growth,” *Sci. Rep.*, vol. 8, no. 1, p. 5640, Dec. 2018, doi: 10.1038/s41598-018-24018-6.
- [59] J. Aubin *et al.*, “Growth and structural properties of step-graded, high Sn content GeSn layers on Ge,” *Semicond. Sci. Technol.*, vol. 32, no. 9, p. 094006, Sep. 2017, doi: 10.1088/1361-6641/aa8084.
- [60] S. Al-Kabi *et al.*, “An optically pumped 2.5 μ m GeSn laser on Si operating at 110 K,” *Appl. Phys. Lett.*, vol. 109, no. 17, p. 171105, Oct. 2016, doi: 10.1063/1.4966141.
- [61] S. Assali, J. Nicolas, and O. Moutanabbir, “Enhanced Sn incorporation in GeSn epitaxial semiconductors via strain relaxation,” *J. Appl. Phys.*, vol. 125, no. 2, p. 025304, Jan. 2019, doi: 10.1063/1.5050273.
- [62] W. Hagen and H. Strunk, “A new type of source generating misfit dislocations,” *Appl. Phys.*, vol. 17, no. 1, pp. 85–87, Sep. 1978, doi: 10.1007/BF00885035.
- [63] V. I. Vdovin, “Misfit Dislocations in Epitaxial Heterostructures: Mechanisms of Generation and Multiplication,” *Phys. Status Solidi A*, vol. 171, no. 1, pp. 239–250, Jan. 1999, doi: 10.1002/(SICI)1521-396X(199901)171:1<239::AID-PSSA239>3.0.CO;2-M.
- [64] N. von den Driesch *et al.*, “Direct Bandgap Group IV Epitaxy on Si for Laser Applications,” *Chem. Mater.*, vol. 27, no. 13, pp. 4693–4702, Jul. 2015, doi: 10.1021/acs.chemmater.5b01327.
- [65] J. Chrétien *et al.*, “GeSn Lasers Covering a Wide Wavelength Range Thanks to Uniaxial Tensile Strain,” *ACS Photonics*, vol. 6, no. 10, pp. 2462–2469, Oct. 2019, doi: 10.1021/acsphotonics.9b00712.
- [66] P. Zaumseil *et al.*, “The thermal stability of epitaxial GeSn layers,” *APL Mater.*, vol. 6, no. 7, p. 076108, Jul. 2018, doi: 10.1063/1.5036728.
- [67] J.-H. Fournier-Lupien *et al.*, “In Situ Studies of Germanium-Tin and Silicon-Germanium-Tin Thermal Stability,” *ECS Trans.*, vol. 64, no. 6, pp. 903–911, Aug. 2014, doi: 10.1149/06406.0903ecst.
- [68] N. von den Driesch *et al.*, “Thermally activated diffusion and lattice relaxation in (Si)GeSn materials,” *Phys. Rev. Mater.*, vol. 4, no. 3, p. 033604, Mar. 2020, doi: 10.1103/PhysRevMaterials.4.033604.
- [69] E. Rosseel *et al.*, “Characterization of Epitaxial Si:C:P and Si:P Layers for Source/Drain Formation in Advanced Bulk FinFETs,” *ECS Trans.*, vol. 64, no. 6, pp. 977–987, Aug. 2014, doi: 10.1149/06406.0977ecst.
- [70] K. Kato *et al.*, “Robustness of Sn precipitation during thermal oxidation of Ge_{1-x}Sn_x on Ge(001),” *Jpn. J. Appl. Phys.*, vol. 53, no. 8S1, p. 08LD04, Aug. 2014, doi: 10.7567/JJAP.53.08LD04.

- [71] É. V. Dobrokhotov, "Diffusion in Dislocation Germanium and the Model of a Liquid Dislocation Core," *Phys. Solid State*, vol. 47, no. 12, p. 2257, 2005, doi: 10.1134/1.2142887.
- [72] J. Nicolas, S. Assali, S. Mukherjee, A. Lotnyk, and O. Moutanabbir, "Dislocation Pipe Diffusion and Solute Segregation during the Growth of Metastable GeSn," *Cryst. Growth Des.*, vol. 20, no. 5, pp. 3493–3498, May 2020, doi: 10.1021/acs.cgd.0c00270.
- [73] S. Mukherjee *et al.*, "Short-range atomic ordering in nonequilibrium silicon-germanium-tin semiconductors," *Phys. Rev. B*, vol. 95, no. 16, p. 161402, Apr. 2017, doi: 10.1103/PhysRevB.95.161402.
- [74] F. Gencarelli *et al.*, "Extended X-ray absorption fine structure investigation of Sn local environment in strained and relaxed epitaxial Ge_{1-x}Sn_x films," *J. Appl. Phys.*, vol. 117, no. 9, p. 095702, Mar. 2015, doi: 10.1063/1.4913856.
- [75] M. J. Hurley and E. R. Rosenbaum, "Performance-Based Design," in *SFPE Handbook of Fire Protection Engineering*, M. J. Hurley, D. Gottuk, J. R. Hall, K. Harada, E. Kuligowski, M. Puchovsky, J. Torero, J. M. Watts, and C. Wieczorek, Eds. New York, NY: Springer New York, 2016, pp. 1233–1261. doi: 10.1007/978-1-4939-2565-0_37.
- [76] L. Rebohle, S. Prucnal, and D. Reichel, *Flash Lamp Annealing: From Basics to Applications*, vol. 288. Cham: Springer International Publishing, 2019. doi: 10.1007/978-3-030-23299-3.
- [77] A. T. Fiory, "Rapid thermal processing for silicon nanoelectronics applications," *JOM*, vol. 57, no. 6, pp. 21–26, Jun. 2005, doi: 10.1007/s11837-005-0131-0.
- [78] P. Liang, P. Han, F. Yujie, and Y. Xing, "Annealing studies of boron implanted emitters for n-silicon solar cells," *Semicond. Sci. Technol.*, vol. 29, no. 3, p. 035011, Mar. 2014, doi: 10.1088/0268-1242/29/3/035011.
- [79] S. Prucnal, L. Rebohle, and W. Skorupa, "Doping by flash lamp annealing," *Mater. Sci. Semicond. Process.*, vol. 62, pp. 115–127, May 2017, doi: 10.1016/j.mssp.2016.10.040.
- [80] S. K. Sundaram and E. Mazur, "Inducing and probing non-thermal transitions in semiconductors using femtosecond laser pulses," *Nat. Mater.*, vol. 1, no. 4, pp. 217–224, Dec. 2002, doi: 10.1038/nmat767.
- [81] P. Baeri and E. Rimini, "Laser annealing of silicon," *Mater. Chem. Phys.*, vol. 46, no. 2–3, pp. 169–177, Nov. 1996, doi: 10.1016/S0254-0584(97)80010-7.
- [82] A. G. Cullis, H. C. Webber, N. G. Chew, J. M. Poate, and P. Baeri, "Transitions to Defective Crystal and the Amorphous State Induced in Elemental Si by Laser Quenching," *Phys. Rev. Lett.*, vol. 49, no. 3, pp. 219–222, Jul. 1982, doi: 10.1103/PhysRevLett.49.219.
- [83] A. G. Cullis, N. G. Chew, H. C. Webber, and D. J. Smith, "Orientation dependence of high speed silicon crystal growth from the melt," *J. Cryst. Growth*, vol. 68, no. 2, pp. 624–638, Sep. 1984, doi: 10.1016/0022-0248(84)90469-X.
- [84] J. A. Yater and M. O. Thompson, "Orientation dependence of laser amorphization of crystal Si," *Phys. Rev. Lett.*, vol. 63, no. 19, pp. 2088–2091, Nov. 1989, doi: 10.1103/PhysRevLett.63.2088.
- [85] S. F. Lombardo *et al.*, "Phase field model of the nanoscale evolution during the explosive crystallization phenomenon," *J. Appl. Phys.*, vol. 123, no. 10, p. 105105, Mar. 2018, doi: 10.1063/1.5008362.
- [86] M. O. Thompson *et al.*, "Melting Temperature and Explosive Crystallization of Amorphous Silicon during Pulsed Laser Irradiation," *Phys. Rev. Lett.*, vol. 52, no. 26, pp. 2360–2363, Jun. 1984, doi: 10.1103/PhysRevLett.52.2360.
- [87] R. Reitano, P. M. Smith, and M. J. Aziz, "Solute trapping of group III, IV, and V elements in silicon by an aperiodic stepwise growth mechanism," *J. Appl. Phys.*, vol. 76, no. 3, pp. 1518–1529, Aug. 1994, doi: 10.1063/1.357728.

- [88] D. P. Brunco, M. O. Thompson, D. E. Hoglund, M. J. Aziz, and H. -J. Gossmann, "Germanium partitioning in silicon during rapid solidification," *J. Appl. Phys.*, vol. 78, no. 3, pp. 1575–1582, Aug. 1995, doi: 10.1063/1.360251.
- [89] R. Reitanot, P. M. Smith, and M. J. Aziz, "Trends in Solute Segregation Behavior During Silicon Solidification," *MRS Proc.*, vol. 321, p. 479, 1993, doi: 10.1557/PROC-321-479.
- [90] F. A. Trumbore, "Solid Solubilities of Impurity Elements in Germanium and Silicon*," *Bell Syst. Tech. J.*, vol. 39, no. 1, pp. 205–233, Jan. 1960, doi: 10.1002/j.1538-7305.1960.tb03928.x.
- [91] V. E. Boisenko and S. G. Yudin, "Steady-state solubility of substitutional impurities in silicon," *Phys. Status Solidi A*, vol. 101, no. 1, pp. 123–127, May 1987, doi: 10.1002/pssa.2211010113.
- [92] A. Bhaduri, T. Kociniewski, F. Fossard, J. Boulmer, and D. Débarre, "Optical and electrical properties of laser doped Si:B in the alloy range," *Appl. Surf. Sci.*, vol. 258, no. 23, pp. 9228–9232, Sep. 2012, doi: 10.1016/j.apsusc.2011.10.077.
- [93] G. Kerrien *et al.*, "Gas immersion laser doping (GILD) for ultra-shallow junction formation," *Thin Solid Films*, vol. 453–454, pp. 106–109, Apr. 2004, doi: 10.1016/j.tsf.2003.11.151.
- [94] L. Romano *et al.*, "Mechanism of de-activation and clustering of B in Si at extremely high concentration," *Nucl. Instrum. Methods Phys. Res. Sect. B Beam Interact. Mater. At.*, vol. 253, no. 1–2, pp. 50–54, Dec. 2006, doi: 10.1016/j.nimb.2006.10.012.
- [95] Y. Takamura, S. H. Jain, P. B. Griffin, and J. D. Plummer, "Thermal stability of dopants in laser annealed silicon," *J. Appl. Phys.*, vol. 92, no. 1, pp. 230–234, Jul. 2002, doi: 10.1063/1.1481975.
- [96] R. T. Young and J. Narayan, "Laser annealing of diffusion-induced imperfections in silicon," *Appl. Phys. Lett.*, vol. 33, no. 1, pp. 14–16, Jul. 1978, doi: 10.1063/1.90164.
- [97] S. Solmi, E. Landi, and F. Baruffaldi, "High-concentration boron diffusion in silicon: Simulation of the precipitation phenomena," *J. Appl. Phys.*, vol. 68, no. 7, pp. 3250–3258, Oct. 1990, doi: 10.1063/1.346376.
- [98] Y. Takamura, P. B. Griffin, and J. D. Plummer, "Physical processes associated with the deactivation of dopants in laser annealed silicon," *J. Appl. Phys.*, vol. 92, no. 1, pp. 235–244, Jul. 2002, doi: 10.1063/1.1481974.
- [99] S. R. Wilson *et al.*, "Thermal stability of electrically active dopants in laser annealed silicon films," *J. Appl. Phys.*, vol. 54, no. 9, pp. 5004–5013, Sep. 1983, doi: 10.1063/1.332768.
- [100] H. Shin *et al.*, "Dopant Activation of In Situ Phosphorus-Doped Silicon Using Multi-Pulse Nanosecond Laser Annealing," *Phys. Status Solidi A*, vol. 217, no. 12, p. 1900988, 2020, doi: 10.1002/pssa.201900988.
- [101] E. Rosseel *et al.*, "(Invited) Selective Epitaxial Growth of High-P Si:P for Source/Drain Formation in Advanced Si nFETs," *ECS Trans.*, vol. 75, no. 8, p. 347, Aug. 2016, doi: 10.1149/07508.0347ecst.
- [102] R.-D. Chang and C.-H. Lin, "Activation and deactivation of phosphorus in silicon-on-insulator substrates," *Mater. Sci. Semicond. Process.*, vol. 42, pp. 219–222, Feb. 2016, doi: 10.1016/j.mssp.2015.09.008.
- [103] E. V. Monakhov *et al.*, "Excimer laser annealing of shallow As and B doped layers," *Mater. Sci. Eng. B*, vol. 114–115, pp. 352–357, Dec. 2004, doi: 10.1016/j.mseb.2004.07.062.
- [104] M. Shayesteh *et al.*, "Optimized Laser Thermal Annealing on Germanium for High Dopant Activation and Low Leakage Current," *IEEE Trans. Electron Devices*, vol. 61, no. 12, pp. 4047–4055, Dec. 2014, doi: 10.1109/TED.2014.2364957.

- [105] R. Milazzo *et al.*, “N-type doping of Ge by As implantation and excimer laser annealing,” *J. Appl. Phys.*, vol. 115, no. 5, p. 053501, Feb. 2014, doi: 10.1063/1.4863779.
- [106] M. Hackenberg *et al.*, “Modeling boron profiles in silicon after pulsed excimer laser annealing,” Valladolid, Spain, 2012, pp. 241–244. doi: 10.1063/1.4766533.
- [107] M. Hackenberg *et al.*, “Simulation of the boron build-up formation during melting laser thermal annealing,” *Phys. Status Solidi C*, vol. 11, no. 1, pp. 89–92, Jan. 2014, doi: 10.1002/pssc.201300156.
- [108] P. Lill, M. Dahlinger, and J. Köhler, “Boron Partitioning Coefficient above Unity in Laser Crystallized Silicon,” *Materials*, vol. 10, no. 2, p. 189, Feb. 2017, doi: 10.3390/ma10020189.
- [109] K. K. Ong, K. L. Pey, P. S. Lee, A. T. S. Wee, X. C. Wang, and Y. F. Chong, “Dopant distribution in the recrystallization transient at the maximum melt depth induced by laser annealing,” *Appl. Phys. Lett.*, vol. 89, no. 17, p. 172111, Oct. 2006, doi: 10.1063/1.2364834.
- [110] G. Fisicaro *et al.*, “Anomalous Impurity Segregation and Local Bonding Fluctuation in $\text{Ge}_{1-x}\text{Si}_x$,” *Phys. Rev. Lett.*, vol. 110, no. 11, p. 117801, Mar. 2013, doi: 10.1103/PhysRevLett.110.117801.
- [111] E. V. Monakhov *et al.*, “Boron distribution in silicon after excimer laser annealing with multiple pulses,” *Mater. Sci. Eng. B*, vol. 124–125, pp. 228–231, Dec. 2005, doi: 10.1016/j.mseb.2005.08.058.
- [112] E. V. Monakhov *et al.*, “Excimer Laser Annealing of Ion-Implanted Silicon: Dopant Activation, Diffusion and Defect Formation,” in *2007 15th International Conference on Advanced Thermal Processing of Semiconductors*, Cannizzaro, Catania, Italy, Oct. 2007, pp. 31–35. doi: 10.1109/RTP.2007.4383815.
- [113] G. Impellizzeri *et al.*, “Role of oxygen on the electrical activation of B in Ge by excimer laser annealing: Role of oxygen on the electrical activation of B in Ge,” *Phys. Status Solidi A*, vol. 211, no. 1, pp. 122–125, Jan. 2014, doi: 10.1002/pssa.201300308.
- [114] G. Impellizzeri *et al.*, “B-doping in Ge by excimer laser annealing,” *J. Appl. Phys.*, vol. 113, no. 11, p. 113505, Mar. 2013, doi: 10.1063/1.4795268.
- [115] R. Milazzo *et al.*, “Impurity and defect interactions during laser thermal annealing in Ge,” *J. Appl. Phys.*, vol. 119, no. 4, p. 045702, Jan. 2016, doi: 10.1063/1.4940737.
- [116] S. F. Lombardo *et al.*, “Laser annealing in Si and Ge: Anomalous physical aspects and modeling approaches,” *Mater. Sci. Semicond. Process.*, vol. 62, pp. 80–91, May 2017, doi: 10.1016/j.mssp.2016.10.047.
- [117] G. Fisicaro *et al.*, “Kinetic Monte Carlo simulations of boron activation in implanted Si under laser thermal annealing,” *Appl. Phys. Express*, vol. 7, no. 2, p. 021301, Feb. 2014, doi: 10.7567/APEX.7.021301.

Chapter II : Experimental Techniques

Chapter II: Experimental Techniques

Chapter II: Experimental Techniques	17
II.1 Reduced Pressure Chemical Vapour Deposition (RP-CVD) ..	Error! Bookmark not defined.
II.1.1 Chemical Vapour Deposition.....	Error! Bookmark not defined.
II.1.2 The Epi Centura 5200 cluster tool.....	Error! Bookmark not defined.
II.1.3 Growth Mechanisms	Error! Bookmark not defined.
II.2 Nanosecond Laser Annealing (NLA)	Error! Bookmark not defined.
II.2.1 The Nanosecond Laser Annealing tool.....	Error! Bookmark not defined.
II.2.2 In-situ Time Resolved Reflectivity Measurements.....	Error! Bookmark not defined.
II.3 X-Ray Diffraction	Error! Bookmark not defined.
II.3.1 Introduction	Error! Bookmark not defined.
II.3.2 Measurement Modes.....	Error! Bookmark not defined.
II.4 Surface Characterization Techniques	Error! Bookmark not defined.
II.4.1 Atomic Force Microscope (AFM).....	Error! Bookmark not defined.
II.4.2 Scanning Electron Microscopy (SEM).....	Error! Bookmark not defined.
II.5 Transmission Electron Microscope (TEM)	Error! Bookmark not defined.
II.6 Composition Characterization Techniques	Error! Bookmark not defined.
II.6.1 Secondary Ion Mass Spectrometry (SIMS).....	Error! Bookmark not defined.
II.6.2 Wavelength Dispersive X-ray Fluorescence (WDXRF).....	Error! Bookmark not defined.
II.6.3 Energy Dispersive X-ray Spectroscopy (EDX)	Error! Bookmark not defined.
II.6.4 X-ray Photoelectron Spectroscopy (XPS)	Error! Bookmark not defined.
II.7 Electrical Characterization Techniques.....	Error! Bookmark not defined.
II.7.1 Transmission Line Method (TLM).....	Error! Bookmark not defined.
II.7.2 Four Point Probe measurements (4PP).....	Error! Bookmark not defined.
II.7.3 Electrochemical Capacitance Voltage (ECV) profiling	Error! Bookmark not defined.
II.8 Conclusion	Error! Bookmark not defined.

Chapter II: Experimental Techniques

I.5 Reduced Pressure Chemical Vapour Deposition (RP-CVD)

I.5.1 Chemical Vapour Deposition

In 1982, an indirect-to-direct bandgap transition was theoretically predicted for (Si)GeSn by Goodman *et al.* [1] As discussed in the first chapter, the growth of GeSn faces some challenges like large lattice mismatch and low Sn solubility. It is solved thanks to growth in out-of-equilibrium conditions. The first epitaxy of monocrystalline GeSn was achieved in 1987 by Shah *et al.* using bias-sputtering deposition. [2] Molecular Beam Epitaxy (MBE) was in the nineties the growth method of choice for (Si)GeSn due to the lack of an adequate Sn precursor for Chemical Vapour Deposition (CVD). [3] Nevertheless, MBE necessitates ultra-high vacuum conditions and suffers from low GeSn growth temperatures (100°C-200°C), with the formation of point defects, then. Moreover, MBE is limited to rather thin layers. [4] The introduction of SnCl₄ [5] enabled CVD to overcome, over the last decade, these limitations, with the first optically pumped GeSn laser grown by RP-CVD in 2015. [6]

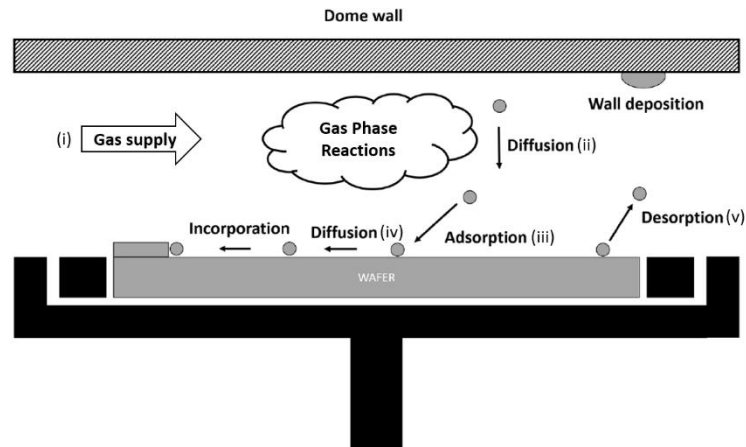


Figure II.1: Working principle of a Reduced Pressure Chemical Vapor Deposition (RP-CVD) cluster tool.

RP-CVD utilizes gaseous precursors for growth. During growth, these gaseous precursor are supplied as a laminar flow to the reactor chamber by forced convection using H₂ as carrier gas (i), shown in **Figure I.4**. Precursor, afterwards, diffuse towards the heated substrate surface (ii). During the diffusion process, precursor gas might start to decompose via gas phase reaction. When the precursor molecules reach the substrate surface, they get absorbed and chemically react, resulting in stepwise full decomposition of precursors (iii). Adatoms diffuse along the surface until they reach an energetically favorable location, like a step-edge, where they are incorporated (iv). Volatile by-products, e.g. leftovers after decomposition of precursors, and undecomposed molecules desorb and are evacuated from the reactor chamber (v).

To enable growth at ultra-low growth temperatures, necessary to grow metastable (Si)GeSn, a proper surface preparation is required. Meyerson *et al.* [7] and Sedgewick *et al.* [8] demonstrated in the 1980s that surface preparation of the substrate was crucial in order to obtain high crystalline quality films at low growth temperature. The fundamental reason is that epitaxy aims at duplicating the substrate's crystalline structure into the thin film. The presence of surface contaminants would significantly degrade the layer quality.

To prepare the surface, high temperatures are combined with high H₂ flows (typically a few tens of standard liter per minute (slm)). This can be performed inside the growth chamber, with the removal of native or chemical oxides if the temperature is high enough. This also results in a (2x1) reconstruction of the surface [9], [10], with a passivation of the Ge dangling bonds by hydrogen atoms and the formation of π -bonds. In the presented study, prior to the growth of the GeSn layer, a H₂ bake of the Ge Strain Relaxed Buffer was performed for 2 minutes at 800 °C.

Moreover, to facilitate the growth of high crystalline quality and limit contamination, ultra-pure carrier and precursor gases should be employed. Purification cartridges are used to achieve purification levels of 99.999999% of carrier gases N₂ and H₂. Loadlocks are used to isolate the growth chambers from the air and maintain them constantly under ultra-pure H₂ or N₂.

I.5.2 The Epi Centura 5200 cluster tool

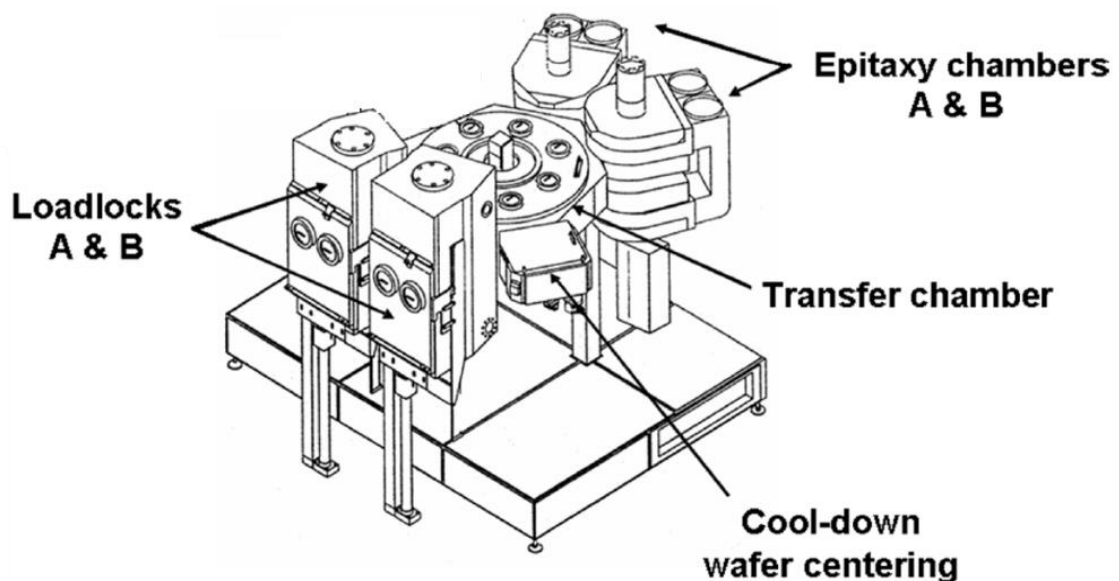


Figure II.2: Schematic of the Epi Centura 5200 Reduced Pressure Chemical Vapor Deposition (RP-CVD) cluster tool.

An Epi Centura 5200 Reduced Pressure Chemical Vapor Deposition (RP-CVD) cluster tool from Applied Materials was used for the growth of Ge Strain-Relaxed Buffers and (Si)GeSn-based stacks. It is shown in **Figure II.2**. It consists of three main components, the load locks, the growth chambers and the transfer chamber. The two load locks act as interfaces for

wafer loading and unloading. During loading and unloading, load locks are exposed to the air. After wafer loading, outer doors close and load-locks are cyclically pumped down to 20 Torr under N_2 . The rest of the tool is thus never exposed to the air. The transfer chamber with a robot under 15 slm of N_2 is used to move wafers from the load locks to the growth chambers and back. The growth occurs in two growth chambers, one of which is equipped for high temperature growth and the other for low temperature growth. A wafer centering and cool down chamber is used to deal with minor misalignments when transferring wafers and to cool down wafers after growth. Moreover, the cluster tool includes (i) an electronic control cabinet delivering power to the lamps, (ii) a pressure-lowering cabinet for the various gases used, (iii) pumping lines and four pumps controlling the pressure in the different chambers, (iv) a burning/scrubbing system for exhaust gases and (v) gas cabinets which contain the various gas bottles. When being used, epitaxy chambers are cooled by a water-cooling system embedded in the metal walls around them and an extensive ventilation system. A growth temperature range of 300 °C to 1100 °C is accessible and a pressure range between 10 and 600 Torr. A 1000 Torr Baraton gauge and a Butterfly valve at the chamber outlet regulate the pressure.

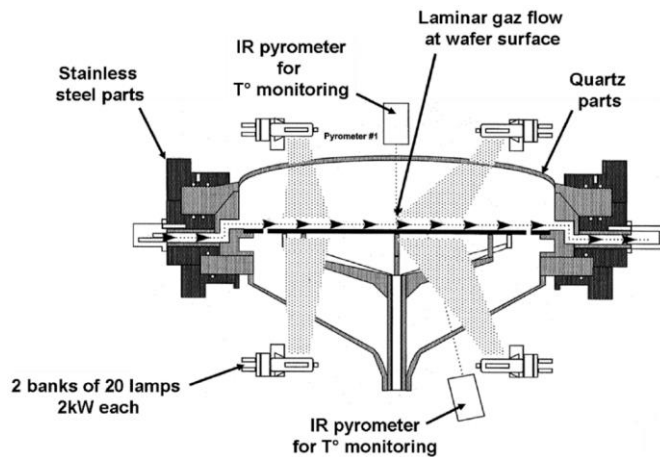


Figure II.3: Schematic of a chamber of the Epi Centura 5200 Reduced Pressure Chemical Vapor Deposition (RP-CVD) cluster tool.

To protect the growth from contamination, the growth chamber is pressurized and enclosed by a quartz dome, shown in **Figure II.3**. To maintain structural integrity under such high pressures, the quartz dome is solidarized to a circular metal support using clamp rings that crush Viton or Teflon gaskets, shown as darker areas around the chamber in **Figure II.3**. Process gases are supplied by laminar flow over the wafer surface. The laminar flow's uniformity can be adjusted by micrometer screws. Gas decomposition is obtained thanks to heating of the chambers, which is achieved by two banks of 20 lamps (2 kW each). One bank of lamps is mounted above and the other bank below the chamber. Eight lamps of each bank are oriented towards the wafer center and the remaining twelve towards the periphery to obtain a good temperature uniformity. Temperature control occurs thanks to two infra-red pyrometers. One looks directly at the wafer surface while the other one looks at the backside of the susceptor on which the wafer lies. The simplified working principle of the pyrometers is the black body principle. According to the black body principle the radiated power P is collected and converted to a temperature T using a power law, shown in **Equation (I.5.1)**.

$$P = \sigma T^4 \quad (\text{I.5.1})$$

With $\sigma \sim 0.65$ for the Si wafer and ~ 0.80 for the graphite susceptor coated with SiC, on which the wafer rests. The lower pyrometer is used to control the temperature during growth because it is not sensitive to surface emissivity changes during growth. The SiC covered susceptor is used because of thermal conduction and heat retention. It is typically rotated at a speed of 30 rotations per minute to obtain a better film uniformity.

To gain access to the low growth temperatures mandatory to grow high quality, high Sn content (Si)GeSn, one chamber of the cluster tool was retroactively modified. It is now equipped with low temperature pyrometers with a linear temperature response between 250 °C and 500 °C, while the other chamber is fit for high temperature growth. Exhaust Sn is trapped by a special Sn trapping cartridge reducing environmental Sn pollution.

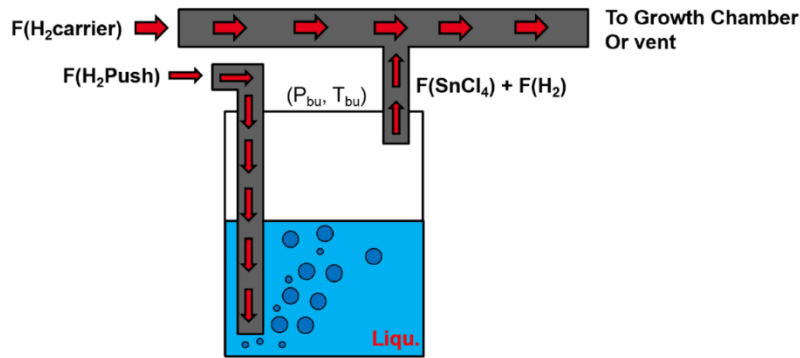


Figure II.4: Working principle of a bubbler.

SnD_4 was one of the first Sn precursors used to grow (Si)GeSn in a CVD reactor. [11] It is highly unstable, however. To overcome this drawback, Vincent *et al.* proposed in 2010 to use SnCl_4 , which is stable and commonly used for glass coatings. [5] To supply SnCl_4 to the growth chamber, a bubbler, shown in **Figure II.4**, is necessary because SnCl_4 is liquidus at room temperature. The working principle of a bubbler is to supply a larger flow of H_2 carrier gas to create bubbles in a SnCl_4 bath. When bubbles rise to the surface of liquid SnCl_4 , some SnCl_4 molecules are trapped inside them. By calculating the vapor pressure of SnCl_4 inside the bubbler at temperature T , shown in **Equation (I.5.3)**, the SnCl_4 flow can be estimated thanks to **Equation (I.5.2)**. [12]

$$F(\text{SnCl}_4) = F(\text{H}_2) \left(\frac{P(\text{SnCl}_4)}{P(\text{Bubbler}) - P(\text{SnCl}_4)} \right) \quad (\text{I.5.2})$$

Where
$$P(\text{SnCl}_4)[\text{bar}] = 10^{A - \frac{B}{T+C}} \quad (\text{I.5.3})$$

Constants are $A = 4.18162$, $B = 184.537 \text{ K}$ and $C = -54.377 \text{ K}$. [13] $P(\text{Bubbler})$ is given by the bubbler pressure. To enable growth at ultra-low temperatures, higher order hydrides Ge_2H_6 and Si_2H_6 are used as Ge and Si precursors, respectively. They have lower

binding energies, dissociate more easily and, therefore, yield higher growth rates at low growth temperatures than for instance GeH_4 and SiH_4 .

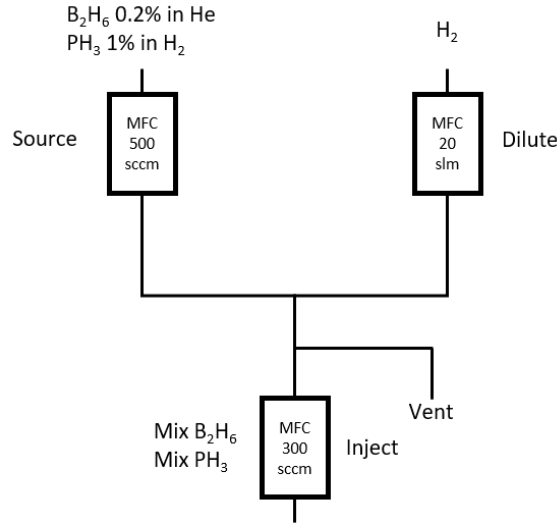


Figure II.5: Working principle of a dopant mixer

To in-situ dope (Si)GeSn, B_2H_6 diluted at 0.2% in H_2 and PH_3 diluted at 1% in H_2 were used as p-type and n-type dopant precursors, respectively. To obtain the ability to vary the dopant concentrations over a broad range, a wide range of dopant precursor flows needs to be accessed. This is achieved thanks to a mixer. A mixer dilutes the dopant precursor flow coming from the gas bottle with H_2 . Dopant concentrations between 5.54 and 2000 parts per million for B_2H_6 and 27.7 and 10 000 ppm for PH_3 can be accessed with B_2H_6 0.2% and PH_3 1% in H_2 bottles, as here. The dopant precursor flow in the chamber is given by **Equation (I.5.4)**, where the source mass-flow F_{Src} is equal to 500 sccm, the dilution mass-flow F_{Dlt} is equal to 20 000 sccm, the bottle's dilution of the dopant precursor and x_{Bot} is equal either to 2000 or 10 000 ppm. The Mixing Ratio $\text{MR}(\%)$ should be in-between 10% and 90% or equal to 100% and the injection mass-flow should be in-between 30 and 295 sccm (300 sccm mass-flows).

$$x_{\text{mix}}(\text{ppm}) = \frac{\text{MR}(\%) \cdot F_{\text{Src}}}{\text{MR}(\%) \cdot F_{\text{Src}} + (100 - \text{MR}(\%)) \cdot F_{\text{Dlt}}} \frac{x_{\text{Bot}}(\text{ppm})}{10^6} F_{\text{Inj}} \quad (\text{I.5.4})$$

I.5.3 Growth Mechanisms

Because the reaction of Ge-hydrides with SnCl_4 is complex, a better knowledge of growth mechanisms is crucial to optimize growth. Attempts have thus been made in the literature to describe the chemical reactions at hand. [14], [15] From experiments in literature, it is known that [14]

- (i) Reactive intermediates are formed.

- (ii) The Ge growth component is more dependent on dissociative adsorption than the Sn growth component.
- (iii) Sn is pre-dissociated in the gas phase, therefore, not thermally activated, while Ge is thermally activated.
- (iv) The surface is covered with H and Cl.
- (v) The lower growth temperature reactivity is given by the Ge-hydride reactivity. This means that no growth occurs without the dissociative adsorption of Ge-hydrides.

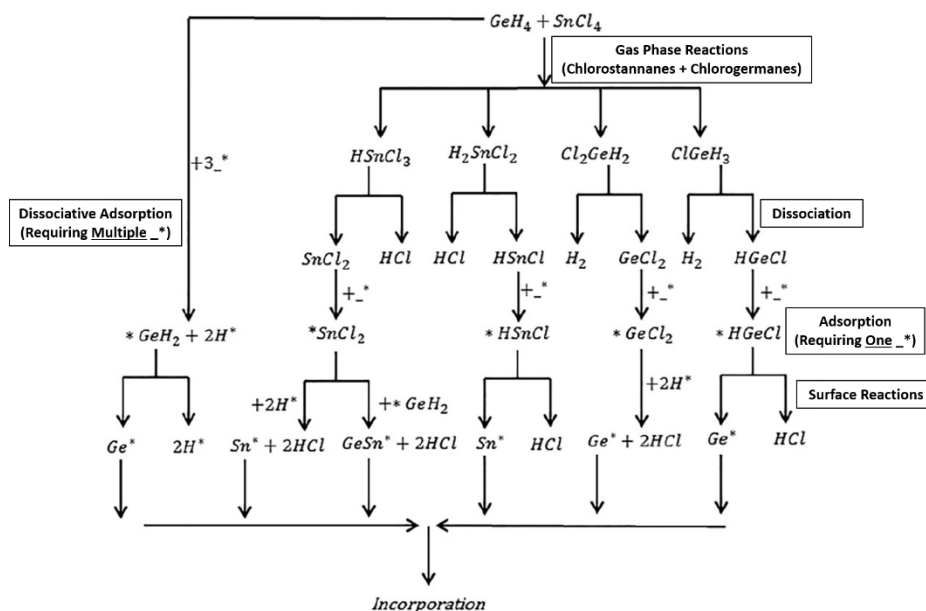
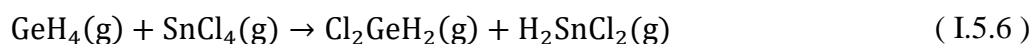
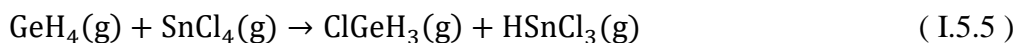


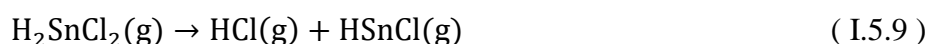
Figure II.6: Schematic of possible reaction pathways for GeH_4 and $SnCl_4$. [14]

Given those findings, Margetis *et al.* proposed a growth model with possible reaction pathways. It is shown in **Figure II.6** for GeH_4 and $SnCl_4$. [14] In the studies presented in the following, Ge_2H_6 was used as Ge precursor. This should result in minor alterations of the growth reactions, but should in general not lead to completely different reaction pathways because similar findings have been observed for Ge_2H_6 . [15]

Margetis *et al.* first proposed that GeH_4 and $SnCl_4$ react in exothermic (not thermally activated) reactions in the gas phase, shown in **Equation (I.5.5)** and **(I.5.6)**.



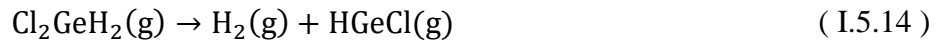
These reaction products further react in other exothermic gas phase reactions, shown in **Equation (I.5.7)** to **(I.5.9)**.



Easy adsorption of products thanks to the reaction described in **Equation (I.5.7)** to **(I.5.9)** occurs, resulting in the Sn growth component being mass-transport limited. Sn reaction products are adsorbed on the surface through first order reactions requiring only one open surface site (denoted $_*$), shown in **Equation (I.5.10)** and **(I.5.11)**.



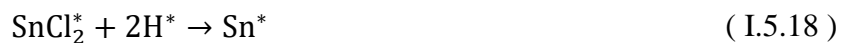
The $*$ stands for surface absorbed products. The reaction pathway $\text{GeH}_4(\text{g}) \rightarrow \text{GeH}_2(\text{g}) + \text{H}_2(\text{g})$ is not significant at 320 °C because, according to calculations, the reaction rate is too low. [16] The decomposition of germane rather proceeds via chlorogermanes $\text{Cl}_x\text{GeH}_{4-x}$ formation, shown in **Equation (I.5.12)** to **(I.5.14)**.



Reactions shown in **Equation (I.5.12)** to **(I.5.14)** are endothermic, which means that they are probably thermally activated. Results shown in the literature show that Ge incorporation increases with SnCl_4 with a scaling factor of 0.5 [14], outlining that a significant amount of Ge is incorporated following chlorogermane reaction paths. In **Equations (I.5.12)** and **(I.5.13)** only one open surface site is required to be absorbed via $\text{HGeCl}(\text{g}) + _* \rightarrow \text{HGeCl}^*$ and $\text{GeCl}_2(\text{g}) + _* \rightarrow \text{GeCl}_2^*$. This highlights that high growth rates at low growth temperatures for this chemistry are not only enabled by Cl and H desorption from surface Sn, but, in addition, thanks to gas phase conversion of SnCl_4 and GeH_4 into more reactive intermediates. Moreover, Ge is incorporated by dissociative adsorption [17], shown in **Equations (I.5.15)** and **(I.5.16)**, which requires two or three open surface sites.



The reaction described in **Equation (I.5.15)** and **(I.5.16)**, are of second or third order, where the second order reaction dominates at high surface coverage and low growth temperatures. The Ge growth rate component might be more dependent on H and Cl desorption and the creation of open surface sites, i.e. thermally activated. The surface adsorbed reaction products reduce further via surface reactions. The chloride species reduce via reactions shown in **Equations (I.5.17)** and **(I.5.18)**.



Equation (I.5.17) and **(I.5.18)** are exothermic and depend on the Ge-hydride reactivity, which means that it ceases when the dissociative adsorption of Ge-hydrides ceases. Another exothermic chloride species reduction reaction is shown in **Equation (I.5.19)**.



Most of the Ge atoms are incorporated via the endothermic reaction shown in **Equation (I.5.20)**. The exothermic reaction in **Equation (I.5.21)** might explain why the GeH₄ incorporation efficiency increases when SnCl₄ is added to the growth mixture. Some Ge is incorporated via **Equation (I.5.22)**.



A schematic overview of possible reaction pathways proposed by Margetis *et al.* [14], is shown in **Figure II.6**. Overall, SnCl₄ increases the Ge efficiency by forming chlorogermanes and the presence of Ge-hydrides is necessary to decompose SnCl₄. The knowledge gained from the proposed reaction pathways enables to better understand the interaction of dopant precursors B₂H₆ and PH₃ with other precursors and how this impacts growth mechanisms.

I.6 Nanosecond Laser Annealing (NLA)

I.6.1 The Nanosecond Laser Annealing tool

As discussed in the previous chapter, (Si)GeSn is a metastable material. This metastability results in Sn segregation and precipitation for annealing strategies commonly used in the semiconductor industry like Rapid Thermal Annealing (RTP) or Flash Annealing. Nanosecond Laser Annealing (NLA) might overcome this limitation by utilizing ultra-short laser pulses (typically a few 100 ns) to anneal.

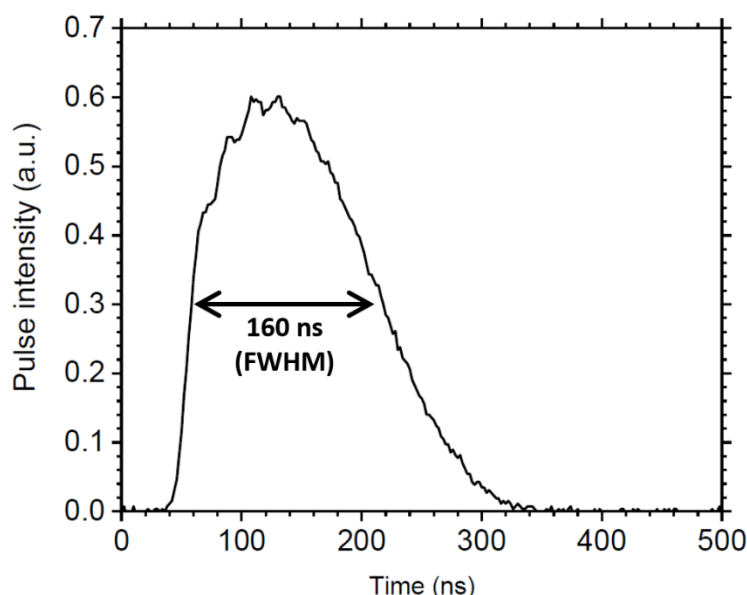


Figure II.7: Screen LT-3100 laser pulse profile (intensity vs. time).

In the presented studies, a Screen LT-3100 tool from SCREEN-LASSE is used. It utilizes a XeCl laser with a wavelength of 308 nm and a pulse duration with a Full Width at Half

Maximum (FWHM) of 160 ns, shown in **Figure II.3**. The pulse duration can be slightly modified (a few ns difference) by mixing Ne, the main gas in the laser cavity, with some Xe, HCl and H₂ within the laser cavity. Ultra-Violet (UV) laser irradiation enables processing at the nanometer scale [18] and the pulse duration is chosen to reach a metastable adiabatic regime for dopant activation, while avoiding surface damage and defect generation. [19]

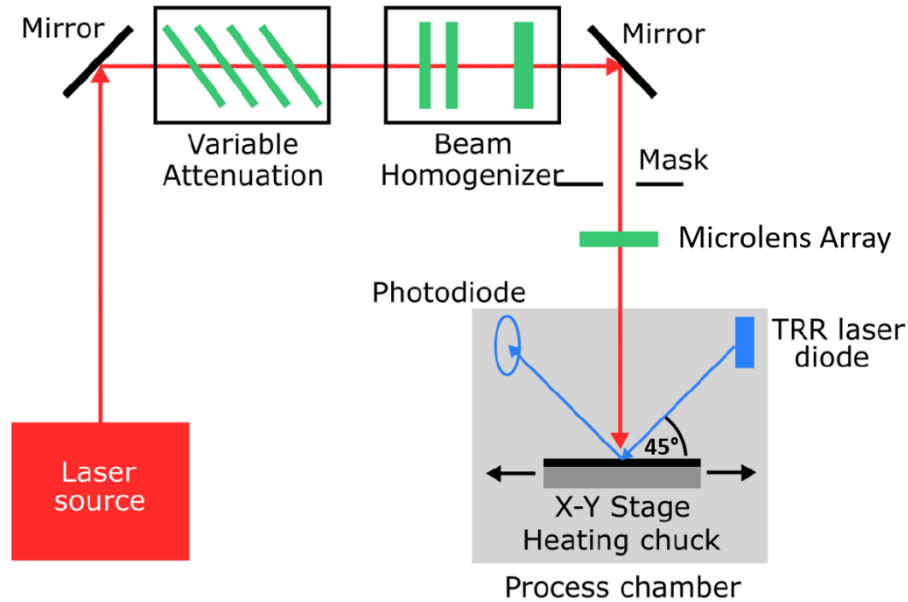


Figure II.8: Screen LT-3100 tool setup. [20]

The voltage applied to the X-ray gun, which excites the gas inside the laser cavity, determines the applied energy density. Attenuation along the optical line, shown in **Figure II.8**, leads to slight adjustments of the energy density sent onto the specimen's surface. The attenuator is made out of semi-reflecting plates, which dampen the incoming beam by regulating the mirror configuration. [21]

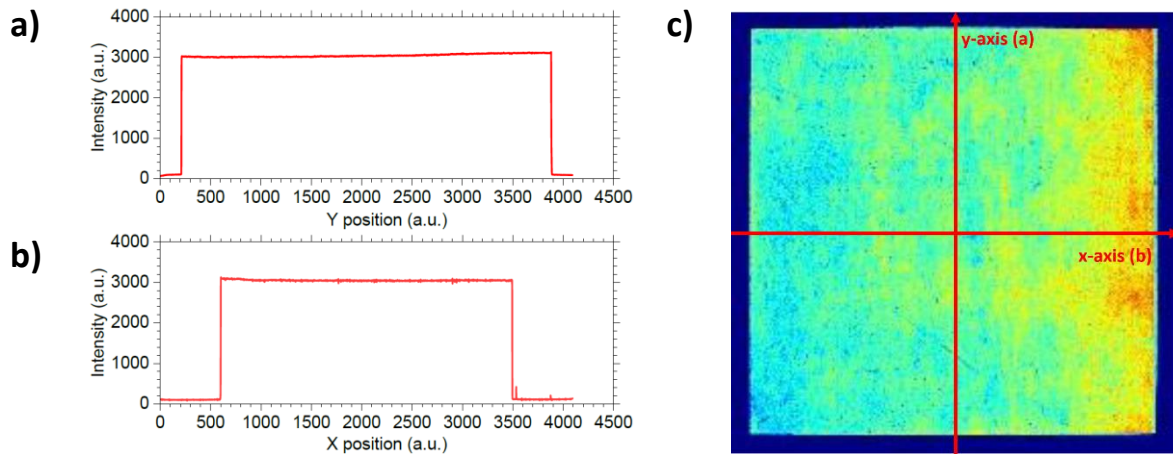


Figure II.9: Screen LT-3100 laser beam uniformity profile (a) along the x-axis and (b) along the y-axis. (c) Laser beam uniformity map with a homogeneity around 2%.

To obtain a homogenous beam, a single microlens array and a Fourier lens [22] are used. The laser beam is split into beamlets that get focused by a spherical lens resulting in an overlapping beam at the homogenization plane. The final beam resembles a rectangle with a flat-top size of 26 mm x 33 mm, shown in **Figure II.9**. The microlens array is modifiable to form smaller beams, which results in a shift of the energy density range to higher values. With a 26 mm by 33 mm spot size, an energy density range from 0.08 Jcm^{-2} to 0.80 Jcm^{-2} can be probed. An energy density range from 0.36 Jcm^{-2} to 3.60 Jcm^{-2} can be probed when the spot size is 15 mm by 15 mm. The uniformity is then around 2%. In the present study, 15 mm by 15 mm areas were irradiated with energy densities ranging from 0.3 to 2.0 Jcm^{-2} in a step-and-repeat mode. In this mode a position is annealed by one or multiple laser pulses. Then, the stage with the wafer on top moves and a new position is annealed. No laser pulse is applied while the stage moves. The position accuracy of the stage is a few μm . Annealing is performed in a N_2 atmosphere on a ceramic chuck, which can be heated up to $450 \text{ }^\circ\text{C}$. The tool can align the wafer notch and includes a post-anneal cooling station when the heated chuck is used. More details about the laser-annealing tool can be found in the literature. [23], [24]

I.6.2 In-situ Time Resolved Reflectivity Measurements

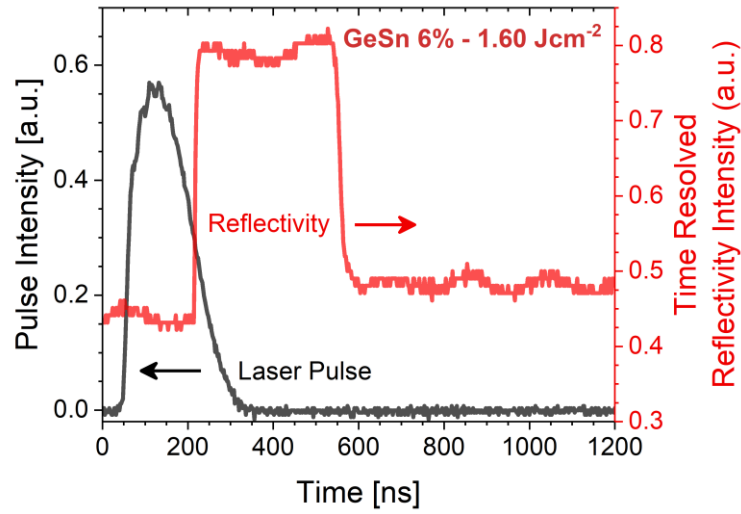


Figure II.10: Screen LT-3100 laser pulse profile (intensity vs. time) and a typical Time Resolved Reflectivity (TRR) profile (intensity vs. time).

The used Nanosecond Laser Annealing tool at LETI is equipped with an in-situ transient reflectivity measurement system with ns resolution to measure temperature and phase changes. UV-NLA results in surface reflectivity changes [25] because the refraction index changes with temperature and phase changes. A laser, with a wavelength of 638 nm, samples the surface at a rate of 0.5 ns^{-1} , probing the intensity by recording the reflected beam with a photodiode. The resulting profile is shown in **Figure II.10**. The measuring laser beam is orientated at 45° to the sample surface resulting in an elliptical spot size of 5 mm by 10 mm. The obtained intensity is arbitrary and does not correspond to the real reflectivity. This allows measuring the complete annealing process including heating, melting, solidification and cool down.

I.7 X-Ray Diffraction

I.7.1 Introduction

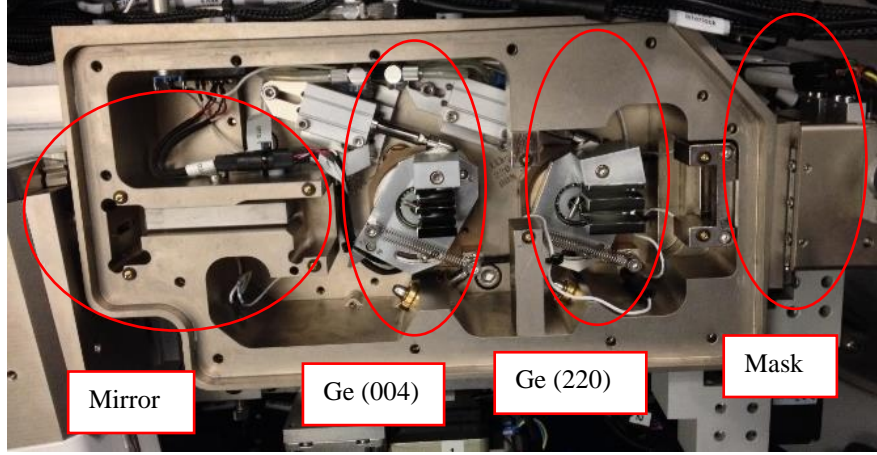


Figure II.11: Description of the XRD measurement setup with two “Channel Cut Crystal” monochromators Ge (0 0 4) and Ge (2 2 0) to form the X-ray beam.

High-Resolution X-Ray Diffraction (HR-XRD) is a characterization technique that uses monochromatic X-ray beams to non-destructively analyze the structural properties of crystalline materials. A DELTA-XM tool from JVM/Bruker was used for all studies. It creates X-rays thanks to a copper X-ray tube. A Ge (220) “Channel Cut Crystal”, shown in **Figure II.11**, is used to obtain monochromatic, parallel X-ray beams corresponding to the copper $K_{\alpha 1}$ line with $\lambda_{\alpha}^{\text{Cu}} = 1.540597 \text{ \AA}$. A crystal analyzer made from asymmetric Ge oriented along (1 1 1) was inserted in front of the detector to increase the measurement accuracy by reducing the probed area of the reciprocal space.

These monochromatic X-ray beams are shone onto a specimen. X-rays are scattered by the potential $V(\vec{r})$ of atoms and the scattered light is detected. The rate of scattering Γ can be calculated using Fermi’s golden rule, seen in **Equation (I.7.1)**.

$$\Gamma(\vec{k}', \vec{k}) = \frac{2\pi}{\hbar} |\langle \vec{k}' | V(\vec{r}) | \vec{k} \rangle|^2 \delta(E - E') \quad (\text{I.7.1})$$

In the case of X-Ray Diffraction, elastic scattering is observed. The momentum and energy, therefore, are conserved. In this case, the scattering amplitude $|\langle \vec{k}' | V(\vec{r}) | \vec{k} \rangle|^2$ is the Fourier transform of the scattering potential.

In the case of a crystalline material a lattice can be defined with a lattice vector \vec{R} , shown in **Equation (I.7.2)**.

$$\vec{R} = n_1 \vec{a}_1 + n_2 \vec{a}_2 + n_3 \vec{a}_3 \quad n_i \in \mathbb{Z}, i = 1, 2, 3 \quad (\text{I.7.2})$$

Where \vec{a}_i ($i = 1, 2, 3$) are lattice vectors. By performing a Fourier transformation of the lattice, the reciprocal space is obtained. The plane wave vector of the reciprocal space is given by \vec{Q} , seen in **Equation (I.7.3)**.

$$\vec{Q} = h\vec{b}_1 + k\vec{b}_2 + l\vec{b}_3 \quad h, k, l \in \mathbb{Z} \quad (\text{I.7.3})$$

The integer numbers h, k and l are know as the Miller indices and \vec{b}_i ($i = 1, 2, 3$) are the reciprocal space lattice vectors. Because every lattice point is included in a lattice plane **Equations (I.7.4)** to **(I.7.6)** must be true.

$$e^{i\vec{Q} \cdot \vec{R}} = 1 \quad (\text{I.7.4})$$

$$\Rightarrow \vec{Q} \cdot \vec{R} = 2\pi n \quad n \in \mathbb{Z} \quad (\text{I.7.5})$$

$$\vec{a}_i \cdot \vec{b}_j = 2\pi \delta_{ij} \quad i, j \in \mathbb{Z} \quad (\text{I.7.6})$$

From **Equation (I.7.6)** the reciprocal lattice vectors can be defined by **Equations (I.7.7)** to **(I.7.9)**.

$$\vec{b}_1 = 2\pi \frac{\vec{a}_2 \times \vec{a}_3}{\vec{a}_1 \cdot (\vec{a}_2 \times \vec{a}_3)} \quad (\text{I.7.7})$$

$$\vec{b}_2 = 2\pi \frac{\vec{a}_3 \times \vec{a}_1}{\vec{a}_1 \cdot (\vec{a}_2 \times \vec{a}_3)} \quad (\text{I.7.8})$$

$$\vec{b}_3 = 2\pi \frac{\vec{a}_1 \times \vec{a}_2}{\vec{a}_1 \cdot (\vec{a}_2 \times \vec{a}_3)} \quad (\text{I.7.9})$$

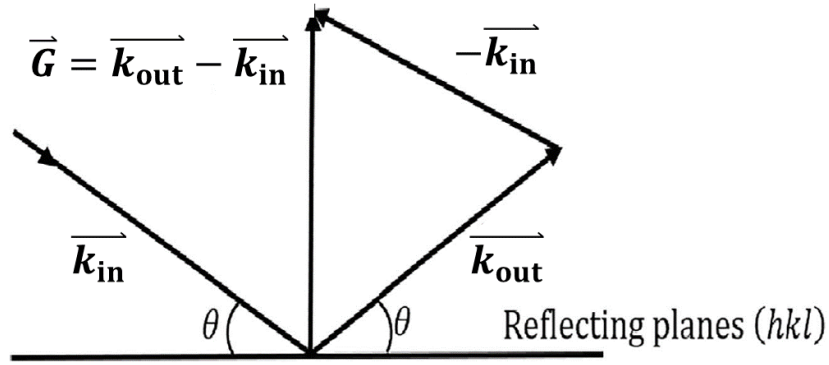


Figure II.12: Visual representation of the Laue equation showing the scattering of an incoming plane wave with \vec{k}_{in} on a reciprocal lattice plane (hkl), resulting in an outgoing plane wave with \vec{k}_{out} . [26] The difference between incoming and outgoing wave vectors is the plane wave vector \vec{Q} .

Considering that the lattice vector \vec{R} and the plane wave vector \vec{Q} are defined by the lattice, the Laue equation, shown in **Equation (I.1.1)**, can be obtained from the scattering amplitude $|\langle \vec{k}' | V(\vec{r}) | \vec{k} \rangle|^2$.

$$\vec{Q} = \vec{k}_{\text{out}} - \vec{k}_{\text{in}} \quad (\text{I.7.10})$$

The Laue equation is a manifestation of momentum conservation. As shown in **Figure II.12**, the incoming plane wave with wave vector \vec{k}_{in} is scattered by the lattice plane (hkl), resulting in an outgoing plane wave with wave vector \vec{k}_{out} . Their difference is equal to the plane wave vector of the reciprocal lattice \vec{Q} . An equivalent of the Laue equation is the Bragg equation, shown in **Equation (I.7.11)**.

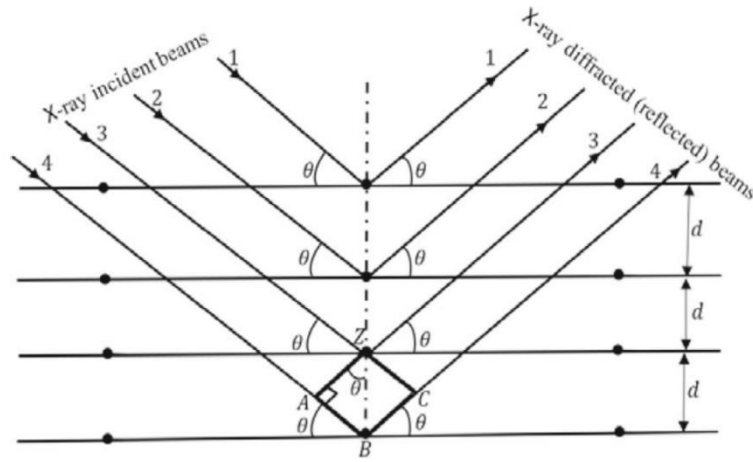
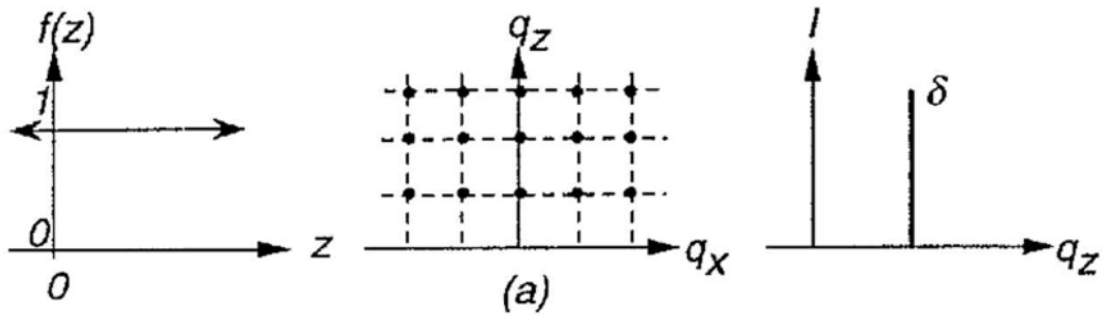


Figure II.13: Schematic representation of geometry to derive Bragg equation showing incoming plane waves being diffracted by the lattice at an angle Θ , resulting in outgoing plane waves with an angle 2Θ to the incoming plane waves. [27] The lattice spacing is given by d_{hkl} .

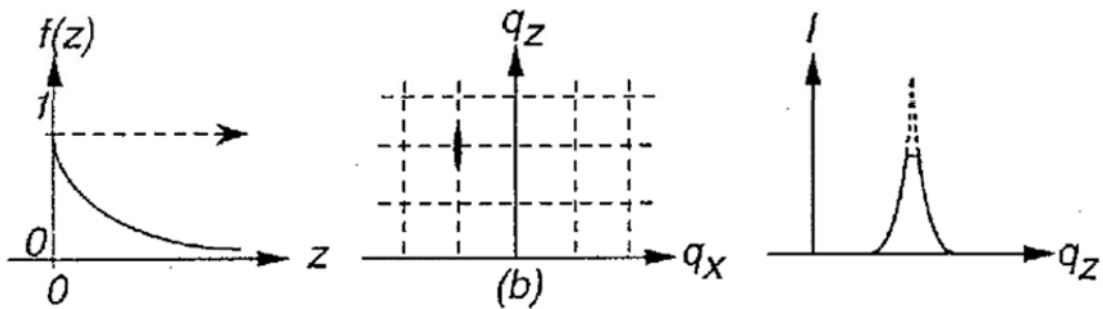
$$\lambda = 2d_{hkl} \sin \theta_{hkl} \quad (\text{I.7.11})$$

A visual representation of the Bragg equation for constructive interference is shown in **Figure II.13**. It shows incoming plane waves with wavelength $\lambda_{\alpha}^{\text{Cu}} = 1.540597 \text{ \AA}$ that are scattered by atoms. The interplanar spacing is given by d_{hkl} and θ_{hkl} describes the angle of diffraction between the plane wave and the scattering plane. The angle between the incoming plane wave and outgoing plane wave is given by $2\theta_{hkl}$.

ideal infinite crystal



attenuated infinite crystal



ideal thin film crystal

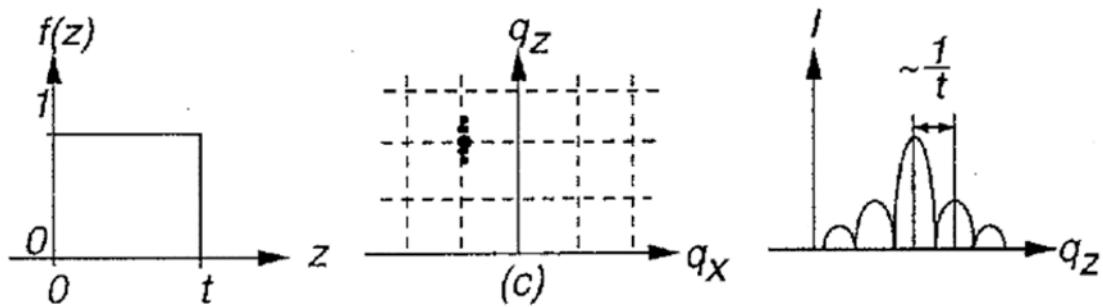


Figure II.14: XRD beam attenuation in a thin film crystal (t = thin film crystal thickness). [28] The δ -function is defined by $\int_{-\infty}^{\infty} f(x) \delta(x - a) dx = f(a)$.

In the case of an ideal infinite crystal, scattering on all lattice planes would result in diffraction with perfect δ -peaks, shown in **Figure II.14 (a)**. In reality, an X-ray beam is interacting with the crystal leading to beam attenuation. This results in some broadening of the diffraction peak and the disappearance of higher order XRD peaks, shown in **Figure II.14 (b)**. Moreover, a crystal is not infinite, but has a specified thickness. Due to reflection of the X-ray beam on the layer surface and at the substrate/film interface, constructive and destructive interferences happen, resulting in satellite peaks, called thickness fringes, along the q_z reciprocal direction, shown in **Figure II.14 (c)**. The spacing of the satellite peaks is inversely proportional to the film thickness t . In addition to these effects, there is some peak broadening due to the measurement setup.

I.7.2 Measurement Modes

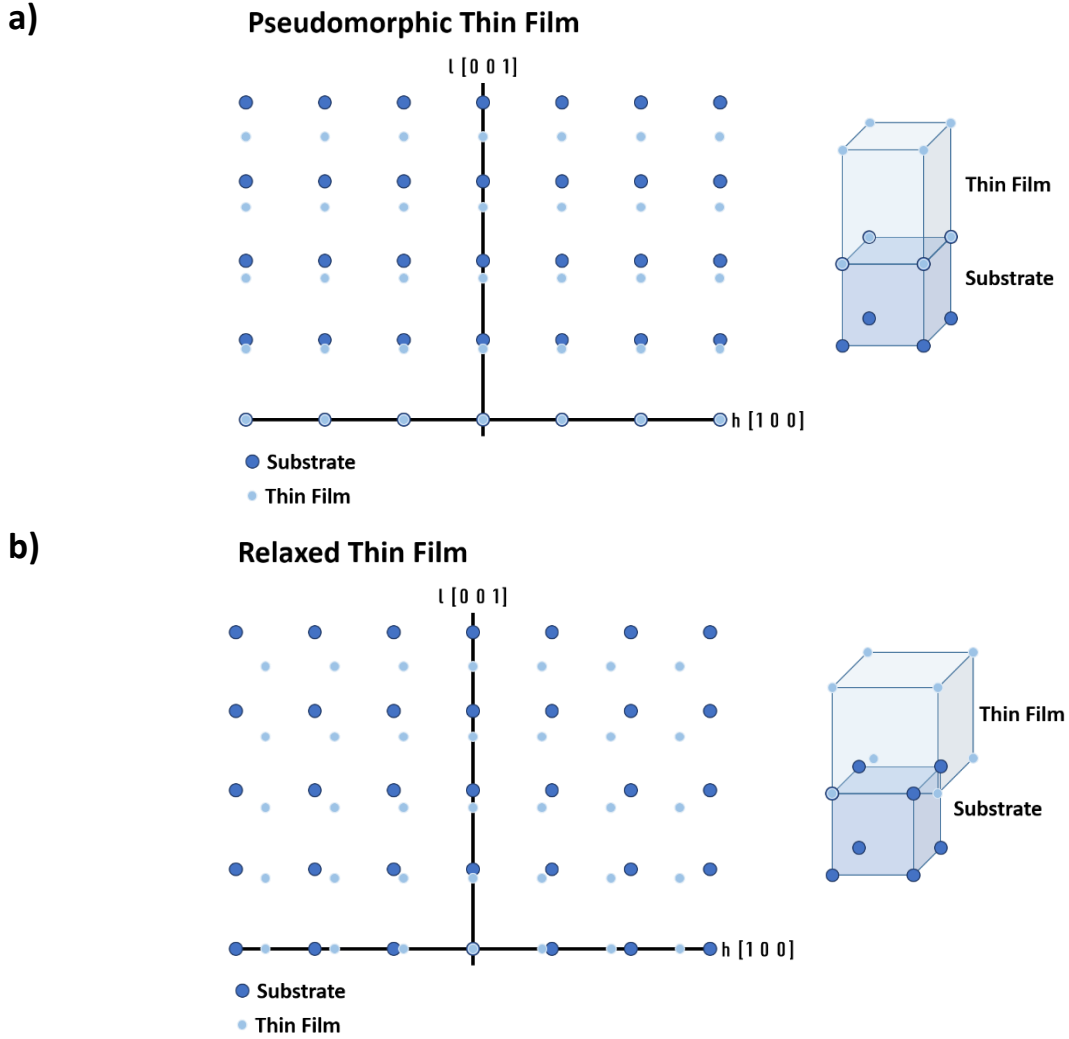


Figure II.15: Schematics of the reciprocal space for a pseudomorphic thin film (a) and a relaxed thin film (b) on top of a substrate.

As discussed in **Chapter I**, the growth of heterostructures typically results in lattice parameter deformations. In-plane and out-of-plane lattice parameters of a thin films grown on top of a substrate are then different, because the thin film is either compressively and tensile strained. These deformations of the lattice plane lead to changes in the interplanar spacing d_{hkl} . The absolute value of the plane wave vector $|\vec{Q}|$ is given by **Equation (I.7.12)**.

$$|\vec{Q}| = \frac{2\pi}{d_{hkl}} \quad (\text{I.7.12})$$

This means that, when growing heterostructures, different diffraction peaks in the reciprocal space are observed for the substrate and thin film. In the case of a thin film grown

pseudomorphically on a substrate, the various diffraction peaks shift along the $\langle 001 \rangle$ directions, to smaller values for larger lattice parameter and therefore compressively strained films as shown in **Figure II.15 (a)**. The absolute value of the plane wave vector $|\vec{Q}|$ can be written as its components in the x- and z-direction as a function of the in- and out-of plane lattice parameter a^{\parallel} and a^{\perp} , respectively, as given in **Equation (I.7.13)** and **(I.7.14)**.

$$q_x = 2\pi \frac{2\sqrt{2}}{a^{\parallel}} \quad (\text{I.7.13})$$

$$q_z = 2\pi \frac{4}{a^{\perp}} \quad (\text{I.7.14})$$

As discussed in the previous section, when the layer reaches its critical thickness it starts to plastically relax, which causes the in- and out-of-plane lattice parameters to change and, therefore, leads to changes of the corresponding diffraction peak positions. As shown in **Figure II.15 (b)** for a fully relaxed thin film on top of a substrate, the interplanar spacing in q_x and q_z directions are the same and, therefore, the diffraction peaks are shifted towards smaller values along the q_x and q_z directions.

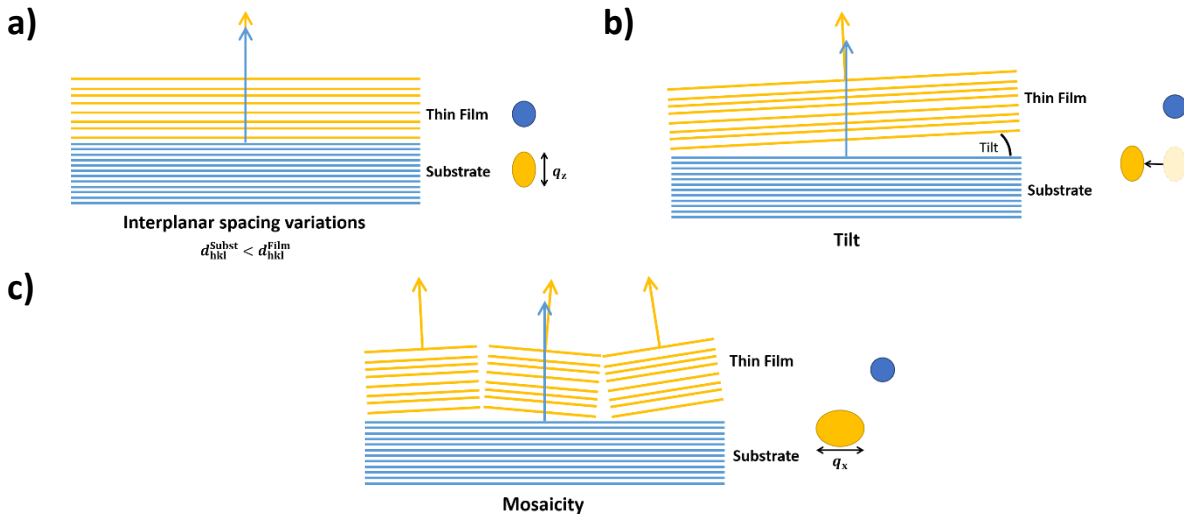


Figure II.16: Schematic showing the effect of interplanar spacing variations (a), tilt (b) and mosaicity (c).

In addition to lattice parameter changes, a real thin film exhibits small interplanar spacing variations due to inhomogeneities. These small interplanar spacing variations cause some slight variations of the plane wave vector \vec{Q} , which in turn results in some broadening of the diffraction peaks along the q_z direction, as shown in **Figure II.16 (a)**.

In general, there is some small tilt between the thin film and the substrate, as shown in **Figure II.16 (b)**. The tilt results in a shift of the diffraction peaks of the thin film along the q_x direction.

Thin film might exhibit regions with different tilts, called mosaicity, as shown schematically in **Figure II.16 (c)**. Mosaicity results in some broadening of the diffraction peaks along the q_x direction because different regions with different tilts shift the diffraction peak to different q_x values.

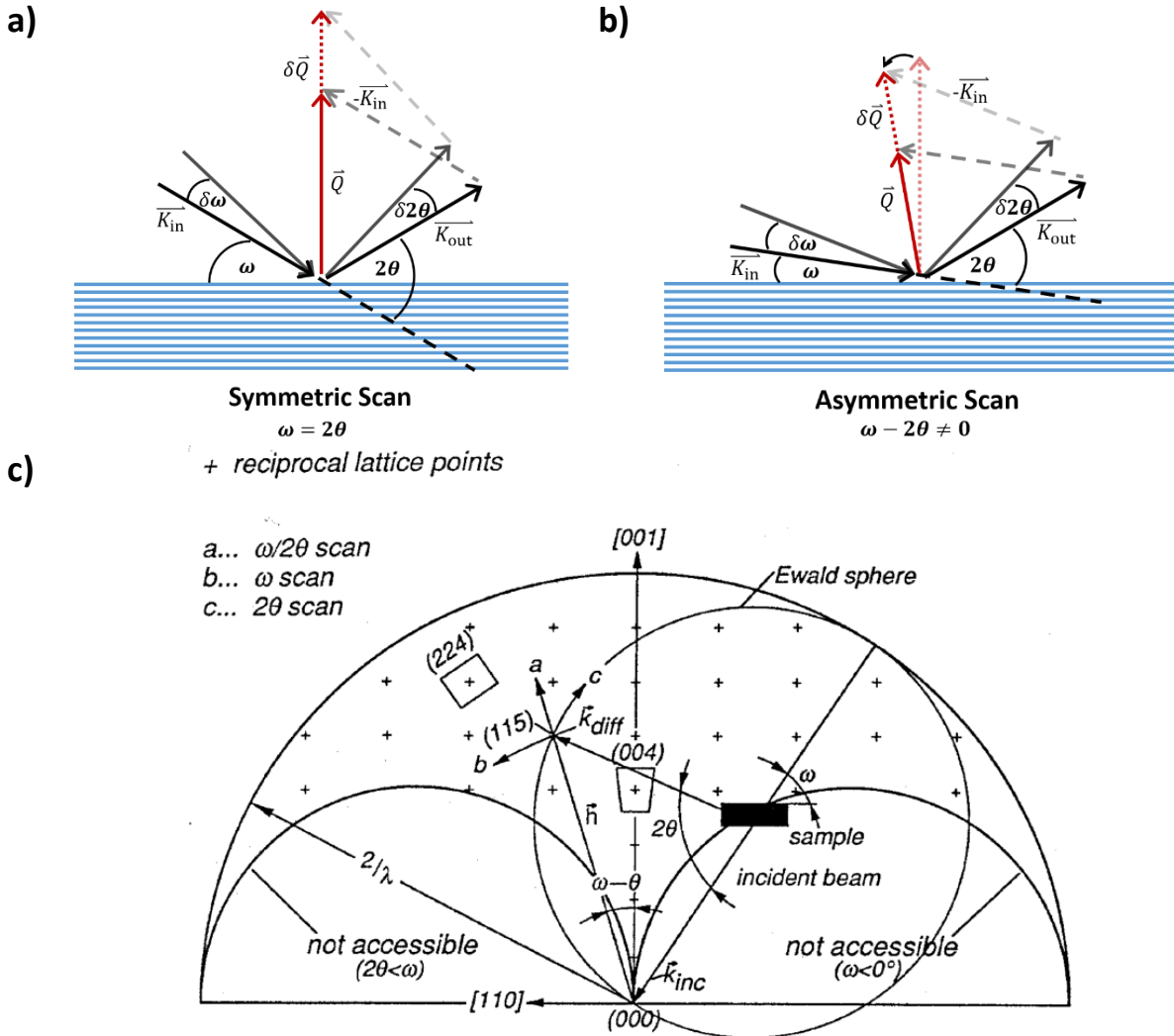


Figure II.17: Schematic of a symmetric (a) and an asymmetric scan (b). Ewald sphere of the reciprocal space outlining the various possible scans (c).

To investigate the crystalline quality and determine strain, composition and film thickness accurately, it is necessary to combine various types of XRD scans. [29]–[32] By performing symmetrical scans, e.g. scans where $\omega = 2\theta$, it is possible to scan the reciprocal space along the q_z direction, as shown in **Figure II.17 (a)**. To investigate a broader range of the reciprocal space, it is necessary to tilt the plane wave vector \vec{Q} . This can be achieved by probing the sample with $\omega - 2\theta \neq 0$, as shown in **Figure II.17 (b)**. The offset that occurs in this scan setup, enables to tilt the plane wave vector.

By combining symmetric and asymmetric scans, a broad range of the reciprocal space is investigated, as outlined in **Figure II.17 (c)**. Due to destructive interference depending on the crystalline structure of the thin film, some diffraction orders are not accessible and therefore cannot be observed. In the present studies, Reciprocal Space Maps (RSMs) around the (0 0 4), (2 2 4) or (1 1 3) diffraction orders were acquired. The strain in the thin film was calculated by determining the in-plane and out-of-plane lattice parameters from the substrate and thin film diffraction peak positions of the RSM. The thin film's in-plane lattice parameter $a_{\text{Film}}^{\parallel}$, the bulk, unstrained lattice parameters of the thin film a_{Film}^0 and the substrate $a_{\text{Substrate}}^0$ were used in **Equation (I.7.15)** to calculate the macroscopic degree of strain relaxation R inside the thin film.

$$R = \frac{a_{\text{Film}}^{\parallel} - a_{\text{Substrate}}^0}{a_{\text{Film}}^0 - a_{\text{Substrate}}^0} \quad (\text{I.7.15})$$

With $a_{\text{Substrate}}^0 = \frac{1-\nu}{1+\nu} a_{\text{Film}}^{\parallel} + \frac{2\nu}{1+\nu} a_{\text{Film}}^{\perp}$, ν being the Poisson ratio for the film ($\nu = 0.278$ for Si, 0.271 for Ge and 0.263 for Sn [33]).

The setup used to record RSMs employed a solid-state 1D detector with 1280 cells with a size of $50 \times 8000 \mu\text{m}^2$. The layer composition of different layers in a complex heterostructure can be calculated from the in-plane and out-of-plane lattice parameters determined by RSM measurements. For pseudomorphic, thin films Takagi-Taupin's dynamical scattering theory was used to extract the thin film thickness and composition from fits of the layer peaks and fringes obtained by $\omega - 2\theta$ scans around the (0 0 4) diffraction order. [34]

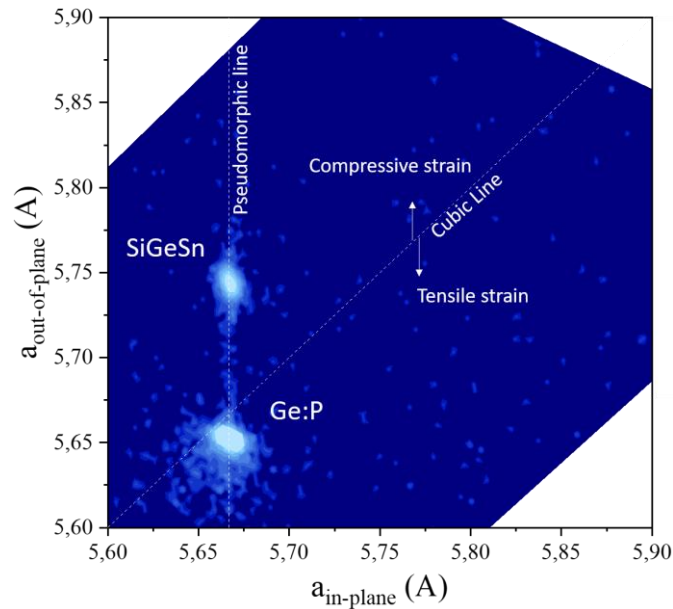


Figure II.18: Reciprocal Space Space Map of the (2 2 4) order of pseudomorphic SiGeSn grown on a Ge:P/Ge SRB.

A typical RSM is given in **Figure II.18** for a pseudomorphic SiGeSn layer on a Ge:P/Ge SRB. The in- and out-of-plane are calculated according to **Equation (I.7.13)** and **(I.7.14)**. The q_z -spread of the SiGeSn peak is due to deformation of the lattice by defects. The slight asymmetry of the Ge peak and the shift towards the Si substrate peak is due to the formation of an interfacial GeSi alloy during the short duration thermal cycling that followed the growth [35] and the slight tensile strain in the Ge SRBs, with a mean macroscopic degree of strain relaxation $R = 104\%$. This slight tensile strain was due to thermal expansion differences between Ge and Si, which came into play during the cooling-down to room temperature after growth [36]–[39]. This deformed the lattice, resulting in a spread of the Ge peak.

I.8 Surface Characterization Techniques

I.8.1 Atomic Force Microscope (AFM)

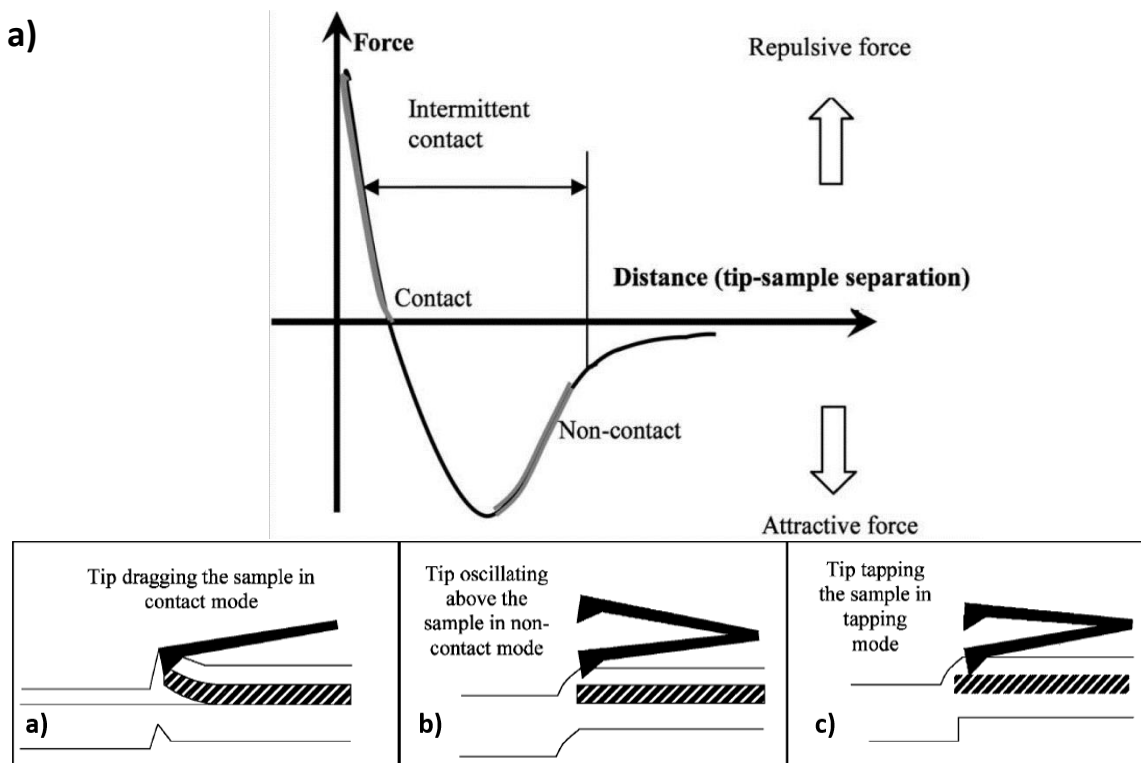


Figure II.19: Force-displacement curve, outlining interatomic force variations when the AFM tip approaches the surface. [40] Schematics of contact mode (b), non-contact mode (c) and tapping mode (d). [40]

Atomic Force Microscopy (AFM) tools, like the Fast-Scan Bruker in-line tool used for the present studies, generally rely on micro-machined, silicon cantilever probes with sharp tips mounted onto Piezoelectric actuators which displace the cantilever. A laser beam, which is reflected on the back of the cantilever, measures the movements of the cantilever and the reflected beam is detected by a four-segment photodiode.

When the tip approaches the surface and gets close enough to interact with it, the tip is attracted by the sample due to van-der-Waals forces, as shown in **Figure II.19 (a)**. In this regime of attractive interaction between tip and surface, the topography is imaged by oscillating near or at its resonance frequency, shown in **Figure II.19 (c)**. This mode is called non-contact mode because the tip is never in contact with the sample surface (distance generally 50 to 150 Å). Topography changes result in shifts of the oscillating frequency away from its resonant frequency. [41] The non-contact mode however suffers from fluid contamination, which can result in measurement failures.

As the tip approaches the surface further, the van-der-Waals force of the electron clouds start to repulse the tip electrostatically. The interaction force between tip and sample surface becomes zero when the tip-sample distance is a few Å and becomes repulsive when the tip is in contact with the surface. In the part of the force-displacement curve (repulsive region) with a steep slope, the topography is probed by measuring the interaction forces due to direct contact. [42] This mode is called contact mode, as shown in **Figure II.19 (b)**. In this mode, the presence of a contamination layer results in constant, attractive forces exerted on the tip by capillary forces. [40] Moreover, the cantilever applies shear forces on itself. [40] The shear forces direction and magnitude depend on the cantilever deflection and its spring constant. Tip damaging can occur in the contact mode as tips can crash into surface features.

Combining both modes, e.g. oscillations and sample impact [43], [44], results in the so-called tapping mode. This mode operates at a tip-sample distance of 20 to 100 Å. Its oscillation is tuned to lightly tap the surface at its maximum amplitude with a frequency between 50 and 500 kHz. The topography is inferred from the amplitude of the oscillation as it loses some energy due to intermittent contact. A feedback loop that compares the recorded signal with a reference signal is usually used in this mode to keep the amplitude constant by adjusting the tip-sample separation accordingly. In this case, the voltage applied to the Piezoelectric actuator is a measure of vertical displacement, which is used to determine the topography.

Generally, the standard deviation of the mean z -value is given as the Root Mean Square (RMS) value and the difference between the maximum and minimum z -value as Z_{range} , **Equations** shown in (**I.8.1**) and (**I.8.2**), respectively.

$$\text{RMS} = \sqrt{\frac{\sum_{i=1}^N (Z_i - \bar{Z})^2}{N}} \quad (\text{I.8.1})$$

$$\sigma_{Z_{\text{range}}} = Z_{\text{Max}} - Z_{\text{Min}} \quad (\text{I.8.2})$$

I.8.2 Scanning Electron Microscopy (SEM)

To overcome the resolution limitation of optical microscopes given by Rayleigh's criterion, shown in **Equation (I.8.3)**,

$$\delta = \frac{0.61\lambda}{n \sin\beta} \quad (\text{I.8.3})$$

where n is the refractive index and λ the wavelength, smaller wavelengths are required. One solution to obtain smaller wavelengths is to switch over to electrons whose wavelength is given by de Broglie's particle wavelength, shown in **Equation (I.8.4)**.

$$\lambda = \frac{h}{mv} \quad (\text{I.8.4})$$

Where h is the Planck constant, m is the particle mass and v its velocity.

Scanning Electron Microscopy (SEM) uses this technique to achieve a resolution of 3×10^5 . The working principle is similar to optical microscopy. An electron beam is formed in an electron gun. An anode accelerates the beam towards the specimen's surface. On its way, the beam is shaped and focused by electromagnetic condenser lenses. When the beam reaches the surface, its electrons interact with the specimen. The incoming electrons inelastically scatter with shell atoms transferring some energy resulting in shell electrons being expelled. These expelled electrons are called Secondary Electrons and a detector collects them. The Secondary Electrons energy is below 50 eV and the contrast is mostly due to the topography of the sample.

If the energy density is larger than 50 eV a Rutherford scattering event occurs close to the nuclei. Those electron are Backscattered Electrons, which can be collected to obtain an image with a contrast given by the atomic weight.

I.9 Transmission Electron Microscope (TEM)

By Focused Ion Beam or mechanical grinding, an ultra-thin lamella (a few tens of nm to one hundred nm, typically) can be prepared, enabling the transmission of electrons. Transmission Electron Microscopy (TEM) utilizes the particle wave properties of electrons and their charge to obtain subatomic resolution of 2.5 Å to 3.0 Å. [45], [46]

A TEM is operated under Ultra High Vacuum to optimize the free path of electrons. It generally consists of a source of electrons which are accelerated at 100 to 400 keV, condenser lenses to form a thin, coherent beam with a small spot size, a specimen holder, an objective lens, a projector lens and a screen/camera. By increasing the applied accelerating voltage, the electron's kinetic energy is increased, which results in a smaller particle wavelength and hence, better resolution. [47], [48] Moreover, higher electron doses yield lower signal-to-noise ratios. [49]

Generated electrons are accelerated towards the specimen. When they get close enough, they interact with the specimen by elastic scattering (electron-nuclei), which gives (high resolution) information thanks to energy conservation and which is proportional to $Z^{1/3}$, and inelastic scattering (electron-electron), which results in radiation damage due to energy transfer and which is proportional to $Z^{4/3}$. The closer the electron gets to a nucleus the more the (screened) electric potential bents the electron's path. This results in a diffraction pattern that gives information about the specimen's crystallinity. [45] An aperture can be used to block either the non-scattered (Bright Field image) or diffracted electrons (Dark Field image). Defects and crystalline planes corresponding to the selected diffraction spot have higher contrast in DF images and can therefore be studied in more details. [45] The obtained image is collected by

the objective lens and magnified by the projector lens behind the specimen. A screen/detector records the image.

I.10 Composition Characterization Techniques

I.10.1 Secondary Ion Mass Spectrometry (SIMS)

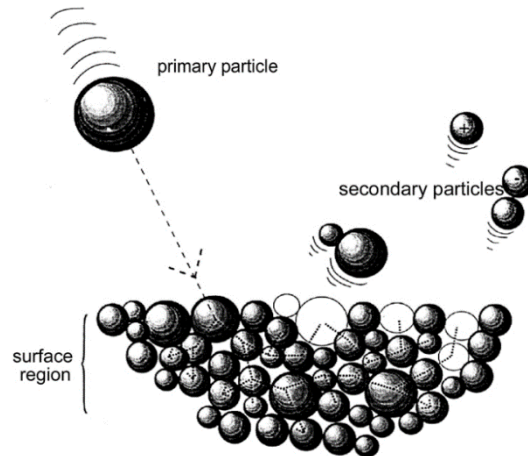


Figure II.20: Schematic of a primary ion beam impacting on a specimen's surface causing the release of secondary, partly ionized particles. [50]

Secondary Ion Mass Spectrometry (SIMS) generally relies on the detection of ions created during the bombardment of a specimen's surface with an ion beam, shown in **Figure II.20**. Primary ions impact on the specimen's surface results in the release of secondary ionized particles. Adequate mass analysis by a mass spectrometer enables to determine the specimen's chemical composition.

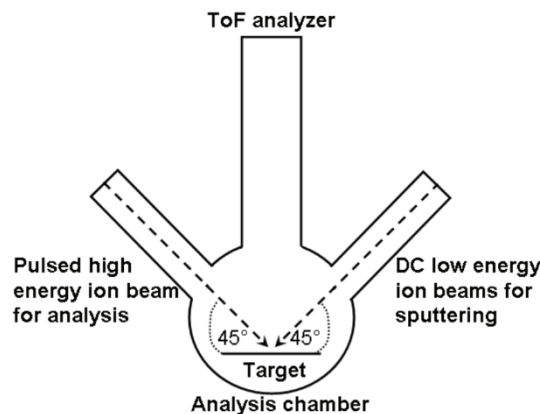


Figure II.21: Schematic of the TOF SIMS V tool from Ion ToF. [50]

In the present studies, an Ion ToF V Time-of-Flight (ToF) SIMS tool was used. It uses two primary ion beams, a low energy oxygen or cesium ion beam for sputtering and a high energy bismuth ion beam for analysis. A liquid Metal Ion Source is used as source for bismuth and cesium. Oxygen is supplied by a gas source. To accelerate, chop and focus the secondary ions ejected from the sample being profiled, columnar optics are used.

When the incoming primary ion beam impacts the specimen's surface, primary ions transfer their kinetic energy causing a cascading knock-on-effect. That results in the removal of particles like atoms and multi-atomic clusters. Only around 1% of all pulverized particles are ionized. The number of ionized particles depends on their relative ionization probabilities and their de-excitation close to the specimen's surface. After ionization, a planar electrode with a small aperture accelerates the ionized particles. Electromagnetic lenses and electrostatic plates collimated a coherent secondary ion beam.

SIMS is operated under Ultra High Vacuum to optimize free drift. Various ion masses are analyzed by natural segregation due to their different kinetic energies. Electrostatic mirrors are used [51]–[53] to increase the free drift length and reduce energy variations between ions with the same mass. A Multi-Channel Plate detector with a dead time of a few nanoseconds is utilized to detect ions.

The secondary ion yield depends directly on the ionization probability. The ionization probability in turn depends on (i) the element/compound, (ii) the chemical environment and (iii) the instrument setup/parameters. To account for varying instrument sensitivities for different elements in a given condition a Relative Sensitivity Factor (RSF) is determined by measuring well known reference samples under the same conditions.

I.10.2 Wavelength Dispersive X-ray Fluorescence (WDXRF)

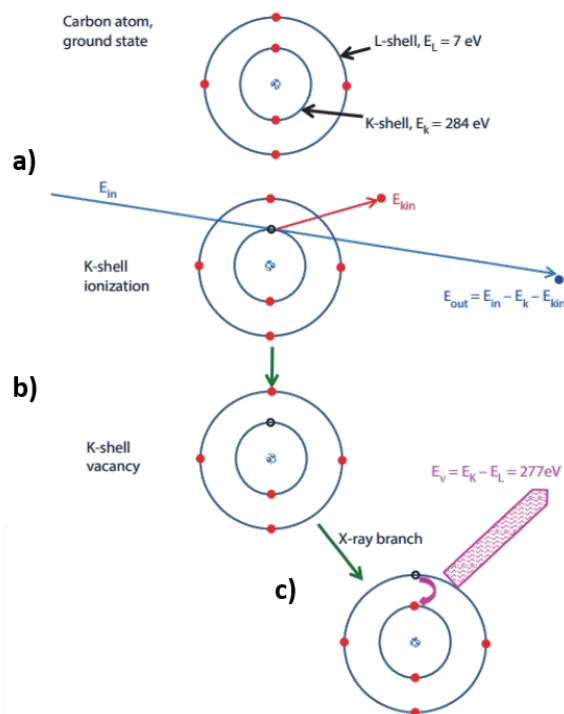


Figure II.22: Schematic diagram depicting the emission of characteristic X-ray radiation. [54]

Wavelength Dispersive X-Ray Fluorescence (WDXRF) uses the characteristic X-ray of an atom created when a core shell electron is ionized, shown in **Figure II.22 (a)** by inelastically scattering with a X-ray photon. The excited ionized state relaxes by filling the core shell vacancy with an electron from a valence orbital, shown in **Figure II.22 (b)**. When the electron from the valence orbital falls into the core shell, radiation is emitted which is specific to the energy difference between the core and valence shells, shown in **Figure II.22 (c)**. These energy levels are specific to each element of the periodic table and enable, therefore, to identify the specimen's composition. Energy dispersive X-Ray Fluorescence directly monitors the energy of the radiation with a detector. This results in a limit resolution (FWHM $>150 \text{ eV}$ [55]) of the various energies and might lead to some inaccurate determination of the composition. To overcome this limitation, WDXRF takes advantage of Bragg's equation, shown in **Equation (I.7.11)** in **Section XRD Introduction**, by using an analyzing crystal that results in some constructive diffraction (26 eV FWHM [55]). By positioning the detector on a goniometer, a broad range of energies is probed.

In the current study, a Rigaku AZX400 XRF spectrometer was used, with a Rhodium target X-ray tube and a detector mounted to a goniometer. The intensities of Si- K_α , Sn- L_α and P- K_α lines were collected for intrinsic, boron or phosphorous doped (Si)GeSn layers.

I.10.3 Energy Dispersive X-ray Spectroscopy (EDX)

Energy Dispersive X-Ray (EDX) uses the characteristic X-ray radiation emitted when a focused ion beam is in-elastically scattered by a specimen, as shown in **Figure II.22**. EDX is commonly used together with SEM or TEM to obtain nanometer scale maps of the composition in addition to topologic and crystallographic information.

I.10.4 X-ray Photoelectron Spectroscopy (XPS)

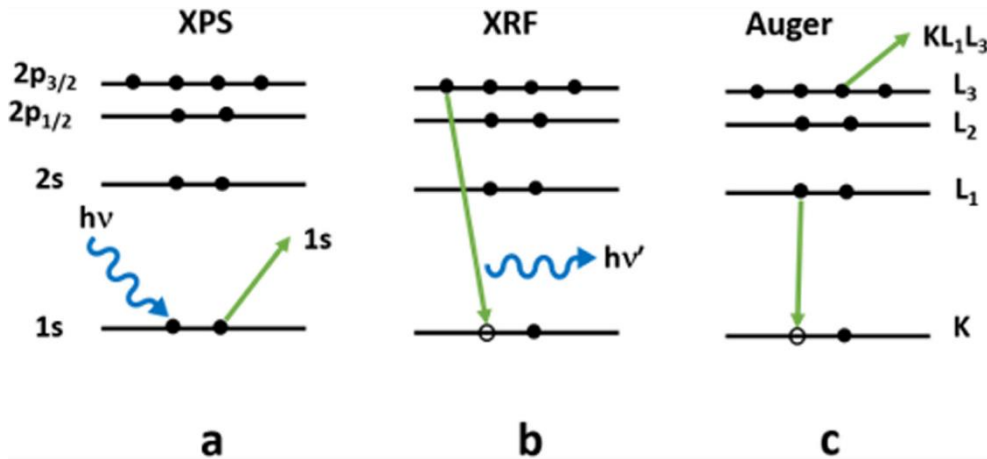


Figure II.23: Schematic diagram depicting various mechanisms occurring when X-ray photons interact with a specimen. [56]

X-ray Photoelectron Spectroscopy (XPS) is based on the photoelectric effect first discovered by Hertz and formally described by Einstein. A monochromatic X-ray source is used to create X-ray photons with a specific energy below 6 keV. These X-ray photons inelastically scatter with a core electron of a specimen's atom, which is ionized, as shown in **Figure II.23 (a)**. Ionized electrons are, then, detected. The detected kinetic energy E_{kin} of the ionized core electron is dependent on the X-ray photons energies with its frequency ν_{Photon} , the binding energy of the core electron E_{bind} and the spectrometer work function ϕ_{Work} , shown in **Equation (I.10.1)**.

$$E_{\text{kin}} = E_{\text{bind}} + \phi_{\text{Work}} - h\nu_{\text{Photon}} \quad (\text{I.10.1})$$

This allows to quantitatively determine the element and the orbit of the electron's origin from the XPS peak. The core shell's vacancy is filled by a valence electron. This results in the release of energy either via X-ray fluorescence, discussed in the previous section, shown in **Figure II.23 (b)** or by releasing a valence electron, called Auger electron, shown in **Figure II.23 (c)**. Auger electrons are detected and their kinetic energy gives information about the state of the ejected core electron, the state of the ejected valence electron and the state of the outer shell electron that filled the core vacancy.

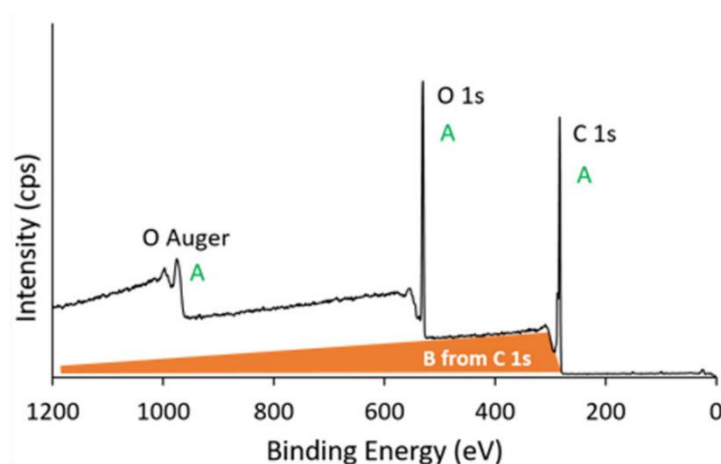


Figure II.24: Example of a X-ray Photoelectron Spectroscopy (XPS) spectrum. [56] The background caused by in-elastic and elastic scattering of the ionized electrons inside the specimen is shown in orange for the C1s XPS peak.

XPS is a surface sensitive characterization method, even though X-ray photons penetrate the specimen over a few μm . This is due to in-elastic and elastic scattering of ionized electrons inside the specimen, resulting in some kinetic energy loss. These ionized electrons lead to some background in the XPS spectra, shown in **Figure II.24**. Electrons that do not scatter and, therefore, contribute to XPS peaks can be observed. The surface sensitivity at a given thickness d is governed by Beer's law for a given attenuation λ , shown in **Equation (I.10.2)**.

$$I = I_0 e^{-\frac{d}{\lambda}} \quad (\text{I.10.2})$$

The attenuation can be estimated by the inelastic mean free path between two scattering events. A surface sensitivity of 10 nm (surface normal sampling/information depth) is typically obtained, with the collection of 95% of all emitted electrons. Due to the temperature dependence of the attenuation length, the information depth can be increased by decreasing the kinetic energy of X-ray photons.

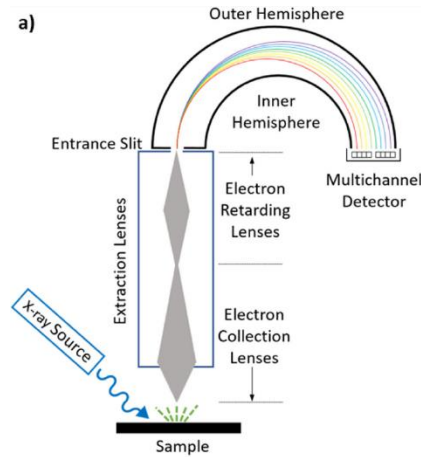


Figure II.25: Typical measurement setup used for X-ray Photoelectron Spectroscopy (XPS). [56]

To perform XPS measurements, an X-ray source, stage, an extraction lens, an analyzer to separate the various probed energies and a detector are required. A typical XPS tool setup is shown in **Figure II.25**. Usually, XPS tools are operated under ultra-high vacuum to increase the electron's free path and reduce surface contamination.

I.11 Electrical Characterization Techniques

I.11.1 Four Point Probe measurements (4PP)

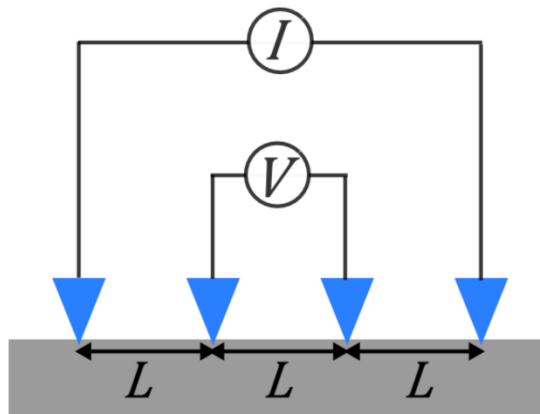


Figure II.26: Typical setup used for Four Point Probe measurements (4PP). [20]

To characterize the electrical resistance of a uniform thin film, its sheet resistance, e.g. the lateral resistance per square, is measured by Four Point Probe (4PP) measurements thanks to four uniformly spaced (spacing L), aligned tips. A current I is applied to the outer two tips and the voltage drop V between the inner two tips is measured. This enables to measure the sheet resistance without any contributions of the contact resistance. If the layer thickness t is

significantly smaller than the tip spacing L , the resistivity can be calculated from the sheet resistance, as shown in **Equation (I.11.1)**.

$$R_S = \frac{\rho}{t} = \Gamma \frac{V}{I} \tag{ I.11.1 }$$

Γ is a geometrical factor due to the point's shape and it is equal to $\Gamma = \frac{\ln 2}{\pi}$. In the present studies, a WS3000 NAPSON tool was used with a point-to-point spacing of 1 mm and a tip curvature around 150 μm .

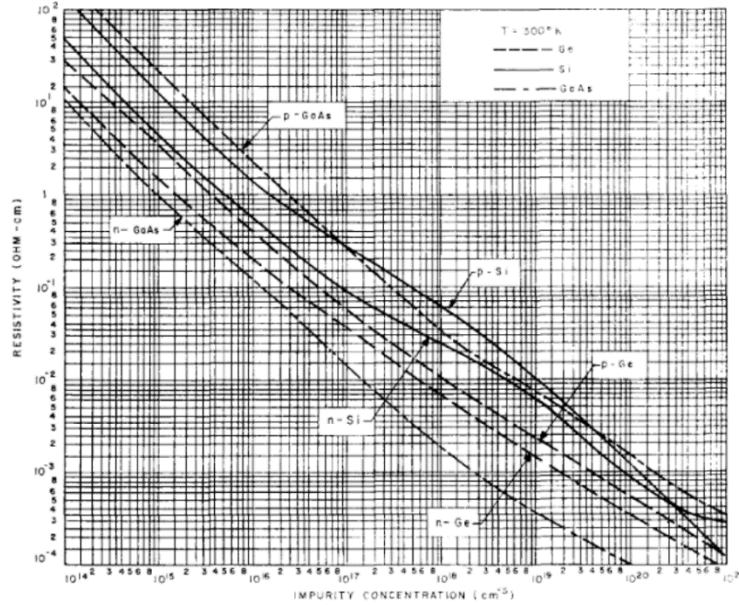


Figure II.27: Sze's resistivity vs. impurity concentration curve for Si, Ge and GaAs. [57]

The resistivity ρ is converted to an active carrier concentration n using Sze's resistivity vs. impurity concentration curve, as shown in **Figure II.27**. [57] To obtain reliable values with this method, p-n-junctions are required. n-type and p-type pure Ge curves were assumed to be valid for (Si)GeSn, as there were then moderate amounts of Si and Sn in Ge.

I.11.2 Electrochemical Capacitance Voltage (ECV) profiling

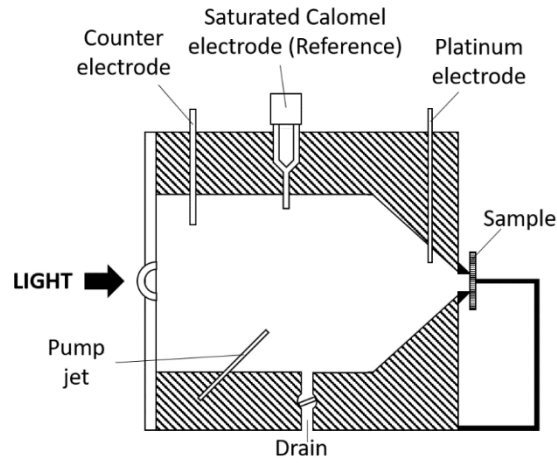


Figure II.28: Typical measurement setup used for Electrochemical Capacitance-Voltage (ECV). [58]

Electrochemical Capacitance-Voltage (ECV) measurements use an electrolyte to form a Schottky junction with a probed semiconductor to perform Capacitance-Voltage (CV) measurements. In addition to CV measurements, the electrolyte is used to etch the semiconductor. A typical ECV measurement setup is shown in **Figure II.28**. The electrolyte, contained in an electrochemical cell, is in contact with the semiconductor via a small seal ring opening with a contact area A . By applying a reverse bias V , the surface region of area A is depleted of majority carriers. This allows to access the ionized dopant concentrations because, in the depleted region, only ionized donors and electrically active defects or traps contribute to CV measurements. The applied bias V causes a potential drop between a probed semiconductor and a platinum electrode, which is measured with respect to a reference saturated calomel electrode. The capacitance C and the derivative of the capacitance $\frac{\partial C}{\partial V}$ are measured by modulating the applied bias with a high frequency. By measuring both the capacitance C and the derivative of the capacitance $\frac{\partial C}{\partial V}$, the capacitance and the ionized concentration are determined according to **Equations (I.11.2)** and **(I.11.3)**.

$$\frac{1}{C^2} = \frac{2(V_{fb} - V)}{\epsilon_r \epsilon_0 q N^* A^2} \quad (\text{I.11.2})$$

$$N^* = \frac{C^3}{\epsilon_r \epsilon_0 q A^2 \frac{\partial C}{\partial V}} \quad (\text{I.11.3})$$

Where V_{fb} is the flatband voltage, ϵ_r the relative permittivity, ϵ_0 the vacuum permittivity and q the electron charge. The (intrinsic) carrier concentration is influenced by deep states, which might lead to its overestimation.

Standard CV measurement's depth resolution is limited by the depletion width w_d . Continuous measurement-etch cycles extend the depth resolution beyond the depletion width w_d and depth dependent dopant profiles are recorded. Etching is achieved by supplying holes. A forward bias is sufficient to supply holes in p-type semiconductors. In n-type semiconductors, electron-hole pairs are created by illumination with an energy greater than the band gap energy $E_{ill} > E_g$. The electron-hole pairs are then separated by reverse biasing the Schottky junction to supply holes to the etching process. The current between the semiconductor and counter electrode I_{dis} controls the etching step and the etch depth w_{etch} is determined by Faraday's law, shown in **Equation (I.11.4)**.

$$w_{etch} = \frac{M}{ZF\rho A} \int I_{dis} dt \quad (\text{I.11.4})$$

Where Z accounts for the dissolution valency, F is the Faraday's constant, ρ the semiconductor's density and M the semiconductor's molecular weight. By adding the depletion depth w_d to the etch depth w_{etch} the total measurement depth w_{total} is obtained.

I.11.3 Transmission Line Method (TLM)

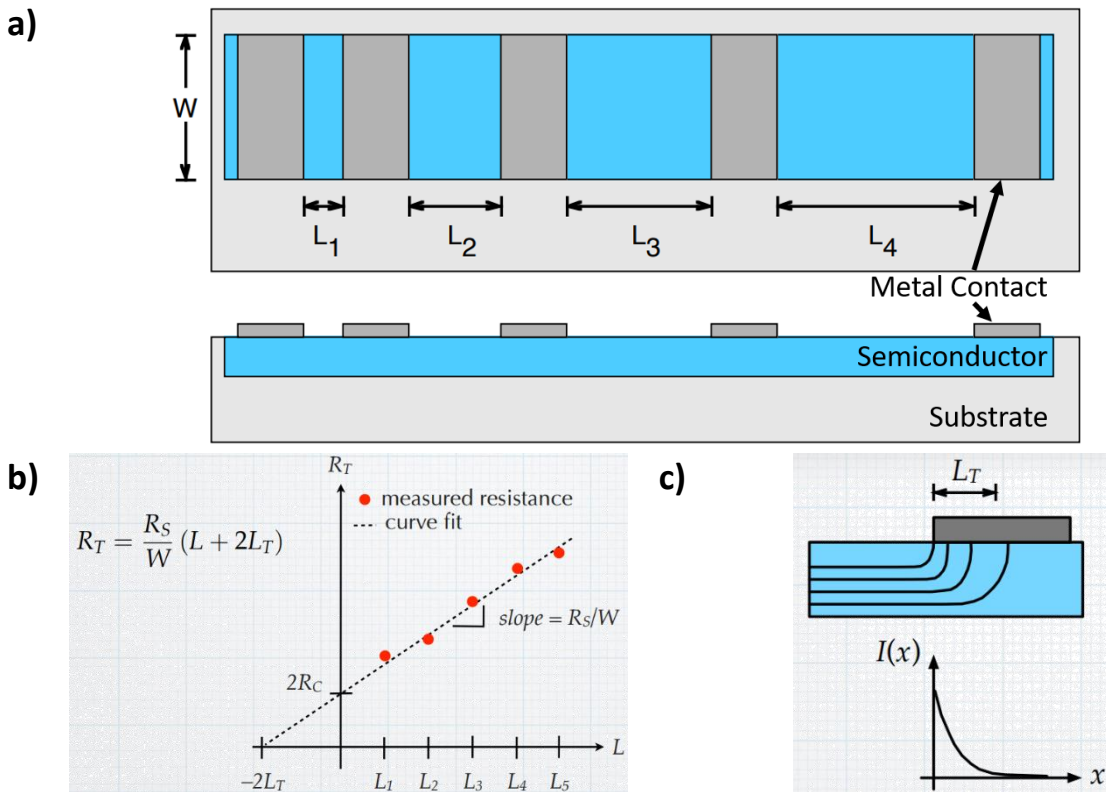


Figure II.29: (a) Schematic of a typical sample layout for Transmission Line Measurement (TLM), (b) typical total resistance R_T vs. contact distance L graph obtained from TLM (b) and (c) schematic of current crowding and the corresponding current distribution graph. [59]

Transmission Line Measurement were proposed by Shockley [60] to determine the contact resistance of semiconductors by forming contacts with the same width W at various distances L on a semiconductor, shown in **Figure II.29 (a)**. By plotting the total resistance R_T against the contact distance L , shown in **Figure II.29 (b)**, the sheet resistance R_S can be determined from the slope and the y-axis intercept corresponds to $2R_C$ with the contact resistance R_C . The current flow is uniform in the semiconductor, but not when the current flows into the semiconductor. Current crowding then occurs and the current flow reduces exponentially with a characteristic transfer length L_T , shown in **Figure II.29 (c)**. The transfer length is the length an electron or hole travels underneath a contact before it flows into the contact.

I.12 Conclusion

Reduced Pressure Chemical Vapour Deposition (RP-CVD) was the growth technique used for the current studies. Its working principle and the tool were introduced. Because the growth of (Si)GeSn is complex, an overview of growth mechanisms was given.

To achieve high dopant activation in (Si)GeSn, an ultrafast non-equilibrium method was required, Nanosecond Laser Annealing (NLA) fulfills this requirement by using nanosecond laser pulses, reaching high temperatures and facilitating high dopant activation. To understand the annealing process, in-situ Time Resolved Reflectivity (TRR) measurements were performed, which were explained in detail.

Characterization techniques like X-ray Diffraction (XRD), Atomic Force Microscopy (AFM), Transmission Electron Microscopy (TEM), Secondary Ion Mass Spectroscopy (SIMS) and Electrochemical Capacitance-Voltage (ECV), used to obtain crystalline, morphological, compositional and electrical information, were also described.

The information gained from the various characterization methods helped us in optimizing processes and material quality and thus improve device performances, as shown in the following.

References

- [1] C. H. L. Goodman, "Direct-gap group IV semiconductors based on tin," *IEE Proc. Solid State Electron Devices*, vol. 129, no. 5, p. 189, 1982, doi: 10.1049/ip-i-1.1982.0043.
- [2] S. I. Shah, J. E. Greene, L. L. Abels, Q. Yao, and P. M. Raccach, "Growth of single-crystal metastable Ge_{1-x}Sn_x alloys on Ge(100) and GaAs(100) substrates," *J. Cryst. Growth*, vol. 83, no. 1, pp. 3–10, May 1987, doi: 10.1016/0022-0248(87)90495-7.
- [3] G. He and H. A. Atwater, "Synthesis of epitaxial Sn_xGe_{1-x} alloy films by ion-assisted molecular beam epitaxy," *Nucl. Instrum. Methods Phys. Res. Sect. B Beam Interact. Mater. At.*, vol. 106, no. 1–4, pp. 126–132, Dec. 1995, doi: 10.1016/0168-583X(95)00690-7.
- [4] S. Wirths, D. Buca, and S. Mantl, "Si–Ge–Sn alloys: From growth to applications," *Prog. Cryst. Growth Charact. Mater.*, vol. 62, no. 1, pp. 1–39, Mar. 2016, doi: 10.1016/j.pcrysgrow.2015.11.001.
- [5] B. Vincent *et al.*, "Undoped and *in-situ* B doped GeSn epitaxial growth on Ge by atmospheric pressure-chemical vapor deposition," *Appl. Phys. Lett.*, vol. 99, no. 15, p. 152103, Oct. 2011, doi: 10.1063/1.3645620.
- [6] S. Wirths *et al.*, "Lasing in direct-bandgap GeSn alloy grown on Si," *Nat. Photonics*, vol. 9, no. 2, pp. 88–92, Feb. 2015, doi: 10.1038/nphoton.2014.321.
- [7] B. S. Meyerson, "Low-temperature Si and Si:Ge epitaxy by ultrahigh-vacuum/chemical vapor deposition: Process fundamentals," *IBM J. Res. Dev.*, vol. 34, no. 6, pp. 806–815, Nov. 1990, doi: 10.1147/rd.346.0806.
- [8] T. O. Sedgwick, P. D. Agnello, and D. A. Grützmacher, "Effects of Trace Surface Oxidation in Low Temperature Epitaxy Grown from Dichlorosilane," *J. Electrochem. Soc.*, vol. 140, no. 12, pp. 3684–3688, Dec. 1993, doi: 10.1149/1.2221150.
- [9] S. D. Kevan, "Surface states and reconstruction on Ge(001)," *Phys. Rev. B*, vol. 32, no. 4, pp. 2344–2350, Aug. 1985, doi: 10.1103/PhysRevB.32.2344.
- [10] H. Bender, S. Verhaverbeke, M. Caymax, O. Vatel, and M. M. Heyns, "Surface reconstruction of hydrogen annealed (100) silicon," *J. Appl. Phys.*, vol. 75, no. 2, pp. 1207–1209, Jan. 1994, doi: 10.1063/1.356478.
- [11] M. Bauer *et al.*, "Synthesis of ternary SiGeSn semiconductors on Si(100) via Sn_xGe_{1-x} buffer layers," *Appl. Phys. Lett.*, vol. 83, no. 11, pp. 2163–2165, Sep. 2003, doi: 10.1063/1.1606104.
- [12] D. Bour, Z. Yang, and C. Chua, "Simple technique for measuring the filled volume of liquid or solid CVD precursor chemicals in bubblers," *J. Cryst. Growth*, vol. 310, no. 10, pp. 2673–2677, May 2008, doi: 10.1016/j.jcrysgro.2008.01.038.
- [13] D. R. Stull, "Vapor Pressure of Pure Substances. Organic and Inorganic Compounds," *Ind. Eng. Chem.*, vol. 39, no. 4, pp. 517–540, Apr. 1947, doi: 10.1021/ie50448a022.
- [14] J. Margetis, S.-Q. Yu, B. Li, and J. Tolle, "Chemistry and kinetics governing hydride/chloride chemical vapor deposition of epitaxial Ge_{1-x}Sn_x," *J. Vac. Sci. Technol. A*, vol. 37, no. 2, p. 021508, Mar. 2019, doi: 10.1116/1.5055620.
- [15] J. Aubin and J. M. Hartmann, "GeSn growth kinetics in reduced pressure chemical vapor deposition from Ge₂H₆ and SnCl₄," *J. Cryst. Growth*, vol. 482, pp. 30–35, Jan. 2018, doi: 10.1016/j.jcrysgro.2017.10.030.
- [16] J. Olivares, J. Sangrador, A. Rodríguez, and T. Rodríguez, "Effect of Deposition Parameters on the Characteristics of Low-Pressure Chemical Vapor Deposited SiGe Films Grown from Si[₂]H[₆] and GeH[₄]," *J. Electrochem. Soc.*, vol. 148, no. 10, p. C685, 2001, doi: 10.1149/1.1399277.

- [17] G. H. Coccoletzi, P. H. Hernández, and N. Takeuchi, “First principles total energy studies of the adsorption of germane on Ge(001)-c(2×4),” *Thin Solid Films*, vol. 490, no. 2, pp. 196–200, Nov. 2005, doi: 10.1016/j.tsf.2005.04.053.
- [18] J. Venturini, “Laser Thermal Annealing: Enabling ultra-low thermal budget processes for 3D junctions formation and devices,” in *2012 12th International Workshop on Junction Technology*, Shanghai, May 2012, pp. 57–62. doi: 10.1109/IWJT.2012.6212810.
- [19] J. Venturini *et al.*, “Excimer laser thermal processing of ultra-shallow junction: laser pulse duration,” *Thin Solid Films*, vol. 453–454, pp. 145–149, Apr. 2004, doi: 10.1016/j.tsf.2003.11.087.
- [20] L. Dagault, “Investigation of Si_{1-x}Gex epilayers behavior upon Ultraviolet Nanosecond Laser Annealing,” Université Toulouse 3 Paul Sabatier, 2021. [Online]. Available: hal.laas.fr/tel-03356506
- [21] R. Delmdahl and R. Pätzl, “Excimer laser technology trends,” *J. Phys. Appl. Phys.*, vol. 47, no. 3, p. 034004, Jan. 2014, doi: 10.1088/0022-3727/47/3/034004.
- [22] Y. Jin, Y. Zhao, and Y. Jiang, “Microlens beam homogenizer for excimer laser processing,” *J. Laser Appl.*, vol. 28, no. 2, p. 022601, May 2016, doi: 10.2351/1.4944448.
- [23] K. Huet, I. Toque-Tresonne, F. Mazzamuto, T. Emeraud, and H. Besaucele, “Laser Thermal Annealing: A low thermal budget solution for advanced structures and new materials,” in *2014 International Workshop on Junction Technology (IWJT)*, Shanghai, China, May 2014, pp. 1–6. doi: 10.1109/IWJT.2014.6842020.
- [24] K. Huet, F. Mazzamuto, T. Tabata, I. Toqué-Tresonne, and Y. Mori, “Doping of semiconductor devices by Laser Thermal Annealing,” *Mater. Sci. Semicond. Process.*, vol. 62, pp. 92–102, May 2017, doi: 10.1016/j.mssp.2016.11.008.
- [25] D. H. Auston, C. M. Surko, T. N. C. Venkatesan, R. E. Slusher, and J. A. Golovchenko, “Time-resolved reflectivity of ion-implanted silicon during laser annealing,” *Appl. Phys. Lett.*, vol. 33, no. 5, pp. 437–440, Sep. 1978, doi: 10.1063/1.90369.
- [26] C. Hammond, *The basics of crystallography and diffraction*, Fourth edition. Oxford: Oxford University Press, 2015.
- [27] D. S. Sivia, *Elementary scattering theory: for X-ray and neutron users*. Oxford ; New York: Oxford University Press, 2011.
- [28] M. A. Herman and H. Sitter, *Molecular Beam Epitaxy: Fundamentals and Current Status*, 2., nd Ed. 1996. Berlin: Springer Berlin, 2013.
- [29] W. J. Bartels, J. Hornstra, and D. J. W. Lobeek, “X-ray diffraction of multilayers and superlattices,” *Acta Crystallogr. A*, vol. 42, no. 6, pp. 539–545, Nov. 1986, doi: 10.1107/S0108767386098768.
- [30] D. K. Bowen and B. K. Tanner, *X-Ray Metrology in Semiconductor Manufacturing*, 0 ed. CRC Press, 2018. doi: 10.1201/9781315222035.
- [31] J. M. Hartmann *et al.*, “Reduced pressure chemical vapour deposition of SiGe virtual substrates for high mobility devices,” *Semicond. Sci. Technol.*, vol. 19, no. 3, pp. 311–318, Mar. 2004, doi: 10.1088/0268-1242/19/3/004.
- [32] J. M. Hartmann, B. Gallas, J. Zhang, and J. J. Harris, “Gas-source molecular beam epitaxy of SiGe virtual substrates: II. Strain relaxation and surface morphology,” *Semicond. Sci. Technol.*, vol. 15, no. 4, pp. 370–377, Apr. 2000, doi: 10.1088/0268-1242/15/4/311.
- [33] F. Gencarelli *et al.*, “Crystalline Properties and Strain Relaxation Mechanism of CVD Grown GeSn,” *ECS J. Solid State Sci. Technol.*, vol. 2, no. 4, pp. P134–P137, 2013, doi: 10.1149/2.011304jss.
- [34] V. Holy, U. Pietsch, and T. Baumbach, *High-Resolution X-Ray Scattering from Thin Films and Multilayers*, vol. 149. Berlin, Heidelberg: Springer Berlin Heidelberg, 1999. doi: 10.1007/BFb0109385.

- [35] J. M. Hartmann *et al.*, “Reduced pressure–chemical vapor deposition of Ge thick layers on Si(001) for 1.3–1.55- μm photodetection,” *J. Appl. Phys.*, vol. 95, no. 10, pp. 5905–5913, May 2004, doi: 10.1063/1.1699524.
- [36] R. E. Camacho-Aguilera *et al.*, “An electrically pumped germanium laser,” *Opt. Express*, vol. 20, no. 10, p. 11316, May 2012, doi: 10.1364/OE.20.011316.
- [37] D. D. Cannon *et al.*, “Tensile strained epitaxial Ge films on Si(100) substrates with potential application in *L*-band telecommunications,” *Appl. Phys. Lett.*, vol. 84, no. 6, pp. 906–908, Feb. 2004, doi: 10.1063/1.1645677.
- [38] T. K. P. Luong *et al.*, “Control of tensile strain and interdiffusion in Ge/Si(001) epilayers grown by molecular-beam epitaxy,” *J. Appl. Phys.*, vol. 114, no. 8, p. 083504, Aug. 2013, doi: 10.1063/1.4818945.
- [39] G. Capellini, M. De Seta, P. Zaumseil, G. Kozlowski, and T. Schroeder, “High temperature x ray diffraction measurements on Ge/Si(001) heterostructures: A study on the residual tensile strain,” *J. Appl. Phys.*, vol. 111, no. 7, p. 073518, Apr. 2012, doi: 10.1063/1.3702443.
- [40] N. Jalili and K. Laxminarayana, “A review of atomic force microscopy imaging systems: application to molecular metrology and biological sciences,” *Mechatronics*, vol. 14, no. 8, pp. 907–945, Oct. 2004, doi: 10.1016/j.mechatronics.2004.04.005.
- [41] M. Basso, L. Giarre, M. Dahleh, and I. Mezic, “Numerical analysis of complex dynamics in atomic force microscopes,” in *Proceedings of the 1998 IEEE International Conference on Control Applications (Cat. No.98CH36104)*, Trieste, Italy, 1998, vol. 2, pp. 1026–1030. doi: 10.1109/CCA.1998.721613.
- [42] R.-F. Fung and S.-C. Huang, “Dynamic Modeling and Vibration Analysis of the Atomic Force Microscope,” *J. Vib. Acoust.*, vol. 123, no. 4, pp. 502–509, Oct. 2001, doi: 10.1115/1.1389084.
- [43] M. V. Salapaka, D. J. Chen, and J. P. Cleveland, “Stability and sensitivity analysis of periodic orbits in tapping mode atomic force microscopy,” in *Proceedings of the 37th IEEE Conference on Decision and Control (Cat. No.98CH36171)*, Tampa, FL, USA, 1998, vol. 2, pp. 2047–2052. doi: 10.1109/CDC.1998.758635.
- [44] A. Sebastien, M. V. Salapaka, D. J. Chen, and J. P. Cleveland, “Harmonic analysis based modeling of tapping-mode AFM,” in *Proceedings of the 1999 American Control Conference (Cat. No. 99CH36251)*, San Diego, CA, USA, 1999, pp. 232–236 vol.1. doi: 10.1109/ACC.1999.782775.
- [45] D. B. Williams and C. B. Carter, *Transmission Electron Microscopy*. Boston, MA: Springer US, 2009. doi: 10.1007/978-0-387-76501-3.
- [46] Y. Jiang *et al.*, “Electron ptychography of 2D materials to deep sub-ångström resolution,” *Nature*, vol. 559, no. 7714, pp. 343–349, Jul. 2018, doi: 10.1038/s41586-018-0298-5.
- [47] L. de Broglie, “XXXV. A tentative theory of light quanta,” *Lond. Edinb. Dublin Philos. Mag. J. Sci.*, vol. 47, no. 278, pp. 446–458, Feb. 1924, doi: 10.1080/14786442408634378.
- [48] E. Abbe, “XV.-The Relation of Aperture and Power in the Microscope (continued)*,” *J. R. Microsc. Soc.*, vol. 3, no. 6, pp. 790–812, Dec. 1883, doi: 10.1111/j.1365-2818.1883.tb05956.x.
- [49] G. McMullan, A. R. Faruqi, and R. Henderson, “Direct Electron Detectors,” in *Methods in Enzymology*, vol. 579, Elsevier, 2016, pp. 1–17. doi: 10.1016/bs.mie.2016.05.056.
- [50] J. C. Vickerman, “ToF-SIMS—an overview,” *ToF-SIMS: surface analysis by mass spectrometry*, pp. 1–40, 2001.
- [51] S. G. Alikhanov, “A NEW IMPULSE TECHNIQUE FOR ION MASS MEASUREMENTS,” *Soviet Phys. JETP*, Apr. 01, 1957.

- [52] E. Niehuis, T. Heller, H. Feld, and A. Benninghoven, "Design and performance of a reflectron based time-of-flight secondary ion mass spectrometer with electrodynamic primary ion mass separation," *Journal of Vacuum Science & Technology A*, p. 1243, Jun. 04, 1998.
- [53] X. Tang, R. Beavis, W. Ens, F. Lafortune, B. Schueler, and K. G. Standing, "A secondary ion time-of-flight mass spectrometer with an ion mirror," *Int. J. Mass Spectrom. Ion Process.*, vol. 85, no. 1, pp. 43–67, Jul. 1988, doi: 10.1016/0168-1176(88)83004-0.
- [54] J. I. Goldstein, D. E. Newbury, J. R. Michael, N. W. M. Ritchie, J. H. J. Scott, and D. C. Joy, *Scanning Electron Microscopy and X-Ray Microanalysis*. New York, NY: Springer New York, 2018. doi: 10.1007/978-1-4939-6676-9.
- [55] "Rigaku AZX400 Data Sheet."
- [56] F. A. Stevie and C. L. Donley, "Introduction to x-ray photoelectron spectroscopy," *J. Vac. Sci. Technol. A*, vol. 38, no. 6, p. 063204, Dec. 2020, doi: 10.1116/6.0000412.
- [57] S. M. Sze and J. C. Irvin, "Resistivity, mobility and impurity levels in GaAs, Ge, and Si at 300°K," *Solid-State Electron.*, vol. 11, no. 6, pp. 599–602, Jun. 1968, doi: 10.1016/0038-1101(68)90012-9.
- [58] S. Y. Wang, J. Simpson, K. A. Prior, and B. C. Cavenett, "Electrochemical capacitance-voltage profiling of *n*-type ZnSe," *J. Appl. Phys.*, vol. 72, no. 11, pp. 5311–5317, Dec. 1992, doi: 10.1063/1.352016.
- [59] C. Honsberg and S. Bowden, "TLM measurement." pveducation.org/pvcdrom/tlm-measurement
- [60] W. Shockley, "Research and investigation of inverse epitaxial UHF power transistors," *Report No. AI-TOR-64-20*, Wright-Patterson Air Force Base, Ohio, Sep. 1964.

Chapter III : In-Situ B and P Doping of GeSn

Chapter III: In-Situ B and P Doping of GeSn

Chapter III: In-Situ B and P Doping of GeSn	56
III.1 Introduction	Error! Bookmark not defined.
III.2 Confirmation of new growth parameters.....	Error! Bookmark not defined.
III.3 Layer thickness and Sn content determination	Error! Bookmark not defined.
III.4 Incorporation of Sn and dopants into the GeSn lattice	Error! Bookmark not defined.
III.5 Catalytic impact of dopants on growth rate	Error! Bookmark not defined.
III.6 Surface morphology and roughness.....	Error! Bookmark not defined.
III.7 Conclusions.....	Error! Bookmark not defined.

Chapter III: In-Situ B and P Doping of GeSn

I.13 Introduction

In this chapter, an in-depth study of the in-situ doping of GeSn with Ge_2H_6 , SnCl_4 , B_2H_6 or PH_3 over a wide range of dopant precursor flows in our Reduced Pressure – Chemical Vapor Deposition (RP-CVD) cluster tool was performed. Those investigations, carried out at 349°C , 100 Torr, to prevent droplet formation on the surface and obtain smooth surfaces [1], [2], give new insights into the growth mechanisms of intrinsic and doped GeSn.

I.14 Confirmation of new growth parameters

In previous studies, notably by Aubin *et al.* [3], the Sn content in GeSn layers was altered by changing the growth temperature. Hence, to prove that this relationship remains unchanged over time, especially after a change of SnCl_4 cartridge and bubbler settings (in December 2019), we performed some undoped GeSn growth before switching over to in-situ doped GeSn.

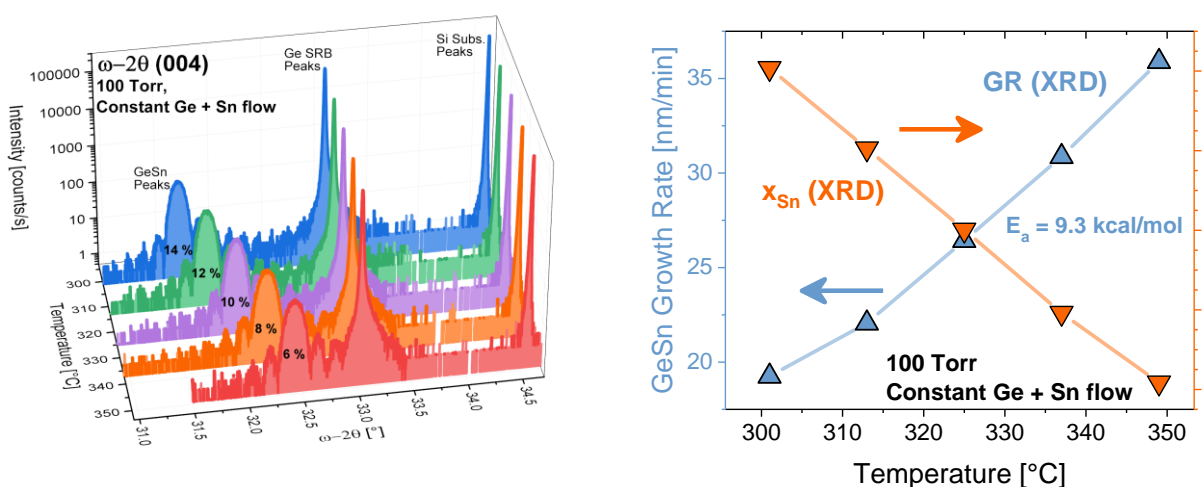


Figure III.1: (left) ω - 2θ scans around the (0 0 4) XRD order associated with pseudomorphic, 35 to 39 nm thick GeSn layers grown at 100 Torr with Ge_2H_6 + SnCl_4 in the 301°C – 349°C temperature range with the new SnCl_4 cartridge and bubbler settings. $F(\text{Ge}_2\text{H}_6)/F(\text{H}_2) = 7.92 \times 10^{-4}$, $F(\text{SnCl}_4)/F(\text{H}_2) = 4.69 \times 10^{-5}$. (right) GeSn growth rates and Sn contents in GeSn layers grown at various temperatures between 301°C and 349°C with the new SnCl_4 bubbler setup.

As in previous studies, the temperature was varied between 349°C and 301°C , while the chamber pressure was 100 Torr. The growth temperature was chosen to eliminate Sn surface

segregation and get rid of droplets. The 35 to 39 nm thick GeSn layers were grown on 2.5 μm thick Ge Strain Relaxed Buffers (SRBs). The $F(\text{Ge}_2\text{H}_6)/F(\text{H}_2)$ and the $F(\text{SnCl}_4)/F(\text{H}_2)$ mass-flow ratios (MFR) were constant at 7.92×10^{-4} and 4.69×10^{-5} . These parameters were the same as in Ref. [3], save for the SnCl_4 flow, which was 12% higher here (because of bubbler setting changes).

Conventional ω - 2θ scans around the (0 0 4) X-ray diffraction (XRD) order were performed to investigate the GeSn growth kinetics (see **Figure I.1 (left)**). All deposited layers were pseudomorphic and exhibited well-defined, intense layer peaks in XRD, with Pendellösung thickness fringes on both sides. As in previous studies, the Ge SRB peak was slightly asymmetric and shifted towards the Si substrate peak. This was due to the formation of an interfacial GeSi alloy during the short duration thermal cycling that followed the growth [2] and the slight tensile strain in the Ge SRBs, with a mean macroscopic degree of strain relaxation $R = 104\%$. This slight tensile strain was due to thermal expansion differences between Ge and Si, which came into play during the cooling-down to room temperature after growth. [4]–[7]

When the temperature was reduced, the GeSn peak moved away from the Ge SRB peak. This was due to a Sn content increase, from 6.1% up to 14.1%, determined by simulations based on the Takagi-Taupin's dynamical scattering theory. [8]

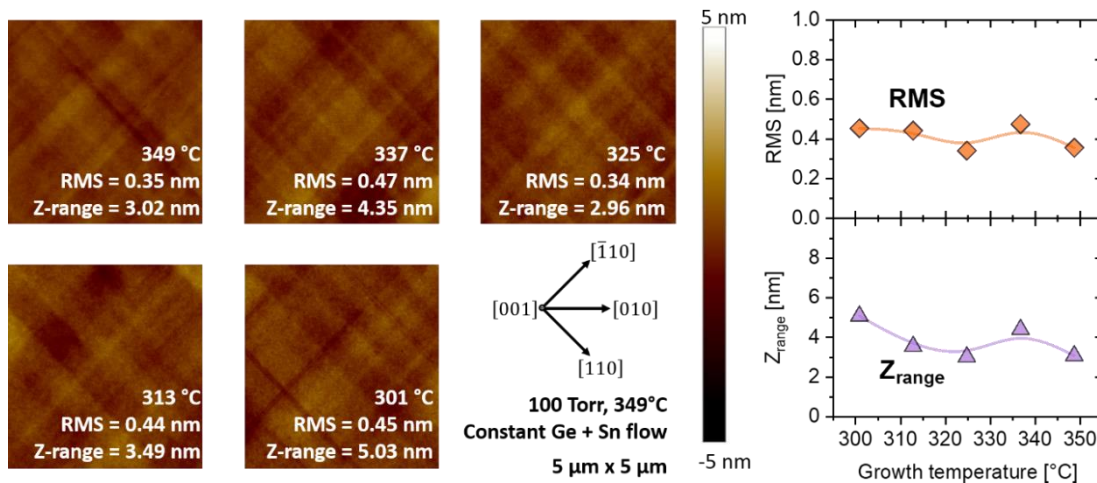


Figure III.2: (left) 5 μm x 5 μm AFM images of intrinsic GeSn layers grown at 100 Torr with $\text{Ge}_2\text{H}_6 + \text{SnCl}_4$ in the 301°C – 349°C temperature range with the new SnCl_4 bubbler setup. $F(\text{GeH}_4)/F(\text{H}_2) = 7.92 \times 10^{-4}$, $F(\text{SnCl}_4)/F(\text{H}_2) = 4.69 \times 10^{-5}$. (right) Corresponding RMS roughness (top) and Z range (bottom) at various temperatures between 301°C and 349°C.

The Sn content changes with a slope of $-1.75\% / 10^\circ\text{C}$ (see **Figure I.1 (right)**), a value close to the $-1.85\% / 10^\circ\text{C}$ value found by Aubin *et al.* [3] Meanwhile, the GeSn growth rate increases exponentially with the temperature (from 19 nm min^{-1} at 301°C up to 41 nm min^{-1} at 349°C), a clear sign that growth is thermally activated. Aubin *et al.* reported a growth rate increase from 15 up to 32 nm min^{-1} [3], i.e. growth rates lower than here. Changes in the bubbler settings, with 1.5% instead of 1% of SnCl_4 flowing out the bubbler, and 12% higher

SnCl_4 flows here than in Ref. [3] may partly explain those differences (indeed, higher SnCl_4 flows result in higher growth rates [3]). A slight temperature increase, by a few degrees, between 2016 [3] and now, cannot be excluded, however. An activation energy E_a of 9.3 kcal mol.⁻¹ can be extracted from **Figure I.1 (right)**. It is quite close to the 10.4 kcal mol.⁻¹ value found by Aubin *et al.* [3], outlining that growth kinetics remained similar.

All layers had smooth surfaces with cross hatches along the $\langle 110 \rangle$ directions, as shown by **Figure III.2** AFM images with $\langle 100 \rangle$ scan directions. This cross-hatch originated from the Ge SRBs on which the GeSn layers were pseudomorphically grown. [2], [3] We conclusively showed in Ref. [3] that a 30 nm thick $\text{Ge}_{0.85}\text{Sn}_{0.15}$ layer grown on a Ge SRB was fully pseudomorphic, although its surface exhibited a cross-hatch. There were indeed, in Fig. (1) of Ref. [3], multiple thickness fringes and a well-defined GeSn layer peak in the Omega-2Theta scan around the (0 0 4) XRD order (as in **Figure III.2** of the current study). Meanwhile, the Ge SRB and the GeSn layer had, once again in Fig. 1 of Ref. [3], the same in-plane lattice parameter in the (2 2 4) Reciprocal Space Map, demonstrating that the layer was indeed fully strained. The only exception was the GeSn layer grown at 301°C, which exhibited tiny holes. Aubin *et al.* [3] previously evidenced those holes, as well. They might be the emergence points of threading dislocations coming from the Ge SRB underneath. In addition, the overall surface coverage of the deposited layer on top of the substrate shrank for the GeSn layer grown at 301°C, without GeSn deposited at the edges of the wafer. This is not yet fully understood. Margetis *et al.* [9] outlined that, for the growth of GeSn at such low growth temperatures, it was necessary to form gas phase intermediates. It might thus be that, at such low temperatures and high SnCl_4 flows, the gas distribution close to the wafer edges was not right to create these intermediates, resulting in a lack of GeSn growth.

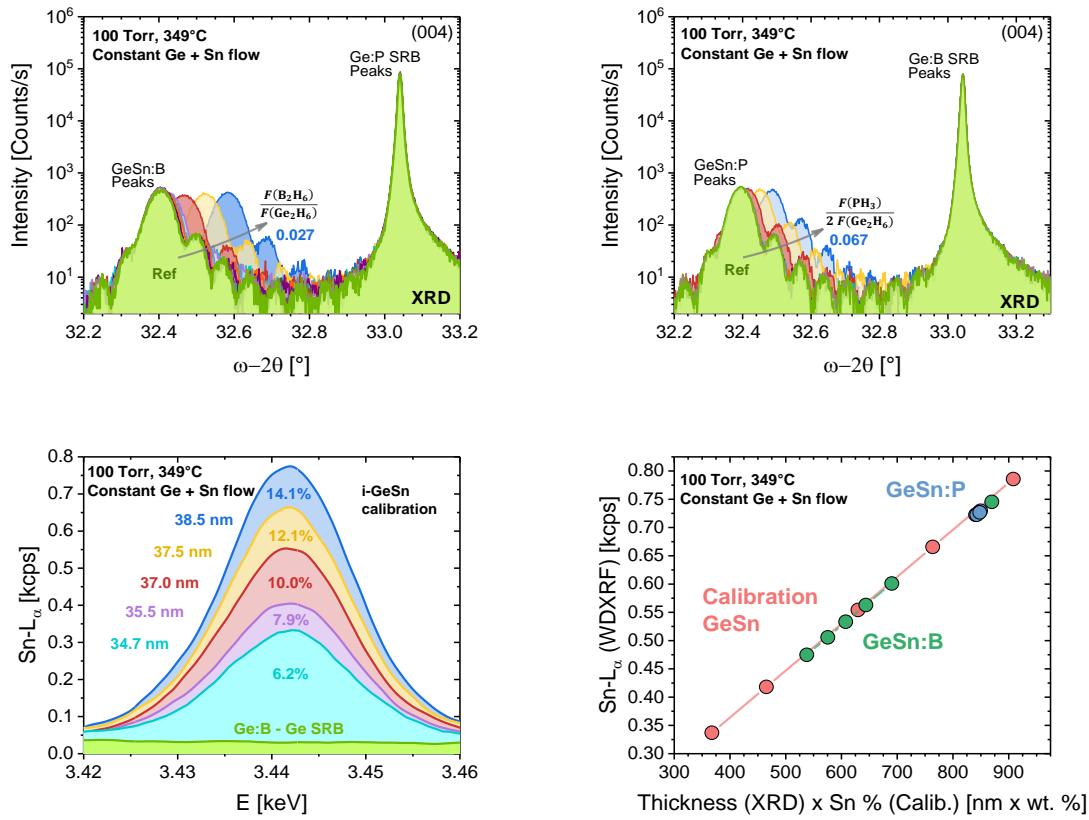
I.15 Layer thickness and Sn content determination


Figure III.3: (top left) $\omega-2\theta$ scans around the (0 0 4) XRD order for 61 nm to 80 nm thick GeSn:B layers grown on Ge SRBs with various diborane flows and (top right) 76 nm to 86 nm thick GeSn:P layers grown on Ge SRBs with various phosphine flows. (bottom left) Sn-L α lines of intrinsic GeSn layers grown on Ge SRBs at various temperatures. (bottom right) Sn-L α line intensity from WDXRF as a function of the product of the GeSn (GeSn:B, GeSn:P) layer thickness by its Sn content. WDXRF data points associated with (i) GeSn:B or GeSn:P layers grown at various dopant flows and (ii) intrinsic GeSn layers with various Sn contents all grown on Ge SRBs.

$\omega-2\theta$ scans around the (004) X-Ray Diffraction (XRD) order gave us access to the apparent Sn content and layer thickness in our in-situ doped layers, as shown in **Figure III.3 top left** for GeSn:B and **Figure III.3 top right** for GeSn:P. Thickness fringes on both sides of the GeSn:B and GeSn:P peaks outline the high crystalline quality of the layers grown and the presence of smooth surfaces / interfaces. When the $F(\text{B}_2\text{H}_6)/F(\text{Ge}_2\text{H}_6)$ and $F(\text{PH}_3)/2F(\text{Ge}_2\text{H}_6)$ MFRs increase from 0 up to 2.68×10^{-2} (GeSn:B) and from 0 to 6.71×10^{-2} (GeSn:P), the layer peak moves slightly towards the Ge SRB peak. This effect is more pronounced for the highest MFRs, with significant shifts towards higher incidence angles. The effect is more significant for GeSn:B than for GeSn:P. This is likely due to the smaller size of B ($a_B = 3.852 \text{ \AA}$) than P ($a_P = 5.014 \text{ \AA}$) atoms, resulting in higher amounts of strain compensation by substitutional incorporation of dopants into the GeSn lattice. Careful fits of the XRD layer peaks and fringes

on both sides yielded GeSn:B thicknesses between 61 nm and 80 nm and GeSn:P thicknesses between 76 nm and 86 nm.

Samples grown with the highest B₂H₆ and PH₃ dopant flows were probed by Rutherford Backscattering Spectrometry (RBS). Thicknesses and compositions trends were confirmed for GeSn:B and GeSn:P. Minimum channeling yields of 3.8% for GeSn:B and 7.5% for GeSn:P confirmed the good crystalline quality already evidenced by XRD.

As the GeSn peak position was determined by the Sn content and also the B or P substitutional concentrations, the actual layer composition could not be determined. Therefore, we conducted WDXRF measurements to unambiguously determine the Sn content. WDXRF yielded the real Sn content thanks to Sn-L_α line intensity measurements, shown in **Figure III.3 bottom left**. The actual Sn content can indeed be determined by plotting the Sn-L_α line intensity of the various GeSn layers as a function of the product of the layer thickness by the real Sn content (which is equal to the Sn content from XRD in intrinsic GeSn layers), as previously shown in Ref. [4]. The expected accuracy of the elemental composition is in the 1% range. Such an accuracy was demonstrated using similar strategies on different thin layered materials such as 2D – MoS₂ [5] and GeSbTe [6]. The calibration curve is shown in **Figure III.3 bottom right**. Intrinsic GeSn layers, with Sn contents ranging from 6% to 14% and GeSn layer thicknesses between 35 nm and 39 nm, were used as calibration samples [7]. Since the absorption of the Sn-L_α line and other matrix effects in the roughly 80 nm thick in-situ doped GeSn layers were negligible, we were able to determine the real Sn content in GeSn:B and GeSn:P layers from this calibration curve, as we knew the layer thickness from XRD.

I.16 Incorporation of Sn and dopants into the GeSn lattice

As the diborane or the phosphine flows increased, the apparent Sn content stayed at first roughly around 6.5%, as shown in **Figure III.4**. This value was the same for intrinsic GeSn, GeSn:B and GeSn:P, in contrast to previous literature findings. [10] As the flows reached the highest values ($F(\text{B}_2\text{H}_6)/F(\text{Ge}_2\text{H}_6) > 4.5 \times 10^{-3}$ and $F(\text{PH}_3)/2 * F(\text{Ge}_2\text{H}_6) > 1.1 \times 10^{-2}$), the apparent Sn content fell from 6.5% down to 4.6% for GeSn:B and from 6.6% down to 5.6% for GeSn:P. The real Sn content from WDXRF is also provided in **Figure III.4**. For GeSn:B, **Figure III.4 left**, the real Sn content stayed constant at around 6.5% and decreased only for the three highest $F(\text{B}_2\text{H}_6)/F(\text{Ge}_2\text{H}_6)$ MFRs, down to 4.9%. A similar behavior was found for GeSn:P, **Figure III.4 right**. For GeSn:P, the Sn content dropped from 6.6% down to 6.0% for the highest four $F(\text{PH}_3)/2 * F(\text{Ge}_2\text{H}_6)$ MFRs. For intermediate phosphine flows, we had a slight dip of the apparent Sn content, which might have been due to a switch from a flow of PH₃ heavily diluted in H₂ to a flow directly from the precursor bottle (i.e. the transition from a mixer in use to none).

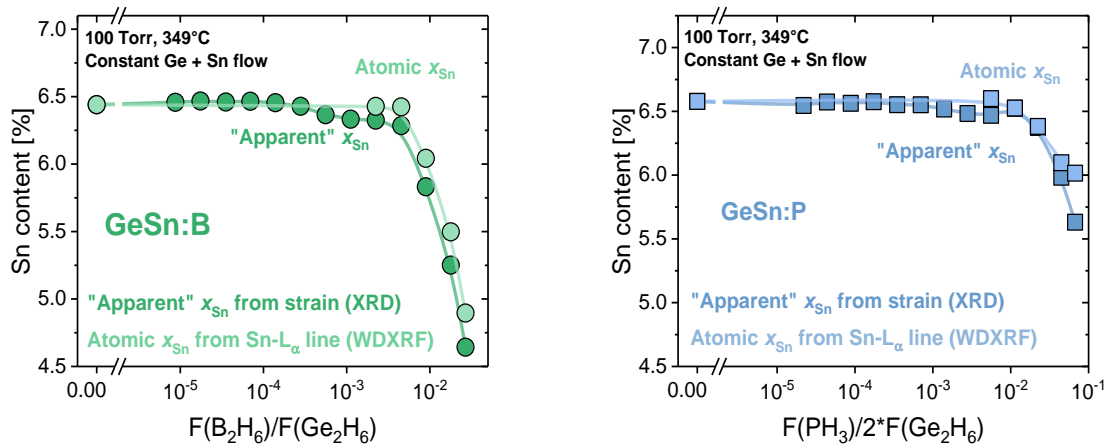


Figure III.4: Apparent and real Sn contents (from XRD and WDXRF, respectively) in GeSn:B (left) and GeSn:P (right) layers grown at 349°C, 100 Torr with various $F(B_2H_6)/F(Ge_2H_6)$ or $F(PH_3)/2 * F(Ge_2H_6)$ MFRs. The $F(Ge_2H_6)/F(H_2)$ and the $F(SnCl_4)/F(H_2)$ MFRs were constant at 7.92×10^{-4} and 4.69×10^{-5} , respectively.

We then calculated the substitutional B and P concentrations by transforming the difference between the apparent Sn contents from XRD and the real Sn contents from WDXRF (incorporation of smaller sized B and P atoms into doped GeSn layers), into substitutional B and P concentrations. This needs to be taken cautiously because of WDXRF and XRD measurement uncertainties. Therefore, we only extracted the substitutional concentrations for the highest two $F(B_2H_6)/F(Ge_2H_6)$ or $F(PH_3)/2 * F(Ge_2H_6)$ MFRs. The resulting values are estimations.

B substitutional concentrations, shown in Figure III.5 top left, were at most $5.2 \times 10^{19} \text{ cm}^{-3}$, i.e. a value nearly ten times lower than the $4.8 \times 10^{20} \text{ cm}^{-3}$ maxima in the literature for Ge:B grown at 350°C, 100 Torr with $Ge_2H_6 + B_2H_6$. [8] Such boron concentrations should nevertheless be high enough for use in GeSn photodiodes and light emitting devices. Substitutional P concentrations up to $2.2 \times 10^{20} \text{ cm}^{-3}$ were achieved for the highest phosphine flows (Figure III.5 top right). This was somewhat close to the highest substitutional P concentration, $4.1 \times 10^{20} \text{ cm}^{-3}$, in Ge:P grown at 350°C, 100 Torr with Ge_2H_6 [9]. PH_3 was diluted at 0.2% in H_2 in Ref. [9], instead of 1% here; however, a four times lower Ge_2H_6 flow was used for Ge:P than here, resulting in similar MFRs, in the end. We thus retained to some extent the P doping capabilities of Ge while benefiting from the specifics of GeSn, which can be grown reliably at 349°C with a better compatibility with high Sn content optically active stacks. We otherwise determined the atomic P concentrations inside the GeSn:P layers by WDXRF, with an InP substrate with a known P concentration as a calibration sample (Figure III.5 bottom). The P atomic concentration increased linearly with the phosphine flow, from $3.0 \times 10^{19} \text{ cm}^{-3}$ up to $3.7 \times 10^{20} \text{ cm}^{-3}$. It was otherwise systematically higher than the substitutional P content (from XRD + WDXRF). It thus seems that a significant amount of P atoms were present in interstitial sites or nanoclusters. To better understand the incorporation of B and P, Secondary Ions Mass Spectrometry (SIMS) depth profiles of the atomic concentration of Ge,

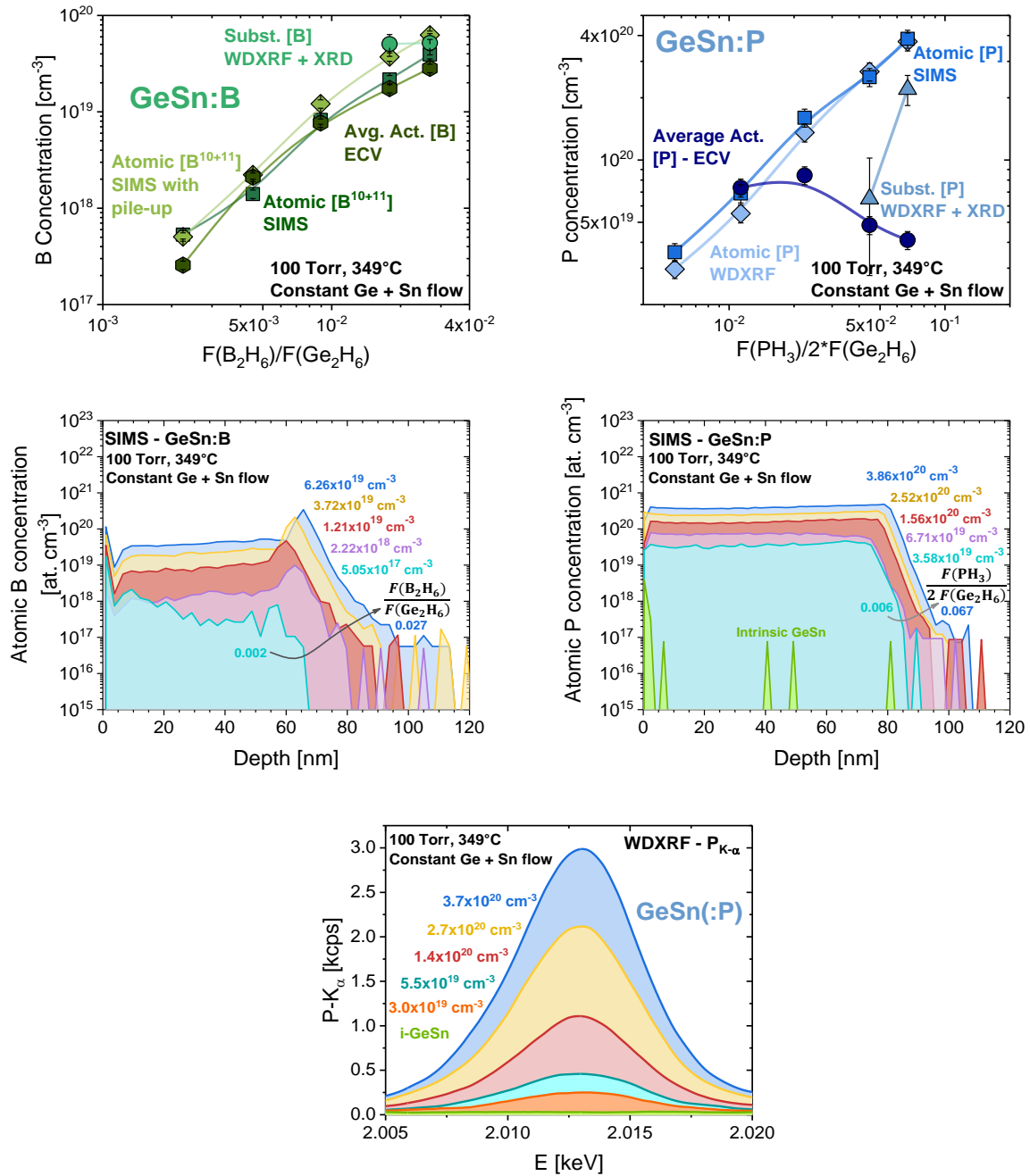


Figure III.5: Substitutional B content (difference between apparent x_{Sn} from XRD and real x_{Sn} from WDXRF), atomic B concentration from SIMS and active carrier concentration from ECV (top left). Substitutional and atomic P concentrations together with active carrier concentrations (top right, $[P]_{Subst.}$ from difference between apparent x_{Sn} from XRD and real x_{Sn} from WDXRF, $[P]_{atomic}$ from WDXRF and from SIMS). SIMS depth profiles of the atomic B concentration in the 61 nm to 80 nm thick GeSn:B layers (middle left) and of the atomic P atomic concentration in the 78 nm to 86 nm thick GeSn:P layers (middle right). P-K α lines of GeSn:P layers grown on Ge SRBs for the five highest $F(PH_3)/2*F(Ge_2H_6)$ MFRs (bottom). $T = 349^\circ C$, $P = 100$ Torr, highest four $F(B_2H_6)/F(Ge_2H_6)$ or five highest $F(PH_3)/2*F(Ge_2H_6)$ MFRs probed. The $F(Ge_2H_6)/F(H_2)$ and the $F(SnCl_4)/F(H_2)$ MFRs were constant at 7.92×10^{-4} and 4.69×10^{-5} , respectively.

Sn, B or P in those layers were also performed. The P concentration profile was steady and abrupt in the GeSn:P layers, with average P atomic concentrations really close to that from WDXRF (Figure III.5 middle right). Meanwhile, there was a gradual increase of the atomic B concentration from the surface towards the GeSn:B/Ge:P interface, with a pile-up at the interface (Figure III.5 middle left). This pile-up might be due to an easier incorporation of B on a hydrogen terminated Ge starting surface or some burst of the B₂H₆ flow at the onset of growth. The atomic B concentrations, obtained by taking the average B concentration of the GeSn:B layer, without or with the B interfacial pile-ups, increased almost linearly with the diborane flow, from 5.3x10¹⁷ cm⁻³ up to 3.9x10¹⁹ cm⁻³ and from 5.0x10¹⁷ cm⁻³ up to 6.3x10¹⁹ cm⁻³, respectively. The atomic B concentrations were close to the substitutional B concentrations, showing that almost all B atoms were actually in substitutional sites.

Electrochemical Capacitance Voltage (ECV) measurements were conducted to quantify the electrical activation of dopants in our in-situ doped layers. Active carrier concentrations increasing from 2.57x10¹⁷ cm⁻³ up to 2.83x10¹⁹ cm⁻³ were obtained, for the highest diborane flows, in GeSn:B. These active carrier concentrations were close to the atomic and substitutional concentrations from SIMS and WDXRF + XRD, outlining that B atoms were almost fully electrically active. Similar findings were previously reported in literature. [11], [12] For GeSn:P, the picture was not as clear. As GeSn is naturally slightly unintentionally p-type doped and because P tends to float on the surface, only ECV values at depths around 70 nm were used. The resulting active carrier concentration for GeSn:P decreased from 6.93x10¹⁹ cm⁻³ down to 4.10 x10¹⁹ cm⁻³ as the PH₃ flow increases. The formation of electrically inactive Sn_mP_n-V complexes between phosphorus donors and double negatively charged Ge vacancy acceptors previously evidenced in the literature for Ge(Sn):P grown at 350°C [9], [13] could explain such a trend.

$x_B/(1-x_B) = m * F(B_2H_6) / ((F(Ge_2H_6) + \frac{1}{2} F(SnCl_4)))$ and $x_P/(1-x_P) = m * F(PH_3) / (2 * F(Ge_2H_6) + F(SnCl_4))$ relationships accounted for the semi-linear increase of the atomic B concentration x_B and P concentration x_P with the diborane and phosphine flows, respectively. m values below 1 meant that the incorporation of dopants was more complicated than the incorporation of Ge or Sn. m was equal to 0.05 for GeSn:B, a value nearly 14 times lower than the $m = 0.68$ value obtained for Ge:B grown at 350°C, 100 Torr with Ge₂H₆ + B₂H₆. [8] For GeSn:P, m was equal to 0.14, a value 3.4 times smaller than the $m = 0.47$ value obtained for Ge:P grown at 350°C, 100 Torr with Ge₂H₆. [9] Dopant incorporation was thus more difficult in GeSn than in pure Ge, especially for boron. The surface site competition between Sn and B reported in the literature [11], [12] might explain the lower m value for GeSn:B.

I.17 Catalytic impact of dopants on growth rate

Margetis *et al.* showed that B₂H₆ had a catalytic impact on the GeSn growth rate (GR). [12] We have thus carefully analyzed the evolution of the GeSn:B or GeSn:P GR with the dopant flow. As the diborane or phosphine flows increased, the overall GR stayed at first constant, with a mean value close to 39 nm min.⁻¹, as shown in **Figure III.6 top**. This GR was significantly higher than the highest GR of 29 nm min.⁻¹ in Ge:B (even with the additional GR increase because of the addition of B₂H₆ to the other precursors). This outlined the catalytic effect SnCl₄ had on the Ge GR, in line with the literature. [3] For the highest dopant flows, the GR rapidly increased, up to 51 nm min.⁻¹ for GeSn:B and less rapidly for GeSn:P, with a maximum at

43 nm min.⁻¹, as shown in **Figure III.6 top**. As we evidenced the same kind of Sn content drop as Margetis *et al.*, we investigated in more details the catalytic impact of dopants.

To that end, we determined elemental growth rates by multiplying the overall GR by the Ge content (**Equation (I.1.1)**) or real and apparent Sn content (**Equation (I.17.2)**) (**Figure III.6 bottom**).

$$GR_{Ge} = (1 - x_{Sn}) * GR_{GeSn} \quad (I.17.1)$$

$$GR_{Sn} = x_{Sn} * GR_{GeSn} \quad (I.17.2)$$

The Sn GR component stayed constant at around 2.5 nm min.⁻¹ for the lowest diborane or phosphine flows probed. For the highest flows, the Sn GR component dropped down a bit when using the apparent Sn content from XRD (**Figure III.6 bottom left**). Meanwhile, the Sn GR component stayed constant for all MFRs when using real Sn contents from WDXRF instead of apparent Sn contents from XRD, as shown in **Figure III.6 bottom right**. Meanwhile, the Ge GR component was constant at around 37 nm min.⁻¹ for low MFRs. For high dopant flows, the Ge GR component significantly increased for GeSn:B, reaching 48 nm min.⁻¹. The increase was less significant for GeSn:P, with at most 40 nm min.⁻¹.

This is to our knowledge, the first time such a GeSn:P GR increase is reported for high dopant flows. Similar increases were found for Ge:B and Ge:P grown at 350°C, however. [8], [9] The constant Sn GR component and the increase of the Ge GR component at high MFRs are likely due to an increased incorporation of Ge thanks to B and P opening surface sites. The Ge GR component is most likely surface reaction rate limited, while the Sn GR component is most likely mass-transport limited, as suggested in the literature. [3], [14]

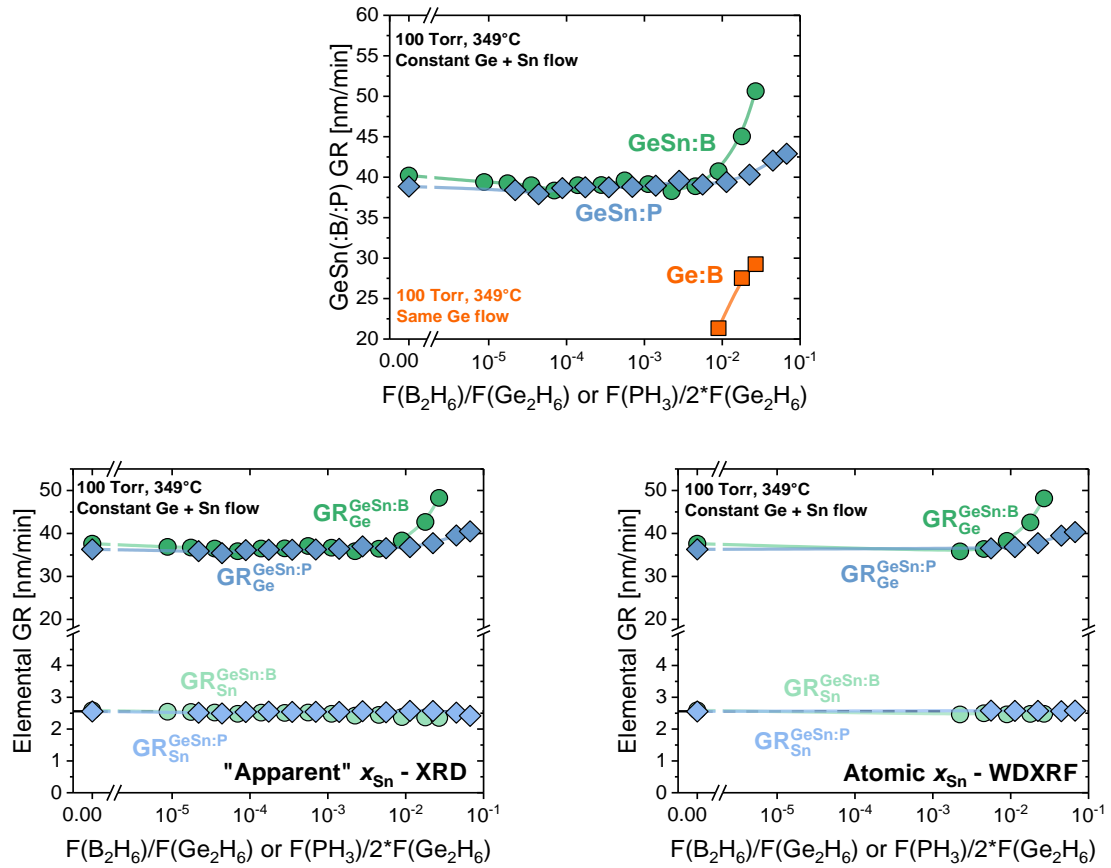


Figure III.6: Ge:B, GeSn:B and GeSn:P Growth Rates at 349°C, 100 Torr for various $F(B_2H_6)/F(Ge_2H_6)$ or $F(PH_3)/2 \cdot F(Ge_2H_6)$ MFRs (top). GeSn:B and GeSn:P elemental Growth Rates from apparent Sn contents (XRD, bottom left) and from real Sn contents (WDXRF, bottom right) at 349°C, 100 Torr for various $F(B_2H_6)/F(Ge_2H_6)$ or $F(PH_3)/2 \cdot F(Ge_2H_6)$ MFRs. The $F(Ge_2H_6)/F(H_2)$ and the $F(SnCl_4)/F(H_2)$ MFRs were constant at 7.92×10^{-4} and 4.69×10^{-5} , respectively.

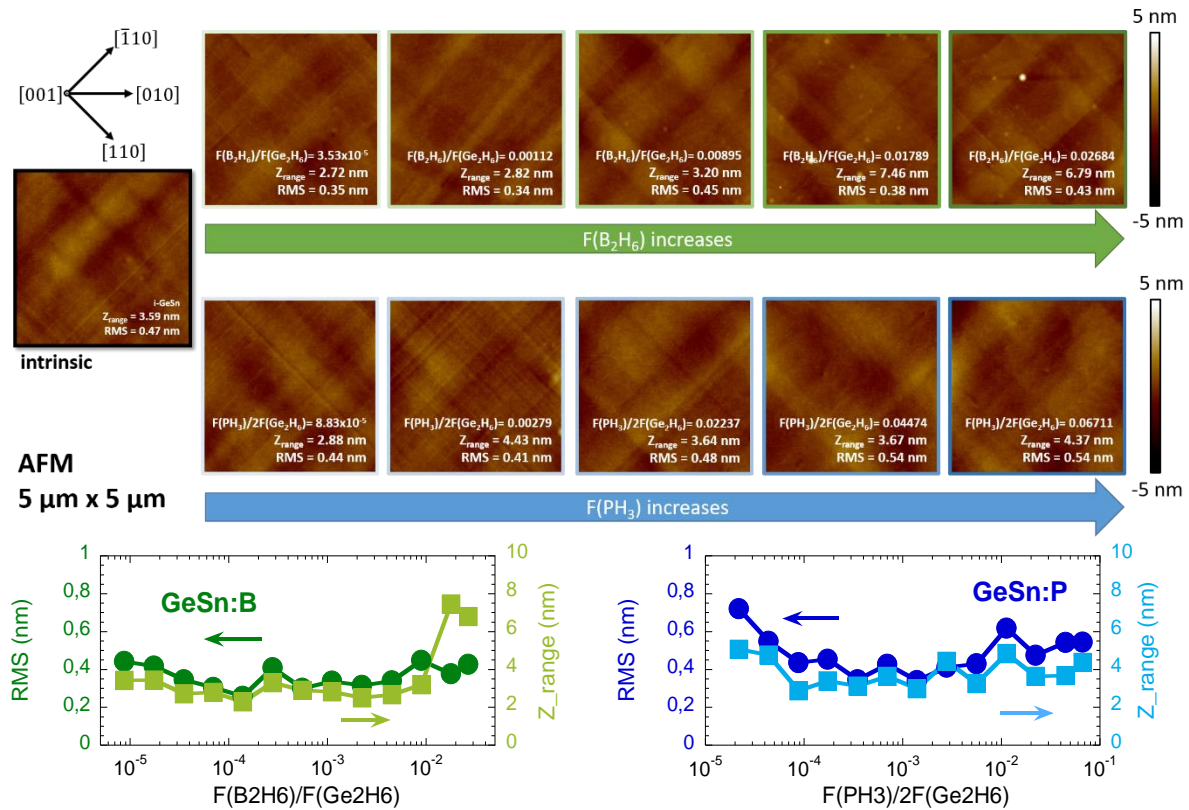
I.18 Surface morphology and roughness


Figure III.7: 5 $\mu\text{m} \times 5 \mu\text{m}$ AFM images of surfaces of 61 nm to 80 nm thick GeSn:B (top) and 76 nm to 86 nm thick GeSn:P (middle) layers grown at 349°C, 100 Torr with various $F(\text{B}_2\text{H}_6)/F(\text{Ge}_2\text{H}_6)$ or $F(\text{PH}_3)/2F(\text{Ge}_2\text{H}_6)$ MFRs. Surface RMS roughness and Z range for GeSn:B (bottom left) and GeSn:P (bottom right) for various $F(\text{B}_2\text{H}_6)/F(\text{Ge}_2\text{H}_6)$ or $F(\text{PH}_3)/2F(\text{Ge}_2\text{H}_6)$ MFRs.

5 $\mu\text{m} \times 5 \mu\text{m}$ AFM images were acquired to image the surface morphology and to determine the surface roughness of our layers. Cross-hatches along $\langle 110 \rangle$, as for the Ge SRBs underneath, were found for all layers, which were otherwise rather smooth, as shown in **Figure III.7 top row** for GeSn:B and **Figure III.7 middle row** for GeSn:P. Mean surface roughness and Z ranges were similar for our in-situ doped layers and for various content intrinsic GeSn layers (0.47 nm and 3.59 nm for GeSn:B and 0.49 nm and 3.85 nm for GeSn:P, to be compared with 0.47 nm and 3.59 nm for i-GeSn): **Figure III.7 bottom row**. The incorporation of B and P atoms into the GeSn lattice did not deteriorate the surface of the grown layers. The only exceptions were the GeSn:B samples grown at the three highest MFRs. There were then some islands, which were likely due to B and/or Sn surface segregation. A similar behavior has been found by Vincent *et al.* [11] A loss of crystallinity was reported in that article, however, which is not the case for our samples.

I.19 Conclusions

The holy grail of group-IV light emission would be electrically pumped lasing at Room Temperature (RT). In CEA-LETI, the performance of p-i-n light emitting diodes is limited by the use of in-situ doped Ge layers beneath and above the active layer stack. To overcome Sn segregation during the growth of the top electrode and, in thick GeSn/Ge stacks, avoid plastic relaxation, it would be ideal to switch over to in-situ doped GeSn grown at temperatures similar to that of the active region. We have therefore explored the in-situ boron and phosphorous doping of GeSn on Ge strain relaxed buffers with $\text{Ge}_2\text{H}_6 + \text{SnCl}_4 + \text{B}_2\text{H}_6$ and $\text{Ge}_2\text{H}_6 + \text{SnCl}_4 + \text{PH}_3$ chemistries. Growth pressure, temperature, $F(\text{Ge}_2\text{H}_6)/F(\text{H}_2)$ and $F(\text{SnCl}_4)/F(\text{H}_2)$ Mass-Flow Ratios (MFRs) were constant at 100 Torr, 349°C, 7.92×10^{-4} and 4.69×10^{-5} .

Then, X-Ray Diffraction measurements were performed to gain access to the GeSn composition and layer thickness. As the GeSn peak position was determined not only by the Sn content, but also by the B or P substitutional concentrations, the actual layer composition could not be unambiguously determined solely from XRD, which gave us access to “apparent” Sn contents. Wavelength Dispersive X-Ray Fluorescence measurements of the Sn- L_α line were thus performed to determine the atomic Sn content in our layers. Well defined, intense layer peaks and thickness fringes confirmed the superior crystalline quality of our intrinsic and in-situ doped GeSn layers and yielded thicknesses (and thus growth rates).

As the diborane or phosphine flows increased, the Sn content (from WDXRF) stayed at first roughly constant around 6.5%. This value was the same for i-GeSn, GeSn:B and GeSn:P, in contrast to previous literature findings. As the dopant flows reached the highest values, the Sn content decreased significantly for GeSn:B (from 6.5% down to 4.9%), less so for GeSn:P (from 6.6% down to 6.0%). Substitutional B concentrations up to $5.2 \times 10^{19} \text{ cm}^{-3}$ and substitutional P concentrations up to $2.2 \times 10^{20} \text{ cm}^{-3}$ were deduced from differences between real and apparent Sn contents (from XRD and WDXRF, respectively). The highest substitutional P concentration was indeed close to that in Ge:P layers grown at 350°C, 100 Torr with $\text{Ge}_2\text{H}_6 + \text{PH}_3$: $4.1 \times 10^{20} \text{ cm}^{-3}$.

Electrochemical capacitance voltage measurement were conducted on GeSn:B and GeSn:P layers. B atoms were almost fully electrically active in GeSn, with carrier concentrations of at most $2.8 \times 10^{19} \text{ cm}^{-3}$. Meanwhile, the presence of large amounts of electrically inactive $\text{Sn}_m\text{P}_n\text{-V}$ complexes could explain why the electrically active carrier concentration in GeSn:P was reduced for the highest PH_3 flows (at most: $6.9 \times 10^{19} \text{ cm}^{-3}$).

We then determined elemental growth rates by multiplying the overall GR by the Ge or Sn content (from WDXRF) to have a more detailed look at the growth mechanics. The introduction of SnCl_4 catalyzed the growth rate of GeSn compared to that of pure Ge. As the diborane or phosphine flows increased, the Sn GR component stayed constant at around 2.5 nm min^{-1} . Meanwhile, the Ge GR component was constant at around 37 nm min^{-1} for lower MFRs. For high dopant flows, the Ge GR component increased significantly for GeSn:B and reached 48 nm min^{-1} . The increase was less significant for GeSn:P, with at most 40 nm min^{-1} . Similar increases were found for Ge:P and Ge:B grown at 350°C, however. The constant Sn GR component and the increase of the Ge GR component at high MFRs were likely due to an increased incorporation of Ge thanks to B and P opening surface sites (indeed, the Ge GR

component is surface reaction rate limited, while the Sn GR component is mass-transport limited).

Cross-hatches along $\langle 110 \rangle$ were evidenced by Atomic Force Microscopy for all layers, which were otherwise rather smooth. The only exceptions were the GeSn:B samples grown with the three highest diborane flows. There were then some islands, which were likely due to B and/or Sn surface segregation.

References

- [1] J.-M. Hartmann, M. Frauenrath, and J. Richy, "Epitaxy of Pseudomorphic GeSn Layers with Germane (GeH₄) or Digermane (Ge₂H₆) as Ge Precursors and Tin Tetrachloride (SnCl₄) as the Sn Precursor," *ECS Trans.*, vol. 98, no. 5, p. 225, Sep. 2020, doi: 10.1149/09805.0225ecst.
- [2] J. M. Hartmann and J. Aubin, "Assessment of the growth/etch back technique for the production of Ge strain-relaxed buffers on Si," *J. Cryst. Growth*, vol. 488, pp. 43–50, Apr. 2018, doi: 10.1016/j.jcrysgr.2018.02.036.
- [3] J. Aubin and J. M. Hartmann, "GeSn growth kinetics in reduced pressure chemical vapor deposition from Ge₂H₆ and SnCl₄," *J. Cryst. Growth*, vol. 482, pp. 30–35, Jan. 2018, doi: 10.1016/j.jcrysgr.2017.10.030.
- [4] R. Khazaka, E. Nolot, J. Aubin, and J.-M. Hartmann, "Growth and characterization of SiGeSn pseudomorphic layers on 200 mm Ge virtual substrates," *Semicond. Sci. Technol.*, vol. 33, no. 12, p. 124011, Dec. 2018, doi: 10.1088/1361-6641/aaea32.
- [5] E. Nolot, S. Cadot, F. Martin, P. Hönicke, C. Zech, and B. Beckhoff, "In-line characterization of ultrathin transition metal dichalcogenides using X-ray fluorescence and X-ray photoelectron spectroscopy," *Spectrochim. Acta Part B At. Spectrosc.*, vol. 166, p. 105788, Apr. 2020, doi: 10.1016/j.sab.2020.105788.
- [6] C. Jeynes *et al.*, "Quantifying nitrogen in GeSbTe:N alloys," *J. Anal. At. Spectrom.*, vol. 35, no. 4, pp. 701–712, 2020, doi: 10.1039/C9JA00382G.
- [7] M. Frauenrath, J.-M. Hartmann, and E. Nolot, "Boron and Phosphorous Doping of GeSn for Photodetectors and Light Emitting Diodes," *ECS Trans.*, vol. 98, no. 5, pp. 325–338, Sep. 2020, doi: 10.1149/09805.0325ecst.
- [8] J.-M. Hartmann, M. Frauenrath, J. Richy, and M. Veillerot, "Ultra-High Boron Doping of Si and Ge for Nanoelectronics and Photonics," *ECS Trans.*, vol. 98, no. 5, pp. 203–214, Sep. 2020, doi: 10.1149/09805.0203ecst.
- [9] J. Aubin, J. M. Hartmann, J. P. Barnes, J. B. Pin, and M. Bauer, "Very Low Temperature Epitaxy of Heavily In Situ Phosphorous Doped Ge Layers and High Sn Content GeSn Layers," *ECS J. Solid State Sci. Technol.*, vol. 6, no. 1, pp. P21–P26, 2017, doi: 10.1149/2.0091701jss.
- [10] J. Margetis *et al.*, "Fundamentals of Ge_{1-x}Sn_x and Si_yGe_{1-x-y}Sn_x RPCVD epitaxy," *Mater. Sci. Semicond. Process.*, vol. 70, pp. 38–43, Nov. 2017, doi: 10.1016/j.mssp.2016.12.024.
- [11] B. Vincent *et al.*, "Undoped and *in-situ* B doped GeSn epitaxial growth on Ge by atmospheric pressure-chemical vapor deposition," *Appl. Phys. Lett.*, vol. 99, no. 15, p. 152103, Oct. 2011, doi: 10.1063/1.3645620.
- [12] J. Margetis *et al.*, "Growth and Characterization of Epitaxial Ge_{1-x}Sn_x Alloys and Heterostructures Using a Commercial CVD System," *ECS Trans.*, vol. 64, no. 6, pp. 711–720, Aug. 2014, doi: 10.1149/06406.0711ecst.
- [13] A. Vohra *et al.*, "Source/Drain Materials for Ge nMOS Devices: Phosphorus Activation in Epitaxial Si, Ge, Ge_{1-x}Sn_x and Si_yGe_{1-x-y}Sn_x," *ECS J. Solid State Sci. Technol.*, vol. 9, no. 4, p. 044010, Jan. 2020, doi: 10.1149/2162-8777/ab8d91.
- [14] J. Margetis, S.-Q. Yu, B. Li, and J. Tolle, "Chemistry and kinetics governing hydride/chloride chemical vapor deposition of epitaxial Ge_{1-x}Sn_x," *J. Vac. Sci. Technol. A*, vol. 37, no. 2, p. 021508, Mar. 2019, doi: 10.1116/1.5055620.

Chapter IV : In-Situ B and P Doping of SiGeSn

Chapter IV: In-Situ B and P Doping of SiGeSn

Chapter IV: In-Situ B and P Doping of SiGeSn.....	73
IV.1 Introduction.....	73
IV.2 Impact of dopant precursors on crystalline quality and layer thickness.....	73
IV.3 Impact of dopant precursors on composition	74
IV.4 Catalytic impact of dopants on growth rate.....	76
IV.5 Surface morphology and roughness	79
IV.6 Incorporation and activation of dopants in the SiGeSn lattice.....	81
IV.7 Conclusions.....	83

Chapter IV: In-Situ B and P Doping of SiGeSn

IV.1 Introduction

For GeSn:P, it was found that, for high dopant flows, P atoms were not fully electrically activated, most likely because of the formation of electrically inactive $\text{Sn}_m\text{P}_n\text{V}$ clusters. In this study, we aimed to overcome these shortcomings by switching over to in-situ doped SiGeSn and investigate the growth mechanics, composition and electrical activation of dopants.

IV.2 Impact of dopant precursors on crystalline quality and layer thickness

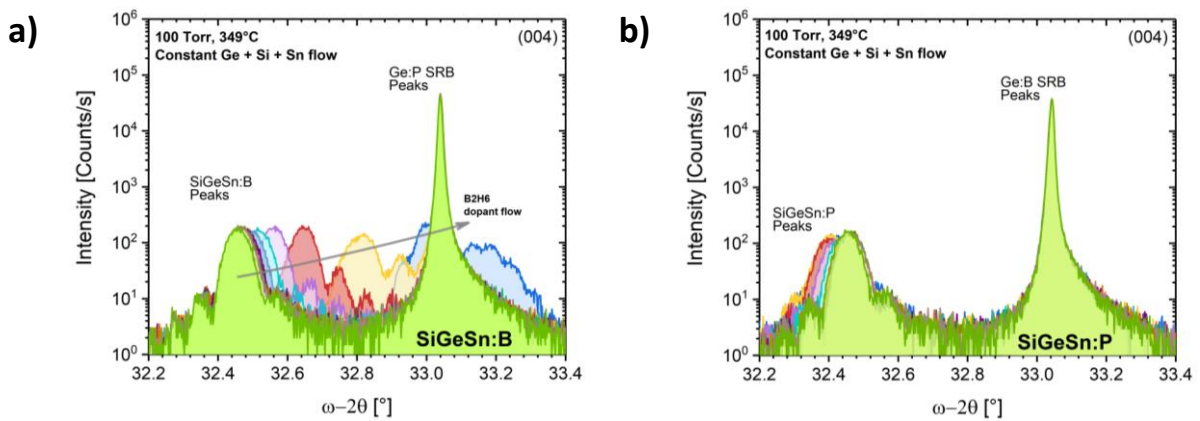


Figure IV.1: ω - 2θ scans around the (0 0 4) XRD order for (a) 69 nm to 76 nm thick SiGeSn:B layers and (b) 60 nm to 72 nm thick SiGeSn:P layers grown with various diborane and phosphine flows on Ge SRBs. The $F(\text{Ge}_2\text{H}_6)/F(\text{H}_2)$, $F(\text{Si}_2\text{H}_6)/F(\text{H}_2)$, and $F(\text{SnCl}_4)/F(\text{H}_2)$ MFRs were constant at 7.92×10^{-4} , 1.25×10^{-3} , and 4.69×10^{-5} , respectively. Growth temperatures and pressures were 349 °C and 100 Torr.

In-situ B and P doped layers were grown at 349 °C, 100 Torr with a constant $F(\text{Ge}_2\text{H}_6)/F(\text{H}_2)$ Mass-Flow Ratio (MFR) of 7.92×10^{-4} , a constant $F(\text{Si}_2\text{H}_6)/F(\text{H}_2)$ MFR of 1.25×10^{-3} and a constant $F(\text{SnCl}_4)/F(\text{H}_2)$ MFR of 4.69×10^{-5} . The $F(\text{B}_2\text{H}_6)/F(\text{Ge}_2\text{H}_6)$ and $F(\text{PH}_3)/2 \cdot F(\text{Ge}_2\text{H}_6)$ MFRs were varied from 0 up to 2.68×10^{-2} and 6.71×10^{-2} , respectively. Thickness fringes on both sides of the SiGeSn:B and SiGeSn:P peaks outlined the high crystalline quality of the grown layers and the presence of smooth surfaces / interfaces, as shown in **Figure IV.1** for SiGeSn:B (a) and SiGeSn:P (b). Rutherford backscattering (RBS) experiments confirmed the good crystalline quality of those pseudomorphic layers with χ_{\min} , i.e. ratios of intensities in channeling and random orientations, below 5%.

When the $F(\text{B}_2\text{H}_6)/F(\text{Ge}_2\text{H}_6)$ MFRs increased from 0 up to 2.68×10^{-2} , the SiGeSn:B layer peak shifted towards the Ge SRB peak, reaching almost the same incidence angle at the highest MFR value. This likely meant that the chemical composition of the SiGeSn:B layers significantly changed as the diborane flow increased, with a perpendicular lattice parameter almost matching that of the Ge SRB for the highest B_2H_6 dopant flow probed.

Meanwhile, the SiGeSn:P XRD peak did not significantly move when the $F(\text{PH}_3)/2 \cdot F(\text{Ge}_2\text{H}_6)$ MFRs increased from 0 up to 6.71×10^{-2} . The XRD peak first shifted slightly to smaller incidence angles then moved back towards its intrinsic position. Most likely, the introduction of PH_3 did not significantly change the composition. This is investigated in a latter section.

Takagi-Taupin's dynamical scattering theory was used to extract the film thickness from fits of the layer peaks and fringes. [1] The thickness increased from 69 nm for intrinsic SiGeSn up to 76 nm for SiGeSn(:B) grown at a $F(\text{B}_2\text{H}_6)/F(\text{Ge}_2\text{H}_6)$ MFR of 2.68×10^{-2} . On the contrary, the SiGeSn:P layer thickness decreased with the PH_3 flow, from 72 nm for intrinsic SiGeSn down to 60 nm for the highest phosphine flow probed.

IV.3 Impact of dopant precursors on composition

WDXRF measurements were performed to obtain the chemical composition of the in-situ doped SiGeSn layers. Pure Si and Sn targets were used as calibrations samples and the Si- K_α and Sn- L_α line spectra were recorded to determine the Si and Sn contents in the SiGeSn:B and SiGeSn:P layers.

The Sn- L_α line spectra of SiGeSn(:B) and of the underlying Ge SRB are shown in **Figure IV.2 (a)**. There was no Sn- L_α peak for the Ge SRB (orange). The Sn- L_α line intensity, which was the highest for the intrinsic SiGeSn layer (green), decreased as the diborane flow increased. The opposite behavior was observed for Si (**Figure IV.2 (b)**). No signal was found for the Ge SRB (orange). The intrinsic SiGeSn layer had the lowest Si- K_α line intensity. Increasing the diborane flow resulted in a Si- K_α line intensity increase. Such Sn content reductions and Si content increases would partly explain the peak shift in **Figure IV.1 (a)** XRDs scans.

Si (dark green) and Sn (light green) contents in SiGeSn(:B) were extracted from Si- K_α and Sn- L_α line spectra shown in **Figure IV.2 (a)** and **(b)**. They are shown as functions of the diborane flow in **Figure IV.2 (c)**. For low dopant flows, the Sn and Si contents stayed relatively constant at 9.1% and 14.5%, respectively. The Sn content decreased slightly for high diborane flows, from 8.5% down to 7.1%, while the Si content drastically increased, from 15.1% up to 25.0%. These significant composition changes were independently confirmed by Rutherford Back Scattering (RBS) and RSM measurements. The $(2 \ 2 \ 4)$ RSM of the highest doped SiGeSn:B sample, shown in **Figure IV.2 (e)**, is characteristic of a pseudomorphic growth, with the SiGeSn:B layer and the Ge SRB having the same in-plane lattice parameter. Perpendicular lattice parameters are also almost the same, in line with the close to perfect lattice match of the two, shown in **Figure IV.1 (a)**. Those composition changes most likely were due to some B_2H_6 - assisted decomposition of Ge_2H_6 and Si_2H_6 . Similar findings for GeSn(:B) were reported before [2] and it will be discussed in more details in the next section.

The Si-to-Sn-ratio of 3.5 for the highest B_2H_6 flow probed, was definitely higher than in previous studies of ours on intrinsic SiGeSn. Fang *et al.* [3] predicted lattice matching of SiGeSn:B with the Ge SRB underneath for a Si / Sn ratio of 3.6, in line with current findings. Such ratio should result in a significant band offset in optical devices with high Sn content GeSn layers for light emission and SiGeSn:B as the p-type doped layers beneath or on top, with therefore a good confinement of carriers and, possibly, better device performances. For

SiGeSn(:P), similar Si- K_{α} and Sn- L_{α} line spectra than for SiGeSn(:B) (not shown here) were obtained. The extracted Sn (light blue) and Si (dark blue) contents are shown in **Figure IV.2 (d)**. The Si content increased very slightly with the phosphine flow, from 13.8% (intrinsic SiGeSn) up to 14.0% (highest PH_3 dopant flow). Meanwhile, the Sn content increased more significantly with the $\text{F}(\text{PH}_3)/2*\text{F}(\text{Ge}_2\text{H}_6)$ MFR, from 8.1% (intrinsic SiGeSn) up to 9.7% (highest PH_3 dopant flow). The combination of Ge_2H_6 , Si_2H_6 and PH_3 might have led to the formation of gas phase intermediates that did not dissociate on the growing surface. This likely resulted in Sn atoms incorporating more easily into the remaining open surface sites. [4]

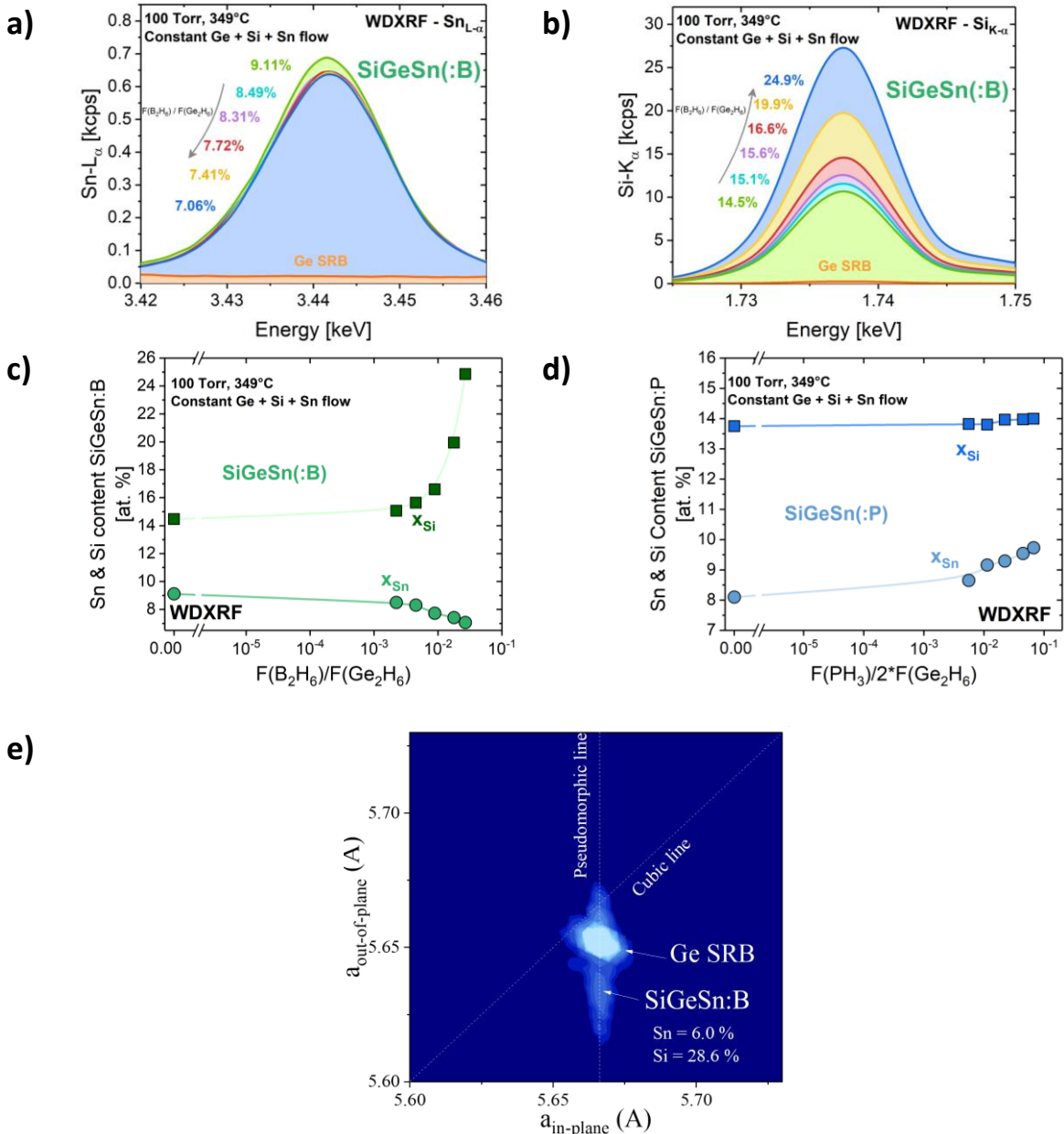


Figure IV.2: (a) Sn- L_{α} and (b) Si- K_{α} lines for SiGeSn(:B) layers grown on Ge SRBs with various $\text{F}(\text{B}_2\text{H}_6)/\text{F}(\text{Ge}_2\text{H}_6)$ MFRs. (c) Sn (light green circles) and Si (dark green squares) contents in SiGeSn(:B) layers determined from (a) and (b). (d) Sn (light blue circles) and Si (dark blue squares) contents for SiGeSn(:P) layers grown with various $\text{F}(\text{PH}_3)/2*\text{F}(\text{Ge}_2\text{H}_6)$ MFRs.

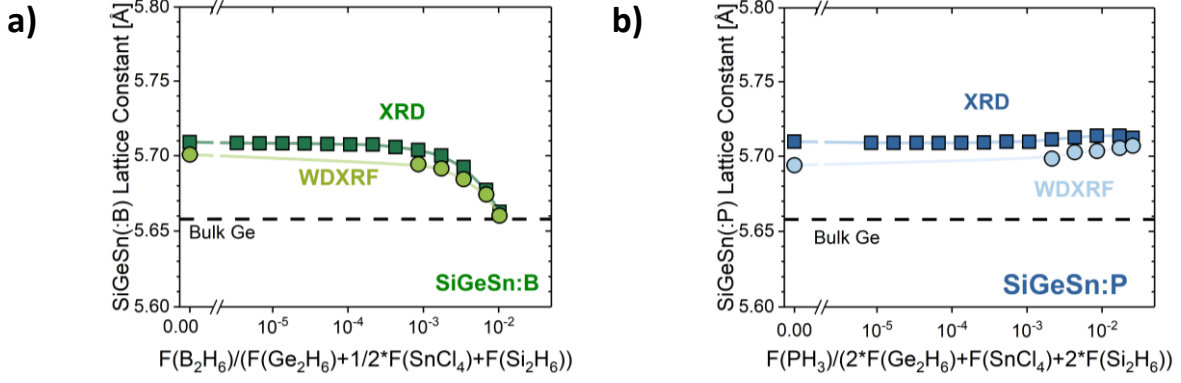


Figure IV.3: (a) SiGeSn(:B) and (b) SiGeSn(:P) perpendicular lattice constants in our layers from XRD (darker colors) and from the atomic Si and Sn content obtained by WDXRF (lighter colors). The expected accuracy of the elemental composition from WDXRF is in the 1% range (absolute).

The trustworthiness of WDXRF measurements was confirmed as follows. Lattice constants were determined from the atomic Si and Sn contents of **Figure IV.2** (WDXRF) and compared to experimental lattice parameter values inferred from **Figure IV.1** XRD peak positions with the assumption that layers were fully pseudomorphic. The resulting values are shown in **Figure IV.3**. A modified Vegard's law was used to compute the SiGeSn lattice constant from WDXRF contents, shown in **Equation (I.1.1)**.

$$a_{\text{SiGeSn}} = a_{\text{Ge}}x_{\text{Ge}} + a_{\text{Si}}x_{\text{Si}} + a_{\text{Sn}}x_{\text{Sn}} - b_{\text{GeSn}}x_{\text{Sn}}(1 - x_{\text{Sn}}) - b_{\text{SiGe}}x_{\text{Si}}(1 - x_{\text{Si}}) \quad (\text{IV.3.1})$$

With $a_{\text{Si}} = 5.43105 \text{ \AA}$, $a_{\text{Ge}} = 5.65785 \text{ \AA}$, $a_{\text{Sn}} = 6.489 \text{ \AA}$ and $x_{\text{Ge}} = 1 - x_{\text{Si}} - x_{\text{Sn}}$. It was opted to use the bowing parameters found by Gencarelli *et al.* for GeSn ($b_{\text{GeSn}} = -0.041$) [5] and by Dismukes *et al.* for SiGe ($b_{\text{SiGe}} = 0.028$). [6] The uncertainty of the XRD measurement is $6 \times 10^{-5}^\circ$. The expected accuracy of the elemental composition is in the 1% range (absolute). This accuracy range has been demonstrated using similar strategies on different thin layered materials such as 2D – MoS₂ [7] and GeSbTe. [8] Negligible differences between the extracted lattice parameters from XRD and WDXRF were found, validating the latter method.

IV.4 Catalytic impact of dopants on growth rate

Compositional changes were also evidenced for in-situ doped GeSn [2] due to growth mechanism changes for high dopant flows. **Figure IV.4 (a)** shows the growth rate of in-situ doped SiGeSn(:B) (light green circles) and in-situ doped SiGeSn(:P) (light blue diamonds) together with the corresponding values for in-situ doped GeSn(:B) (dark green circles), in-situ doped GeSn(:P) (dark blue diamonds) and in-situ doped Ge:B (orange squares). Flows, pressures and temperatures were the same, the only differences being the presence of SnCl₄ or Si₂H₆. The SiGeSn(:B) growth rate stayed constant for intrinsic and doped layers grown with low diborane flows, at $31.0 \frac{\text{nm}}{\text{min}}$. It increased slightly up to $31.8 \frac{\text{nm}}{\text{min}}$ for the highest B₂H₆ flows probed, at which it seemed to stabilize. A similar trend was found by RBS measurements.

The SiGeSn:P growth rate was lower than that of intrinsic SiGeSn when moderate amounts of PH₃ flowed into the growth chamber ($\sim 30 \frac{\text{nm}}{\text{min}}$ instead of $32 \frac{\text{nm}}{\text{min}}$ (intrinsic)). There was otherwise a gradual reduction of the SiGeSn:P growth rate from $32 \frac{\text{nm}}{\text{min}}$ down to $26.8 \frac{\text{nm}}{\text{min}}$ for the highest four phosphine flows probed. Although Ge₂H₆ and SnCl₄ flows were the same for intrinsic or in-situ doped SiGeSn, SiGeSn growth rates for dopant MFRs below 5×10^{-3} were otherwise $\sim 30\%$ lower than GeSn growth rates. Previously, Khazaka *et al.* obtained similar results when comparing intrinsic SiGeSn and GeSn growth rates. [9], [10]

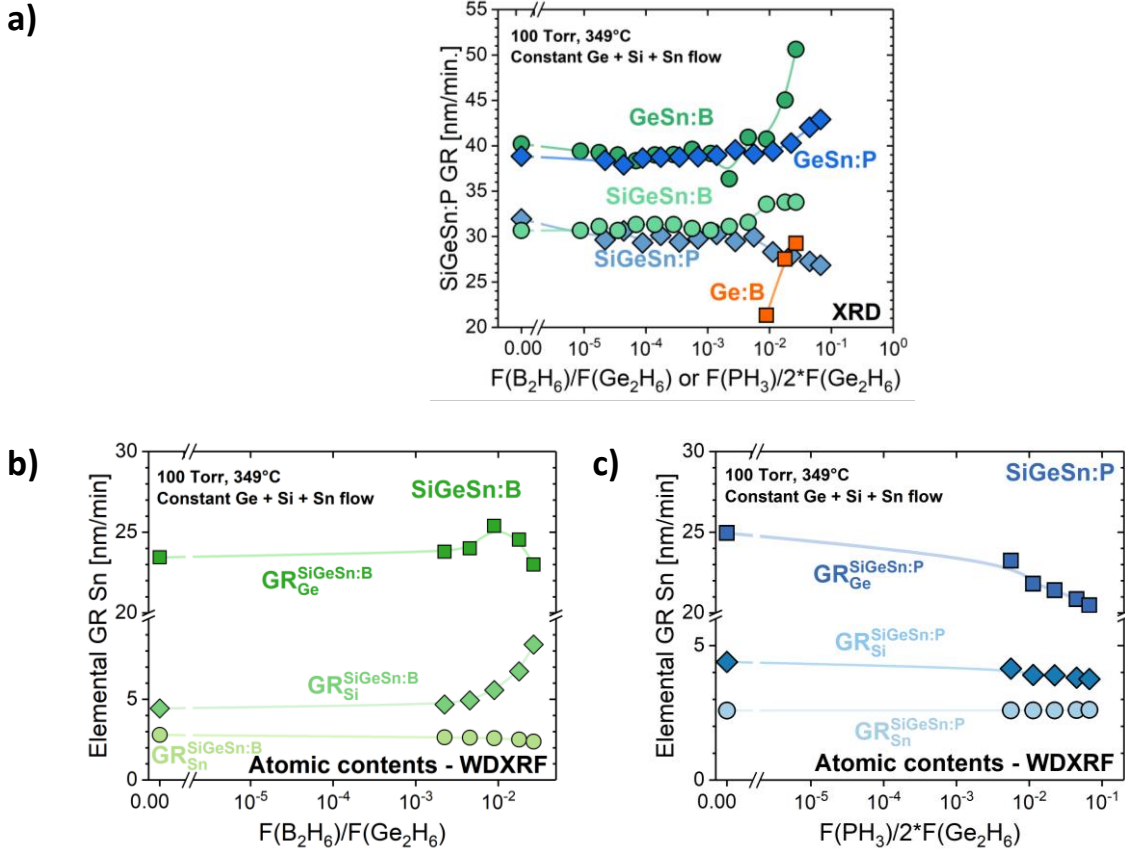


Figure IV.4: (a) Ge:B (orange squares), GeSn:B (dark green circles), GeSn:P (dark blue diamonds), SiGeSn:B (light green circles) and SiGeSn:P (light blue diamonds) growth rates at 349 °C, 100 Torr for various $F(\text{B}_2\text{H}_6)/F(\text{Ge}_2\text{H}_6)$ or $F(\text{PH}_3)/2 \cdot F(\text{Ge}_2\text{H}_6)$ MFRs. (b) SiGeSn:B (green) and (c) SiGeSn:P (blue) elemental growth rates from atomic Sn (circles) and Si (diamonds) contents (WDXRF) at 349 °C, 100 Torr for various $F(\text{B}_2\text{H}_6)/F(\text{Ge}_2\text{H}_6)$ or $F(\text{PH}_3)/2 \cdot F(\text{Ge}_2\text{H}_6)$ MFRs. The $F(\text{Ge}_2\text{H}_6)/F(\text{H}_2)$, $F(\text{Si}_2\text{H}_6)/F(\text{H}_2)$ and the $F(\text{SnCl}_4)/F(\text{H}_2)$ MFRs were constant at 7.92×10^{-4} , 1.25×10^{-3} and 4.69×10^{-5} , respectively.

It should be pointed out that such a growth rate drop when switching over from intrinsic SiGeSn to P doped SiGeSn was not evidenced in other literature articles. [3], [11] This might be due to the use of other precursors and growth chamber setups.

To better apprehend the impact of B₂H₆ and PH₃ on growth mechanisms and see how this influenced the composition, elemental growth rates were calculated, GR_x ($x = \text{Si}, \text{Ge}$ or Sn),

yielding the individual contributions of each element to the overall growth rate GR_{SiGeSn} . They were obtained by multiplying the overall growth rate by the atomic contents x_{Sn} or x_{Si} from WDXRF ($x_{\text{Ge}} = 1 - x_{\text{Sn}} - x_{\text{Si}}$). Contributions of dopants were neglected as their concentrations were significantly below 1%, as shown in the following. Formulas used to compute elemental growth rates were **Equations (3.1) to (3.3)**.

$$GR_{\text{Ge}} = (1 - x_{\text{Sn}} - x_{\text{Si}}) * GR_{\text{SiGeSn}} \quad (\text{IV.4.1})$$

$$GR_{\text{Sn}} = x_{\text{Sn}} * GR_{\text{SiGeSn}} \quad (\text{IV.4.2})$$

$$GR_{\text{Si}} = x_{\text{Si}} * GR_{\text{SiGeSn}} \quad (\text{IV.4.3})$$

Elemental growth rates for SiGeSn(:B) are shown in **Figure IV.4 (b)**. The Ge elemental growth rate (dark green squares) stayed constant at $23.5 \frac{\text{nm}}{\text{min}}$ for intrinsic SiGeSn and low diborane flows. It increased to $25.4 \frac{\text{nm}}{\text{min}}$ for higher B_2H_6 flows. The injection of diborane also led to an increase of the Ge elemental growth rate for in-situ B doped GeSn [2], albeit more pronounced. Such an increase was explained through surface sites being opened by large amounts of B_2H_6 molecules. As Ge growth was surface reaction rate limited [4], the Ge growth rate component increased. In contrast to in-situ B doped GeSn, the Ge elemental growth rate decreased for the highest two B_2H_6 flows probed when growing in-situ B doped SiGeSn. This can be understood when looking at the Si elemental growth rate (**Figure IV.4 (b)**, light green diamonds). It stayed constant at $4.5 \frac{\text{nm}}{\text{min}}$ for low diborane flows and, then, monotonously increased for high B_2H_6 flows, reaching $8.4 \frac{\text{nm}}{\text{min}}$ for the highest diborane flow probed. It might thus be that Si and Ge were competing for incorporation on open surface sites. Given the reactions proposed by Perrin *et al.* [12], it might have been that Si_2H_6 decomposition and incorporation was preferred over that of Ge_2H_6 , explaining why there was such a peculiar drop of the Ge elemental growth rate for really high diborane flows.

Finally, the Sn elemental growth rate component (**Figure IV.4 (b)**, lime green circles) stayed almost constant at $2.8 \frac{\text{nm}}{\text{min}}$ for low B_2H_6 flows. It dropped a bit, to $2.4 \frac{\text{nm}}{\text{min}}$ for the highest diborane flows probed. Such a stability was expected as Margetis *et al.* showed that the Sn growth rate component was most likely mass-transport limited. [4]

The elemental growth rate components of in-situ doped SiGeSn(:P) are shown in **Figure IV.4 (c)**. The Sn elemental growth rate component stayed almost constant at $2.6 \frac{\text{nm}}{\text{min}}$, a value close to that of SiGeSn:B ($2.4 \frac{\text{nm}}{\text{min}}$) (light blue circles). The same trend was highlighted for in-situ P doped GeSn. [2] The Si elemental growth rate component for intrinsic SiGeSn was $4.4 \frac{\text{nm}}{\text{min}}$. It dropped to $4.1 \frac{\text{nm}}{\text{min}}$ when PH_3 was flown into the growth chamber, then slightly decreased to $3.8 \frac{\text{nm}}{\text{min}}$ for the highest PH_3 flow probed. The Ge growth rate component also dropped when adding PH_3 to the growth mixture (dark blue squares). It monotonously decreased with the phosphine flow, from $25 \frac{\text{nm}}{\text{min}}$ for intrinsic SiGeSn down to $20.5 \frac{\text{nm}}{\text{min}}$ for the highest phosphine flow probed. Such a trend is in contrast with our findings for in-situ P doped GeSn, with then an increase of the Ge elemental growth rate component for high PH_3 flows.

The combination of Ge_2H_6 , Si_2H_6 and PH_3 might have resulted, besides some surface poisoning, in the formation of gas phase intermediates that reduced the incorporation of Ge.

IV.5 Surface morphology and roughness

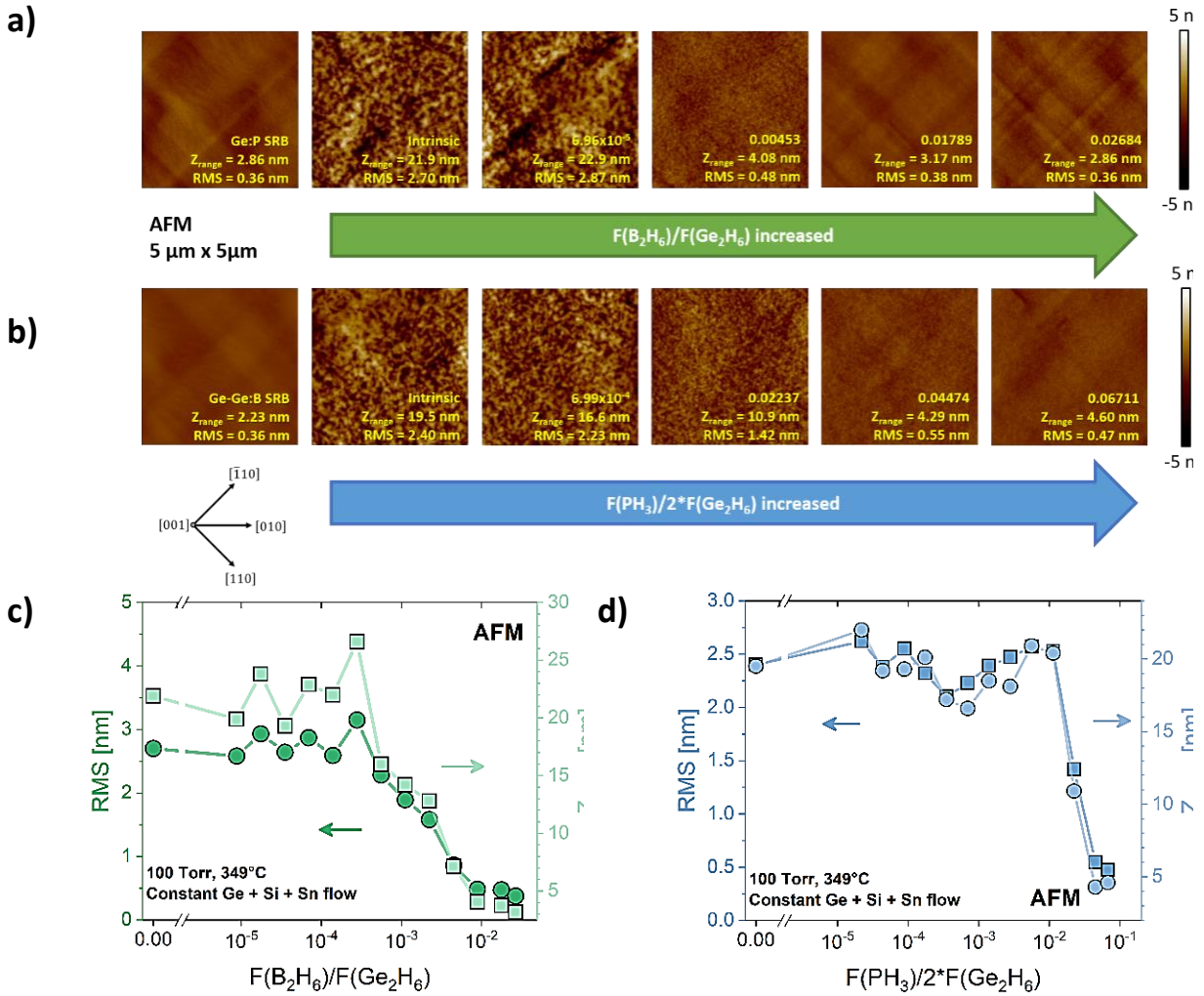


Figure IV.5: 5 μm x 5 μm AFM images of the surfaces of 69 nm to 76 nm thick SiGeSn:B layers (a) and 72 nm to 60 nm thick SiGeSn:P layers (b) grown at 349 °C, 100 Torr with various $F(\text{B}_2\text{H}_6)/F(\text{Ge}_2\text{H}_6)$ or $F(\text{PH}_3)/2 \cdot F(\text{Ge}_2\text{H}_6)$ MFRs on Ge/Ge:P or Ge/Ge:B SRBs. Surface RMS roughness and Z_{range} values for SiGeSn:B (c) and SiGeSn:P (d) for various $F(\text{B}_2\text{H}_6)/F(\text{Ge}_2\text{H}_6)$ or $F(\text{PH}_3)/2 \cdot F(\text{Ge}_2\text{H}_6)$ MFRs. The $F(\text{Ge}_2\text{H}_6)/F(\text{H}_2)$, $F(\text{Si}_2\text{H}_6)/F(\text{H}_2)$ and the $F(\text{SnCl}_4)/F(\text{H}_2)$ MFRs were constant at 7.92×10^{-4} , 1.25×10^{-3} and 4.69×10^{-5} , respectively. Growth temperatures and pressures were equal to 349 °C and 100 Torr.

Figure IV.5 (a) shows 5 μm x 5 μm AFM images for SiGeSn:B. The starting Ge-Ge:P SRB had a smooth surface, with a well-defined cross-hatch along the $\langle 110 \rangle$ directions. Some terraces can even be seen, outlining its good surface quality. [13] As soon as intrinsic SiGeSn was grown on top of such SRBs, the surface became rough and the cross-hatch grainy, with a Root-Mean-Square (RMS) roughness of 2.70 nm and a Z_{range} of 21.9 nm, similar to what

Khazaka *et al.* observed. [9] The surface stayed rough and the cross-hatch grainy for low B_2H_6 flows. At a $F(B_2H_6)/F(Ge_2H_6)$ MFR of 4.53×10^{-3} , the surface started to become smooth again. However, the cross-hatch was not recovered. The surface was smoother still for a $F(B_2H_6)/F(Ge_2H_6)$ MFR of 1.79×10^{-2} , with a cross-hatch re-appearing. The cross-hatch was fully recovered for a $F(B_2H_6)/F(Ge_2H_6)$ MFR of 2.68×10^{-2} and metrics were then that of the starting SRB underneath.

RMS roughness (dark green circles) and Z_{range} values (light green squares) are shown for SiGeSn:B in **Figure IV.5 (c)**. They were close to that of intrinsic SiGeSn for low diborane flows. As seen in **Figure IV.5 (a)**, the surface became smoother and the cross-hatch was gradually recovered when the diborane flow increased. This resulted in lower RMS roughness and Z_{range} , with values as low as 0.36 nm and 2.86 nm for the highest diborane flows probed. Such values are similar to that for intrinsic and doped GeSn. [2], [14] Drastically improved SiGeSn:B surfaces compared to that of intrinsic SiGeSn were obtained. [9], [10]

Figure IV.5 (b) shows $5 \mu m \times 5 \mu m$ AFM images for SiGeSn:P. The Ge / Ge:B buffer used for the growth of SiGeSn(:P) was of similar quality than the Ge / Ge:P one used for SiGeSn(:B). It had a well-defined cross-hatch along the $\langle 110 \rangle$ directions and a smooth surface. Again, as soon as Si_2H_6 was added to the growth mixture, the surface became rough and the cross-hatch grainy. The RMS roughness and Z_{range} values were 2.40 nm and 19.5 nm, then. The SiGeSn:P surface remained rough and grainy for low phosphine flows. It stayed that way for higher $F(PH_3)/2 * F(Ge_2H_6)$ MFRs than for SiGeSn:B. At a $F(PH_3)/2 * F(Ge_2H_6)$ MFR of 2.24×10^{-2} , the SiGeSn:P surface started to become smooth, while the cross-hatch stayed grainy. At a $F(PH_3)/2 * F(Ge_2H_6)$ MFR of 4.47×10^{-2} , the surface became significantly smoother with RMS roughness and Z_{range} values of 0.55 nm and 4.29 nm, respectively. However, no clear surface cross-hatch was visible. At the highest $F(PH_3)/2 * F(Ge_2H_6)$ MFR of 6.71×10^{-2} , a cross-hatch started to appear. RMS roughness and Z_{range} were 0.47 nm and 4.60 nm, respectively. Those values were slightly higher than that for intrinsic and in-situ P doped GeSn. [2], [14] In **Figure IV.5 (d)**, the SiGeSn(:P) surface became drastically smoother only for the highest three PH_3 flows probed, while, for SiGeSn(:B), the surface became smoother over a wider range of high B_2H_6 flows. It should be pointed out that the in-situ B or P doped SiGeSn layers with the highest dopant flows were grown twice in order to confirm those smoothing trends; similar results were obtained.

The incorporation, for high diborane flows, of large amounts of Si atoms likely resulted in a reduction of the built-in compressive strain (see **Figure IV.1 (a)** XRD profiles), which might have contributed to the recovery of the SiGeSn:B surface cross-hatch. The Si lattice parameter ($a_{Si} = 5.43105 \text{ \AA}$) is indeed much smaller than the Ge and Sn ones ($a_{Sn} = 6.489 \text{ \AA}$ and $a_{Ge} = 5.65785 \text{ \AA}$). Moreover, it was previously shown, by Atom Probe Tomography (APT), that there was some small Si-Si attraction inside intrinsic SiGeSn that led to a non-standard Si distribution where Si neighbors were more likely Si atoms than expected for a random Si distribution. [15] Such a distribution might have led to this grainy aspect for intrinsic and weakly doped SiGeSn surfaces. The addition of small size B ($a_B = 3.852 \text{ \AA}$) and P ($a_P = 4.94 \text{ \AA}$) atoms might have modified the atomic distribution in heavily in-situ doped SiGeSn layers, which became more random, resulting in some cross-hatch recovery and smoother surfaces. To confirm such a hypothesis, APT measurements would need to be performed and next-nearest-neighbor-distributions analyzed, which is beyond the scope of this PhD thesis.

IV.6 Incorporation and activation of dopants in the SiGeSn lattice

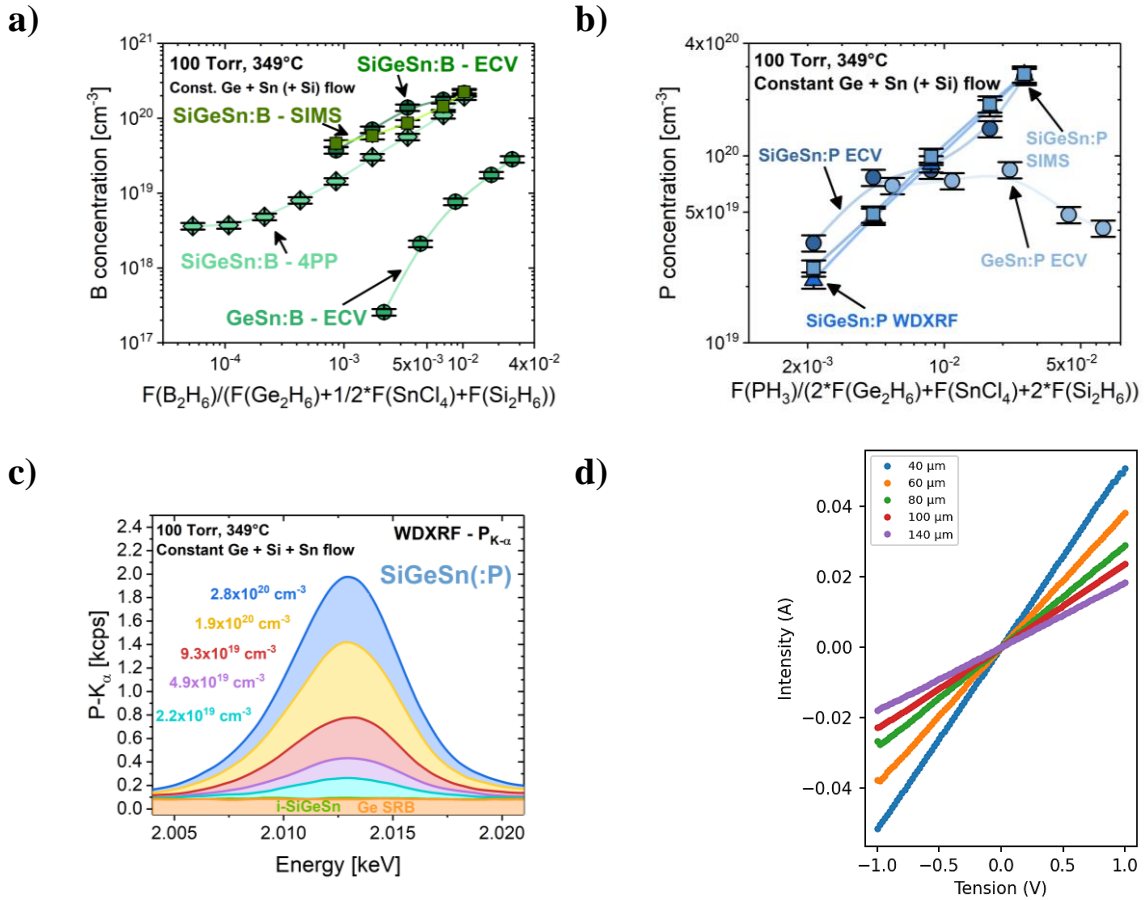


Figure IV.6: (a) Atomic B concentration from SIMS and active carrier concentration from ECV and Four Point Probe (4PP) measurements. (b) Atomic P concentrations from WDXRF and SIMS together with active carrier concentrations from ECV. (c) P-K_α lines of SiGeSn:P layers grown on Ge SRBs for the five highest $F(PH_3)/2*F(Ge_2H_6)$ MFRs. (d) Transmission line measurements of in-situ B doped SiGeSn grown with a $F(B_2H_6)/F(Ge_2H_6)$ MFR of 2.68×10^{-2} . The five highest $F(B_2H_6)/F(Ge_2H_6)$ or five highest $F(PH_3)/2*F(Ge_2H_6)$ MFRs were probed. The $F(Ge_2H_6)/F(H_2)$ and the $F(SnCl_4)/F(H_2)$ MFRs were constant at 7.92×10^{-4} and 4.69×10^{-5} , respectively. Growth temperatures and pressures were equal to 349 °C and 100 Torr.

Figure IV.6 (a) shows how the electrically active carrier concentration in in-situ doped SiGeSn(:B) changed when the diborane flow increased. The electrically active carrier concentration determined by Four Point Probe (4PP) (**Figure IV.6 (a)** light green diamonds) increased at first slowly then more rapidly, from $3.6 \times 10^{18} \text{ cm}^{-3}$ up to $2.0 \times 10^{20} \text{ cm}^{-3}$, as the B_2H_6 flow increased. For low diborane flows, the electrically active carrier concentration was too low to be reliably detected by 4PP. It should otherwise be mentioned that the abacus plot of Sze for pure Ge was used to convert 4PP measurements into boron ions concentrations. [16] Because high amounts of Si and Sn were present in our SiGeSn:B layers, such an assumption is not that accurate. It however seemed to yield rather good estimations of the B ions concentrations, which were in line with data from other techniques. Over the common range probed, 4PP values

were confirmed by ECV measurements (**Figure IV.6 (a)** dark green circles). To obtain the ECV mean values, data was averaged between 10 nm (to avoid surface effects) and 40 nm (to avoid buffer contributions). ECV values were slightly higher than 4PP values, maybe because of the small energy band gap of SiGeSn that resulted in a small inversion region for CV measurements, making the extraction of the electrically active carrier concentration more difficult. The error on the electrically active carrier concentration from 4PP and ECV was nevertheless estimated to be 10%. The electrically active carrier concentration was significantly higher in SiGeSn:B than in GeSn:B [2], shown in **Figure IV.6 (a)** green circles. This was likely due to a higher solid solubility of B atoms thanks to Si contents of up to 25%. It is indeed known that the B solid solubility increases with the Si content in a Ge lattice. [17] The atomic concentration of B from SIMS, shown in **Figure IV.6 (a)**, increased with the diborane flow from $4.6 \times 10^{19} \text{ cm}^{-3}$ up to $2.2 \times 10^{20} \text{ cm}^{-3}$ (from a depth of 10 nm up to the layer thickness). Such atomic concentrations were in line with the electrically active carrier concentration from ECV, outlining that close to full activation was achieved. The boron SIMS depth profiles were box-like, without any surface or interface peaks. To obtain even higher dopant concentrations (at most $6 \times 10^{20} \text{ cm}^{-3}$ in in-situ B doped Ge [18] grown at 320°C with $\text{Ge}_2\text{H}_6 + \text{B}_2\text{H}_6$), further improvements of the growth parameters will be necessary. Nevertheless, the very high electrically active carrier concentration should result in significantly lower contact resistances and better performances of (Si)GeSn based devices.

The dark blue squares in **Figure IV.6 (b)** show the electrically active carrier concentration from ECV for SiGeSn:P. Indeed, our 4PP setup did not yield trustworthy electrically active carrier concentrations for SiGeSn:P, likely because no good np-junction was formed with the substrate. The electrical active carrier concentration from ECV increased significantly, up to $2.7 \times 10^{20} \text{ cm}^{-3}$, when more P was supplied by increasing the phosphine flow. To obtain the ECV mean values for SiGeSn:P, an average between 5 nm (to avoid surface effects) and 30 nm (to avoid buffer contributions) was taken. The electrically active carrier concentration in SiGeSn:P was significantly higher than that in in-situ P doped GeSn, with a maximum electrically active carrier concentration of at most $6.9 \times 10^{19} \text{ cm}^{-3}$. [2] This was due to a reduction of the electrically active carrier concentration in GeSn:P layers for the highest phosphine flows probed, as shown in **Figure IV.6 (b)** (light blue circles). Then, P atoms most likely formed electrically inactive $\text{Sn}_m\text{P}_n\text{-V}$ clusters. [19], [20] The electrically active carrier concentration in SiGeSn:P was even higher than in Ge:P, with at most $7.5 \times 10^{19} \text{ cm}^{-3}$ at 350°C , then. [19] Thanks to the larger mass of P compared to B, it was possible to obtain the atomic P concentration in in-situ doped SiGeSn, shown as blue triangles in **Figure IV.6 (b)**, by recording the P- K_α line intensity with WDXRF. Spectra are shown in **Figure IV.6 (c)**. For the Ge-Ge:B SRB and the intrinsic SiGeSn layer, no P- K_α line peak was recorded, confirming the lack of P atoms. The atomic P concentration increased almost linearly with the phosphine flow, outlined by the increasing P- K_α line intensity, reaching at most $2.8 \times 10^{20} \text{ cm}^{-3}$ for in-situ P doped SiGeSn. SIMS profiles were box like and confirmed the atomic P concentration obtained by WDXRF. It was close to the electrically active carrier concentration in SiGeSn(:P) from ECV, showing that P atoms were almost fully electrically activated. It thus seemed like that no or significantly less electrically inactive $\text{Sn}_m\text{P}_n\text{-V}$ clusters formed when Si was present in large amounts in the GeSn alloy.

To assess whether or not in-situ doped layers had an impact on the performance of contacts, some Transmission Line Measurement (TLM) structures were fabricated. Mesas were defined

by anisotropic dry etching. To deposit the metal, first some Ar plasma etching was performed, 10 nm of NiPt were sputtered on top and it was capped with 7 nm of TiN. Then, the structure was covered by 10 nm of Ti and 200 nm of Au. TLM results for the highest in-situ B doped SiGeSn layer grown with a $F(\text{B}_2\text{H}_6)/F(\text{Ge}_2\text{H}_6)$ MFR of 2.68×10^{-2} are shown in **Figure IV.6 (d)**. Ohmic contacts were obtained, with a contact resistivity of $2 \times 10^{-5} \Omega \text{ cm}^2$.

In previous studies on in-situ B or P doped SiGeSn [3], [11], the maximum p-type and n-type doping were $2 \times 10^{20} \text{ cm}^{-3}$ and $8 \times 10^{19} \text{ cm}^{-3}$, respectively. Electrically active carrier concentrations in the current study were higher or equal than those values.

$x_{\text{B}}/(1-x_{\text{B}}) = m * F(\text{B}_2\text{H}_6) / ((F(\text{Ge}_2\text{H}_6) + \frac{1}{2} F(\text{SnCl}_4) + F(\text{Si}_2\text{H}_6))$ and $x_{\text{P}}/(1-x_{\text{P}}) = m * F(\text{PH}_3) / (2 * F(\text{Ge}_2\text{H}_6) + F(\text{SnCl}_4) + 2 * F(\text{Si}_2\text{H}_6))$ relationships accounted for the semi-linear increase of the atomic B concentration x_{B} and P concentration x_{P} with the diborane and phosphine flows, respectively. m values below 1 meant that the incorporation of dopants was more complicated than the incorporation of Ge, Si or Sn. m was equal to 0.05 for GeSn:B [2], 0.42 for SiGeSn:B (current results) and 0.68 for Ge:B. [21] Meanwhile, m was equal to 0.14 for GeSn:P [2], 0.25 for SiGeSn:P (current results) and 0.47 for Ge:P [43]. As all layers were grown at 350°C , 100 Torr with a $\text{Ge}_2\text{H}_6 + \text{Si}_2\text{H}_6 + \text{SnCl}_4 + \text{PH}_3$ or B_2H_6 chemistry, it thus meant that dopant incorporation was more efficient in SiGeSn than in GeSn and close to that in Ge.

IV.7 Conclusions

In the current study, the in-situ B and P doping of SiGeSn was investigated. Ge_2H_6 , SnCl_4 and Si_2H_6 were used as precursors for the growth of SiGeSn at 349°C , 100 Torr. PH_3 and B_2H_6 were the n-type and p-type gaseous precursors, respectively. For high dopant flows, the SiGeSn:B or SiGeSn:P surface quality was improved with a recovering of a cross-hatch along the $\langle 110 \rangle$ directions, RMS roughness as low as 0.36 nm (SiGeSn:B) and 0.47 nm (SiGeSn:P) and Z_{range} values down to 2.86 nm (SiGeSn:B) and 4.60 nm (SiGeSn:P). Adding B_2H_6 or PH_3 to the growth mixture resulted, for high dopant flows, in significantly higher Si contents and slightly lower Sn incorporation (SiGeSn:B) or steady Si contents and slightly higher Sn incorporation (SiGeSn:P). Si / Sn ratios of 3.5 with Si contents of up to 25% were achieved in SiGeSn:B. Ge and Si competing for surface sites might partly explain those composition changes. It might also be that the addition of B_2H_6 or PH_3 resulted in the formation of gas phase intermediates that reduced the incorporation of Ge, but further investigations would be needed to fully understand growth mechanisms. The electrically active carrier concentrations were improved, reaching $2.0 \times 10^{20} \text{ cm}^{-3}$ for SiGeSn:B and $2.7 \times 10^{20} \text{ cm}^{-3}$ for SiGeSn:P, e.g. values higher than for in-situ B and P doped GeSn grown with the same process conditions (save for the lack of Si_2H_6). Those values are interesting for (Si)GeSn based devices, especially electrically pumped (Si)GeSn lasers.

References

- [1] V. Holy, U. Pietsch, and T. Baumbach, *High-Resolution X-Ray Scattering from Thin Films and Multilayers*, vol. 149. Berlin, Heidelberg: Springer Berlin Heidelberg, 1999. doi: 10.1007/BFb0109385.
- [2] M. Frauenrath *et al.*, “An In-Depth Study of the Boron and Phosphorous Doping of GeSn,” *ECS J. Solid State Sci. Technol.*, vol. 10, no. 8, p. 085006, Aug. 2021, doi: 10.1149/2162-8777/ac1d27.
- [3] Y.-Y. Fang, J. Tolle, A. V. G. Chizmeshya, J. Kouvetakis, V. R. D’Costa, and J. Menendez, “Practical B and P doping via SixSnyGe_{1-x-y-z}Mz quaternaries lattice matched to Ge: Structural, electrical, and strain behavior,” *Appl. Phys. Lett.*, vol. 95, no. 8, p. 081113, Aug. 2009, doi: 10.1063/1.3204456.
- [4] J. Margetis, S.-Q. Yu, B. Li, and J. Tolle, “Chemistry and kinetics governing hydride/chloride chemical vapor deposition of epitaxial Ge_{1-x}Sn_x,” *J. Vac. Sci. Technol. A*, vol. 37, no. 2, p. 021508, Mar. 2019, doi: 10.1116/1.5055620.
- [5] F. Gencarelli *et al.*, “Crystalline Properties and Strain Relaxation Mechanism of CVD Grown GeSn,” *ECS J. Solid State Sci. Technol.*, vol. 2, no. 4, pp. P134–P137, 2013, doi: 10.1149/2.011304jss.
- [6] J. P. Dismukes, L. Ekstrom, and R. J. Paff, “Lattice Parameter and Density in Germanium-Silicon Alloys ¹,” *J. Phys. Chem.*, vol. 68, no. 10, pp. 3021–3027, Oct. 1964, doi: 10.1021/j100792a049.
- [7] E. Nolot, S. Cadot, F. Martin, P. Hönicke, C. Zech, and B. Beckhoff, “In-line characterization of ultrathin transition metal dichalcogenides using X-ray fluorescence and X-ray photoelectron spectroscopy,” *Spectrochim. Acta Part B At. Spectrosc.*, vol. 166, p. 105788, Apr. 2020, doi: 10.1016/j.sab.2020.105788.
- [8] C. Jeynes *et al.*, “Quantifying nitrogen in GeSbTe:N alloys,” *J. Anal. At. Spectrom.*, vol. 35, no. 4, pp. 701–712, 2020, doi: 10.1039/C9JA00382G.
- [9] R. Khazaka, J. Aubin, E. Nolot, and J.-M. Hartmann, “Investigation of the Growth of Si-Ge-Sn Pseudomorphic Layers on 200 mm Ge Virtual Substrates: Impact of Growth Pressure, HCl and Si₂H₆ Flows,” *ECS Trans.*, vol. 86, no. 7, pp. 207–218, Jul. 2018, doi: 10.1149/08607.0207ecst.
- [10] R. Khazaka, E. Nolot, J. Aubin, and J.-M. Hartmann, “Growth and characterization of SiGeSn pseudomorphic layers on 200 mm Ge virtual substrates,” *Semicond. Sci. Technol.*, vol. 33, no. 12, p. 124011, Dec. 2018, doi: 10.1088/1361-6641/aaea32.
- [11] S. Wirths *et al.*, “Growth Studies of Doped SiGeSn/Strained Ge(Sn) Heterostructures,” *ECS Trans.*, vol. 64, no. 6, pp. 689–696, Aug. 2014, doi: 10.1149/06406.0689ecst.
- [12] J. Perrin, Y. Takeda, N. Hirano, Y. Takeuchi, and A. Matsuda, “Sticking and recombination of the SiH₃ radical on hydrogenated amorphous silicon: The catalytic effect of diborane,” *Surf. Sci.*, vol. 210, no. 1–2, pp. 114–128, Mar. 1989, doi: 10.1016/0039-6028(89)90106-4.
- [13] J. M. Hartmann and J. Aubin, “Assessment of the growth/etch back technique for the production of Ge strain-relaxed buffers on Si,” *J. Cryst. Growth*, vol. 488, pp. 43–50, Apr. 2018, doi: 10.1016/j.jcrysgro.2018.02.036.
- [14] J. Aubin and J. M. Hartmann, “GeSn growth kinetics in reduced pressure chemical vapor deposition from Ge₂H₆ and SnCl₄,” *J. Cryst. Growth*, vol. 482, pp. 30–35, Jan. 2018, doi: 10.1016/j.jcrysgro.2017.10.030.
- [15] S. Mukherjee *et al.*, “Short-range atomic ordering in nonequilibrium silicon-germanium-tin semiconductors,” *Phys. Rev. B*, vol. 95, no. 16, p. 161402, Apr. 2017, doi: 10.1103/PhysRevB.95.161402.

- [16] S. M. Sze and J. C. Irvin, "Resistivity, mobility and impurity levels in GaAs, Ge, and Si at 300°K," *Solid-State Electron.*, vol. 11, no. 6, pp. 599–602, Jun. 1968, doi: 10.1016/0038-1101(68)90012-9.
- [17] C. Porret *et al.*, "(Invited) Very Low Temperature Epitaxy of Group-IV Semiconductors for Use in FinFET, Stacked Nanowires and Monolithic 3D Integration," *ECS Trans.*, vol. 86, no. 7, pp. 163–175, Jul. 2018, doi: 10.1149/08607.0163ecst.
- [18] C. Porret *et al.*, "Low-Temperature Selective Growth of Heavily Boron-Doped Germanium Source/Drain Layers for Advanced pMOS Devices," *Phys. Status Solidi A*, vol. 217, no. 3, p. 1900628, Feb. 2020, doi: 10.1002/pssa.201900628.
- [19] J. Aubin, J. M. Hartmann, J. P. Barnes, J. B. Pin, and M. Bauer, "Very Low Temperature Epitaxy of Heavily In Situ Phosphorous Doped Ge Layers and High Sn Content GeSn Layers," *ECS J. Solid State Sci. Technol.*, vol. 6, no. 1, pp. P21–P26, 2017, doi: 10.1149/2.0091701jss.
- [20] A. Vohra *et al.*, "Source/Drain Materials for Ge nMOS Devices: Phosphorus Activation in Epitaxial Si, Ge, $\text{Ge}_{1-x}\text{Sn}_x$ and $\text{Si}_y\text{Ge}_{1-x-y}\text{Sn}_x$," *ECS J. Solid State Sci. Technol.*, vol. 9, no. 4, p. 044010, Jan. 2020, doi: 10.1149/2162-8777/ab8d91.
- [21] J.-M. Hartmann, M. Frauenrath, J. Richey, and M. Veillerot, "Ultra-High Boron Doping of Si and Ge for Nanoelectronics and Photonics," *ECS Trans.*, vol. 98, no. 5, pp. 203–214, Sep. 2020, doi: 10.1149/09805.0203ecst.

**Chapter V : Nanosecond Laser
Annealing of In-Situ B Doped Ge**

Chapter V: Chapter V: Nanosecond Laser Annealing of In-Situ B doped Ge

<u>Chapter V: Nanosecond Laser Annealing of In-Situ B Doped Ge.....</u>	90
V.1 Introduction.....	90
V.2 Impact of the substitutional B concentration on the melt threshold	90
V.3 Single pulse nanosecond laser annealing: Dopant activation	91
V.4 Single pulse nanosecond laser annealing: Surface morphology evolution.....	92
V.5 Single pulses nanosecond laser annealing on Ge:B: Crystalline structure	96
V.6 Multipulse nanosecond laser annealing: Surface morphology evolution	97
V.7 Multipulse nanosecond laser annealing: Crystalline structure evolution	99
V.8 Multipulse nanosecond laser annealing: Dopant activation	100
V.9 Conclusions.....	100

Chapter V: Nanosecond Laser Annealing of In-Situ B Doped Ge**V.1** Introduction

In previous studies, it was shown that the electrically active carrier concentration in binary Si:P could be significantly increased by nanosecond laser annealing thanks to its ability to dissolve P clusters. [1] In binary Si:B, superconductivity was achieved by electrically activating ultra-high B concentrations. [2] In-situ doping Ge with B resulted in binary alloys [3] with metastable, ultra-high substitutional concentrations. The difference between B ion concentration and substitutional concentration was due to the formation of electrically inactive clusters. [4]

Layers with the highest possible electrically active carrier concentrations are generally used to lower the contact resistances and benefit from higher performance devices. In this study, we sought to enhance the electrical activation of highly in-situ boron-doped Ge thanks to nanosecond laser annealing (NLA).

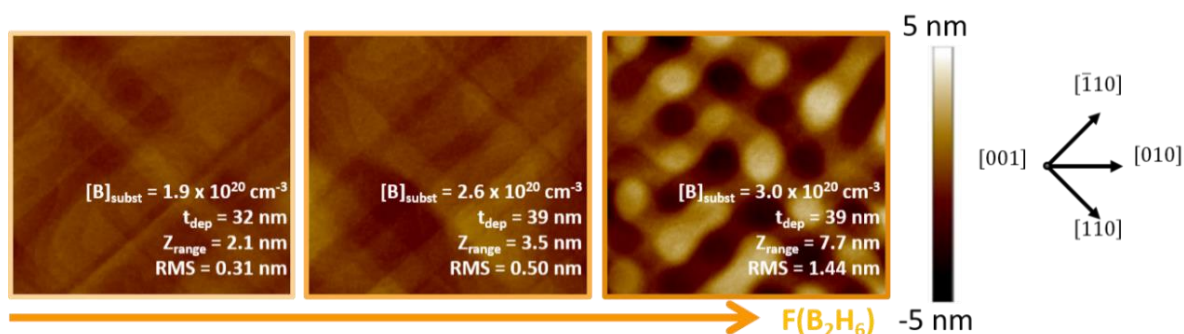
V.2 Impact of the substitutional B concentration on the melt threshold

Figure V.1: 5 μm x 5 μm atomic force microscopy (AFM) images of Ge:B layers grown with various $F(\text{B}_2\text{H}_6)/F(\text{Ge}_2\text{H}_6)$ MFRs. The z-scale ranges from -5 nm to 5 nm and the crystallographic directions are shown on the right. The $F(\text{Ge}_2\text{H}_6)/F(\text{H}_2)$ MFR was constant at 7.92×10^{-4} . Growth temperatures and pressures were equal to 349°C and 100 Torr. The $F(\text{B}_2\text{H}_6)/F(\text{Ge}_2\text{H}_6)$ MFRs were 8.95×10^{-3} , 1.79×10^{-2} and 2.68×10^{-2} (from left to right).

5 μm x 5 μm Atomic Force Microscopy (AFM) images of the surface for 32 to 39 nm thick in-situ boron-doped Ge layers are shown, with a 5 nm z-scale, in **Figure V.1**. The substitutional B concentration, from XRD, increased from $1.9 \times 10^{20} \text{ cm}^{-3}$ on the left up to $3.0 \times 10^{20} \text{ cm}^{-3}$ on the right (through a B_2H_6 dopant flow increase). For the lowest two diborane flows, surfaces were rather smooth, with Root Mean Square (RMS) roughness below 0.5 nm and Z_{range} values below 4 nm. Both layers exhibited a surface cross-hatch along the $\langle 110 \rangle$ crystalline directions, as for the Ge SRBs underneath. The Ge:B layer grown with the highest $F(\text{B}_2\text{H}_6)/F(\text{Ge}_2\text{H}_6)$ Mass Flow Ratio (MFR) was much rougher. The RMS roughness and Z_{range} were then of 1.44 nm and 7.7 nm, respectively.

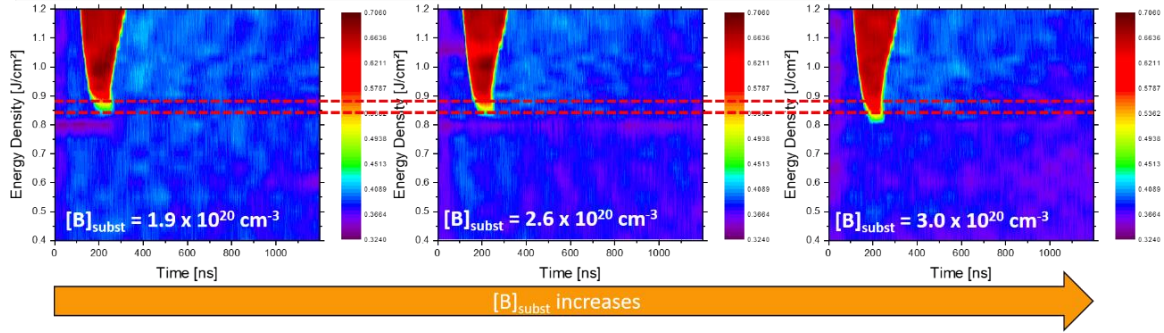


Figure V.2: Time Resolved Reflectivity Maps for different $F(B_2H_6)/F(Ge_2H_6)$ MFRs. The red dashed lines show the energy densities at which the top Ge:B layers first melted. The $F(Ge_2H_6)/F(H_2)$ MFR was constant at 7.92×10^{-4} . Growth temperatures and pressures were equal to $349^\circ C$ and 100 Torr. The $F(B_2H_6)/F(Ge_2H_6)$ MFRs were 8.95×10^{-3} , 1.79×10^{-2} and 2.68×10^{-2} (from left to right).

Figure V.2 shows various Time Resolved Reflectivity (TRR) Maps. The construction of TRR maps is detailed elsewhere. [5] Due to the higher reflectivity of liquid compared to solid semiconductors, we could easily detect the energy density at which a solid to liquid transition occurred upon annealing. [6], [7] The melt threshold shifted from 0.875 Jcm^{-2} down to 0.85 Jcm^{-2} as the substitutional B concentration increased. This was likely due to differences in terms of crystalline quality and/or surface roughness, but might also be due to the increased B concentration itself. This might in part explain why the melt threshold shifted to lower energy densities. In the following, we will focus on the 39 nm thick Ge:B layer grown with the intermediate B_2H_6 flow because it was smooth and the substitutional B concentration was high indeed ($2.6 \times 10^{20} \text{ cm}^{-3}$).

V.3 Single pulse nanosecond laser annealing: Dopant activation

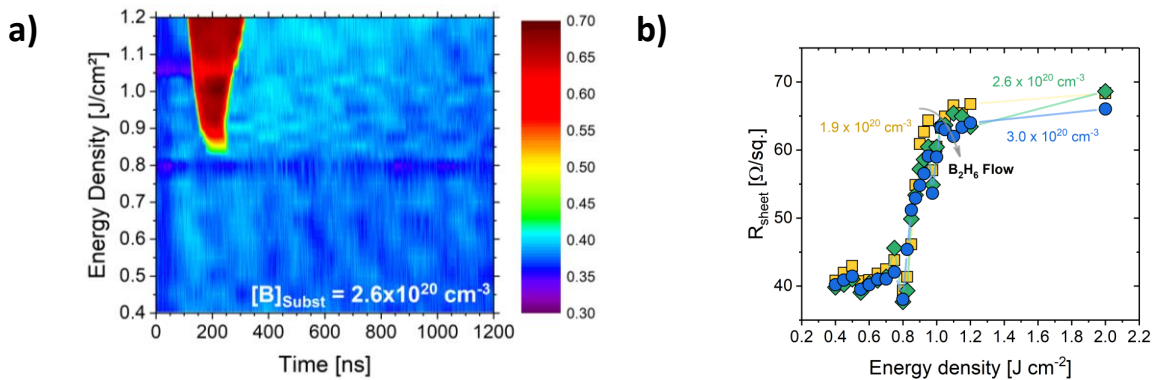


Figure V.3: (a) Time Resolved Reflectivity Map for a 39 nm thick Ge:B layer with a substitutional B concentration of $2.6 \times 10^{20} \text{ cm}^{-3}$ grown with a $F(B_2H_6)/F(Ge_2H_6)$ MFR of 1.79×10^{-2} . (b) Four point probe measurements of sheet resistance R_s for various diborane flows and different energy densities. The $F(Ge_2H_6)/F(H_2)$ MFR was constant at 7.92×10^{-4} . Growth temperatures and pressures were equal to $349^\circ C$ and 100 Torr.

The TRR map for the Ge:B layer with the intermediate diborane flow is shown in **Figure V.3 (a)**. At low Energy Densities (i.e. up to 0.80 Jcm^{-2}), the TRR signal did not significantly change. At an ED around 0.825 Jcm^{-2} , the reflectivity signal increased when the laser pulse was shone onto the surface. Some small and localized areas were melted at this ED. At 0.85 Jcm^{-2} , the TRR signal started to saturate. Significant amounts of the surface were melted, then. It enabled the determination of the melt threshold at 0.85 Jcm^{-2} . As the ED further increased, the time during which the TRR signal saturated increased. This was due to an increase of the Ge:B melt depth, resulting in the detection of a liquid layer by TRR over longer durations.

The sheet resistance was probed for all EDs by four-point probe measurements, as shown in **Figure V.3 (b)** for the various Ge:B layers grown. The sheet resistance's evolution did not significantly depend on the substitutional B concentration. Therefore, only the second highest diborane flow probed is discussed. Below the melt threshold, the sheet resistance did not significantly change. When the layer started melting, the sheet resistance rapidly increased, from $39.82 \text{ } \Omega/\square$ up to $68.62 \text{ } \Omega/\square$ (+70%). At an ED around 1.00 Jcm^{-2} , it began to saturate. Above that ED, the sheet resistance continued to increase, but much more slowly. We assume that, around this ED, the whole Ge:B layer was melted. Such an assumption was based on LIAB simulations [8], which showed full melt after nanosecond laser annealing at 1.05 Jcm^{-2} . This will be discussed in more details in the next section.

There were multiple reasons as to why the sheet resistance increased. It might be that the crystalline quality or surface morphology worsened. Moreover, dopant redistribution could explain an increase of the sheet resistance. Atomic Force Microscopy (AFM) and X-Ray Diffraction (XRD) measurements were thus performed in order to gain some insight about the mechanisms leading to this sheet resistance evolution.

V.4 Single pulse nanosecond laser annealing: Surface morphology evolution

Figure V.4 shows $5 \text{ } \mu\text{m} \times 5 \text{ } \mu\text{m}$ AFM images of in-situ doped Ge:B for various NLA energy densities. **Figure V.4 (a)** shows the layer after NLA with an energy density of 0.60 Jcm^{-2} (and a z-scale of 5 nm). The surface remained smooth with a RMS roughness and a Z_{range} of 0.60 nm and 5.4 nm, respectively.

This meant that the surface morphology did not significantly change below the melt threshold. For comparison, the as-grown Ge:B layer is shown in **Figure V.1 (b)**. This regime was previously identified as being the sub-melt regime. [9] When the ED increased up to the melt threshold (0.825 Jcm^{-2}), the TRR signal significantly changed (see **Figure V.3 (a)**). Actually, localized surface structures melted, as shown in **Figure V.4 (b)** with a 30 nm z-scale. Surface structures were rectangular and their sides were aligned along the $\langle 110 \rangle$ directions, as the cross-hatch of the as-grown layer. The size of all surface structures was quite constant. Comparable surface structures were previously seen for SiGe. [10] When the energy density further increased, up to 0.85 Jcm^{-2} , surface structures multiplied and merged, as shown in **Figure V.4 (c)**. We were then in the partial melt regime. [9] A High Resolution Transmission Electron Microscope (HR-TEM) image of the Ge:B layer after NLA with an ED of 0.85 Jcm^{-2} is shown in **Figure V.4 (f)**. The Ge:B layer had a thickness of 33 nm, which was slightly lower than that of the as-grown layer, i.e. 39 nm. It might be that some material agglomerated in the

12 nm high surface structures. Recrystallization was complete but gave rise to three-dimensional islands on the surface, with a brighter contrast. This latter was due to a lack of material in the surface convex structure compared to the thickness of the TEM foil. The crystalline quality of this layer was somewhat good, as outlined by the Fast Fourier Transform of the TEM image, with (011) pole orientation and well defined spots. However, they were less well defined than for a superior quality epitaxial layer.

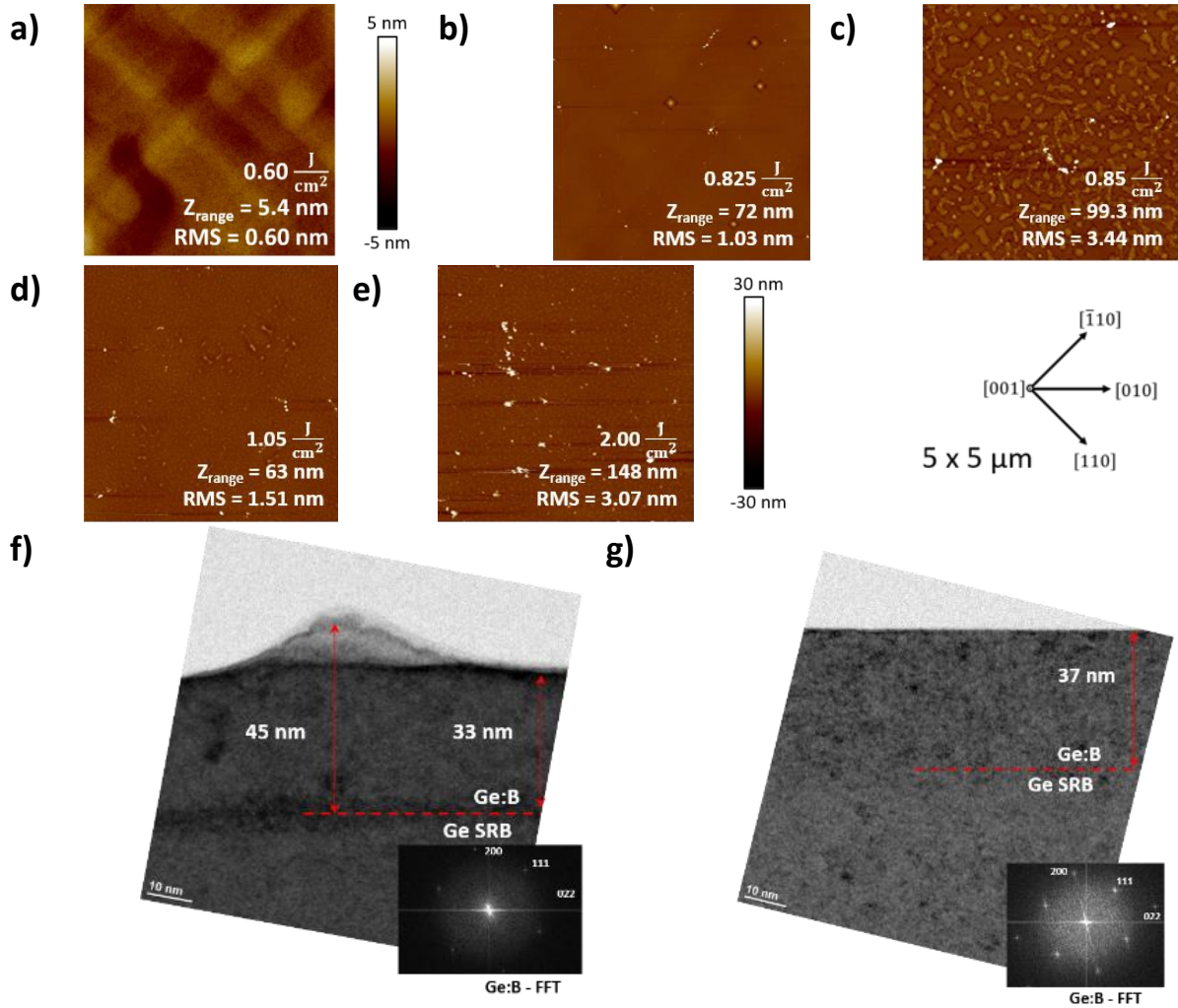


Figure V.4: 5 μm x 5 μm atomic force microscopy images of, initially, a 39 nm thick Ge:B layer with $[B]_{\text{subst.}} = 2.6 \times 10^{20} \text{ cm}^{-3}$ after nanosecond laser anneals at 0.60 Jcm⁻² ((a), Z_{range} scale between -5 nm and 5 nm), 0.825 Jcm⁻² (b), 0.85 Jcm⁻² (c), 1.05 Jcm⁻² (d) and 2.00 Jcm⁻² (e) (all z-scales range from -30 nm to 30 nm). The crystallographic directions are shown in the middle on the right. High Resolution Transmission Electron Microscope (HR-TEM) image of in-situ B doped Ge after NLA at 0.85 Jcm⁻² (f) and 1.05 Jcm⁻² (g).

At 1.05 Jcm⁻², shown in **Figure V.4 (d)**, surface structures merged and a smoother surface was obtained, with a RMS roughness of 1.51 nm compared to 3.44 nm at 0.85 Jcm⁻². Where the surface structures merged, some undulations appeared. **Figure V.4 (g)** shows a HR-TEM image

for 1.05 Jcm^{-2} . The surface was smooth and it seemed that the whole Ge:B layer had melted. This confirmed our hypothesis on the sheet resistance saturation occurring when reaching the full melt regime at higher energy densities. [9] For 2.00 Jcm^{-2} , shown in **Figure V.4 (e)**, the surface did not significantly change. There were still undulations, because of the merging of surface structures, together with a limited number of larger surface structures. The indiffusion of oxygen during the annealing process might have led to the formation of clusters that resulted in those larger surface structures. Although experiments were performed while flowing large amounts of N_2 over the annealed surface (to prevent as much as possible oxygen incorporation). Oxygen indiffusion can not be excluded, however, as previously reported in the literature. [11]–[13]

In order to better understand the formation of surface structures above the melt threshold, quantitative analyzes of the surface structures were performed utilizing the Particle Analysis feature of the NanoScope analyzing software from Bruker. To obtain comparable datasets, a threshold at 2 nm above the mean plane of the various surfaces was used and all recorded AFM images were flattened by a 6th order fit to guaranty that long range undulations (because of the surface cross-hatch of the Ge SRBs underneath) were not counted as surface structures.

At the melt threshold, some surface structures were detected, shown in **Figure V.5 (a)**. Their surface density rapidly increased with the energy density. It reached a peak of $27.36 \mu\text{m}^{-2}$ at an energy density of 0.925 Jcm^{-2} . The surface density then decreased and reached a minimum of $0.32 \mu\text{m}^{-2}$ at an energy density of 1.10 Jcm^{-2} .

This occurred when surface structures started to merge. Similarly, the surface coverage by those surface structures reached its maximum of 20% at the same energy density and its minimum around the full melt, as shown in **Figure V.5 (c)**. Above 1.10 Jcm^{-2} , significant amounts of the Ge SRB layer underneath were expected to melt, which might be the reason as to why surface structure were once again formed because of a rougher liquid-solid-interface. Degault *et al.* previously outlined the importance of the liquid-solid-interface roughness on the surface roughness. [10]

The surface structure diameter continuously decreased, from 118 nm down to 71 nm, when reaching the full melt, as shown in **Figure V.5 (b)**. The surface structure height dropped to values around 10 nm at intermediate energy densities then went back to 15 nm at full melt, as shown in **Figure V.5 (d)**. For higher ED, the surface structure height increased, most likely because of oxygen indiffusion that led to clustering. [11]–[13] Similarly, the RMS roughness and Z_{range} values peaked around the melt threshold when surface structures were formed, shown in **Figure V.5 (e)**. They then decreased until full melt was reached then re-increased due to clustering most likely caused by oxygen indiffusion.

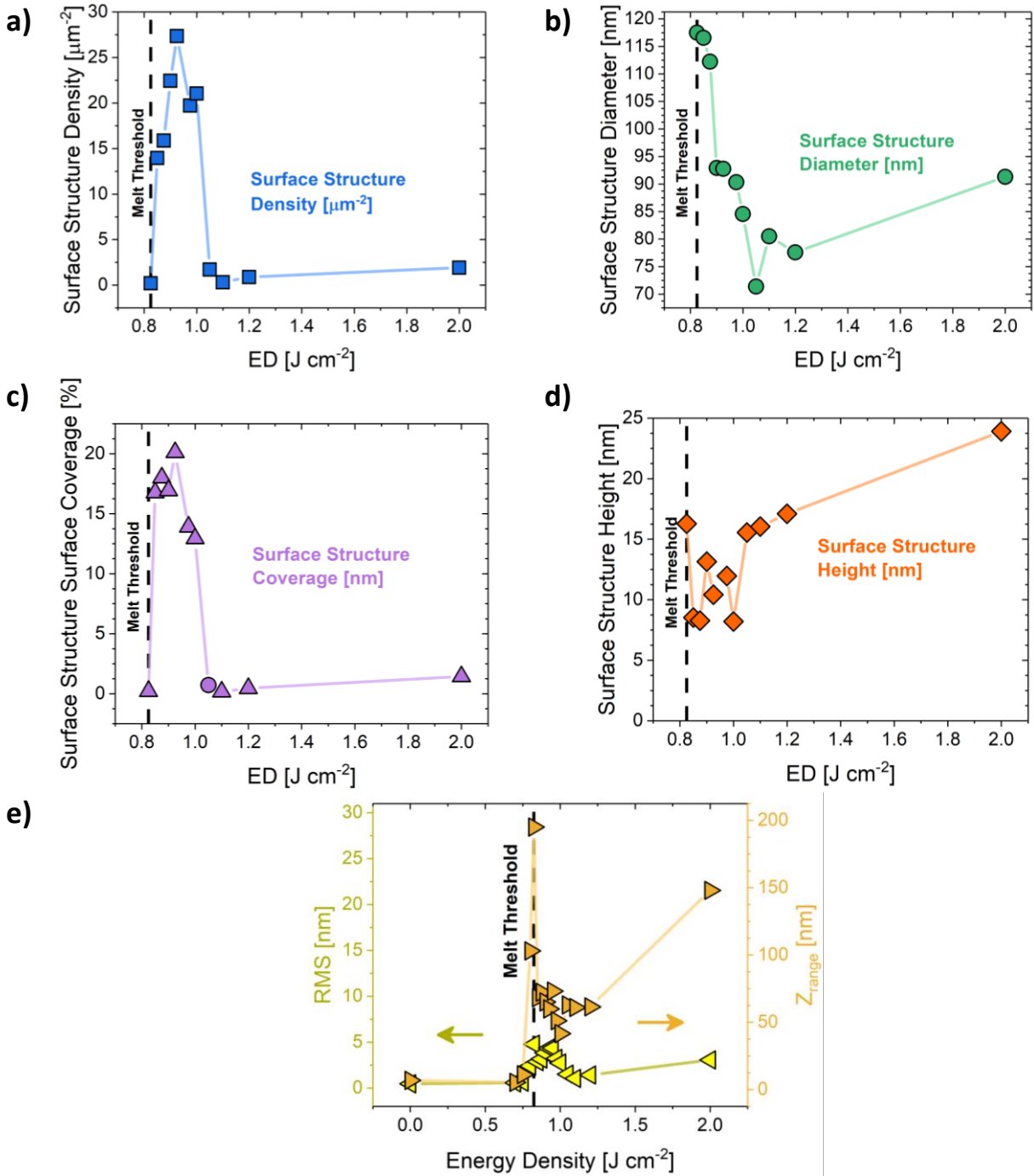


Figure V.5: Evolution of the surface structures' density (a), diameter (b), coverage (c) and height (d) together with the evolution of the surface RMS roughness and Z_{range} (e) as functions of the NLA ED for, initially, a 39 nm thick Ge:B layer thick with $[\text{B}]_{\text{subst.}} = 2.6 \times 10^{20} \text{ cm}^{-3}$. The vertical, black, dashed lines outline the melt threshold.

V.5 Single pulses nanosecond laser annealing on Ge:B: Crystalline structure

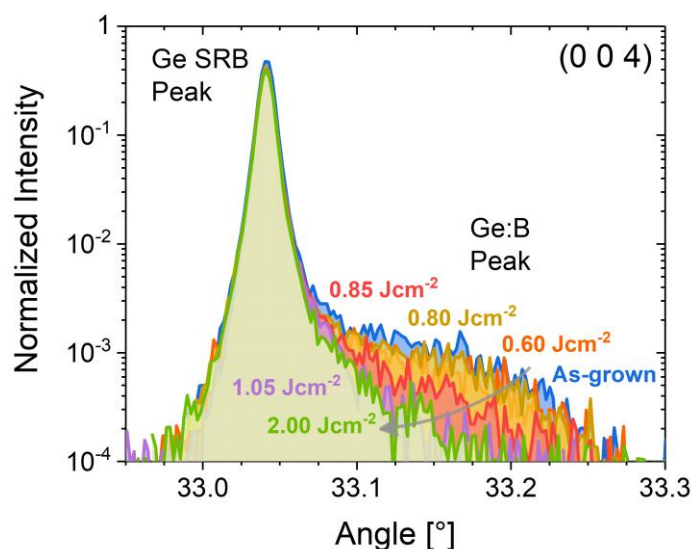


Figure V.6: Normalized ω - 2θ scans around the (0 0 4) XRD order for an as-grown Ge:B layer 39 nm thick with $[B]_{\text{subst.}} = 2.6 \times 10^{20} \text{ cm}^{-3}$ (blue) and after its NLA with Energy Densities ranging from 0.60 Jcm^{-2} (orange) up to 2.00 Jcm^{-2} (green).

The increased sheet resistance could be the result of dopant redistribution or loss of crystalline quality. **Figure V.6** shows normalized ω - 2θ scans around the (0 0 4) XRD order for a 39 nm thick layer with $[B]_{\text{subst.}} = 2.6 \times 10^{20} \text{ cm}^{-3}$ either in its as-grown state (blue) or after NLA anneals with various EDs (orange to green). Profiles were normalized by the Si peak intensity (not shown here). For the as-grown layer, a Ge:B shoulder peak can be found at higher angles than that of the well-defined, high intensity Ge SRB peak. This was due to the incorporation of large amounts of B atoms which are much smaller than that of Ge ($a_{\text{B}} = 3.852 \text{ \AA} \Leftrightarrow a_{\text{Ge}} = 5.658 \text{ \AA}$), resulting in a tensile strained Ge:B layer on top of the Ge SRB. The Ge:B peak stayed almost the same (in terms of intensity and angular position) below the melt threshold, as shown for 0.60 Jcm^{-2} (orange) and 0.80 Jcm^{-2} (yellow). At the melt threshold, when the first surface structures formed and merged, some of the peak intensity was lost, shown for 0.85 Jcm^{-2} in red in **Figure V.6**. B atoms indeed redistributed. The fact that the sheet resistance increased and that the Ge:B shoulder peak position did not change indicated that some electrically inactive clusters that did not contribute to tensile strain might have formed for such NLA conditions. At the full melt ED, shown at 1.05 Jcm^{-2} in purple in **Figure V.6**, the Ge:B shoulder peak was completely lost, emphasizing that even more B was redistributed and likely formed clusters. Porret *et al.* previously reported the formation of boron-interstitial clusters for in-situ ultra-highly B doped Ge. [4] The Ge:B shoulder peak was not recovered when the Ge SRB layer underneath was melted at 2.00 Jcm^{-2} , shown in green in **Figure V.6**.

V.6 Multipulse nanosecond laser annealing: Surface morphology evolution

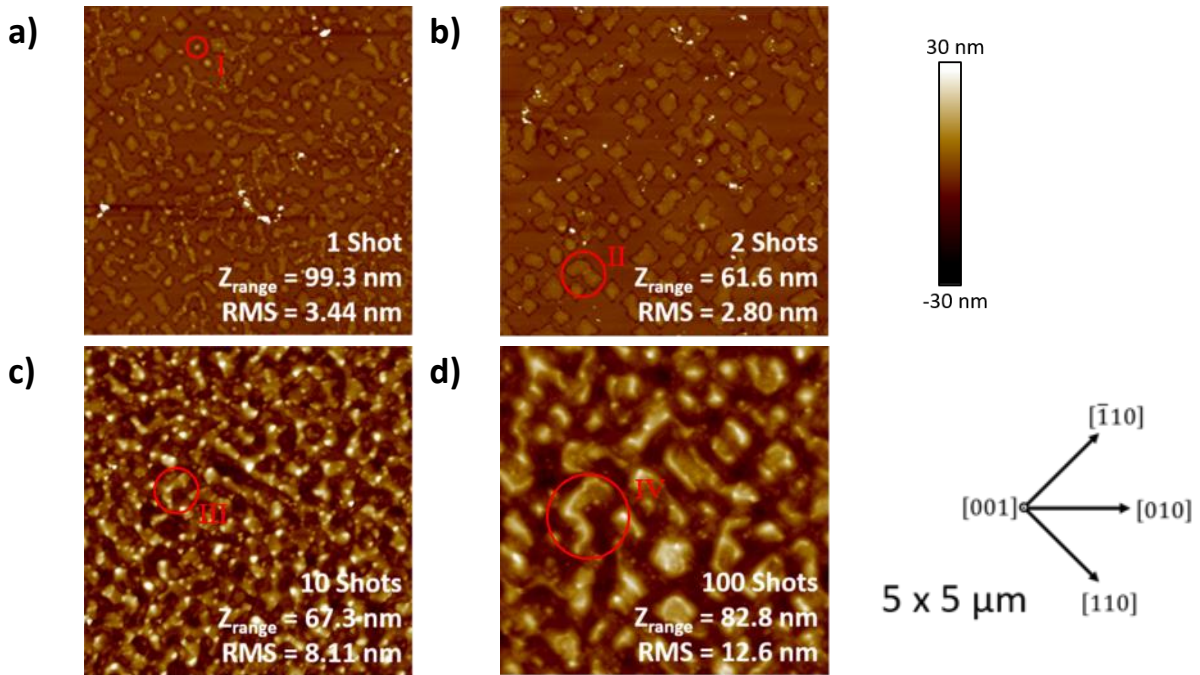


Figure V.7: (a) 5 μm x 5 μm atomic force microscope images of, initially, a 39 nm thick Ge:B layer with $[B]_{\text{subst.}} = 2.6 \times 10^{20} \text{ cm}^{-3}$ after single pulse NLA (a), 2 pulses NLA (b), 10 pulses NLA (c) and 100 pulses NLA (d) at the same ED of 0.85 Jcm^{-2} (z-scales range from -30 nm to 30 nm). Crystallographic directions are provided in the bottom right.

When shooting multiple laser pulses on the same position, the same depth melted repeatedly. This might result in the dissolution of electrically inactive clusters. **Figure V.7 (a) to (d)** shows AFM images of the surface of, initially, a 39 nm thick Ge:B layer with $[B]_{\text{subst.}} = 2.6 \times 10^{20} \text{ cm}^{-3}$ after the use of up to 100 pulses at 0.85 Jcm^{-2} at the same position. After a single pulse at 0.85 Jcm^{-2} , shown in **Figure V.7 (a)**, rectangular surface structures formed, highlighted by a red circle labeled I, and merged. After two pulses, shown in **Figure V.7 (b)**, surface structures further merged, forming larger surface structures, marked by a red circle labeled II. After ten pulses, shown in **Figure V.7 (c)**, almost all surface structures merged, forming continuous structures, marked by a red circle labeled III. The RMS roughness increased from around 3 nm for one and two pulses up to 8 nm after ten pulses. One hundred pulses at an energy density of 0.85 Jcm^{-2} , shown in **Figure V.7 (d)**, resulted in the formation of larger surface structures, marked by a red circle labeled IV, and a surface with a RMS roughness around 13 nm. The formation of larger surface structures was expected because the same volume of the surface was melted every time a laser pulse was shone onto the surface, resulting in surface structures merging and the formation of larger surface structures.

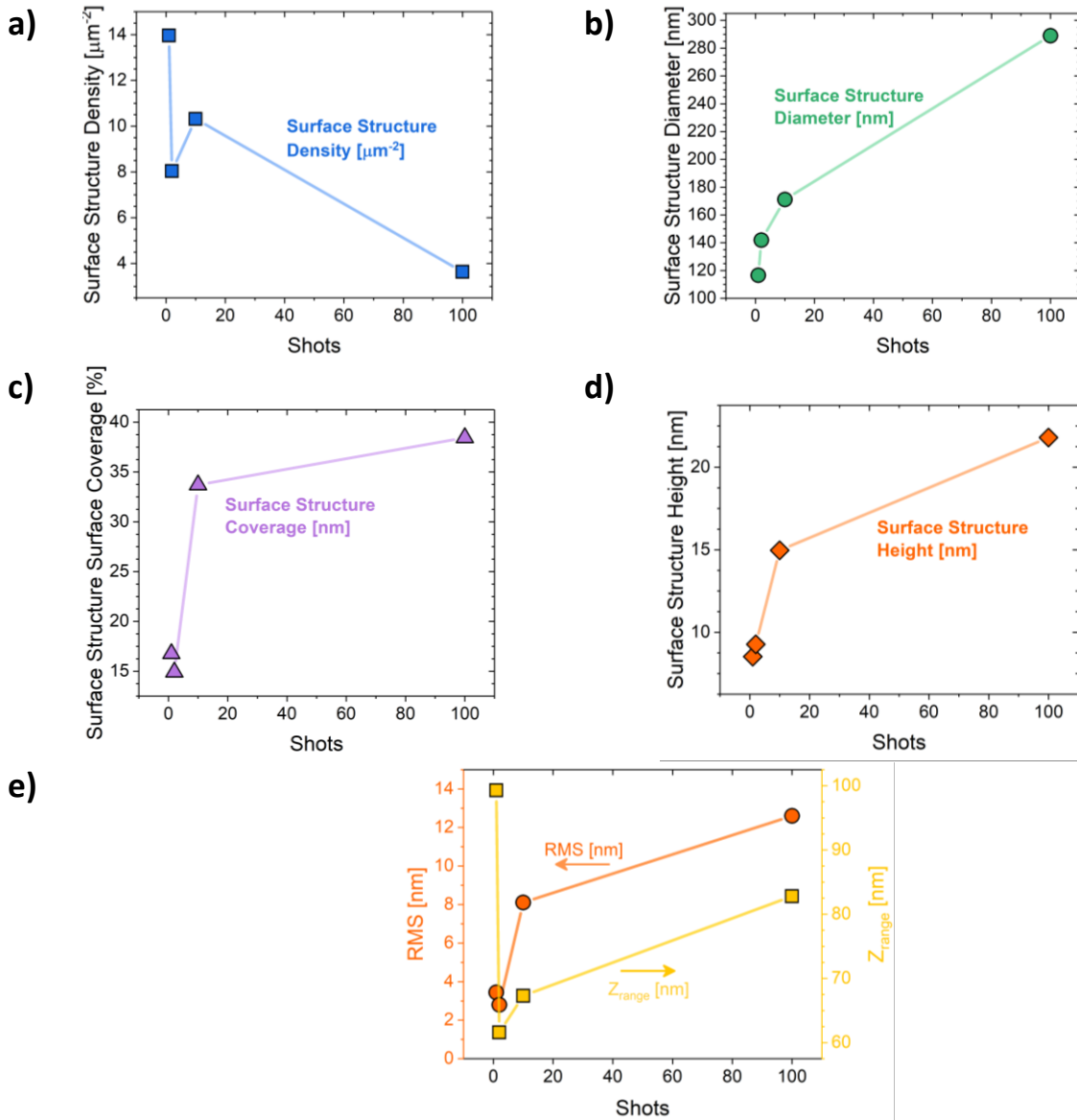


Figure V.8: Evolution of surface structures' density (a), diameter (b), coverage (c) height (d) and evolution of the RMS roughness (e) as functions of the number of NLA pulses with 0.85 Jcm^{-2} applied at the same position for, initially, a 39 nm thick Ge:B layer with $[\text{B}]_{\text{subst.}} = 2.6 \times 10^{20} \text{ cm}^{-3}$.

After two pulses, surface structures, formed after a single pulse, merged. This resulted in a reduction of the surface structure density, shown in **Figure V.8 (a)**. After ten pulses, new surface structures were formed and the surface structures density slightly re-increased, most likely because most of the surface had melted. After 100 pulses, small surface structures merged and formed large surface structures, resulting in a significantly reduced surface structures density.

When more pulses were used, the surface structures' diameter significantly increased, as shown in **Figure V.8 (b)**. This was due to the merging of small surface structures and the formation of larger ones. Increasing the amount of pulses led to an increased surface coverage by surface structures, shown in **Figure V.8 (c)**. The surface coverage seemed to saturate after

ten and 100 pulses. It might be that almost the entire surface was melted after ten and 100 pulses.

Increased surface structure height because of the merging of surface structures (**Figure V.8 (d)**) was at the root of the RMS roughness and Z_{range} increases with the number of pulses shown in **Figure V.8 (e)**.

V.7 Multipulse nanosecond laser annealing: Crystalline structure evolution

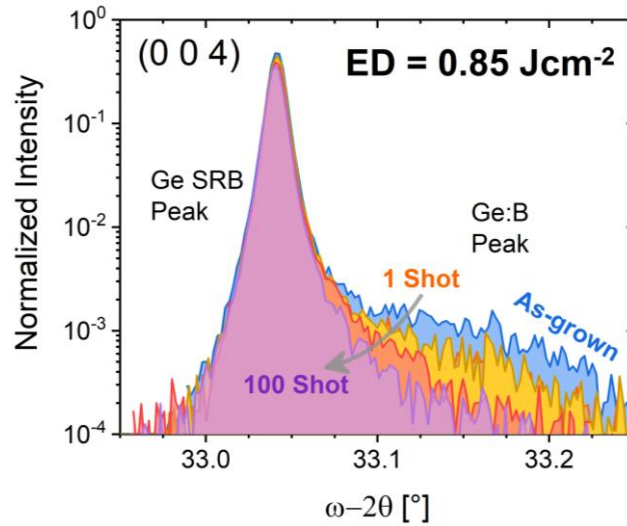


Figure V.9: (a) Normalized ω - 2θ scans around the (0 0 4) XRD order for, initially, a 39 nm thick Ge:B layer with $[B]_{\text{subst.}} = 2.6 \times 10^{20} \text{ cm}^{-3}$ annealed at 0.85 Jcm^{-2} with either a single pulse (orange) or various amounts of pulses (yellow: 2 pulses, red: 10 pulses and purple: 100 pulses).

The normalized ω - 2θ scans around the (0 0 4) XRD order for a 39 nm thick Ge:B layer with $[B]_{\text{subst.}} = 2.6 \times 10^{20} \text{ cm}^{-3}$ either in its as-grown state (blue) or after NLA with up to 100 laser pulses at 0.85 Jcm^{-2} (orange to purple) are shown in **Figure V.9**. Scans were normalized by the Si peak intensity (not shown here). The Ge:B shoulder peak intensity stayed constant for two instead of one pulse. This outlined that there was no significant difference in B distribution inside Ge after one or two pulses. B was significantly redistributed after ten pulses (red profile), with a significantly reduced Ge:B shoulder peak intensity. The Ge:B shoulder was completely lost after 100 pulses. Clusters that did not contribute to the layer's tensile strain state were thus not dissolved after the use of multiple pulses, quite the opposite, instead.

V.8 Multipulse nanosecond laser annealing: Dopant activation

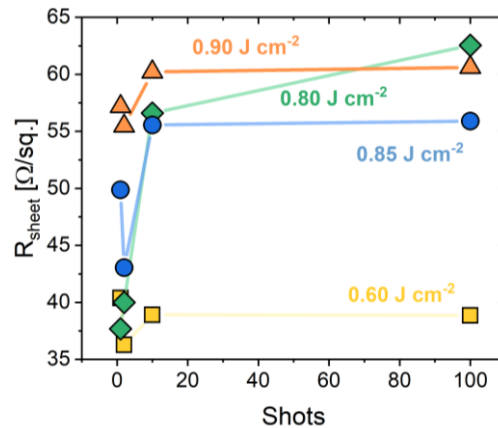


Figure V.10: Four point probe measurements of sheet resistance for, initially, a 39 nm thick Ge:B layer with $[B]_{subst.} = 2.6 \times 10^{20}\ cm^{-3}$ annealed 1, 2, 10 and 100 times at various energy densities.

These clusters were electrically inactive because the sheet resistance increased when multiple pulses were used, as shown in **Figure V.10**. To quantify the impact of the energy density on the B electrical activation, the initially 39 nm thick Ge:B layer with $[B]_{subst.} = 2.6 \times 10^{20}\ cm^{-3}$ was laser annealed at various energy densities with different numbers of pulses. The sheet resistance improved slightly for two pulses at an energy density of $0.85\ Jcm^{-2}$. This might be due to the non-uniformity of the wafer and should be confirmed in future experiments. At $0.60\ Jcm^{-2}$, the sheet resistance improved slightly when applying multiple pulses. This opens up a processing window for future experiments in the sub melt regime, which already showed promising results for other materials. [14], [15]

V.9 Conclusions

Single pulse or multiple pulses nanosecond laser annealings were performed with various energy densities on heavily in-situ boron-doped Ge layers grown on thick Ge:P/Ge strain-relaxed buffers, themselves on Si substrates. The sheet resistance increased when increasing the energy density, resulting in a larger melt depth. Even the use of multiple pulses with the same energy density at the same position did not improve the sheet resistance. Nanosecond laser annealing rather led to the formation of (i) surface structures that merged and (ii) electrically inactive clusters that did not contribute to strain. With the use of multiple pulses, surface structures merged and formed even larger surface structures. This led to more B redistribution and likely to the formation of more electrically inactive boron-interstitial clusters in the melt regime. In the sub melt regime, multi pulse NLA might improve contact resistance. Nanosecond laser annealing in the melt regime therefore seemed not to be able to improve the electrical activation of heavily in-situ boron-doped Ge layers as it did for heavily in-situ phosphorous doped Si.

References

- [1] E. Rosseel *et al.*, “Characterization of Epitaxial Si:C:P and Si:P Layers for Source/Drain Formation in Advanced Bulk FinFETs,” *ECS Trans.*, vol. 64, no. 6, pp. 977–987, Aug. 2014, doi: 10.1149/06406.0977ecst.
- [2] R. Daubriac *et al.*, “Superconducting Polycrystalline Silicon Layer Obtained by Boron Implantation and Nanosecond Laser Annealing,” *ECS J. Solid State Sci. Technol.*, vol. 10, no. 1, p. 014004, Jan. 2021, doi: 10.1149/2162-8777/abdc41.
- [3] J.-M. Hartmann, M. Frauenrath, J. Richey, and M. Veillerot, “Ultra-High Boron Doping of Si and Ge for Nanoelectronics and Photonics,” *ECS Trans.*, vol. 98, no. 5, pp. 203–214, Sep. 2020, doi: 10.1149/09805.0203ecst.
- [4] C. Porret *et al.*, “Low-Temperature Selective Growth of Heavily Boron-Doped Germanium Source/Drain Layers for Advanced pMOS Devices,” *Phys. Status Solidi A*, vol. 217, no. 3, p. 1900628, Feb. 2020, doi: 10.1002/pssa.201900628.
- [5] M. Frauenrath *et al.*, “Nanosecond Laser Annealing of pseudomorphic GeSn layers – Impact of Sn content,” *to be published*.
- [6] S. Adachi, “Optical dispersion relations in amorphous semiconductors,” *Phys. Rev. B*, vol. 43, no. 15, pp. 12316–12321, May 1991, doi: 10.1103/PhysRevB.43.12316.
- [7] G. E. Jellison, “Optical functions of GaAs, GaP, and Ge determined by two-channel polarization modulation ellipsometry,” *Opt. Mater.*, vol. 1, no. 3, pp. 151–160, Sep. 1992, doi: 10.1016/0925-3467(92)90022-F.
- [8] K. Huet *et al.*, “Pulsed laser annealing for advanced technology nodes: Modeling and calibration,” *Appl. Surf. Sci.*, vol. 505, p. 144470, Mar. 2020, doi: 10.1016/j.apsusc.2019.144470.
- [9] L. Dagault *et al.*, “Investigation of recrystallization and stress relaxation in nanosecond laser annealed Si_{1-x}Ge_x/Si epilayers,” *Appl. Surf. Sci.*, vol. 527, p. 146752, Oct. 2020, doi: 10.1016/j.apsusc.2020.146752.
- [10] L. Dagault *et al.*, “Impact of UV Nanosecond Laser Annealing on Composition and Strain of Undoped Si_{0.8}Ge_{0.2} Epitaxial Layers,” *ECS J. Solid State Sci. Technol.*, vol. 8, no. 3, pp. P202–P208, 2019, doi: 10.1149/2.0191903jss.
- [11] G. Impellizzeri *et al.*, “Role of oxygen on the electrical activation of B in Ge by excimer laser annealing: Role of oxygen on the electrical activation of B in Ge,” *Phys. Status Solidi A*, vol. 211, no. 1, pp. 122–125, Jan. 2014, doi: 10.1002/pssa.201300308.
- [12] R. Milazzo *et al.*, “Oxygen behavior in germanium during melting laser thermal annealing,” *Mater. Sci. Semicond. Process.*, vol. 42, pp. 196–199, Feb. 2016, doi: 10.1016/j.mssp.2015.07.066.
- [13] R. Milazzo, M. Linser, D. Scarpa, A. Carnera, A. Andrighetto, and E. Napolitani, “Indiffusion of oxygen in germanium induced by pulsed laser melting,” *Mater. Sci. Semicond. Process.*, vol. 88, pp. 93–96, Dec. 2018, doi: 10.1016/j.mssp.2018.07.036.
- [14] S. B. Felch *et al.*, “Ultra-Shallow Junctions Formed By Sub-Melt Laser Annealing,” in *AIP Conference Proceedings*, Marseille (France), 2006, vol. 866, pp. 129–132. doi: 10.1063/1.2401478.
- [15] V. Mazzocchi *et al.*, “Boron and Phosphorus dopant activation in Germanium using laser annealing with and without preamorphization implant,” in *2009 17th International Conference on Advanced Thermal Processing of Semiconductors*, Albany, NY, Sep. 2009, pp. 1–5. doi: 10.1109/RTP.2009.5373447.

Chapter VI : Single Pulse Nanosecond Laser Annealing of GeSn

Chapter VI: Single Pulse Nanosecond Laser Annealing of GeSn

Chapter VI: Single Pulse Nanosecond Laser Annealing of GeSn.....	106
VI.1 Introduction.....	106
VI.2 Wafer uniformity	106
VI.3 Impact of different Sn contents on Time Resolved Reflectivity Response	107
VI.4 Effect of Nanosecond Laser Annealing on Surface Morphology	110
VI.5 Effect of Nanosecond Laser Annealing on Crystalline Structure.....	115
VI.6 Effect of Nanosecond Laser Annealing on Sn redistribution	120
VI.7 Conclusions.....	122

Chapter VI: Single Pulse Nanosecond Laser Annealing of GeSn**VI.1 Introduction**

In the current study, we investigate the impact of nanosecond laser annealing (NLA), an ultrafast, non-equilibrium process, on GeSn. One of our aims was to assess the crystal recovery after NLA (and therefore melting and solidification) and investigate whether or not Sn redistribution occurred during recrystallization. Such know-how would be crucial if ion implantation together with NLA were used in order to locally dope GeSn-based heterostructures. Recent studies by L. Casiez *et al.* showed the formation of Sn-rich vertical structures near the surface in thick, partially relaxed GeSn 8% layers. [1]

We more specifically focused on pseudomorphic, intrinsic GeSn layers on Ge Strain-Relaxed Buffers (SRBs) with Sn contents between 6% and 14%. As hinted previously, GeSn is a highly complex material. Therefore, we first aimed at better understanding the interaction of the laser with the material in simple stacks. Here, we focused on single pulse experiments. This meant applying a single laser pulse with a specific Energy Density (ED) at a predefined position, moving over to the next position on the same wafer and repeating the experiment with a different ED and so on. This procedure enabled us to gain a detailed understanding of mechanisms at play.

VI.2 Wafer uniformity

Table VI.I Results from an uniformity study. RMS roughness and Z range coming from $5\ \mu\text{m} \times 5\ \mu\text{m}$ AFM images of the surface of our samples. The Sn content and thickness were extracted from ω -2 θ scans around the (0 0 4) XRD order. The sheet resistance values were obtained thanks to four point probe measurements.

	Sn content [%]	GeSn thickness [nm]	RMS roughness [nm]	Z range [nm]	Sheet Resistance [$\Omega/\text{sq.}$]
GeSn 6%	6.29±0.12	41.52±0.60	0.38±0.08	3.25±0.61	154.36±0.59
GeSn 10%	10.11±0.12	39.44±1.46	0.39±0.08	3.08±0.49	155.05±0.73
GeSn 14%	14.13±0.08	38.30±1.39	0.39±0.03	4.43±1.77	293.30±1.56

We obtained Sn contents of 6.3%, 10.1% and 14.1% in as-grown layers by setting the growth temperature to 349°C, 325°C and 301°C, respectively. The as-grown layer thicknesses were 41.5 nm, 39.4 nm and 38.3 nm, respectively. Atomic force microscopy (AFM) and X-ray diffraction (XRD) profiles were typical of high crystalline quality stacks with smooth surfaces and interfaces. We performed a uniformity study on as-grown wafers by recording five AFM

images (center and 6 cm from the center in positive and negative x- and y- direction), performing five ω -2 Θ XRD scans (same positions as for AFM) and doing 69 (32 for GeSn 14%, same positions used for NLA) four-point-probe measurements at various positions over the wafer surfaces. Wafers were indeed uniform, as shown by average values and standard deviations in **Table VI.I**. More details on wafer uniformity are given in **Appendix A**.

VI.3 Impact of different Sn contents on Time Resolved Reflectivity Response

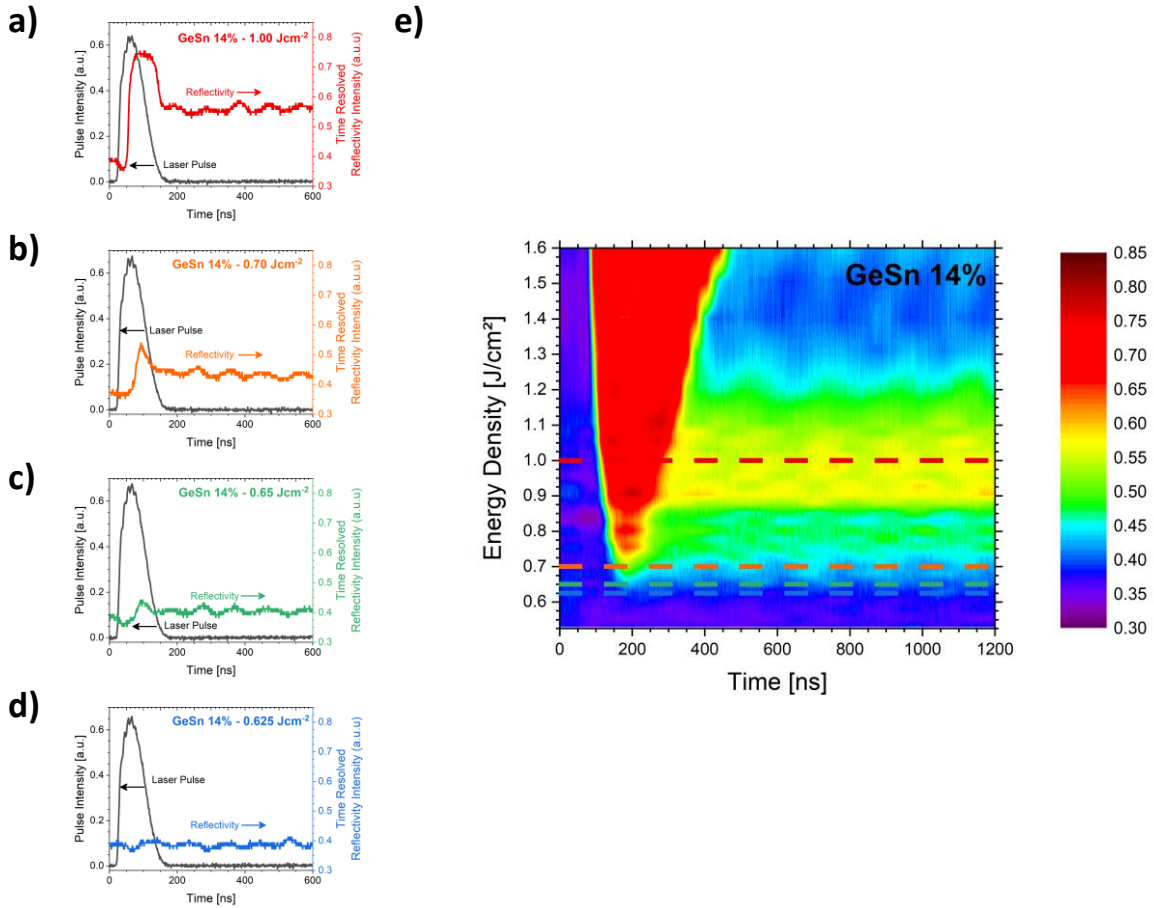


Figure VI.1: TRR spectra of a 41 nm thick pseudomorphic GeSn 14% layer annealed at 1.00 Jcm⁻² (red (a)), 0.70 Jcm⁻² (orange (b)), 0.65 Jcm⁻² (green (c)) and 0.625 Jcm⁻² (blue (d)). The black curve in each graph shows the pulse intensity for the corresponding ED. (e) Time Resolved Reflectivity map with a stacking of all spectra (ED step 0.025 Jcm⁻²). Colored lines are guidances to locate the TRR spectra of (a) to (d) in the TRR map.

To determine the melt threshold, i.e. the energy density at which local melt started to occur, we examined the TRR signal recorded during the laser annealing process. Due to the higher reflectivity of liquid semiconductors compared to solid semiconductors, the energy density at which a solid to liquid transition occurred during the annealing process could easily be identified. We assumed that the properties of GeSn alloys were close to that of pure Ge. [2], [3] We recorded the TRR signal for each laser pulse. In **Figure VI.1 (a) to (d)**, we present some recorded TRR signals, in addition to their specific laser pulse, shown in black, for the GeSn 14% layer. Before the appearance of any local surface melt, the TRR signal oscillated randomly

and we could not discern any specific peak, as shown in blue in **Figure VI.1 (d)**, after laser annealing at 0.625 Jcm^{-2} .

When ED reached 0.65 Jcm^{-2} , we started to detect a distinguishable peak in the TRR signal as the laser pulse reached its maximum intensity. The spectrum is shown in **Figure VI.1 (c)** in green. This was due to some melting of some very small areas on the surface. We recorded a more distinct peak at an ED of 0.75 Jcm^{-2} , **Figure VI.1 (b)** in orange. At this ED, a significant amount of the surface melted. We had a broad peak of the TRR signal at an ED of 1.0 Jcm^{-2} , red curve in **Figure VI.1 (a)**. The whole irradiated surface melted and the melt depth was significant, then, resulting in a continuous liquid layer just after the laser pulse.

By stacking the various TRR spectra, shown in **Figure VI.1 (a) to (d)**, we could construct a TRR map, shown in **Figure VI.1 (e)**. The TRR map enabled us to more easily determine the melt threshold and gain a better understanding of how the molten layer evolved when applying various pulses with different energy densities. The colored lines in **Figure VI.1 (e)** correspond to the TRR spectra in the same color in **Figure VI.1 (a) to (d)**.

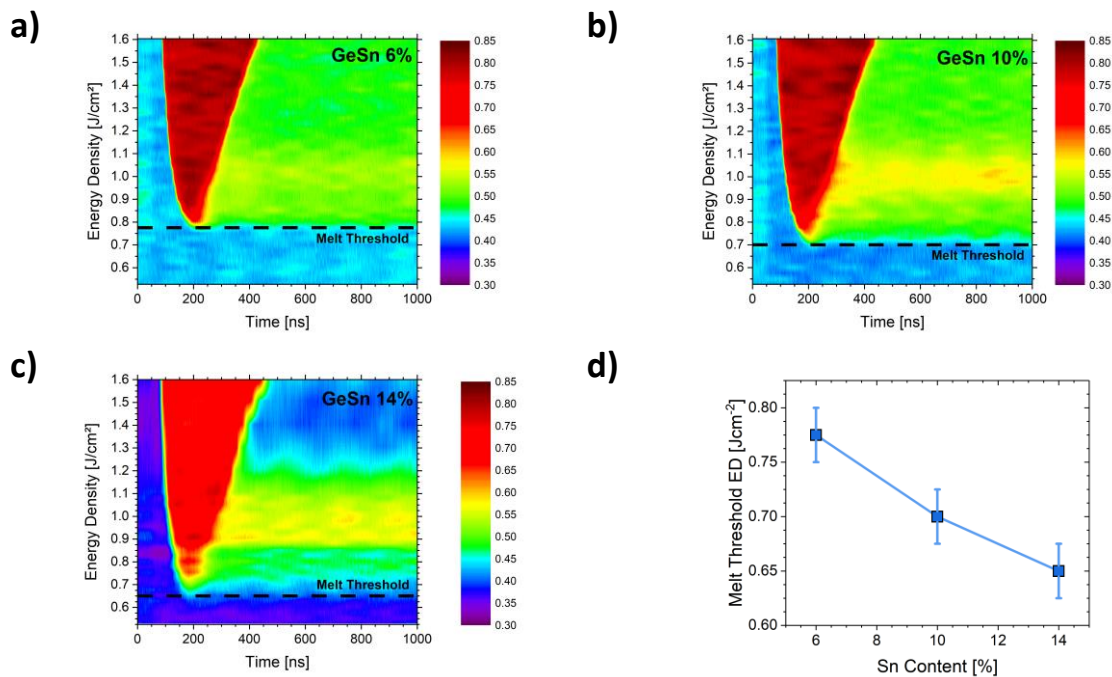


Figure VI.2: TRR maps (step size 0.025 Jcm^{-2}) for 38-41 nm thick pseudomorphic GeSn 6% (a), 10% (b) and 14% (c) layers. The black line corresponds to the melt threshold, the energy density at which the material started to melt. (d) Sn content dependence of the melt threshold with an error of 0.025 Jcm^{-2} .

The melt threshold was at 0.65 Jcm^{-2} based on the TRR map. The TRR peak lasted longer and increased in intensity as the ED increased more and more above the melt threshold. After melting the top GeSn surface, we indeed melted more and more of the film as the melt depth increased with the applied energy density. At some point, the whole surface melted and we only increased the melt depth. At intermediate ED, we observed a peculiar behavior. A high reflectivity (yellow) tail appeared after the melting (red) peak. It was visible in the TRR spectra

of **Figure VI.1 (a)**, too. Compared to other spectra in **Figure VI.1 (b) to (d)**, the TRR signal of the final state (after solidification and cooling) was significantly higher. This was the first time we had such a behavior. Since then, we also had a similar behavior for SiGe on Si.

To understand the origins of this tail, we also constructed TRR maps for GeSn 6% and 10%. They are shown in **Figure VI.2 (a) and (b)**, as well as the TRR map for GeSn 14% in **Figure VI.2 (c)**. From these maps, we determined the melt threshold to be 0.775 Jcm^{-2} for GeSn 6% and 0.70 Jcm^{-2} for GeSn 10%. As outlined in **Figure VI.2 (d)**, the melt threshold shifted to lower energy densities as the as-grown Sn content increased. Such a behavior was expected because the melting temperature was 938°C for pure Ge, while it was only 232°C for $\beta\text{-Sn}$. [4] Therefore, a higher Sn content should be associated with a lower melt threshold energy density. In addition to the lowering of the melt threshold, we had TRR tails for the various Sn contents. The tail could be due to changes in the surface morphology or to a different surface composition. Indeed, Sn is known to segregate towards the surface of GeSn. [5]–[7]

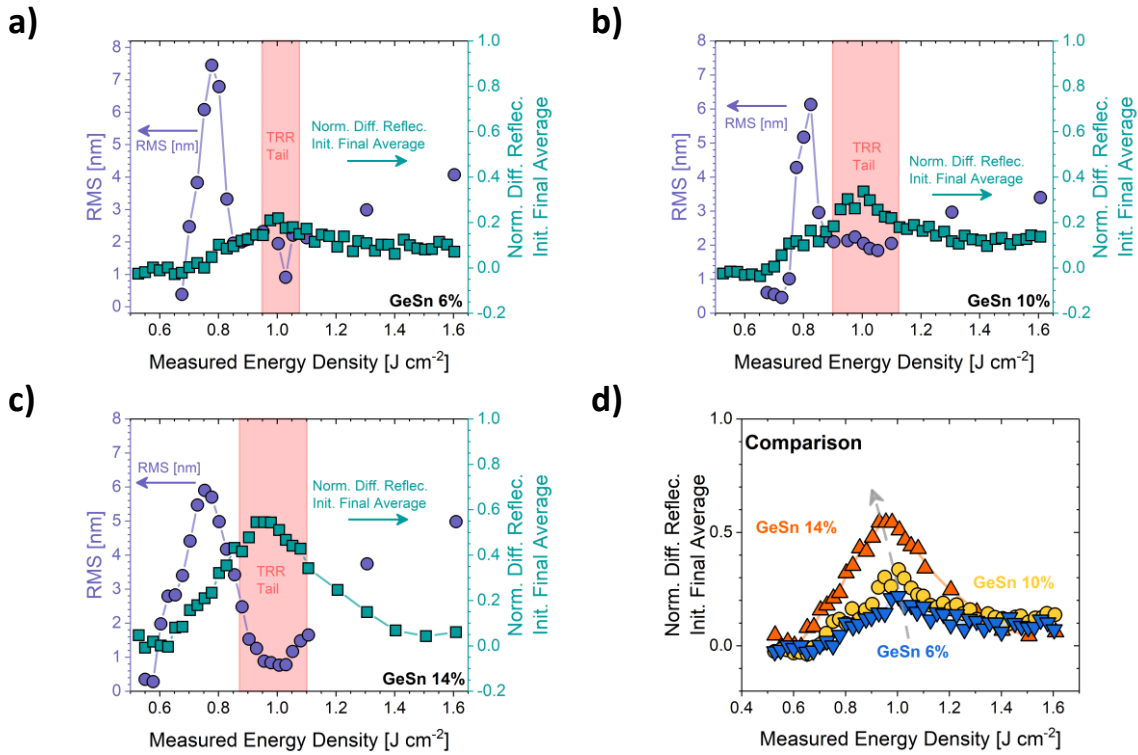


Figure VI.3: Differences between average final and initial TRR signals divided by the average initial reflectivity (green squares) and surface RMS roughness (purple circles) at various energy densities for GeSn 6% (a), 10% (b) and 14% (c). Red areas show energy density ranges with tails in the TRR maps. (d) Differences between average final and initial TRR signals divided by the average initial reflectivity as functions of the measured energy for GeSn 6% (blue squares), 10% (yellow circles) and 14% (orange triangles).

We quantified the importance of the TRR tail by calculating the mean TRR signal of the first 10 recorded data points and the mean TRR signal of the last 10 recorded data points for various energy densities. Subtracting the mean initial from the mean final signal and dividing the difference by the mean initial signal (called thereafter the “normalized

initial-final-difference”) yielded a quantification of the TRR tail for various EDs and Sn contents. When plotting this so called “normalized initial-final-difference” against the energy density, peaks were seen, as shown in **Figure VI.3 (a) to (c)**. In addition, to the initial-final difference, we plotted the surface RMS roughness value from AFM. There were clear correlations between TRR tails and surface roughness. The “initial-final-difference” TRR signal peaked at ED around 1.00 Jcm^{-2} , at which the RMS roughness values were the lowest for the various Sn contents.

For comparison purposes, we plotted the “normalized initial-final-difference” curves in **Figure VI.3 (d)** for the various Sn contents probed (6% blue, 10% yellow and 14% orange). The graph highlighted that the TRR tail reflectivity increased as the as-grown Sn content increased. Moreover, the tail widened. Besides widening and becoming more intense, the TRR tail also slightly shifted to lower ED. The formation of a continuous, smooth layer at lower ED most likely caused this. We expect Sn to have segregated to the surface, resulting in a Sn richer surface. As the Sn content increased, this layer formed at lower energy densities above the melt threshold. These results would suggest that the TRR tail did not only depend on the surface morphology, but also on the as-grown Sn content.

VI.4 Effect of Nanosecond Laser Annealing on Surface Morphology

The TRR maps showed a correlation with the surface roughness. Hence, the following presents a detailed look at the surface morphology of NLA annealed, various Sn content GeSn layers. **Figure VI.4 (a) to (h)** show a selection of AFM images of the GeSn 6% layer laser annealed at various energy densities. The surface of the as-grown layer was cross-hatched and rather smooth, as shown in **Figure VI.4 (a)**. Similar aspect images were obtained for the various Sn contents layers and for different positions on the as-grown wafers (not shown here). The RMS roughness and Z_{range} were equal to 0.26 nm and 2.70 nm for that layer, i.e. values typical of such pseudomorphic GeSn layers.¹³

At an ED of 0.775 Jcm^{-2} for GeSn 6%, local melt was observed, leading to the surface shown in **Figure VI.4 (b)**. Continuous, elongated, cross-shaped surface structures with ridge-like features were observed. Secondary Electron Microscopy showed that even smaller structures formed at 0.725 Jcm^{-2} and 0.75 Jcm^{-2} . The structures were cross shaped for 0.75 Jcm^{-2} and rectangular at 0.725 Jcm^{-2} . From this, a melt threshold of 0.725 Jcm^{-2} was extracted. Dagault *et al.* previously found similar structures for compressively strained SiGe on Si.¹⁴ For SiGe, the shape of the surface structures depended on the composition. For pure Si, structures were rectangular, while for SiGe with Ge contents above 20%, structures were crosses. The higher the Ge content was, the more elongated and the less ridge-like (less continuous) structures were. The shape of these structures was likely due to melting and recrystallization anisotropy. [8]–[10] A recent publication on melting after laser irradiation showed the formation of a liquid-solid interface with inverted pyramids with $\langle 110 \rangle$ sides. [11] This could be the origin of such surface structures.

Our cross-shaped structures were along $\langle 100 \rangle$ crystallographic directions. Fournier-Lupien *et al.* reported a similar behavior in GeSn layers after conventional anneals. [5] They showed that Sn segregated to the surface during annealing, forming droplets which propagated along specific crystallographic directions. In our case, structures were too small, a few nm

compared to μm for Fournier-Lupien *et al.*, to be the result of droplets propagating on the surface. Still, this was a first hint that the surface structures were most likely Sn rich. The reason as to why these surface structures formed at these specific locations is not yet fully understood. A defective crystalline structure (e.g. the threading arm of a misfit dislocation) or a slightly higher Sn content might have caused the localized melt. A detailed study at the same spot of as-grown and laser annealed layers would be required, which is beyond the scope of the current work.

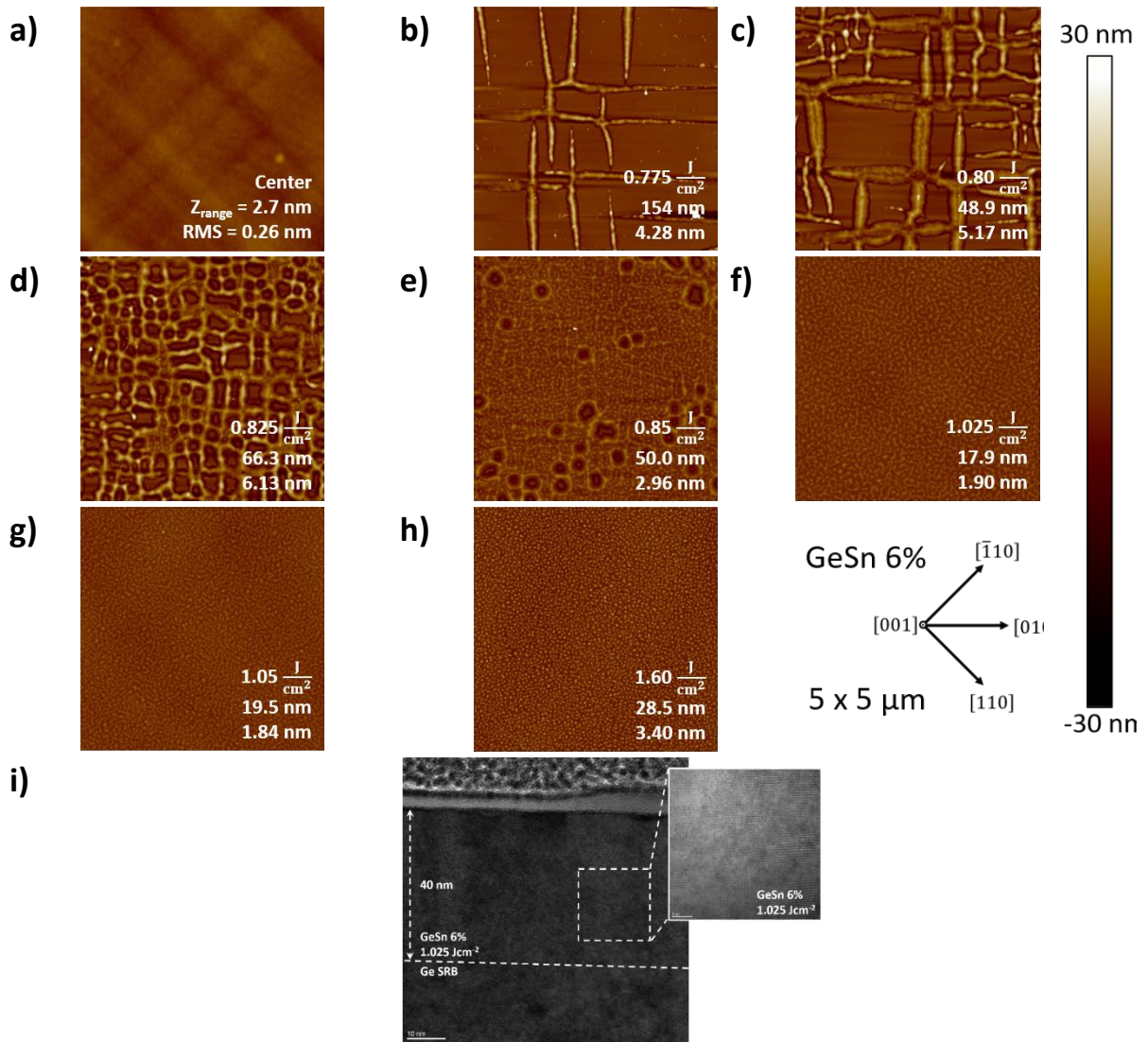


Figure VI.4: $5 \mu\text{m} \times 5 \mu\text{m}$ AFM images of 41 nm thick pseudomorphic GeSn 6% layers as-grown ((a), 5 nm z-scale) and after laser annealing at 0.775 J cm^{-2} (b), 0.80 J cm^{-2} (c), 0.825 J cm^{-2} (d), 0.85 J cm^{-2} (e), 1.025 J cm^{-2} (f), 1.05 J cm^{-2} (g) and 1.60 J cm^{-2} (h) ((b) to (h) with 30 nm z-scale). The schematic on the bottom right shows the crystallographic directions. (i) Cross-sectional HR-TEM image with a 10 nm scale bar of the GeSn 6% layer on the Ge SRB and zoom with a 5 nm scale bar after NLA at 1.025 J cm^{-2} , corresponding to (f).

When the ED increased to 0.80 Jcm^{-2} , shown in **Figure VI.4 (c)**, cross-shaped surface structures multiplied. In addition, tails broadened and their ends started to connect. At an ED of 0.825 Jcm^{-2} , shown in **Figure VI.4 (d)**, a street-grid like pattern appeared. Structures multiplied significantly and covered a large part of the surface. When ED further increased to 0.85 Jcm^{-2} , shown in **Figure VI.4 (e)**, features started to merge. This led to a surface that was slightly smoother with a RMS roughness around 3 nm compared to 6 nm at 0.825 Jcm^{-2} . Moreover, the surface had some “holes” where surface features did not yet completely merge and some specific surface undulations where surface structures had merged. The merging of islands continued as the energy density further increased. This led to a smoothing of the surface.

At an ED of 1.025 Jcm^{-2} , shown in **Figure VI.4 (f)**, and an ED of 1.05 Jcm^{-2} , **Figure VI.4 (g)**, the surface RMS roughness reached its minimum around 2 nm. This likely corresponded to energy densities at which the entire GeSn layer was melted without melting the Ge SRB underneath. This will be, in the following, called the ‘full melt’ regime. Such an assumption was based on numerical simulations using LIAB [12] for pure Ge. Simulations indeed revealed that the ED difference between melt threshold and full melt should be around 0.3 Jcm^{-2} , a difference close to that here ($1.05 - 0.775 = 0.275 \text{ Jcm}^{-2}$). As the energy density further increased to 1.60 Jcm^{-2} , shown in **Figure VI.4 (h)**, the surface became rougher again, with a RMS roughness of 3.4 nm. Small islands formed on the surface.

Dagault *et al.* had identified different melt regimes for compressively strained SiGe on Si. [13] At the melt threshold, a surface melt regime was evidenced. Only localized regions had melted, resulting in the formation of surface structures. At higher energy densities, i.e. in the partial melt regime, the surface became smoother. In that regime, a continuous liquid SiGe layer formed on the solid SiGe layer, but the melt depth was still smaller than the full SiGe layer thickness. When the melt depth was equal to the SiGe layer thickness, the full melt regime was reached. The same regimes were evidenced here for compressively strained GeSn on Ge. Between 0.775 Jcm^{-2} and 0.85 Jcm^{-2} , we were in the surface melt regime. Up to 1.05 Jcm^{-2} , we were in the partial melt regime. For even higher energy densities, we were in the full melt regime.

The High Resolution Transmission Electron Microscopy (HR-TEM) image shown in **Figure VI.4 (i)** outlined that the entire GeSn 6% layer recrystallized after laser annealing at 1.025 Jcm^{-2} . The crystalline quality was excellent, with no difference with the Ge SRB underneath. Since the Sn content was only 6% and the crystalline qualities of the GeSn layer and the buffer were good, there was no contrast difference between the buffer and the GeSn layer in the HR-TEM image. As the real thickness of the GeSn layer could not be determined with such a HR-TEM image, the white dashed line highlights a 40 nm depth (e.g. the thickness of the as-grown layer). **Figure VI.4 (i)** shows the ability of nanosecond laser annealing to form high quality GeSn layers after a complete melt then recrystallization.

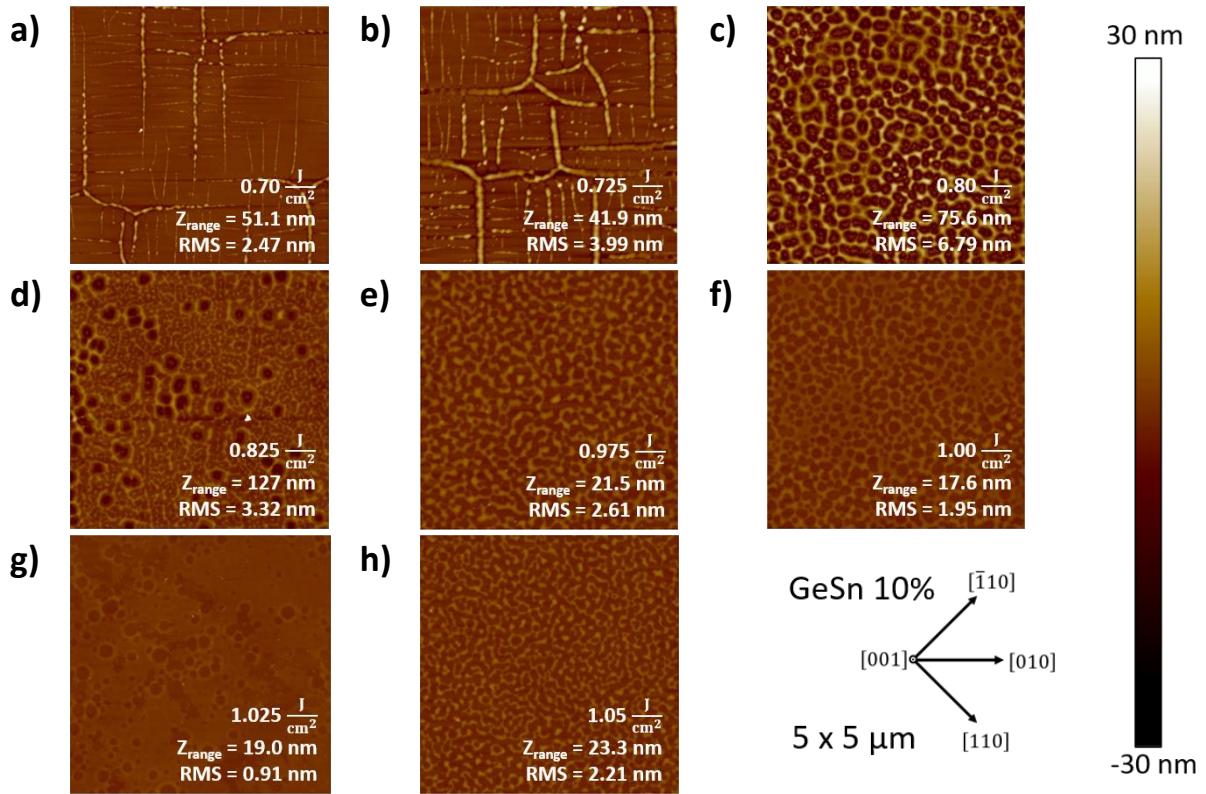


Figure VI.5: $5 \mu\text{m} \times 5 \mu\text{m}$ AFM images of 40 nm thick pseudomorphic GeSn 10% layers after laser annealing at 0.70 Jcm^{-2} (a), 0.725 Jcm^{-2} (b), 0.80 Jcm^{-2} (c), 0.825 Jcm^{-2} (d), 0.975 Jcm^{-2} (e), 1.00 Jcm^{-2} (f), 1.025 Jcm^{-2} (g) and 1.05 Jcm^{-2} (h) ((a) to (h) all with 30 nm z-scale). The schematic on the bottom right shows the crystallographic directions.

To understand the impact of Sn content on the surface structures shape, we also recorded several AFM images on NLA annealed GeSn 10% layers. **Figure VI.5** shows some of them. In **Figure VI.5 (a)**, at 0.70 Jcm^{-2} , i.e. the melt threshold of GeSn 10%, elongated crosses appeared. Structures were orientated along the [100] and [010] directions. This was the first energy at which surface structures appeared, in line with the melt threshold from TRR. These structures were more elongated, thinner and less continuous (ridge-like) than those on GeSn 6%, shown in **Figure VI.4**. A similar behavior was previously reported by Dagault *et al.* [13] The impact of Sn (in a Ge lattice) on the shape of structures was more pronounced than that of Ge (in a Si lattice), i.e. smaller Sn content changes led to more significant changes of the shape of surface structures. One possible explanation could be the larger lattice parameter difference between Sn (6.489 \AA) and Ge (5.658 \AA), 0.831 \AA compared to Si (5.431 \AA) and Ge, 0.227 \AA only. The pronounced impact of higher amounts of Sn on the shape of structures thus highlighted the importance of compressive strain on the formation of such structures. Recent, unpublished laser annealing studies of relaxed SiGe strengthened this hypothesis.

At 0.725 Jcm^{-2} , **Figure VI.5 (b)**, cross-shaped structures multiplied and thickened. The crystalline orientation of the surface structures was the same than at 0.70 Jcm^{-2} . The surface structure merged and formed a street-grid like pattern at 0.80 Jcm^{-2} , **Figure VI.5 (c)**. No dominant orientation of the surface structures in any crystalline directions was observed for this energy density. Neither was a dominant preferential orientation in any crystalline directions

recovered for higher ED. It might be that the formation of a continuous liquid layer led to a surface structure formation that did not take the underlying crystalline structure into account. Therefore, the surface structures were not aligned along specific crystalline directions. At 0.825 Jcm^{-2} , the structures began to merge with some “holes”, **Figure VI.5 (d)**. Holes closed at higher energy densities, leaving behind some specific surface undulations. These specific surface undulations increased in size when ED reached 0.975 Jcm^{-2} , as shown in **Figure VI.5 (e)**. We did not observe this behavior for GeSn 6%, as shown in **Figure VI.4**. This was likely because a critical Sn concentration was necessary to form those larger islands out of the specific surface undulations. At 1.00 Jcm^{-2} , shown in **Figure VI.5 (f)**, surface undulations-islands merged, forming a continuous layer with some “holes” at 1.025 Jcm^{-2} , shown in **Figure VI.5 (g)**. This layer was significantly smoother with a RMS roughness of 0.90 nm. At higher energy densities, 1.05 Jcm^{-2} , shown in **Figure VI.5 (h)**, islands formed.

For GeSn 10% we can again distinguish the three melt regimes: the surface melt regime from 0.70 Jcm^{-2} up to 0.85 Jcm^{-2} , the partial melt regime from 0.875 Jcm^{-2} up to 1.025 Jcm^{-2} and the full melt regime above. It should, at that stage, be reminded that there was most likely a Sn rich layer on top of such NLA GeSn 10% layers, which showed three melt regimes. Additional TEM observations would be needed to confirm that.

Finally, we have investigated the impact of NLA on GeSn 14% layers. At 0.60 Jcm^{-2} , shown in **Figure VI.6 (a)**, the first surface structures appeared. This was at a lower energy density than in TRR. Such structures were most likely too small to be detectable by TRR. They were indeed much thinner than those observed for GeSn 6% and GeSn 10%, respectively shown in **Figure VI.4** and **Figure VI.5**. Moreover, those surface structures were more discontinuous, like “beads on a necklace” instead of ridges. This was in line with findings for SiGe on Si [14], but at lower Sn concentrations.

At 0.65 Jcm^{-2} , shown in **Figure VI.6 (b)**, surface structures multiplied and formed a street-grid like pattern. Again, ridges were thinner and not continuous. Slightly larger islands formed at intersections. At 0.75 Jcm^{-2} , **Figure VI.6 (c)**, large islands formed that merged at 0.80 Jcm^{-2} , **Figure VI.6 (d)**. The layer was almost continuous, with some holes, however, at 0.90 Jcm^{-2} , as shown in **Figure VI.6 (e)**. It became continuous at higher energy densities, shown for 0.95 Jcm^{-2} in **Figure VI.6 (f)**. At 1.00 Jcm^{-2} , the RMS roughness reached a minimum value of 0.76 nm, shown in **Figure VI.6 (g)**. Some surface regions were discontinuous, but the difference in height with the rest of the surface was 3.0 nm only. At 1.05 Jcm^{-2} , shown in **Figure VI.6 (h)**, the layer became less continuous, with “holes”. At even higher energy densities, islands formed (not shown).

There were once again three melt regimes for the GeSn 14% layer. The surface melt regime occurred from 0.60 Jcm^{-2} to 0.80 Jcm^{-2} . The partial melt regime was between 0.825 Jcm^{-2} to 1.025 Jcm^{-2} . Above that ED, most likely full melt occurred. There was some uncertainty because the transition from partial to full melt regime was less abrupt than for lower Sn contents.

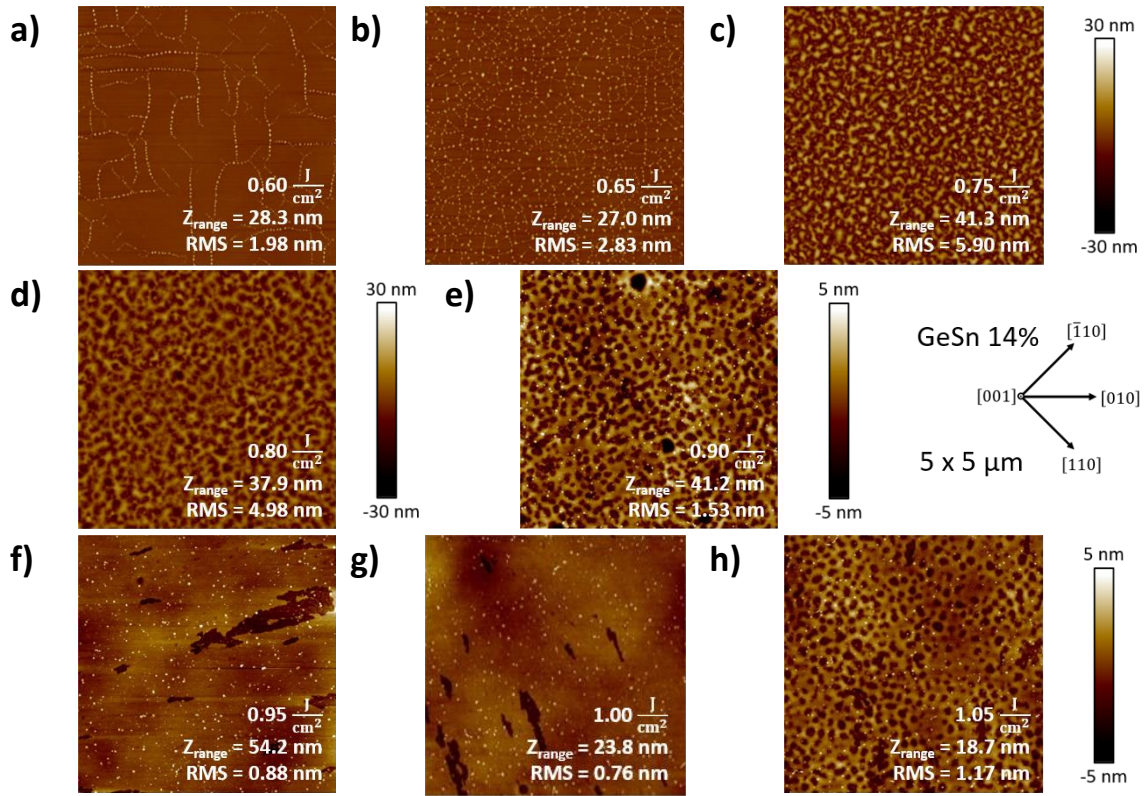


Figure VI.6: $5 \mu\text{m} \times 5 \mu\text{m}$ AFM images of 38 nm thick pseudomorphic GeSn 14% layers after laser annealing at 0.60 Jcm^{-2} (a), 0.65 Jcm^{-2} (b), 0.75 Jcm^{-2} (c), 0.80 Jcm^{-2} (d) ((a), (b), (c), (d) with 30 nm z-scale), 0.90 Jcm^{-2} (e), 0.95 Jcm^{-2} (f), 1.025 Jcm^{-2} (g) and 1.05 Jcm^{-2} (h) ((e) to (h) with 5 nm z-scale). The schematic in the middle on the right shows the crystallographic directions.

A detailed quantitative analysis of the surface structure density and dimensions was performed. It can be found in **Appendix**. It showed that, for GeSn 6% and 10%, surface structures increased in size and the surface structure density stayed rather constant for energy densities just above the melt threshold. Meanwhile, for GeSn 14%, the surface structure diameter did not directly increase for energy densities just above the melt threshold. Instead, the surface structure density increased. When a high enough amount of large enough surface structures were formed, they merged and formed a continuous surface layer. For GeSn 6%, the surface coverage was not high enough to form a continuous surface layer. The surface coverage increased with the as-grown Sn content. This was an indication that the surface structures might be Sn-rich.

VI.5 Effect of Nanosecond Laser Annealing on Crystalline Structure

AFM investigations outlined that Sn might be redistributed during nanosecond laser annealing. Sn redistribution most likely led to the formation of Sn rich structures on the surface or even a Sn rich surface layer. ω - 2θ scans around the (0 0 4) XRD order enabled us to assess the crystalline structure, Sn content and layer thickness for various EDs. **Figure VI.7 (a) to (d)** show Ω - 2θ scans for the GeSn 14% layer. The as-grown GeSn 14% layer, shown in **Figure VI.7 (d)**, was pseudomorphic and exhibited a well-defined, intense GeSn peak with well

separated, periodic thickness fringes on each side. This outlined the very good crystalline quality of that layer and the fact that the surface and interfaces were smooth. [15] The as-grown Sn content was 14.02% and the thickness 38.4 nm at that location on the wafer. We recorded scans of similar quality for the various Sn contents and over the entirety of as-grown wafers.

As in previous studies, the Ge SRB peak was slightly asymmetric and shifted towards the Si substrate peak. This was due to the formation of an interfacial GeSi alloy during the short duration thermal cycling [16] and the slight tensile strain in the Ge SRBs, with a mean macroscopic degree of strain relaxation $R = 104\%$. This slight tensile strain was due to thermal expansion differences between Ge and Si, which came into play during the cooling-down to room temperature. [17]–[19]

At the melt threshold, shown in **Figure VI.7 (c)**, the GeSn XRD peak intensity decreased slightly and shifted towards slightly higher incidence angles. That resulted in a decrease of the “apparent” Sn content to 13.69%. By “apparent” Sn content, we mean the Sn content that can be inferred from such XRD profiles assuming that the GeSn layer was fully compressively strained on the Ge SRB underneath, which might not always be the case. Moreover, the intensity of the thickness fringes was significantly reduced. This was most likely due to the formation of surface structures.

When the energy density further increased, the GeSn peak shifted to higher angles and its intensity decreased. The peak shift was linked to a reduction of the “apparent” Sn content. Similar observations were previously made in the literature for laser annealed GeSn. [20] At 0.85 Jcm^{-2} , shown in **Figure VI.7 (b)**, the GeSn XRD peak had almost entirely disappeared. This coincided with the energy density leading to the formation of a continuous layer (surface structures merged) shown in **Figure VI.7**. This was another indication that a Sn-rich surface layer might have formed on the surface. Further investigations on thick (relaxed), P implanted GeSn indicated that β -Sn layers (regions) might be formed. This would explain why we did not record any GeSn XRD signal. At even higher energy densities, 1.025 Jcm^{-2} shown in **Figure VI.7 (a)**, multiple GeSn peaks appeared at different angles. This might be due to the presence of multiple GeSn layers with different Sn contents. The highest “apparent” Sn content estimated from these peaks was 6.3%, a value significantly above the equilibrium solid solubility limit of 1%. [21] A Sn content above the solid solubility limit after some conventional annealing was not evidenced up to now. [6], [22]

Figure VI.7 (e) shows the Raman shift measured for GeSn 14% layers laser annealed at various energy densities. The Raman peak shifted to lower wavelengths above the melt threshold (vertical black dashed line) and reached a plateau for intermediate energy densities, where we recorded the loss of the XRD peak, shown in **Figure VI.7 (b)**. When the high crystalline quality, high Sn content XRD peaks appeared for high energy densities, shown in **Figure VI.7 (a)**, the Raman peak returned to its original position. This might be explained by Sn redistribution which led to the formation of a β -Sn layer.

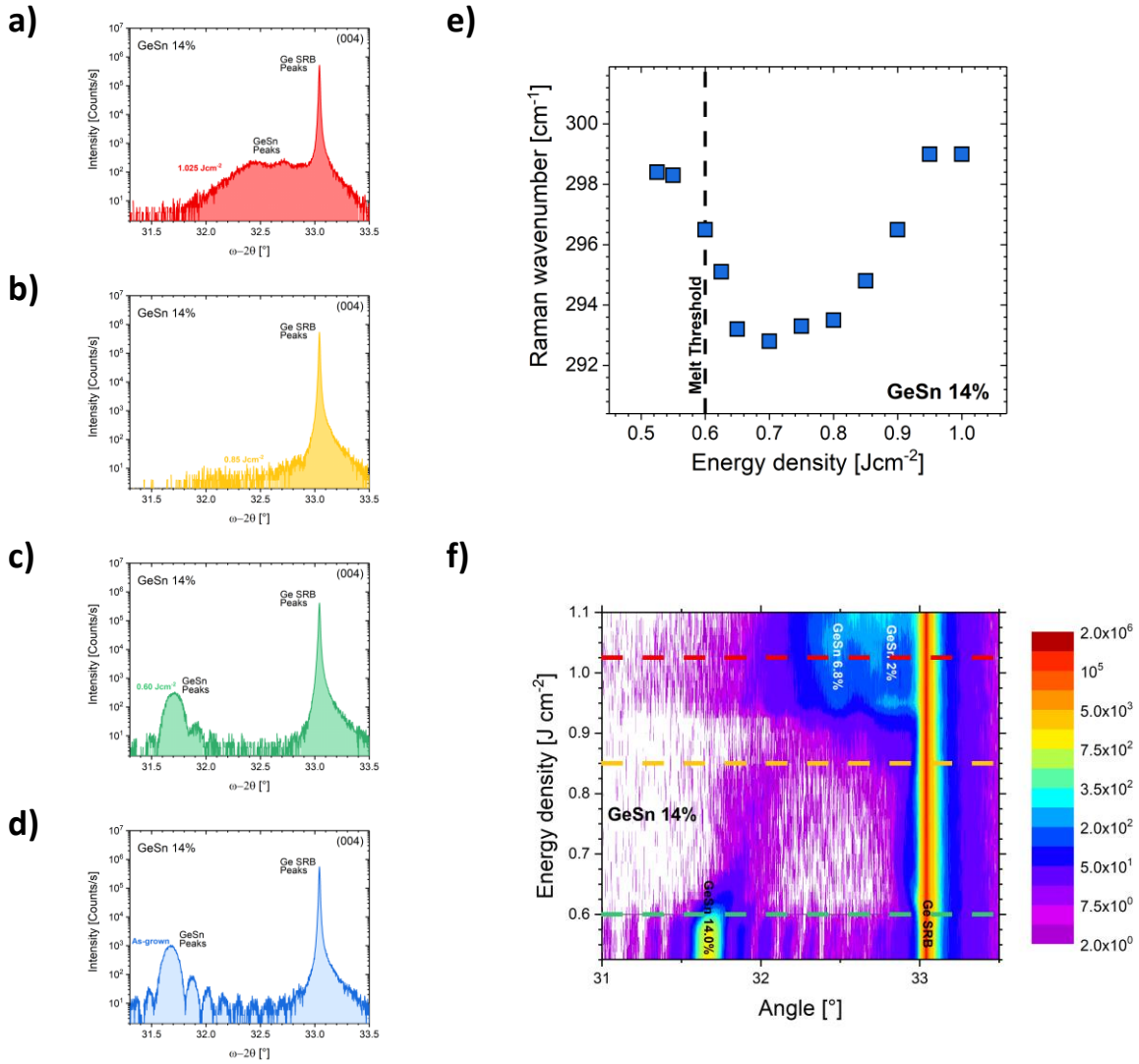


Figure VI.7: ω - 2θ scans around the (0 0 4) XRD order for GeSn 14% after laser annealing at 1.00 Jcm^{-2} (red (a)), 0.85 Jcm^{-2} (yellow (b)) and 0.60 Jcm^{-2} (green (c)) and as-grown profile (blue (d)). (e) Raman wavenumber at various energy densities for GeSn 14%. The vertical black dashed line outlines the melt threshold (determined by AFM). (f) ω - 2θ scan map obtained by stacking XRD scans at various ED (step size 0.025 Jcm^{-2}). Colored lines show at which energy density (a) to (d) ω - 2θ scans were acquired.

Reciprocal space maps around the (2 2 4) XRD order were recorded for GeSn 6% and 10%. They are provided in **Appendix I**. GeSn peaks shifted, after NLA, towards the Ge SRB peaks, most likely because of Sn redistribution. It is worth noting that the GeSn layers remained fully compressively strained on the Ge SRB underneath (same in-plane reciprocal space coordinates). Similar results were previously obtained for higher Sn contents. [20]

To gain a better overview of the way the GeSn XRD peak shifted, a XRD map was constructed. To achieve this, ω - 2θ scans were stacked on top of each other with an ED step size of 0.025 Jcm^{-2} . **Figure VI.7 (f)** shows such a XRD map for GeSn 14%. Colored horizontal lines correspond to the ω - 2θ scans in the same color shown in **Figure VI.7 (a) to (c)**.

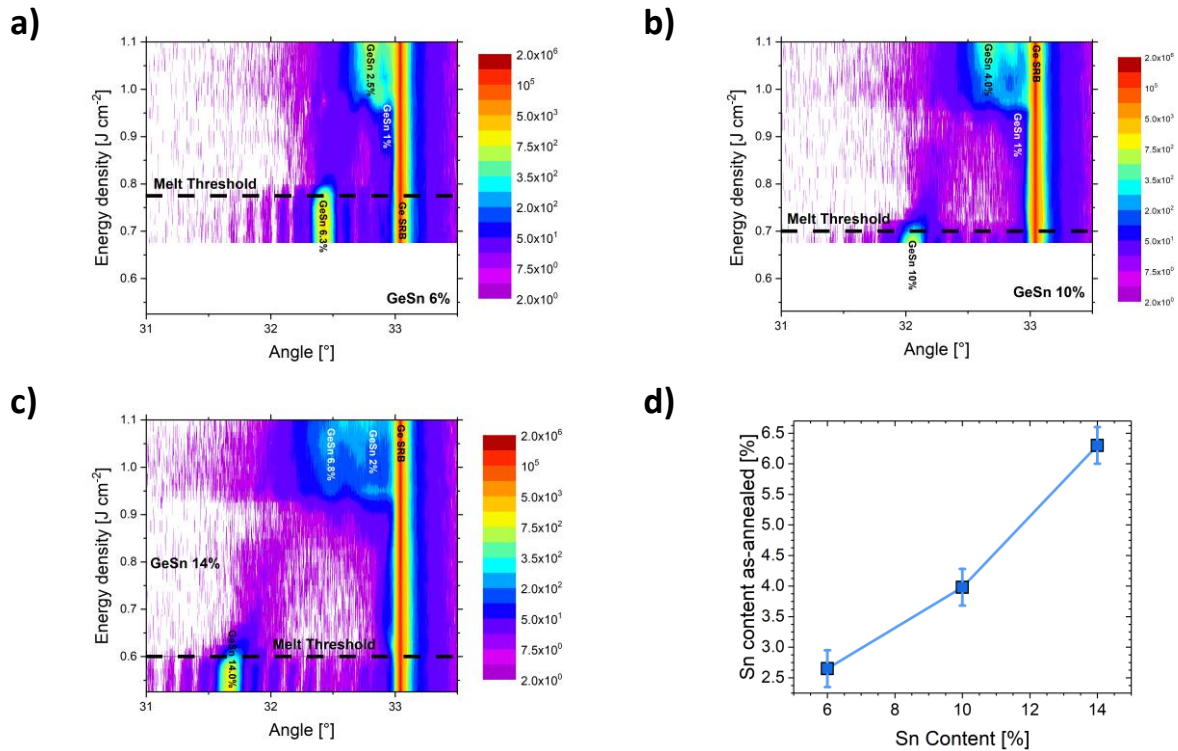


Figure VI.8: ω - 2θ scan maps (step size 0.025 J cm^{-2}) around the (0 0 4) XRD order of laser annealed pseudomorphic GeSn 6% (a), 10% (b) and 14% (c) layers. The black dashed lines outline the melt threshold (determined by AFM). (d) Dependence of the Sn content after laser annealing at energy densities above 1.00 J cm^{-2} on the as-grown Sn content (absolute error bars: 0.3%).

The XRD maps for the various samples, shown in **Figure VI.8**, revealed that the GeSn XRD peak did not change in intensity or position below the melt threshold, this whatever the as-grown Sn content. Moreover, they did confirm the melt threshold obtained by AFM. This outlined that, as soon as surface structures formed, however small they were, there was some Sn redistribution, strengthening the hypothesis that the surface structures might be Sn-rich. Above the melt threshold, the GeSn XRD peak shifted to higher angles because of lower “apparent” Sn contents and lost intensity. This was most likely due to Sn redistribution, strain relaxation or surface roughening. The higher the as-grown Sn content was, the lower the GeSn XRD peak intensity was. As shown in **Figure VI.7 (b)**, the GeSn peak for GeSn 14% was completely lost at intermediate energy densities. That was not the case for lower as-grown Sn contents. Additionally, at energy densities above 0.95 J cm^{-2} , a new GeSn XRD peak appeared at angles corresponding to lower “apparent” Sn contents than the as-grown Sn contents.

For GeSn 6%, shown in **Figure VI.8 (a)**, this peak corresponded to an “apparent” Sn content of around 2.7%, which was above the solid solubility limit of 1%. The resulting GeSn XRD peak was not well defined, but still clearly distinguishable. For GeSn 10%, shown in **Figure VI.8 (b)**, a GeSn peak formed at an angle corresponding to a Sn content of 4.0%. This was, once again, significantly above the solid solubility limit. There was an additional GeSn XRD peak between the GeSn 4% peak and the Ge SRB peak. This might be a thickness fringe or another GeSn layer with a different Sn concentration.

Plotting the as-grown Sn content against the annealed “apparent” Sn content revealed, in **Figure VI.8 (d)**, an increase of the annealed Sn content with the as-grown Sn content. Nanosecond laser annealing might have resulted in a recrystallization that was so fast that Sn segregation was prevented, resulting in a solid phase solubility limit higher than with longer anneals. Higher as-grown Sn contents would result in higher annealed Sn contents, then.

Figure VI.9 (a) shows the thickness at the various energy densities probed for the different as-grown Sn contents. We subtracted, for each as-grown Sn content, the melt threshold ED from the measured ED, to facilitate comparison between datasets. The black dashed line outlined the melt threshold. Thicknesses provided in **Figure VI.9 (a)** were estimations because the loss of thickness fringes made the extraction inaccurate.

Below the melt threshold, the thickness did not significantly change. Above the melt threshold, the thickness remained constant up to lower energy densities above the melt threshold when the as-grown Sn content was higher. As the ED further increased, the thickness dropped. The thickness dropped at energy densities for which the surface structure density reached a maximum value, as shown in **Appendix I**. This was just when surface structures merged and started forming a continuous Sn rich layer. Because of the redistribution of Sn, which probably led to the formation of this layer, the as-grown layer thickness was reduced.

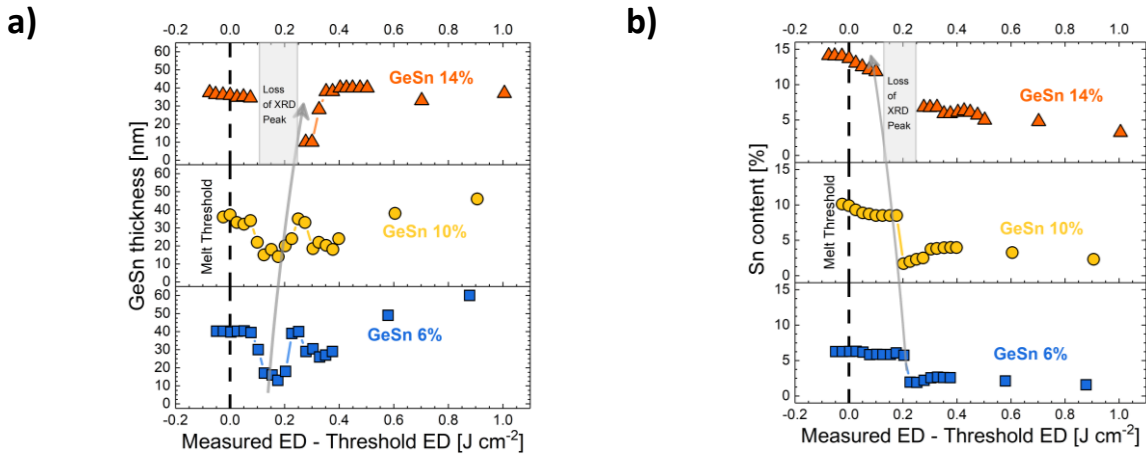


Figure VI.9: GeSn layer thickness (a) and Sn content (b) extracted from ω - 2θ scans around the (0 0 4) XRD order as a function of measured energy density minus the melt threshold energy density for GeSn 6% (blue squares), GeSn 10% (yellow circles) and GeSn 14% (orange triangles) layers. The black dashed lines show the melt thresholds. The melt threshold was 0.775 Jcm^{-2} for GeSn 6%, 0.70 Jcm^{-2} for GeSn 10% and 0.60 Jcm^{-2} for GeSn 14% (from AFM). The gray arrow shows the shift towards higher EDs of the thickness reduction when the as-grown Sn content increases. Meanwhile, grey boxes show the ED regions over which the GeSn 14% XRD peak was too ill defined to be fitted.

When the higher Sn content layer formed above EDs of 0.95 Jcm^{-2} , the GeSn thickness recovered its as-grown value. Afterwards, GeSn 6% and 10% layer thicknesses slightly shrank, probably because of surface structure formation at EDs just above those for which smooth layers were obtained. For an as-grown Sn content of 14%, the layer thickness was more stable because the surface structure formation occurred at higher EDs. When the melt depth reached the GeSn-Ge SRB interface, some of the Ge SRB melted and the thickness increased.

Above the melt threshold, the Sn content was slightly reduced, as shown in **Figure VI.9 (b)**. As in **Figure VI.9 (a)**, we subtracted, for each as-grown Sn content, the melt threshold ED from the measured ED, to facilitate the comparison between datasets. At energy densities slightly above the melt threshold, when only small surface structures formed (**Figure VI.4 to Figure VI.6**), the Sn content remained constant in the GeSn 6% (blue) and 10% (yellow) samples. For GeSn 14% (orange), the Sn content dropped until the GeSn XRD peak was lost. For GeSn 14% at EDs above 0.675 Jcm^{-2} , surface structures rather increased in density. For GeSn 6% and 10%, they increased in size. This might explain why the Sn content evolved differently. When surface structures merged, the Sn content dropped then slightly re-increased. For GeSn 14%, no Sn contents could be determined because of the loss of the GeSn XRD peak. The Sn contents for all probed layers then stabilized. The Sn content was slightly reduced at the highest energy densities probed, most likely because of the melting of the Ge SRBs that resulted in a dilution of Sn with more Ge.

VI.6 Effect of Nanosecond Laser Annealing on Sn redistribution

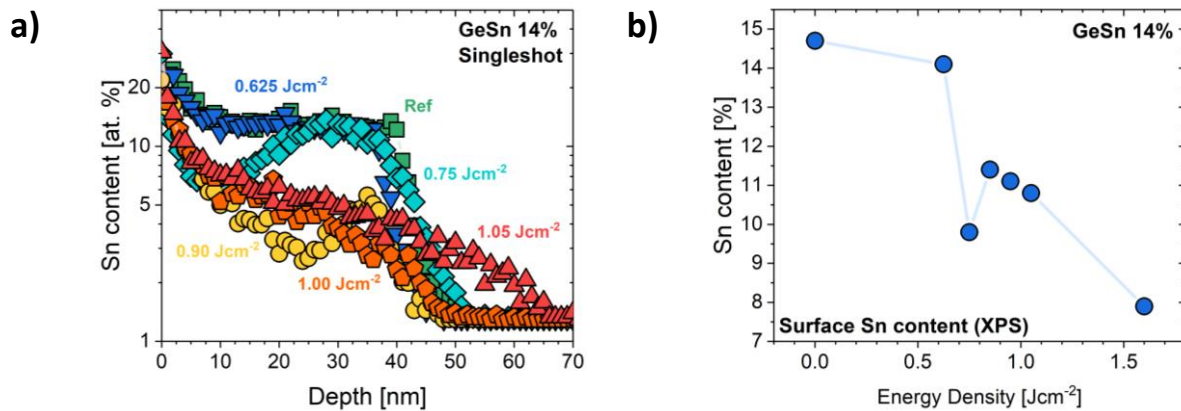


Figure VI.10: (a) SIMS profile of GeSn 14% layer with an as-grown thicknesses close to 40 nm for various EDs and (b) surface Sn content probed by XPS.

For GeSn 6 % at the melt threshold of 0.775 Jcm^{-2} the SIMS profile, shown in **Appendix I**, showed no significant Sn redistribution. For GeSn 10%, also shown in **Appendix I**, and GeSn 14%, shown in **Figure VI.10 (a)**, there were, at the melt threshold, no significant differences between as-grown layers (green squares) and layers laser annealed at 0.70 Jcm^{-2} or 0.625 Jcm^{-2} (blue triangles). SIMS was limited by measurement artifacts in the first few nanometers profiled. We were thus not able to properly track the redistribution of Sn into small surface islands at the melt threshold. For GeSn 14% and an energy density of 0.75 Jcm^{-2} , there was some Sn redistribution (light blue diamonds in **Figure VI.10 (a)**), with a Sn concentration drop and a plateau around 6.5% close to the surface. The Sn content gradually increased towards the as-grown Sn concentration after that plateau. The depth where the as-grown Sn content was reached corresponded to the melt depth during laser annealing, 28 nm in that case. The ill-defined peak in **Figure VI.7 (b)** XRD profile was thus due to Sn redistribution. For 0.90 Jcm^{-2} (yellow circles in **Figure VI.10 (a)**), the melt depth increased to 35 nm. The Sn content increased towards the surface and towards the liquid/solid interface. A minimum of around 2.5% Sn, around the solid solubility limit and corresponding to the appearance of a XRD peak in line with such a Sn content, was found at 24 nm. Around the full melt threshold (orange

pentagons in **Figure VI.10 (a)**), the Sn content increased continuously towards the surface and an abrupt decrease close to the GeSn/Ge SRB interface was evidenced. This outlined that the melt depth was slightly below the thickness of the whole GeSn layer.

SIMS profiles of “full melt” GeSn 6% and 10% layers (**Appendix I**) showed a drastic increase of the Sn concentration in the first ten nm close to the surface. This might be due to the formation of Sn rich islands on the surface. Meanwhile, the surface oxide on the GeSn 14% sample was removed *prior to SIMS* to perform X-ray photoelectron spectroscopy (XPS) measurements. The Sn rich islands on the surface might have been highly oxidized and removed during that oxide removal, explaining the lack of a Sn surface peak in **Figure VI.10 (a)**.

When the energy density further increased to 1.05 Jcm^{-2} (red triangles in **Figure VI.10 (a)**), Sn redistributed into the Ge SRB underneath, with therefore some significant Sn signal above 50 nm. The melt depth for this energy density was 66 nm (from SIMS).

X-ray photoelectron spectroscopy (XPS) was performed to obtain the Sn content on the surface of GeSn 14% samples, shown in **Figure VI.10 (b)**. The oxide was removed just before XPS measurements and the exposure time after oxide removal limited as much as possible to obtain more accurate values of the Sn content. XPS data were in line with SIMS data for GeSn 14%. No Sn enriched surface was evidenced by XPS. Instead, the surface Sn content decreased as the ED increased. That decrease was slight at the melt threshold, more drastic at higher energy densities, reaching 9.8% for 0.75 Jcm^{-2} . Such a reduction was likely due to a loss of Sn during oxide removal (etching of Sn rich oxidized islands). At 0.85 Jcm^{-2} , the Sn surface content re-increased to 11.4%. This corresponded to the ED where surface structures started to merge and form a continuous layer that might have been more robust against oxide removal, as shown in **Appendix I**. The surface Sn content monotonously decreased for higher ED. It was 7.9% at 1.60 Jcm^{-2} , most likely because Sn was redistributed into the Ge SRB. Previous studies found Sn contents above 20%. [20], [23], [24] In these studies, no oxide removal was performed and Sn rich islands were highly oxidized. To gain a more detailed understanding of where Sn was redistributed to and if the Sn rich islands were removed during oxide removal, cross-sectional Transmission Electron Microscopy together with Energy Dispersive X-Ray Spectroscopy (EDX) are required. Moreover, Sn might have desorbed from the surface due to its low binding energy. The Sn-Sn bond energy is 184 kJ/mol only, compared to 230 kJ/mol and 264 kJ/mol for Ge-Sn and Ge-Ge bonds, respectively. [25]

The as-grown GeSn 14% layer exhibited good crystalline quality and abrupt surface/interfaces, as shown by the Bright Field Scanning Transmission Electron Microscopy (BF-STEM) image in **Figure VI.11 (a)**. The depth of the GeSn / Ge SRB interface was in line with the XRD thickness. When applying a laser pulse with an energy density of 1.00 Jcm^{-2} , shown in **Figure VI.11 (b)**, some roughening of the surface was seen, in line with **Figure VI.6 (g)** AFM data. The crystalline quality was good. No significant difference in contrast was found between the GeSn layer and the Ge SRB.

Figure VI.11 (c) EDX map showed that Sn was homogeneously distributed in the as-grown GeSn 14% layer. The mean Sn content was around 14%, in line with XRD data. Moreover, the surface was smooth and the GeSn/Ge interface abrupt. On the other hand, Sn was significantly redistributed towards the surface after NLA with 1.00 Jcm^{-2} , as outlined by the EDX map shown in **Figure VI.11 (d)**. The Sn-rich surface layer had a Sn content around 11%, in line with the Sn contents from SIMS and XPS. There was otherwise a gradual increase of the Sn content in

this NLA GeSn layer, from around 3% at the bottom towards 11% close to the surface. There was no significant Sn redistribution for thicknesses larger than 40 nm, outlining that 1.00 Jcm^{-2} was close to the full melt energy density.

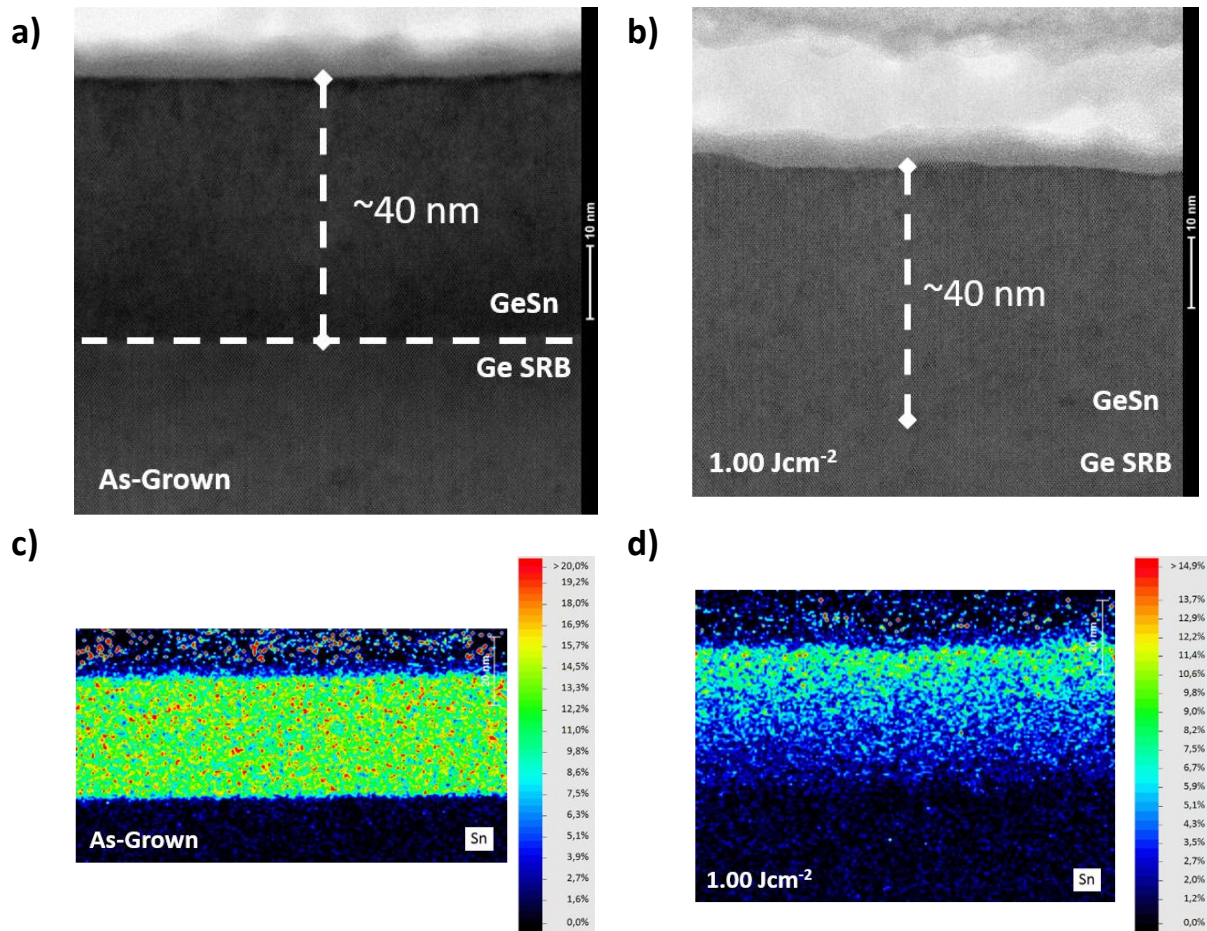


Figure VI.11: BF-STEM images of as-grown (a) GeSn 14% and after NLA with 1.00 Jcm^{-2} (b). The vertical dashed line corresponds to the GeSn / Ge SRB interface, which was at a thickness of around 40 nm. EDX of Sn in as-grown GeSn 14% (c) and after NLA with 1.00 Jcm^{-2} (d). The colorscale is not the same in (c) and (d).

VI.7 Conclusions

In this study, the recrystallization of pseudomorphic GeSn with various Sn contents was investigated. The goal was to better understand how ultrafast nanosecond laser annealing interacted with that metastable material. It was shown that the melt threshold shifted to lower energy densities as the as-grown Sn content in pseudomorphic GeSn layers on Ge Strain-Relaxed Buffers increased. We found a peculiar tail for all Sn contents in TRR maps, which was likely due to surface roughness and the formation of a Sn rich layer. We otherwise evidenced the same melt regimes as for SiGe on Si and the same dependence of the shape of surface structures on the Sn composition. The impact of compositional changes was more

pronounced in GeSn than in SiGe, however, most likely because of the much larger atomic size of Sn compared to Ge than Ge compared to Si. TEM showed the high crystalline quality of the GeSn 6% and 14% layers after laser annealing around the full melt regime (1.025 Jcm^{-2}). At energy densities close to the full melt, smooth surfaces were formed and ω - 2θ XRD scans showed the formation of GeSn layers with Sn contents of up to 6.3%. Such layers had not been reported previously in the literature for annealed samples. Those layers were of good crystalline quality, as outlined by high intensity XRD peaks. This opens up a new process option for the activation of dopants after ion implantation. All results hinted at the fact that a Sn rich layer was formed on the surface after laser annealing at high energy densities. SIMS measurements evidenced the redistribution of Sn towards the surface, which was confirmed by TEM EDX measurements.

References

- [1] L. Casiez *et al.*, “Recrystallization of thick implanted GeSn layers with nanosecond laser annealing,” *J. Appl. Phys.*, vol. 131, no. 15, p. 153103, Apr. 2022, doi: 10.1063/5.0085107.
- [2] S. Adachi, “Optical dispersion relations in amorphous semiconductors,” *Phys. Rev. B*, vol. 43, no. 15, pp. 12316–12321, May 1991, doi: 10.1103/PhysRevB.43.12316.
- [3] G. E. Jellison, “Optical functions of GaAs, GaP, and Ge determined by two-channel polarization modulation ellipsometry,” *Opt. Mater.*, vol. 1, no. 3, pp. 151–160, Sep. 1992, doi: 10.1016/0925-3467(92)90022-F.
- [4] R. W. Olesinski and G. J. Abbaschian, “The Ge–Sn (Germanium–Tin) system,” *Bull. Alloy Phase Diagr.*, vol. 5, no. 3, pp. 265–271, Jun. 1984, doi: 10.1007/BF02868550.
- [5] J.-H. Fournier-Lupien *et al.*, “In Situ Studies of Germanium-Tin and Silicon-Germanium-Tin Thermal Stability,” *ECS Trans.*, vol. 64, no. 6, pp. 903–911, Aug. 2014, doi: 10.1149/06406.0903ecst.
- [6] P. Zaumseil *et al.*, “The thermal stability of epitaxial GeSn layers,” *APL Mater.*, vol. 6, no. 7, p. 076108, Jul. 2018, doi: 10.1063/1.5036728.
- [7] J. Nicolas, S. Assali, S. Mukherjee, A. Lotnyk, and O. Moutanabbir, “Dislocation Pipe Diffusion and Solute Segregation during the Growth of Metastable GeSn,” *Cryst. Growth Des.*, vol. 20, no. 5, pp. 3493–3498, May 2020, doi: 10.1021/acs.cgd.0c00270.
- [8] K.-H. Heinig, “Effects of local melting on semiconductor surfaces,” *Energy Pulse Modif. Semicond. Relat. Mater.*, pp. 265–279, 1984.
- [9] H. A. Atwater, C. V. Thompson, and H. I. Smith, “Mechanisms for crystallographic orientation in the crystallization of thin silicon films from the melt,” *J. Mater. Res.*, vol. 3, no. 6, pp. 1232–1237, Dec. 1988, doi: 10.1557/JMR.1988.1232.
- [10] J. C. Brice and P. A. C. Whiffin, “The temperature distribution in pulled germanium crystals during growth,” *Solid-State Electron.*, vol. 7, no. 2, pp. 183–187, Feb. 1964, doi: 10.1016/0038-1101(64)90143-1.
- [11] G. Calogero *et al.*, “Multiscale modeling of ultrafast melting phenomena,” *Npj Comput. Mater.*, vol. 8, no. 1, p. 36, Dec. 2022, doi: 10.1038/s41524-022-00720-y.
- [12] K. Huet *et al.*, “Laser Thermal Annealing for Low Thermal Budget Applications: From Contact Formation to Material Modification,” *ECS Trans.*, vol. 89, no. 3, pp. 137–153, Apr. 2019, doi: 10.1149/08903.0137ecst.
- [13] L. Dagault *et al.*, “Impact of UV Nanosecond Laser Annealing on Composition and Strain of Undoped Si_{0.8}Ge_{0.2} Epitaxial Layers,” *ECS J. Solid State Sci. Technol.*, vol. 8, no. 3, pp. P202–P208, 2019, doi: 10.1149/2.0191903jss.
- [14] L. Dagault *et al.*, “Investigation of recrystallization and stress relaxation in nanosecond laser annealed Si_{1-x}Ge_x/Si epilayers,” *Appl. Surf. Sci.*, vol. 527, p. 146752, Oct. 2020, doi: 10.1016/j.apsusc.2020.146752.
- [15] V. Holy, U. Pietsch, and T. Baumbach, *High-Resolution X-Ray Scattering from Thin Films and Multilayers*, vol. 149. Berlin, Heidelberg: Springer Berlin Heidelberg, 1999. doi: 10.1007/BFb0109385.
- [16] J. M. Hartmann and J. Aubin, “Assessment of the growth/etch back technique for the production of Ge strain-relaxed buffers on Si,” *J. Cryst. Growth*, vol. 488, pp. 43–50, Apr. 2018, doi: 10.1016/j.jcrysgro.2018.02.036.
- [17] R. E. Camacho-Aguilera *et al.*, “An electrically pumped germanium laser,” *Opt. Express*, vol. 20, no. 10, p. 11316, May 2012, doi: 10.1364/OE.20.011316.
- [18] D. D. Cannon *et al.*, “Tensile strained epitaxial Ge films on Si(100) substrates with potential application in L-band telecommunications,” *Appl. Phys. Lett.*, vol. 84, no. 6, pp. 906–908, Feb. 2004, doi: 10.1063/1.1645677.

- [19] T. K. P. Luong *et al.*, “Control of tensile strain and interdiffusion in Ge/Si(001) epilayers grown by molecular-beam epitaxy,” *J. Appl. Phys.*, vol. 114, no. 8, p. 083504, Aug. 2013, doi: 10.1063/1.4818945.
- [20] L. Wang *et al.*, “Post-growth annealing of germanium-tin alloys using pulsed excimer laser,” *J. Appl. Phys.*, vol. 118, no. 2, p. 025701, Jul. 2015, doi: 10.1063/1.4926484.
- [21] F. A. Trumbore, “Solid Solubilities and Electrical Properties of Tin in Germanium Single Crystals,” *J. Electrochem. Soc.*, vol. 103, no. 11, p. 597, 1956, doi: 10.1149/1.2430167.
- [22] N. von den Driesch *et al.*, “Thermally activated diffusion and lattice relaxation in (Si)GeSn materials,” *Phys. Rev. Mater.*, vol. 4, no. 3, p. 033604, Mar. 2020, doi: 10.1103/PhysRevMaterials.4.033604.
- [23] P. Onufrijevs *et al.*, “Direct-indirect GeSn band structure formation by laser Radiation: The enhancement of Sn solubility in Ge,” *Opt. Laser Technol.*, vol. 128, p. 106200, Aug. 2020, doi: 10.1016/j.optlastec.2020.106200.
- [24] P. Ščajev *et al.*, “Extension of spectral sensitivity of GeSn IR photodiode after laser annealing,” *Appl. Surf. Sci.*, vol. 555, p. 149711, Jul. 2021, doi: 10.1016/j.apsusc.2021.149711.
- [25] Y.-R. Luo, *Handbook of Bond Dissociation Energies in Organic Compounds*, 0 ed. CRC Press, 2002. doi: 10.1201/9781420039863.

Chapter VII : Multi Pulse Nanosecond Laser Annealing of GeSn

Chapter VII: Multi Pulse Nanosecond Laser Annealing of GeSn

<u>Chapter VII: Multi Pulse Nanosecond Laser Annealing of GeSn</u>	<u>130</u>
VII.1 Introduction.....	130
VII.2 Multi Pulse NLA - Evolution of Time Resolved Reflectivity	130
VII.3 Multi Pulse NLA - Evolution of surface structure at the melt threshold	136
VII.4 Multi Pulse NLA - Evolution of surface morphology at the full melt threshold	139
VII.5 Multi Pulse NLA - Evolution of crystalline structure at the melt threshold	146
VII.6 Multi Pulse NLA – Sn redistribution	147
VII.7 Conclusions.....	150

Chapter VII: Multi Pulse Nanosecond Laser Annealing of GeSn**VII.1 Introduction**

In this chapter, we focus on the impact of multi-pulse NLA on pseudomorphic, intrinsic GeSn layers with Sn contents between 6% and 14% that were grown on Ge Strain-Relaxed Buffers (SRBs). As previously hinted, GeSn alloys are metastable, the lattice mismatch of Sn with Ge, 14%, is high ($a_{\text{Ge}} = 5.658 \text{ \AA} \Leftrightarrow a_{\text{Sn}} = 6.489 \text{ \AA}$) and melting temperatures are very different. [1] Therefore, in our previous study [2], we strove to better understand the interaction between a single laser pulse and such metastable GeSn alloys in simple stacks. Different melt regimes were found in this study, which are outlined **Table VII.I**. In the current study, we extended previous findings on single pulse experiments to multiple laser pulses. This meant applying a single laser pulse with a specific energy density at a predefined position multiple times, moving over to the next position on the same wafer and repeating the experiment with a different energy density and so on. This procedure enabled us to gain a detailed understanding of mechanisms at play.

Table VII.I The various melt regimes for pseudomorphic 6%, 10% and 14% GeSn on Ge depending on the energy density (in Jcm^{-2}) of the laser pulse. [10]

	GeSn 6% [Jcm^{-2}]	GeSn 10% [Jcm^{-2}]	GeSn 14% [Jcm^{-2}]
Submelt regime	< 0.775	< 0.70	< 0.60
Surface melt regime	0.775 to 0.85	0.70 to 0.85	0.60 to 0.80
Partial melt regime	0.875 to 1.05	0.875 to 1.025	0.825 to 1.025
Full melt regime	> 1.05	> 1.025	> 1.025

VII.2 Multi Pulse NLA - Evolution of Time Resolved Reflectivity

TRR maps shown in **Figure VII.1** for GeSn 6% were similar to that for GeSn single pulse laser annealing. [2] Here, the energy density was constant and multiple laser pulses sent onto the very same position. The TRR signal was recorded for each laser pulse. By stacking the various TRR signals on top of one another, a multishot TRR map was obtained. Sub-melt, partial met and full melt regimes previously found for SiGe on Si [3] were also seen during the single pulse laser annealing of GeSn on Ge. [2] In the current study, we used multiple laser pulse shots with EDs spanning the various melt regimes, on the same position. Below the melt threshold, shown in **Figure VII.1 (a)**, i.e. for an energy density of 0.40 Jcm^{-2} , there were no significant changes in the TRR curves as the number of laser pulses increased.

At the melt threshold of 0.775 Jcm^{-2} for GeSn 6%, shown in **Figure VII.1 (b)**, no significant changes occurred. This was even more obvious when comparing the TRR profiles after a single laser pulse, shown in **Figure VII.1 (f)**, and after the hundredth laser pulse, shown

in **Figure VII.1 (g)**. No significant changes were visible. A single laser pulse at the melt threshold resulted in the formation of surface structures in our previous studies. [2] These structures were too small, however, to be detected by TRR. This was most likely the same for multiple laser pulses.

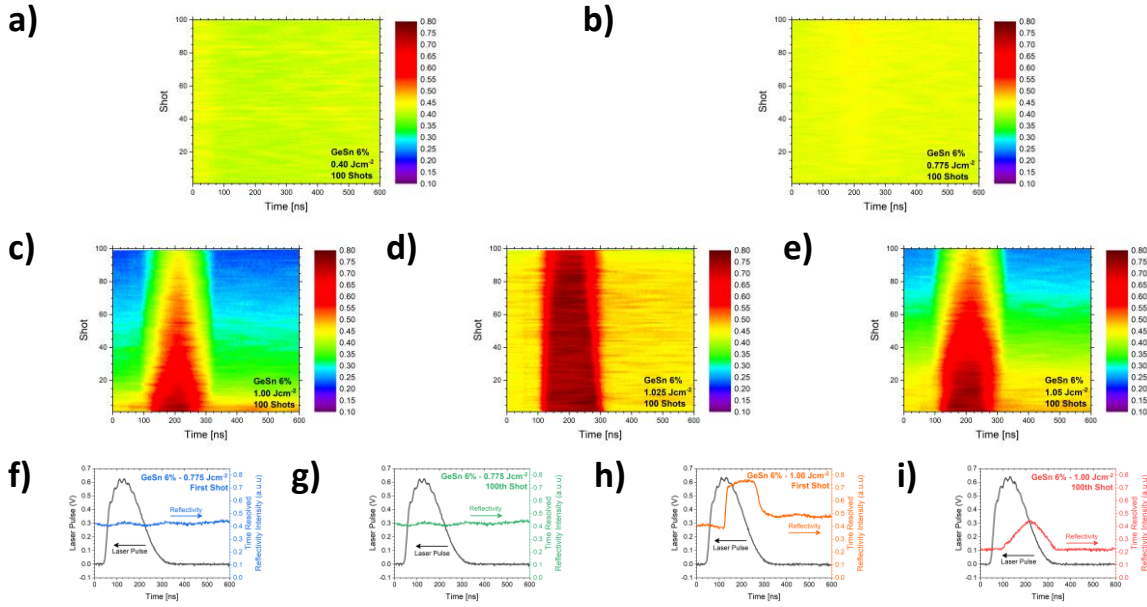


Figure VII.1: Multi laser pulses TRR maps (y-axis: amount of applied laser pulses) for a 42 nm thick pseudomorphic GeSn 6% layer on a Ge SRB laser annealed with Energy Densities of (a) 0.40 Jcm^{-2} , (b) 0.775 Jcm^{-2} , (c) 1.00 Jcm^{-2} , (d) 1.025 Jcm^{-2} and (e) 1.05 Jcm^{-2} . TRR profile with $\text{ED} = 0.775 \text{ Jcm}^{-2}$ for the first (f) and the one-hundredth laser pulse (g). First (h) and one-hundredth (i) laser pulses' TRR profiles with $\text{ED} = 1.00 \text{ Jcm}^{-2}$. The black curve in each graph shows the laser pulse for that ED.

Due to time limitations, we focused on the melt and full melt thresholds (i.e. the energy density for which the entire GeSn layer was melted [2]). Just below the full melt threshold at an energy density of 1.00 Jcm^{-2} , shown in **Figure VII.1 (c)**, significant changes were recorded. At this energy density, almost the entire GeSn layer was melted, resulting in a saturation of the TRR signal for a long time while the layer remained liquid. In Ref. [2], melting after a single laser pulse resulted in the formation of larger, connected islands and to the redistribution of Sn towards the surface. The starting conditions were thus not the same for the next laser pulse. Such differences had a definite impact on melting, as outlined by the shortened duration of the melt peak. The melt peak duration was shortened more and more when the number of laser increased. The TRR profiles after a single pulse, shown in **Figure VII.1 (h)**, and after 100 laser pulses, shown in **Figure VII.1 (i)**, outline that point. The melt peak after 100 pulses is significantly less intense and much shorter. Most likely, the formation of larger and larger, probably Sn-rich, surface structures resulted in different melting conditions. Smaller and smaller portions of the surface melted, explaining why the TRR signal changed.

Curiously, this behavior was completely different at 1.025 Jcm^{-2} , shown in **Figure VII.1 (d)**. The TRR signal for each of the 100 applied laser pulses did not drastically change. It was

slightly reduced for high numbers of laser pulses, but stayed otherwise rather constant. The melting of the entire GeSn 6% layer without any melting of the Ge SRB layer underneath was evidenced in our previous study on single pulse NLA of GeSn at this energy density. We assume that, at this ED, the liquid / solid interface stayed rather smooth because of the melting temperature differences between Sn (232°C) and Ge (938°C). [4] Hence, at this energy density only the GeSn layer was melted. The liquid / solid interface roughness was thus close to that of the GeSn / Ge interface, which was low indeed. At EDs that did not correspond to the full melt ED, the liquid / solid interface was by contrast much rougher. [5], [6] The smooth liquid / solid interface thus resulted in the formation of a smooth surface after NLA. This yielded a steadier TRR signal after multiple laser pulses. We would venture that, for high numbers of laser pulses where the TRR signal slightly changed, the first few nanometers of the Ge SRB were molten, resulting in a roughening of the liquid / solid interface. Surface structures therefore formed, with then a lowering and a shortening of the TRR peak.

At a slightly higher energy density of 1.05 Jcm^{-2} , shown in **Figure VII.1 (e)**, the TRR signal for the various applied laser pulses did change again. It stayed almost constant with slight changes for the first 20 to 30 laser pulses. It might be that, for the first 20 to 30 laser pulses, only the GeSn layer melted. This resulted in the formation of a smooth liquid / solid interface close to the GeSn / Ge SRB interface. When more than 30 laser pulses were applied, significant amounts of the Ge SRB were molten, resulting in a rough liquid / solid interface and the formation of surface structures, which reduced the TRR signal and changed the melt behavior by changing the starting conditions of the annealed area.

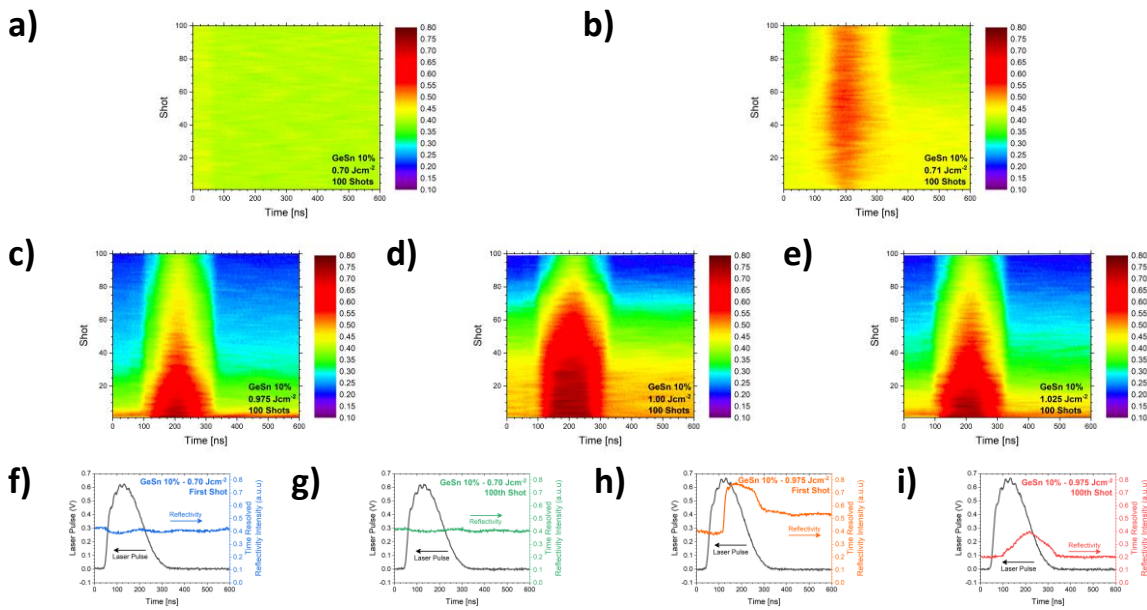


Figure VII.2: Multi laser pulses TRR maps (y-axis amount of applied laser pulses) for a 39 nm thick pseudomorphic GeSn 10% layer on a Ge SRB laser annealed with EDs of (a) 0.70 Jcm^{-2} , (b) 0.71 Jcm^{-2} , (c) 0.975 Jcm^{-2} , (d) 1.00 Jcm^{-2} and (e) 1.025 Jcm^{-2} . TRR profiles for the (f) first and (g) one-hundredth laser shot at 0.70 Jcm^{-2} . First (h) and one-hundredth (i) laser pulses' TRR profiles with 0.975 Jcm^{-2} . The black curve in each graph shows the laser pulse for that ED.

Let us now shift to GeSn 10%. For an ED of 0.70 Jcm^{-2} , i.e. the melt threshold of GeSn 10%, no significant changes were observed when applying multiple laser pulses, as shown in **Figure VII.2 (a)**. As for GeSn 6%, laser annealing at the melt threshold most likely resulted in the formation of surface structures that were too small to be detected by TRR. **Figure VII.2 (f)** and **(g)**, show TRR profiles after one and 100 laser pulses, respectively. Profiles were very similar, with some random oscillations of the TRR signal. Just increasing ED from 0.70 Jcm^{-2} to 0.71 Jcm^{-2} , shown in **Figure VII.2 (b)**, drastically changed the TRR signal for multiple laser pulses. The TRR signal was the highest when the laser pulse reached its highest intensity, outlining some local melting. The TRR peak widened when more laser pulses were used, most likely because larger surface areas melted. When around 50 laser pulses were sent on the GeSn 10% surface, the TRR signal did not significantly change anymore. In our previous study on laser annealing of GeSn with a single laser pulse [9], it was found thanks to AFM that the surface structures formed at an ED of 0.71 Jcm^{-2} were larger than those at 0.70 Jcm^{-2} . Hence, the formation of larger surface structures has a significant influence on the TRR signal. These surface structures most likely increased in size when more laser pulses were used. After 50 laser pulses, a critical surface structures' area was likely reached, which did not really change for higher numbers of laser pulses (the surface structures melted over and over again). This would explain the broadening of the TRR peak for the first 50 laser pulses and why it stayed constant when more laser pulses were used.

At an energy density of 0.975 Jcm^{-2} , shown in **Figure VII.2 (c)**, large surface structures seemed to continuously form. This was most likely the reason why the TRR signal continuously decreased in intensity and melt peak width.

The behavior for the first 20 to 30 laser pulses at an energy density of 1.00 Jcm^{-2} , shown in **Figure VII.2 (d)**, was quite similar to that at 1.025 Jcm^{-2} for GeSn 6%. The width of the melt peak and the value of the initial and final TRR signal for the first 20 to 30 laser pulses were almost the same than at 1.025 Jcm^{-2} for GeSn 6%. For higher numbers of laser pulses, the TRR melt peak's intensity and width were reduced. This was most likely due to the melting of the very top part of the Ge SRB, resulting in a rough liquid / solid interface and the formation of surface structures. The shift to lower energy densities was due to the higher Sn content (10% instead of 6%). When the Sn content increased, the melting temperature was lower as the melting temperature for β -Sn, 232°C , was definitely lower than that for pure Ge, 938°C . [4]

At 1.025 Jcm^{-2} , for GeSn 6%, the behavior was similar to that at 1.05 Jcm^{-2} for GeSn 10%, as shown in **Figure VII.2 (e)**. Here, the liquid / solid interface after the use of laser pulses was most likely rough again because the energy density was high enough to melt part of the Ge SRB. This led to the formation of Sn-rich surface structures that continuously increased in size when more laser pulses were used, resulting in TRR signal changes. The corresponding TRR profiles are shown in **Figure VII.2 (h)** and **(i)**.

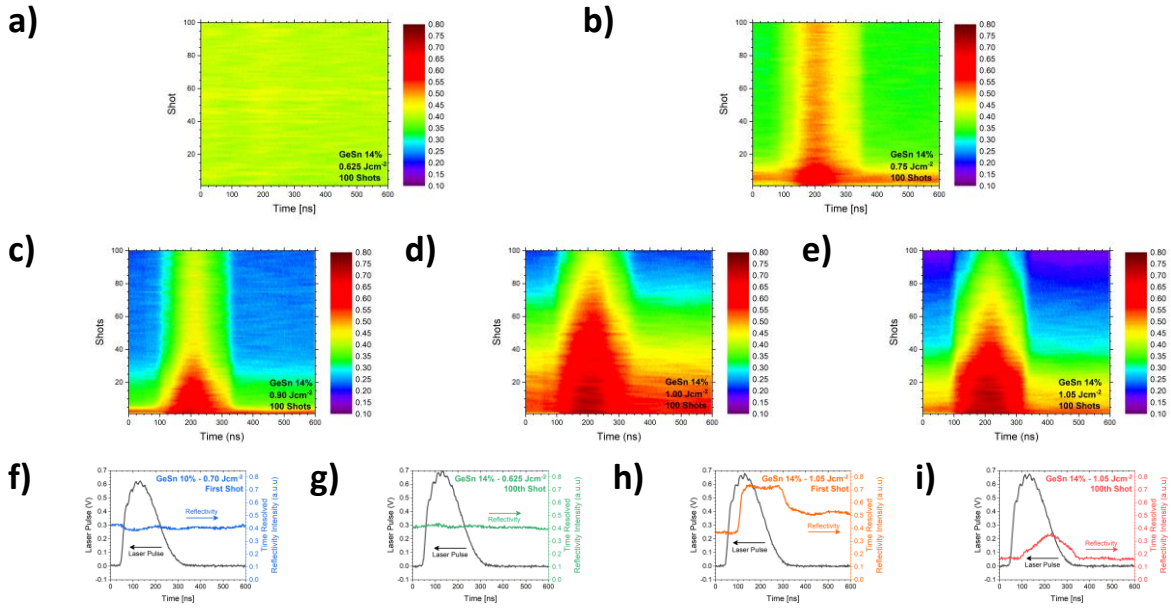


Figure VII.3: Multi laser pulses TRR map (y-axis amount of applied laser pulses) of a 36 nm thick pseudomorphic GeSn 14% layer annealed with EDs of (a) 0.625 Jcm^{-2} , (b) 0.75 Jcm^{-2} , (c) 0.90 Jcm^{-2} , (d) 1.00 Jcm^{-2} and (e) 1.05 Jcm^{-2} . TRR profiles for the (f) first and (g) one-hundredth laser shot at 0.625 Jcm^{-2} . First (h) and one-hundredth (i) laser pulses' TRR profile with 1.05 Jcm^{-2} . The black curve in each graph shows the laser pulse for that ED.

For GeSn 14%, a similar TRR signal behavior was evidenced after the use of multiple laser pulses. At the melt threshold of 0.625 Jcm^{-2} , the TRR signal did not change significantly, shown in **Figure VII.3 (a)**. TRR profiles of the first and one hundredth laser pulses, shown in **Figure VII.3 (f)** and **(g)**, respectively, support this observation.

The TRR profile at an intermediate energy density of 0.75 Jcm^{-2} , where the melt depth was a couple of nanometers inside the GeSn 14% layer, but not close to the GeSn / Ge SRB interface, is shown in **Figure VII.3 (b)**. At this energy density, the liquid solid interface was assumed to be rough and large surface structures were present on the surface, as in [2]. When the surface structures reached a critical size, they did not change anymore and the TRR stayed constant. This occurred after around 10 laser pulses. AFM images corresponding to 0.75 Jcm^{-2} are shown in **Appendix B**.

The behavior around the full melt of the GeSn 14% layer was similar to that for lower Sn contents. Again, the TRR signal changed rapidly when using multiple laser pulses below and above the full melt threshold (**Figure VII.3 (c)** and **(e)**). At 1.00 Jcm^{-2} , shown in **Figure VII.3 (d)**, the TRR signal stayed constant for the first 10 to 20 laser pulses then changed gradually, losing TRR peak intensity and width, as outlined in **Figure VII.3 (h)** and **(i)**. The Ge SRB was most likely molten. The rougher liquid / solid interface resulted in the formation of surface structures having an impact on the TRR signal.

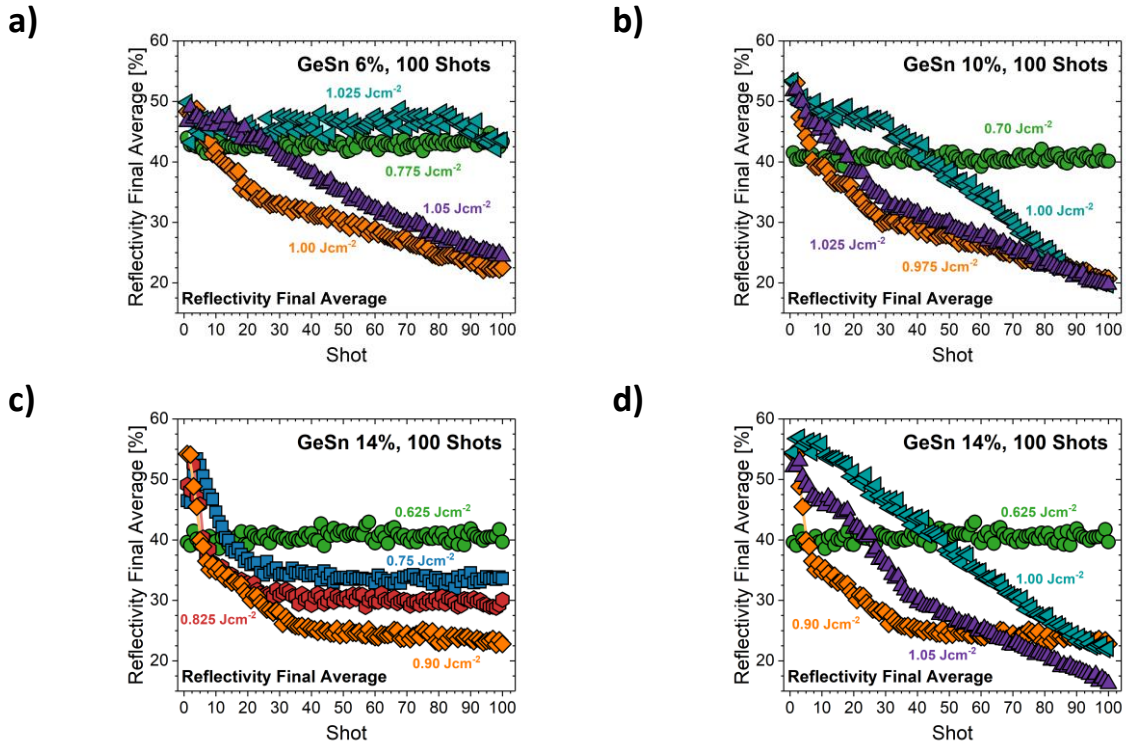


Figure VII.4: Final average TRR signal after each applied laser pulse for GeSn 6% (a), GeSn 10% (b), GeSn 14% with intermediate energy densities (melt threshold to below full melt threshold) (c) and GeSn 14% with energy densities around the full melt threshold (d).

The evolution of the reflectivity final average (last 10 TRR data points), a measure of the reflectivity of the sample's surface after each laser pulse, is shown in **Figure VII.4** for the various Sn contents probed. The average final TRR signal did not change at 0.775 Jcm^{-2} , the melt threshold of GeSn 6%. This is shown as green circles in **Figure VII.4 (a)**. At 1.00 Jcm^{-2} , shown as orange diamonds, the final TRR signal decreased rapidly then more slowly. This was most likely due to the surface structure size, which increased rapidly then more slowly. It might be that Sn redistribution towards the surface impacted the final TRR signal, too. The average final TRR signal did only slightly change for more than 80 laser pulses at 1.025 Jcm^{-2} , shown as light blue triangles. For less than 80 laser pulses, the final TRR value stayed close to the value obtained at the melt threshold. Most likely, the Ge SRB did not melt and the surface stayed smooth. When increasing the energy density to 1.05 Jcm^{-2} , shown as purple triangles, the final average TRR signal was almost constant for the first 20 laser pulses, which might be because, for less than 20 laser pulses, the Ge SRB did not melt. Then it reduced continuously to a value close to the one obtained after 100 laser pulses at 1.00 Jcm^{-2} .

Figure VII.4 (b), shows the average final TRR signal for GeSn 10%. Shown as green circles, the final average TRR signal did not change at the melt threshold. For 0.975 Jcm^{-2} , shown as orange diamonds, and 1.025 Jcm^{-2} , shown as purple triangles, the behavior was similar. The final average TRR signal decreased at first rapidly then more slowly, likely because of some evolution of the surface roughness and maybe because of Sn redistribution towards the surface. At 1.00 Jcm^{-2} , shown as light blue triangles, the average final TRR stayed almost constant for the first 30 laser pulses then continuously decreased to the value obtained after

100 laser pulses at 0.975 Jcm^{-2} and 1.025 Jcm^{-2} . This was likely due to the melting of the Ge SRB.

No changes were observed at the melt threshold for GeSn 14% (green circles in **Figure VII.4 (c)**). The average final TRR signal after 100 laser pulses shifted to lower reflectivity intensities when the energy density increased, shown in **Figure VII.4 (c)**, most likely because of a surface roughness increase. The rapid change of final average TRR signal during the first few laser pulses could be explained by a rapid evolution of surface structures or Sn redistribution towards the surface. Around the full melt, shown in **Figure VII.4 (d)**, results were similar to that at lower Sn contents. The energy density might not have been perfectly tuned to the full melt because a constant plateau of the average final TRR value was recorded for the first 10 laser pulses. The TRR signal did change more continuously for more than 10 laser pulses, which might be a sign that it was not that far from the full melt ED, however.

VII.3 Multi Pulse NLA - Evolution of surface structure at the melt threshold

Previous studies on single pulse NLA of GeSn showed that Sn was distributed towards the surface and surface structures formed above the melt threshold. The latter became thinner, less continuous and denser at higher Sn contents. The influence of multiple laser pulses at the melt threshold energy density on various Sn content layers was imaged with AFM. Pictures are shown in **Figure VII.5**. When applying 10 laser pulses, surface structures seemed to contract and become more circular. A more detailed picture is shown in **Appendix B** for 3 and 5 laser pulses. It highlights the continuous contraction of ridges into rounder surface structures for a higher number of laser pulses.

For GeSn 10%, dense amounts of surface structures formed, while for 6% only a few surface structures remained when more laser pulses were applied. Meanwhile, the surface structure density seemed to stay constant for GeSn 14%. It might be that the surface was somehow richer in Sn for GeSn 10%. Therefore, larger surface structures formed that broke into a denser surface structure network compared to GeSn 6% and 14%. This was supported by the TRR map of GeSn 10% at the melt threshold, shown in **Figure VII.2 (b)**, which changed when more laser pulses were applied. For GeSn 6% and 14%, that did not occur. At some point, the size of melted areas and surface structures saturated and the TRR signal did not significantly change when more laser pulses were applied. After 100 laser pulses, large circular surface structures formed. They were uniformly distributed on the surface and did not vary much in size. There was not so much similarity anymore with surface structures after a single laser pulse. There was indeed a switch from rather continuous ridges after a single laser pulse to lines of circular surface structures after 100 laser pulses. Similar observations were made for GeSn 6% and 14%. Surface structures were randomly uniformly distributed, similar in size and not oriented in networks after 100 laser pulses compared to networks after single laser pulses.

Melt Threshold

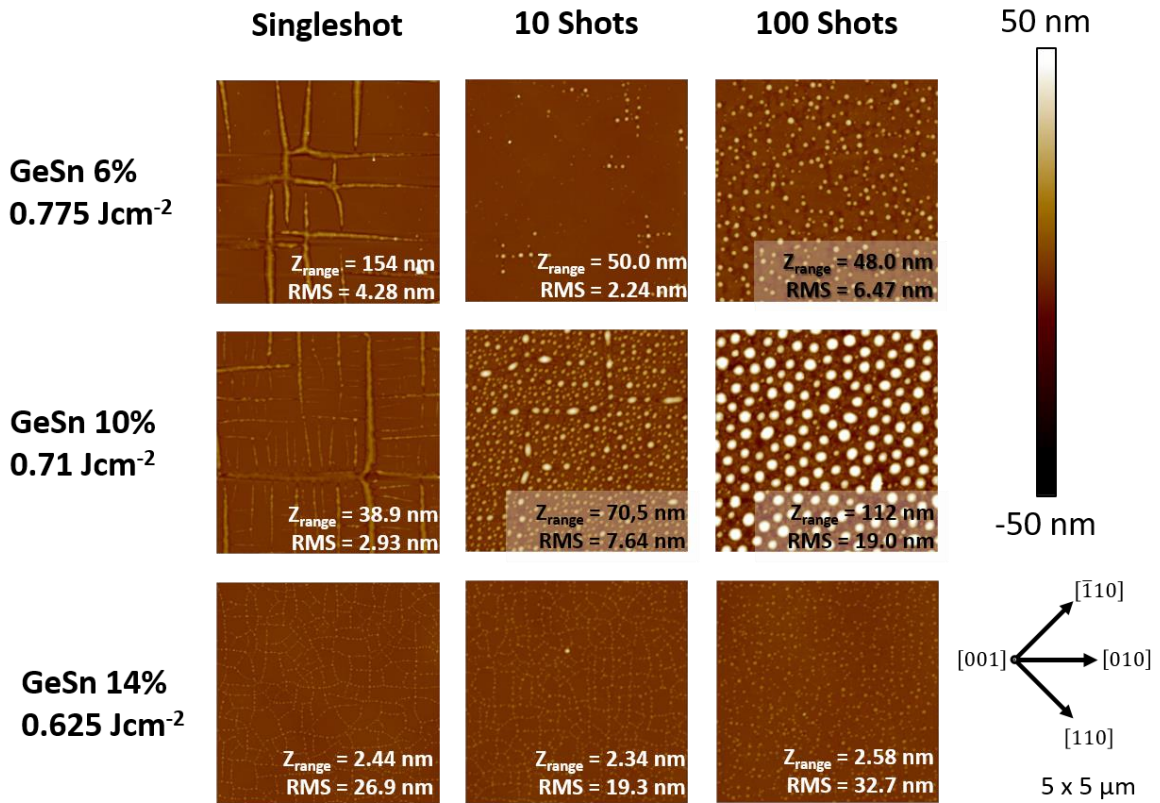


Figure VII.5: 5 μm x 5 μm AFM images of 36 to 41 nm thick pseudomorphic GeSn 6%, 10% and 14% (top to bottom) after annealing with various numbers of pulses up to 100 (left to right) at the melt threshold energy density. The z-scale was 50 nm for all shown images. The schematic on the bottom right shows the crystallographic directions.

For GeSn 14%, surface structures were already less continuous and more like “beads on a necklace” after a single laser pulse. As more laser pulses were applied, surface structures started to agglomerate at intersections, with the formation of larger surface structures.

After 100 laser pulses and for a Sn content of 6%, large, round surface structures formed. Along the directions where, after a single laser pulse, surface structures formed, some darker traces could also be observed. They were most likely the signature of the surface diffusion of Sn to form Sn-rich surface structures.

Utilizing the Particle Analysis feature of the Bruker analyzing software NanoScope, we performed a quantitative evaluation of the impact of the as-grown Sn content on the metrics of surface structures at the melt threshold. Results are shown in **Figure VII.6**. To obtain comparable datasets, a threshold at 2 nm above the mean plane of the various surfaces was used and all recorded AFM images were flattened by a 6th order fit to ensure that long range undulations (because of the surface cross-hatch of the Ge SRBs underneath) were not counted as surface structures.

The surface structure density increased from around 15% to around 60% when the as-grown Sn content increased, shown in **Figure VII.6 (a)**, most likely because the surface

structures were Sn rich. For GeSn 6% (blue triangles), the surface structure density increased slightly when applying 100 laser pulses because the large surface structures formed after a single laser pulse broke into smaller surface structures. More surface structures formed as more laser pulses were used.

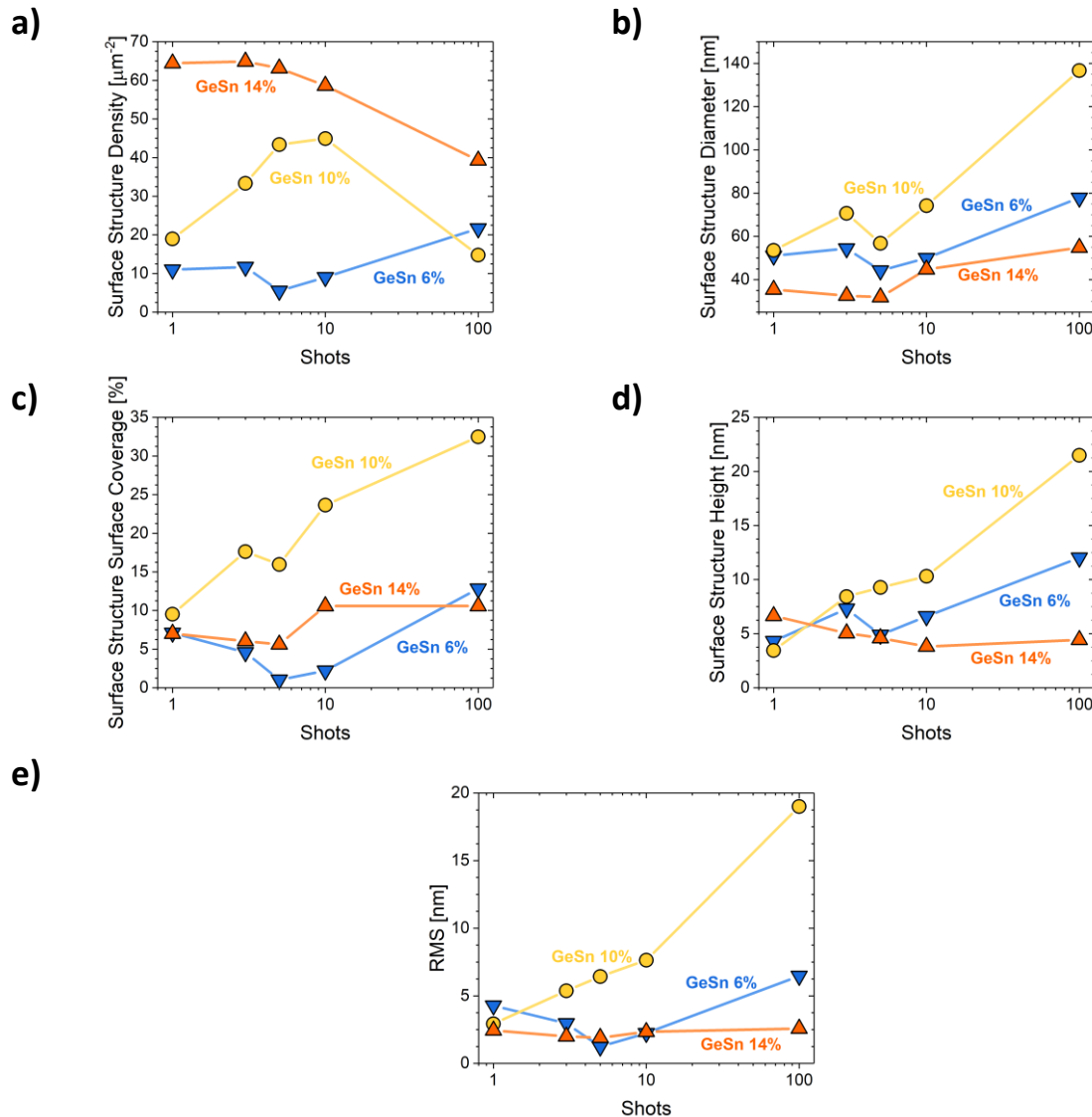


Figure VII.6: Comparison of surface structure density (a), diameter (b), coverage (c), height (d) and RMS roughness (e) as functions of how many laser pulses were shot at the melt threshold on GeSn 6% (blue squares), GeSn 10% (yellow circles) and GeSn 14% (orange triangles). Densities, diameters, heights and surface coverages were extracted by assuming a threshold of 2 nm above the surface mean plane.

The surface structure density, shown in **Figure VII.6 (a)**, increased significantly for GeSn 10% (yellow circles) when applying up to 10 laser pulses because larger surface structures broke into smaller surface structures. For 100 laser pulses, it then decreased because surface structures merged and formed larger surface structures once again. For GeSn 14% (orange triangles), surface structures merged when applying more and more laser pulses. The surface

structure density, therefore, decreased when shooting more laser pulses. Meanwhile, it was rather steady for GeSn 6%. Only for 100 laser pulses more surface structures formed.

There was an increase of surface structure diameter with the number of laser pulses for GeSn 6% and 14%, shown in **Figure VII.6 (b)**. It might be that a critical amount of Sn on the surface was needed to form larger surface structures. For GeSn 10%, the surface structure diameter increased significantly when applying 100 laser pulses. A high concentration of Sn on the surface might have resulted in the formation of larger surface structures.

The surface coverage did not change much when applying more laser pulses for GeSn 6% and 14%, shown in **Figure VII.6 (c)**. It continuously increased for GeSn 10% when more laser pulses were applied. For GeSn 10%, the surface might be richer in Sn. Larger surface structures, therefore, formed and merged, covering more of the surface.

For GeSn 6%, shown in **Figure VII.6 (d)**, the surface structure height slightly increased when applying more laser pulses. It was most likely due to the merging of surface structures. The surface structure height increased more drastically for GeSn 10% because of the larger surface coverage. When applying more laser pulses, the surface structure height decreased slightly for GeSn 14%. This and the almost constant surface coverage, shown in **Figure VII.6 (c)**, might be an indication that some of the surface structures evaporated when using more laser pulses.

The RMS roughness, shown in **Figure VII.6 (e)**, did not increase significantly for GeSn 6% and 14% because surface structures were not sufficiently large or dense enough to form large surface structures by merging. For GeSn 10%, on the other hand, surface structures merged and formed larger surface structures resulting in an increase of the surface roughness.

Figure VII.4 showed that the final reflectivity was highly depended on the applied energy density. In a previous study [2], it was found that the surface roughness had a significant impact on the final reflectivity.

VII.4 Multi Pulse NLA - Evolution of surface morphology at the full melt threshold

AFM images of the surface of GeSn 6% at various EDs now close to the full melt energy density are shown in **Figure VII.7**. When applying laser pulses at 1.00 Jcm^{-2} , shown in the first line of **Figure VII.7**, small surface structures that were randomly distributed on the surface formed (**top left**) formed. When increasing the amount of laser pulses, surface structures merged, forming larger surface structures, as shown for 10 laser pulses (**top middle**). After 100 laser pulses (**top right**), larger surface structures formed a discontinuous surface with RMS and Z_{range} values of 53 nm and 287 nm, respectively.

At 1.025 Jcm^{-2} , shown in the middle line of **Figure VII.7**, surface structures did not merge or merged much more slowly. Only when 100 laser pulses were applied (**middle right**), did some of the surface structures merge. Surface structures were a lot smaller than at 1.00 Jcm^{-2} (**top right**). Accordingly, the RMS roughness and Z_{range} values were smaller at 10 nm and 80 nm, respectively. We must have, at that specific ED, melted close to the entire GeSn layer on top of the Ge SRB. Meanwhile, the Ge SRB did not melt because of its higher melting temperature. The liquid / solid interface must have been close to the GeSn / Ge SRB interface, which was smooth, resulting in a comparatively smooth surface on top. As more laser pulses

were shot, likely some of the Ge SRB melted, resulting in a rougher liquid / solid interface and the formation of larger surface structures.

The behavior at 1.05 Jcm^{-2} , bottom line in **Figure VII.7**, was similar to that at 1.00 Jcm^{-2} . Small surface structures formed after a single laser pulse (**bottom left**) that merged and formed larger surface structures when more laser pulses were applied (**bottom middle and right**). The RMS and Z_{range} values were 53 nm and 253 nm, respectively, after 100 laser pulses at 1.05 Jcm^{-2} . This highlighted that 1.025 Jcm^{-2} was a specific energy density. When ED was lower or above that value, the surface evolved significantly differently. This supported our hypothesis that, at 1.025 Jcm^{-2} , a smooth liquid / solid interface was obtained by only melting the GeSn layer on top, resulting in the formation of a smoother surface.

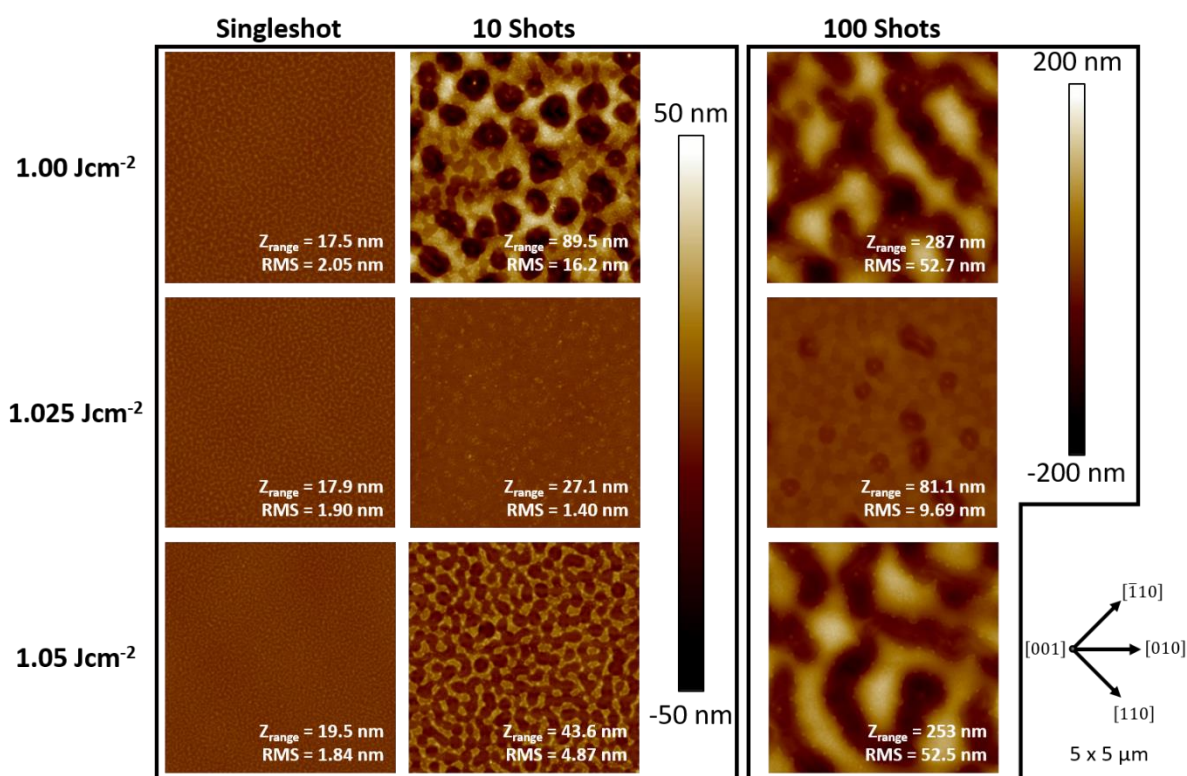


Figure VII.7: $5 \mu\text{m} \times 5 \mu\text{m}$ AFM images of a 41 nm thick pseudomorphic GeSn 6% layer on a Ge SRB after NLA with energy densities around the full melt threshold (increasing from top to bottom) and up to 100 laser pulses (left to right). The z-scale was 50 nm for all images up to 10 laser pulses and 200 nm for 100 laser pulses. The schematic on the bottom right shows the crystallographic directions.

When increasing the Sn content to 10% a similar behavior than at 6% was recorded close to the full melt energy, as shown in **Figure VII.8**. At $\text{ED} = 0.975 \text{ Jcm}^{-2}$, surface structures merged forming larger surface structures. The RMS and Z_{range} values after 100 laser pulses were 52 nm and 382 nm, respectively.

At $\text{ED} = 1.00 \text{ Jcm}^{-2}$, shown in **Figure VII.8**, surface structures merged when more laser pulses were used. Meanwhile, the surface layer stayed continuous, without significant holes

formed, up to 10 laser pulses (**middle left** and **middle middle**). For more than 10 pulses (**middle right**) the behavior was similar to that at 0.975 Jcm^{-2} . Large surface structures were formed after merging, resulting in a surface with significant height differences. The RMS and Z_{range} values were 53 nm and 274 nm, respectively, close to those at 0.975 Jcm^{-2} . The behavior at 1.025 Jcm^{-2} (**bottom line**) was similar to 0.975 Jcm^{-2} . Surface structures merged forming larger surface structures when more laser pulses were used. It was likely that the energy density was not as well adjusted to the full melt as it was for GeSn 6%. When applying more laser pulses some of the Ge SRB melted, resulting in some surface roughening.

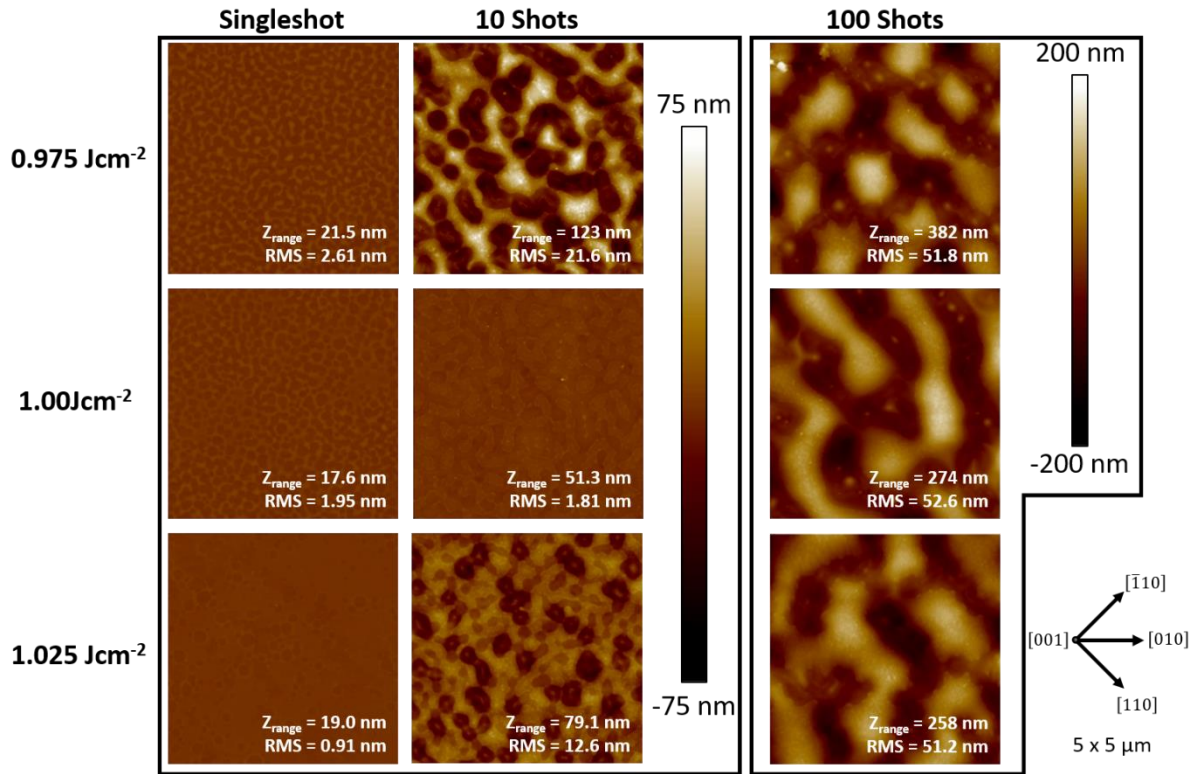


Figure VII.8: $5 \mu\text{m} \times 5 \mu\text{m}$ AFM images of a 39 nm thick pseudomorphic GeSn 10% layer on a Ge SRB after NLA with energy densities around the full melt threshold (increasing from top to bottom) and up to 100 laser pulses (left to right). The z-scale was 75 nm for all images up to 10 laser pulses and 200 nm for 100 laser pulses. The schematic on the bottom right shows the crystallographic directions.

A broader range of smooth surfaces was previously found for GeSn 14% close to the full melt threshold. [2] A wide range of energy densities were, therefore, investigated for GeSn 14%. AFM images are shown in **Figure VII.9**. At $\text{ED} = 0.90 \text{ Jcm}^{-2}$, the surface was smooth after a single laser pulse (top left). When 10 pulses were used (**top middle**), the small undulations on the surface after a single pulse merged, forming larger elongated surface structures. The RMS roughness and Z_{range} values increased significantly from 1.6 nm and 16 nm up to 26.0 nm and from 16 nm to 169 nm, respectively. The surface got even rougher when 100 pulses were applied (**top right**). The elongated surface structures after 10 laser pulses kept

on merging when more pulses were applied (100 pulses, **top right**). The resulting surface structures were more rectangular and less elongated.

At $ED = 1.00 \text{ Jcm}^{-2}$, shown in **Figure VII.9 (middle line)**, a smooth surface with only minor roughness deviations was obtained after a single pulse (**middle left**). The RMS roughness and Z_{range} were 0.83 nm and 34 nm, respectively. The surface stayed smooth after 10 pulses (**middle middle**) with RMS roughness and Z_{range} of 2.25 nm and 43 nm, respectively. There was a circular surface structure in the top right corner. This was likely due to some contamination or defects present prior to laser annealing. After 100 laser pulses (**middle right**), large surface structures formed with RMS roughness and Z_{range} of 55 nm and 282 nm, respectively, close to that at slightly lower or higher energy densities after 100 pulses. This was most likely due to the melting of the Ge SRB.

Surface undulations were present after a single pulse with 1.05 Jcm^{-2} (**Figure VII.9 bottom left**). Undulations merged after 10 laser pulses (**bottom middle**), forming larger surface structures and a less continuous surface with some significant height deviations. Large connected surface structures were present after 100 laser pulses (**bottom right**). The RMS and Z_{range} were 58 nm and 300 nm, respectively.

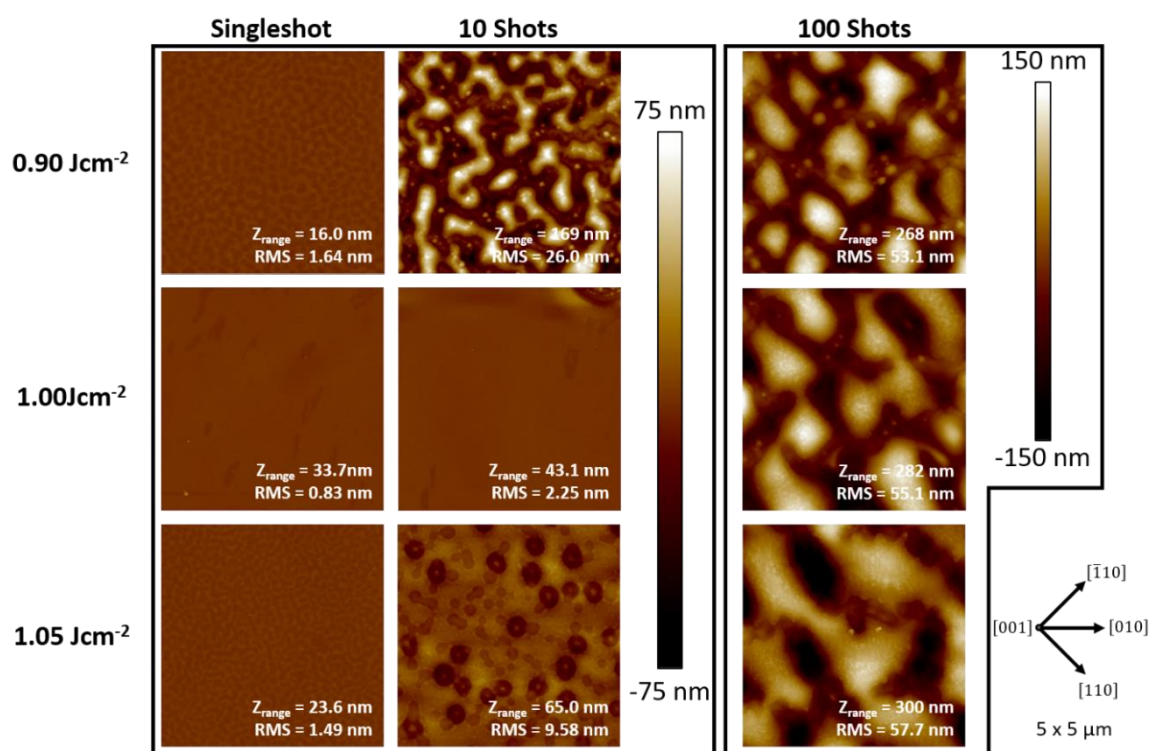


Figure VII.9: $5 \mu\text{m} \times 5 \mu\text{m}$ AFM images of a 36 nm thick pseudomorphic GeSn 14% layer on a Ge SRB after NLA with energy densities around the full melt threshold (increasing from top to bottom) and up to 100 laser pulses (left to right). The z-scale was 75 nm for all shown images up to 10 laser pulses and 150 nm for 100 laser pulses. The schematic on the bottom right shows the crystallographic directions.

The AFM images recorded for the different Sn contents were in line with the final TRR values shown in **Figure VII.4**. AFM images highlighted that, indeed, the formation of big

surface structures resulted in a TRR drop. At energy densities close to the full melt, the TRR did drop more slowly because smaller surface structures were formed when the Ge SRB was not melted and the liquid / solid interface was smooth.

To better understand the impact of the energy densities on the surface structures' dimensions when applying various amounts of laser pulses, a quantitative analysis of the surface structures' dimensions for GeSn 14% is shown in **Figure VII.10**. The same procedure as in **Figure VII.7** was used to extract values from the images.

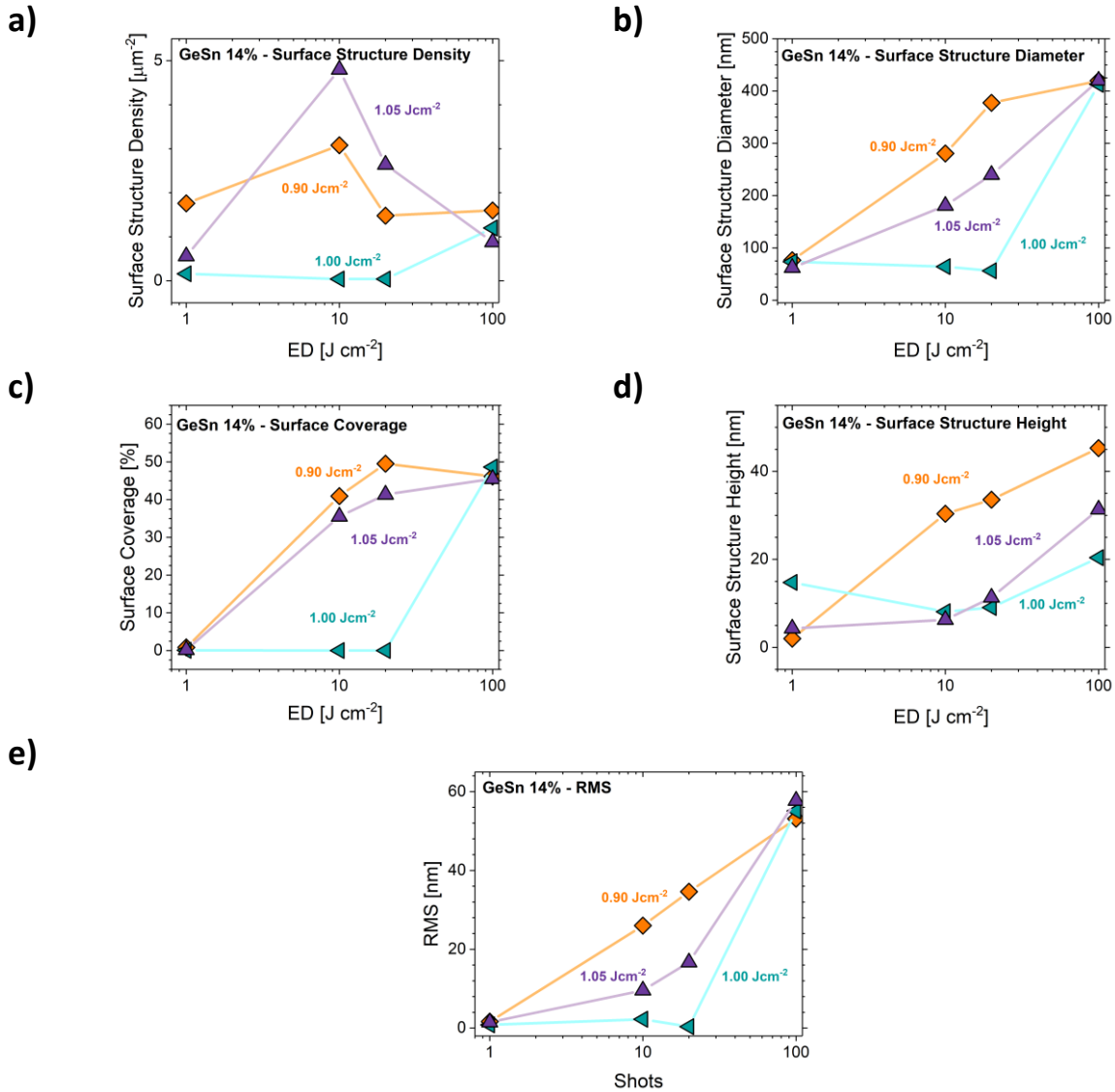


Figure VII.10: Comparison of surface structure density (a), diameter (b), coverage (c), height (d) and RMS roughness (e) for GeSn 14% as functions of how many laser pulses were applied at $\text{ED} = 0.90 \text{ Jcm}^{-2}$ (orange diamonds), 1.00 Jcm^{-2} (blue triangles) and 1.05 Jcm^{-2} (purple triangles). Densities, diameters, heights and surface coverages were extracted by assuming a threshold of 2 nm above the surface mean plane.

When increasing the amount of applied laser pulses up to 10 pulses, the surface structure density, shown in **Figure VII.10 (c)**, increased for laser pulses with EDs of 0.90 Jcm^{-2} (orange diamonds) and 1.05 Jcm^{-2} (purple triangles). It might be that a rough liquid / solid interface was formed after a single laser pulse at these energy densities, which became rougher when more laser pulses were applied, leading to the formation of more surface structures. The surface structure density for these energy densities decreased when up to 100 laser pulses were used because surface structures merged. At an ED of 1.00 Jcm^{-2} , on the other hand, the surface structure density stayed constant when applying up to 20 laser pulses. It only increased for 100 laser pulses. The melting of the Ge SRB might be at the origin of a rougher liquid / solid interface and, therefore, the formation of surface structures.

The surface structures diameter (**Figure VII.10 (b)**) and surface coverage (**Figure VII.10 (c)**) increased and then saturated when applying multiple laser pulses at 0.90 Jcm^{-2} and 1.05 Jcm^{-2} . At $\text{ED} = 1.00 \text{ Jcm}^{-2}$, when applying multiple laser pulses, the surface structure diameter and coverage only increased for 100 pulses. This behavior was likely because of the melting of the Ge SRB.

Applying more laser pulses at $\text{ED} = 0.90 \text{ Jcm}^{-2}$ resulted in an increase of the surface structure height, shown in **Figure VII.10 (d)**, because surface structures merged. It stayed constant at $\text{ED} = 1.05 \text{ Jcm}^{-2}$ or slightly dropped at $\text{ED} = 1.00 \text{ Jcm}^{-2}$. Because the liquid / solid interface was in the GeSn layer for 0.90 Jcm^{-2} , at the GeSn / Ge SRB interface for 1.00 Jcm^{-2} and in the Ge SRB for 1.05 Jcm^{-2} , the surface structure height might have evolved differently. When applying 100 pulses the surface structure height increased with 1.00 Jcm^{-2} and 1.05 Jcm^{-2} , most likely because a rough liquid / solid interface was formed.

The RMS value, shown in **Figure 10 (e)**, stayed constant for up to 20 laser pulses with 1.00 Jcm^{-2} . Meanwhile, it continuously increased for laser pulses with $\text{ED} = 0.90 \text{ Jcm}^{-2}$ and 1.05 Jcm^{-2} , possibly because of the liquid / solid interface roughness. The RMS increased for all energy densities when 100 laser pulses were applied. This might be because of the presence of a rough liquid / solid interface even for $\text{ED} = 1.00 \text{ Jcm}^{-2}$.

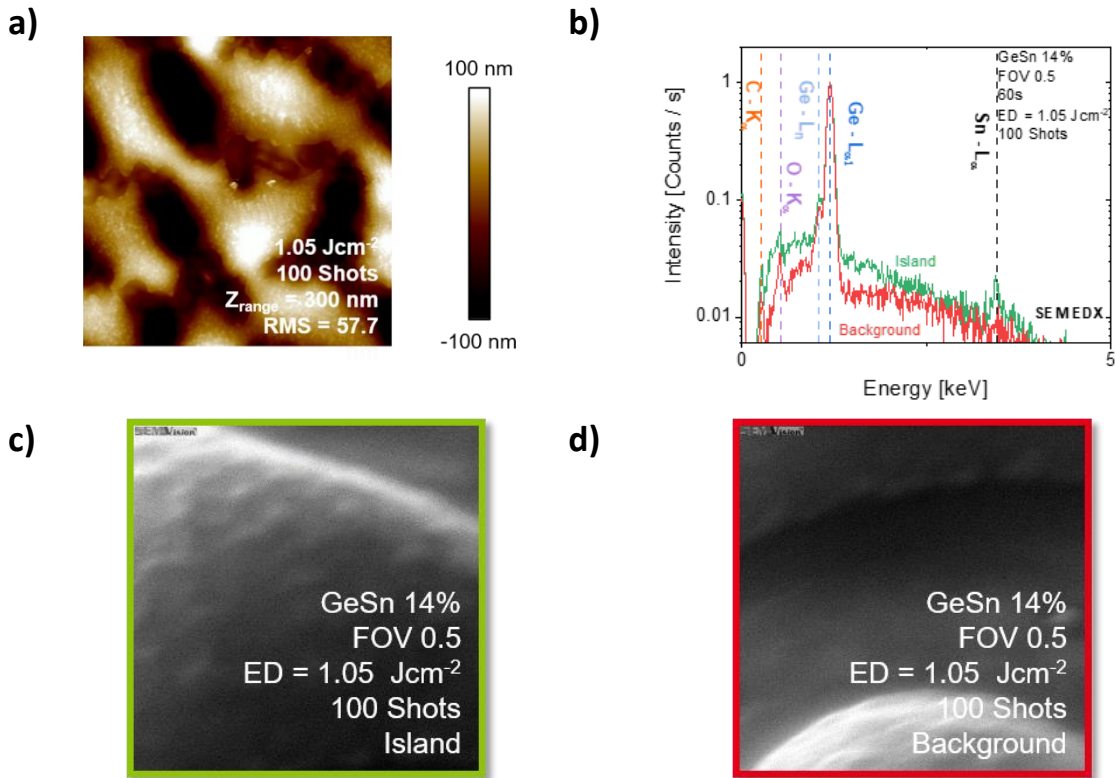


Figure VII.11: (a) 5 $\mu\text{m} \times 5 \mu\text{m}$ AFM images of 36 nm thick pseudomorphic GeSn 14% after annealing with 100 laser pulses at $\text{ED} = 1.05 \text{ Jcm}^{-2}$. The z-scale was 100 nm. (b) EDX profiles of an area covered by surface structures, shown in (c) in green, and of an area not covered by surface structures, shown in (d) in red.

Energy Dispersive X-ray Spectroscopy (EDX) was performed on a GeSn 14% layer annealed at $\text{ED} = 1.05 \text{ Jcm}^{-2}$ with 100 laser pulses in a Secondary Electron Microscope (SEM). The aim was to determine the composition of surface structures. The corresponding AFM image is shown in **Figure VII.11 (a)**. EDX profiles are shown in **Figure VII.11 (b)**. The green curve corresponds to an area mostly covered by surface structures, as shown in **Figure VII.11 (c)**. Meanwhile, the red curve corresponds to an area mostly free of surface structures, shown in **Figure VII.11 (d)**. EDX profiles exhibited the same kind of Ge peaks. O and C peaks were more pronounced in the area covered by surface structures. This might be a sign that surface structures might be contaminated by O and/or C. The Sn peak was almost absent from spectra on zones not covered by surface structures. Meanwhile, there was a defined peak for the area covered with surface structures, outlining that it was most likely Sn rich.

VII.5 Multi Pulse NLA - Evolution of crystalline structure at the melt threshold

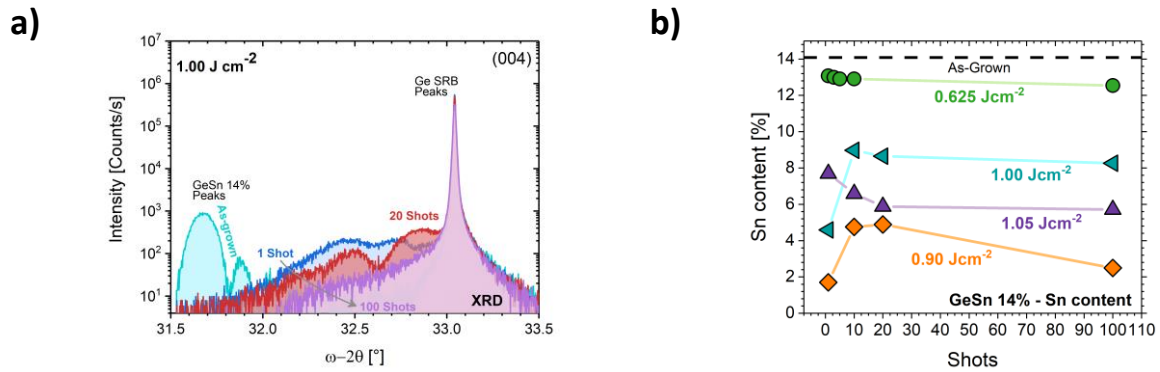


Figure VII.12: (a) $\omega-2\theta$ scans around the (0 0 4) XRD order for a 36 nm thick GeSn 14% layer on a Ge SRB after laser annealing at 1.00 Jcm^{-2} with various laser pulses (1 (blue), 20 (red) and 100 (purple) laser pulses). (b) Sn content extracted from $\omega-2\theta$ scans after laser annealing at (a) 0.625 Jcm^{-2} (green circles), 0.90 Jcm^{-2} (orange diamonds), 1.00 Jcm^{-2} (blue triangles) and 1.05 Jcm^{-2} (purple triangles).

Applying multiple laser pulses led to the formation of large surface structures and also had an impact on the crystalline structure. **Figure VII.12 (a)** shows $\omega-2\theta$ scans around the (0 0 4) XRD order for a 36 nm thick GeSn 14% layer annealed with multiple laser pulses at an energy density of 1.00 Jcm^{-2} . The as-grown layer exhibited a well-defined GeSn peak with thickness fringes. A Sn content of 14.08% and a thickness of 36.3 nm were extracted. A more detailed discussion of as-grown GeSn XRD profiles can be found in [7].

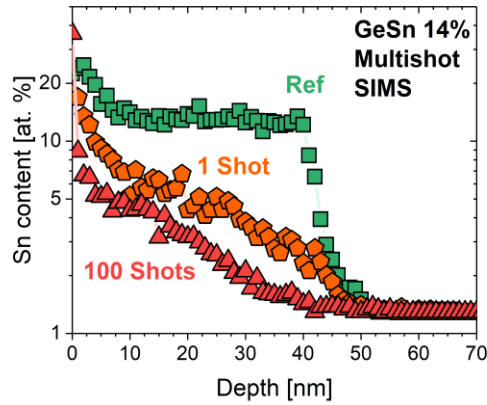
When a single laser pulse with $\text{ED} = 1.00 \text{ Jcm}^{-2}$ was used, the GeSn XRD peak shifted towards the Ge SRB's peak. This was likely due to Sn redistribution. The Sn content seemed not to be uniform because multiple maxima could be found in the broad XRD peak. After 20 pulses, the different maxima shaped into more defined peaks. It might be that different layers with different and discrete Sn contents were formed. After 100 pulses, no defined peaks nor any maxima were recorded. Moreover, the GeSn peak definitely shifted towards the Ge SRB XRD peak and lost intensity. Sn most likely moved towards the surface, with only a low Sn content GeSn layer with some grading towards the surface remaining beneath.

The Sn content after laser annealing at 0.625 Jcm^{-2} (melt threshold, green circles), shown in **Figure VII.12 (b)**, was lower than the as-grown Sn content around 13.1%. It decreased slightly to 12.5% after 100 laser pulses. This might be a sign of Sn evaporating when using more laser pulses. [8] The fact that the Sn content at 0.625 Jcm^{-2} was lower than the as-grown Sn content might outline that even the formation of small surface structures on the surface had a significant impact on the Sn content.

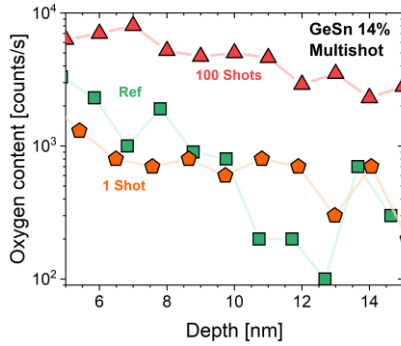
At 0.90 Jcm^{-2} (orange diamonds), the Sn content, 1.7%, was almost at the solid solubility limit of Sn in Ge, i.e. 1%. [1] It increased to 4.9% when 20 laser pulses were applied. After 100 laser pulses, the Sn content decreased to 2.5%. This was likely due to Sn redistribution.

VII.6 Multi Pulse NLA – Sn redistribution

a)



b)



c)

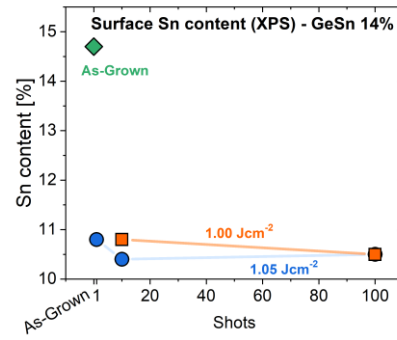


Figure VII.13: SIMS depth profiles of Sn (a) and O (b) in a 36 nm GeSn 14% layer on a Ge SRB for various amounts of laser pulses at $ED = 1.00 \text{ Jcm}^{-2}$ and (c) surface Sn content probed by XPS: as-grown (green diamonds), $ED = 1.00 \text{ Jcm}^{-2}$ (orange squares) and 1.05 Jcm^{-2} (blue circles).

To investigate the redistribution of Sn and the incorporation of O into the laser annealed layers, SIMS measurements were performed on GeSn 14% for $ED = 1.00 \text{ Jcm}^{-2}$. Profiles are shown in **Figure VII.13 (a)**. SIMS was limited by measurement artifacts in the first few nanometers profiled. The as-grown reference sample (green squares) exhibited a box-shaped Sn profile. Sn was redistributed towards the surface after a single pulse (orange pentagons). The Sn content increased from around 3% at the bottom to 10% close to the surface of the layer. Not all of the GeSn layer had likely melted. There was indeed a definite drop of the Sn content at the GeSn/Ge SRB interface. There was no such drop after 100 laser pulses (red triangles), outlining that the entire GeSn layer and possibly a bit of the Ge SRB underneath were melted. This supported the hypothesis that melting the Ge SRB led to the formation of surface structures. The Sn content increased from around 1.5% at the GeSn / Ge interface to around 5% close to the surface. The low Sn content might be because surface structures merged, creating areas with low and high Sn contents. The SIMS profile was likely taken in a low Sn content area.

SIMS profiles of the O incorporation, shown in **Figure VII.13 (b)**, outlined that the O concentration after a single laser pulse (orange pentagons) was the same than in the as-grown

layer (green squares). After 100 pulses (red triangles), the O concentration in the first 5 to 15 nm was significantly higher as outlined by the SIMS profile. The repeated melting of the layer over a long time span likely led to some O incorporation.

The Sn content assessments by SIMS were completed by XPS measurements, shown in **Figure VII.13 (c)**. The as-grown layer has a surface Sn content of around 14.6%, in line with XRD data. The surface Sn content dropped to around 11% for a single laser pulse and saturated at around 10.5% for 10 and 100 laser pulses. For 100 pulses, a Sn rich area with more surface structures was likely investigated by XPS, while SIMS investigated an area with less Sn-rich surface structures.

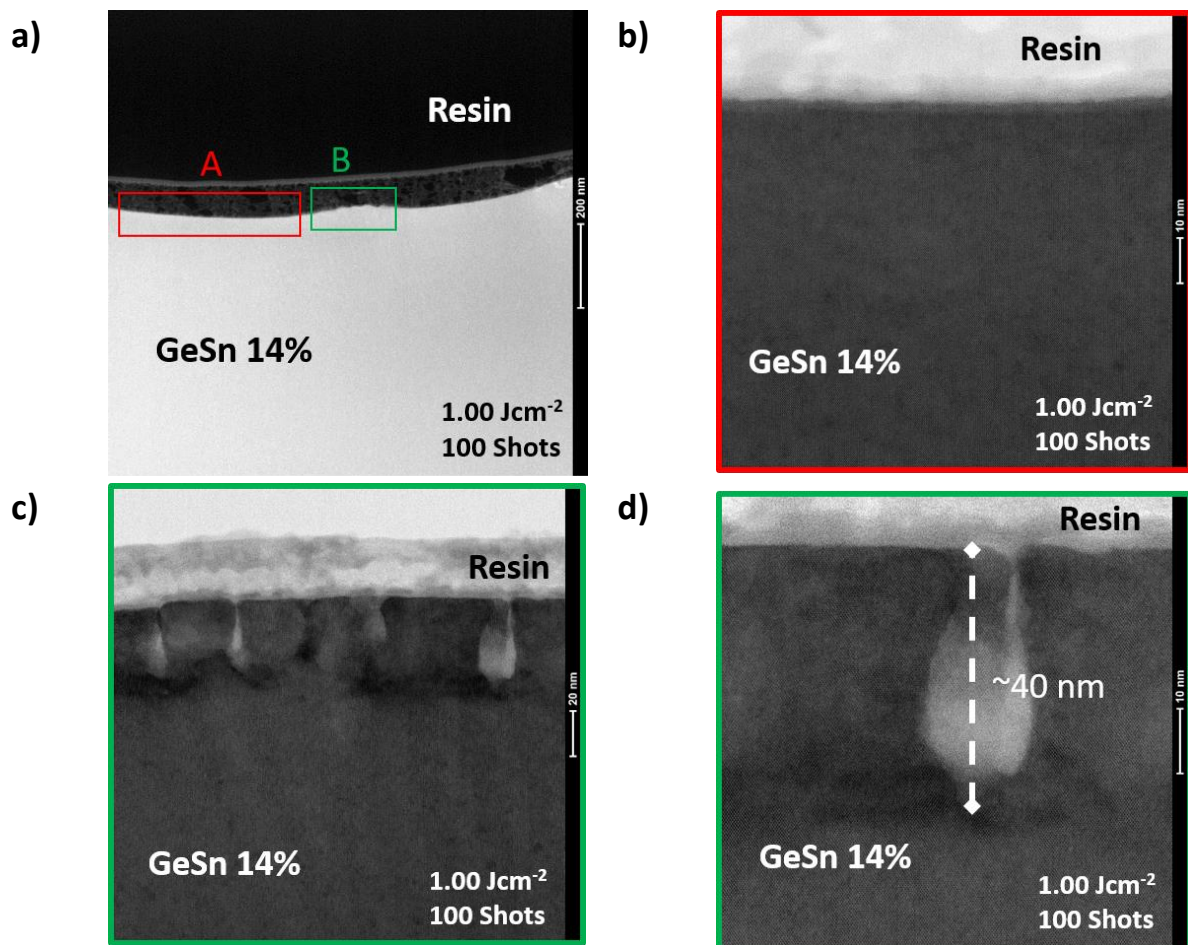


Figure VII.14: Cross-sectional TEM images of a 36 nm thick GeSn 14% layer on a Ge SRB laser annealed 100 times with $ED = 1.00 \text{ Jcm}^{-2}$: (a) overview, (b) valley region, (c) hill region and (d) zoom on vertical structures (hill region).

The redistribution of Sn and the formation of large surface structures should have a significant impact on the crystalline structure. Bright Field Transmission Electron Microscope (BF-TEM) images are shown in **Figure VII.14**. Nanosecond laser annealing with 100 pulses at $ED = 1.00 \text{ Jcm}^{-2}$ resulted in the formation of a rough surface, shown in **Figure VII.14 (a)**. Valleys and hills formed due to the redistribution of material and the merging of surface structures. A closer look at the valley region is given in **Figure VII.14 (b)**. The surface was

rather smooth in this region. Moreover, there was no significant contrast difference, making the determination of the GeSn / Ge interface difficult. This was either due to a low Sn content in the valley or the lack thereof of a GeSn layer anymore in this region.

Vertical structures with an oval root formed near the surface in the hill region, shown in **Figure VII.14 (c)**. The vertical structures were brighter in contrast. It might be that they were Sn-rich. Below the root of the vertical structures, a layer with darker contrast was observed. This was either because the layer was more defective in that region or the Sn concentration was lower.

A closer look at the vertical structure is provided in **Figure VII.14 (d)**. Vertical structures were roughly 50 nm long, i.e. more than the layer thickness of 36 nm. This outlined that significant amounts of material were redistributed and accumulated in the hill regions. No clear conclusion on how good the crystalline quality of the vertical structures was could be drawn, however. Indeed, as seen in the AFM image (**Figure VII.9 middle right**), vertical structures corresponded to smaller surface structures all over larger surface structures (hill regions in TEM). Due to the small size, there might be layers with a good crystalline structure surrounding the vertical structure. The unambiguous determination of the crystalline quality of the vertical structures was, therefore, difficult.

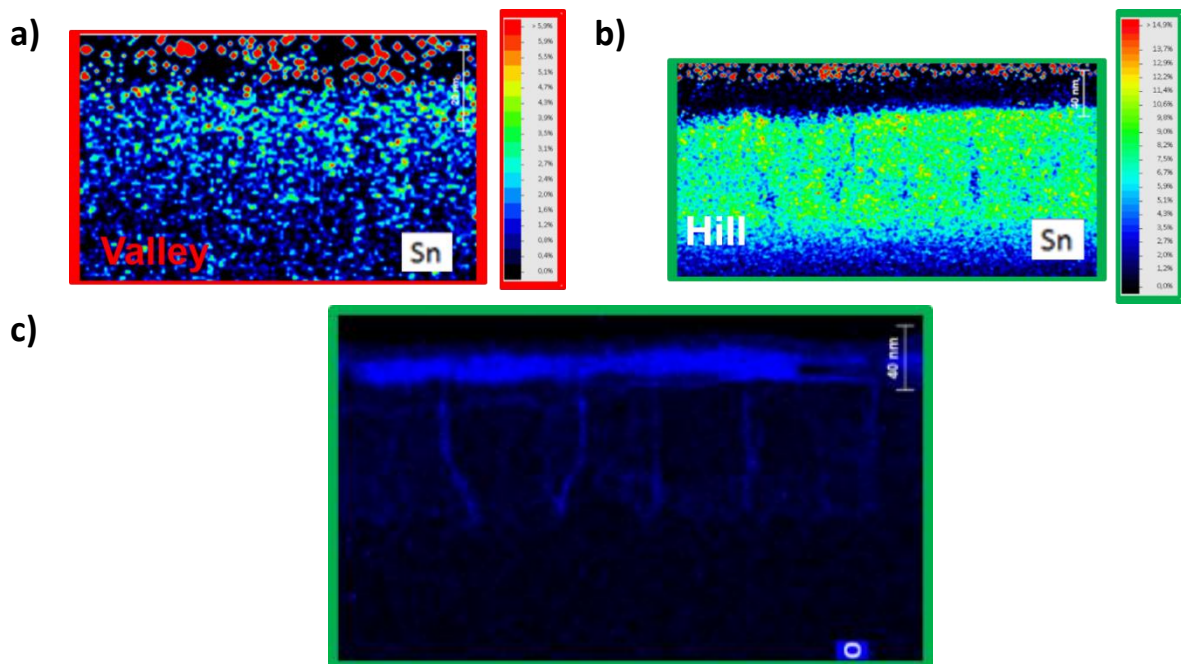


Figure VII.15: TEM EDX maps of a 36 nm thick GeSn 14% layer on a Ge SRB after laser annealing for 100 times at $ED = 1.00 \text{ Jcm}^{-2}$: (a) Sn map of the valley region, (b) Sn and (c) O map of the hill region.

To better understand if the formation of hills and valleys led to some redistribution of Sn, Energy Dispersive X-Ray Spectroscopy (EDX) measurements of the TEM cross section were performed. Maps are shown in **Figure VII.15**. The EDX profile of the valley region is shown in **Figure VII.15 (a)**. It shows that the Sn content increases from around 1% (the solid solubility

limit) to around 4% at the surface in roughly 40 nm. This was a significant reduction compared to the as-grown Sn content of 14.1%. This highlights that Sn was redistributed to the hill region.

The hill region, shown in **Figure VII.15 (b)**, was a lot richer in Sn. Moreover, the Sn content was homogeneously distributed over the hill region and was around 10%. The Sn rich layer was close to 80 nm thick, outlining the significant redistribution of material. Below the homogeneously Sn rich layer, the Sn content reduced gradually until it was too small for detection.

The only exception to the homogenous Sn distribution were the vertical structures. These structures were poorer in Sn, with a concentration of around 4 to 5%. **Figure VII.15 (c)** shows the EDX oxygen profile. It outlines that the vertical structures were, indeed, oxygen rich and that there was a highly oxidized surface layer present. It confirms SIMS findings, shown in **Figure VII.13 (b)**, with some oxygen incorporation for 100 laser pulses at 1.00 Jcm^{-2} . Previous NLA studies indeed showed some incorporation of oxygen during experiments. [9]–[11] In this study, a nitrogen atmosphere was used during the laser annealing in order to minimize oxygen incorporation, but it was not completely prevented, as outlined by current findings.

VII.7 Conclusions

In this study, our understanding on the nanosecond laser annealing of GeSn was improved by performing multishot experiments. Pseudomorphic GeSn layers with Sn contents of 6%, 10% and 14% on Ge thick Strain-Relaxed Buffers were laser annealed with up to 100 laser pulses applied to the same position. Time Resolved Reflectivity (TRR) profiles recorded in-situ during annealing changed depending on the energy density and number of laser pulses used. When applying multiple laser pulses, large surface structures were formed and Sn was redistributed towards the surface. At the full melt threshold, i.e. the energy density at which the entire GeSn layer melted without melting the Ge SRB, the surface stayed smooth and the TRR signal stayed mostly constant. This was because of the difference in melt temperature of Ge and GeSn. A smooth liquid / solid was formed, reducing the amount of surface structures. SIMS and TEM revealed that oxygen was incorporated near the surface in vertical structures in GeSn 14% after 100 laser pulses at $ED = 1.00 \text{ Jcm}^{-2}$. Overall, the experiments enabled us to gain a better understanding of the interaction of the laser light with GeSn. The study revealed the importance of the liquid / solid interface roughness for the formation of surface structures and the information in-situ TRR gave on how the material evolved during multiple laser pulses. This might be useful to optimize future NLA experiments. Concerning GeSn devices, the results showed that multiple laser pulses with high energy density did not improve material quality. To benefit from higher device performances, we should perform solid phase epitaxial regrowth experiments at low energy densities.

References

- [1] F. A. Trumbore, “Solid Solubilities and Electrical Properties of Tin in Germanium Single Crystals,” *J. Electrochem. Soc.*, vol. 103, no. 11, p. 597, 1956, doi: 10.1149/1.2430167.
- [2] M. Frauenrath *et al.*, “Nanosecond Laser Annealing of pseudomorphic GeSn layers – Impact of Sn content,” *to be published*.
- [3] L. Dagault *et al.*, “Impact of UV Nanosecond Laser Annealing on Composition and Strain of Undoped Si_{0.8}Ge_{0.2} Epitaxial Layers,” *ECS J. Solid State Sci. Technol.*, vol. 8, no. 3, pp. P202–P208, 2019, doi: 10.1149/2.0191903jss.
- [4] R. W. Olesinski and G. J. Abbaschian, “The Ge–Sn (Germanium–Tin) system,” *Bull. Alloy Phase Diagr.*, vol. 5, no. 3, pp. 265–271, Jun. 1984, doi: 10.1007/BF02868550.
- [5] L. Dagault *et al.*, “Investigation of recrystallization and stress relaxation in nanosecond laser annealed Si_{1-x}Gex/Si epilayers,” *Appl. Surf. Sci.*, vol. 527, p. 146752, Oct. 2020, doi: 10.1016/j.apsusc.2020.146752.
- [6] G. Calogero *et al.*, “Multiscale modeling of ultrafast melting phenomena,” *Npj Comput. Mater.*, vol. 8, no. 1, p. 36, Dec. 2022, doi: 10.1038/s41524-022-00720-y.
- [7] M. Frauenrath, J.-M. Hartmann, and E. Nolot, “Boron and Phosphorous Doping of GeSn for Photodetectors and Light Emitting Diodes,” *ECS Trans.*, vol. 98, no. 5, pp. 325–338, Sep. 2020, doi: 10.1149/09805.0325ecst.
- [8] Y.-R. Luo, *Handbook of Bond Dissociation Energies in Organic Compounds*, 0 ed. CRC Press, 2002. doi: 10.1201/9781420039863.
- [9] G. Impellizzeri *et al.*, “Role of oxygen on the electrical activation of B in Ge by excimer laser annealing: Role of oxygen on the electrical activation of B in Ge,” *Phys. Status Solidi A*, vol. 211, no. 1, pp. 122–125, Jan. 2014, doi: 10.1002/pssa.201300308.
- [10] R. Milazzo *et al.*, “Oxygen behavior in germanium during melting laser thermal annealing,” *Mater. Sci. Semicond. Process.*, vol. 42, pp. 196–199, Feb. 2016, doi: 10.1016/j.mssp.2015.07.066.
- [11] R. Milazzo, M. Linser, D. Scarpa, A. Carnera, A. Andrighetto, and E. Napolitani, “Indiffusion of oxygen in germanium induced by pulsed laser melting,” *Mater. Sci. Semicond. Process.*, vol. 88, pp. 93–96, Dec. 2018, doi: 10.1016/j.mssp.2018.07.036.

**Chapter VIII : Nanosecond Laser
Annealing of Phosphorus Implanted
GeSn**

Chapter VIII: Nanosecond Laser Annealing on phosphorous implanted GeSn

Chapter VIII: Nanosecond Laser Annealing of Phosphorus Implanted GeSn **156**

VIII.1 Introduction.....	156
VIII.2 Time Resolved Reflectivity evolution.....	156
VIII.3 P implanted GeSn NLA – Surface Morphology Evolution	157
VIII.4 P implanted GeSn NLA – Crystalline Structure	159
VIII.5 P implanted GeSn NLA – Tin and phosphorus redistribution	162
VIII.6 P implanted GeSn NLA – Solid Phase Epitaxial Regrowth	164
VIII.7 Conclusions.....	167

Chapter VIII: Nanosecond Laser Annealing of Phosphorus Implanted GeSn**VIII.1** Introduction

In the previous chapters, the mechanisms governing the nanosecond annealing of intrinsic, pseudomorphic GeSn layers were investigated. However, high dopant active concentrations are required in order to reduce the contact resistance and improve device performances. In this last chapter, Nanosecond Laser Annealing (NLA) is performed on phosphorous-implanted GeSn 6%, the goal being to obtain high active dopant concentrations, while preserving good crystalline quality. The implantation dose was $1 \times 10^{15} \text{ cm}^{-2}$ and an ion implantation energy of 9 keV, which induced an amorphization depth 25 nm (total GeSn thickness 41 nm). To complete the study, Solid Phase Epitaxial Regrowth was evaluated by performing laser annealing with energy densities lower than the melting threshold observed for our GeSn layer.

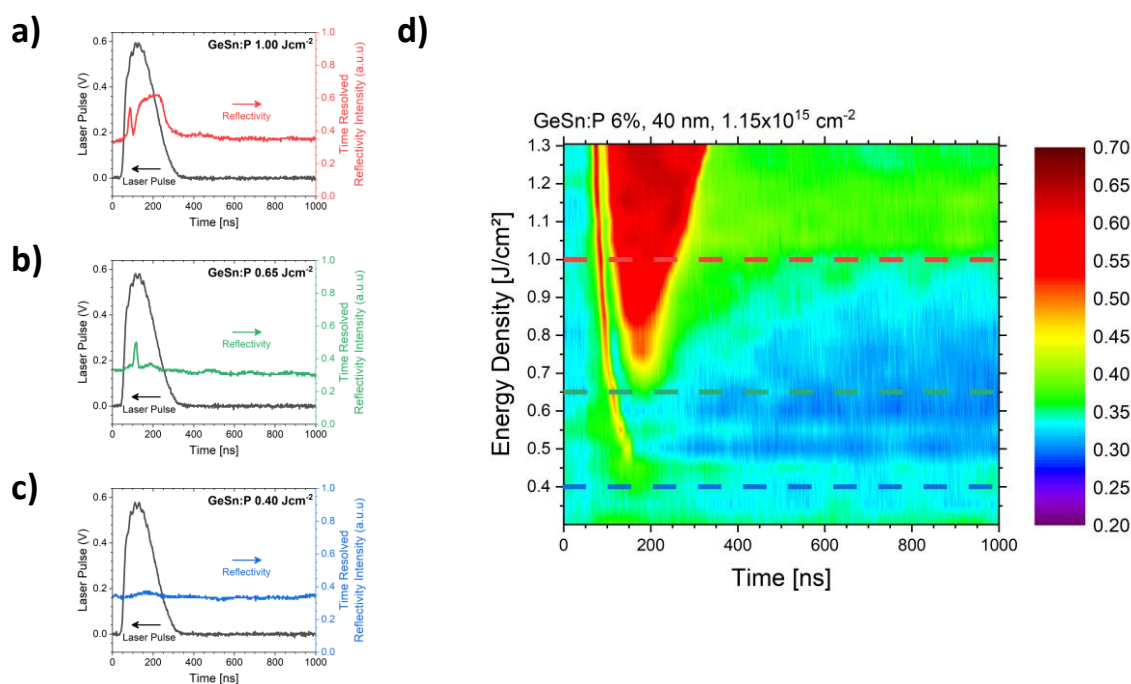
VIII.2 Time Resolved Reflectivity evolution

Figure VIII.1: Time Resolved Reflectivity (TRR) profiles for a 41 nm thick pseudomorphic, P implanted ($1 \times 10^{15} \text{ cm}^{-2}$, 25 nm amorphized) GeSn 6% layer annealed at 1.00 Jcm^{-2} (red (a)), 0.85 Jcm^{-2} (green (b)) and 0.40 Jcm^{-2} (blue (c)). The black curve in each graph shows the pulse intensity vs. time for different ED. (d) TRR map with a stacking of all spectra (ED increment = 0.025 Jcm^{-2}). Colored lines are guidances to locate (a) to (c) TRR spectra in the TRR map.

A 41 nm thick pseudomorphic GeSn 6% layer grown on a Ge SRB was implanted with phosphorous ions (dose : $1 \times 10^{15} \text{ cm}^{-2}$, 25 nm amorphized). The Time-Resolved Reflectivity (TRR) profile of that GeSn:P layer after NLA at 0.40 Jcm^{-2} is shown in **Figure VIII.1** (c). The

TRR signal is constant with no peak observed during NLA, outlining that no melt occurred [1], [2]. At 0.65 Jcm^{-2} , a very short TRR peak (a few nanoseconds) is visible when the laser pulse reaches its maximum intensity, as shown in **Figure VIII.1 (b)**. This is due to explosive recrystallization caused by recrystallization of the amorphous GeSn layer into almost polycrystalline GeSn. This is, as previously described, attributed to the release of latent heat during the solidification of the molten amorphous layer, which consecutively fuels the melting of a small part of the deeper amorphous layers that was already at a high temperature. The melting of this small part of the deeper amorphous layer fueled the melting of an even deeper, small part of the amorphous layer continuously fueling the recrystallization of the entire amorphous layer into an almost polycrystalline layer [3]–[6]. At 1.00 Jcm^{-2} , shown in **Figure VIII.1 (a)**, a second melt was recorded which corresponded to the melt of the polycrystalline GeSn layer.

By stacking the TRR profiles recorded at various EDs, a TRR map was obtained, shown in **Figure VIII.1 (d)**. The explosive melt threshold was around 0.475 Jcm^{-2} and the second melt threshold around 0.725 Jcm^{-2} .

VIII.3 P implanted GeSn NLA – Surface Morphology Evolution

Table 1 Surface structure metrics extracted by assuming a threshold of 2 nm above the surface mean plane and using the Particle Analysis feature of the Bruker analyzing software NanoScope. AFM images were flattened by a 6th order fit to ensure that long range undulations (because of the surface cross-hatch of the Ge SRBs underneath) were not counted as surface structures.

Energy Density [Jcm^{-2}]	Surface Structure Density [μm^{-2}]	Surface Structure Diameter [nm]	Surface Structure Height [nm]
0.55	10.8	63.4	10.6
0.85	27.8	122.2	16.0
1.00	45.4	80.6	7.6
1.30	27.5	61.1	10.1

NLA on intrinsic GeSn layers resulted in the formation of surface structures, as here for GeSn:P. [7] The evolution of the surface morphology is characterized by AFM (Flattened by a second order function to remove the effects of bowing while maintaining surface undulations) and shown in **Figure VIII.2**. The as-implanted surface exhibited a cross-hatch along the $\langle 110 \rangle$ directions and a smooth surface, as shown in **Figure VIII.2 (a)**, with Root Mean Square (RMS) roughness and Z_{range} values of 0.40 nm and 4.06 nm, respectively. Smaller surface structures formed at higher EDs, as shown for 0.55 Jcm^{-2} in **Figure VIII.2 (b)**. RMS and Z_{range} values were then 2.11 nm and 19.8 nm, respectively. When the ED further increased, surface structures merged and RMS and Z_{range} values increased to 4.38 nm and 35.0 nm, respectively, as shown for 0.85 Jcm^{-2} in **Figure VIII.2 (c)**. A high density of small isolated surface structures formed

at 1.00 Jcm^{-2} , as shown in **Figure VIII.2 (d)**. They did not significantly change for 1.30 Jcm^{-2} , as shown in **Figure VIII.2 (e)**.

In intrinsic GeSn, there was a definite correlation between the surface RMS roughness and the normalized TRR difference between average initial and final values (e.g. the following ratio: (mean intensity of the last 10 TRR data points - mean intensity of the first 10 TRR data points)/(mean intensity of the first 10 TRR data points), then normalized to range from 0 to 1). [7] When the entire top layer melted a smooth layer with a smaller RMS roughness was formed, resulting in a peak of the normalized TRR difference. A similar correlation was found for P implanted GeSn, shown in **Figure VIII.2 (f)**. The RMS roughness reached a minimum and the normalized TRR difference a maximum around 1.00 Jcm^{-2} . Those might indicate that the entire top amorphous GeSn:P layer or the entire GeSn layer (amorphous + crystalline) was melted.

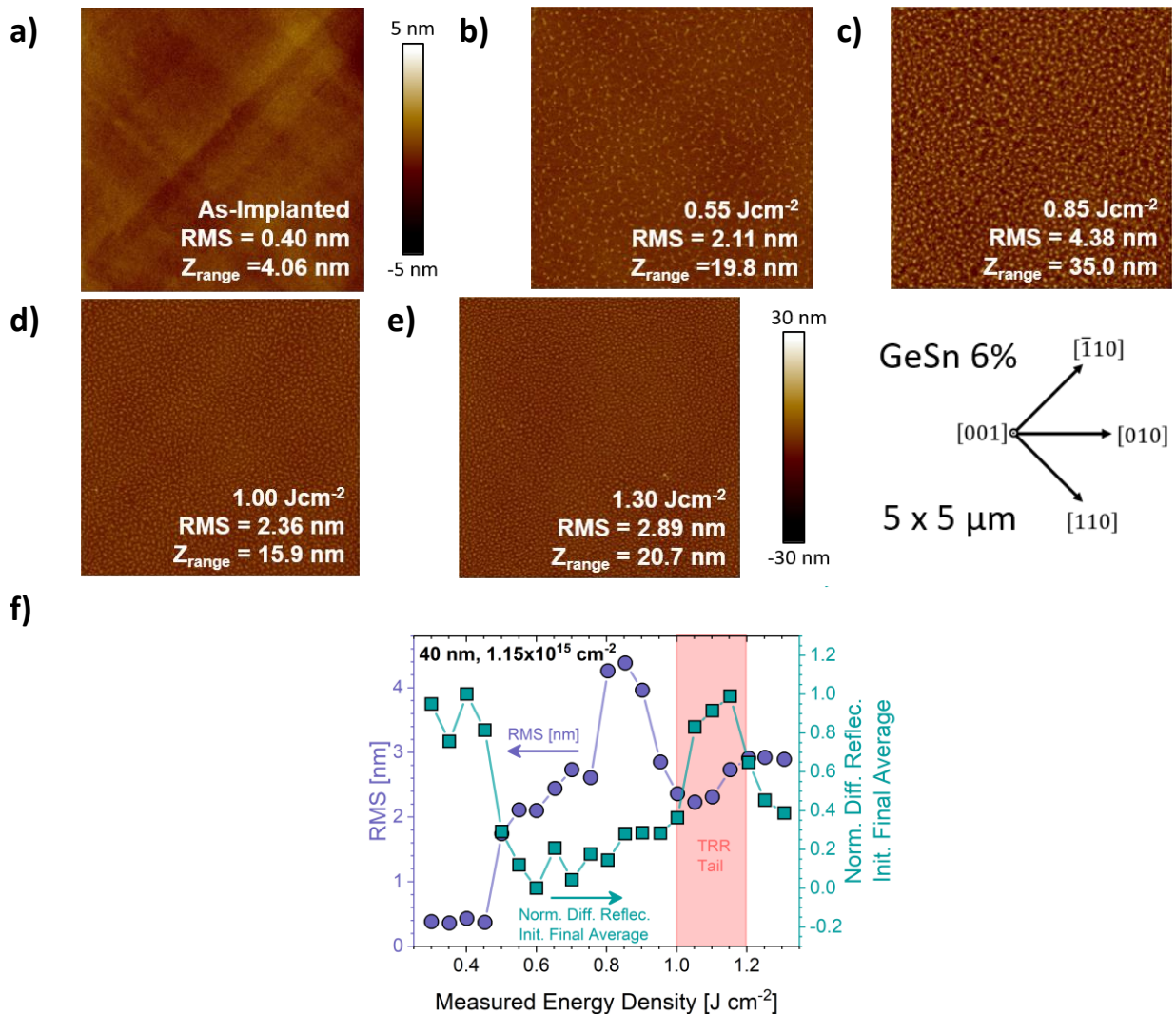


Figure VIII.2: $5 \mu\text{m} \times 5 \mu\text{m}$ AFM images of a 41 nm thick pseudomorphic, GeSn:P 6% layer either as-implanted ((a), 5 nm z-scale) and after laser annealing at 0.55 Jcm^{-2} (b), 0.85 Jcm^{-2} (c), 1.00 Jcm^{-2} (d) and 1.30 Jcm^{-2} (e) ((b) to (e) with 30 nm z-scales). The schematic on the bottom right shows the crystallographic directions. (f) Differences between average final and initial TRR signals divided by the average initial reflectivity (green squares) and surface RMS roughness (purple circles) at various energy densities for GeSn 6%. The red area shows energy density ranges with tails in the TRR maps.

VIII.4 P implanted GeSn NLA – Crystalline Structure

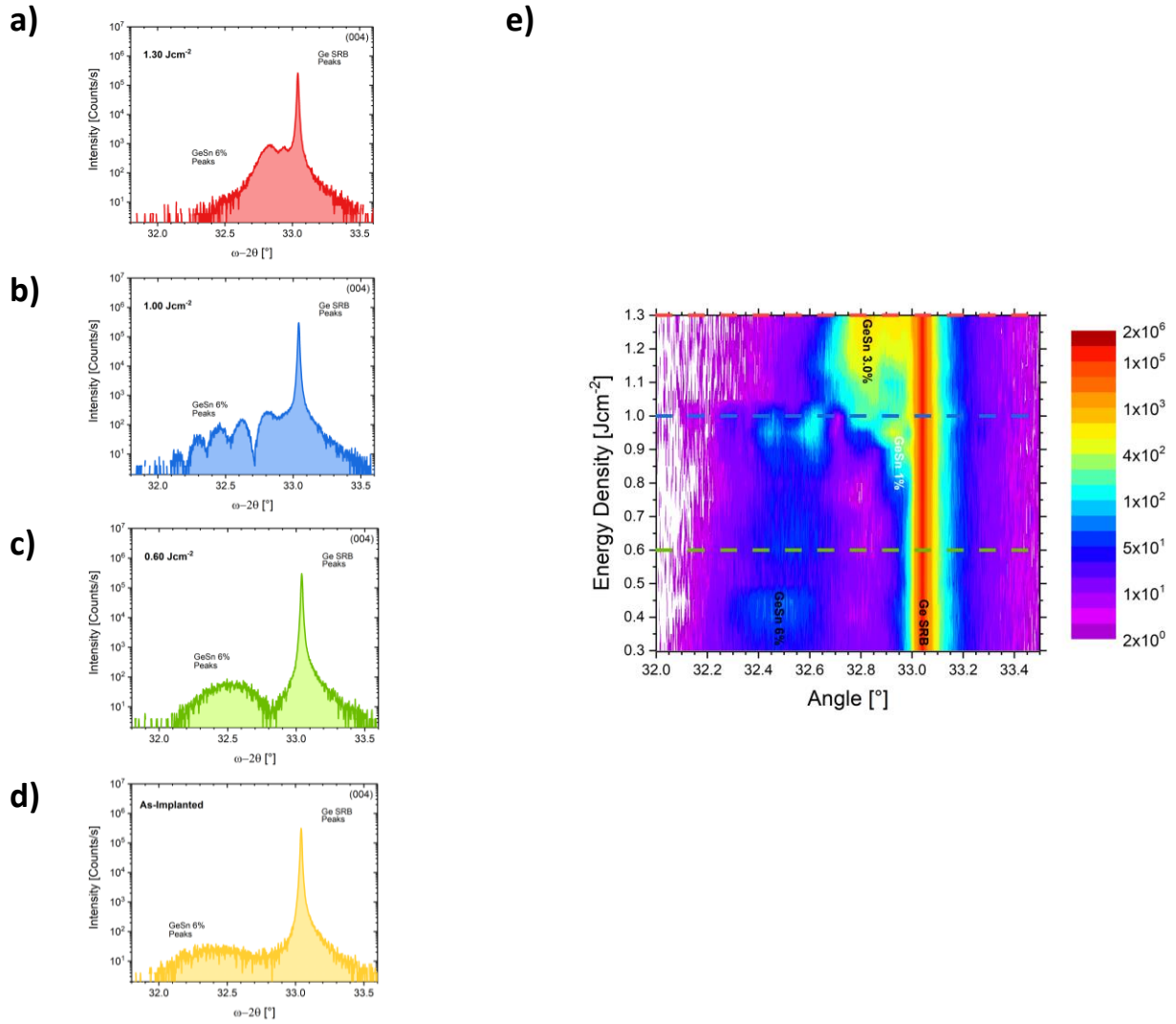


Figure VIII.3: ω - 2θ scans around the (0 0 4) XRD order for a 41 nm GeSn:P layer after laser annealing at 1.30 Jcm⁻² (red (a)), 1.00 Jcm⁻² (blue (b)) and 0.60 Jcm⁻² (green (c)) and as-implanted profile (yellow (d)). (e) ω - 2θ scan map obtained by stacking XRD scans at various EDs (step size: 0.025 Jcm⁻²). Colored lines show at which energy density (a) to (d) ω - 2θ scans were acquired.

The as-implanted GeSn layer was of low crystalline quality because of ion implantation damage that resulted in defects deteriorating the crystalline quality, as outlined by the broad peak in the ω - 2θ XRD profile around the (0 0 4) order shown in **Figure VIII.3 (d)**. The GeSn peak intensity increased and the XRD peak width reduced when laser annealed at 0.60 Jcm⁻² thanks to the recrystallization and hence, healing of some defects introduced during ion implantation, as shown in **Figure VIII.3 (c)**. Well defined XRD peaks and possibly thickness fringes, outlining the presence of smooth surfaces / interfaces, were found for 1.00 Jcm⁻², as shown in **Figure VIII.3 (b)**. The formation of various GeSn layers with different Sn contents might, indeed, resulted in thickness fringes - like peaks. Cross-sectional transmission electron

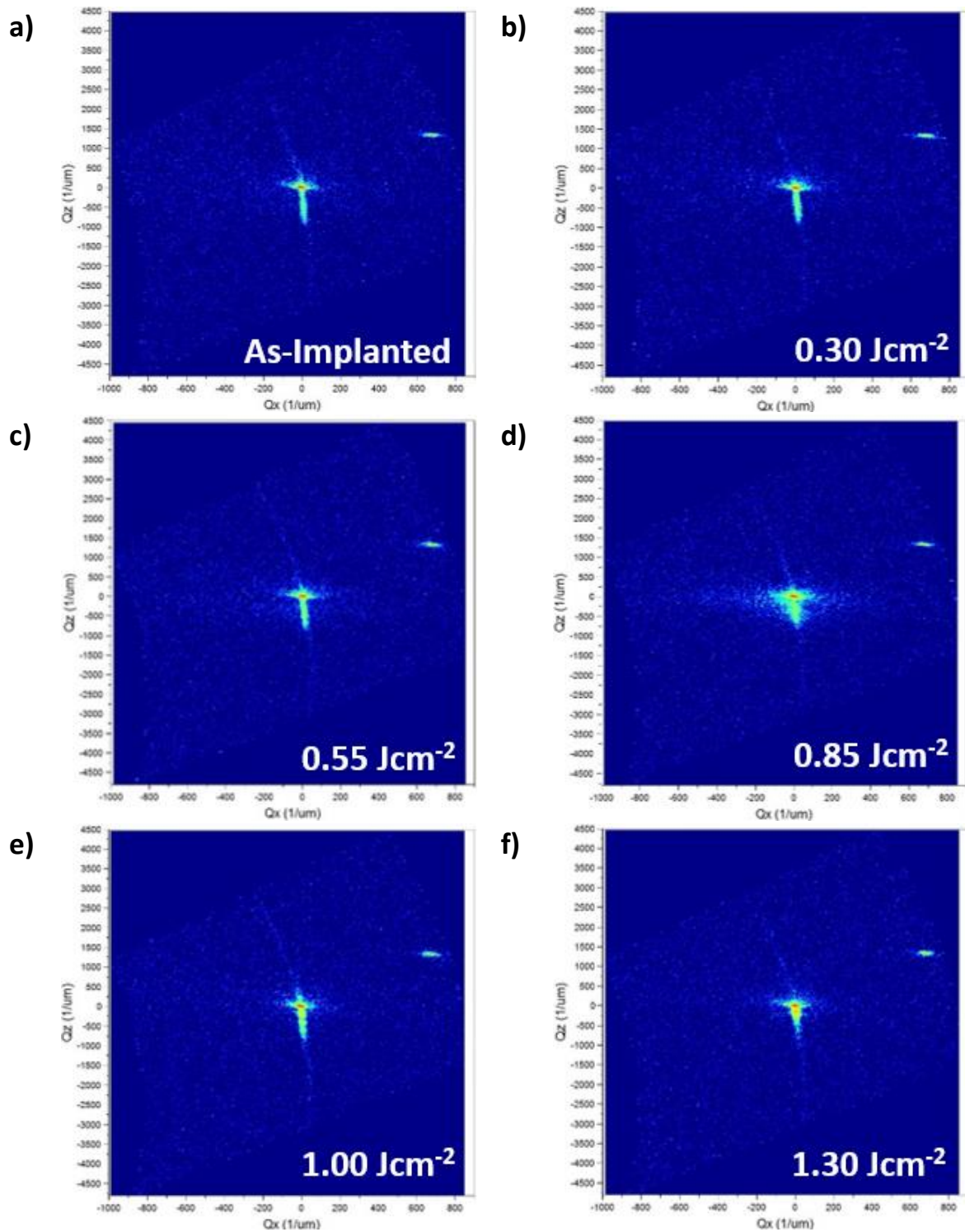


Figure VIII.4: (1 1 3) RSM of 41 nm phosphore implanted GeSn layer (a) as implanted and after laser annealing at (b) 0.30 Jcm^{-2} , (c) 0.55 Jcm^{-2} , (d) 0.85 Jcm^{-2} , (e) 1.00 Jcm^{-2} and (f) 1.30 Jcm^{-2} .

microscopy (TEM) images would be required for a better understanding. At 1.30 Jcm^{-2} , the GeSn XRD peak positions were close to that expected for a Sn concentration of 1%, e.g. the

equilibrium concentration. Sn was thus redistributed when the layer melted and regions with Sn concentrations close to the equilibrium one formed. [8]

By stacking ω -2 Θ XRD scans obtained at various EDs (step-size 0.025 Jcm^{-2}), an overview of Sn redistribution and recrystallization is obtained, shown in **Figure VIII.3 (e)**. Before explosive recrystallization occurred, the XRD peak stayed broad. As the ED further increased, the GeSn XRD peak intensity increased and the peak shifted towards the higher angle Ge SRB peak, most likely because of Sn redistribution. Around 0.90 Jcm^{-2} , there were multiple high intensity GeSn peaks, which might be thickness fringes or due to different Sn content layers. Above 1.05 Jcm^{-2} , the high intensity GeSn peaks disappeared and a GeSn peak corresponding to 1% to 2% of Sn appeared (**Figure VIII.3 (a)**).

Figure VIII.4 shows (1 1 3) Reciprocal Space Maps of GeSn:P after ion implantation and laser annealed. Well defined Si and Ge SRB peak were observed. A GeSn peak of reduced intensity was found close to the Ge SRB peak. The peak was elongated along Q_z and rather well defined along Q_x for the as-implanted layer, shown in **Figure VIII.4 (a)**. No thickness fringes were observed outlining that the crystalline quality was lower than in as-grown pseudomorphic GeSn layers because of defects introduced by ion implantation. Below explosive recrystallization occurred, at an ED of 0.30 Jcm^{-2} , shown in **Figure VIII.4 (b)**, no changes compared to the as-implanted layer occurred. When ED reached 0.55 Jcm^{-2} and explosive recrystallization occurred, shown in **Figure VIII.4 (c)**, the GeSn peak became more defined and “thickness fringe”-like features appeared, most likely because the crystalline structure was more ordered after the occurrence of explosive recrystallization. Those features disappeared and the GeSn peak significantly broadened and shifted closer to the Ge SRB peak at 0.85 Jcm^{-2} , shown in **Figure VIII.4 (d)**. This was likely due to a significant area of the amorphous (almost polycrystalline) GeSn melting and recrystallizing imperfectly because of the surrounding solid, amorphous (almost polycrystalline) GeSn and because of the redistribution of Sn. When the entire amorphous (almost polycrystalline) layer was molten at 1.00 Jcm^{-2} , shown in **Figure VIII.4 (d)**, high crystalline quality GeSn crystallized because of the underlying crystalline GeSn layer. This was highlighted by “thickness fringe”-like features, outlining the curing of most implantation damages. At 1.30 Jcm^{-2} , shown in **Figure VIII.4 (e)**, the GeSn peak without “thickness fringe”-like features anymore shifted closer to the Ge SRB peak due to Sn redistribution. Moreover, it was shown that the GeSn layer stayed compressively strained for all annealing conditions. Similar behaviors were reported before. [9], [10]

Scanning Transmission Electron Microscope –High Angle Annular Dark Field (STEM-HAADF) images of as-implanted GeSn:P are shown in **Figure VIII.5 (a)**. Some implantation damage close to the surface was visible. The rest of the layer stack was of high crystalline quality. A contrast variation was found around 25 nm, which corresponded to end of range defects formed at the amorphous/crystalline interface. [8], [9]

Surface structures seen for $ED = 1.00 \text{ Jcm}^{-2}$ in **Figure VIII.2 (d)** AFM images were also visible in **Figure VIII.5 (b)** TEM image. **Figure VIII.5 (d)** Energy Dispersive X-Ray Spectroscopy (EDX) map showed that Sn redistribution towards the surface resulted in the formation of Sn rich surface structures. Similar Sn rich surface structures were found when laser annealing intrinsic, various Sn contents GeSn layers. [7], [10], [11] EDX signals with varying intensities highlighted inhomogeneous Sn distribution around the surface structures. This might explain why multiple XRD peaks were found when laser annealing with

ED = 1.00 Jcm⁻². Implantation defects were recovered after laser annealing, as outlined by the good crystalline structure. The crystalline structure of Sn rich regions was blurry, which might be due to the high Sn content. Surface structures and regions below were nevertheless well aligned, as shown in the inset of **Figure VIII.5 (b)**.

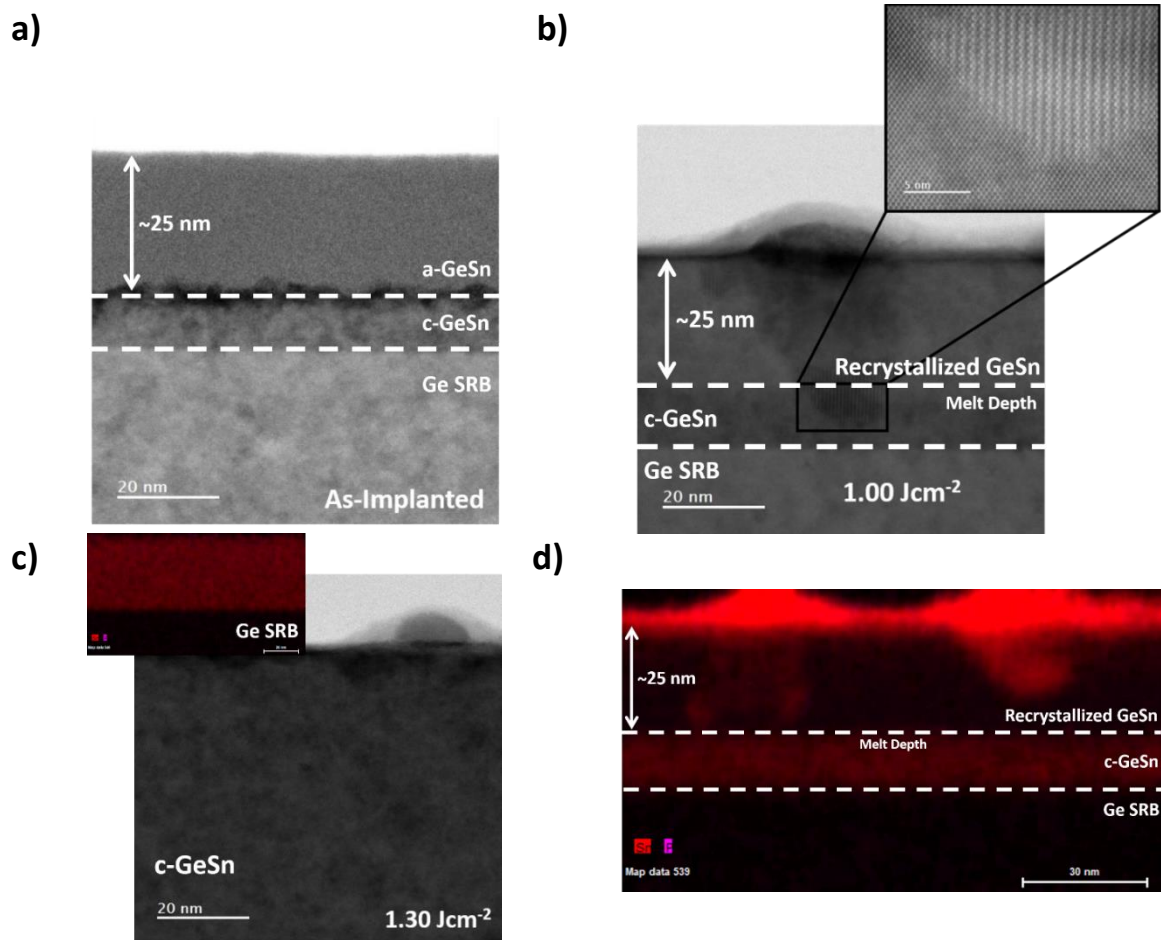


Figure VIII.5: Scanning Transmission Electron Microscopy – High Angle Annular Dark Field (STEM-HAADF) images of a 41 nm thick pseudomorphic GeSn:P 6% layer either (a) as-implanted or after laser annealing at EDs of (b) 1.00 Jcm⁻² and (c) 1.30 Jcm⁻². (d) Energy Dispersive X-Ray Spectroscopy (EDX) map of Sn in the GeSn:P layer annealed at ED = 1.00 Jcm⁻².

The surface structures extended less into the GeSn layer for ED = 1.30 Jcm⁻², as shown in **Figure VIII.5 (c)**. It resulted therefore in less lattice disturbances. EDX mapping, shown in the inset of **Figure VIII.5 (c)**, highlighted a uniform Sn distribution.

VIII.5 P implanted GeSn NLA – Tin and phosphorus redistribution

A SIMS depth profile of the P concentration in the as-implanted layer is shown in **Figure VIII.6 (a)**. The amorphisation depth was around 25 nm. Laser annealing at 0.55 Jcm⁻², corresponding to explosive melt, did not result in any significant change of the P concentration

profile. When the ED increased to 0.85 Jcm^{-2} , the top part of the GeSn:P layer was molten, as outlined in **Figure VIII.1 (d)**. This resulted in a shift of the P profile to deeper thicknesses. At 1.00 Jcm^{-2} , the maximum profile concentration was close to the GeSn / Ge SRB interface and decreased linearly towards the surface. When the Ge SRB melted at 1.30 Jcm^{-2} , P was distributed over a wide depth, resulting in an almost homogenous profile up to around 125 nm, as shown in the inset of **Figure VIII.6 (a)**.

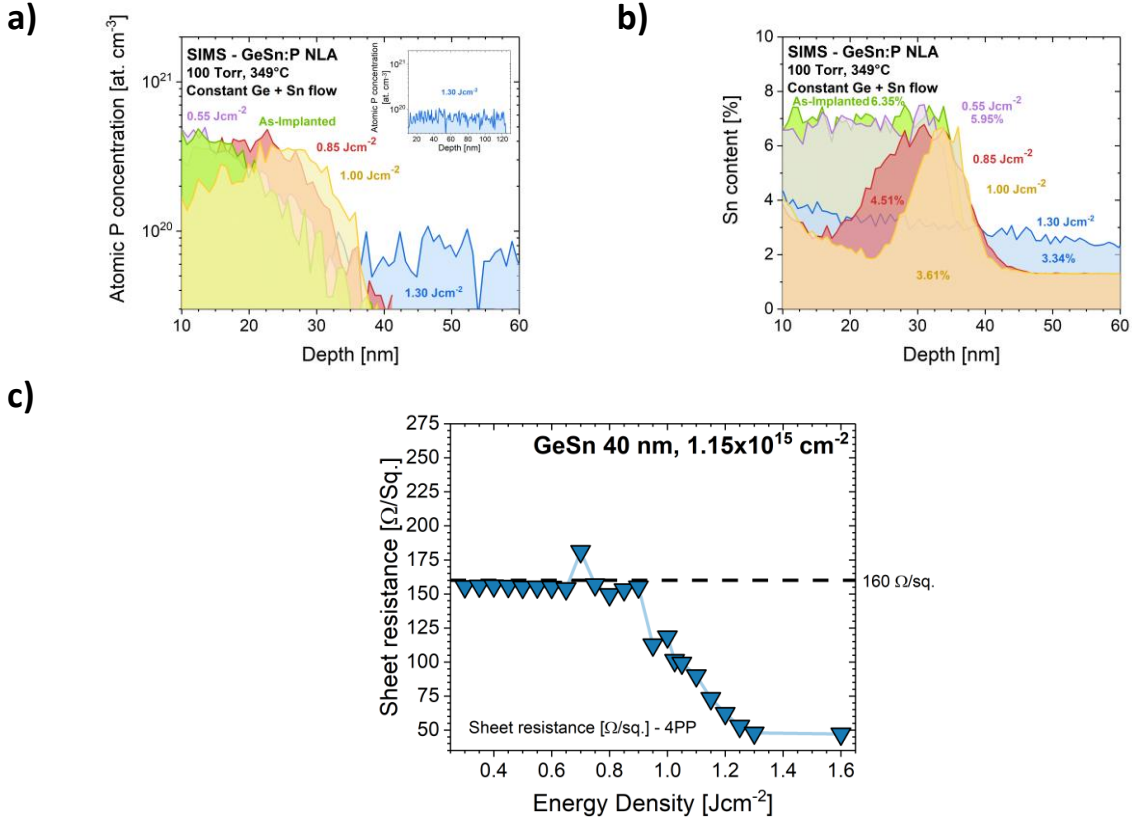


Figure VIII.6: SIMS P (a) and Sn (b) depth profiles in a GeSn:P 6% layer with an as-grown thicknesses close to 41 nm after NLA with various EDs. (c) Four point probe measurements of the sheet resistance for various EDs.

Sn was also redistributed during NLA. SIMS depth profiles are shown in **Figure VIII.6 (b)**. The as-implanted layer and the layer laser annealed at 0.55 Jcm^{-2} exhibited box-like Sn profiles with an average Sn concentration around 6%, as expected. The average Sn concentration was determined by calculating the average value from 10 nm (to exclude surface artifacts) to 40 nm (the layer thickness). When the ED increased to 0.85 Jcm^{-2} , the melt depth increased and Sn was redistributed, with a reduction of the Sn content at intermediate thicknesses and a linear increase towards the surface. The melt depth can be determinate to approximately $22.5 \text{ nm} \pm 2.5 \text{ nm}$. Indeed, below that thickness, the Sn concentration was unchanged compared to the as-implanted sample. The average Sn concentration in the sample laser annealed at 0.85 Jcm^{-2} was 4.51%, with therefore some significant Sn redistribution towards the surface. The melt depth increased to around 30 nm when laser annealed with ED with 1.00 Jcm^{-2} , and the Sn content was 3.61%, a clear sign of further Sn redistribution towards

the surface. At 1.30 Jcm^{-2} , the Ge SRB melted and Sn was distributed in the buffer, resulting in an average Sn content of 3.34% and a linear increase towards the surface.

The influence of P and Sn redistribution as well as recrystallization on dopant activation was investigated thanks to four point probe measurements (4PP). At EDs up to 0.90 Jcm^{-2} , the sheet resistance remained constant at around $155 \text{ }\Omega/\text{square}$, the value of the as-implanted layer. It then gradually decreased as the ED increased, saturating at $48 \text{ }\Omega/\text{square}$ after laser annealing at 1.30 Jcm^{-2} . One reason for the decreased sheet resistance was the redistribution of P, resulting in a thicker conducting layer. Because the sheet resistance did saturate, it can be concluded that some of the sheet resistance reduction is due to dopant activation and due to the thicker P doped layer. In general, this study showed that highly crystalline GeSn with high dopant activation and no significant remaining implantation damage was obtained when combining ion implantation and UV-NLA. This offers a possibility to obtain good quality, low sheet resistance layers in configurations where Sn redistribution has no impact on device performances, as for example contacts layers.

VIII.6 P implanted GeSn NLA – Solid Phase Epitaxial Regrowth

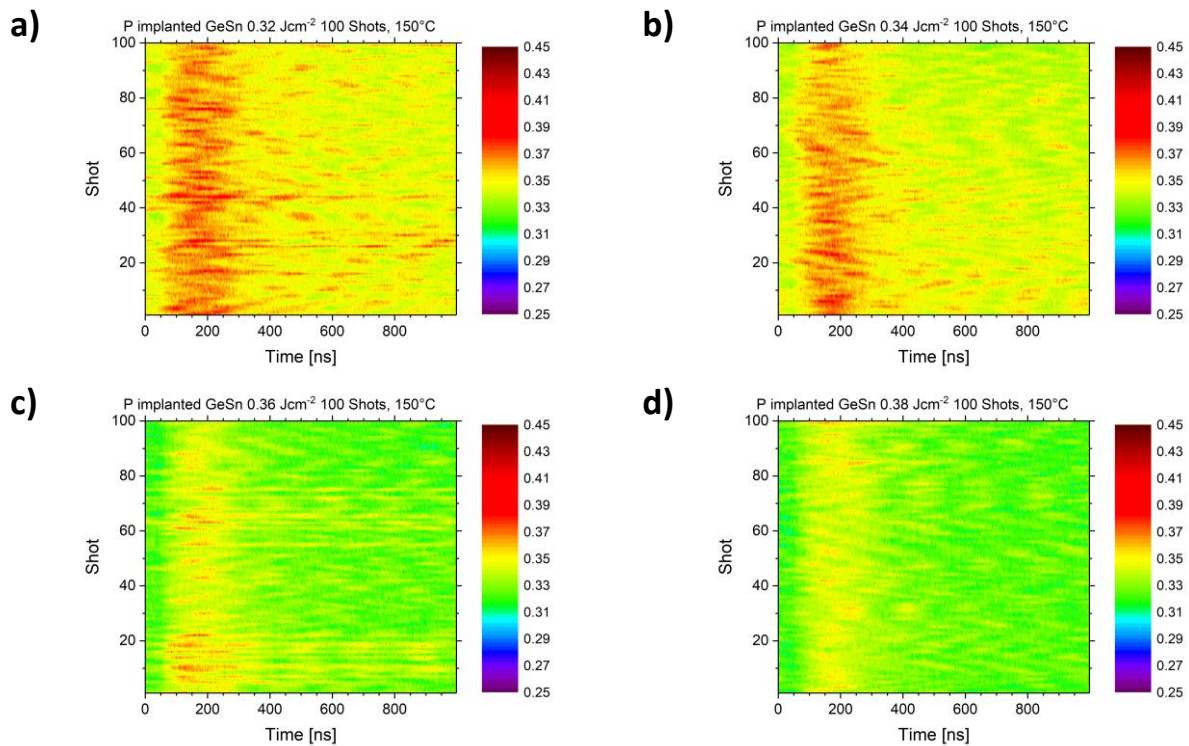


Figure VIII.7: Solid Phase Epitaxial Regrowth (SPER) TRR maps (y-axis: amount of applied laser pulses) for a 41 nm thick pseudomorphic, P implanted ($1 \times 10^{15} \text{ cm}^{-2}$, 25 nm amorphized) GeSn 6% layer on a Ge SRB laser annealed with (a) Round 1, (b) Round 2 (c) Round 3 and (d) Round 4.

As previously shown, the NLA of P implanted GeSn resulted in an activation of P when significant melt occurred. However, Sn redistribution towards the surface occurred during the melting process. To prevent Sn redistribution, Solid Phase Epitaxial Regrowth (SPER) was

investigated. High dopant activation was indeed achieved in Si thanks to SPER without melting the layer. [11] Here, the P implanted, 41 nm thick GeSn 6% layer was placed on a chuck that was heated at 150 °C. Four rounds of laser annealing were performed. First, 100 laser pulses at 0.32 Jcm^{-2} (Round 1), then 100 laser pulses at 0.34 Jcm^{-2} (Round 2), followed by 100 laser pulses at 0.36 Jcm^{-2} (Round 3) and finally, 100 laser pulses at 0.38 Jcm^{-2} (Round 4) were used. All laser pulses were cumulated onto the same position. The ED was chosen to prevent any melting (explosive and second melt) to always maintain a solid layer and hence, prevent Sn redistribution.

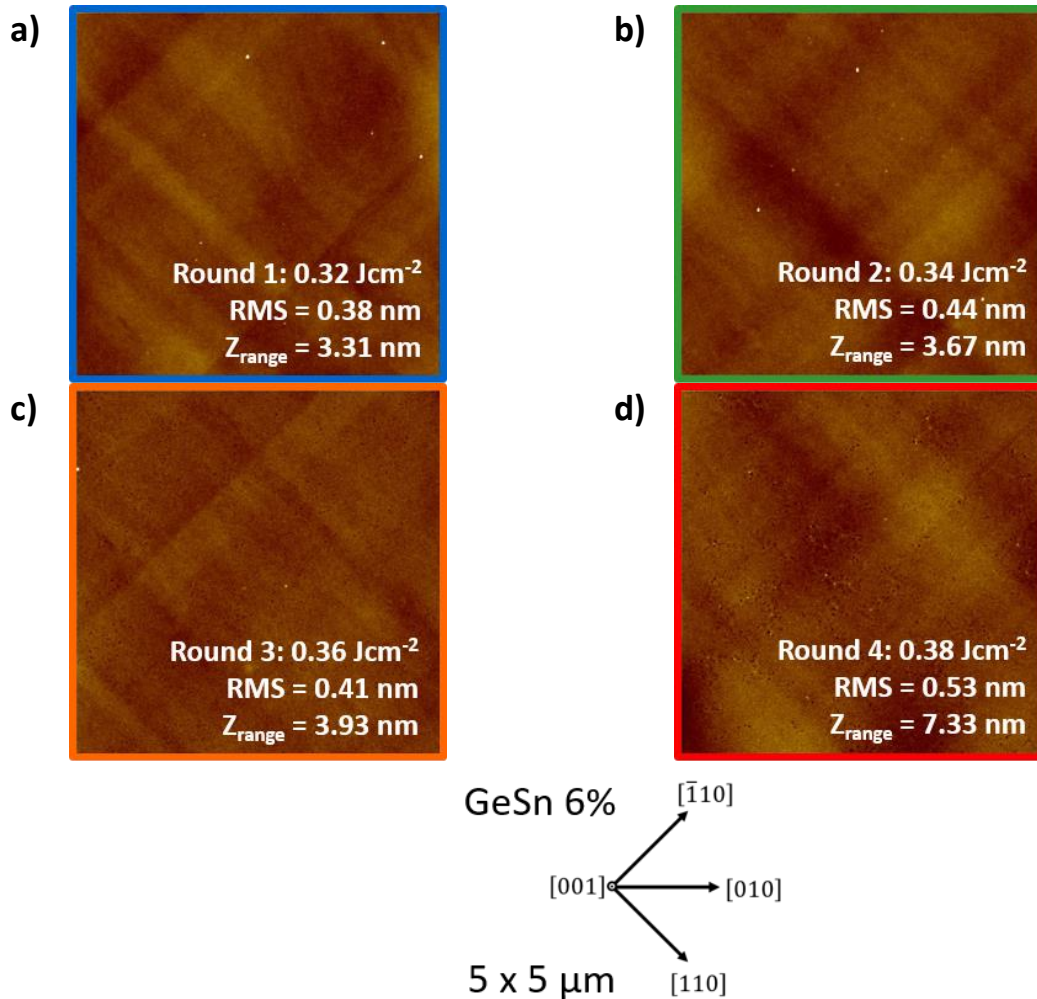


Figure VIII.8: $5 \mu\text{m} \times 5 \mu\text{m}$ AFM images of a 41 nm thick GeSn:P 6% layer as-implanted ((a), 5 nm z-scale) and after laser annealing after SPER rounds one to four ((a) to (d)). The schematic on the bottom shows the crystallographic directions.

In order to check whether or not melting occurred, stacked TRR profile maps were constructed by stacking the TRR profiles for each pulse. They are shown in **Figure VIII.7**. The slight reflectivity peaks observed in **Figure VIII.7** were due to changes of the optical parameters caused by the heating of the layer when laser pulses were applied. The differences in reflectivity between the first two rounds with 0.32 Jcm^{-2} and 0.34 Jcm^{-2} , respectively, shown

Figure VIII.7 (a) and **(b)**, compared to the third and fourth round with 0.36 Jcm^{-2} and 0.38 Jcm^{-2} , respectively, shown **Figure VIII.7 (a)** and **(b)**, were due to some slight non-uniformity of the wafer. It was thus concluded that no melt occurred.

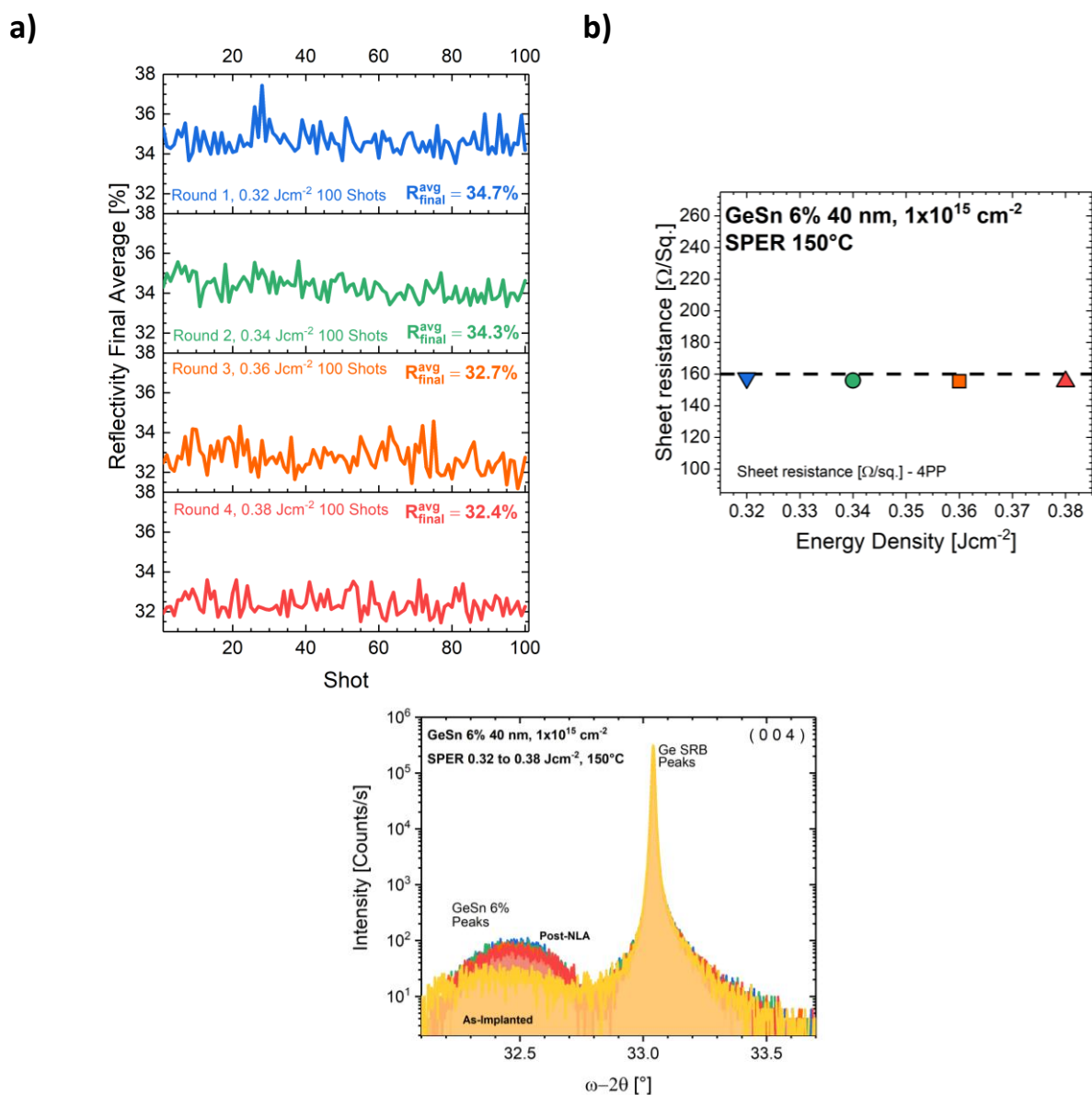


Figure VIII.9: (a) Average final Time Resolved Reflectivity value evolution as a function of applied pulses (first to fourth round of SPER (top to bottom)). (b) Four point probe measurement of the sheet resistance and (c) ω - 2θ scans around the (0 0 4) XRD order for the first to fourth SPER rounds, with the same colors as the curves in (a).

The formation of a few tiny islands on the surface was observed after the first and second round, shown in **Figure VIII.8 (a)** and **(b)**. Except for islands, the surface was smooth with RMS roughness and Z_{range} values around 0.40 nm and 3.50 nm, respectively. A cross-hatch along the $\langle 110 \rangle$ directions was visible after each round. The density of those islands decreased significantly after round three, as shown in **Figure VIII.8 (c)**, and no islands were recorded

after the fourth round, shown in **Figure VIII.8 (d)**. There is some slight surface roughening after the third round with a Z_{range} value of 3.93 nm and some slight surface “patterning”. The surface roughening and “patterning” was more significant after the fourth round with RMS roughness and Z_{range} values of 0.53 nm and 7.33 nm, respectively. No large surface structures were formed like it did when melting the GeSn layer, shown in **Figure VIII.2**, and the surface morphology did not really change, highlighting that melt was prevented, while the structure was altered.

To gain a better understanding how the final material parameters changed after applying each laser pulse, the average final TRR (last 20 ns of the measurement when the heat of the laser pulse has already dissipated) was plotted as a function of the number of laser pulses for the four EDs probed. The resulting data are shown in **Figure VIII.9 (a)**. For the first round (blue curve), the average final TRR signal did not significantly change. It stayed more or less constant around 34.7%. A similar result was obtained for the second round (green curve), the TRR signal stayed almost constant at a value of 34.3%. A reduction of the average final TRR signal was obtained for the third round, with a mean value of 32.7%. It did not further decrease during the fourth round, with a mean value of 32.4%. The sheet resistance from 4PP measurements was steady after rounds 1 to 4, as shown in **Figure VIII.9 (b)**. It stayed close to the as-implanted value at 155 Ω/square . Some XRD measurements were performed, as shown in **Figure VIII.9 (c)**, outlining that for each round some of the implantation damage was recovered, but no significant change was observed when comparing the various rounds.

The fact that the TRR final average was slightly reduced when applying more laser pulses during the second and third rounds might mean that some significant structural changes would happen for numbers of pulses higher than 100 at those EDs of 0.34 Jcm^{-2} and 0.36 Jcm^{-2} . Further investigations while changing laser annealing parameters like ED, maximum amount of pulses and amount of rounds would be required to potentially succeed in reducing the layer resistivity. SPER might indeed allow dopant activation without Sn redistribution. In the literature, it was shown that SPER by UV-NLA yielded total crystal recovery and high dopant activation rates. [12] Most recent results showed that for amorphous layer thicker than 15 nm it was best to adopt a different ED for each applied laser pulse to obtain total crystal recovery and high dopant activation. [13] This kind of approach should be investigated for GeSn in the future.

VIII.7 Conclusions

In this last chapter, we showed that the sheet resistance was lower after NLA than after ion implantation in a phosphorous-implanted GeSn 6% layer. NLA recrystallized the implantation damage, resulting in a monocrystalline layer without the formation of Sn precipitates. Sn was, however, redistributed towards the surface, resulting in Sn rich surface structures with monocrystalline, Sn rich GeSn regions underneath with, however, a lower crystalline quality than that of the as-grown layer. These types of layers with low sheet resistance are of interest to improve the performance of for example contact layers. To prevent Sn redistribution, Solid Phase Epitaxial Regrowth was investigated. No large Sn surface structures were observed after SPER. TRR measurements showed that some small structural changes occurred, however, without sheet resistance reductions. This outlined that SPER might thus result in dopant activation without Sn redistribution, provided that annealing parameters are further improved.

References

- [1] S. Adachi, “Optical dispersion relations in amorphous semiconductors,” *Phys. Rev. B*, vol. 43, no. 15, pp. 12316–12321, May 1991, doi: 10.1103/PhysRevB.43.12316.
- [2] G. E. Jellison, “Optical functions of GaAs, GaP, and Ge determined by two-channel polarization modulation ellipsometry,” *Opt. Mater.*, vol. 1, no. 3, pp. 151–160, Sep. 1992, doi: 10.1016/0925-3467(92)90022-F.
- [3] M. O. Thompson *et al.*, “Melting Temperature and Explosive Crystallization of Amorphous Silicon during Pulsed Laser Irradiation,” *Phys. Rev. Lett.*, vol. 52, no. 26, pp. 2360–2363, Jun. 1984, doi: 10.1103/PhysRevLett.52.2360.
- [4] C. Buchner and W. Schneider, “Explosive crystallization in thin amorphous layers on heat conducting substrates,” *J. Appl. Phys.*, vol. 117, no. 24, p. 245301, Jun. 2015, doi: 10.1063/1.4922787.
- [5] G. C. Egan, T. T. Li, J. D. Roehling, J. T. McKeown, and G. H. Campbell, “In situ dynamic TEM characterization of unsteady crystallization during laser processing of amorphous germanium,” *Acta Mater.*, vol. 143, pp. 13–19, Jan. 2018, doi: 10.1016/j.actamat.2017.10.003.
- [6] G. C. Egan, T. W. Heo, A. Samanta, and G. H. Campbell, “A novel liquid-mediated nucleation mechanism for explosive crystallization in amorphous germanium,” *Acta Mater.*, vol. 179, pp. 190–200, Oct. 2019, doi: 10.1016/j.actamat.2019.08.026.
- [7] M. Frauenrath *et al.*, “Nanosecond Laser Annealing of pseudomorphic GeSn layers – Impact of Sn content,” *to be published*.
- [8] D. -S. Wen, P. Smith, C. M. Osburn, and G. A. Rozgonyi, “Elimination of End-of-Range Shallow Junction Implantation Damage during CMOS Titanium Silicidation,” *J. Electrochem. Soc.*, vol. 136, no. 2, pp. 466–471, Feb. 1989, doi: 10.1149/1.2096656.
- [9] P.-S. Chen, T. E. Hsieh, and C.-H. Chu, “Removal of end-of-range defects in Ge+-pre-amorphized Si by carbon ion implantation,” *J. Appl. Phys.*, vol. 85, no. 6, pp. 3114–3119, Mar. 1999, doi: 10.1063/1.369694.
- [10] M. Frauenrath, P. Acosta Alba, N. Gauthier, E. Nolot, D. Cooper, and J. M. Hartmann, “Multi Pulse Nanosecond Laser Annealing of pseudomorphic GeSn layers – Impact of Sn content.”
- [11] L. Wang *et al.*, “Post-growth annealing of germanium-tin alloys using pulsed excimer laser,” *J. Appl. Phys.*, vol. 118, no. 2, p. 025701, Jul. 2015, doi: 10.1063/1.4926484.
- [12] P. Acosta Alba, J. Aubin, S. Perrot, F. Mazzamuto, A. Grenier, and S. Kerdilès, “Solid phase recrystallization induced by multi-pulse nanosecond laser annealing,” *Appl. Surf. Sci. Adv.*, vol. 3, p. 100053, Mar. 2021, doi: 10.1016/j.apsadv.2020.100053.
- [13] A. Alvarez Alonso and P. Acosta Alba, “Adaptive Energy Density Solid Phase Recrystallization of Thick Si Layers by UV-NLA,” *IIT 2022*, To be published.

Conclusions and Perspectives

Conclusions and perspectives

To meet the demands of environmental sensing, which is growing at a rapid pace, Si integrated photonics should be extended from the Near to the Mid-Infrared. This requires efficient, CMOS compatible lasers and photodiodes. A direct group IV semiconductor can be obtained by tensile straining Ge and/or alloying it with at least 7.5% of Sn (unstrained). In 2020, electrically pumped lasing in GeSn at temperatures up to 100 K was shown. [1], [2] To further increase the lasing temperature, efficient doping is required.

Doping studies on (Si)GeSn are however rather scarce in the literature. As far as in-situ doping is concerned, a few papers showed growth mechanism changes and gave hints about achievable doping levels, but data were incomplete. Similarly, literature on ex-situ doping based on the combination of ion implantation and annealing was limited, too. In the current manuscript, we thus thoroughly explored (i) the in-situ doping of GeSn and SiGeSn and (ii) the impact of Nanosecond Laser Annealing (NLA) on Ge:B, GeSn and GeSn:P layers. Out of the laser annealed layers, the latter was implanted with phosphorus ions while the first one was in-situ doped with boron. Our aim was to benchmark both approaches and identify their strengths and weaknesses, while understanding the physical behavior of GeSn when submitted to NLA.

Detailed studies by X-Ray Diffraction (XRD) and Wavelength Dispersive X-Ray Fluorescence of GeSn:B and GeSn:P layers unveiled that, as the B_2H_6 or PH_3 flows increased, the Ge Growth Rate (GR) component increased while the Sn GR component stayed constant. Indeed, B_2H_6 and PH_3 helped in opening surface sites. Because the Ge GR component was surface reaction rate limited while the Sn GR component was mass-transport limited, a Sn concentration reduction was observed and the in-situ doped GeSn growth rate increased as the dopant flows increased. Electrically active B concentrations up to $2.8 \times 10^{19} \text{ cm}^{-3}$ were achieved in GeSn:B 6% layers grown at 350 °C, 100 Torr with $Ge_2H_6 + SnCl_4 + B_2H_6$. Meanwhile, the electrically active concentration in GeSn:P 6% grown at 350 °C, 100 Torr with $Ge_2H_6 + SnCl_4 + PH_3$ was limited to $6.9 \times 10^{19} \text{ cm}^{-3}$. This was likely due to the formation of large amounts of electrically inactive Sn_mP_n-V complexes.

Those rather low doping concentrations were overcome by injecting large amounts of Si atoms into the GeSn lattice. Electrically active dopant concentrations as high as $2.0 \times 10^{20} \text{ cm}^{-3}$ for SiGeSn:B and $2.7 \times 10^{20} \text{ cm}^{-3}$ for SiGeSn:P were then obtained for layers grown at 350 °C, 100 Torr with the same gas flows than above, save for the addition of Si_2H_6 . It thus seemed that significantly less electrically inactive Sn_mP_n-V clusters were formed when Si was present in large amounts in SiGeSn:P alloys. In addition, the introduction of high dopant flows resulted in improved SiGeSn:B or SiGeSn:P surface qualities over that of intrinsic layers by recovering a cross-hatch along the $\langle 110 \rangle$ directions and obtaining Root Mean Square roughness as low as 0.36 nm (SiGeSn:B) and 0.47 nm (SiGeSn:P) and Z_{range} values down to 2.86 nm (SiGeSn:B) and 4.60 nm (SiGeSn:P). Si / Sn ratios of 3.5 with Si contents up to 25% were otherwise achieved in SiGeSn:B. Ge and Si competing for surface sites might partly explain those composition changes.

Nanosecond Laser Annealing, utilizing laser pulses with Full Widths at Half Maximum of a few tens of nanoseconds, in combination with ion implantation takes advantage of ultra-short

pulse durations to create ultra-shallow temperature gradients to achieve defect-free monocrystalline layers with active dopant concentrations above the solid solubility.

Laser annealing of pseudomorphic, in-situ B doped Ge was first investigated. Increased sheet resistances were obtained, most likely because of the formation of electrically inactive boron-interstitial clusters that did not contribute to strain. Rectangular surface structures formed around the melt threshold and merging of surface structures resulted in larger surface structures at higher energy densities.

Nanosecond laser annealing studies were then performed on thin, pseudomorphic GeSn 6%, 10% and 14% layers to better understand the impact of NLA on such alloys, which are prone to Sn segregation / agglomeration. Peculiar tails in Time Resolved Reflectivity (TRR) maps were found. They were due to the formation of smooth surfaces. The energy density at which such TRR tails appeared corresponded to the melting of the entire GeSn layer on top of Ge Strain-Relaxed Buffers, resulting in smooth liquid/solid interfaces (melting temperature 938°C for pure Ge and 232°C for β -Sn [3]). At those energy densities, high crystalline quality layers with up to 6.3% Sn were obtained. These high Sn concentrations are unique to this kind of non-equilibrium annealing techniques. The same melt regimes than those observed for SiGe were evidenced and Secondary Ion Mass Spectrometry showed Sn redistribution towards the surface.

Our understanding on GeSn Nanosecond Laser Annealing was improved by applying up to 100 pulses at the same position. These studies revealed the importance of the melt depth for the formation of surface structures. Laser annealing at the full melt threshold, where the liquid/solid interface was at the GeSn/Ge SRB interface, yielded smooth surfaces, as long as the Ge SRB did not melt and the liquid/solid interface remained smooth. Cross-sectional Transmission Electron Microscopy and Energy Dispersive X-Ray Spectroscopy (EDX) revealed that oxygen was incorporated when multiple laser pulses were sent on the same position. Secondary Electron Microscopy together with EDX showed that surface structures were Sn rich.

Finally, Nanosecond Laser Annealing was performed on phosphorous-implanted GeSn 6% layers to investigate ex-situ doping. Implantation damage was suppressed and high crystalline quality GeSn:P layers, with well-defined XRD peaks and improved sheet resistance, thanks to dopant activation, obtained. However, dopant activation required rather high energy densities, which resulted in some Sn redistribution. Finally, Solid Phase Epitaxial Regrowth was investigated, aiming at removing implantation damages and activating dopants without melting the layer. Some recrystallization was achieved but annealing parameters would need to be further optimized to obtain proper dopant activation.

The knowledge gained during these studies was used to enhance the performance of devices. Constant composition and step-graded heterostructures with Sn concentrations up to 16.9% and 17.2%, respectively, were grown. The temperature and precursor flow management during growth was improved compared to previous studies, resulting in higher Sn contents, better material quality and improved carrier confinement in the high Sn content layers. The stacks were then bonded to Al(N) pillars for improved heat dissipation and the defective low Sn content layers removed. Moreover, a SiN stressor layer was deposited on the constant composition stack to inject some tensile strain in it and increase the differences between L- and

Γ bandgaps. This enabled us to obtain the first optically pumped lasers operating at room temperature [4], [5], as shown in **Appendix IV and V**.

The following provides some hints about studies that could be performed to improve the performance of future devices.

First, the lasing threshold should be drastically lowered. To achieve this, the amount of vacancies (and dislocations) should be reduced. [6] Recent results showed that microstructuring and selective etching of heavily dislocated regions enabled to anneal GeSn heterostructures without Sn segregation. [7] In the future, it might be beneficial to use nanosecond laser annealing to precisely control such processes.

Heterostructures for photodiodes, detectors and electrically pumped lasers are otherwise complex, with the presence of thin and thick partially relaxed layers. As shown in previous studies, the strain state in the bottom GeSn layers has a definite impact on GeSn layers grown on top. [8] Because Sn incorporation is impacted by strain, it would be interesting to further investigate the mechanisms at play. Moreover, the interaction of dopants and strain relaxation has not yet been investigated. It was indeed shown that strain relaxation reduced boron incorporation in SiGe. [9] This might be the case in (Si)GeSn, too. In the current studies, it was shown that the incorporation of dopants into (Si)GeSn changed the layer compositions and resulted in improved surface morphologies. Both would have an impact on the quality of thick layer stacks and should therefore be investigated in complex heterostructures. Layer stacks for devices make use of low growth temperatures (313°C – 325°C, typically) to achieve higher Sn contents. Reducing the growth temperature of in-situ doped (Si)GeSn might be advantageous to avoid potentially dangerous temperature ramps. Better electrical confinement thanks to high Si/Sn ratio SiGeSn barriers might also help in improving device performances. The expertise gained during the present studies would be a good starting point to grow even higher quality intrinsic and in-situ doped SiGeSn layers with a broad range of compositions.

References

- [1] Y. Zhou *et al.*, “Electrically injected GeSn lasers on Si operating up to 100 K,” *Optica*, vol. 7, no. 8, p. 924, Aug. 2020, doi: 10.1364/OPTICA.395687.
- [2] Y. Zhou *et al.*, “Electrically injected GeSn lasers with peak wavelength up to 2.7 μm ,” *Photonics Res.*, vol. 10, no. 1, p. 222, Jan. 2022, doi: 10.1364/PRJ.443144.
- [3] R. W. Olesinski and G. J. Abbaschian, “The Ge–Sn (Germanium–Tin) system,” *Bull. Alloy Phase Diagr.*, vol. 5, no. 3, pp. 265–271, Jun. 1984, doi: 10.1007/BF02868550.
- [4] J. Chrétien *et al.*, “Room temperature optically pumped GeSn microdisk lasers,” *Appl. Phys. Lett.*, vol. 120, no. 5, p. 051107, Jan. 2022, doi: 10.1063/5.0074478.
- [5] A. Bjelajac *et al.*, “Up to 300 K lasing with GeSn-On-Insulator microdisk resonators,” *Opt. Express*, vol. 30, no. 3, p. 3954, Jan. 2022, doi: 10.1364/OE.449895.
- [6] S. Assali *et al.*, “Vacancy complexes in nonequilibrium germanium-tin semiconductors,” *Appl. Phys. Lett.*, vol. 114, no. 25, p. 251907, Jun. 2019, doi: 10.1063/1.5108878.
- [7] V. Bonino *et al.*, “Microstructuring to Improve the Thermal Stability of GeSn Layers,” *ACS Appl. Mater. Interfaces*, vol. 14, no. 19, pp. 22270–22277, May 2022, doi: 10.1021/acsami.2c01652.
- [8] S. Assali, J. Nicolas, and O. Moutanabbir, “Enhanced Sn incorporation in GeSn epitaxial semiconductors via strain relaxation,” *J. Appl. Phys.*, vol. 125, no. 2, p. 025304, Jan. 2019, doi: 10.1063/1.5050273.
- [9] G. Rengo *et al.*, “(Invited) Highly Doped $\text{Si}_{1-x}\text{Ge}_x$ Epitaxy in View of S/D Applications,” *ECS Trans.*, vol. 98, no. 5, pp. 27–36, Sep. 2020, doi: 10.1149/09805.0027ecst.

Acknowledgements

To begin, I would like to thank you for taking your time to read this section and to give respect to the people that contributed to this work. Notably, I would like to express my appreciation to Jean-Michel HARTMANN and Pablo ACOSTA-ALBA. They, in their position as thesis director and supervisor donated so much of their valuable time to me. I deeply appreciated the opportunity to be able to learn from their scientific experience. Moreover, I have grown in professional and non-professional life experiences under their tutorship in the various conversations we had. Thank you so much and I hope we stay in contact in the future.

A great amount of appreciation needs to go to Sylvain MAITREJEAN and Cécile MOULIN, the head of SSURF and the laboratory management. Thank you for your continued support and leadership. Also, thank you for the advice you shared and the interesting questions you posed during meetings. Moreover, I would like to thank Véronique BOURDON and Barbara COYNEL for their assists in administrative matters and for helping me setup for conferences.

Most definitely, this research would have been limited to material research without the great collaboration of the colleagues at DOPT and IRIG who contribute a lot of knowledge and fabricated the devices. I did always look forward to the meetings with you. It was a lot of fun. Remember the chances are always 50%-50%. Either it works or it does not.

While mentioning great collaborations, I would be foolish to not mention my older laboratory of Dan BUCA at the Forschungszentrum Jülich, who continued to contribute to my research even after I finished my master's degree and moved to France. Thank you, also, for the continued support and advice.

To obtain some material to investigate running tools are required, for this I would express my appreciation to T. MARION, L. SAIDI, C. CHAFFARD, F. GONZATTI, T. BRAIZAZ, S. ROUSSEAU, B. ASSUE, P. ROCHE, S. LAGRANGE, V. RIPOCHE, J.B. PIN, S. PUGET and J. BISSERIER. Moreover, I would like to thank everyone how contributed to characterizing my samples E. NOLOT, M. VEILLEROT, N. GAUTHIER, N. BERNIER, A.-M. PAPON, D. COOPER, S. M. N'HARI, J; RICHY and C. LECOUEY.

A. BSIESY, I. BERBEZIER, C. BONAFOS, M. GROS-JEAN and D. BUCA I would like to thank for participating in my thesis jury, as well, F. CRISTIANO and F. BASSANI for taking part in my CSI.

Thank you Hélène for sharing insides into French culture with me and for all of the numerous conversation we shared in our office. I most definitely helped me to improve my French. Thank you to Joel for all the enlightening conversation about science. Not to forget, thank you to all the PhD students (interns, alternants) at SSURF (DOPT) Lucas, Laurent, Mayara, Azilliz, Quentin, Thomas, Océane, Reda, Angela, Antoine, Lea, Clément and Lara who kept me for not working too much and reminded me to eat. Thank you for all the laughter shared. Merci à Anne-Flore et Lucas pour la correction de mon abstrait française. Best of luck to all of you.

Luk Yi, I can't thank you enough for all our conversations about science or just life and for you supporting me and lifting me up even in the darkest moments. You are truly a best friend.

Bella, I know you for so long, you have always been a friend and I appreciate our conversations. Sven thank you for the distraction of watching all Marvel movies and for the good friend advice.

Meinen Eltern gehört ein großer Anteil meines Dankes. Ohne eure kontinuierliche und bedingungslose Unterstützung wäre mein Weg deutlich schwieriger gewesen. Ich bin euch unendlich dankbar und ich habe euch ganz doll lieb. Auch ein Dank an meine Schwester, die mich immer noch lehrt auf andere Menschen zu achten.

Merci à Flo pour l'accueil bienveillant et pour créer le sentiment que j'ai une famille française. Je l'apprécie beaucoup

Appendix A : Résumé Français Etendu

Appendix A Résumé Français Etendu

A.I.1. Introduction

La détection environnementale est un secteur ayant une valeur marchande de 1.40 milliard de dollars US (en 2020) et qui croit de quasiment 10% par an, pour un chiffre d'affaire attendu de 2.17 milliards de dollars US en 2026. L'industrie 4.0, qui fait appel à la détection de gaz, la ville intelligente, l'internet des objets (IdO) et le réchauffement climatique, qui nécessite une réduction de l'émission des gaz à effet de serre, ont depuis quelques années un impact majeur sur ce secteur économique.

Les communications optiques de données à courte distance ont engendré, ces douze dernières années, un développement fort de la photonique intégrée sur Silicium dans le domaine du proche infra-rouge (NIR), avec des longueurs d'onde au maximum de 1.6 μm . Le moyen infra-rouge (MIR), avec une longueur d'onde de 2 à 5 μm , est cependant intéressant pour nombreux applications [1]–[3] comme la détection environnementale, la détection de vie, le diagnostic médical [4] et la sécurité, avec la détection de vibrations moléculaires spécifiques au monoxyde de carbone (CO) et des gaz à effet de serre comme dioxyde de carbone (CO_2) et le méthane (CH_4). [5], [6]

Une pleine compatibilité avec une intégration de type CMOS pour le Si (i.e. le fait de ne pas engendrer de défauts profonds et d'éviter toute incompatibilité chimique avec des procédés CMOS usuels), avec des composants unitaires uniquement à base de semi-conducteurs IV-IV, serait le Graal afin d'obtenir un plateforme MIR efficace et à prix bas. Jusqu'à présent, les sources de lumière dans de telles plateformes provenaient du collage de lasers III-V sur Si [7]–[10] ou de la croissance d'empilements de semiconducteurs III-V directement sur Si [11], [12], avec un certain nombre d'incompatibilités chimiques et des thermiques différentes.

Afin de bénéficier d'un semi-conducteur de la colonne IV avec une structure de bande interdite directe et, par conséquence, d'une émission efficace de lumière, il est possible de contraindre fortement en tension le Ge pur (tension biaxiale au-dessus de 1.7% [13], [14]) et/ou de basculer sur des alliages GeSn avec au moins 7.5% de Sn (sans contraintes) selon des simulations k.p. [15], [16]. La première démonstration de laser GeSn pompé optiquement à 90 K a été apportée en 2015. [17] Depuis, des progrès remarquables ont été faits, avec un effet laser avec un rendement de conversion de puissance pompe proche de l'unité en 2019 [18], un effet laser avec une densité de puissance seuil ultra-basse en 2020 [19], et des lasers pompés optiquement émettant à température ambiante en 2022 [20], [21]. Un effet laser dans du GeSn pompé électriquement a par ailleurs été obtenu, à une température maximale de 100 K, en 2020 [22], [23]. Le rêve d'une plateforme photonique intégrée avec uniquement des semi-conducteurs de la colonne IV ne semble plus si inaccessible que cela.

La température maximale pour un effet laser dans du GeSn pompé électriquement se doit toutefois d'être significativement augmentée et le seuil d'effet laser diminué. De même, le courant d'obscurité de photodétecteurs GeSn et leur responsivité se doivent d'être diminués et augmentés, respectivement. A ces fins, le confinement des porteurs de charge dans des structures pin doit être possible et la résistance de contact réduite. On peut bénéficier d'un tel confinement grâce à l'injection d'atomes de Si, un semi-conducteur avec une bande interdite plus élevée et un paramètre de maille plus petit, dans du GeSn. On peut alors bénéficier de degrés de liberté

supplémentaires du point de vue contrainte et structure de bande interdite. [24] La résistance de contact peut quant à elle être réduite grâce à l'introduction de hautes concentrations de dopants électriquement actifs dans la maille cristalline. Des alliages ternaires (Si)GeSn sont toutefois sensibles à la ségrégation et la précipitation de l'étain. [25] L'implantation ionique se doit d'être combinée à un recuit afin de guérir les défauts d'implantation et bénéficier de dopants électriquement actifs dans la maille cristalline. De hauts budgets thermiques lors de ces recuits ne seraient pas compatibles avec la faible stabilité d'alliages (Si)GeSn.

Des dopants peut être incorporés directement lors de l'épitaxie des empilements. On parlera alors de dopage in-situ. Les dopants sont alors injectés, lors de la croissance, directement dans des sites de la maille cristalline et sont électriquement actifs. Aucun défaut n'est créé à dessin pendant l'épitaxie qui pourrait, plus tard, exiger des recuits pour le supprimer, contrairement à l'implantation ionique. Par conséquent, le dopage in-situ n'est pas en première lecture confronté à la ségrégation et précipitation de l'étain.

Un autre technique pour doper des alliages (Si)GeSn serait de combiner l'implantation ionique avec un procès de recuit ultra-rapide. Le recuit laser nanoseconde utilise des pulses laser avec une largeur à mi-hauteur des quelques dizaines des nanosecondes et une faible longueur d'absorption dépendant des matériaux et la longueur d'onde du laser utilisé. L'énergie du pulse laser est absorbé par la couche et l'interaction lumière/matière transforme l'énergie en chaleur. Grâce à la courte durée du pulse laser, un gradient de température très peu profond est formé, permettant un contrôle précis de la profondeur de fusion et la formation de couches monocristallines sans défauts. En plus, la courte durée du pulse engendre une faible diffusion des dopants en phase solide et une diffusion significative en phase liquide, qui permet d'obtenir une concentration de dopants au-dessus la limite de solubilité en phase solide et une résistance de contact réduite. [26]

A.I.2. Une étude profonde de dopage bore et phosphores de GeSn

Le Graal en ce qui concerne l'émission lumière dans le moyen infra-rouge serait un laser à base de semiconducteurs de la colonne IV pompé électriquement et fonctionnant à température ambiante. Au CEA-LETI, la performance de diodes électroluminescente (DEL) p-i-n à base de GeSn est jusqu'à présent limitée par l'utilisation de couche Ge dopées in-situ au-dessous et au-dessus des couches actives en GeSn. Pour (i) minimiser la ségrégation de l'étain pendant la croissance, à relativement haute température, de l'électrode du dessus et (ii) dans des empilements GeSn/Ge épais, éviter toute relaxation plastique des contraintes emmagasinées, il serait idéal de remplacer les couches de Ge dopées in-situ par des couches de GeSn dopées in-situ aux températures proches de cela de la zone active. Par conséquence, le dopage in-situ du GeSn avec bore et phosphore a été exploré sur des substrats virtuels Ge, avec des chimies de croissance $\text{Ge}_2\text{H}_6 + \text{SnCl}_4 + \text{B}_2\text{H}_6$ et $\text{Ge}_2\text{H}_6 + \text{SnCl}_4 + \text{PH}_3$. La pression de croissance, la température, les rapports de flux $F(\text{Ge}_2\text{H}_6)/F(\text{H}_2)$ et $F(\text{SnCl}_4)/F(\text{H}_2)$ étaient constants à 100 Torr, 349 °C, 7.92×10^{-4} et 4.69×10^{-5} , respectivement.

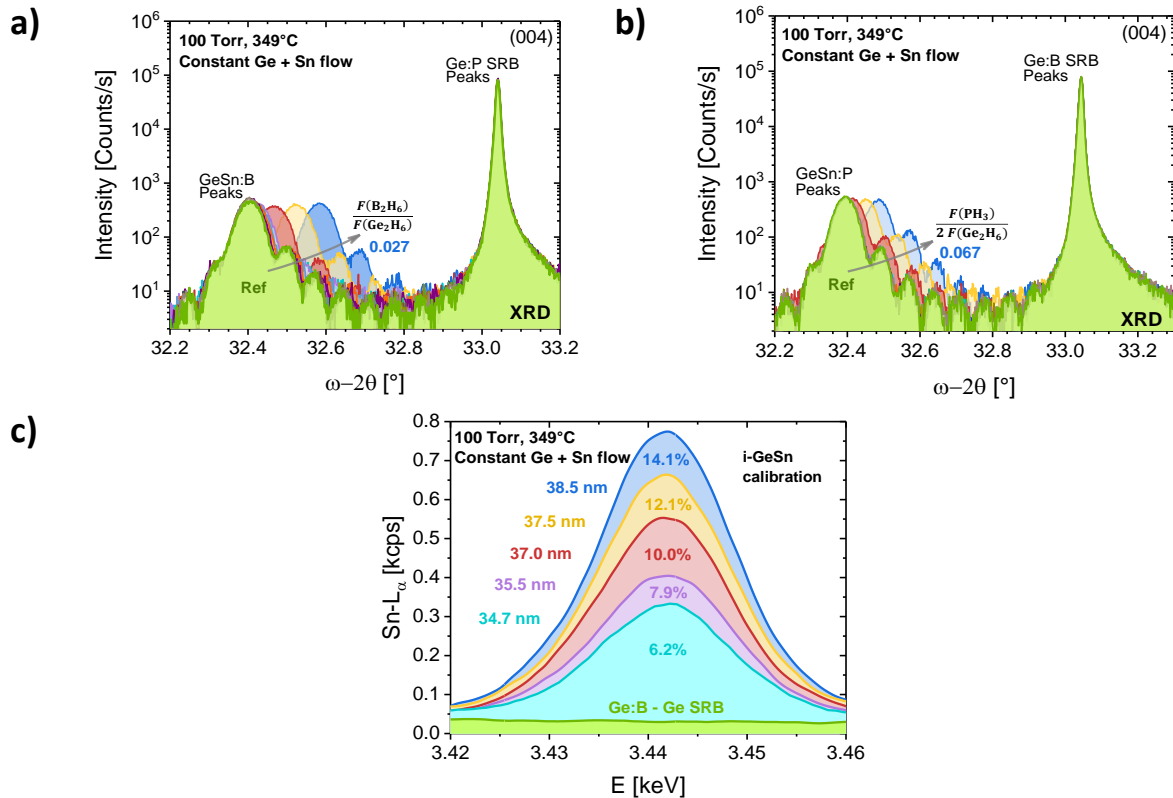


Figure A.1: (a) Balayages $\omega-2\theta$ autour de l'ordre (0 0 4) de la diffraction X pour (a) 61 nm à 80 nm de GeSn:B déposés sur des couches tampons en Ge:P avec des rapports de flux $F(B_2H_6)/F(Ge_2H_6)$ variables and (b) 76 nm à 86 nm de GeSn:P déposés sur des couches tampons en Ge:B avec des rapports de flux $F(PH_3)/2F(Ge_2H_6)$ variables. (c) Pics Sn- L_{α} en WDXRF pour des couches GeSn intrinsèques de concentrations variables en étain déposées sur couches tampons Ge. [27]

Des balayages $\omega-2\theta$ autour de l'ordre (0 0 4) de la diffraction X, présentés en **Figure A.1 (a)** et **(b)**, ont été menés afin d'avoir accès à la composition apparente en étain et à l'épaisseur de ces couches GeSn:B et GeSn:P. On gardera à l'esprit que la position angulaire des pics GeSn n'est pas été seulement déterminée par la concentration en étain, mais aussi par les concentrations substitutionnelles en bore et phosphore (ceux-ci sont beaucoup plus petits que les atomes de Ge et surtout de Sn). La composition réelle de ces couches dopées in-situ n'a donc pas pu être déterminée sans ambiguïté uniquement à partir de mesures en diffraction de rayons X. Des mesures en spectroscopie de fluorescence de rayons X à dispersion de longueur d'onde (WDXRF) de l'intensité des pics Sn- L_{α} ont donc été menées afin de déterminer la concentrations atomique en Sn dans ces couches, comme illustré en **Figure A.1**. Des pics intenses et bien définis en diffraction de rayons X et la présence de franges d'interférence ont confirmé l'excellente qualité cristalline de ces couches GeSn:B et GeSn:P et nous ont donné accès à leurs épaisseurs (et donc aux vitesses de croissance).

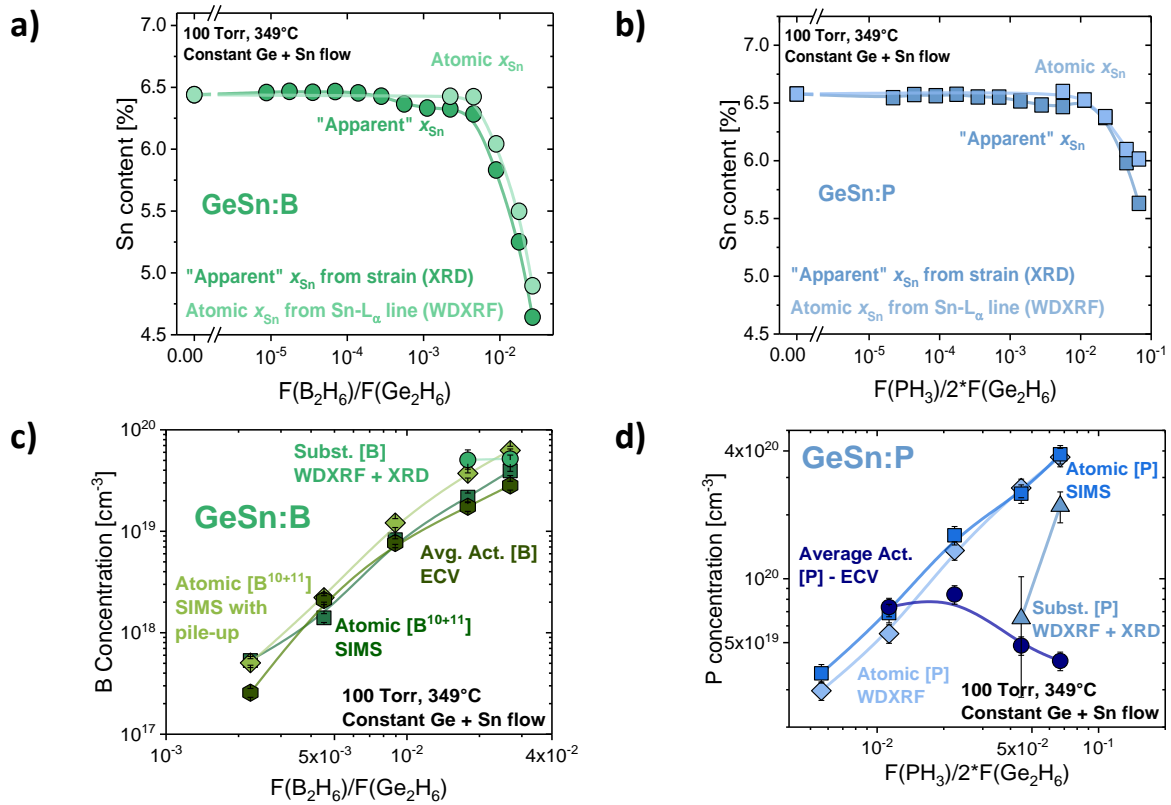


Figure A.2: Concentrations « apparentes » (DRX) et atomiques (WDXRF) en étain dans des couches GeSn:B (a) et GeSn:P (b). Les concentrations substitutionnelles en bore (déduites des différences entre concentrations apparentes en étain (DRX) et réelles (WDXRF)), les concentrations atomiques en bore d'après le SIMS et les concentrations en ions bore d'après des mesures d'ECV sont données dans le graphe (c). Les concentrations substitutionnelles provenant de la la différence entre la concentration d'Sn réelle (DRX) et « présumé » (WDXRF), les concentrations atomiques en atomes de phosphore (WDXRF et SIMS) ainsi que les concentrations en ions P^+ sont données dans la figure (d). $T = 349 \text{ °C}$, $P = 100 \text{ Torr}$, flux variables de B_2H_6 ou de PH_3 . Les rapports de flux $F(Ge_2H_6)/F(H_2)$ et $F(SnCl_4)/F(H_2)$ étaient constants à 7.92×10^{-4} et 4.69×10^{-5} , respectivement.

La concentration atomique en Sn (de WDXRF) dans nos couches GeSn:B ou GeSn:P est restée quasiment constante à 6.5% pour des rapports de flux $F(B_2H_6)/F(Ge_2H_6)$ ou $F(PH_3)/2 * F(Ge_2H_6)$ faibles à moyens, comme présenté en **Figure A.2**. Pour des flux élevés de B_2H_6 ou de PH_3 , la concentration en Sn chute significativement dans du GeSn:B (de 6.5% vers 4.9%), comme illustré **Figure A.2 (a)**, moins dans du GeSn:P (de 6.6% vers 6.0%), comme montré en **Figure A.2 (b)**. La concentration substitutionnelle en atomes de bore est au maximum de $5.2 \times 10^{19} \text{ cm}^{-3}$, comme présenté en **Figure A.2 (c)**, tandis que l'incorporation en atomes de P, au maximum de $2.2 \times 10^{20} \text{ cm}^{-3}$, est sans doute caractérisée par la formation d'amas nanométriques de type $Sn_m P_n V$ électriquement inactifs, comme illustré en **Figure A.2** (différence entre la concentration atomique en atomes de P et concentration ionique).

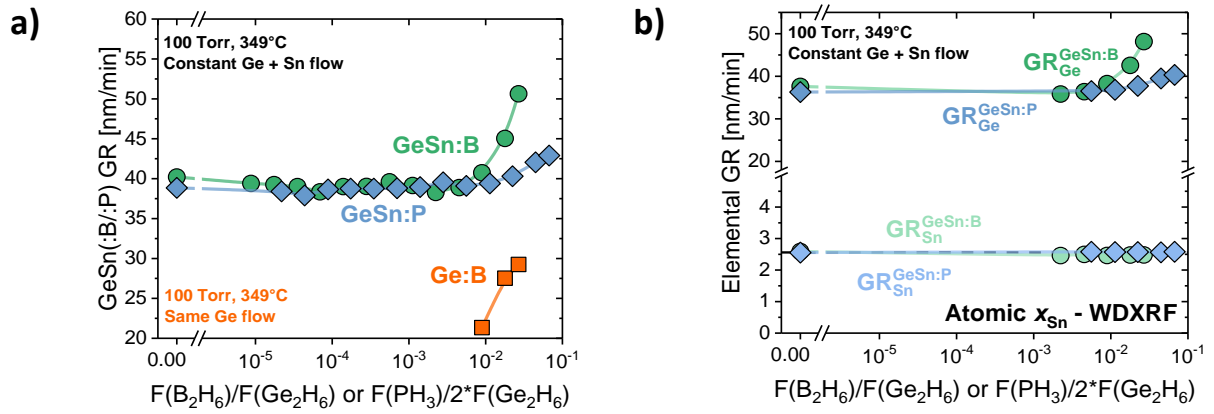


Figure A.3: Vitesses de croissance du Ge:B, du GeSn:B et du GeSn:P à 349 °C, 100 Torr pour des rapports de flux $F(B_2H_6)/F(Ge_2H_6)$ ou $F(PH_3)/2 * F(Ge_2H_6)$ variables (a). Vitesses de croissance élémentaires du germanium et de l'étain pour des couches GeSn:B et GeSn:P déduites à partir de la concentration atomique en Sn, (b). T = 349 °C, P = 100 Torr. Rapports de flux $F(Ge_2H_6)/F(H_2)$ et $F(SnCl_4)/F(H_2)$ constants à 7.92×10^{-4} et 4.69×10^{-5} , respectivement.

Les vitesses de croissance élémentaires ont été déterminées en multipliant la vitesse de croissance des alliages GeSn:B ou GeSn:P, présenté en **Figure A.3 (a)**, par la concentration en Ge ou Sn (provenant de la WDXRF) afin de mieux appréhender les mécanismes de croissance. L'introduction de $SnCl_4$ a catalysé la vitesse de croissance de GeSn comparée à du Ge pur, comme illustré en **Figure A.3 (a)**. Quand les rapports de flux $F(B_2H_6)/F(Ge_2H_6)$ ou $F(PH_3)/2 * F(Ge_2H_6)$ augmentent, la vitesse de croissance élémentaire du Sn reste constante à $2.5 \text{ nm} \cdot \text{min}^{-1}$ (**Figure A.3 (b)**). La vitesse élémentaire de croissance du Ge reste quand à elle constante vers $37 \text{ nm} \cdot \text{min}^{-1}$ pour des flux bas ou médians de dopants. Pour des flux élevés, la vitesse de croissance élémentaire augmente significativement, jusqu'à $48 \text{ nm} \cdot \text{min}^{-1}$ pour le GeSn:B ($40 \text{ nm} \cdot \text{min}^{-1}$ pour le GeSn:P). Des augmentations comparables ont été trouvées pour Ge:P et Ge:B épitaxiés à 350 °C. Cette stabilité de la vitesse de croissance élémentaire de l'étain et cette augmentation de la vitesse de croissance élémentaire du Ge sont des signes clairs d'une incorporation augmentée des atomes de Ge grâce aux atomes de bore et de phosphore en surface qui ont ouverts des sites d'incorporation (la vitesse de croissance du Ge est limitée par des réactions de surface, tandis que celle du Sn est limitée par le transport de masse [28]).

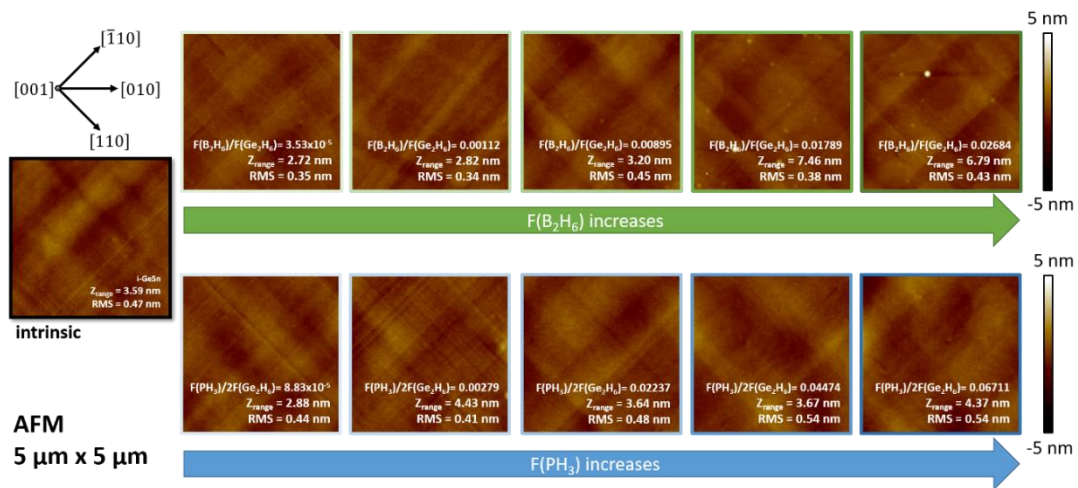


Figure A.4: Images AFM $5 \mu m \times 5 \mu m$ de la surface de couches GeSn:B de 61 nm à 80 nm d'épaisseur (en haut) GeSn:P de 76 nm à 86 nm d'épaisseur (en bas) épitaxiées à $349 \text{ }^\circ C$, 100 Torr avec des flux variables de B_2H_6 ou de PH_3 .

Des structures en double tôle ondulée dites « cross-hatches » dans les directions $\langle 110 \rangle$ ont été observées en microscopie à force atomique (AFM), comme illustré **Figure A.4**. Les surfaces GeSn:B comme GeSn:P étaient par ailleurs plutôt glisses. Les seules exceptions étaient les couches GeSn:B déposées avec les trois flux de diborane le plus élevés. Quelques îlots, sans doute dus à de la ségrégation en surface de bore et/ou d'étain, étaient alors présents en surface.

A.I.3. Dopage in-situ du GeSn et SiGeSn pour des dispositifs optiques et électroniques

La concentration en ions phosphore dans le GeSn:P était sans doute limitée par la formation d'amas Sn_mP_nV électriquement inactifs de taille nanométrique. De même, la concentration en ions bore dans le GeSn:B n'était au maximum que de quelques 10^{19} cm^{-3} . Nous avons donc cherché si l'ajout de Si et donc la formation d'alliages SiGeSn permettait l'obtention de couches significativement plus dopées. Le mécanisme de croissance, la composition et l'activation électrique ont donc été étudiés. Le passage à des couches SiGeSn dopées in-situ pourrait présenter un autre avantage, i.e. le confinement électrique des porteurs de charges dans des couches GeSn optiquement actives avec de hautes concentrations en Sn et donc d'énergies de bande interdite plus faibles, avec à la clef une augmentation de la performance des dispositifs.

Les vitesses de croissance du SiGeSn dopé in-situ bore ou phosphore étaient de l'ordre de 30 nm min^{-1} , i.e. des valeurs inférieures à celles pour GeSn:B et GeSn:P (40 nm min^{-1}) et les mêmes flux de Ge_2H_6 et $SnCl_4$. Les vitesses de croissance de ces dernières augmentaient par ailleurs significativement pour de hauts flux de dopants. En comparaison, la vitesse de croissance de SiGeSn:B augmente légèrement tandis que celle du SiGeSn:P diminue lorsque le flux de dopants augmente (**Figure A.5**). Alors que B_2H_6 comme PH_3 ouvrent sans doute des sites d'incorporation en surface pour le GeSn:(B/:P) et le SiGeSn:B, il se pourrait que la formation de composés intermédiaires en phase gazeuse ait réduit la vitesse de croissance du SiGeSn:P.

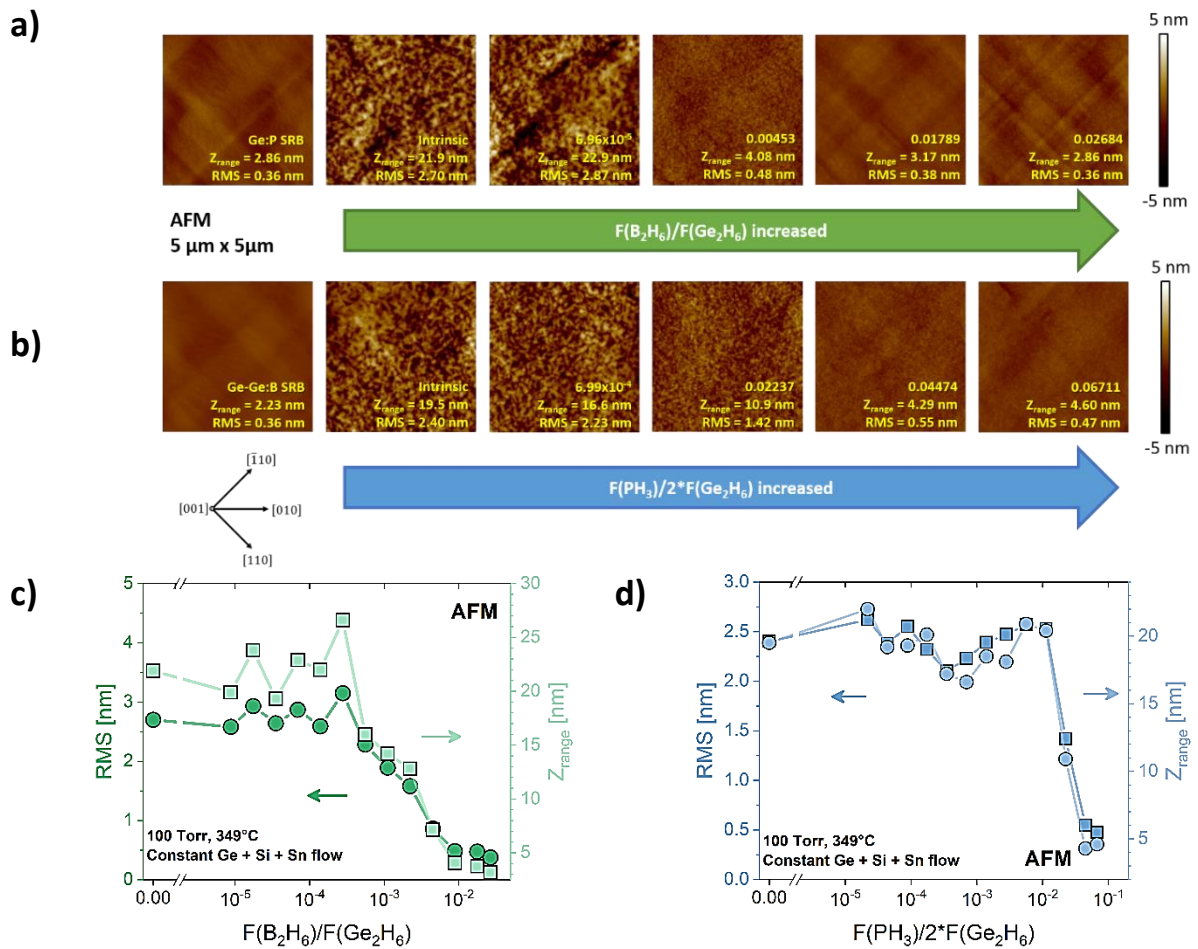
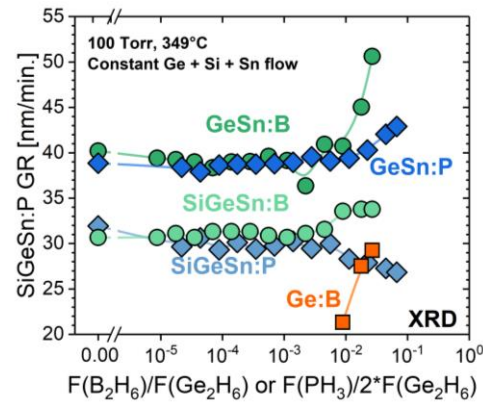


Figure A.5: Des images AFM 5 μm x 5 μm des surfaces de couches SiGeSn:B (de 69 nm à 76 nm d'épaisseur) (a) and SiGeSn:P (de 72 nm à 60 nm d'épaisseur) (b) épitaxiées à 349 °C, 100 Torr avec des flux B_2H_6 ou PH_3 variés sur des couches tampons Ge/Ge:P ou Ge/Ge:B. Rugosités RMS de surface et Z_{range} pour SiGeSn:B (c) et SiGeSn:P (d) et des flux variés de B_2H_6 ou de PH_3 . Les rapports de flux $F(Ge_2H_6)/F(H_2)$, $F(SnCl_4)/F(H_2)$ et $F(Si_2H_6)/F(H_2)$ étaient constants à 7.92×10^{-4} , 4.69×10^{-5} et 1.25×10^{-3} , respectivement.

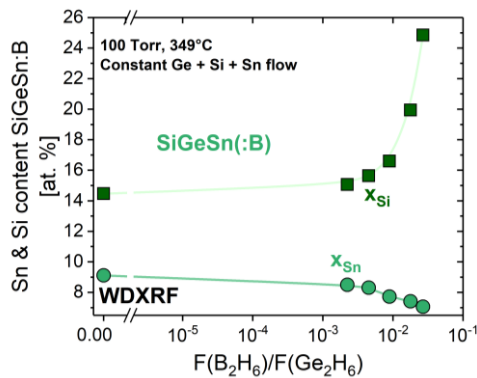
La qualité de surface de couches SiGeSn fortement dopées est fortement améliorée par rapport à celle de couches SiGeSn intrinsèques, avec la même morphologie en double tôle ondulée et la même rugosité de surface (RMS 0.40 nm) que pour le GeSn pour des hauts flux des dopants (**Figure A.5**).

A flux constants de Ge_2H_6 , de Si_2H_6 et de $SnCl_4$, on a constaté, lorsque le flux de gaz dopants augmentait, (i) dans SiGeSn:B, une légère diminution de la concentration en Sn et une très forte augmentation de la concentration en Si et (ii) dans SiGeSn:P, une augmentation de la concentration en Sn ainsi qu'une légère augmentation de la concentration en Si (**Figure A.6 (b) et (c)**). Des rapports entre concentrations de Si et de Sn de 3.5, avec des concentrations en Si de 25%, ont été obtenus dans SiGeSn :B, ce qui devrait permettre de bénéficier d'un fort confinement électrique.

a)



c)



d)

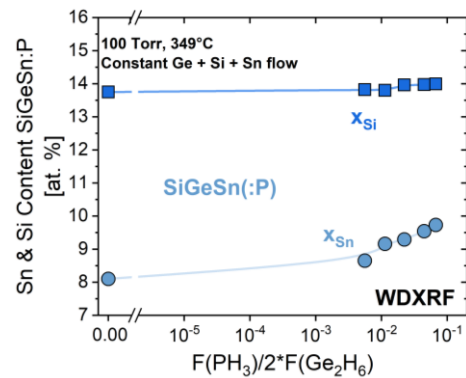


Figure A.6: Vitesses de croissance du SiGeSn:B comme SiGeSn:P (a) et concentrations atomiques (WDXRF) en Sn et Si dans des couches SiGeSn:B (b) comme SiGeSn:P (c) en fonction du flux de gaz dopants. $T = 349\text{ }^{\circ}\text{C}$, $P = 100\text{ Torr}$. Les rapports de flux $F(\text{Ge}_2\text{H}_6)/F(\text{H}_2)$, $F(\text{SnCl}_4)/F(\text{H}_2)$ et $F(\text{Si}_2\text{H}_6)/F(\text{H}_2)$ étaient constants à 7.92×10^{-4} , 4.69×10^{-5} et 1.25×10^{-3} , respectivement.

Des concentrations ioniques maximales de $2.1 \times 10^{20}\text{ cm}^{-3}$ ont été atteintes dans le SiGeSn:B. Ces concentrations sont sept fois plus élevées que dans le GeSn:B avec $3 \times 10^{19}\text{ cm}^{-3}$ (**Figure A.7 (a)**). Des concentrations trois fois plus élevées en ions phosphore que dans du GeSn:P (au maximum : $7 \times 10^{19}\text{ cm}^{-3}$) ont par ailleurs été obtenues dans du SiGeSn:P (**Figure A.7 (b)**). Aucune chute de la concentration en ions phosphore a par ailleurs été observée pour de hauts flux de PH_3 . Tout ceci pourrait être dû à une concentration moindre d'amas $\text{Sn}_m\text{P}_n\text{V}$ de taille nanométrique dans le SiGeSn:P.

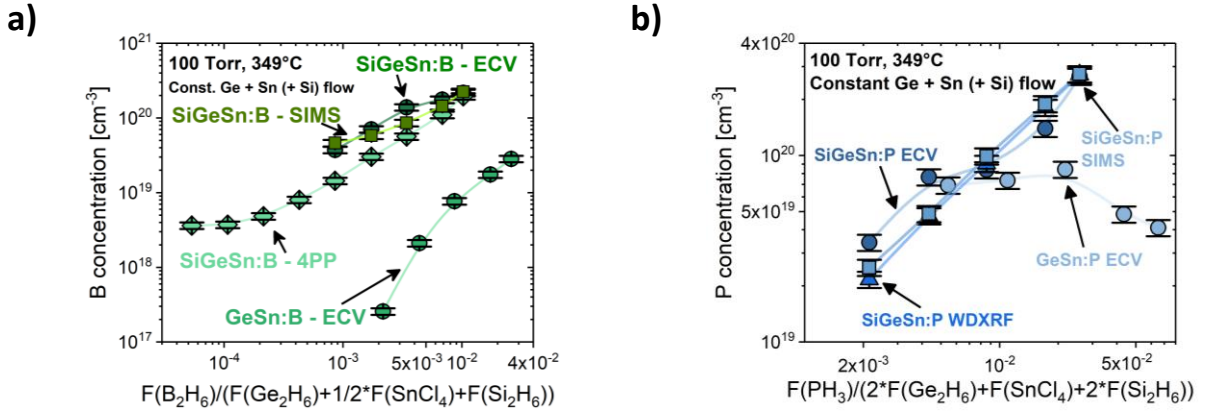


Figure A.7: Concentrations en atomes ou ions B (a) et en atomes ou ions P (b) dans des couches SiGeSn:B ou SiGeSn:P. $T = 349\text{ }^{\circ}\text{C}$, $P = 100\text{ Torr}$. Les rapports de flux $F(\text{Ge}_2\text{H}_6)/F(\text{H}_2)$, $F(\text{SnCl}_4)/F(\text{H}_2)$ et $F(\text{Si}_2\text{H}_6)/F(\text{H}_2)$ étaient constants à 7.92×10^{-4} , 4.69×10^{-5} et 1.25×10^{-3} , respectivement.

A.I.4. Recuit Laser Nanoseconde des couches de Ge dopé bore in-situ pour l'activation des dopants

Le germanium dope peut être utilisé pour des sources et drains des transistors pMOS Ge [29] ou comme couche de type p-type dans des photodétecteurs Ge (PDs) de type p-i-n Ge [30]. Si sa température de croissance est suffisamment basse, du Ge dopé bore peut même être utilisé pour des PDs et diodes électroluminescentes à base de GeSn. [31] Les dispositifs NIR et MIR pompés électriquement gagnent rapidement en intérêt, notamment depuis la démonstration d'un effet laser pompé électriquement jusqu'à 100 K dans des structures à base de GeSn par l'Université d'Arkansas. [22], [23]

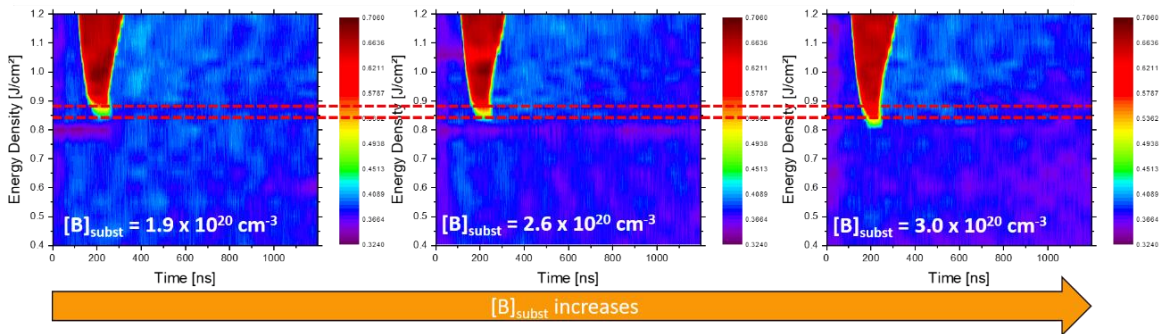


Figure A.8: Cartes TRR pour des rapports de flux $F(\text{B}_2\text{H}_6)/F(\text{Ge}_2\text{H}_6)$ variées. La ligne rouge montre la densité d'énergie pour laquelle on est au seuil de fusion. Les couches Ge:B ont été épitaxiées à $349\text{ }^{\circ}\text{C}$, $P = 100\text{ Torr}$ avec rapports de flux $F(\text{B}_2\text{H}_6)/F(\text{Ge}_2\text{H}_6)$ de 8.95×10^{-3} , 1.79×10^{-2} and 2.68×10^{-2} (de gauche à droite), tandis que rapport de flux $F(\text{Ge}_2\text{H}_6)/F(\text{H}_2)$ était constant à 7.92×10^{-4} .

La concentration ionique dans des binaires Si:P a été augmenté significativement grâce à la dissolution d'amas P par NLA. Des alliages Ge:B avec d'ultra-haute concentrations en bore peuvent être obtenus, de manière métastable, grâce au dopage in-situ. Cependant, l'activation

électrique dans ces binaires Ge:B semble limitée par la formation d'amas électriquement inactifs. Nous avons donc étudié la dissolution de ces amas grâce au NLA et la possibilité d'améliorer ainsi les propriétés électriques de ces couches Ge:B.

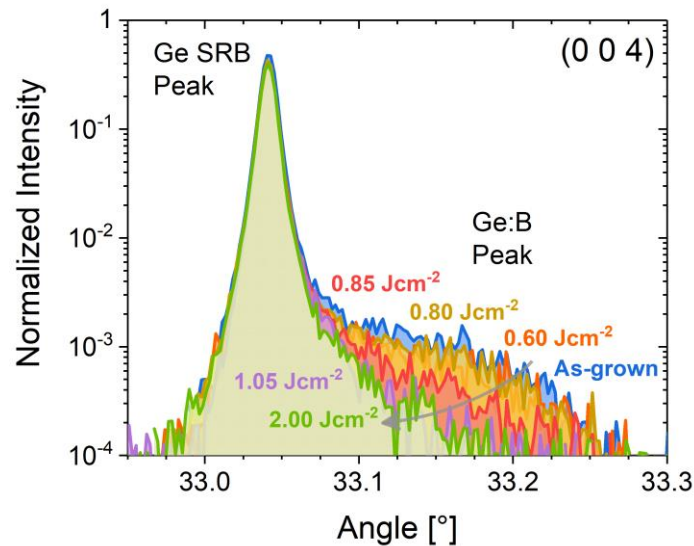


Figure A.9: Balayages ω - 2θ normalisés en intensité autour de l'ordre (0 0 4) de la diffraction X pour une couche Ge:B après croissance (39 nm) avec $[B]_{\text{subst.}} = 2.6 \times 10^{20} \text{ cm}^{-3}$ (bleu) et après NLA avec des densités d'énergie allant de 0.60 Jcm^{-2} (orange) jusqu'à 2.00 Jcm^{-2} (vert).

Le seuil de fusion, qui peut être déterminé grâce à des cartes de type Time Resolved Reflectivity acquises lors du NLA du Ge:B (**Figure A.8**), chute de 0.875 Jcm^{-2} à 0.85 Jcm^{-2} en augmentant la concentration substitutionnelle en bore. Ceci pourrait être dû à des différences de qualité cristalline, de rugosité de surface et/ou de concentrations en B.

La **Figure A.9** montre des balayages ω - 2θ normalisés autour de l'ordre (0 0 4) de la DRX pour ces couches Ge :B recuites. Le pic Ge:B ne change pas significativement en dessous du seuil de fusion à 0.825 Jcm^{-2} . Au-dessus de celui-ci, le pic Ge:B devient de moins en moins intense et disparaît au seuil de fusion complète de la couche Ge:B (1.05 Jcm^{-2}). Des recuits NLA à des densités d'énergie encore plus élevées (2.00 Jcm^{-2}) n'ont pas engendré une réapparition du pic Ge:B.

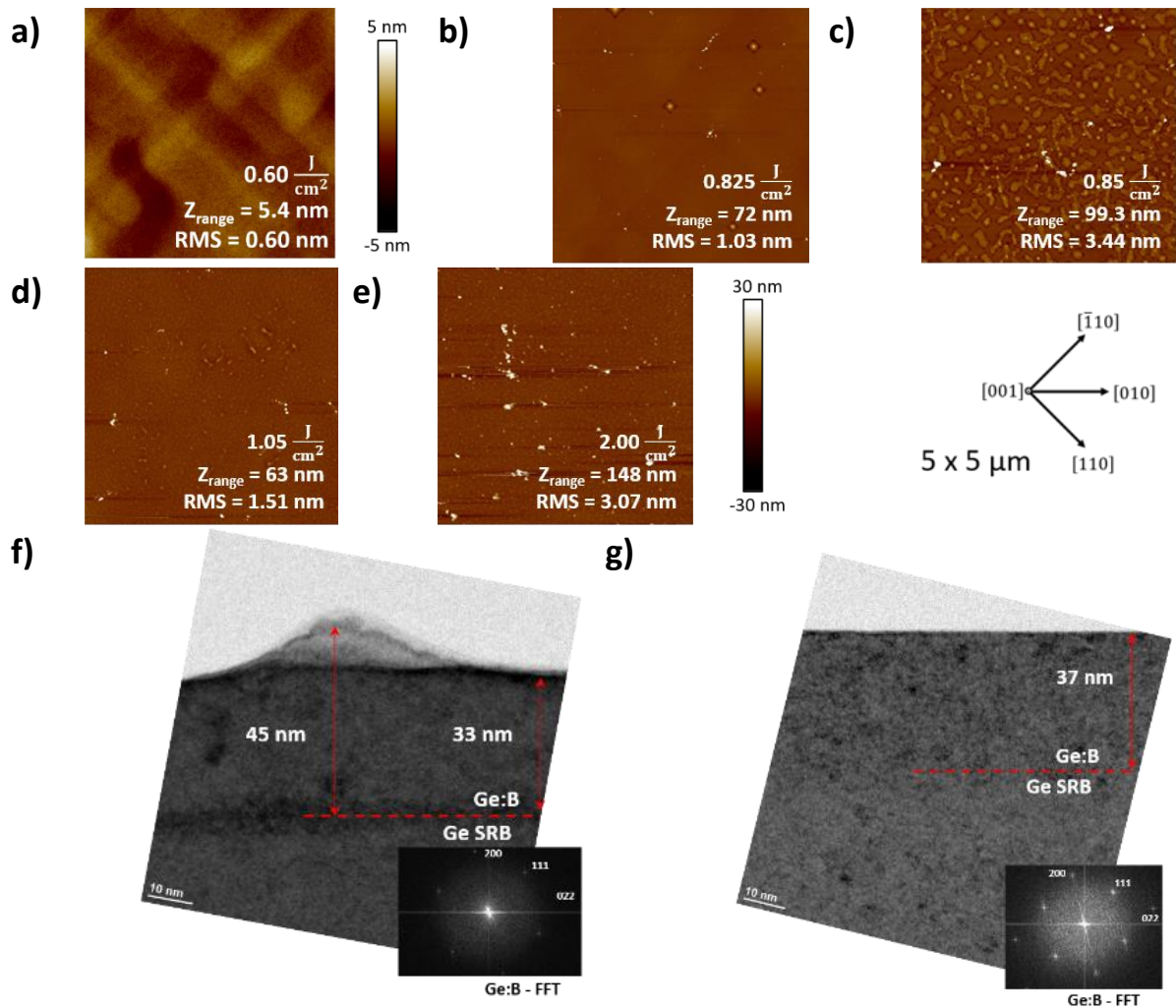


Figure A.10: Images AFM $5 \mu\text{m} \times 5 \mu\text{m}$ de la surface d'une couche Ge:B (de 39 nm d'épaisseur, initialement) avec $[\text{B}]_{\text{subst.}} = 2.6 \times 10^{20} \text{ cm}^{-3}$, ceci après NLA à 0.60 Jcm^{-2} ((a), échelle en z de -5 nm à 5 nm), 0.825 Jcm^{-2} (b), 0.85 Jcm^{-2} (c), 1.05 Jcm^{-2} (d) and 2.00 Jcm^{-2} (e) (avec une échelle en z de -30 nm à 30 nm). Les directions cristallographiques sont données au milieu à droite. Images HR-TEM de couches Ge dopées B in-situ après recuits NLA à 0.85 Jcm^{-2} (f) et 1.05 Jcm^{-2} (g).

Au seuil de la fusion, des structures de surface localisées ont fondu, comme montré par les images AFM $5 \mu\text{m} \times 5 \mu\text{m}$ en **Figure A.10 (a) à (e)**. Celles-ci étaient plutôt de forme rectangulaire, avec des faces selon dans les directions cristalline $\langle 110 \rangle$, comme la structure en double tôle ondulée après croissance. La taille de ces structures étaient plutôt constante. Des structures de surface similaires ont été reportées pour SiGe sur Si.

Des images en microscopie électronique en transmission à haute résolution de couches Ge:B après recuits NLA à 0.85 Jcm^{-2} sont montrées en **Figure A.10 (f) et (g)**. La couche Ge:B semble avoir une épaisseur de 33 nm, ce qui un peu moins épais que celle de la couche après croissance, c.-à-d. 39 nm. Il se pourrait donc qu'une partie de la matière ait migré dans les structures de surface de 12 nm de haut. [32] Ces dernières sont plus claires en TEM, ce qui pourrait être dû à une accumulation des atomes bore plus légers ou à cause d'une épaisseur de la

lamelle plus mince. La spectroscopie infrarouge à transformée de Fourier a montré une qualité cristalline dégradée pour le Ge:B après le NLA.

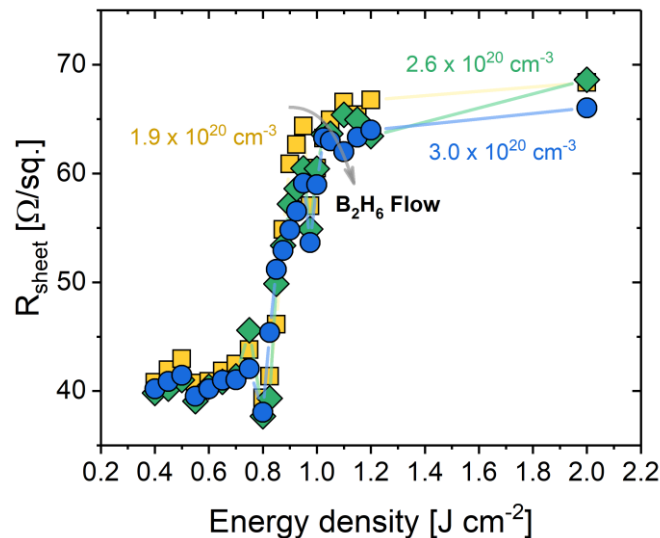


Figure A.11: Mesure de la résistance carrée R_S avec la technique 4 pointes pour différentes concentrations de B et des densités d'énergie variées.

Le recuit laser a conduit à une redistribution du bore, avec la formation d'amas électriquement inactifs qui n'ont pas contribué au courant. Par conséquent, la résistance carrée a augmenté de 70% de $39.82 \Omega/\square$ à $68.62 \Omega/\square$, quand la couche a fondu, illustré en **Figure A.11**. Ce comportement semble indépendant de la concentration substitutionnelle de bore après croissance. Même des recuits avec plusieurs pulses laser envoyés sur la même position et différentes densités d'énergie n'ont pas été en capacité d'augmenter l'activation électrique. Une légère amélioration de la résistance carrée sous le seul de fusion a toutefois été constaté, qui devra être confirmé lors de futures expériences.

Plusieurs pulses laser ont conduit à la formation (i) de structures en surface, dont la taille augmentait avec le nombre de pulses et la densité d'énergie et (ii) d'amas électriquement inactifs qui n'ont pas contribué à la conduction. Plus d'atomes de bore ont été redistribués et plus d'amas de bore en sites interstitiels électriquement inactifs ont semblé-t-il être formés dans le régime de fusion. Des recuits NLA dans le régime de fusion n'ont pas été en capacité d'améliorer l'activation électrique des atomes de B dans des couches de Ge fortement dopées, contrairement à ce qui avait été obtenu pour des couches de Si fortement dopées phosphore.

A.I.5. Recuit laser nanoseconde des couches GeSn pseudomorphes avec des concentrations variées en étain

Des recuits NLA pourraient être en capacité d'améliorer les performances de dispositifs d'émission de lumière à base de GeSn sur Si grâce à une amélioration de la qualité structural et une modification de la structure de bande (relaxation de la contrainte résiduelle et compression). L'emploi de procédés standards de recuit durant quelques secondes à quelques dizaines de secondes est complexe à cause de la ségrégation de surface de l'étain. Le NLA offre, par contre,

une opportunité unique de recuire des hétérostructures GeSn de manière très contrôlé et hors équilibre.

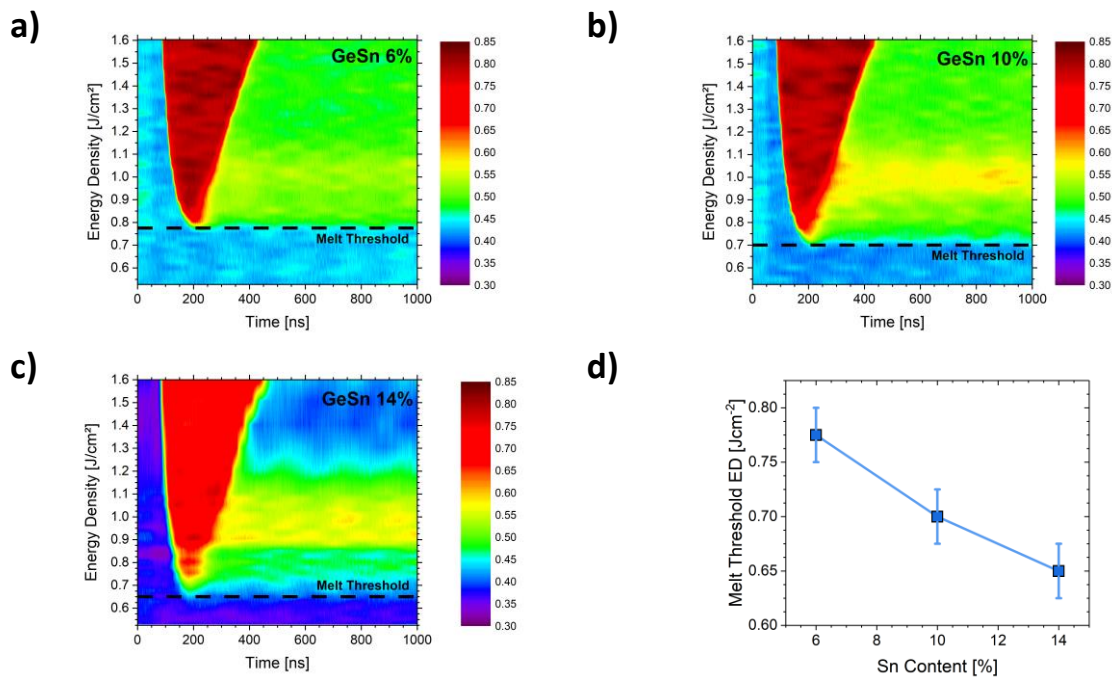


Figure A.12: Des cartes TRR (taille d'échelon 0.025 Jcm^{-2}) pour des couches GeSn 6% (a), 10% (b) and 14% (c) pseudomorphique (38-41 nm). La ligne noire correspondent au seuil de la fusion. (d) Le seuil de la fusion pour chaque concentration d'étain.

Des recuits NLA ont donc été menés sur des couches GeSn 6%, 10% et 14% de plusieurs dizaines de nanomètres d'épaisseur épitaxiées sur des couches tampons en Ge. La gamme de densités d'énergie explorée était de 0.525 Jcm^{-2} jusqu'à 1.60 Jcm^{-2} . Les cartes TRR en **Figure A.12** montrent que le seuil de fusion se déplace vers des densités d'énergie plus faible lorsque la concentration en étain est plus élevée.

Au seuil de fusion, des lignes sont apparues sur la surface de GeSn, comme illustré, pour 14% d'étain, en **Figure A.13**. Ces structures de surface étaient, toutefois, plus petites qu'avec des recuits plus standards, sans gouttelettes d'Sn en bout de traces. [33] Pour des densité d'énergie légèrement au-dessus du seuil de la fusion, des structures de surface fondues ont été observées en AFM et le pic DRX associé à la couche de GeSn s'est décalé vers de plus grands angles d'incidence, selon toutes probabilités à cause de la redistribution de l'étain. Les structures de surfaces fondues se sont multipliées et ont commencé à se rejoindre quand la densité d'énergie a continué à augmenter. La fusion de structures de surface a engendré des surfaces significativement plus rugueuses avec une Z_{range} autour de 50 nm. En se rapprochant de la fusion de la couche entière à 1.00 Jcm^{-2} , les surfaces sont devenues plus glisses, avec une rugosité RMS autour de 1.20 nm.

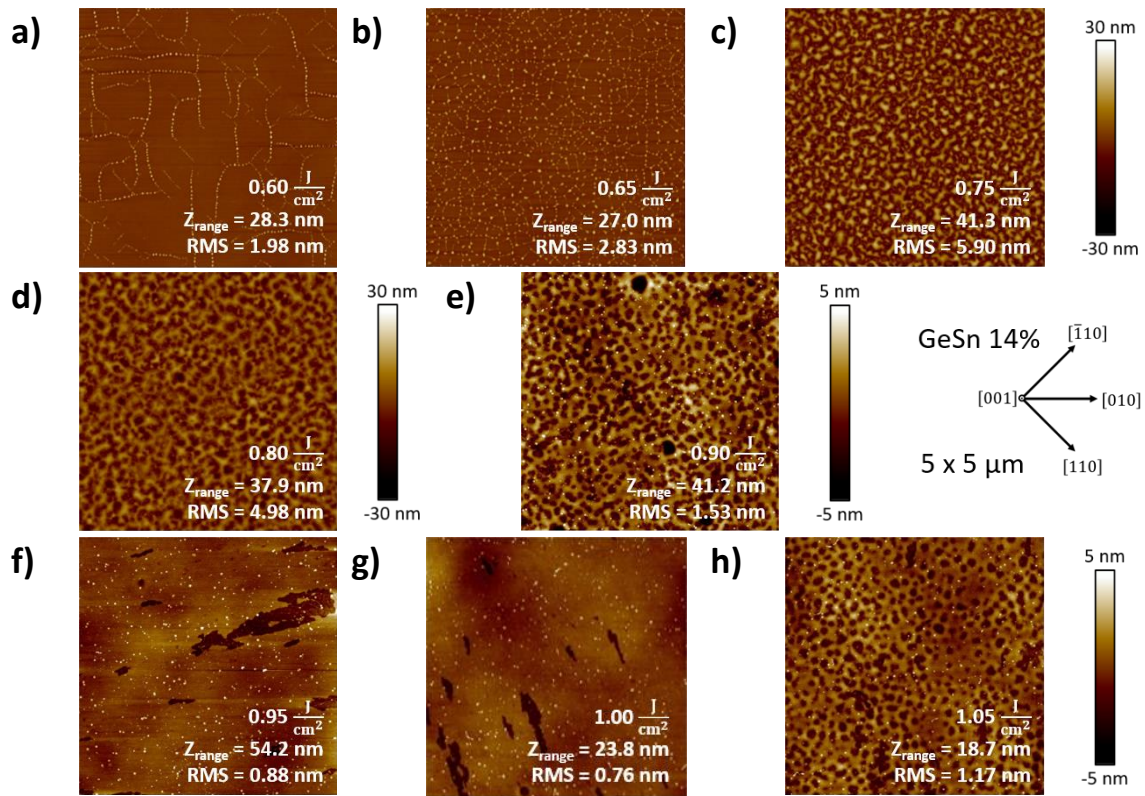


Figure A.13: Images $5 \mu\text{m} \times 5 \mu\text{m}$ de couches GeSn 14% pseudomorphes après recuit NLA à 0.60 Jcm^{-2} (a), 0.65 Jcm^{-2} (b), 0.75 Jcm^{-2} (c), 0.80 Jcm^{-2} (d) ((a), (b), (c), (d) échelle de -30 nm à 30 nm), 0.825 Jcm^{-2} (b), 0.85 Jcm^{-2} (c), 1.05 Jcm^{-2} (d) and 2.00 Jcm^{-2} (e) (tous avec une échelle de -30 nm à 30 nm) 0.90 Jcm^{-2} (e), 0.95 Jcm^{-2} (f), 1.025 Jcm^{-2} (g) and 1.05 Jcm^{-2} (h) ((e) à (h) avec une échelle de 5 nm). Les directions cristallographiques sont données en milieu à droite.

Le pic DRX s'est déplacé, post recuit NLA, à des angles caractéristique de hautes concentrations en Sn, illustré en **Figure A.14**, avec une dépendance claire en fonction de la concentration en Sn de départ. A titre d'exemple, une concentration en étain de 6.8% a été obtenue après recuit NLA d'une couche GeSn 14%. La qualité cristalline de couche étaient plus élevée que celles de couches GeSn recuites avec des densités d'énergie intermédiaires. La formation de telles couches à concentrations d'étain plutôt élevée n'a pas été reportée auparavant pour des recuits plus standards et serait spécifique aux recuits NLA ultra-rapides.

Dans la gamme de densités d'énergie explorée, la résistance carrée a chuté de 38% et le signal TRR était plus élevé après recuit. Quand la densité d'énergie a augmenté, la partie haute des substrats virtuels en Ge en dessous de nos couches de GeSn a fondu, conduisant à une augmentation de la rugosité de surface (formation de nombreuses petites structures). La concentration en étain a lentement et continuellement chuté, comme montré par le déplacement du pic DRX associé à la couche de GeSn vers le pic du substrat virtuel Ge (**Figure A.14**).

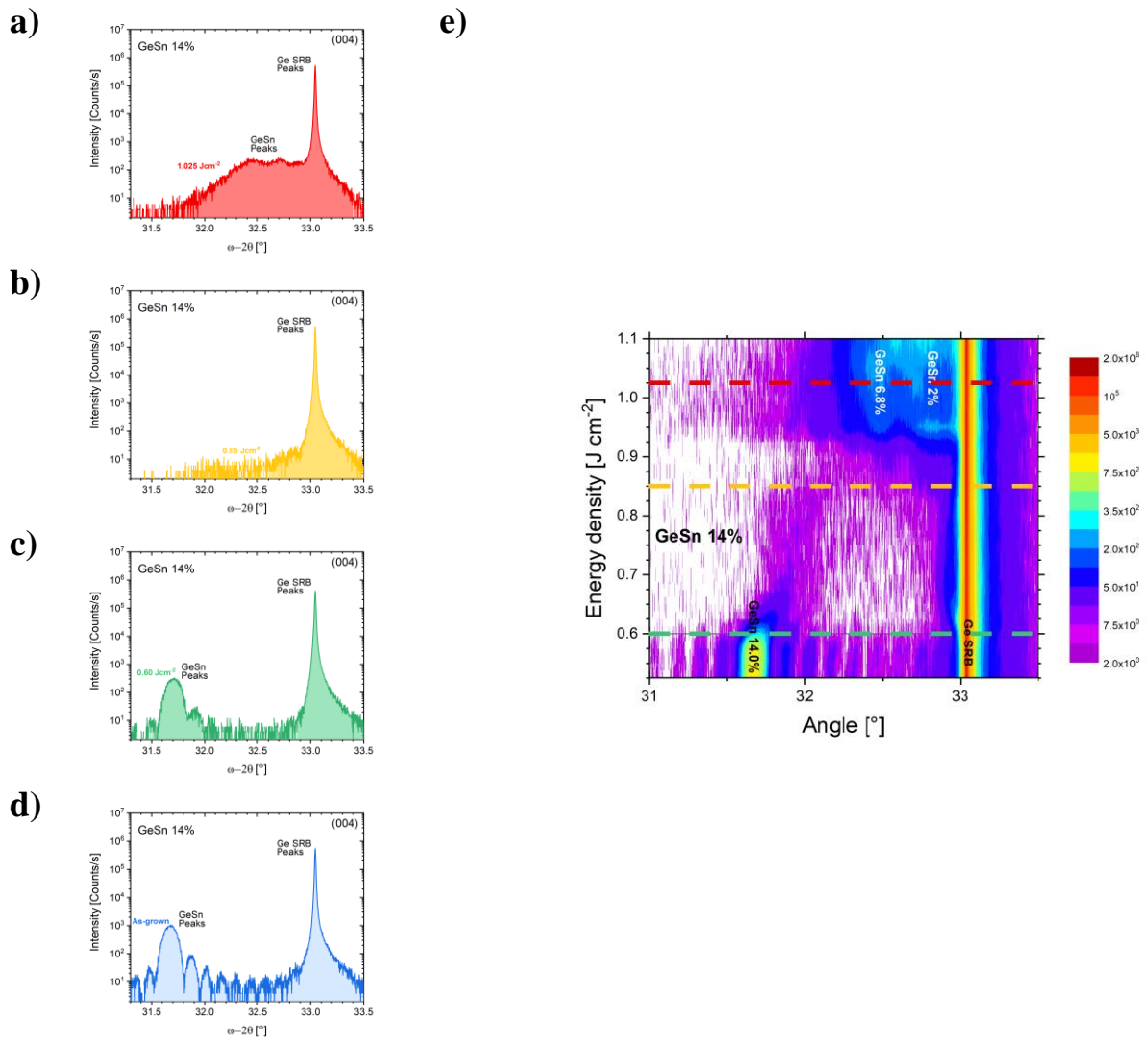


Figure A.14: Balayages $\omega-2\theta$ normalisés autour de l'ordre (0 0 4) de la diffraction X pour une couche GeSn 14% recuite NLA à 1.00 Jcm^{-2} (rouge (a)), 0.85 Jcm^{-2} (jaune (b)) and 0.60 Jcm^{-2} (verte (c)) ou sans recuit NLA (bleu (d)). (f) Carte montrant la résultante de balayages $\omega-2\theta$ à différentes densités d'énergie (échantillonnage tous les 0.025 Jcm^{-2}). Les lignes colorées montrent les densités d'énergie des figures (a) à (d).

A.I.6. Recuit laser nanoseconde en pulsation des couches GeSn intrinsèque et implanté phosphore

Des recuits NLA pulsés ont été menés sur des couches GeSn intrinsèque 6%, 10% et 14% et (ii) GeSn 6% implanté P ($1 \times 10^{15} \text{ cm}^{-2}$) de quelques dizaines de nanomètres d'épaisseur épitaxiées pseudomorphiquement sur de substrat virtuel Ge sur de substrats Si. La maximum de densité d'énergie sondée était de 1.60 Jcm^{-2} .

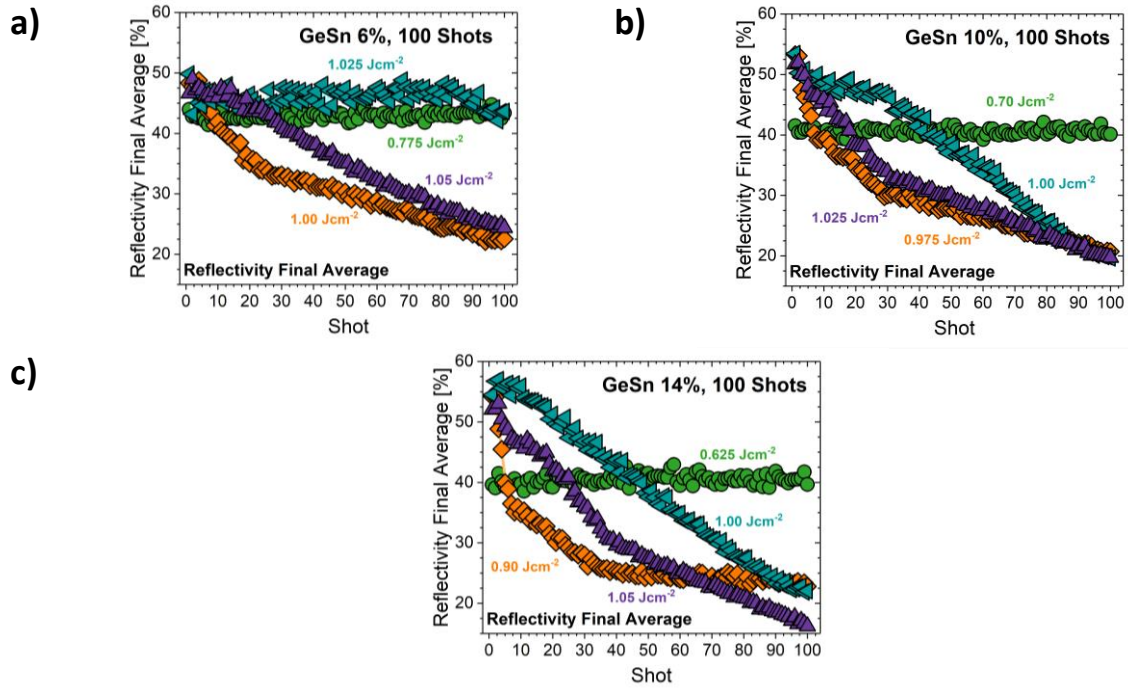


Figure A.15: Augmentation (par rapport à la réflectivité de surface initiale) de la réflectivité de surface pour différents nombres de recuits NLA à différentes énergies pour GeSn 6% (a), GeSn 10% (b) et GeSn 14% (c).

Des petites structures de surfaces sont apparues au seuil de la fusion ($ED = 0.60 \text{ Jcm}^{-2} - 0.775 \text{ Jcm}^{-2}$), sans impact toutefois sur le signal TRR lorsque le nombre de pulses a augmenté. Pour de plus grandes densité d'énergie, de grandes structures de surface sont apparus, avec une réduction du signal TRR, comme illustré **Figure A.15**.

Une surface lisse a été formée lorsque la totalité de la couche GeSn a fondu ($ED = 1.00 \text{ Jcm}^{-2} - 1.025 \text{ Jcm}^{-2}$), comme illustré en **Figure A.16**. L'interface liquide / solide était alors l'interface lisse GeSn / Ge, avec la formation, après solidification, d'une surface lisse. [34], [35] Pour plus de 10 pulses laser à une densité d'énergie $ED = 1.00 \text{ Jcm}^{-2} - 1.025 \text{ Jcm}^{-2}$, le haut du substrat virtuel Ge a fondu et de grandes structures ont été formées en surface.

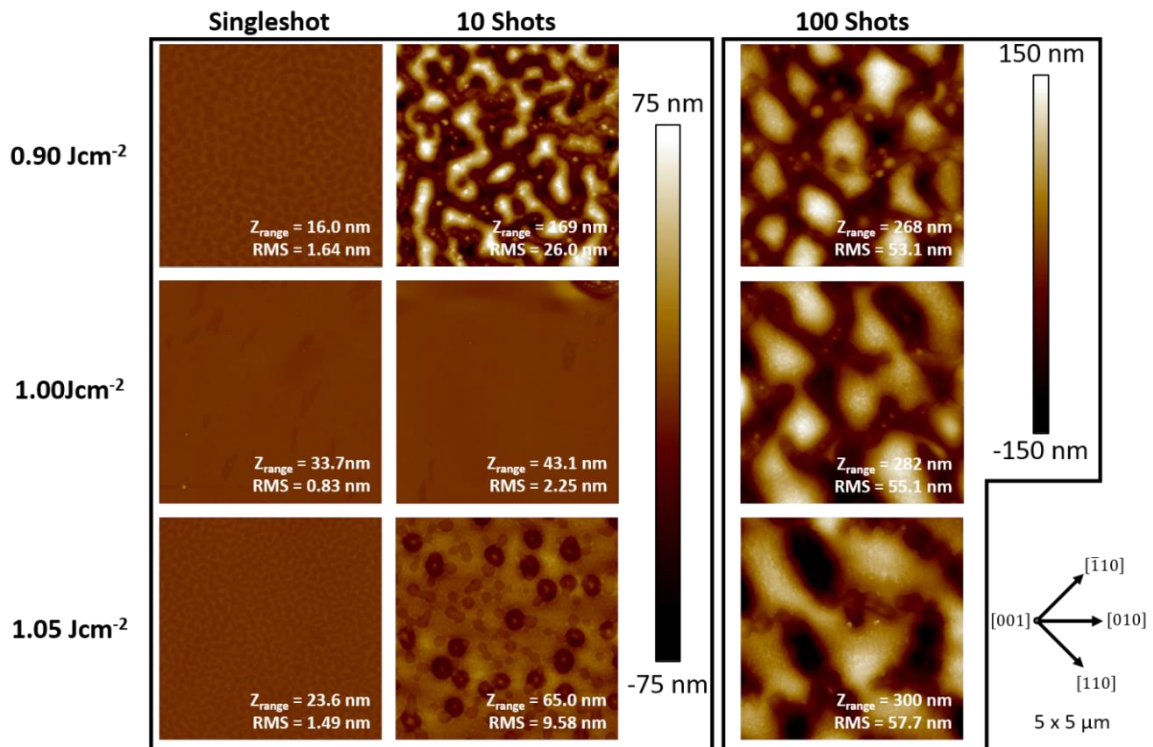


Figure A.16: $5 \mu\text{m} \times 5 \mu\text{m}$ AFM de couche GeSn 14% pseudomorphique (36 nm) après NLA avec des EDs autour du seuil de la fusion (augmentation de haut en bas) et au maximum 100 pulsation (de gauche à droite). L'échelle de 75 nm pour de pulsations au maximum 10 et 150 nm pour des pulsations de 100. Les directions cristallographiques sont données en bas à droite.

Des mesures en microscopie électronique à balayage avec spectroscopie de rayons X à dispersion d'énergie ont montré que ces structures de surface étaient riches en Sn, comme illustré en **Figure A.17 (a) à (d)**. Un déplacement du pic DRX GeSn vers le pic de substrat virtuel Ge a été mis en évidence pour de multiples pulses laser, comme illustré en **Figure A.17 (e)**. Des profils de spectrométrie de masse des ions secondaires, **Figure A.17 (f)**, ont montré une redistribution des atomes d'étain dans l'empilement (premier dix nanomètres avec des incertitudes significatif (limitation SIMS)).

En ce qui concerne le GeSn implanté phosphore, une recristallisation explosive [36]–[38] a été mise en évidence, grâce à la carte TRR de la **Figure 1.6.4**, pour $ED = 0.45 Jcm^{-2}$ et une deuxième fusion autour de $0.70 Jcm^{-2}$. La queue d'intensité aux alentours des $1.10 Jcm^{-2}$ était sans doute due à la formation d'une surface lisse pour une fonte complète de la couche GeSn:P.

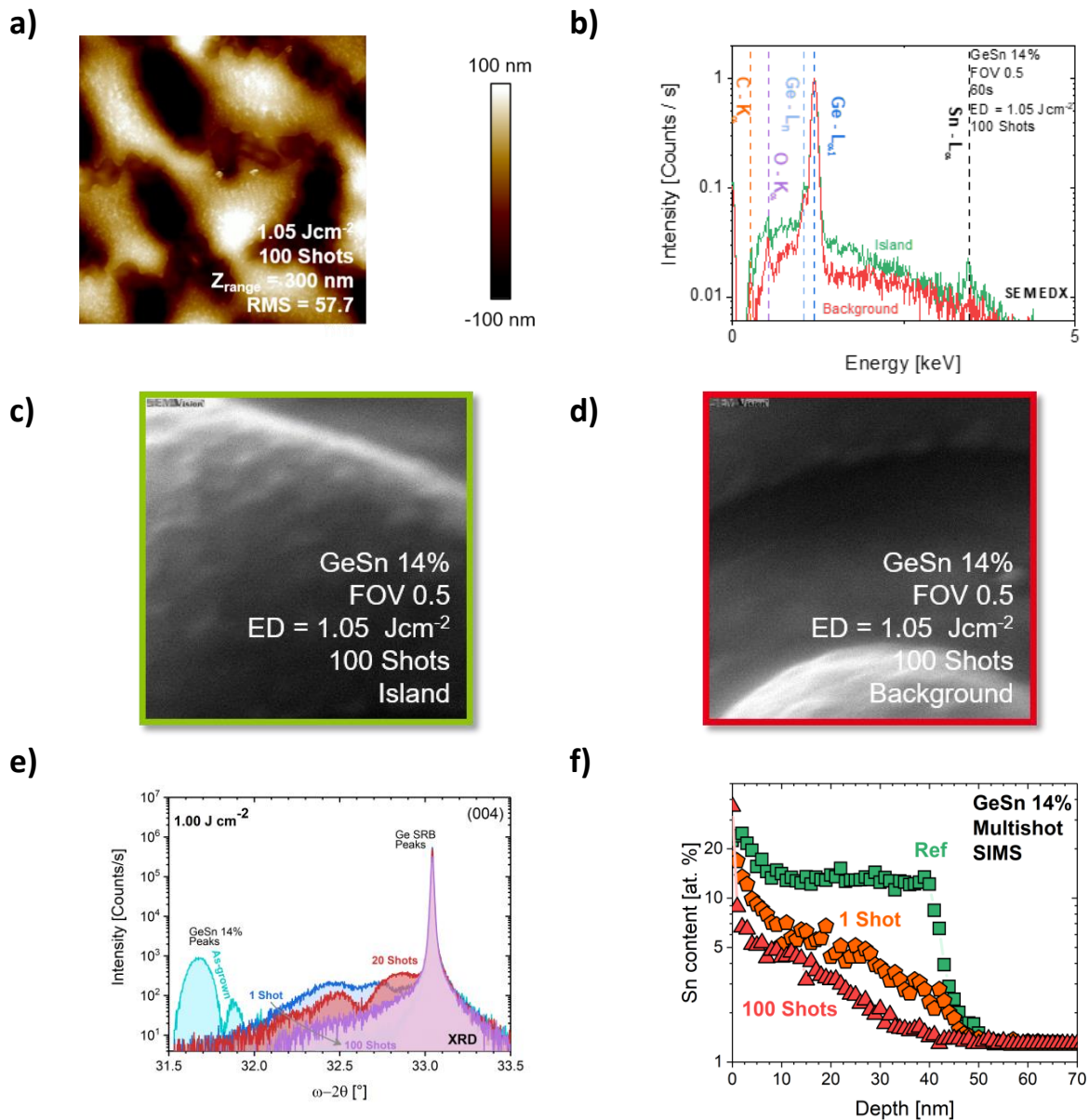


Figure A.17: image AFM $5 \mu\text{m} \times 5 \mu\text{m}$ de la surface d'une couche GeSn 14% de 36 nm d'épaisseur après NLA avec $ED = 1.05 \text{ Jcm}^{-2}$. Echelle des z: 100 nm. (b) Profils EDX pour une région avec des structures de surface, comme en (c), et d'une région sans structures de surface, comme en (d). (e) Balayages $\omega-2\theta$ normalisé autour de l'ordre (0 0 4) de la diffraction X pour une couche de GeSn 14% sur couche tampon Ge après NLA à 1.00 Jcm^{-2} et différents nombres de pulses (1 (bleu), 20 (rouge) et 100 (violet)). (f) Profils SIMS d'étain dans une GeSn 14% (de 36 nm d'épaisseur) sur couche tampon Ge après 1 (orange) ou 100 (rouge) recuits NLA à 1.00 Jcm^{-2} .

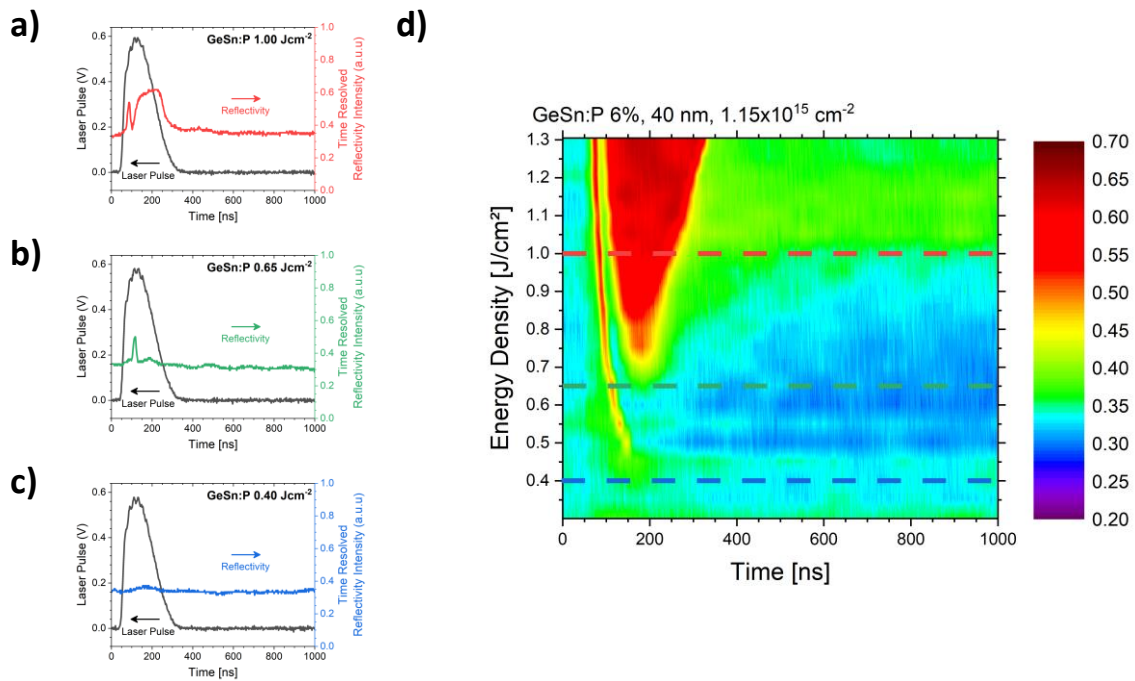


Figure A.18: Profils post recuit NLA (ED = 0.40 Jcm⁻² en bleu, 0.65 Jcm⁻² en vert et 1.00 Jcm⁻² en rouge) et carte TRR (échantillonnage tous les 0.025 Jcm⁻²) pour une couche de GeSn 6% implantée P (41 nm d'épaisseur) Les lignes colorées montrent les EDs des figures (a) à (c).

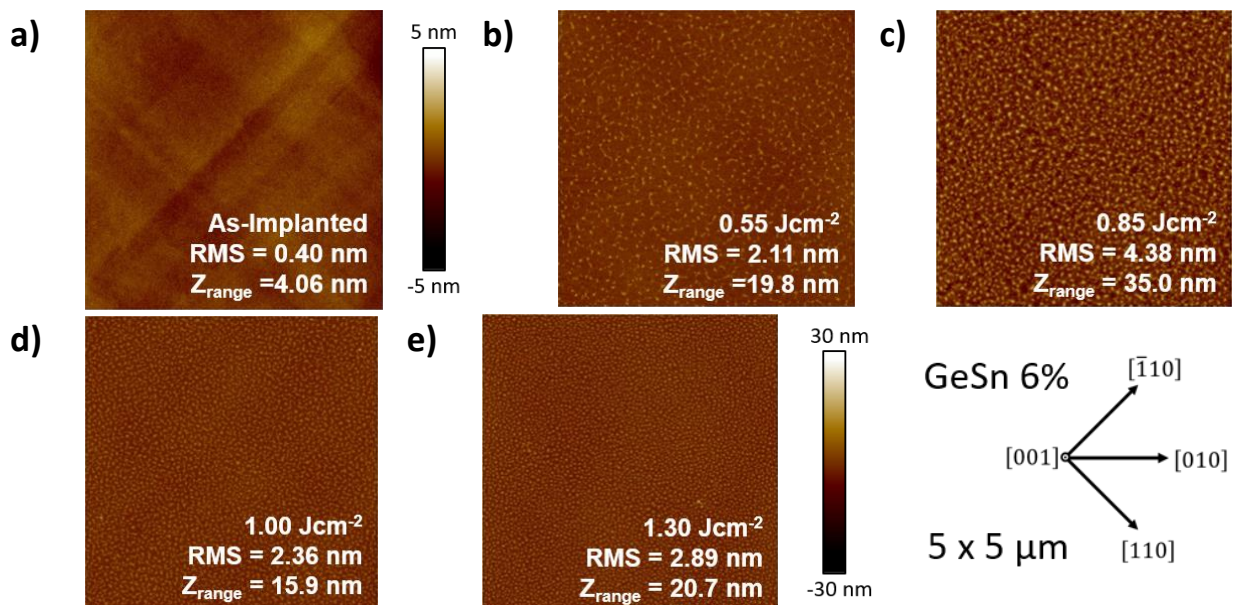


Figure A.19: Images AFM 5 μm x 5 μm de couches GeSn 6% implantées P (41 nm) avant NLA ((a), échelle des z: 5 nm) et après recuits NLA à 0.55 Jcm⁻² (b), 0.85 Jcm⁻² (c), 1.00 Jcm⁻² (d) et 1.30 Jcm⁻² (e) ((b) à (e): échelle des z de 30 nm). Les directions cristallographiques sont données en bas à droite.

Les images AFM de la surface de cette couche GeSn:P avant et après recuits NLA à différents ED montrent la présence d'une structure en double ondulée post épitaxie (**Figure A.19 (a)**) et de surfaces plus rugueuses post recuit NLA. La surface était toutefois plus lisse, à ED = 1.00 Jcm⁻² et 1.30 Jcm⁻² (**Figure A.19 (d)** et **(e)**) qu'à ED = 1.00 Jcm⁻² (**Figure A.19 (c)**), avec des structures de surface plus petites.

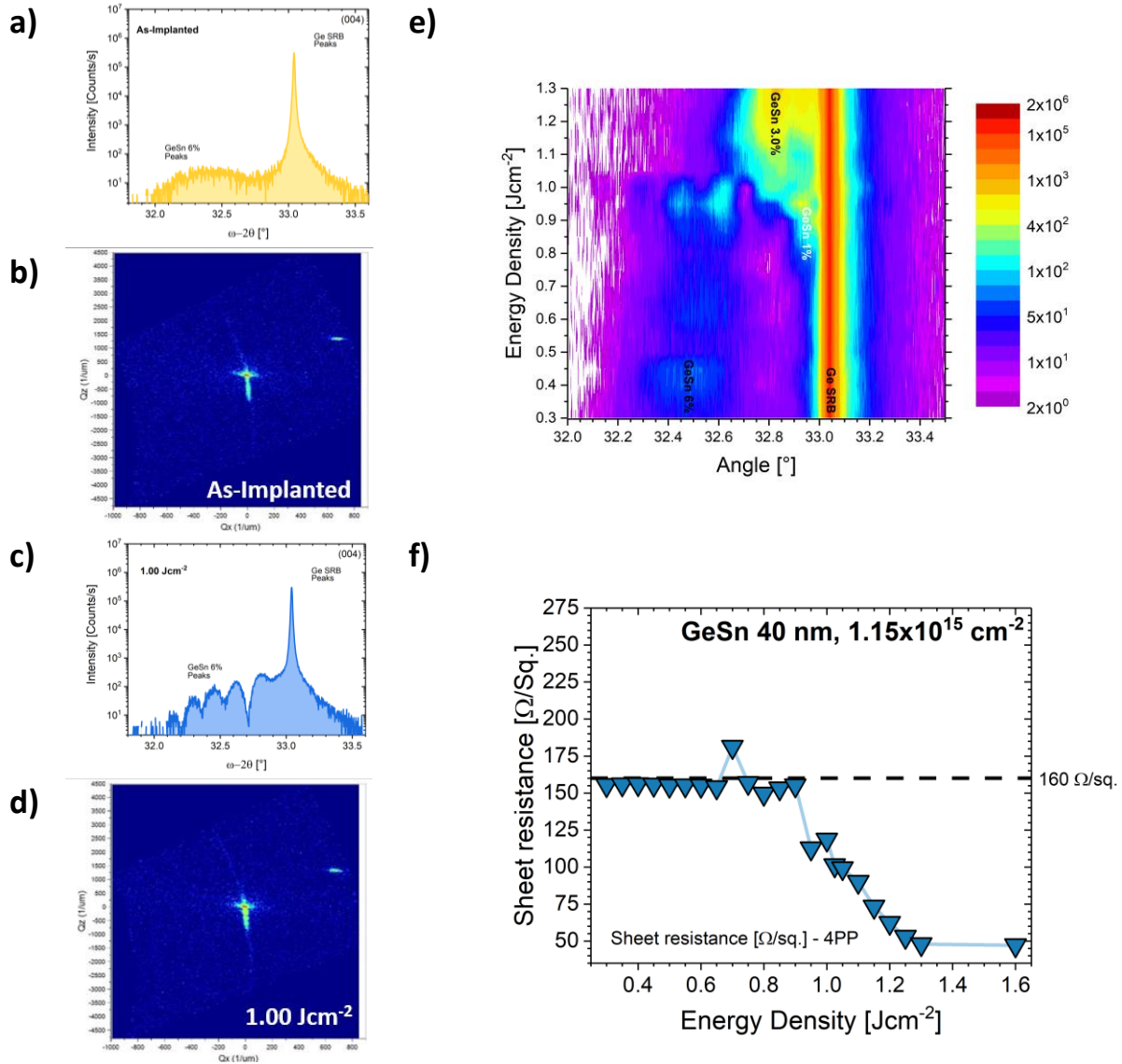


Figure A.20: Balayages $\omega-2\theta$ normalisé autour de l'ordre (0 0 4) de la diffraction X et cartes RSM de l'ordre (1 1 3) de GeSn 6% implanté P sur de tampons de Ge:B/Ge sans NLA ((a) jaune et (b)) et après NLA à 1.00 Jcm⁻² ((c) bleu et (d)). (e) De carte $\omega-2\theta$ de balayages $\omega-2\theta$ à des EDs variées (taille d'échelon 0.025 Jcm⁻²). (f) Mesure 4PP de la résistance carré pour des EDs variées.

Des cartographies de l'espace réciproque et des balayages $\omega-2\theta$ ont montré, en DRX, que les couches GeSn:P sont restées pleinement en compression après NLA, comme illustré en **Figure A.20 (b)** et **(d)**, même si une redistribution de l'étain a eu lieu. Des couches GeSn:P de haute qualité avec plusieurs pic DRX bien-définis (**Figure A.20 (a)**, **(c)** et **(e)**), et une résistance carrée réduite ont été obtenues pour ED = 1.00 Jcm⁻², comme illustré en **Figure A.20 (f)**. La

résistance carrée a chuté de 160 à 48 Ω/sq . après un NLA à 1.30 Jcm^{-2} , avec toutefois une partie du substrat virtuel Ge sous-jacent fondue. Celui démontre que les recuits NLA sont avantageux afin d'améliorer la performance de couches GeSn de contact implantées ioniquement.

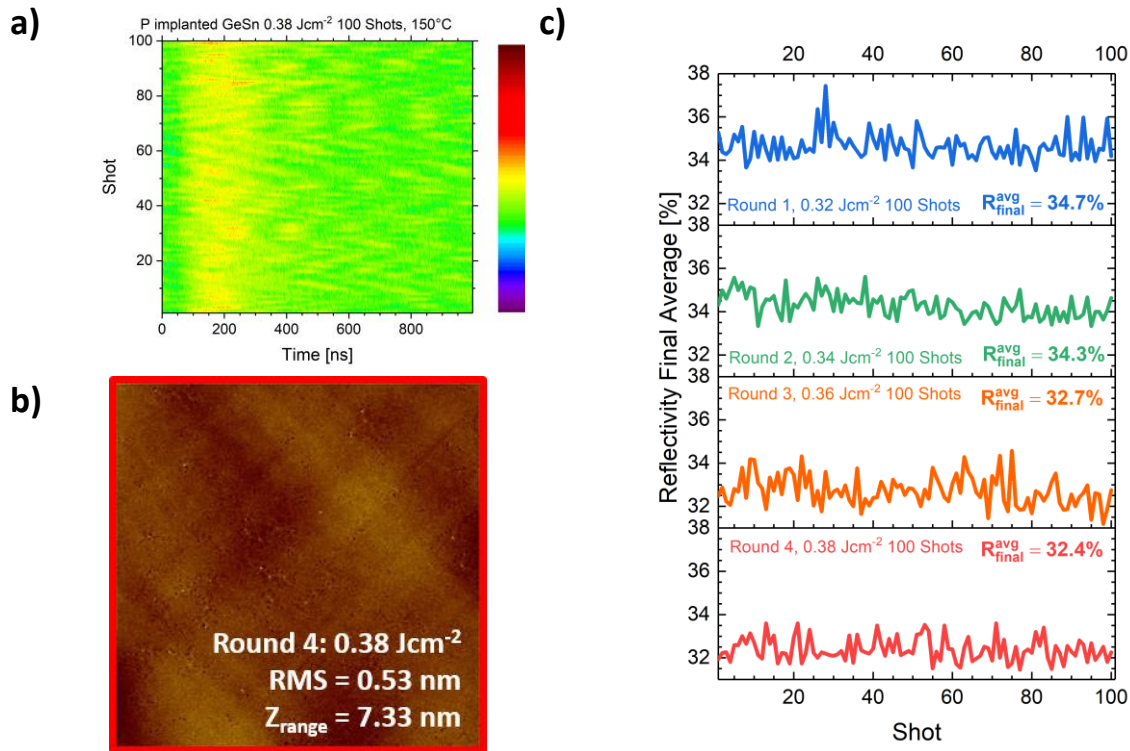


Figure A.21: (a) Carte TRR en fonction du nombre de pulses laser pour du GeSn 6% implanté P (41 nm) à ED = 0.38 Jcm^{-2} (avant: 100 pulsations à 0.32 Jcm^{-2} , 0.34 Jcm^{-2} et enfin 0.36 Jcm^{-2}). (b) Image AFM $5\ \mu\text{m} \times 5\ \mu\text{m}$ (échelle des z: 5 nm) pour cette couche GeSn:P après ces 400 pulses de recuit laser. (c) Réflectivités finales de surface (derniers 20 ns de mesure en TRR (chaleur déjà dissipée)) pour du GeSn 6% implanté P (41 nm) après 100 pulses à 0.32 Jcm^{-2} (bleu), 0.34 Jcm^{-2} (vert), 0.36 Jcm^{-2} (orange) et 0.38 Jcm^{-2} (rouge).

La recristallisation épitaxiale en phase solide [39] a été étudiée pour des densités d'énergie faible et donc des températures réduites (au maximum 150 °C). Une réduction de la résistance carrée n'a pas été obtenue, mais un changement de structure a été observé sans formation de structure de surface, comme illustré en **Figure A.21**. Ceci devrait permettre, à l'avenir, d'activer des dopants dans des couches GeSn implantées sans redistribution de l'étain.

A.I.7. Conclusion

Des papiers sur le dopage in-situ du (Si)GeSn sont peu fréquents dans la littérature. Des changements au niveau des mécanismes de croissance ont été identifiés et des indications en ce qui concerne le dopage publiés, sans étude rigoureuse, toutefois. De même, la littérature en ce qui concerne le dopage ex-situ du GeSn à base d'implantation ionique et de recuit est incomplète. Nous avons, dans ce manuscrit, exploré (i) le dopage in-situ du GeSn et SiGeSn et (ii) l'impact de recuit laser nanoseconde (NLA) sur des couches Ge:B, GeSn et GeSn:P, Les couches de Ge:B étaient dopées B in-situ tandis que les couches GeSn:P l'avaient été par

implantation ionique.. Notre but était de comparer les deux approches pour le dopage du (Si)GeSn et de mieux appréhender les phénomènes physiques inhérents au recuit laser nanoseconde de couches GeSn.

Des études détaillées par Diffraction de Rayons X (DRX) et spectroscopie de fluorescence de rayons X à dispersion de longueur d'onde (WDXRF) de couches GeSn:B et GeSn:P ont dévoilé que, lorsque les flux B_2H_6 ou PH_3 augmentent, le composant Ge de la vitesse de croissance (GR) augmente, tandis que le composant Sn reste constant (dé-passivation de sites d'incorporation en surface par le B_2H_6 et le PH_3). Parce que la composante Ge de la vitesse de croissance est limitée par les réactions de surface tandis que la composante Sn est limitée par le transport de masse, une réduction de la concentration en Sn a été observé ainsi qu'une augmentation de la vitesse de croissance du GeSn dopé in-situ avec les flux de dopant. Des concentrations de bore électriquement actif au maximum de $2.8 \times 10^{19} \text{ cm}^{-3}$ ont été atteints dans des couches GeSn:B 6% épitaxiées à $350 \text{ }^\circ\text{C}$, 100 Torr avec un mélange $Ge_2H_6 + SnCl_4 + B_2H_6$. La concentration en phosphore électriquement actif dans du GeSn:P 6% épitaxié à $350 \text{ }^\circ\text{C}$, 100 Torr avec un mélange $Ge_2H_6 + SnCl_4 + PH_3$ est quant à elle limitée à $6.9 \times 10^{19} \text{ cm}^{-3}$. Ceci était sans doute dû à la formation d'amas Sn_mP_nV électriquement inactifs.

Cette difficulté afférente à ces concentrations plutôt faibles en dopants électriquement actifs dans le GeSn a été surmontée en injectant de fortes quantités d'atomes Si dans la maille du GeSn. Des concentrations en dopants électriquement actifs aussi élevées que $2.0 \times 10^{20} \text{ cm}^{-3}$ dans du SiGeSn:B et $2.7 \times 10^{20} \text{ cm}^{-3}$ dans du SiGeSn:P ont été obtenues pour des couches épitaxiées à $350 \text{ }^\circ\text{C}$, 100 Torr avec les mêmes gaz que ci-dessus, avec bien sûr l'ajout de Si_2H_6 . Significativement moins d'amas Sn_mP_nV électriquement actifs ont sans doute été formés pour des concentrations élevées d'étain (~ 9%) dans les alliages SiGeSn:P. L'emploi de hauts flux de dopants a entraîné une amélioration de la morphologie de surface des couches SiGeSn:B ou SiGeSn:P par rapport à celle de couches intrinsèques. La structure en double tôle ondulée (cross-hatch) selon les directions $\langle 110 \rangle$ a été récupérée et des surfaces lisses obtenues, avec des rugosités RMS de 0.36 nm (SiGeSn:B) et 0.47 nm (SiGeSn:P) et Z_{range} au minimum de 2.86 nm (SiGeSn:B) et 4.60 nm (SiGeSn:P). Des rapports Si/Sn de 3.5, avec des concentrations en silicium au maximum de 25% ont par ailleurs été obtenus pour SiGeSn:B. Une compétition entre atomes de germanium et silicium au niveau des sites d'incorporation en surface qui serait impactée par la présence d'atomes de B expliquerait en partie ces changements de composition.

Des recuits laser nanoseconde faisant appel à des pulses laser avec des largeurs à mi-hauteur de quelques dizaines de nanosecondes, en combinaison avec l'implantation ionique permettrait de tirer partie d'une durée de pulse ultra-court afin de créer des gradients de température très abrupts et générer ainsi des couches monocristallines sans défauts avec des concentrations en dopants électriquement actifs au-dessus de la limite de solubilité à l'état solide.

Le recuit laser de couches de Ge dopées bore in-situ a dans un premier temps été étudié. Des résistances carrées plus élevées ont malheureusement été obtenues, peut-être parce que des amas de bore en sites interstitiels électriquement inactifs se sont formés qui n'ont pas contribué à la contrainte en tension. Des structures de surface de forme rectangulaire sont apparues autour du seuil de fusion et la coalescence des structures de surface a conduit à la présence de structures de surface plus grandes à plus hautes densités d'énergie laser.

Des études de recuit laser nanoseconde ont ensuite été menées sur des couches minces pseudomorphes de GeSn 6%, 10% et 14% afin de mieux appréhender l'impact du NLA sur ces alliages, qui sont sensibles à la ségrégation / l'agglomération de l'étain. Des queues particulières sur les cartes TRR permettant de suivre l'évolution de la réflectivité de surface lors des recuits laser ont été identifiées. Elles sont dues à la formation de surfaces glisse. Les densités d'énergie pour lesquelles ces queues de TRR ont apparu correspondent à celles pour une fusion complète de la couche GeSn au-dessus du substrat Ge virtuel, avec une interface liquide/solide lisse (température de fusion 938 °C pour Ge pure et 232 °C pour β -Sn [40]). A ces densités d'énergie, des couches GeSn de haute qualité cristalline, avec au maximum 6.3% d'étain, ont été obtenues. De telles concentrations sont spécifiques à cette technique de recuit très hors-équilibre. Les mêmes régimes de fusion que ceux observés pour SiGe ont été trouvés pour le GeSn et des mesures SIMS ont démontré la redistribution des atomes d'étain vers la surface.

Notre compréhension du recuit laser nanoseconde de GeSn a été améliorée par l'application d'au maximum 100 pulses laser à la même position. Ces études ont révélé l'importance de la profondeur de fusion pour la formation de structures de surface. Des recuits laser au seuil de la fusion entière de la couche GeSn, i.e. où l'interface liquide/solide était à l'interface GeSn/substrat virtuel de Ge, ont engendré des surfaces lisses tant que le substrat virtuel en Ge n'avait pas fondu et que l'interface GeSn/substrat virtuel Ge était resté lisse. Des images TEM en section transverse combinées à des mesures EDX ont montré une incorporation d'oxygène lors de l'envoi de plusieurs pulses laser sur la même position. Des observations SEM et EDX a montré que les structures de surface étaient riches en Sn.

Enfin, des recuits laser nanoseconde ont été employées sur des couches GeSn 6% implantées phosphore afin d'étudier la faisabilité de doper ex-situ du GeSn par implantation ionique (et donc amorphisation d'une partie de la couche). Les défauts d'implantation ont été guéris par le NLA et des couches GeSn:P de haute qualité cristalline, avec des pics DRX bien-définis et une résistance carrée amélioré, grâce à l'activation des dopants, obtenus. Néanmoins, l'activation des dopant a demandé des densités d'énergie plutôt élevées, avec une redistribution de l'étain dans la couche. Nous avons donc étudié la faisabilité d'une recroissance épitaxiale en phase solide pour ces couches GeS:P, le but étant de guérir les défauts d'implantation et d'activer les dopants sans fusion de couche (et donc sans redistribution de l'étain). Des recristallisations ont été obtenus grâce à un nombre important de pulses laser à faible densité d'énergie, mais les paramètres de recuit devront encore être optimisés afin d'obtenir une bonne activation des dopants.

Le savoir acquit lors de ces études a été utilisé pour améliorer la performance de dispositifs à base de GeSn. Des hétérostructures avec soit des compositions nominalelement constantes, soit en escalier, avec des concentrations en étain au maximum de 16.9% et 17.2%, respectivement, ont été épitaxiées. La gestion de la température et des flux de précurseur pendant la croissance a été amélioré comparé aux études précédents, permettant d'atteindre des concentrations en Sn plus élevées, de meilleures qualités de matériaux et un confinement amélioré des porteurs de charge dans les couches à haut %Sn amélioré. Ces empilements ont été collés sur des piliers en Al(N) afin d'améliorer la dissipation de chaleur et les couches défectueuses de faible concentration en Sn retirées. Une couche de SiN permettant d'injecter de la contrainte en tension a été déposée sur l'empilement avec nominalelement une composition afin d'augmenter la différence entre les vallées L et Γ de la bande de conduction. Ceci nous a permis d'obtenir les premiers lasers pompés optiquement opérant à température ambiante au monde [20], [21].

On trouvera dans les lignes qui suivent quelques études qu'il serait bon de mener afin d'améliorer les performances de futurs dispositifs.

Tout d'abord, le seuil laser devra être réduit de manière drastique. Pour ceci, il faudra réduire la quantité de lacunes (et de dislocations) dans les empilements. [41] Des résultats récents ont montré que la micro-structuration et la gravure sélective de régions fortement disloquées permettent de recuire à relativement haute température des empilements GeSn sans ségrégation d'étain et d'améliorer leurs propriétés optiques. [42] A l'avenir, il serait avantageux d'utiliser le recuit laser nanoseconde pour contrôler précisément un tel processus.

Les hétérostructures pour des photo-détecteurs et des lasers pompés électriquement sont très complexes, avec la présence de couche minces et épaisses plus ou moins relaxées. Comme montré précédemment, l'état de contrainte de couches tampon à base de GeSn a un fort impact sur les couches GeSn déposées au-dessus. [43] Vu que l'incorporation d'Sn est définitivement impacté par la contrainte, il serait intéressant de mieux comprendre les mécanismes en jeu. Par ailleurs, les interactions entre l'incorporation de dopants et la contrainte n'ont pas encore été étudiés. Il a par exemple été montré que la relaxation de la contrainte en compression réduisait l'incorporation du bore dans le SiGe [44]. Cela pourrait également être le cas dans (Si)GeSn. Nous avons par ailleurs montré que la présence de fortes concentrations de dopants dans du (Si)GeSn changeait la composition de la couche et pouvait conduire à des surfaces plus lisses. Ces deux phénomènes auront un impact sur les propriétés et la qualité cristalline d'empilements épais complexes et devront être étudiés. Les couches les plus riches en étain d'empilements pour les LEDs et les lasers sont épitaxiées à basse température (typiquement 313 °C – 325 °C), tandis que les études menées ici sur le dopage in-situ du (Si)GeSn ont été menées à 349°C. Des études similaires du dopage in-situ, mais à plus basse température, pourraient avantageusement être menées afin de compléter notre savoir-faire et minimiser les excursions en températures dangereuses lors de la croissance d'hétérostructures complexes. Un meilleur confinement grâce à un rapport Si/Sn élevé dans des couches barrières SiGeSn dopées in-situ pourrait également contribuer à une amélioration des performances des dispositifs. L'expertise acquise lors des études en cours serait un bon point de départ afin de déposer des couches SiGeSn intrinsèques et dopées in-situ de meilleur qualité encore avec une gamme de compositions élargie.

References

- [1] D. Stange *et al.*, « Optically Pumped GeSn Microdisk Lasers on Si », *ACS Photonics*, vol. 3, n° 7, p. 1279-1285, juill. 2016, doi: 10.1021/acsp Photonics.6b00258.
- [2] S. Al-Kabi *et al.*, « An optically pumped 2.5 μ m GeSn laser on Si operating at 110 K », *Appl. Phys. Lett.*, vol. 109, n° 17, p. 171105, oct. 2016, doi: 10.1063/1.4966141.
- [3] V. Reboud *et al.*, « Optically pumped GeSn micro-disks with 16% Sn lasing at 3.1 μ m up to 180 K », *Appl Phys Lett*, p. 5, 2017.
- [4] J. Juan-Colás, A. Parkin, K. E. Dunn, M. G. Scullion, T. F. Krauss, et S. D. Johnson, « The electrophotonic silicon biosensor », *Nat. Commun.*, vol. 7, n° 1, p. 12769, nov. 2016, doi: 10.1038/ncomms12769.
- [5] M. Sieger et B. Mizaikoff, « Toward On-Chip Mid-Infrared Sensors », *Anal. Chem.*, vol. 88, n° 11, p. 5562-5573, juin 2016, doi: 10.1021/acs.analchem.5b04143.
- [6] R. Wang *et al.*, « III–V-on-Silicon Photonic Integrated Circuits for Spectroscopic Sensing in the 2–4 μ m Wavelength Range », *Sensors*, vol. 17, n° 8, p. 1788, août 2017, doi: 10.3390/s17081788.
- [7] T. Spuesens, D. Van Thourhout, P. Rojo-Romeo, P. Regreny, et J.-M. Fedeli, « CW operation of III-V microdisk lasers on SOI fabricated in a 200 mm CMOS pilot line », in *8th IEEE International Conference on Group IV Photonics*, London, United Kingdom, sept. 2011, p. 199-201. doi: 10.1109/GROUP4.2011.6053762.
- [8] G. Roelkens *et al.*, « III-V-on-Silicon Photonic Devices for Optical Communication and Sensing », *Photonics*, vol. 2, n° 3, p. 969-1004, sept. 2015, doi: 10.3390/photonics2030969.
- [9] G. Crosnier *et al.*, « Hybrid indium phosphide-on-silicon nanolaser diode », *Nat. Photonics*, vol. 11, n° 5, p. 297-300, mai 2017, doi: 10.1038/nphoton.2017.56.
- [10] H. Guan *et al.*, « Widely-tunable, narrow-linewidth III-V/silicon hybrid external-cavity laser for coherent communication », *Opt. Express*, vol. 26, n° 7, p. 7920, avr. 2018, doi: 10.1364/OE.26.007920.
- [11] R. Chen *et al.*, « Material characterization of high Sn-content, compressively-strained GeSn epitaxial films after rapid thermal processing », *J. Cryst. Growth*, vol. 365, p. 29-34, févr. 2013, doi: 10.1016/j.jcrysgro.2012.12.014.
- [12] T. Stettner *et al.*, « Direct Coupling of Coherent Emission from Site-Selectively Grown III–V Nanowire Lasers into Proximal Silicon Waveguides », *ACS Photonics*, vol. 4, n° 10, p. 2537-2543, oct. 2017, doi: 10.1021/acsp Photonics.7b00805.
- [13] P. Vogl, M. M. Rieger, J. A. Majewski, et G. Abstreiter, « How to convert group-IV semiconductors into light emitters », *Phys. Scr.*, vol. T49B, p. 476-482, janv. 1993, doi: 10.1088/0031-8949/1993/T49B/017.
- [14] Y. M. Niquet, D. Rideau, C. Tavernier, H. Jaouen, et X. Blase, « Onsite matrix elements of the tight-binding Hamiltonian of a strained crystal: Application to silicon, germanium, and their alloys », *Phys. Rev. B*, vol. 79, n° 24, p. 245201, juin 2009, doi: 10.1103/PhysRevB.79.245201.
- [15] M. Bertrand *et al.*, « Experimental Calibration of Sn-Related Varshni Parameters for High Sn Content GeSn Layers », *Ann. Phys.*, vol. 531, n° 6, p. 1800396, juin 2019, doi: 10.1002/andp.201800396.
- [16] D. Sukhdeo, Y. Kim, S. Gupta, K. Saraswat, B. Dutt, et D. Nam, « Theoretical Modeling for the Interaction of Tin Alloying With N-Type Doping and Tensile Strain for GeSn Lasers », *IEEE Electron Device Lett.*, vol. 37, n° 10, p. 1307-1310, oct. 2016, doi: 10.1109/LED.2016.2603162.
- [17] S. Wirths *et al.*, « Lasing in direct-bandgap GeSn alloy grown on Si », *Nat. Photonics*, vol. 9, n° 2, p. 88-92, févr. 2015, doi: 10.1038/nphoton.2014.321.

- [18] F. T. Armand Pilon *et al.*, « Lasing in strained germanium microbridges », *Nat. Commun.*, vol. 10, n° 1, p. 2724, déc. 2019, doi: 10.1038/s41467-019-10655-6.
- [19] A. Elbaz *et al.*, « Ultra-low-threshold continuous-wave and pulsed lasing in tensile-strained GeSn alloys », *Nat. Photonics*, vol. 14, n° 6, p. 375-382, juin 2020, doi: 10.1038/s41566-020-0601-5.
- [20] J. Chrétien *et al.*, « Room temperature optically pumped GeSn microdisk lasers », *Appl. Phys. Lett.*, vol. 120, n° 5, p. 051107, janv. 2022, doi: 10.1063/5.0074478.
- [21] A. Bjelajac *et al.*, « Up to 300 K lasing with GeSn-On-Insulator microdisk resonators », *Opt. Express*, vol. 30, n° 3, p. 3954, janv. 2022, doi: 10.1364/OE.449895.
- [22] Y. Zhou *et al.*, « Electrically injected GeSn lasers on Si operating up to 100 K », *Optica*, vol. 7, n° 8, p. 924, août 2020, doi: 10.1364/OPTICA.395687.
- [23] Y. Zhou *et al.*, « Electrically injected GeSn lasers with peak wavelength up to 2.7 μm », *Photonics Res.*, vol. 10, n° 1, p. 222, janv. 2022, doi: 10.1364/PRJ.443144.
- [24] P. Moontragoon, R. A. Soref, et Z. Ikonc, « The direct and indirect bandgaps of unstrained $\text{Si}_x\text{Ge}_{1-x-y}\text{Sn}_y$ and their photonic device applications », *J. Appl. Phys.*, vol. 112, n° 7, p. 073106, oct. 2012, doi: 10.1063/1.4757414.
- [25] S. Takeuchi, A. Sakai, O. Nakatsuka, M. Ogawa, et S. Zaima, « Tensile strained Ge layers on strain-relaxed $\text{Ge}_{1-x}\text{Sn}_x$ /virtual Ge substrates », *Thin Solid Films*, vol. 517, n° 1, p. 159-162, nov. 2008, doi: 10.1016/j.tsf.2008.08.068.
- [26] E. Rosseel *et al.*, « Characterization of Epitaxial Si:C:P and Si:P Layers for Source/Drain Formation in Advanced Bulk FinFETs », *ECS Trans.*, vol. 64, n° 6, p. 977-987, août 2014, doi: 10.1149/06406.0977ecst.
- [27] M. Frauenrath, J.-M. Hartmann, et E. Nolot, « Boron and Phosphorous Doping of GeSn for Photodetectors and Light Emitting Diodes », *ECS Trans.*, vol. 98, n° 5, p. 325-338, sept. 2020, doi: 10.1149/09805.0325ecst.
- [28] J. Margetis, S.-Q. Yu, B. Li, et J. Tolle, « Chemistry and kinetics governing hydride/chloride chemical vapor deposition of epitaxial $\text{Ge}_{1-x}\text{Sn}_x$ », *J. Vac. Sci. Technol. A*, vol. 37, n° 2, p. 021508, mars 2019, doi: 10.1116/1.5055620.
- [29] A. Vohra *et al.*, « Low temperature epitaxial growth of Ge:B and $\text{Ge}_{0.99}\text{Sn}_{0.01}$:B source/drain for Ge pMOS devices: in-situ and conformal B-doping, selectivity towards oxide and nitride with no need for any post-epi activation treatment », *Jpn. J. Appl. Phys.*, vol. 58, n° SB, p. SBBA04, avr. 2019, doi: 10.7567/1347-4065/ab027b.
- [30] J. Osmond *et al.*, « 40 Gb/s surface-illuminated Ge-on-Si photodetectors », *Appl. Phys. Lett.*, vol. 95, n° 15, p. 151116, oct. 2009, doi: 10.1063/1.3243694.
- [31] L. Casiez *et al.*, « GeSn heterostructures LEDs for gas detection », in *2020 IEEE Photonics Conference (IPC)*, Vancouver, BC, Canada, sept. 2020, p. 1-2. doi: 10.1109/IPC47351.2020.9252514.
- [32] L. Dagault *et al.*, « Impact of UV Nanosecond Laser Annealing on Composition and Strain of Undoped $\text{Si}_{0.8}\text{Ge}_{0.2}$ Epitaxial Layers », *ECS J. Solid State Sci. Technol.*, vol. 8, n° 3, p. P202-P208, 2019, doi: 10.1149/2.0191903jss.
- [33] J.-H. Fournier-Lupien *et al.*, « In Situ Studies of Germanium-Tin and Silicon-Germanium-Tin Thermal Stability », *ECS Trans.*, vol. 64, n° 6, p. 903-911, août 2014, doi: 10.1149/06406.0903ecst.
- [34] L. Dagault *et al.*, « Investigation of recrystallization and stress relaxation in nanosecond laser annealed $\text{Si}_{1-x}\text{Ge}_x$ /Si epilayers », *Appl. Surf. Sci.*, vol. 527, p. 146752, oct. 2020, doi: 10.1016/j.apsusc.2020.146752.
- [35] G. Calogero *et al.*, « Multiscale modeling of ultrafast melting phenomena », *Npj Comput. Mater.*, vol. 8, n° 1, p. 36, déc. 2022, doi: 10.1038/s41524-022-00720-y.

- [36] M. O. Thompson *et al.*, « Melting Temperature and Explosive Crystallization of Amorphous Silicon during Pulsed Laser Irradiation », *Phys. Rev. Lett.*, vol. 52, n° 26, p. 2360-2363, juin 1984, doi: 10.1103/PhysRevLett.52.2360.
- [37] C. Buchner et W. Schneider, « Explosive crystallization in thin amorphous layers on heat conducting substrates », *J. Appl. Phys.*, vol. 117, n° 24, p. 245301, juin 2015, doi: 10.1063/1.4922787.
- [38] G. C. Egan, T. T. Li, J. D. Roehling, J. T. McKeown, et G. H. Campbell, « In situ dynamic TEM characterization of unsteady crystallization during laser processing of amorphous germanium », *Acta Mater.*, vol. 143, p. 13-19, janv. 2018, doi: 10.1016/j.actamat.2017.10.003.
- [39] L. Wang *et al.*, « Post-growth annealing of germanium-tin alloys using pulsed excimer laser », *J. Appl. Phys.*, vol. 118, n° 2, p. 025701, juill. 2015, doi: 10.1063/1.4926484.
- [40] R. W. Olesinski et G. J. Abbaschian, « The Ge–Sn (Germanium–Tin) system », *Bull. Alloy Phase Diagr.*, vol. 5, n° 3, p. 265-271, juin 1984, doi: 10.1007/BF02868550.
- [41] S. Assali *et al.*, « Vacancy complexes in nonequilibrium germanium-tin semiconductors », *Appl. Phys. Lett.*, vol. 114, n° 25, p. 251907, juin 2019, doi: 10.1063/1.5108878.
- [42] V. Bonino *et al.*, « Microstructuring to Improve the Thermal Stability of GeSn Layers », *ACS Appl. Mater. Interfaces*, vol. 14, n° 19, p. 22270-22277, mai 2022, doi: 10.1021/acsmi.2c01652.
- [43] S. Assali, J. Nicolas, et O. Moutanabbir, « Enhanced Sn incorporation in GeSn epitaxial semiconductors via strain relaxation », *J. Appl. Phys.*, vol. 125, n° 2, p. 025304, janv. 2019, doi: 10.1063/1.5050273.
- [44] G. Rengo *et al.*, « (Invited) Highly Doped Si_{1-x}Ge_x Epitaxy in View of S/D Applications », *ECS Trans.*, vol. 98, n° 5, p. 27-36, sept. 2020, doi: 10.1149/09805.0027ecst.

Appendix B : NLA of Pseudomorphic GeSn Layers : Impact of Sn Content

Appendix B Nanosecond Laser Annealing of pseudomorphic GeSn layers: Impact of Sn content

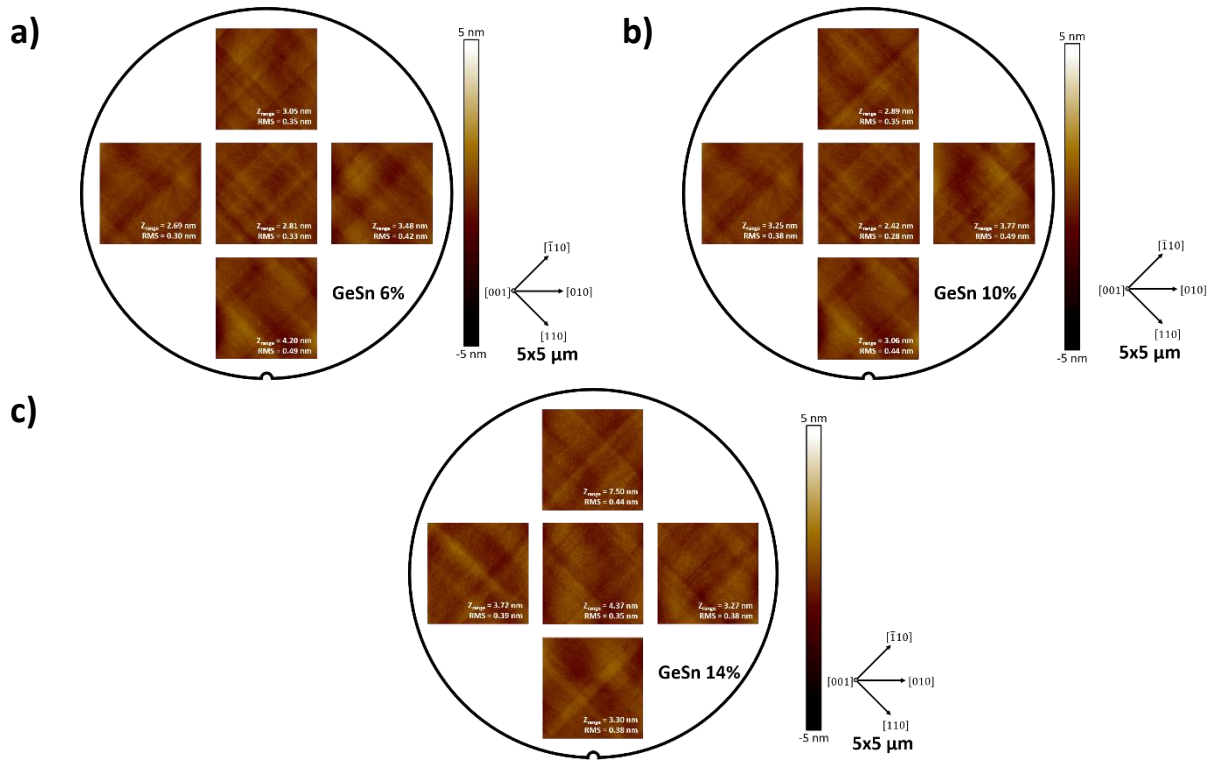


Figure B.1: Atomic force images of as-grown GeSn 6%, 10% and 14% (a, b, c) at various positions.

Smooth surfaces and well-defined cross-hatches along the $\langle 110 \rangle$ directions were recorded by AFM on the various Sn content samples, this whatever the position over the wafers, as shown in **Figure B.1**.

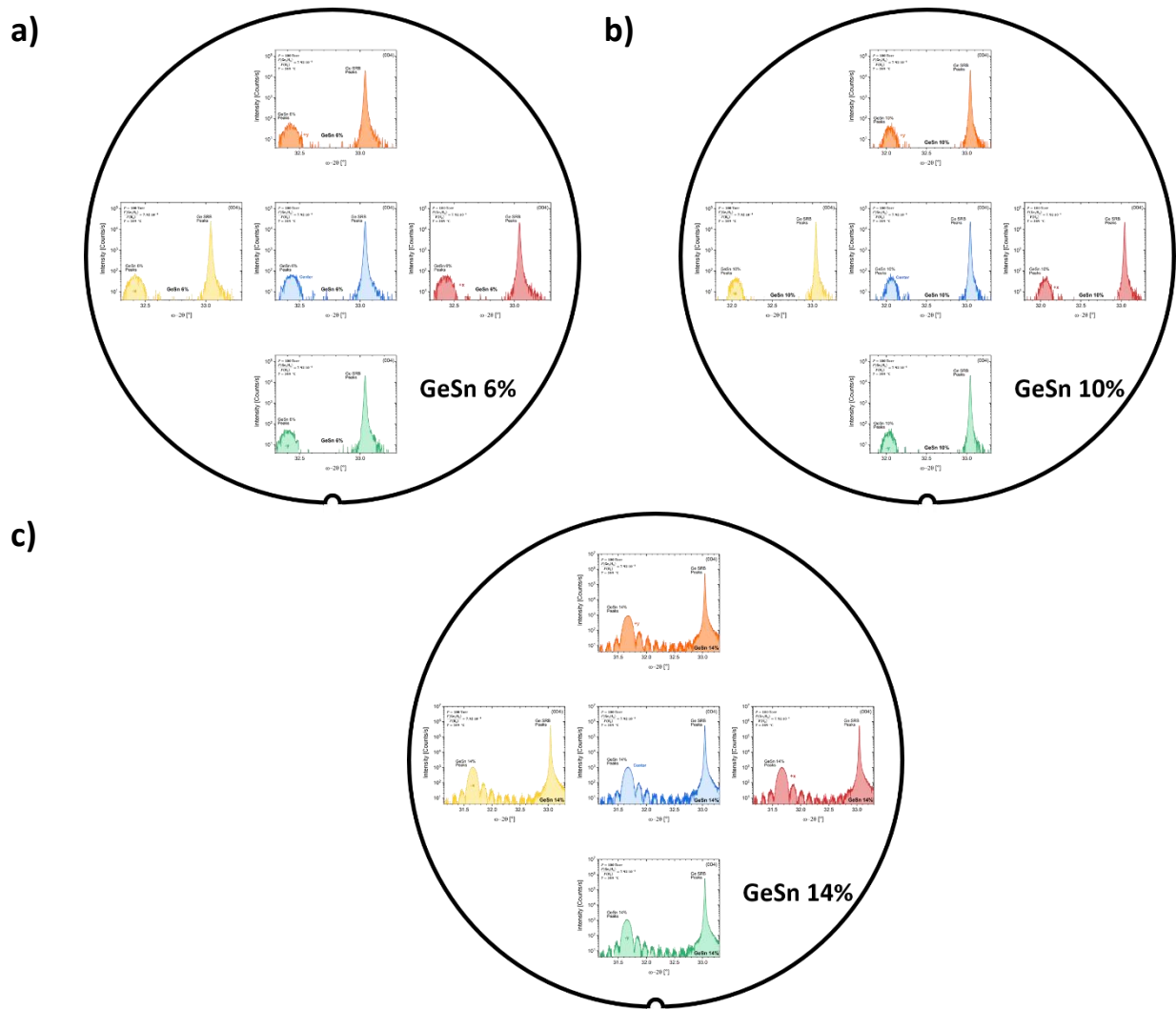


Figure B.2: ω - 2θ XRD scans around the (0 0 4) XRD order for GeSn 6%, 10% and 14% (a, b, c) at various positions.

Thickness fringes were always well defined and the angular position of the GeSn XRD peak did not significantly change in the ω - 2θ scans around the (0 0 4) order performed at various locations on the surfaces of the GeSn 6%, 10% and 14% wafers, as shown in **Figure B.2**.

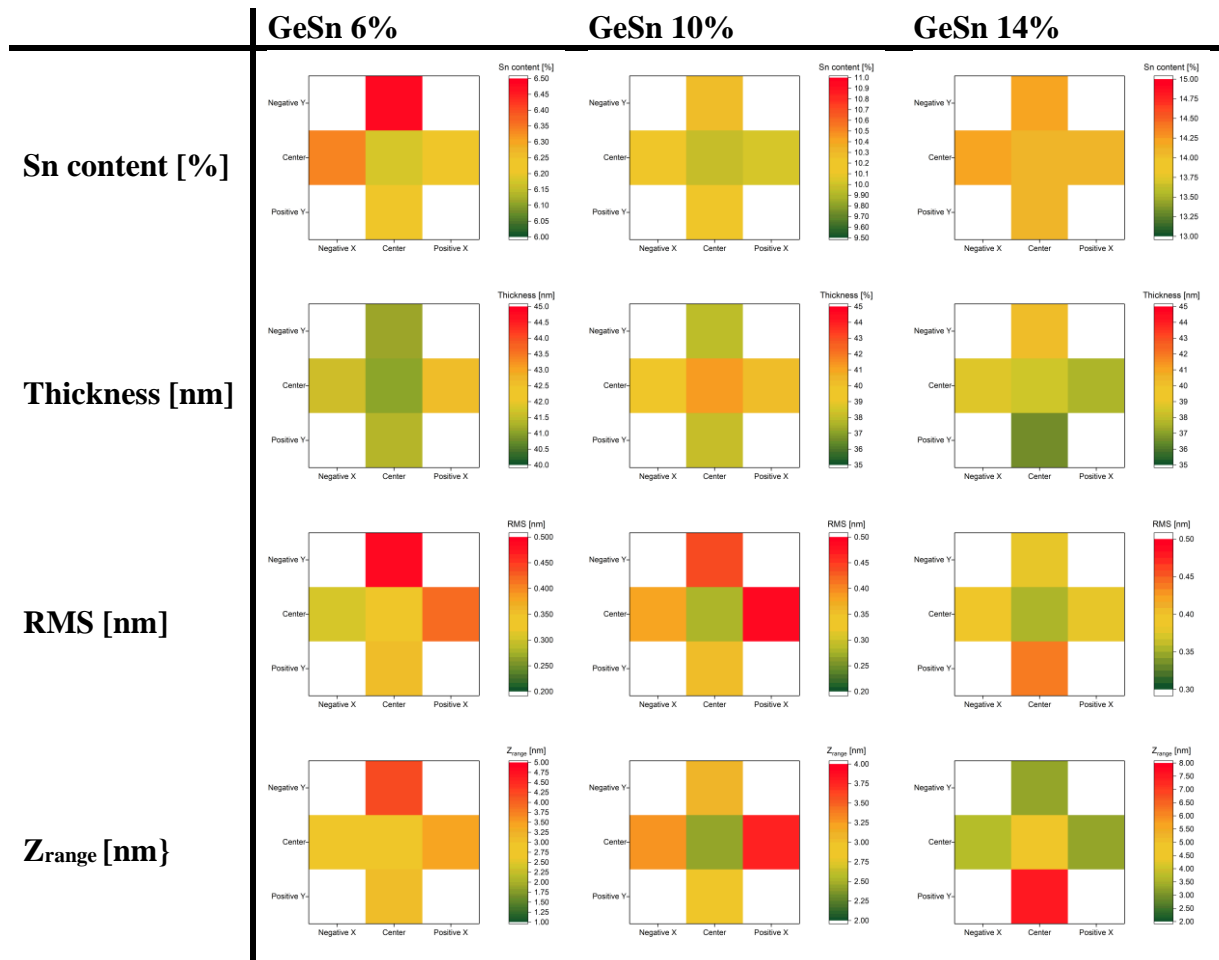


Figure B.3: GeSn 6%, 10% and 14% (left to right) Sn content, GeSn layer thickness, RMS and Z_{range} (top to bottom) uniformity study from XRD and AFM. The Takagi-Taupin's dynamical scattering theory was used to extract the Sn content and GeSn layer thickness.

As-grown GeSn layers were uniform in terms of Sn content, GeSn layer thickness, RMS roughness and Z_{range} , as shown in **Figure B.3**.

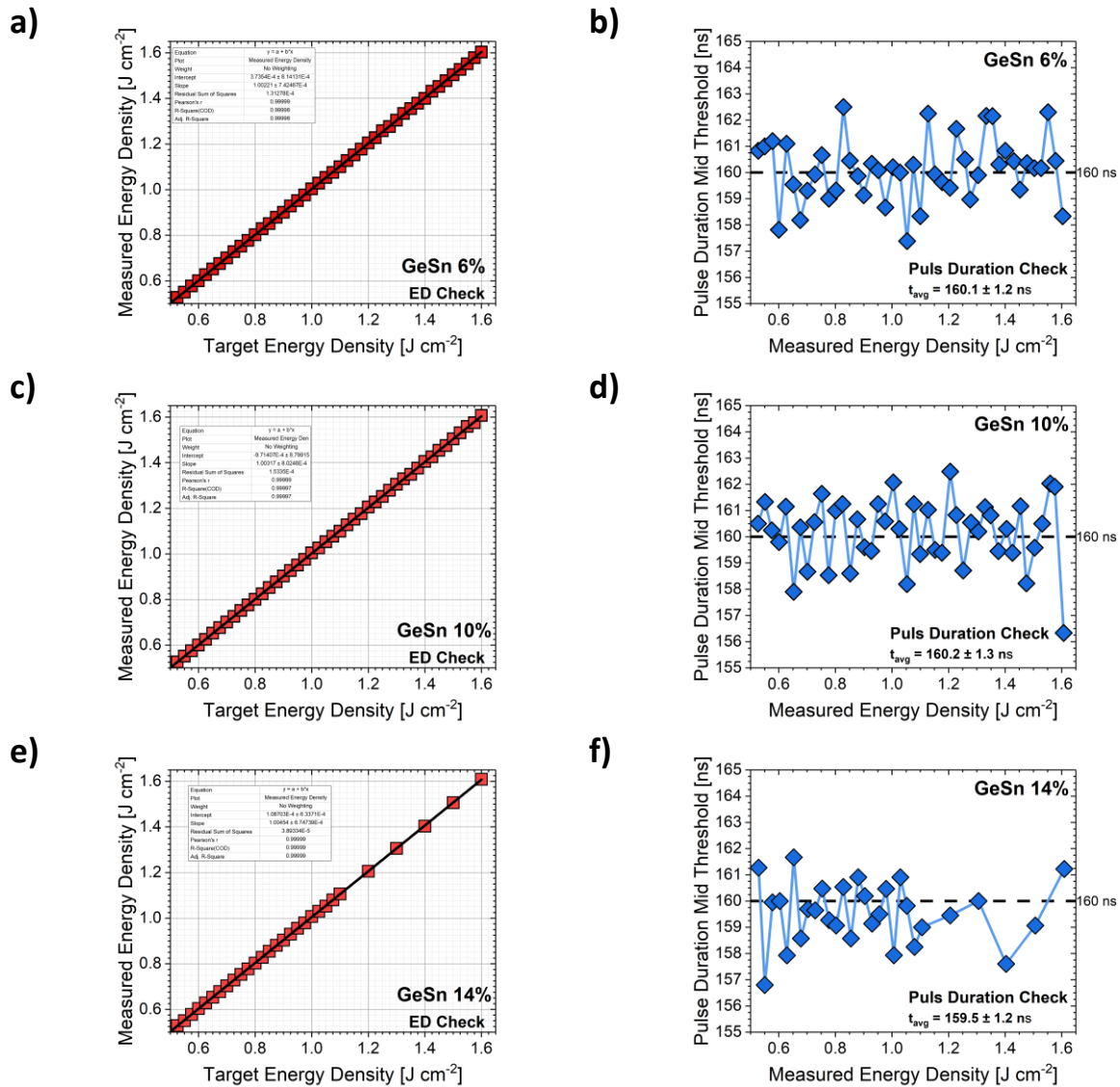


Figure B.4: Targeted vs. measured energy (a, c, e) and pulse duration (b, d, f) for various EDs probed on GeSn 6%, 10% and 14% (top to bottom).

As far as laser pulses were concerned, targeted EDs were in very good agreement with measured EDs, as shown in **Figure B.4 (a, c, e)**. The pulse duration did not change significantly and stayed almost constant for all laser pulses, as shown in **Figure B.4 (b, d, f)**.

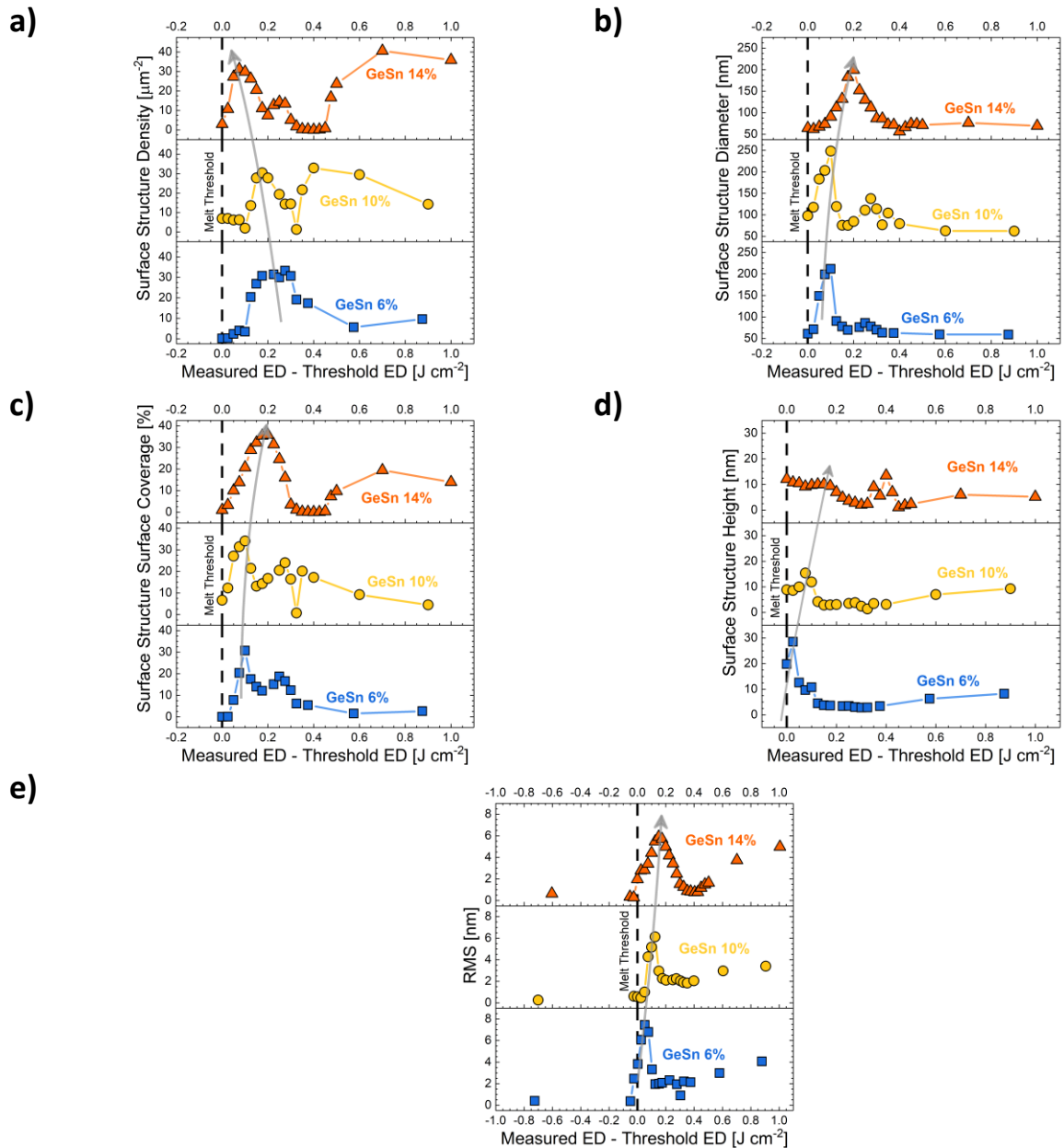


Figure B.5: Comparison of surface structure density (a), surface structure diameter (b), surface coverage by structures (c), surface structure height (d) and RMS roughness (e) as functions of measured energy density minus melt threshold energy density for GeSn 6% (blue squares), GeSn 10% (yellow circles) and GeSn 14% (orange triangles). Black dashed lines show the melt threshold. It was 0.725 J cm^{-2} for GeSn 6%, 0.70 J cm^{-2} for GeSn 10% and 0.60 J cm^{-2} for GeSn 14% (from AFM). Densities, diameters, heights and surface coverages were extracted by assuming a threshold of 2 nm above the surface mean plane. The gray arrows outline the shifts of the various peaks.

Utilizing the Particle Analysis feature of the Bruker analyzing software NanoScope, we performed a quantitative evaluation of the impact of the as-grown Sn content on the metrics of surface structures. Results are shown in **Figure B.5**. To obtain comparable datasets, a threshold at 2 nm above the mean plane of the various surfaces was used and all recorded AFM images

were flattened by a 6th order fit to ensure that long range undulations (because of the surface cross-hatch of the Ge SRBs underneath) were not counted as surface structures.

For an easier comparison between the various Sn contents considered, we subtracted, on the x-axis, the melt threshold ED (determined by AFM) from the measured energy density. The threshold appears as a vertical black dashed line in the figures. All x-axis in **Figure B.5** are presented the same way. **Figure B.5 (a)** shows the evolution of the surface structure density for the various Sn contents. For GeSn 6% (blue squares) and 10% (yellow circles), the surface structure density did not increase immediately above the melt threshold. It rather stayed constant up to 0.100 Jcm⁻² above the melt threshold then continuously increased. This was most likely because, for GeSn 6% and 10%, the surface structures increased in diameter, as shown in **Figure B.5 (b)**, and did not multiply. Hence, the surface structure density stayed constant just above the melt threshold. The surface structure density reached its maximum of 30 μm⁻² at 0.175 Jcm⁻² above the melt threshold for GeSn 6% and 10%. This was the energy density at which the surface structures started to merge.

When increasing the energy density further, the surface structure density remained at a plateau of 0.30 μm⁻² for GeSn 6% up to 0.30 Jcm⁻² above the melt threshold. For GeSn 6%, the surface coverage, shown in **Figure B.5 (c)**, was not high enough to form a coalescent surface layer. This was why no immediate drop of the surface structure density occurred when surface structures merged. At higher energy densities, the surface structure density dropped and saturated at a value below 10 μm⁻² when most likely the Ge SRB melted.

For GeSn 10%, at energy density higher than 0.175 Jcm⁻² above the melt threshold, the surface structure density dropped significantly, reaching 1.32 μm⁻² at 0.325 Jcm⁻² above the melt threshold. In the case of GeSn 10%, when a significant surface structure density was reached the surface structures merged and formed an almost continuous surface layer. At energy density higher than 0.325 Jcm⁻² above the melt threshold, the surface structure density increased to 32.88 μm⁻² at 0.40 Jcm⁻² above the melt threshold. This was most likely because the Ge SRB was melted. At even higher energy densities Sn might be diluted in the melted Ge SRB, resulting in the formation of less surface structures.

For GeSn 14%, the surface structure density, shown in **Figure B.5 (a)** as orange triangles, increased directly after the melt threshold. Meanwhile, the surface structures' diameter increased with a delay of 0.075 Jcm⁻², shown in **Figure B.5 (b)**. For GeSn 14%, the surface structures therefore became more numerous instead of increasing in size when the energy density was increased. A maximum of 31.24 μm⁻² was reached at 0.075 Jcm⁻² above the melt threshold. At higher energy densities, the surface structure density dropped for GeSn 14% because surface structures started to merge. A plateau of around 12 μm⁻² was reached at 0.175 Jcm⁻². This was when the merging surface structures started to form an almost continuous surface layer with some surface undulations formed where surface structures merged. At energy densities higher than 0.275 Jcm⁻² above the melt threshold those surface undulations merged, resulting in the formation of an almost continuous surface layer and a surface structure density of 0.20 μm⁻². It stayed constant up to 0.45 Jcm⁻² and then increased. This increase was most likely due to the start of the melt of the Ge SRB.

The surface structure diameter, shown in **Figure B.5 (b)**, did not immediately increase above the melt threshold for GeSn 14% while it did for GeSn 6% and 10. Nevertheless, it reached a similar maximum between 200 and 250 nm at 0.1 Jcm⁻² above the melt threshold for

GeSn 6% and 10%. The maximum was at 0.20 Jcm^{-2} above the melt threshold for GeSn 14%. The shift towards higher energy densities above the melt threshold and the slow increase just above the melt threshold was because, for GeSn 14%, numerous small surface structures were formed that only merged, forming larger surface structures, at higher energy densities above the melt threshold. At higher energy densities above the melt threshold, the surface structure diameter decreased to a value of around 50 nm. Only for GeSn 10%, the surface structure diameter increased to 140 nm at 0.275 Jcm^{-2} when surface undulations formed. When these surface undulations merged, the surface structure diameter dropped to 50 nm again.

The surface coverage (the percentage of the surface covered with structures) continuously increased for all samples, as shown in **Figure B.5 (c)**. The maximum surface coverage shifted to higher values, from 31% up to 36% at 0.1 Jcm^{-2} above the melt threshold for GeSn 6% and 10%, and at 0.2 Jcm^{-2} above the melt threshold for GeSn 14%. The higher maximum surface coverage value for higher Sn contents could be another indication that the surface became Sn rich after NLA. Meanwhile, the smaller surface structures size for lower energy densities above the melt threshold **Figure B.5 (b)**, were most likely the origin of the shift of the maximum surface coverage towards higher energy densities for the GeSn 14% sample.

For all as-grown Sn contents, the surface structure height, shown in **Figure B.5 (d)**, stayed at a plateau of around 10 nm for low energy densities above the melt threshold. This plateau extended to higher energy densities as the as-grown Sn content increased, most likely because surface structures presented smaller diameters. When the surface structures merged at higher energy densities above the melt threshold, the surface structure height dropped to values below 5 nm. There were peaks when some tiny islands appeared.

The RMS surface roughness, shown in **Figure B.5 (e)**, peaked at a value of 7.45 nm at the melt threshold for GeSn 6% and shifted to higher energy densities than the melt threshold when the as-grown Sn content increased. This was in line with the surface structure diameter and height, which reached peaks at energy densities higher than the melt threshold for high as-grown Sn contents (**Figure B.5 (b)** and **(d)**). The maximum RMS value decreased slightly down to 5.90 nm for GeSn 14%. When the surface structures' diameter and height increased, so did the RMS roughness. For energy densities above 1.00 Jcm^{-2} (i.e. 0.25 Jcm^{-2} to 0.40 Jcm^{-2} over the melt threshold), the RMS roughness increased continuously because of the formation of small islands and the appearance of big droplets (a few hundreds of nm in diameter). These might be due to impurities like oxygen. Previous studies of nanosecond laser annealing indeed showed some incorporation of oxygen during annealing experiments. During the laser annealing a nitrogen atmosphere was used in order to minimize oxygen incorporation, but it was not completely prevented.

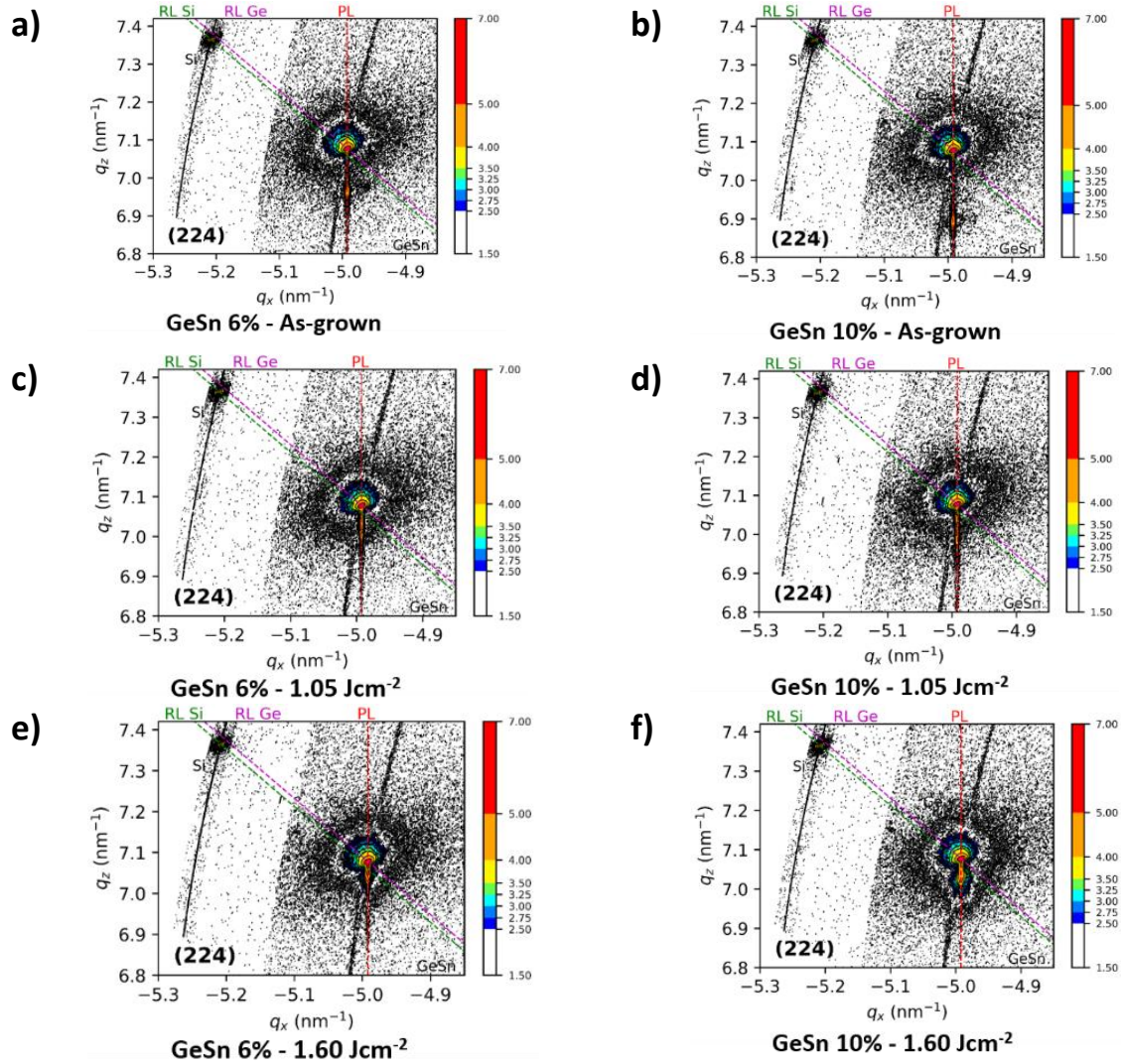


Figure B.6: (2 2 4) RSM of as-grown GeSn 6% (a) and 10% (b), annealed at 1.05 Jcm⁻² (c), (d) and 1.60 Jcm⁻² (e), (f). Dashed green lines outline the position of relaxed Si and purple dashed lines that of Ge. Red dashed lines show layers which are pseudomorphic on the Ge SRBs underneath.

While the “apparent” Sn content dropped, laser annealed GeSn layers were still fully compressively strained on the Ge SRBs underneath. This is obvious in **Figure B.6** (2 2 4) RSMs of GeSn 6% and 10% samples, with vertical shifts of the GeSn peaks towards the Ge SRB peaks (same q_x coordinates) as the energy density increased. A similar behavior was previously reported in the literature for laser annealed, pseudomorphic GeSn layers [4].

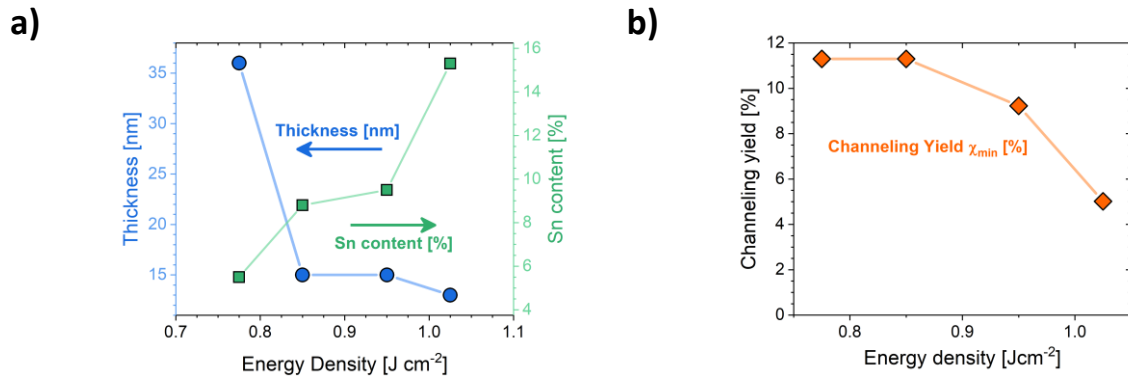


Figure B.7: GeSn 6% layer thickness and Sn content from RBS (a) and minimum channeling yield (ratio of channel and random orientation intensity) from RBS. The thickness and Sn content are values for the highest Sn content layer.

Rutherford BackScattering measurement were otherwise performed to confirm XRD results. Due to time constraints, only measurements on the GeSn 6% layer were performed. When increasing the energy density, the layer thickness decreased, shown by the blue points in **Figure B.7 (a)**. The thickness was, for ED = 0.75 Jcm⁻², equal to 36 nm, a value close to that of the as-grown layer (39 nm from XRD). It then decreased down to around 15 nm and stayed constant at higher energy densities. An increase of the layer thickness at higher energy densities was found by XRD. When the layer thickness decreased, an additional layer with a Sn content between 1.5% and 3% and a thickness of around 30 nm was formed because of Sn redistribution, resulting in multiple layers with different Sn contents. The Sn content of the high Sn content Sn layer increased from 5.5% up to 15.3%, shown in **Figure B.7 (a)** in green. This outlined a significant increase of the Sn content, even higher than with XRD. RBS gave us a more depth sensitive profile of the layer, while XRD gave access to a composition average. This might be one reason for the difference. The good crystalline quality of the layers was confirmed by **Figure B.7 (b)** minimum channeling yield measurements, i.e. ratios between RBS spectra's intensities in channeling and random orientations. It dropped from 11.3% at the melt threshold down to 5.0% at the full melt energy density, outlining the high crystalline quality of annealed layers. It might that the redistribution of Sn towards the surface caused less de-channeling and resulted therefore in a lower channeling yield. Overall, RBS measurements showed that Sn was redistributed and that high Sn content, good crystalline quality NLA layers were formed.

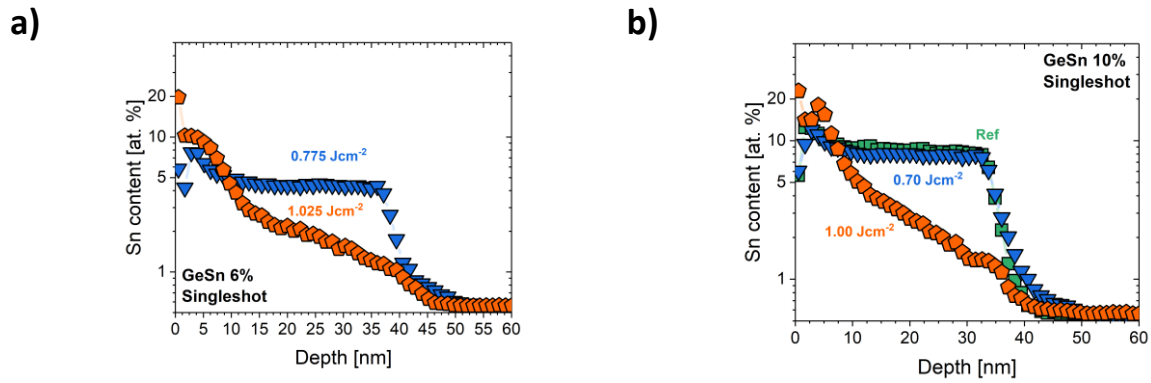


Figure B.8: (a, b) SIMS depth profiles in GeSn 6% and 10% and 14% layers with as-grown thicknesses close to 40 nm, this for various EDs.

Figure B.8 (a, b) SIMS depth profiles of annealed GeSn 6% and 10% showed Sn content increases towards the surface when significant amounts of the GeSn layers were melted (ED = 1.025 and 1.00 J cm⁻²). At the melt threshold (i.e. at ED = 0.70 J cm⁻² for 10% of Sn), Sn depth profiles of annealed samples were by contrast very close to that of as-grown layers.

References

- [1] G. Impellizzeri *et al.*, “Role of oxygen on the electrical activation of B in Ge by excimer laser annealing: Role of oxygen on the electrical activation of B in Ge,” *Phys. Status Solidi A*, vol. 211, no. 1, pp. 122–125, Jan. 2014, doi: 10.1002/pssa.201300308.
- [2] R. Milazzo *et al.*, “Oxygen behavior in germanium during melting laser thermal annealing,” *Mater. Sci. Semicond. Process.*, vol. 42, pp. 196–199, Feb. 2016, doi: 10.1016/j.mssp.2015.07.066.
- [3] R. Milazzo, M. Linser, D. Scarpa, A. Carnera, A. Andrighetto, and E. Napolitani, “Indiffusion of oxygen in germanium induced by pulsed laser melting,” *Mater. Sci. Semicond. Process.*, vol. 88, pp. 93–96, Dec. 2018, doi: 10.1016/j.mssp.2018.07.036.
- [4] L. Wang *et al.*, “Post-growth annealing of germanium-tin alloys using pulsed excimer laser,” *J. Appl. Phys.*, vol. 118, no. 2, p. 025701, Jul. 2015, doi: 10.1063/1.4926484.

Appendix C : Multi Pulse Nanosecond Laser Annealing of GeSn

Appendix C Multi Pulse Nanosecond Laser Annealing of GeSn

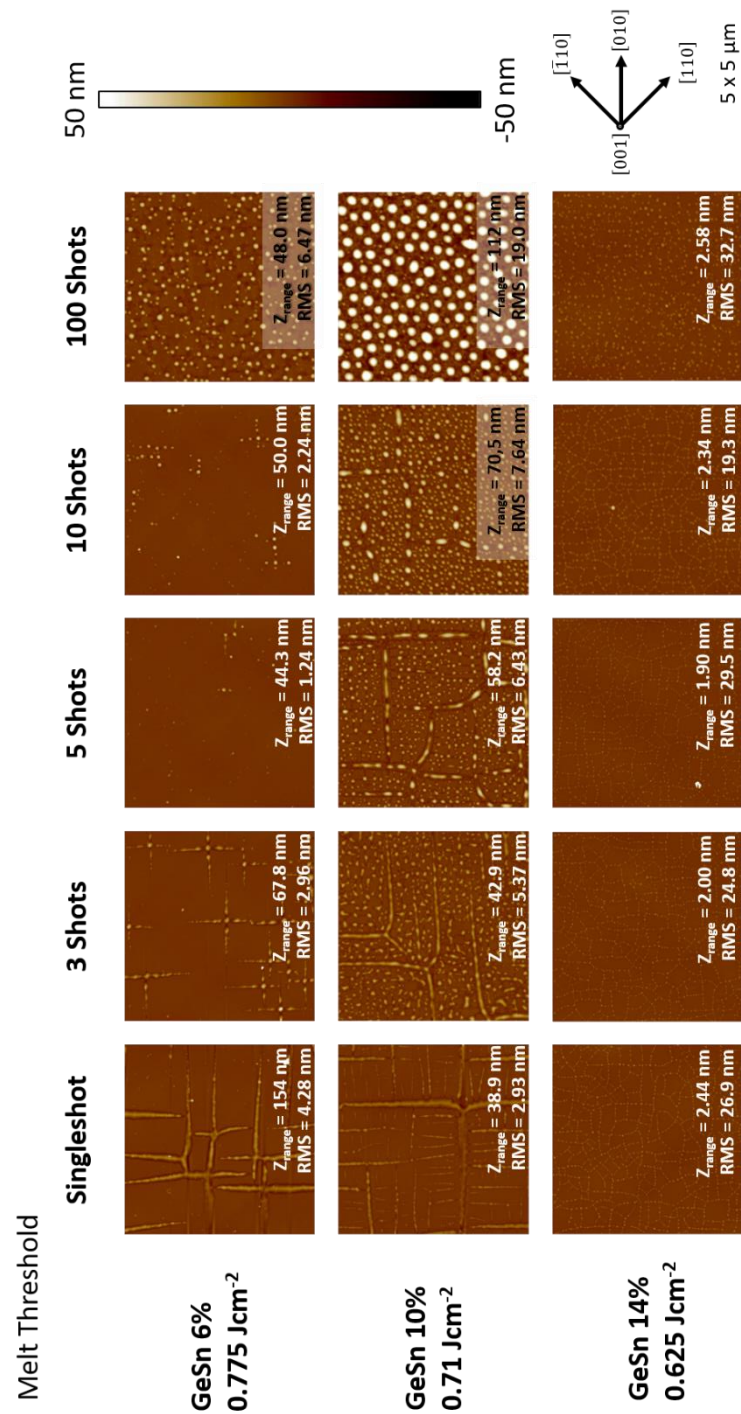


Figure C.1: $5 \mu\text{m} \times 5 \mu\text{m}$ AFM images of 36 to 41 nm thick pseudomorphic GeSn 6%, 10% and 14% (top to bottom) after annealing with various numbers of pulses up to 100 (left to right) at the melt threshold energy density. The z-scale was 50 nm for all shown images. The schematic on the bottom right shows the crystallographic directions.

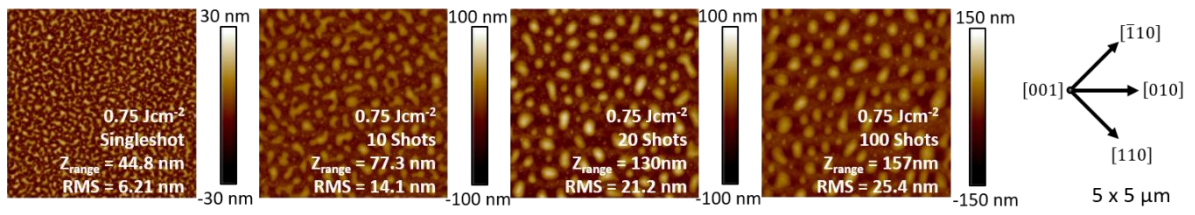


Figure C.2: Atomic force images of GeSn 14% laser annealed with 1 (z-scale 30 nm), 10, 20 (both z-scale 100 nm) and 100 laser pulses (z-scale 150 nm) at $0.75 Jcm^{-2}$. The schematic on the bottom right shows the crystallographic directions.

Appendix D :
GeSnOI
Mid-Infrared Laser Technology

ARTICLE

Open Access

GeSnOI mid-infrared laser technology

Binbin Wang¹, Emilie Sakat¹, Etienne Herth¹, Maksym Gromovyi¹, Andjelika Bjelajac¹, Julien Chaste¹, Gilles Patriarche¹, Philippe Boucaud², Frédéric Boeuf³, Nicolas Pauc⁴, Vincent Calvo⁴, Jérémie Chrétien⁴, Marvin Frauenrath⁵, Alexei Chelnokov⁵, Vincent Reboud⁵, Jean-Michel Hartmann⁵ and Moustafa El Kurdi¹✉

Abstract

GeSn alloys are promising materials for CMOS-compatible mid-infrared lasers manufacturing. Indeed, Sn alloying and tensile strain can transform them into direct bandgap semiconductors. This growing laser technology however suffers from a number of limitations, such as poor optical confinement, lack of strain, thermal, and defects management, all of which are poorly discussed in the literature. Herein, a specific GeSn-on-insulator (GeSnOI) stack using stressor layers as dielectric optical claddings is demonstrated to be suitable for a monolithically integration of planar Group-IV semiconductor lasers on a versatile photonic platform for the near- and mid-infrared spectral range. Microdisk-shape resonators on mesa structures were fabricated from GeSnOI, after bonding a Ge_{0.9}Sn_{0.1} alloy layer grown on a Ge strain-relaxed-buffer, itself on a Si(001) substrate. The GeSnOI microdisk mesas exhibited significantly improved optical gain as compared to that of conventional suspended microdisk resonators formed from the as-grown layer. We further show enhanced vertical out-coupling of the disk whispering gallery mode in-plane radiation, with up to 30% vertical out-coupling efficiency. As a result, the GeSnOI approach can be a valuable asset in the development of silicon-based mid-infrared photonics that combine integrated sources in a photonic platform with complex lightwave engineering.

Introduction

Low-cost and CMOS-compatible Si-based photonic technologies, like Silicon-On-Insulator (SOI), has enabled significant advances for on-chip optical processing in the near-infrared (IR) wavelength range, especially for high-speed detection and modulation of optical signals¹. One of its major drawbacks, though, is the lack of monolithically integrated group-IV lasers. Indeed, group-IV alloys are indirect bandgap semiconductors. To compensate for the lack of such laser sources, strong efforts were devoted these past few years to the integration of III–V compounds with high lasing performances to boost silicon photonic technologies². It was particularly true for telecom applications in the near-infrared wavelength range. So far, III–V lasers are the most standard and reliable light

sources on silicon despite their high manufacturing cost and their complex integration in Si CMOS-compatible manufacturing processes^{3,4}. GeSn semiconductor alloys, with a direct bandgap for tin contents larger than 7% (for strain-free materials)⁵ and which are compatible with large-scale and low-cost silicon processing and manufacturing tools, are promising for low-cost lasers^{6–8}. In addition, GeSn alloys have a narrow bandgap as compared to Ge and are thus suitable to shift the photonic wavelength from near-IR to mid-IR where many application domains exist: biochemical detection, gas monitoring, and thermal imaging. Integrating GeSn on silicon opens up new application fields for Si photonics^{9,10}.

In practice, the epitaxial growth of GeSn on silicon is quite challenging. The very low thermal equilibrium solubility of Sn in Ge, of only 1%, requires the development of metastable growth methods to increase the Sn content above 7%. Moreover, the very high lattice mismatch between GeSn and silicon makes their growth tricky. The use of Ge strain-relaxed buffer (Ge SRB) on silicon is the only approach used so far yielding high

Correspondence: Moustafa El Kurdi (moustafa.el-kurdi@c2n.upsaclay.fr)

¹Université Paris-Saclay, CNRS, C2N, 10 boulevard Thomas Gobert, 91120 Palaiseau, France

²Université Côte d'Azur, CNRS, CRHEA, Rue Bernard Grégory, 06905 Sophia-Antipolis, France

Full list of author information is available at the end of the article

© The Author(s) 2021



Open Access This article is licensed under a Creative Commons Attribution 4.0 International License, which permits use, sharing, adaptation, distribution and reproduction in any medium or format, as long as you give appropriate credit to the original author(s) and the source, provide a link to the Creative Commons license, and indicate if changes were made. The images or other third party material in this article are included in the article's Creative Commons license, unless indicated otherwise in a credit line to the material. If material is not included in the article's Creative Commons license and your intended use is not permitted by statutory regulation or exceeds the permitted use, you will need to obtain permission directly from the copyright holder. To view a copy of this license, visit <http://creativecommons.org/licenses/by/4.0/>.

enough material quality for lasing. However, it still faces major issues^{11–13}. For example, the active GeSn layers are usually grown beyond their critical thickness for plastic relaxation of the compressive strain at the GeSn/Ge interface¹⁴. Compressive strains are unfavorable since they worsen the optical gain properties of GeSn alloys, and, specifically, their sustainability with increasing temperature. Indeed, they reduce the energy barrier between the direct E_T and indirect E_L conduction band valleys (the so-called material directness parameter)¹⁵. Compressive strain in pseudomorphically grown GeSn alloys can turn, even for high Sn contents, the bandgap from direct to indirect, preventing gain and lasing¹⁶. Moreover, the relaxation of this compressive strain during the growth of really thick layers results in the formation of a dense array of misfit dislocations network close to the interface, at the bottom of the optically active region^{5,8}. Thus, many strategies have been employed these past few years to address this compressive strain issue while attempting to reach the highest material quality possible: growth of thick GeSn layers with gradually increasing tin content in order to limit the propagation of misfit defects into the bulk of the GeSn layer, use of SiGeSn barriers to confine the carriers away from the interfacial defects or, even, multi-quantum wells^{11,17–21}. All of those methods are based on in situ strain and defects management and have thus limited flexibility due to metastable growth mechanism constraints.

In this framework, the active injection of tensile strain into GeSn, via external stressor layers, is theoretically and experimentally known to offer further degrees of freedom to tune the strain and consequently the electronic band structure²². It also opens up new possibilities of enhancing gain properties and tuning the laser wavelength^{23,24}. Mainstream technological approaches for strain management call upon external stressor layers such as SiN^{25–27} or mechanical pulling of microbridges by external pads^{28–30}. They were mainly used for pure germanium, up to now. In both cases, layers should be suspended in order to increase the tensile stress injection and reach high enough optical confinement. Indeed, blanket GeSn on Ge SRB structures suffers from a low optical index contrast between GeSn and Ge, resulting in low optical confinement factors in the active region³¹. The active layer thickness has then to be increased in order to reach values in the range of the operating wavelength, e.g. $1\ \mu\text{m}$ ⁶, making external tensile strain injection more challenging. Suspended microdisk (MD) cavities or microbridges were thus the main structures evaluated up to now for such strained laser devices^{22,32}.

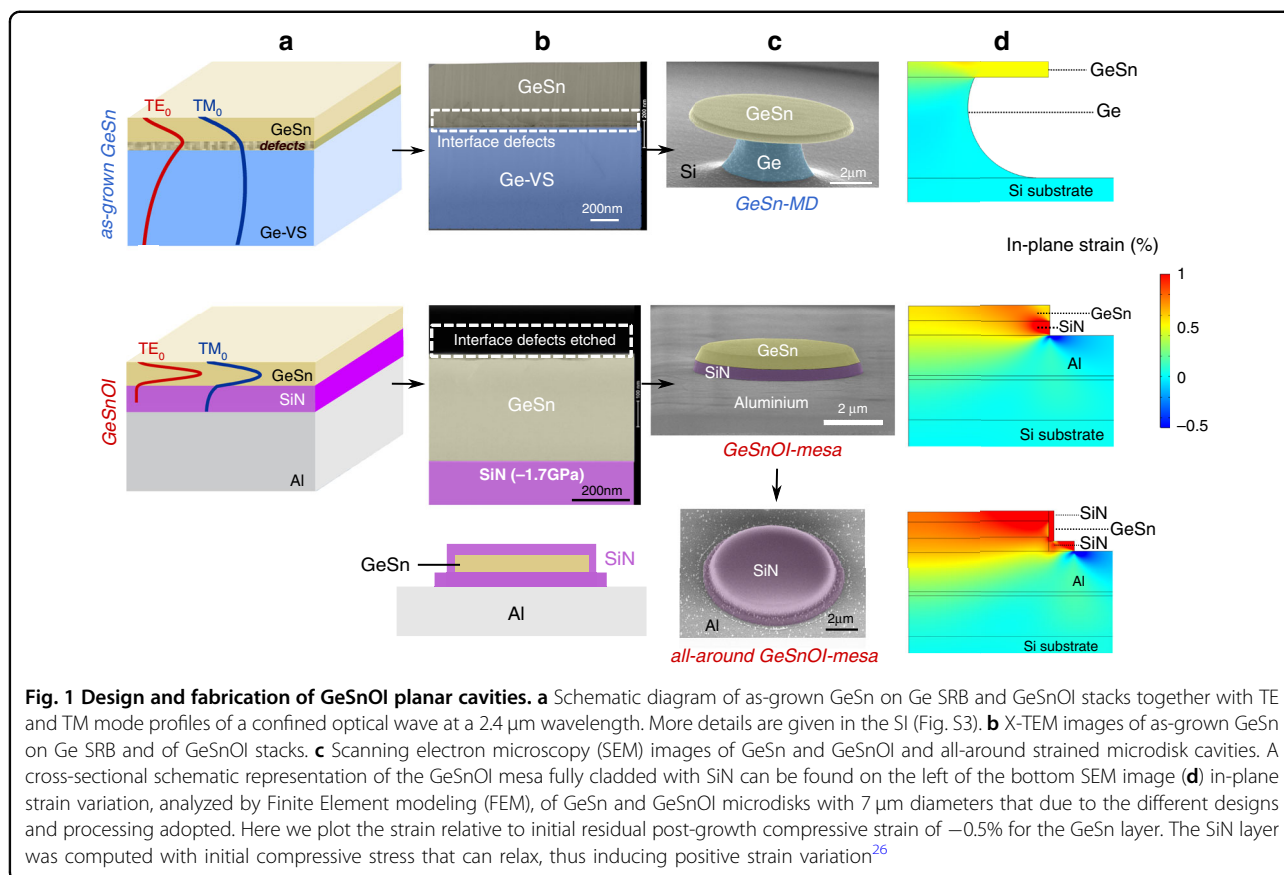
In this work, we show that GeSnOI stacks obtained through the bonding of GeSn active layers tackle all the above-mentioned issues: lattice mismatch interface defects management, compressive/tensile strain management, and

optical confinement. This is demonstrated through a systematic comparison of two structures with equivalent optical confinements: a suspended MD cavity fabricated from a GeSn layer on a Ge SRB, as in the existing literature, and another one, fabricated using the GeSnOI approach, with the use of specific SiN stressor films as insulating layers and with a simple disk-shape mesa as the cavity. The SiN layers used for tensile strain engineering yielded high index contrast with GeSn, which was required for optical confinement. After the bonding of the GeSn layer, the dense array of misfit dislocations close to the GeSn/Ge interface was removed thanks to a simple etching step, resulting in a better active layer quality that should result in an improved carrier injection efficiency. Another advantage offered by such bonded structures was the possibility of having the GeSn layer standing on an aluminum layer, resulting in a better heat dissipation^{27,33}. Moreover, such disk cavities being bonded to the substrate without any under-etching, it was also possible to down-scale their diameters to $3\ \mu\text{m}$, which was not feasible with as-grown GeSn-MD (lowest achievable diameters of $5\ \mu\text{m}$) for mechanical and thermal robustness reasons (the Ge pedestals cannot be too thin). Last but not least, the MD-shape mesa cavity obtained with this new approach also offered the possibility of managing the whispering gallery modes (WGM) in-plane radiation that made the collection of the laser light tricky. A specific design with circular diffraction grating around the MD was proposed to redirect the emission pattern vertically without changing the MD design or the lasing characteristics.

Results

We start with a presentation of the two kinds of structures. Both were based on a 500-nm-thick GeSn layer with 10.5% of Sn grown on a 2.5- μm -thick Ge SRB, itself on a 200 mm Si (001) wafer (Fig. 1a). The growth was performed in an industrial reduced-pressure chemical vapor deposition (RP-CVD). The as-grown GeSn layer had a residual compressive strain of -0.5% as estimated from X-ray diffraction reciprocal space mapping⁵. For such GeSn layer on Ge SRB, the critical thickness is around 100 nm. A dense array of misfit dislocations loops occurs up to a depth of typically 100 nm from the GeSn/Ge interface, can clearly be seen by cross-sectional transmission electron microscopy (X-TEM) (Fig. 1b), a zoomed view is provided in the SI (Fig. S1).

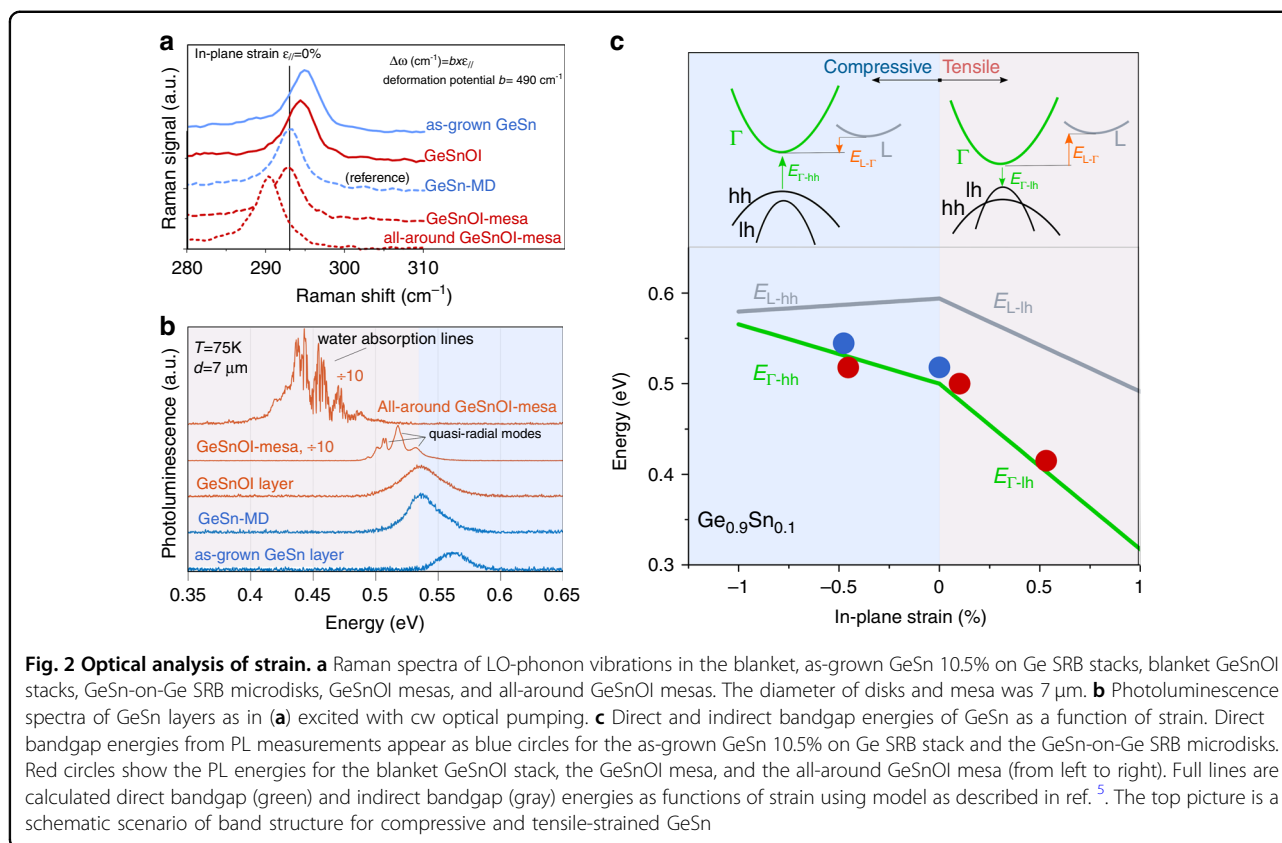
The optical index contrast is low in such a GeSn on the Ge SRB stack, resulting in a poor mode overlap with the active GeSn layer (Fig. 1a). The transverse electric (TE)-polarized propagating wave indeed has an overlap of only 37% with the GeSn active layer and its electrical field maximum is close indeed to the dislocated interfacial region. Similarly, a blanket GeSn on Ge stack provides a very weak transverse magnetic (TM)-polarized light



confinement, with an overlap of only 11% with the GeSn active layer. To circumvent such bad optical confinements, an isotropic under-etching of the Ge SRB is generally performed in order to obtain suspended GeSn-MD laser devices (Fig. 1c). In this configuration, the WGM situated at the edges of the disk experiment a GeSn/air optical index contrast which yields optical confinement factors of 95% and 78% for TE and TM, respectively.

For the MD-shape mesa laser cavity, the approach was different: a piece of the very same GeSn on Ge SRB was bonded on a host Si substrate coated with aluminum and SiN layers to obtain the GeSnOI structure shown in Fig. 1b, c (process detailed in the section A of the SI). The aluminum layer acted as a heat sink while the SiN layer acted as a stressor and provided optical confinement. After bonding, the Si substrate used to grow the Ge SRB was removed by selective etching. The Ge SRB and defects at the GeSn/Ge interface were then removed by another etching step. The final GeSn layer was then thinned from the as-grown 500 nm down to 400 nm, to get rid of the defective interfacial layer, which was then on top, and benefit from improved crystalline quality. The GeSn/SiN index contrast was high enough to provide excellent optical confinement for TE and TM-polarized modes: optical confinement factors were 93% for TE and 77% for

TM, e.g., values very close to that in GeSn MDs (Fig. 1c). This enabled us to suppress the impact of confinement on the optical gain when comparing the lasing performances of conventional GeSn/Ge MDs and MD-shape mesas based on bonded GeSnOI. Confining the modes in a few hundreds of nm-thick-GeSn layer was suitable for homogeneously distributed external tensile strain injection (Fig. 1d). The SiN insulator was initially compressively stressed, by typically -1.7 GPa. The strain was partly released and transferred to the GeSn layer after patterning the GeSnOI layers into MD-shape mesas, as shown by the FEM analysis. The GeSn layer had an initial compressive strain of -0.5% which vanished after the bottom SiN layer had partially released its built-in stress. This led to a very moderately tensile-strained structure (Fig. 1d). To further increase the tensile strain, an additional top SiN stressor layer can be deposited, resulting in an all-around structure. The tensile strain is then homogeneously distributed in the GeSn disk, as shown in Fig. 1d. An SiN stressor layer could also be deposited on top of the GeSn-on-Ge SRB MD, as proposed recently^{24,34}. The distributed tensile strain would be very inhomogeneous, then, which would not be favorable for lasing, as discussed in the SI (section F). Raman analysis of the strain (Fig. 2a) was performed using the strain and alloy potentials of



ref. ⁵. To identify the influence of strain on the band structure, we have performed a continuous wave (cw) photoluminescence (PL) analysis at 75 K under 1550 nm wavelength optical pumping. Different configurations, blanket GeSn on Ge SRB stacks, GeSn-on-Ge SRB MDs, blanket GeSnOI stacks, GeSnOI mesas and all-around GeSnOI mesas, were studied under the same experimental conditions, as shown in Fig. 2.

The suspended GeSn MDk has a PL emission red-shifted by 25 meV with respect to the PL emission from the blanket, unprocessed GeSn layer, which is due to compressive strain relaxation through the under-etching of the Ge SRB at the disk edges. The continuous wave PL spectrum of the GeSnOI mesa has red-shifted by 18 meV only with respect to the PL spectrum of the strain-relaxed GeSn-MD (without SiN stressor). This indicates that the mesa is very weakly tensile-strained, as confirmed by Raman analysis which gives only around 0.1% of in-plane strain, in line with FEM analysis. On the other hand, the all-around GeSnOI disk-shape mesa has a 100 meV red-shifted emission compared to the GeSn-MD. An injected equivalent biaxial tensile strain of 0.55% was measured with Raman spectroscopy, once again in good agreement with FEM analysis. We have plotted in Fig. 2c the bandgap energies extracted from PL spectra as a function of the strain measured by Raman spectroscopy. Full curves are

theoretical direct bandgap Γ -hh (Γ -lh) and indirect bandgap L-hh (L-lh) energies as functions of compressive (or tensile) strain⁵. A quite good agreement is obtained with experimental results (points in blue or red). The SiN stressor thus enabled us to modify the strain state of our GeSn 10.5% alloy, from a -0.5% compressive state to a 0.55% tensile state, e.g., a shift by $\sim +1\%$ of the strain. Band structure engineering was thus feasible without changing the Sn content.

To conclude this section, let us summarize the improvements provided by MD-shape mesas etched in bonded GeSnOI stacks as compared to suspended GeSn MDs. First, a GeSnOI disk-shape mesa has no interfacial defects anymore, while the suspended GeSn-MD still has defects at the pedestal's GeSn/Ge interface. Second, the bonded structure is not under-etched and incorporates an aluminum layer which acts as a heat sink, enabling a better thermal management. The optical confinement factor of optical modes with the active GeSn layer is as good in GeSnOI mesas than in under-etched structures suspended in the air. Finally, a full cladding of the GeSn mesa with SiN insulator layers yields high levels of homogeneously distributed tensile strain, something which is not really feasible with a suspended GeSn-MD. In the latter case, the only practical option is to add a stressor on the top of the suspended GeSn layer^{24,34}. Such

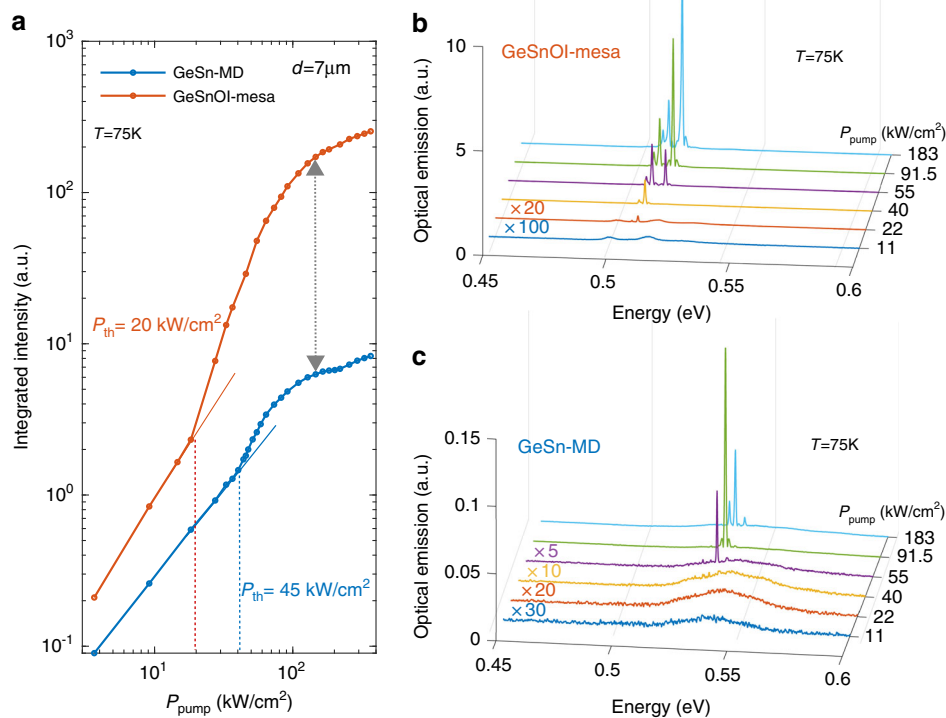


Fig. 3 GeSnOI mesa versus as-grown GeSn microdisk laser. **a** Light-Light (L-L) curves of 7 μm diameter GeSn microdisks and GeSnOI mesas with 360-nm-thick GeSn at 75 K under pulsed pumping (**b**) and **c** PL spectra at 75 K for various pulsed excitation powers for the GeSnOI mesa and the GeSn-MD, respectively. Excitation levels are given by the peak power densities

configuration results in an inhomogeneous tensile strain which is not convenient for lasing (see the SI section). Let us now show, in the next sections, how these improvements enabled us to enhance lasing performances.

Lasing performances were compared for the same 7 μm diameter mesas and MDs. The GeSnOI mesa has an active layer thickness of 360 nm, while the GeSn-MD active layer thickness is 500 nm. The analysis of the MD emission was performed with a 1550 nm wavelength pulsed optical pumping with a pulse width of 3.5 ns and a 25 MHz repetition rate. This illumination condition yielded high excitation densities while avoiding any significant thermal heating (SI section C). As shown in Fig. 3a–c, we observed clear lasing for mesas and MDs in the pulsed excitation regime. However, a two times lower threshold was obtained with the GeSnOI mesa (20 kW/cm^2), as compared to the GeSn-MD (45 kW/cm^2). In addition, the GeSnOI mesa had a peak intensity above lasing threshold which was 60 times higher than that of the GeSn-MD (Fig. 3b, c), while the spontaneous emission below threshold was typically four times more intense (Fig. 3a). We can note that the PL enhancement, below threshold with GeSnOI mesa due to the presence of the reflective Al layer with respect to the GeSn-MD, can be

estimated to be 1.7, which is lower than the observed enhancement. Furthermore (i) the GeSnOI mesa absorbs less efficiently, by a factor of 1.7, the incident pump beam (as discussed below); (ii) the GeSnOI active layer is a factor of 1.4 thinner than the GeSn-MD and thus has less emitters in its volume. We can thus assume that the improved PL signal below the threshold, despite the given above consideration, goes to the sense that carrier losses from non-radiative recombination process are partly reduced with the GeSnOI mesa, which could also partly explain such gain dynamic and threshold improvements^{35,36}. In previous work, we already demonstrated that the power density threshold in suspended GeSn MDs was one order of magnitude lower after the partial removal of interfacial defects from the MD edge region during the Ge under-etching⁵. However, interface defects above the Ge pillars were still present. Here, defects in GeSnOI mesas were removed from the whole surface, most likely explaining why power density thresholds were further reduced. The tensile strain in the GeSnOI mesa was small (only around 0.1%), with a limited impact on band structure and gain. We can note that the presence of the reflective Al layer, in the case of GeSnOI stack, may induce an enhancement of the pump beam absorption by

reflection effect from the bottom Al layer. However depending on the SiN layer thickness, one may have constructive or destructive interference between the incident and the reflected pump beam, inside the active GeSn region. In our specific case, the GeSnOI stack dimensions were not favorable, and the GeSn active layer is positioned at a node of the electrical field distribution along the GeSn/SiN/Al stacking. We estimated that in this configuration, the absorbed power of incident pump is significantly larger here for the GeSn-MD case, by typically a factor 1.7. The absorption coefficient is estimated to be 30% for the GeSn-MD while the GeSnOI mesa have an absorption coefficient of 18%. We can thus assume that the improved lasing thresholds were not induced by enhanced pump power absorption in the GeSnOI mesa. However further improvement of the laser characteristics could be reached thanks to appropriate design of the GeSnOI stack, for example, by using an SiN layer thickness of 600 nm, instead of 400 nm as in the present case. With such SiN layer thickness the GeSn active layer would thus be positioned favorably at the antinode of the electrical field distribution of the pump such that one could reach a strongly improved efficiency of the pump absorption, typically by a factor of 4.5. In this case the absorption coefficient of the pump could reach 80%. It is additionally important to note here that the quality (Q) factor of the GeSnOI mesa is two times lower than that of the GeSn-MD, which should have increased the GeSnOI mesa's lasing threshold. It is however lower than that of the GeSn-MD, illustrating the importance of defects removal to improve the gain. One can also observe in Fig. 2b that the GeSnOI mesa features multimodal lasing, which is the signature of spatial and spectral broadening of the gain, whereas the GeSn-MD has mostly a mono-mode lasing signature.

This can be explained by the presence of the Ge pedestal in the GeSn-MD. Indeed, the edges of the pedestal are 1.5–2 μm away from the MD periphery, resulting in optical losses for higher-order radial modes, i.e., those which have a higher overlap of the optical field with the pedestal. The Q -factor of these modes decreases and they are not able to lase. On the contrary, the same diameter GeSnOI mesa has the whole surface isolated from the substrate by the bottom SiN layer. Therefore, the higher-order radial modes do not incur any pedestal losses. This is also confirmed by the PL spectra of the GeSnOI mesa below threshold, with the presence of high-order radial mode resonances (denoted as quasi-radial modes in Fig. 2b), which were not observed for the GeSn-MD. The multimodal features thus could also be explained by a higher spatial gain broadening with the GeSnOI mesa.

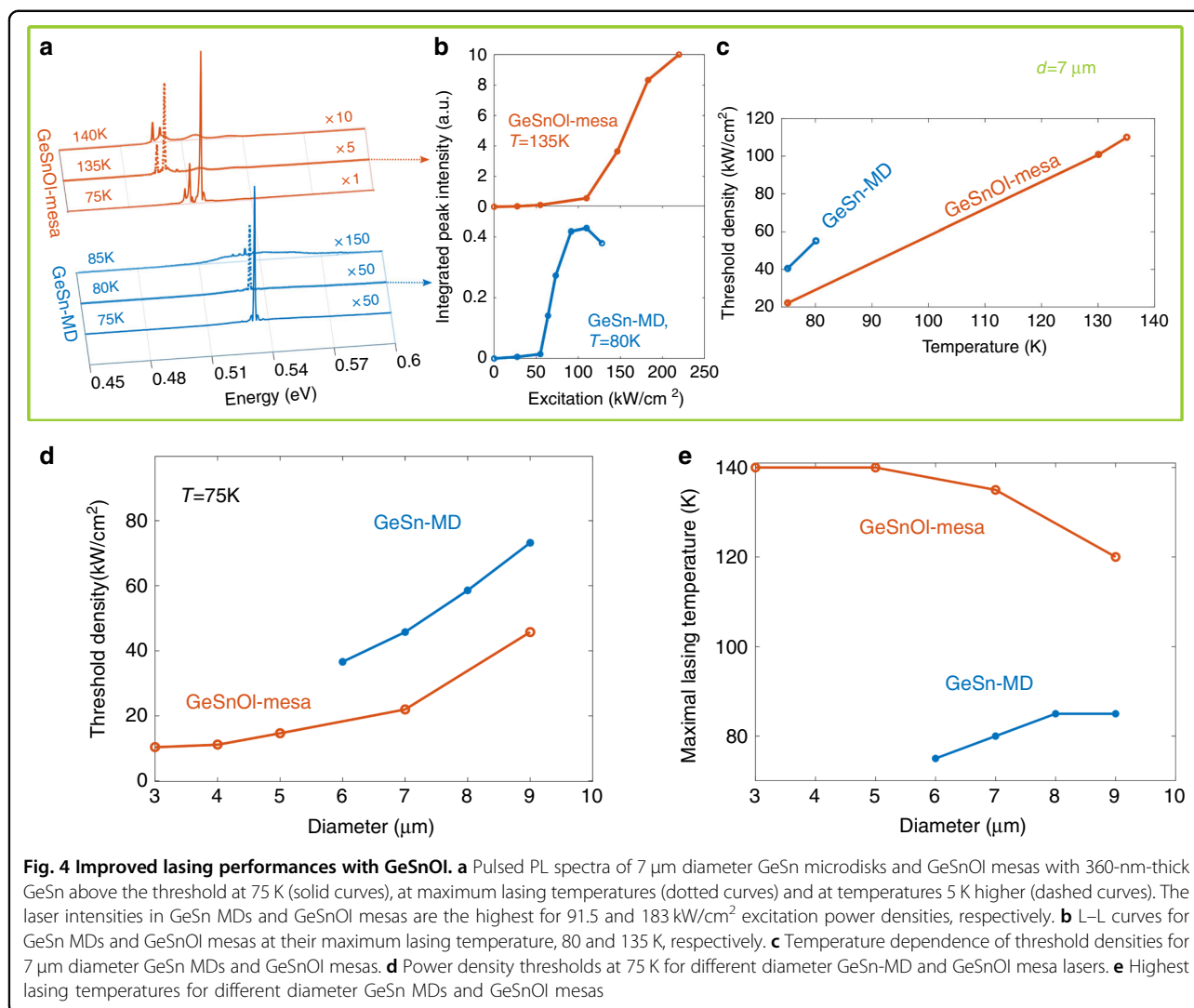
The GeSnOI mesa gain also persists at higher temperature. Lasing spectra above threshold (Fig. 4a) along with L–L curves and lasing thresholds (Fig. 4b, c) at

different temperatures clearly show the improvement when switching from 7 μm diameter GeSn MDs to GeSnOI mesas, with maximum lasing temperatures of 80 and 135 K, respectively. One can estimate, from threshold dependence with temperature of Fig. 4c, a T_0 value of 40 K. This value can be associated with activation of non-radiative recombination process, and intervalley scattering that weaken the optical gain when increasing the temperature. The slope efficiency is as well better above threshold for GeSnOI mesas and this feature is attributed to higher quantum efficiency associated with better carrier distribution in the gain region.

Then, different diameter GeSn MDs and GeSnOI mesas were systematically studied to compare their lasing threshold and their maximum lasing temperature. Thresholds at 75 K are provided in Fig. 4d and maximum lasing temperatures in Fig. 4e, both as functions of the MDs diameter. We reproducibly obtained lower thresholds and higher maximum lasing temperature for GeSnOI mesas than for GeSn MDs.

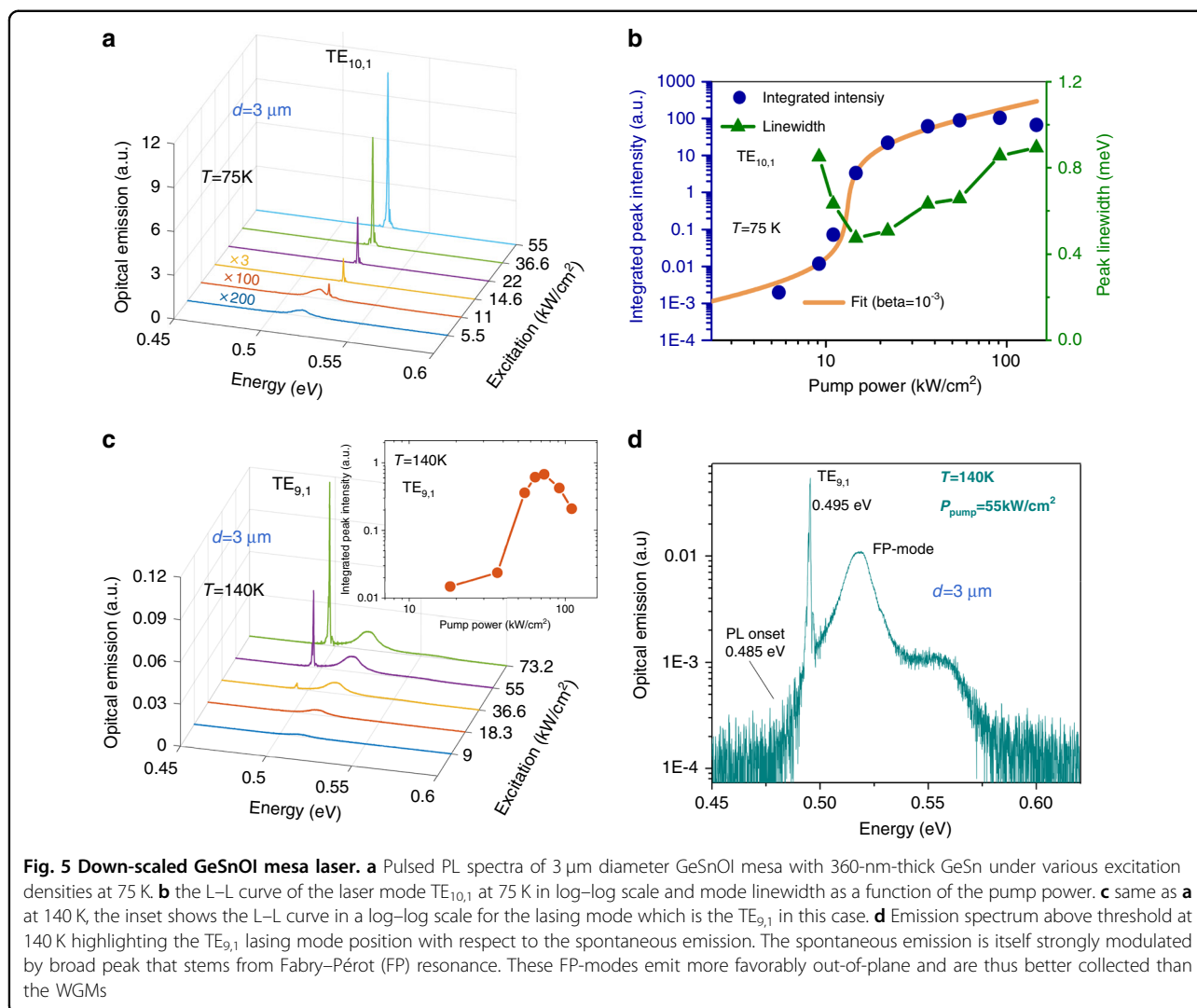
A heat dissipation study was conducted for suspended GeSn MDs (see SI section C). It showed that thermal cooling strongly depended on the MD geometry. We did not observe lasing for MD diameters smaller than 6 μm with therefore very narrow Ge pedestals. Since the under-etching was the same for all diameters, MDs with the largest diameters had larger pedestals and evacuated heat more effectively. For GeSn-MD diameters between 7 and 9 μm , the temperature increase upon optical injection should be around 15 K for a 200 kW/cm^2 excitation density in a pulsed regime, as used in the current experiments. Yet, MDs were not able to reach lasing at temperatures higher than 85 K. This maximum lasing temperature is similar to that in a previous work where MDs were fabricated from the very same GeSn 10.5% layer with equivalent disk diameters but smaller undercuts (1.5 μm instead of 2 μm here). Such reduced lasing temperatures are likely due to limited heat dissipation and gain decrease as the temperature increases.

In GeSnOI mesas, the maximum lasing temperature is 140 K, i.e., 55 K higher than in suspended GeSn MDs. Such an improvement is attributed to a higher crystalline quality, i.e., a lower number of non-radiative recombination channels making the temperature dependence of gain more robust, and to the increased heat dissipation. With such mesa structures, disk diameters can be shrunk down to 3 μm without degrading thermal dissipation upon optical pumping. A reduced size seems to help heat dissipation. Indeed, as seen in Fig. 4e, the lowest diameter mesa has the highest lasing temperatures. Such 3 μm diameter MD mesa also features the smallest lasing thresholds, only 12 kW/cm^2 at 75 K and 40 kW/cm^2 at 140 K (Fig. 5a, b).



Lasing thresholds decrease with the mesa or MD diameters. This was expected as smaller volume cavities have larger spontaneous coupling factors with the optical modes^{36,37}. Here, the coupling factor β was found to be 10^{-3} from a fit of L–L curve of the lasing mode using laser rate equations (Fig. 5b). The 3 μm smallest diameter mesa indeed features single-mode lasing at 0.525 eV at 75 K, which is attributed to a $\text{TE}_{10,1}$ WGM resonance. The sharp linewidth decrease at threshold for this mode allows for an estimate of an equivalent Q -factor value at transparency of typically 1000. A linewidth increase is observed above threshold due to thermal effects. This Q -factor value at transparency has to be compared with modeled values of Q -factor around 10,000–13,000 (see Fig. 6). Note that the measurements are performed in pulsed excitation and the linewidth might vary over the pulse duration, thus inducing larger experimental linewidth than modeled ones in the framework of steady-state regime. The

differences may also stem from fabrication imperfections such as surface roughness of the GeSnOI layer after bonding (Fig. S1) as well as the sidewall roughness of the mesas. The modeled free spectral range is equal to 35 meV for the fundamental radial mode $n = 1$ in such small diameter mesas, which is of the same order of the spontaneous emission broadening. It is thus expected that such a small cavity has a reduced number of modes that overlap with gain, resulting in single-mode lasing as obtained on Fig. 5a–c. At 140 K, the laser emission peak has shifted by 30 meV to lower energy as compared to the laser emission peak at 75 K. Note that the bandgap energy, and thus the optical gain is expected to redshift by typically 10 meV when increasing temperature from 75 to 140 K (see Fig. S7c of the SI). Lasing at 140 K is thus observed with the next available confined optical mode that has a better overlap with gain at 140 K, i.e., the $\text{TE}_{9,1}$ mode instead of $\text{TE}_{10,1}$ (Fig. 5c). The $\text{TE}_{9,1}$ mode energy is

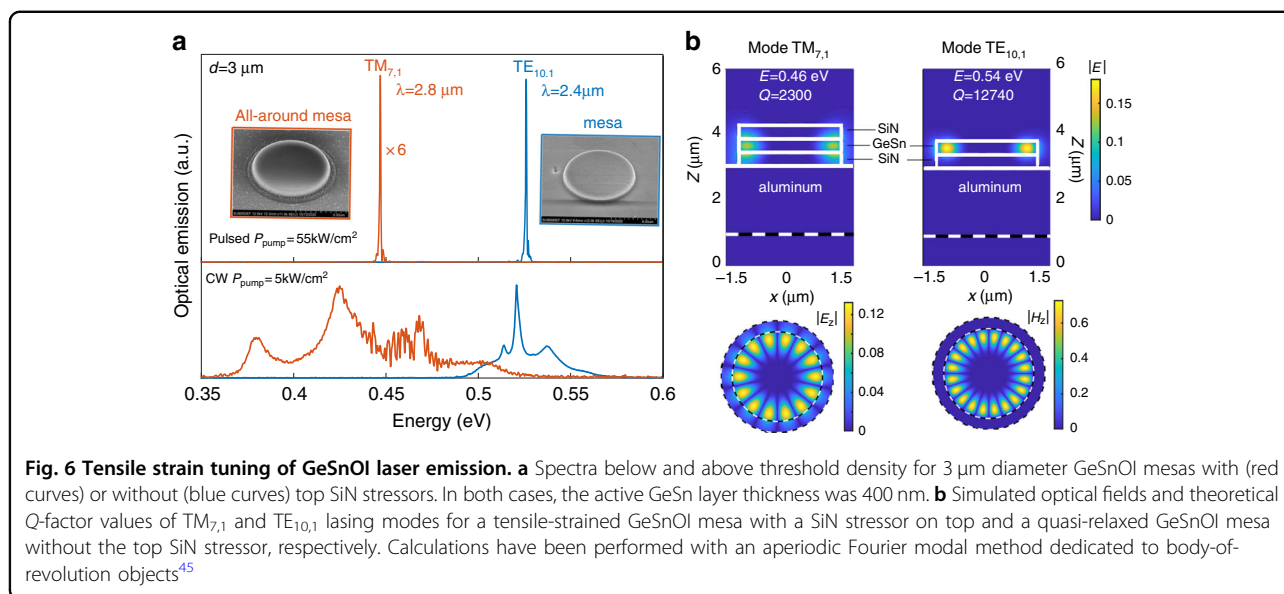


above the onset of spontaneous emission (Fig. 5d). This mode switching when changing the temperature is nonetheless not systematically observed. As discussed in the SI (Fig. S7a, b), we did not observe such mode switching for 400-nm-thick disk mesas with 3 μm diameter. We can note that the $\text{TE}_{10,1}$ mode for sample with 400-nm-thick GeSn is red-shifted by 7 meV with respect to the $\text{TE}_{10,1}$ mode in the 360-nm-thick GeSn sample (see Fig. S8 of the SI). With this sample the $\text{TE}_{10,1}$ mode should thus maintain a better spectral overlap with the optical gain than the $\text{TE}_{9,1}$ mode when the temperature increases from 75 to 140 K. The slope drop at high pump intensity as observed in the inset of Fig. 5c corresponds to the roll-off of the lasers³⁸, as a consequence of self-heating and modified carrier distribution spatially and in k -space.

As proof of the feasibility of tuning, in GeSnOI mesas, the laser wavelength and bandgap with external tensile strain, we also probed with pulsed excitation all-around GeSnOI mesas. After the conformal deposition of the top

SiN stressor layer, an additional etching of the SiN around the MD was performed to avoid compressive strain injection at the edges of the mesas. In that case, as shown in Fig. 6a, we see a clear redshift of the emission, from 2.4 to 2.8 μm , be it below and above the lasing threshold. Such a redshift is due to the applied in-plane tensile strain of 0.5% as deduced from Raman, PL, and FEM analysis.

A more detailed analysis of the lasing performances presented in the SI (section E) however showed that all-around GeSnOI mesas did not have improved lasing performances despite a stronger lifting of the valence band degeneracy, which should have resulted in a transparency threshold reduction. The strain-induced increase of the Γ -L conduction band energy barrier was also expected to improve the maximum lasing temperature. Here, the lasing threshold of 3 μm diameter, tensile-strained GeSnOI all-around mesas was 15.5 kW/cm^2 , to be compared with 12 kW/cm^2 for quasi-relaxed GeSnOI mesas without SiN stressors on top. The maximum lasing

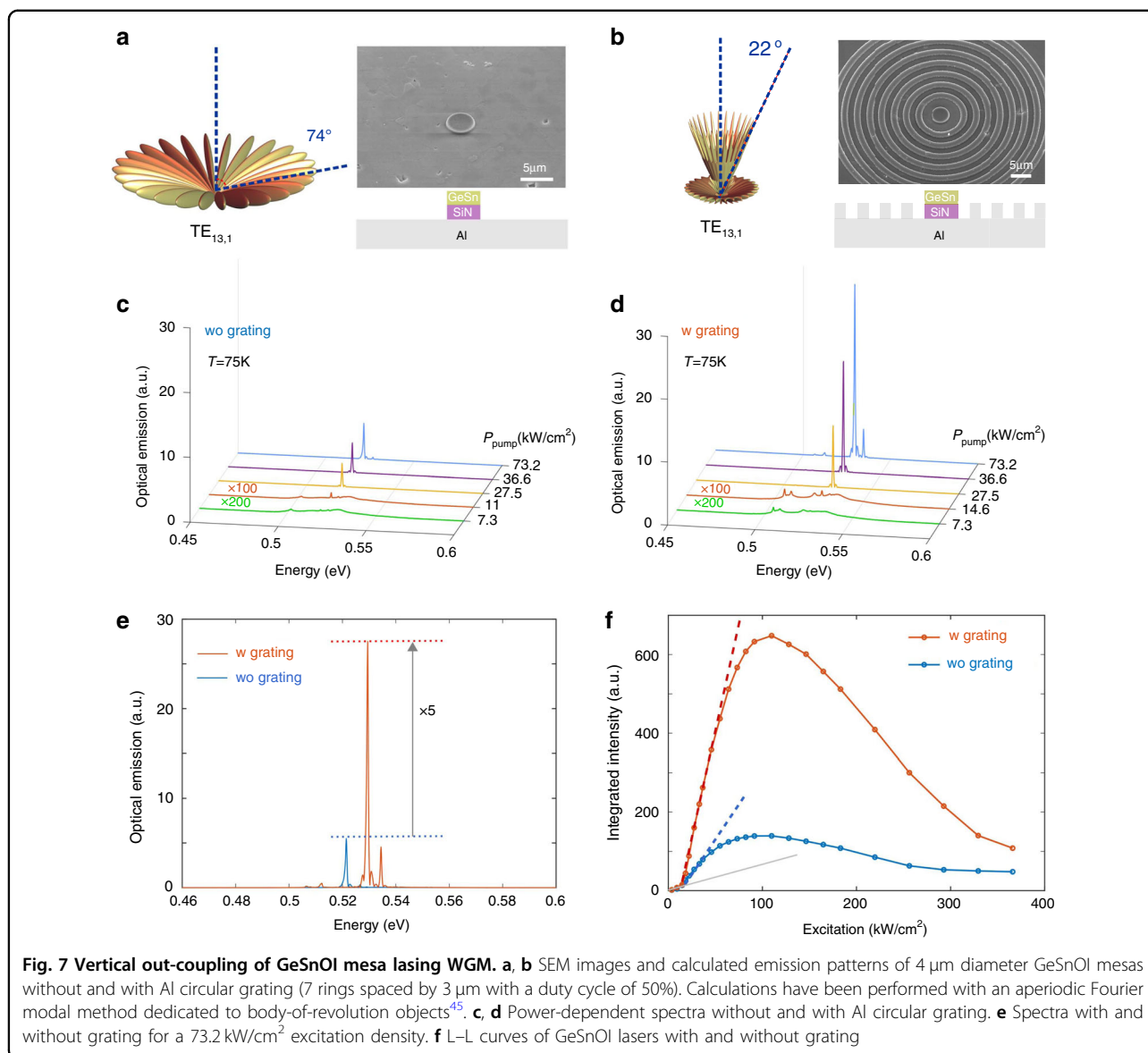


temperature was also slightly lower, 130 K for all-around mesas instead of 140 K without SiN stressors on top (SI section E). The optical gain was thus weaker. Tensile-strained mesas featured TM-polarized optical gain. The lasing mode at 2.8 μm of all-around GeSnOI mesas can be assigned the $\text{TM}_{7,1}$ resonance. Since TM-polarized modes, here at a longer wavelength, have a stronger overlap with the Al metallic layer, it seems likely that the lower performances are due to higher TM losses (Fig. 6b). The Q -factor was of 2300 for the $\text{TM}_{7,1}$ mode, a value significantly lower than the Q -factor of 12,740 we had for the $\text{TE}_{10,1}$ laser mode of GeSnOI mesas without SiN on top. Increasing the bottom SiN thickness, in order to limit the TM field overlap with aluminum and improve the WGM Q -factors, should enable enhanced performances of GeSnOI all-around mesas as shown in the SI (Fig. S4). Aluminum could also be replaced by a dielectric cladding layer to avoid such optical losses. Several strategies using SiO_2 layer as dielectric are proposed in the SI (Fig. S5). However, since SiO_2 is a poor thermal conductor, one should use thin layers in the order of 100-nm-thick to maintain a good thermal dissipation. Despite degradation of thermal dissipation with thick SiO_2 dielectric layers (e.g., 400 nm) as replacement of Al, the planar GeSnOI structure maintains a clear superiority as compared to the suspended GeSn-MD approach for down-scaled geometries (Fig. S5c). Aluminum was selected here as it could be etched selectively with respect to GeSn and SiN in order to fabricate suspended structures, as in ref. ²². We show here the interest of using a GeSnOI approach with a bottom stressor that is compatible with an all-around strain transfer scheme without suspending the active GeSn layer, thereby improving thermal dissipation while benefiting from high optical confinement. In the SI

(Fig. S10), we show that, in contrast, the use of a single side SiN stressor on the top surface of a suspended MD^{24,25,34} is not suitable for homogeneous strain injection into the GeSn active layer. Such a single stressor approach indeed resulted in optical gain quenching.

MD mesas with SiN stressors have many advantages as optical laser cavities, such as scalability with the operating wavelength and high Q -factor provided by WGMs. One of their drawbacks, though, is the in-plane circular spread of the WGM radiation pattern. It differs markedly from the auto-collimated beam from conventional lasers, making emitted power collection tricky. The two common approaches to extract power are (i) side or top collection of radiated power with optical apparatus such as microscope objectives (ii) evanescent coupling of the disk WGM with expanded waveguide modes. The first does not yield a total collection of the in-plane radiation pattern, due to the limited numerical aperture of the collecting objectives. The second approach, with addition of some process complexity, requires an optimization of light injection into the waveguide. Critical coupling conditions have to be met by fine-tuning the gap between waveguides and MDs. Such an evanescent coupling also occurs over a limited fraction of the disk periphery and has an impact on the cavity Q -factor and therefore on its lasing properties. We show here that GeSnOI mesas are advantageous for a proper light collection. Indeed, circular diffraction gratings can be added around disk-shape mesas to redirect the light vertically.

Here, we collect the MD emission vertically with an $\times 50$ objective with a 0.65 numerical aperture. Light is thus collected from the sample surface within a solid angle of 40° . Yet, standard MDs have a radiation pattern which is mainly out of this solid angle, as shown in Fig. 7a, with a



modeling of the WGM radiation for a 4 μm diameter GeSnOI mesa MD. A small MD diameter was chosen as it simplified the modal analysis. Such a mesa features a monomode lasing at 0.52 eV which can be assigned to the $\text{TE}_{13,1}$ mode at an energy of 0.54 eV. The maximum radiation angle is situated around 74° with respect to the normal incidence (Fig. 7a). These simulations also show an extremely small coupling factor from such WGM pattern to the collecting objective, of the order of 10^{-5} only. The collected emission from WGM lasing therefore comes from out-of-plane leakage rather than from radiative emission. Such leakage paths stem from imperfection introduced during fabrication (sidewall and surface roughness, circular symmetry breaking). These imperfections, useful to collect more light into the collection angle, are obviously unwanted in practice since

they result in lower Q -factors and increase lasing thresholds.

One way of overcoming this issue would be to have an optimized process flow in order to reach the highest Q -factors possible and use external gratings to redirect the WGM in-plane radiation pattern. This is feasible with GeSnOI mesas, while it would be very tricky with GeSn suspended MDs. We thus designed a circular diffraction grating with optimal period and duty cycle to maximize the redirection of the WGMs light into the 40° solid angle for a 4 μm diameter GeSnOI mesa (see the SI). Figure 7b radiation diagram with such additional circular grating is drastically modified for the $\text{TE}_{13,1}$ mode, with then a maximal radiation angle of 22° compared to normal incidence. The total flux integrated into our objective collection angle becomes theoretically of 30% as

compared to 2.4×10^{-5} without grating. Such a power collection improvement is expected for lasing WGM mode specifically coupled to the grating. The GeSnOI mesa laser emission spectra and integrated collected intensity, below and above laser threshold, are shown in Fig. 7c–f with and without grating. Below the threshold, spontaneous emission dominates the spectrum and the contribution from WGM is weak as it is not amplified. Intensities with and without grating are thus equivalent. On the contrary, above a threshold which was around 15 kW/cm^2 in both cases, the WGM contribution dominates the spectrum and a clear improvement of collected intensity is observed, typically by a factor of 5 for mesas with gratings. The maximum collected peak power is around $20\text{--}30 \mu\text{W}$.

The modeling predicted an improvement by 12,500 of the intensity collected by the objective with such a grating. It is thus very clear that initially, the collected light without the grating mainly stems from leak paths, as mentioned above, due to roughness scattering not accounted for in the modeling. The very weak estimated coupling factor of the WGM radiation to the objective, of the order of 10^{-5} for mesa MDs, is thus not representative of the power collected experimentally. Such scattering obviously tends to reduce the cavity quality factor of the $\text{TE}_{13,1}$ mode calculated to be $Q_{\text{rad}} = 8160$ for perfectly smooth surfaces and sidewalls. Such a method would thus yield a better control of the total power radiated from the cavity without changing the cavity geometry and its lasing characteristics. The same emission control is feasible for larger diameter cavities. The $4 \mu\text{m}$ diameter featuring single-mode lasing was chosen here to simplify the experimental analysis, but similar results with higher diameter disks have been simulated (data not shown). Gratings without aluminum could as well be envisaged.

Discussion

On the basis of our proposed GeSnOI platform, one could also obtain in-plane coupling of radiated emission into waveguides if the aim was to inject the laser emission into a photonic circuit. The most obvious way would be to use SiN, which offers a high optical index and high transparency in the mid-infrared, as the waveguide material. SiN was indeed proven to be suitable for mid-IR photonic circuits in the literature^{39,40} and could be combined with GeSn as active materials. This should be feasible with our proposed GeSnOI stack. Selective deposition of SiN could be used if an increase in the waveguide core thickness in some places was needed. Blanket SiN deposition followed by selective etching of some of it in specific places, as used here to fabricate all-around mesas, could be selected to construct the in-plane photonic circuit. SiN etching can for instance be performed using fluoride-based plasma, which is very

selective to GeSn⁴¹. The aluminum layer might have to be replaced by low index dielectrics cladding such as silicon dioxide, then⁴². As discussed above and detailed in the SI (section C), the replacement of the Al layer requires specific designs with the aim to maintain a good thermal dissipation for the laser devices. We note that the mesa structure offers superior thermal dissipation than under-etched GeSn/Ge SRB layer while having equivalent optical confinement factors. In this work, we used Al grating for light beam engineering with GeSnOI. There are many others possibilities, using dielectric instead of Al material for that purpose when using infrared compatible materials. In the latter cases, the periodicity and the dimension will depend on the optical parameters of the chosen material. We can further envision more complex mode radiation shaping as compared to the one provided in the present work, by using phase engineering of the wave fronts.

We have shown here the interest of using GeSn active layers bonded on dielectric stressors to fabricate GeSnOI stacks, resulting in optimized group-IV laser designs in terms of defects, strain, modal, and thermal engineering. Additionally, bandgap energy and directness parameters could be tuned via tensile strain. The strain can be varied by using different parameters for the SiN stressor deposition, by varying the Sn content of the alloy, and the degree of relaxation of the GeSn layer through the conditions of epitaxial growth. Obviously, such an approach can be applied to different GeSn active layers with varying Sn contents, as well as complex heterostructures with quantum wells, to provide additional electronic band and gain engineering. The first purpose of the present work was to show the relevance of GeSnOI MD mesas compared to more conventional structures such as suspended GeSn MDs on Ge pillars. The same as-grown 500-nm-thick GeSn 10.5% layer was used for such a comparison. GeSnOI mesas have approximately the same high index contrast than suspended MDs and are suitable for the fabrication of planar structures, free from interface defects, such as ridge Fabry–Perot waveguides, ring cavities, or even photonic crystals. Enhanced performances were obtained with the GeSnOI approach as compared to conventional approaches. We highlighted that planar emission can be redirected vertically thanks to additional gratings, illustrating the flexibility provided by such a technology.

The key advantage of this GeSnOI platform is its ability to combine active laser structures with passive SiN circuitry from the near-infrared to the mid-infrared. It represents a new paradigm for infrared Group-IV photonics that eliminates the need for III–V laser integration.

To be able to reach temperature with this GeSnOI approach, one of the most obvious way is to increase the tin content of the alloy. Here we have reported a complete

study as a first proof of concept to assess the GeSnOI laser technology with respect to the conventional GeSn/Ge SRB, starting from a GeSn with a 10.5% tin content. It has been shown in the literature that lasing up to 270 K can be reached in suspended structures, thus with poor thermal management, using under-etched GeSn/Ge SRB cavities³². In this case, a tin content of 16% in the active region was used. The increase of tin content induces an increase of the directness of the band structure that is one of the main key ingredient which allowed for the higher-temperature laser operation as compared with lower tin content materials. As the GeSnOI approach exhibits improved performances, we can thus expect that this approach, if applied to materials with higher tin content than in this work, could lead to even higher temperatures of laser operation.

One second challenging goal is to demonstrate electrically driven devices. We emphasize that this is completely compatible with our approach if we start with GeSn pin junctions since the bonding can be applied to any kind of GeSn heterostructures. Bonding GeSn diodes is completely feasible and the electrical injection can be made with such GeSnOI active layers. The GeSnOI can even offer better performances as compared to a standard approach since the high index contrast offers more flexibilities in the design to reduce the overlap of the laser modes with doped contacts and the electrodes. It has been shown that electrical injection in optical microcavities is compatible with the use of the SiN stressor transfer method, as long as specific designs are used to define the electrode geometries⁴³.

Materials and methods

GeSn on Ge SRB material growth on silicon

Epitaxial growth of close to 500-nm-thick GeSn 10.5% was performed in a 200 mm Epi Centura 5200 cluster tool from Applied Materials on a Ge SRB on silicon. The Ge SRB was grown with GeH₄ and a low temperature/high temperature approach, followed by some short duration Thermal cycling to reduce the threading dislocations densities to values around 10⁷ cm⁻², typically. Meanwhile, the GeSn layer was grown close to 337 °C at 100 Torr thanks to Ge₂H₆ and SnCl₄ precursors⁴⁴. The as-grown layers was analyzed by X-ray diffraction reciprocal space mapping. The layer has a residual compressive strain of -0.5%.

WGM radiation modeling

The WGM analysis and their scattering by the Al grating was performed in the framework of the aperiodic Fourier modal method that was detailed in ref.⁴⁵. The permittivity model considered, here and in previous sections, for aluminum was a realistic Lorentz–Drude model⁴⁶. More details are provided in the SI (section G) for the design of the Al grating.

Acknowledgements

This work was supported by the French RENATECH network, the French National Research Agency (Agence Nationale de la Recherche, ANR) through funding of the ELEGANTE project (ANR-17-CE24-0015). B.W. was supported by Nano2022 IPCEI project with STMicroelectronics.

Author details

¹Université Paris-Saclay, CNRS, C2N, 10 boulevard Thomas Gobert, 91120 Palaiseau, France. ²Université Côte d'Azur, CNRS, CRHEA, Rue Bernard Grégory, 06905 Sophia-Antipolis, France. ³STMicroelectronics, Rue Jean Monnet, 38054 Crolles, France. ⁴Université Grenoble Alpes, CEA, IRIG-DePhy, 17 rue des Martyrs, 38000 Grenoble, France. ⁵Université Grenoble Alpes, CEA, Leti, 17 rue des Martyrs, 38000 Grenoble, France

Conflict of interest

The authors declare no competing interests.

Supplementary information The online version contains supplementary material available at <https://doi.org/10.1038/s41377-021-00675-7>.

Received: 11 May 2021 Revised: 25 October 2021 Accepted: 29 October 2021

Published online: 17 November 2021

References

- Soref, R., Buca, D. & Yu, S. Q. Group IV photonics: driving integrated optoelectronics. *Opt. Photonics News* **27**, 32–39 (2016).
- Thomson, D. et al. Roadmap on silicon photonics. *J. Opt.* **18**, 073003 (2016).
- Wang, Z. C. et al. Novel light source integration approaches for silicon photonics. *Laser Photonics Rev.* **11**, 1700063 (2017).
- Seifried, M. et al. Monolithically integrated CMOS-compatible III-V on silicon lasers. *IEEE J. Sel. Top. Quantum Electron.* **24**, 8200709 (2018).
- Elbaz, A. et al. Reduced lasing thresholds in GeSn microdisk cavities with defect management of the optically active region. *ACS Photonics* **7**, 2713–2722 (2020).
- Zhou, Y. Y. et al. Electrically injected GeSn lasers on Si operating up to 100 K. *Optica* **7**, 924–928 (2020).
- Zhou, Y. Y. et al. Optically pumped GeSn lasers operating at 270 K with broad waveguide structures on Si. *ACS Photonics* **6**, 1434–1441 (2019).
- Wirhns, S. et al. Lasing in direct-bandgap GeSn alloy grown on Si. *Nat. Photonics* **9**, 88–92 (2015).
- Singh, V. et al. Mid-infrared materials and devices on a Si platform for optical sensing. *Sci. Technol. Adv. Mater.* **15**, 014603 (2014).
- Hodgkinson, J. & Tatam, R. P. Optical gas sensing: a review. *Meas. Sci. Technol.* **24**, 012004 (2013).
- Reboud, V. et al. Optically pumped GeSn micro-disks with 16% Sn lasing at 3.1 μm up to 180 K. *Appl. Phys. Lett.* **111**, 092101 (2017).
- Al-Kabi, S. et al. An optically pumped 2.5 μm GeSn laser on Si operating at 110 K. *Appl. Phys. Lett.* **109**, 171105 (2016).
- Dou, W. et al. Investigation of GeSn strain relaxation and spontaneous composition gradient for low-defect and high-Sn alloy growth. *Sci. Rep.* **8**, 5640 (2018).
- von den Driesch, N. et al. Direct bandgap group IV epitaxy on Si for laser applications. *Chem. Mater.* **27**, 4693–4702 (2015).
- Gupta, S. et al. Achieving direct band gap in germanium through integration of Sn alloying and external strain. *J. Appl. Phys.* **113**, 073707 (2013).
- Pezzoli, F. et al. Temperature-dependent photoluminescence characteristics of GeSn epitaxial layers. *ACS Photonics* **3**, 2004–2009 (2016).
- Stange, D. et al. Short-wave infrared LEDs from GeSn/SiGeSn multiple quantum wells. *Optica* **4**, 185–188 (2017).
- Stange, D. et al. GeSn/SiGeSn heterostructure and multi quantum well lasers. *ACS Photonics* **5**, 4628–4636 (2018).
- Grant, P. C. et al. Direct bandgap type-I GeSn/GeSn quantum well on a GeSn- and Ge- buffered Si substrate. *AIP Adv.* **8**, 025104 (2018).
- Thai, Q. M. et al. GeSn heterostructure micro-disk laser operating at 230 K. *Opt. Express* **26**, 32500–32508 (2018).
- Du, W. et al. Study of Si-based GeSn optically pumped lasers with micro-disk and ridge waveguide structures. *Front. Phys.* **7**, 147 (2019).

22. Elbaz, A. et al. Ultra-low-threshold continuous-wave and pulsed lasing in tensile-strained GeSn alloys. *Nat. Photonics* **14**, 375–382, <https://doi.org/10.1038/s41566-020-0601-5> (2020).
23. Thai, Q. M. et al. GeSn optical gain and lasing characteristics modelling. *Phys. Rev. B* **102**, 155203 (2020).
24. Rainko, D. et al. Impact of tensile strain on low Sn content GeSn lasing. *Sci. Rep.* **9**, 259 (2019).
25. Ghrib, A. et al. Tensile-strained germanium microdisks. *Appl. Phys. Lett.* **102**, 221112 (2013).
26. Ghrib, A. et al. All-around SiN stressor for high and homogeneous tensile strain in germanium microdisk cavities. *Adv. Opt. Mater.* **3**, 353–358 (2015).
27. Elbaz, A. et al. Germanium microlasers on metallic pedestals. *APL Photonics* **3**, 106102 (2018).
28. Armand Pilon, F. T. et al. Lasing in strained germanium microbridges. *Nat. Commun.* **10**, 2724 (2019).
29. Süess, M. J. et al. Analysis of enhanced light emission from highly strained germanium microbridges. *Nat. Photonics* **7**, 466–472 (2013).
30. Nam, D. et al. Study of carrier statistics in uniaxially strained Ge for a low-threshold Ge laser. *IEEE J. Sel. Top. Quantum Electron.* **20**, 16–22 (2014).
31. Imbrenda, D. et al. Infrared dielectric response, index of refraction, and absorption of germanium-tin alloys with tin contents up to 27% deposited by molecular beam epitaxy. *Appl. Phys. Lett.* **113**, 122104 (2018).
32. Chrétien, J. et al. GeSn lasers covering a wide wavelength range thanks to uniaxial tensile strain. *ACS Photonics* **6**, 2462–2469 (2019).
33. Elbaz, A. et al. Solving thermal issues in tensile-strained Ge microdisks. *Opt. Express* **26**, 28376–28384 (2018).
34. Moutanabbir, O. et al. Monolithic infrared silicon photonics: the rise of (Si)GeSn semiconductors. *Appl. Phys. Lett.* **118**, 110502 (2021).
35. Tabataba-Vakili, F. et al. Analysis of low-threshold optically pumped III-nitride microdisk lasers. *Appl. Phys. Lett.* **117**, 121103 (2020).
36. Baba, T. & Sano, D. Low-threshold lasing and Purcell effect in microdisk lasers at room temperature. *IEEE J. Sel. Top. Quantum Electron.* **9**, 1340–1346 (2003).
37. Baba, T. et al. Spontaneous emission factor of a microcavity DBR surface-emitting laser. *IEEE J. Quantum Electron.* **27**, 1347–1358 (1991).
38. Piprek, J., White, J. K. & SpringThorpe, A. J. What limits the maximum output power of long-wavelength AlGaInAs/InP laser diodes? *IEEE J. Quantum Electron.* **38**, 1253–1259 (2002).
39. Mashanovich, G. Z. et al. Low loss silicon waveguides for the mid-infrared. *Opt. Express* **19**, 7112–7119 (2011).
40. Miller, S. A. et al. Low-loss silicon platform for broadband mid-infrared photonics. *Optica* **4**, 707–712 (2017).
41. Gupta, S. et al. Highly selective dry etching of germanium over germanium-tin (Ge1-xSnx): a novel route for Ge1-xSnx nanostructure fabrication. *Nano Lett.* **13**, 3783–3790 (2013).
42. Lin, P. T. et al. Planar silicon nitride mid-infrared devices. *Appl. Phys. Lett.* **102**, 251121 (2013).
43. Prost, M. et al. Tensile-strained germanium microdisk electroluminescence. *Opt. Express* **23**, 6722–6730 (2015).
44. Aubin, J. et al. Growth and structural properties of step-graded, high Sn content GeSn layers on Ge. *Semicond. Sci. Technol.* **32**, 094006 (2017).
45. Bigourdan, F., Hugonin, J.-P. & Lalanne, P. Aperiodic-Fourier modal method for analysis of body-of-revolution photonic structures. *J. Opt. Soc. Am. A* **31**, 1303–1311 (2014).
46. Rakić, A. D. et al. Optical properties of metallic films for vertical-cavity optoelectronic devices. *Appl. Opt.* **37**, 5271–5283 (1998).

Appendix E :
Room Temperature Optically Pumped
GeSn Microdisk Lasers

Room temperature optically pumped GeSn microdisk lasers

Cite as: Appl. Phys. Lett. **120**, 051107 (2022); <https://doi.org/10.1063/5.0074478>

Submitted: 08 October 2021 • Accepted: 24 January 2022 • Published Online: 02 February 2022

 J. Chrétien,  Q. M. Thai,  M. Frauenrath, et al.



View Online



Export Citation



CrossMark

ARTICLES YOU MAY BE INTERESTED IN

[Monolithic infrared silicon photonics: The rise of \(Si\)GeSn semiconductors](#)

Applied Physics Letters **118**, 110502 (2021); <https://doi.org/10.1063/5.0043511>

[Colloidal II-VI–Epitaxial III-V heterostructure: A strategy to expand InGaAs spectral response](#)

Applied Physics Letters **120**, 051101 (2022); <https://doi.org/10.1063/5.0076708>

[Transparent ultrathin Ag nanomesh electrode fabricated by nanosphere lithography for organic light-emitting devices](#)

Applied Physics Letters **120**, 051106 (2022); <https://doi.org/10.1063/5.0079505>

Lock-in Amplifiers
up to 600 MHz



Zurich
Instruments



Room temperature optically pumped GeSn microdisk lasers

Cite as: Appl. Phys. Lett. **120**, 051107 (2022); doi: [10.1063/5.0074478](https://doi.org/10.1063/5.0074478)

Submitted: 8 October 2021 · Accepted: 24 January 2022 ·

Published Online: 2 February 2022



View Online



Export Citation



CrossMark

J. Chrétien,^{1,a)} Q. M. Thai,¹ M. Frauenrath,² L. Casiez,² A. Chelnokov,² V. Reboud,² J. M. Hartmann,² M. El Kurdi,³ N. Pauc,¹ and V. Calvo¹

AFFILIATIONS

¹University Grenoble Alpes, CEA, Grenoble INP, IRIG, PHELIQS, Grenoble, France

²University Grenoble Alpes, CEA, LETI, Grenoble, France

³Université Paris-Saclay, CNRS, C2N, 10 boulevard Thomas Gobert, 91120 Palaiseau, France

^{a)} Author to whom correspondence should be addressed: jeremie.chretien@outlook.com

ABSTRACT

GeSn alloys are promising materials for light emitters monolithically grown on silicon. In this work, we demonstrate room temperature (RT) lasing in a GeSn hetero-structure with 17.2% of Sn. We report a threshold of 3.27 MW cm^{-2} at 305 K with peak emission at 353 meV. We ascribe these improvements to a higher tin concentration in the GeSn active layer with lower Sn content barriers on each side and to a better thermal dissipation provided by an adapted pedestal architecture beneath the GeSn micro-disk. This outcome is a major milestone for a fully integrated group-IV semiconductor laser on Si.

Published under an exclusive license by AIP Publishing. <https://doi.org/10.1063/5.0074478>

GeSn materials are appealing candidates for many applications, ranging from photodetectors^{1–3} to molecular spectroscopy and gas sensing in the mid-infrared (2–5 μm). However, they are still behind III–V counterparts in terms of lasing performance (laser threshold and maximum lasing temperature), even if recent progress in GeSn doping yielded the first electrically pumped GeSn laser with a limited temperature of 100 K.⁴ According to theoretical works,^{5,6} the maximum operating laser temperature is dependent on the energy offset between Γ and L valleys. High Sn contents and high amounts of tensile strain are two strategies that can be leveraged to increase the energy offset between the Γ and L valleys and enhance the optical gain through a carrier density increase in the Γ valley. Experimental efforts were spent since the early 2010s to increase the Sn concentration (over 8%) in GeSn alloys and have a direct bandgap, which are mandatory for stimulated light emission. Since the first demonstration, in 2015, of lasing up to 90 K (Ref. 7) in a Fabry–Pérot (FP) cavity with its core at a thick GeSn layer with 12.6% of Sn (called “GeSn 12.6%” from now on), the maximum operating temperature has steadily improved from 180 up to 270 K by increasing the Sn concentration from 16% up to 20%, using FP^{8–10} or relaxed microdisk cavities.^{11–13} Inserting the active layer between lower Sn content layers was also shown to improve the lasing performance.^{12,13} Tensile strain engineering was also investigated to increase the maximum lasing temperature. It resulted in a maximum lasing temperature of 273 K for tensile strained

GeSn 16% suspended microbridges¹⁴ with a high laser threshold of 2 MW cm^{-2} , however. Lasing under continuous-wave optical pumping was also demonstrated in 5.4% Sn bi-dimensionally tensile strained microdisks¹⁵ with removal of Ge/GeSn interfacial dislocations during layer transfer.

Room temperature (RT) lasing in GeSn is, thus, closely dependent on the interplay between a relatively high laser threshold near RT and the dissipation of heat generated in the resonators.¹⁶ Decreasing thresholds could help in reaching RT operation, even in non-thermally optimized devices. Here, we demonstrate RT lasing in Sn rich layers sandwiched between lower Sn content layers with an improved heat transfer scheme and without the help of tensile strain.

The 1080 nm thick GeSn heterostructure was grown in a 200 mm Epi Centura 5200 reduced pressure-chemical vapor deposition cluster tool from Applied Materials on top of a 2.5 μm thick Ge strain relaxed buffer (SRB), itself grown on the (001) Si substrate. Ge_2H_6 , SnCl_4 , and Si_2H_6 were used as precursor gases. A step graded Sn concentration approach was adopted here with constant Ge_2H_6 and SnCl_4 flows and temperatures, which gradually decreased from 349 °C down to 307 °C during growth at 100 Torr, as described in Ref. 17. The thick, optically active GeSn 17.2% layer grown at 307 °C was capped at 313 °C by GeSn 16.1% and 14.1% layers. The Sn concentration lowering, from 16.1% down to 14.1%, was achieved through a reduction of the SnCl_4 flow. Reducing the Sn content by lowering the SnCl_4 flow instead of

increasing the growth temperature reduced the risk of having Sn surface segregation/precipitation. The Sn contents and the macroscopic degrees of strain relaxation of the various GeSn layers were determined experimentally thanks to the Reciprocal Space Map around the (224) asymmetric x-ray diffraction (XRD) order shown in Fig. 1(a). Data are gathered in Table S1. The optically active part of the heterostructure was made up of a ~ 430 nm GeSn 17.2% \pm 0.3% optically active layer sandwiched in-between ~ 110 nm thick GeSn 16.1% \pm 0.3% barriers, themselves embedded in ~ 110 nm thick GeSn 14.1% \pm 0.3% layers [stack schematics in Fig. 1(a)].

The as-grown GeSn stack shows maximum peak emission at 0.406 eV (3052 nm) at 25 K and under continuous wave optical pumping, as shown in Fig. 1(b), indicating a higher Sn concentration in the active GeSn layer than in Ref. 13 with a photoluminescence peak located at 0.428 eV (2900 nm) at 15 K. This emission wavelength is in good agreement with the 17.2% Sn content obtained in XRD. Two sets of resonators were fabricated from the very same heterostructure. The final microdisks did not differ in terms of an optically active stack. They were drastically different in terms of the thermal management strategy, however. Dimensions and underlying pedestals were indeed not the same. Sample 1 was obtained via anisotropic and isotropic dry etching of the blanket stack in a similar approach to previous works.^{12,18} The final thickness of the GeSn stack after isotropic buffer etching was ~ 900 nm, corresponding (from the bottom to the top) to

the GeSn 14.1%, 16.1%, 17.2%, 16.1%, and 14.1% layers in Fig. 1(a) schematics. The heavily dislocated GeSn 7.4% and the “transition layer” were removed during fabrication. Sample 2 was obtained following the steps presented in Fig. 1(c). It was made of the as-grown stack (sample A) bonded upside-down on a host pedestal (sample B). To that end, a 500 nm thick AlN layer was sputter deposited on sample A, followed by a 40 nm-10 nm-200 nm thick TiN-Cr-Au trilayer. TiN is indeed expected to reduce metallic diffusion taking place in the metallic bonding step that follows, as this material is known for its diffusion barrier properties.¹⁹ Sample A and sample B surfaces were then placed face to face with a small In layer sandwiched between the two samples then annealed at a temperature around 160–180 °C. An InAu alloy, with a high In concentration, formed upon cooling, creating a solder between samples A and B.²⁰ The backside of sample A was then removed with first some polishing followed by selective SF_6 -based dry etching of the last tens of μm of the Si substrate, the whole Ge buffer, and the low Sn content GeSn layers, leaving intact the high Sn content GeSn layers underneath. The final stack thickness was 770 nm, corresponding to (from the end sample's bottom to the top) the GeSn 14.1%, 16.1%, 17.2%, and 16.1% layers. E-beam lithography and anisotropic etching steps were then used. Microdisks were underetched over 2 μm by dipping samples in a 326MIF developer, an aqueous developer containing tetramethylammonium hydroxide, during 40 min, with afterwards a rinse in de-ionized water. The choice of the

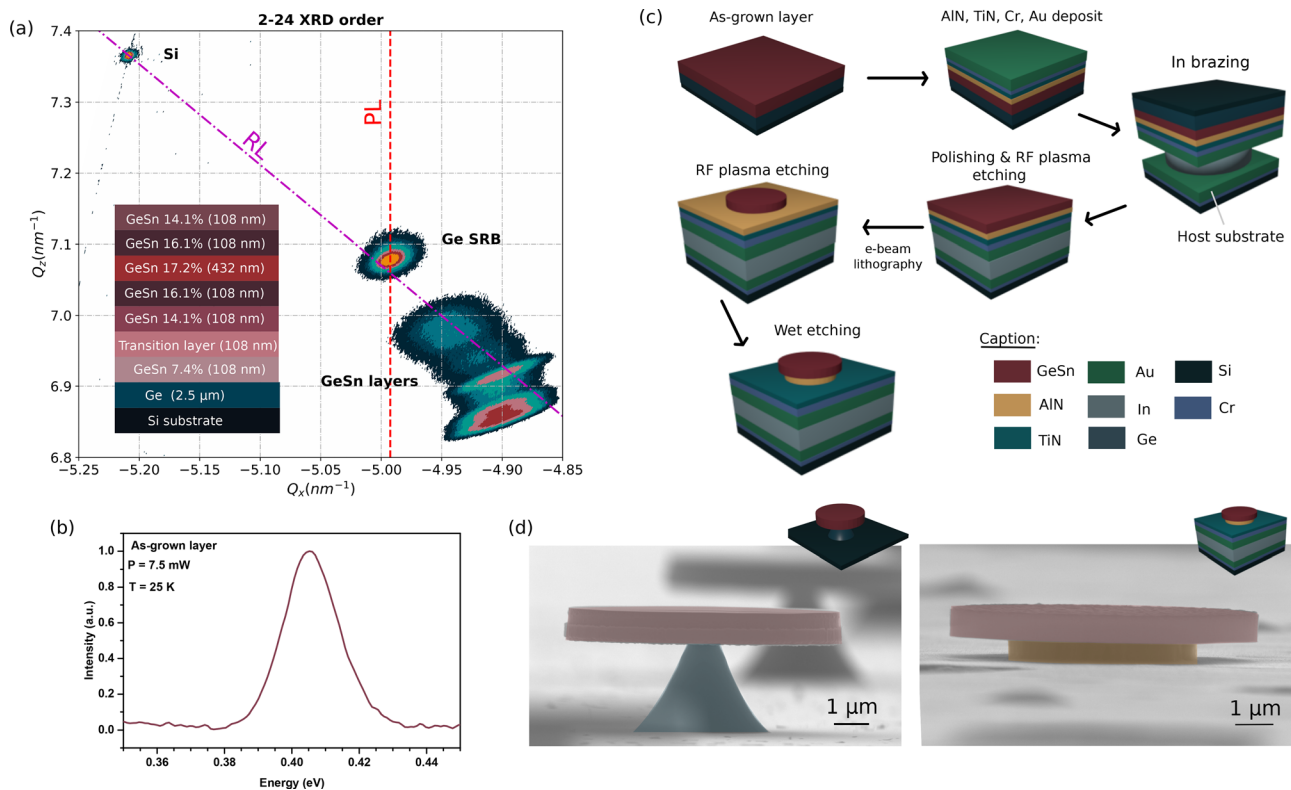


FIG. 1. (a) Reciprocal space map around the (224) XRD asymmetric reflection for the GeSn 17.2% heterostructure epitaxially grown on a 2.5 μm thick Ge SRB, itself on a Si (001) substrate (layer stack shown in the inset). (b) Photoluminescence spectrum of the as-grown stack at 25 K. (c) Sketch of the different steps of the GeSn layer transfer with indium brazing. (d) Scanning electron microscopy images of 8 μm diameters GeSn microdisks on Ge (left) and AlN (right) pedestals.

bonding strategy was dictated here by the bonding temperature, which had to be kept as low as possible to avoid Sn segregation/precipitation in the GeSn layers. This phenomenon is known to happen at temperatures close to the growth temperature,²¹ which was 307 °C only for the 17.2% layer.

A recent work²² on the thermal properties of GeSn alloys showed a conductivity drop as the Sn content increased from 58 W m⁻¹ K⁻¹ (Ref. 23) (pure Ge) down to 4 W m⁻¹ K⁻¹ only (for GeSn 14%). Thus, heat transport in GeSn microdevices is expected to be hindered compared with their pure Ge counterparts. The dissipation of the laser induced heating from the GeSn microdisk to the substrate is dependent on (i) the nature and the thickness of the pedestal, (ii) the underetching, and (iii) the suspended GeSn active area. GeSn epilayers are traditionally grown on top of thick (2.5 μm) Ge strain-relaxed buffers, themselves on Si substrates, minimizing the amount of misfit dislocations in the GeSn layers. Playing on the heat transport properties of this thermal sink adds an extra lever to mitigate the heat of the gain medium under very high pump power, near RT. Changing the thermal conductivity of the pedestal material, by replacing Ge [$k_{Ge} = 58 \text{ W} \cdot \text{m}^{-1} \text{ K}^{-1}$ (Ref. 23)] with AlN [$k_{AlN} = 285 \text{ W} \cdot \text{m}^{-1} \text{ K}^{-1}$ (Ref. 23)], increases the heat flux toward the substrate. Thinning down the pedestal by 5 (from 2.5 μm for Ge to 0.5 μm for AlN) and increasing the heat exchange area at the disk

pedestal interface drastically decrease the pedestal's thermal resistance. Reducing the disk undercut while avoiding mode overlap with the pedestal also reduces the thermal resistance contribution from the crown shaped region between the undercut line and the modal region. A thin AlN pedestal with a short undercut, thus, offers, in principle, a better alternative to Ge, mostly used to date, for heat evacuation. Thick Ge buffers are indeed necessary to grow high quality GeSn epilayers. In addition, AlN is a wideband gap semiconductor, which does not absorb infrared radiation, preventing any mode overlap loss with the pedestal.

In the following, we compare 15 μm diameter microdisk lasers on (i) a Ge pedestal (with a 2.5 μm pedestal thickness and 3.5 μm under-etches) and (ii) an AlN pedestal (with a 0.54 μm pedestal thickness and 1.55 μm under-etches). We show that lasing performances are better for the latter. We estimate the modal confinement factors to be 69.6% for the disk on AlN and 66.2% for the disk on Ge. In addition, there are no noticeable layer bending for both types of disks. Given that radii are the same and confinement factors are very close, we, thus, expect photon propagation conditions to be the same in both types of disks. It is important to note that the step graded approach concentrates the dislocations in the low Sn content layers, etched in both samples, and that the active 17.2% medium along its interfaces is preserved for both configurations. This is in sharp contrast with previous work,²⁴ where severe

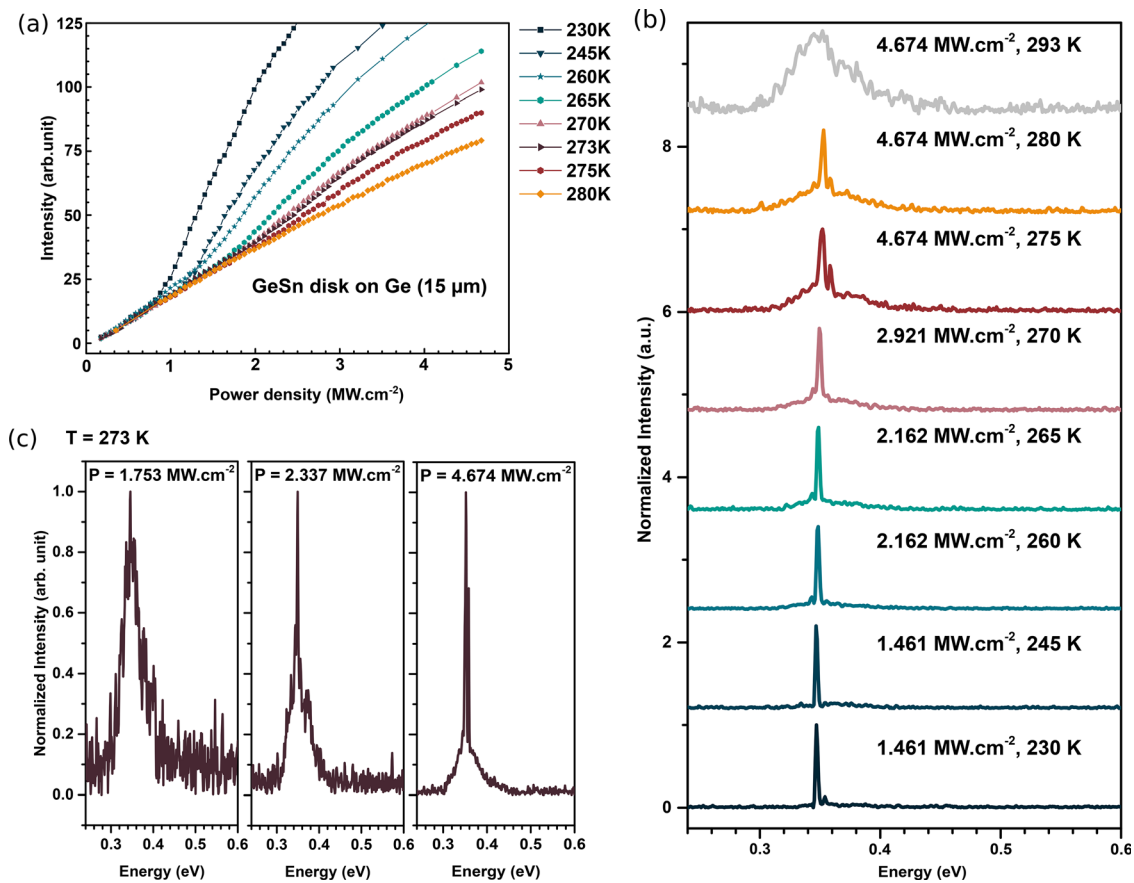


FIG. 2. (a) L-L curves at different temperatures from 230 up to 280 K and (b) corresponding temperature-dependent spectra for a 15 μm diameter GeSn microdisk on a Ge pedestal. (c) Spectra at 273 K under a pulsed density power excitation of 1.753 (under the threshold), 2.337 (near the threshold), and 4.674 MW cm⁻² (above the threshold).

non-radiative recombination by interface defects in the active medium directly grown onto the Ge buffer was mitigated by GeSn bonding and partial back etching of the defective part of the active medium at different degrees after GeSn bonding in GeSnOI or underetching in microdisks on Ge structures. Here, the recombination activity not only near the mode area but also the strain state (relaxed) and photon propagation properties in the gain medium are similar for both samples. This makes heat conduction properties the main discriminating mechanism with differences not only in heat conduction properties arising from different thermal resistances in the pedestals but also and more importantly in the undercut resistance rather high for these concentrations (see the [supplementary material](#)), which depends not only on its length but also on the GeSn conductivity.

A pulsed 1064 nm Nd:YAG laser, with a 0.6 ns pulse duration and a repetition rate of 50 kHz, was used to optically pump the GeSn microdisks. The laser beam was focused on the sample in a 25 μm

diameter circular spot with a 13.8 \times magnification Cassegrain objective. The backscattered PL signal was analyzed with a Fourier transform infrared interferometer equipped with an InSb detector. [Figure 2](#) shows the optical characterization of a 15 μm diameter GeSn microdisk on a Ge pedestal. Light in–light out (L–L) curves for several temperatures are presented in [Fig. 2\(a\)](#). We clearly observed slope breaks from 230 up to 275 K with a laser threshold increase from 791 kW cm^{-2} up to 2.54 MW cm^{-2} , respectively.²⁵ Lasing spectra are shown in [Fig. 2\(b\)](#) as a function of the temperature. A single mode can be observed at 230 K with photon energies around 0.347 eV. Spectra acquired below, near, and above the threshold at 273 K are provided in [Fig. 2\(c\)](#). The mode is still visible at 280 K, but the corresponding L–L curve does not show a slope break anymore.

A 15 μm diameter GeSn microdisk on an AlN pedestal was otherwise investigated. [Figure 3\(a\)](#) shows photoluminescence spectra at various temperatures ranging from 230 to 308 K. The maximum lasing

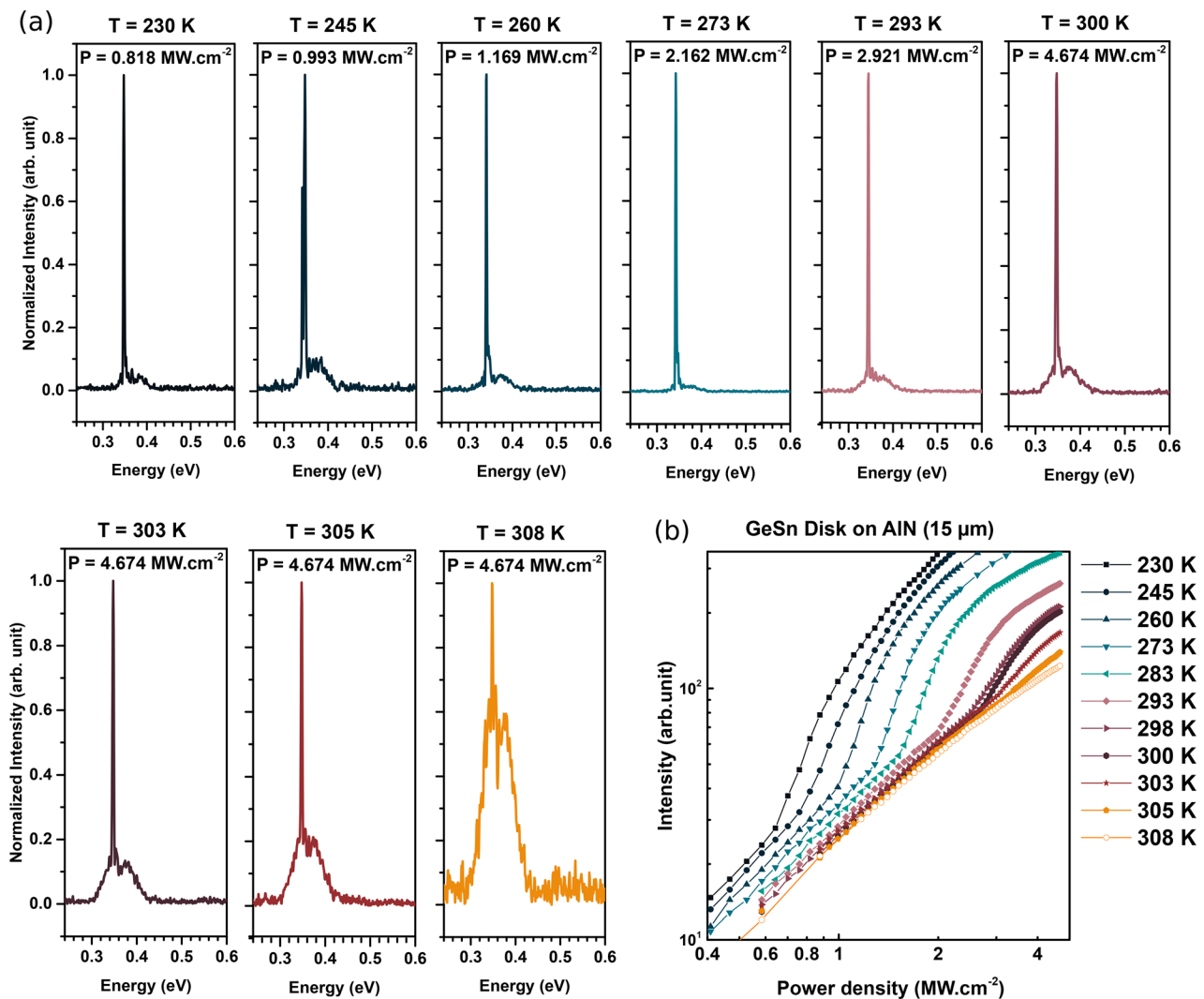


FIG. 3. (a) Spectra of a 15 μm diameter GeSn microdisk resonator on an AlN pedestal from 230 up to 308 K. (b) L–L curves for the same temperature range.

temperature was improved up to 305 K compared to the Ge case. A strong single lasing mode is clearly visible at 0.348 eV, i.e., at nearly the same energy than for the micro-disk on a Ge pedestal. It should be noted that spontaneous emission at 0.38 eV is still significant even at 273 K. We attribute this contribution to the AlN pedestal, since its low refractive index (around 2) increases the interface reflection coefficient compared to the Ge pedestal. It results in an enhancement of the PL signal at the center of the microdisk. The ratio between the lasing peak and spontaneous PL maxima, however, drops from 54 down to 5 when the temperature increases from 273 up to 305 K. The lasing

mode disappears at 308 K. L-L curves are plotted in Fig. 3(b) for temperatures in the 230–308 K range.

From 230 to 305 K, we clearly observe both the optical mode and the nonlinearity of the L-L curve, which sets an upper lasing limit between 305 and 308 K.

Figure 4(a) shows the experimental thresholds $P_{th}(T)$ for both types of microdisks as a function of the temperature (Ge pedestal: blue full squares and AlN pedestal: red full circles). Lasing thresholds were, in Figs. 2(a) and 3(b), power densities at which there were slope breaks in the L-L curves. Extracted data show a biexponential behavior,

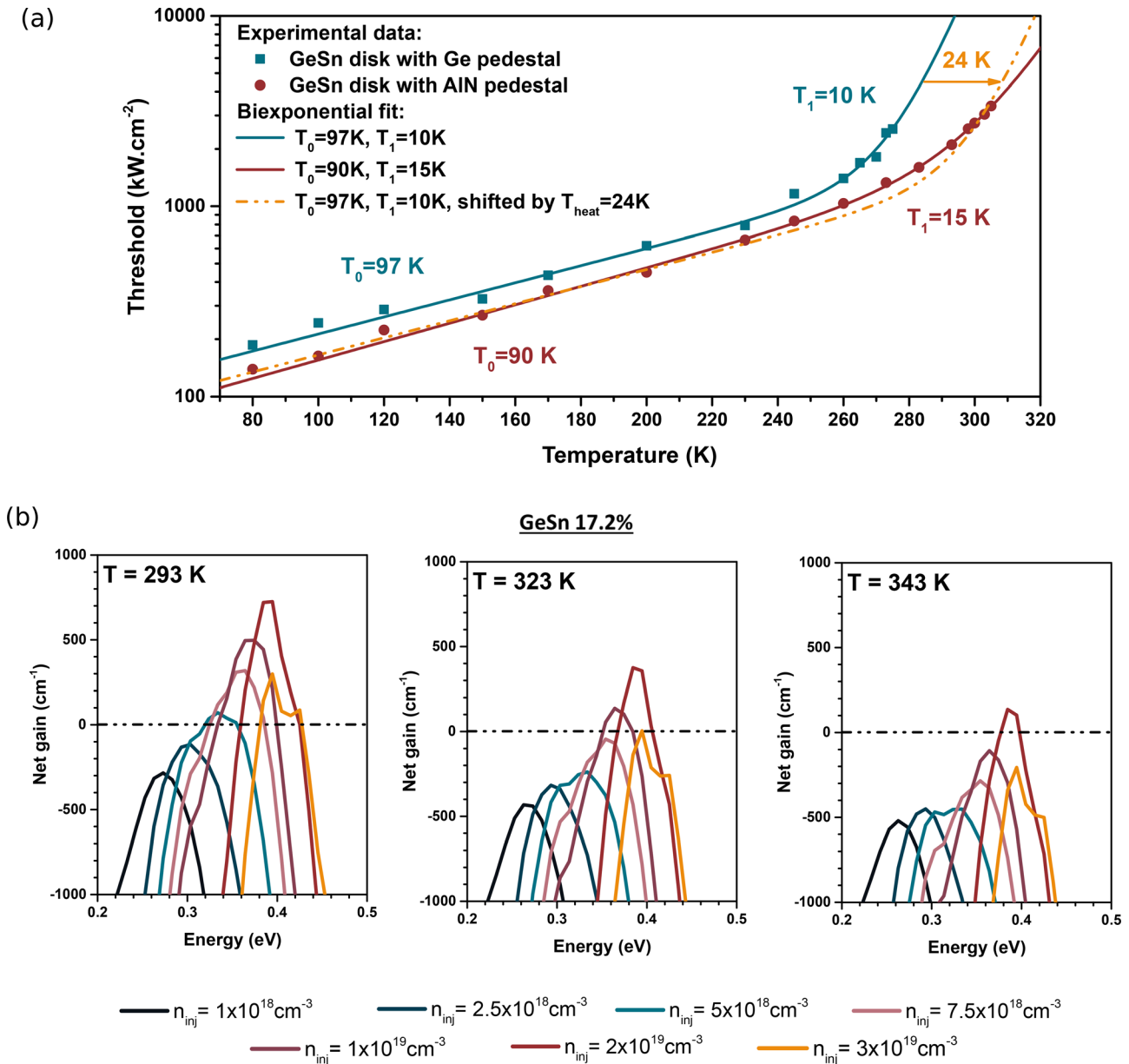


FIG. 4. (a) Threshold as a function of the temperature for 15 μm diameter GeSn disks on Ge (blue full squares) and AlN (red full circles) pedestals. (b) Computed net gain of GeSn 17.2% as a function of the photon energy at different values of n_{inj} between 1×10^{18} and $3 \times 10^{19} \text{ cm}^{-3}$ calculated for 293, 323, and 343 K.

$P_{th}(T) = P_0 \exp\left(\frac{T}{T_0}\right) + P_1 \exp\left(\frac{T}{T_1}\right)$ with $T_0^{Ge} = 97$ K, $T_1^{Ge} = 10$ K and $T_0^{AlN} = 90$ K, $T_1^{AlN} = 15$ K. Similar characteristic temperatures in both samples reveal identical processes for gain loss with temperature (thermal broadening of carriers in the bands, thermal escape from the barriers, Auger recombination...) as a consequence of the basically identical nature of the gain medium and its environment. The thermal shift between both curves is slightly power dependent, and a mean shift of 24 K (see the dotted curve) is deduced by fitting the AlN data with the Ge parameters while introducing a thermal shift as the only fitting parameter in the biexponential law. This is definitely indicative of overheating of the gain medium in the Ge pedestal case compared to the AlN pedestal case. At 230 K, a roll-off is only observed on the L-L curve of the Ge pedestal case (see the [supplementary material](#)), indicating heating of the device contrary to the AlN pedestal case. For the highest temperatures, diffusion of carriers from the modal to the inner zone might induce extra electronic losses through escape to the unattacked and defective low tin content layers in the pedestal of the microdisk on Ge and could contribute to slight increase in the threshold. RT lasing operation in our free-standing system is, thus, made possible by changing the pedestal architecture.

We performed theoretical calculations of the optical gain near RT. The simulation methodology was described in detail in Ref. 6. It takes into account contributions from the interband transition—i.e., from valence bands (VBs) to conduction bands (CBs), the intervalence band transition (VB–VB), and the free carrier absorption (FCA—using the empirical formula established by Liu *et al.* for Ge,²⁶ and extended here for GeSn). We plot in Fig. 4(b) the net gain as a function of the photon energy for GeSn 17.2% at different values of n_{inj} between 1×10^{18} and $3 \times 10^{19} \text{ cm}^{-3}$ and for three temperatures: 293, 323, and 343 K. At 293 K, i.e., the cryostat temperature, a robust net gain (300 cm^{-1}) is reached for $n_{inj} = 7.5 \times 10^{18} \text{ cm}^{-3}$. The maximum of the net gain curve is 750 cm^{-1} for $n_{inj} = 2 \times 10^{19} \text{ cm}^{-3}$. It progressively drops by a factor of two between 293 and 323 K and vanishes for $T = 343$ K. Furthermore, increasing the Sn content leads to maximizing the net gain at room temperature and above, as pointed out in Ref. 6, where an optimum of the concentration for maintaining positive net gains at RT is found for Sn rich layers.

We have just shown that effective temperatures were different for AlN and Ge pedestals (24 K, experimentally). Because of laser heating, they were also different from the cryostat temperature. The thermal profile at the steady-state was also derived from finite element method (FEM) simulations (the [supplementary material](#)). Simulation showed that the disk underetch, i.e., the suspended active zone, was a key parameter to be tuned to cooldown the laser cavity. Taking into account pump-laser overheating and the computed optical gain, we could expect to have lasing at even higher temperatures for better cooled cavities like pillar or released microdisks on a thermal conductive layer, which leads to the same conclusion of Kim *et al.*²⁷

To conclude, we demonstrated lasing in a 17.2% GeSn microdisk under optical pumping up to 305 K in strain free, underetched microdisks on pedestals. By changing the pedestal architecture, we managed to have room temperature lasing, a significant milestone for industrial applications. We estimated that such thermally optimized GeSn layers have the potential to lase up to 330–340 K without strain assistance. Such results are very promising for group-IV light emitters and could be improved via thermal and tensile strain management.

See the [supplementary material](#) for more information on reciprocal space mapping, thermal simulations, the optical spectrum, and gain computations.

This work was supported by the Elegante ANR Project and Gelato Carnot Project. The authors acknowledge the assistance of the staff belonging to CEA-LETI's clean rooms and CEA Advanced technological platform (PTA). They are also grateful for help during GeSn morphological characterization experiments.

AUTHOR DECLARATIONS

Conflict of Interest

The authors have no conflicts to disclose.

DATA AVAILABILITY

The data that support the findings of this study are available from the corresponding author upon reasonable request.

REFERENCES




- A. Gassenq, F. Gencarelli, J. V. Campenhout, Y. Shimura, R. Loo, G. Narcy, B. Vincent, and G. Roelkens, *Opt. Express* **20**, 27297 (2012).
- M. R. M. Atalla, S. Assali, A. Attiaoui, C. Lemieux-Leduc, A. Kumar, S. Abdi, and O. Moutanabbir, *Adv. Funct. Mater.* **31**, 2006329 (2021).
- H. Tran, T. Pham, J. Margetis, Y. Zhou, W. Dou, P. C. Grant, J. M. Grant, S. Al-Kabi, G. Sun, R. A. Soref, J. Tolle, Y.-H. Zhang, W. Du, B. Li, M. Mortazavi, and S.-Q. Yu, *ACS Photonics* **6**, 2807 (2019).
- Y. Zhou, Y. Zhou, Y. Miao, S. Ojo, S. Ojo, H. Tran, G. Abernathy, G. Abernathy, J. M. Grant, J. M. Grant, S. Amoah, G. Salamo, G. Salamo, W. Du, J. Liu, J. Margetis, J. Tolle, Y. Zhang, G. Sun, R. A. Soref, B. Li, S.-Q. Yu, and S.-Q. Yu, *Optica* **7**, 924 (2020).
- D. Rainko, Z. Ikonik, A. Elbaz, N. von den Driesch, D. Stange, E. Herth, P. Boucaud, M. E. Kurdi, D. Grützmacher, and D. Buca, *Sci. Rep.* **9**, 259 (2019).
- Q. M. Thai, J. Chretien, M. Bertrand, L. Casiez, A. Chelnokov, V. Reboud, N. Pauc, and V. Calvo, *Phys. Rev. B* **102**, 155203 (2020).
- S. Wirths, R. Geiger, N. von den Driesch, G. Mussler, T. Stoica, S. Mantl, Z. Ikonik, M. Luysberg, S. Chiussi, J. M. Hartmann, H. Sigg, J. Faist, D. Buca, and D. Grützmacher, *Nat. Photonics* **9**, 88 (2015).
- S. Al-Kabi, S. A. Ghetmiri, J. Margetis, T. Pham, Y. Zhou, W. Dou, B. Collier, R. Quinde, W. Du, A. Mosleh, J. Liu, G. Sun, R. A. Soref, J. Tolle, B. Li, M. Mortazavi, H. A. Naseem, and S.-Q. Yu, *Appl. Phys. Lett.* **109**, 171105 (2016).
- J. Margetis, S. Al-Kabi, W. Du, W. Dou, Y. Zhou, T. Pham, P. Grant, S. Ghetmiri, A. Mosleh, B. Li, J. Liu, G. Sun, R. Soref, J. Tolle, M. Mortazavi, and S.-Q. Yu, *ACS Photonics* **5**, 827 (2018).
- Y. Zhou, W. Dou, W. Du, S. Ojo, H. Tran, S. A. Ghetmiri, J. Liu, G. Sun, R. Soref, J. Margetis, J. Tolle, B. Li, Z. Chen, M. Mortazavi, and S.-Q. Yu, *ACS Photonics* **6**, 1434 (2019).
- D. Stange, S. Wirths, R. Geiger, C. Schulte-Braucks, B. Marzban, N. von den Driesch, G. Mussler, T. Zabel, T. Stoica, J.-M. Hartmann, S. Mantl, Z. Ikonik, D. Grützmacher, H. Sigg, J. Witzens, and D. Buca, *ACS Photonics* **3**, 1279 (2016).
- V. Reboud, A. Gassenq, N. Pauc, J. Aubin, L. Milord, Q. M. Thai, M. Bertrand, K. Guillois, D. Rouchon, J. Rothman, T. Zabel, F. Armand Pilon, H. Sigg, A. Chelnokov, J. M. Hartmann, and V. Calvo, *Appl. Phys. Lett.* **111**, 092101 (2017).
- Q. M. Thai, N. Pauc, J. Aubin, M. Bertrand, J. Chretien, V. Delaye, A. Chelnokov, J.-M. Hartmann, V. Reboud, and V. Calvo, *Opt. Express* **26**, 32500 (2018).
- J. Chretien, N. Pauc, F. Armand Pilon, M. Bertrand, Q.-M. Thai, L. Casiez, N. Bernier, H. Dansas, P. Gergaud, E. Delamadeleine, R. Khazaka, H. Sigg, J. Faist, A. Chelnokov, V. Reboud, J.-M. Hartmann, and V. Calvo, *ACS Photonics* **6**(10), 2462–2469 (2019).
- A. Elbaz, D. Buca, N. von den Driesch, K. Pantzas, G. Patriarce, N. Zerounian, E. Herth, X. Checoury, S. Sauvage, I. Sagnes, A. Foti, R. Ossikovski, J.-M.

- Hartmann, F. Boeuf, Z. Ikonic, P. Boucaud, D. Grützmacher, and M. E. Kurdi, *Nat. Photonics* **14**, 375–382 (2020).
- ¹⁶D. Burt, H.-J. Joo, Y. Jung, Y. Kim, M. Chen, Y.-C. Huang, and D. Nam, *Opt. Express* **29**, 28959 (2021).
- ¹⁷J. Aubin, J. M. Hartmann, A. Gassenq, J. L. Rouviere, E. Robin, V. Delaye, D. Cooper, N. Mollard, V. Reboud, and V. Calvo, *Semicond. Sci. Technol.* **32**, 094006 (2017).
- ¹⁸S. Gupta, R. Chen, Y.-C. Huang, Y. Kim, E. Sanchez, J. S. Harris, and K. C. Saraswat, *Nano Lett.* **13**, 3783 (2013).
- ¹⁹W. E. Martinez, G. Gregori, and T. Mates, *Thin Solid Films* **518**, 2585 (2010).
- ²⁰W. W. So and C. C. Lee, *IEEE Trans. Comp. Packag. Technol.* **23**, 377 (2000).
- ²¹P. Zaumseil, Y. Hou, M. A. Schubert, N. von den Driesch, D. Stange, D. Rainko, M. Virgilio, D. Buca, and G. Capellini, *APL Mater.* **6**, 076108 (2018).
- ²²D. Spirito, N. von den Driesch, C. L. Manganelli, M. H. Zoellner, A. A. Corley-Wiciak, Z. Ikonic, T. Stoica, D. Grützmacher, D. Buca, and G. Capellini, *ACS Appl. Energy Mater.* **4**(7), 7385–7392 (2021).
- ²³Ioffe Institute, see <http://www.ioffe.ru/SVA/> for “New Semiconductor Materials. Characteristics and Properties” (2020).
- ²⁴B. Wang, E. Sakat, E. Herthl, M. Gromovyi, A. Bjelajac, J. Chaste, G. Patriarche, P. Boucaud, F. Boeuf, N. Pauc, V. Calvo, J. Chrétien, M. Frauenrath, A. Chelnokov, V. Reboud, J.-M. Hartmann, and M. El Kurdi, *Light: Sci. Appl.* **10**, 232 (2021).
- ²⁵“Scrutinizing lasers,” *Nat. Photonics* **11**, 139 (2017).
- ²⁶J. Liu, X. Sun, D. Pan, X. Wang, L. C. Kimerling, T. L. Koch, and J. Michel, *Opt. Express* **15**, 11272 (2007).
- ²⁷Y. Kim, S. Assali, D. Burt, Y. Jung, H.-J. Joo, M. Chen, Z. Ikonic, O. Moutanabbir, and D. Nam, *Adv. Opt. Mater.* **10**, 2101213 (2022).

Appendix F :
Up to 300 K Lasing with
GeSn On-Insulator Microdisk Resonators



Up to 300 K lasing with GeSn-On-Insulator microdisk resonators

A. BJELAJAC,¹ M. GROMOVYI,¹ E. SAKAT,¹  B. WANG,¹ G. PATRIARCHE,¹  N. PAUC,² V. CALVO,² P. BOUCAUD,³  F. BOEUF,⁴ A. CHELNOKOV,⁵ V. REBOUD,⁵ M. FRAUENRATH,⁵ J.-M. HARTMANN,⁵ AND M. EL KURDI^{1,*}

¹Université Paris-Saclay, CNRS, C2N, 10 boulevard Thomas Gobert, 91120 Palaiseau, France

²Université Grenoble Alpes, CEA, IRIG-DePhy, 17 rue des Martyrs, 38000 Grenoble, France

³Université Côte d'Azur, CNRS, CRHEA, Rue Bernard Grégory, 06905 Sophia-Antipolis, France

⁴STMicroelectronics, Rue Jean Monnet, 38054 Crolles, France

⁵Université Grenoble Alpes, CEA, Leti, 17 rue des Martyrs, 38000 Grenoble, France

*moustafa.el-kurdi@c2n.upsaclay.fr

Abstract: GeSn alloys are the most promising direct band gap semiconductors to demonstrate full CMOS-compatible laser integration with a manufacturing from Group-IV materials. Here, we show that room temperature lasing, up to 300 K, can be obtained with GeSn. This is achieved in microdisk resonators fabricated on a GeSn-On-Insulator platform by combining strain engineering with a thick layer of high Sn content GeSn.

© 2022 Optica Publishing Group under the terms of the [Optica Open Access Publishing Agreement](#)

1. Introduction

The first demonstration of low-temperature lasing with direct band gap GeSn, published in 2015 [1], was followed by several breakthroughs like electrically-injected lasing up to 100 K [2] and continuous wave (CW) laser operation up to 70 K [3]. An important milestone towards real-field applications is the ability to operate at room temperature (RT). A critical parameter to have a performant laser at high temperature is the directness of the band structure, defined as the energy barrier between the zone center (Γ) and the indirect (L) valleys of the conduction band. This energy barrier should typically be around 150-200 meV, to maintain the Γ -state electron population up to room temperature and have an optical gain involving direct transitions with the valence band hole states [4]. To reach such directness, a high amount of tin (Sn) in the alloys is required, of the order of 16%. Such high Sn contents are challenging to achieve. In practice, the use of Ge strain relaxed buffers (SRBs) on silicon was proven to be most appropriate to grow GeSn alloys and mitigate the large lattice mismatch with Si substrates. However, increasing the Sn content results in a large compressive strain that reduces the band gap directness and degrades the gain. The mainstream approach, to overcome compressive strain issues, is to grow layers definitely above their critical thickness for plastic relaxation, with a strain relaxation typically around 75%. [5] However, dense arrays of misfit dislocations near the GeSn/Ge SRB interface are then formed, resulting in non-radiative processes detrimental to lasing [6]. So far, the highest temperatures achieved for laser operation were 273 K for 16% of Sn and 270 K for 17% of Sn, although the directness parameter was expected then to be high enough to reach RT lasing in [7] and [8]. In Ref. [7], bandgap directness was reinforced by some uniaxial strain.

To go to higher temperatures, we propose a strategy relying on a specific GeSn-On-Insulator (GeSnOI) mesa structure with the use of SiN as stressor as recently proposed in Ref. [9]. The GeSnOI stack is fabricated with layer bonding onto a metallic film for improved thermal management [10]. The main assets of this platform is, first, to enable the removal of the GeSn/Ge SRB interfacial defects by simple etching after bonding. Second, the optical confinement is improved compared to conventional GeSn /Ge SRB stacks thanks to the higher optical index

contrast between GeSn and the SiN layer underneath. Third, the strain transfer yields a higher directness of the alloy [4]. The combination of these advantages leads to RT lasing in microdisk resonators, as shown in the following.

2. Fabrication

Our strategy was to use a 720 nm thick GeSn layer with 16.9% of Sn on top of a 2.5 μm thick Ge SRB, itself on a silicon (Si) (001) substrate. A $\text{Ge}_2\text{H}_6 + \text{SnCl}_4$ chemistry was used to grow that layer, at 313°C, 100 Torr with a growth rate of 22 nm/min. Reciprocal Space Maps around the (004) and (224) X-Ray Diffraction orders gave us access to the Sn concentration and macroscopic degree of strain relaxation R of that GeSn layer. As expected from [11], we had some Sn enrichment in the GeSn layer as soon as the built-in compressive strain started to plastically relax. This resulted in a higher Sn content, less compressively strained GeSn layer (16.9%, $R = 84\%$) on top of a lower Sn content, more dislocated and almost fully relaxed GeSn layer (13.3%, $R = 98\%$), as shown in Fig. 1. The residual compressive strain in the top, optically active part of the GeSn layer was thus -0.5%. Meanwhile, the Ge SRB underneath was slightly tensile strained. This was due to thermal dilatations coefficients' differences between the fully relaxed Ge SRB and the Si substrate that came into play during the cooling-down to room temperature after growth [12]. This was the reason why the Ge SRB peak was not, in Fig. 1(a), on the Si fully Relaxed Line.

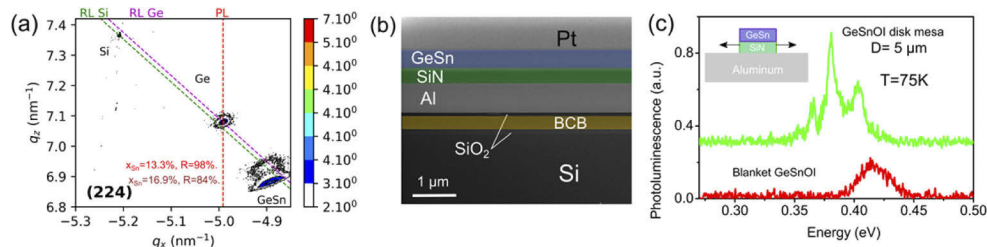


Fig. 1. (a) Reciprocal Space Map around the (224) X-Ray Diffraction order gave access to the in-plane and out-of-plane lattice parameter of the bottom and top parts of the thick GeSn layer on the Ge-buffered Si(001) substrate and thus, to their Sn contents and macroscopic degrees of strain relaxation ([Sn] 13.3% and $R = 98\%$ and [Sn] 16.9% and $R = 84\%$). RL are acronyms for the fully Relaxed Lines (from the origin of the reciprocal space to the Si or the Ge peaks; if the GeSn layers were fully relaxed, they would be on the Ge RL). Meanwhile, PL is an acronym for the Pseudomorphic Line (same in-plane lattice parameter and thus, same q_x coordinate than the Ge SRB; if the GeSn layers were fully strained on the Ge SRB underneath, they would be on that vertical line). (b) cross-sectional scanning electron microscope image of the GeSnOI stack (after bonding with BenzoCycloButene (BCB) on a Si wafer) showing the active GeSn layer, the SiN stressor and the Al heat sink. The Pt layer on top was used to protect the surface during the Focused Ion Beam (FIB) etching of microdisk mesas. (c) 75 K photoluminescence spectra under continuous-wave optical pumping of blanket GeSnOI and of a GeSnOI microdisk mesa. The spectrum of the latter was vertically offset for clarity purposes. The microdisk emission is strongly modulated by cavity resonances.

The GeSnOI layer was thinned down after bonding, with therefore a removal of interfacial defects (Fig. 1(b)). The overall thermal budget was lowered as much as possible, as thermal stress could result in local Sn precipitation [13]. Bonding, which lasted 30 minutes, was thus performed at a temperature of 210°C, i.e. far below the GeSn growth temperature of 313°C (and a similar duration). The final bonded layer thickness was 450 nm and we did follow the procedure recommended by the supplier for the bonding. In the following, we will assume that the Sn composition was the same in microdisks than in the epitaxial stack, as we did not observe

any precipitation by transmission electron microscopy. After patterning into microdisk mesa, the layer became slightly tensile-strained by the bottom SiN stressor layer, by 0.1%, typically. The in-plane strain change, from -0.5% to 0.1%, resulted in a red shift, by typically 40 meV, of the photoluminescence emission spectrum for the microdisk mesa as compared to the one of the blanket GeSnOI stack (Fig. 1(c)) [9]. The emission spectrum of the microdisk mesa showed typical cavity resonance patterns that were not present on the blanket photoluminescence spectrum. The 40 meV shift was estimated from the envelope of the photoluminescence spectra, i.e. without accounting for the resonances.

3. Optically pumped laser characterizations

Figure 2 shows a scanning electron microscopy (SEM) image of a microdisk mesa resonator fabricated from the GeSnOI stack. The emission from the cavities is optically excited and analyzed as a function of temperature and excitation power density using the setup and excitation conditions shown in Fig. 2. Emission spectra at 293 K (20°C) from a 5 μm diameter GeSnOI microdisk mesa under 400 kW cm^{-2} and 800 kW cm^{-2} pulsed excitation densities in Fig. 2 show a clear change from a broad spontaneous emission regime to lasing.

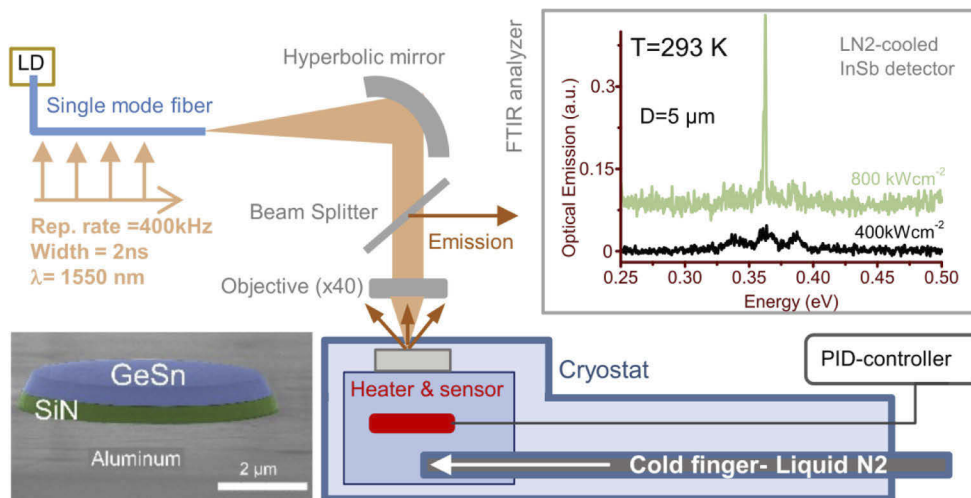


Fig. 2. Experimental set-up. A SEM image of a GeSnOI microdisk mesa is shown in the bottom left. The inset shows emission spectra of a GeSnOI microdisk mesa with a 5 μm diameter, below and above lasing threshold, at 20°C.

We started our investigation of lasing at 273 K, i.e. the highest lasing temperature reported in the literature. Figure 3 shows the emission spectra of a GeSnOI microdisk mesa with a 5 μm diameter for different pump power densities, with a clear transition from a spontaneous emission regime to lasing, also noticeable in the Light in-Light out curve in the inset. The threshold density at 273 K was 240 kW cm^{-2} and lasing occurred at 0.355 eV, in line with the $\text{TE}_{11,1}$ whispering gallery mode resonance (at 0.358 eV from modeling). The adjacent $\text{TE}_{10,1}$ and $\text{TE}_{12,1}$ modes were indeed at 0.333 eV and 0.38 eV (free spectral range around 25 meV), without a good overlap with the maximum of optical gain.

The WGM resonances of the microdisk were calculated a two-dimensional (2D) analytical model, as described in Ref. [3]. The resonance wavelength of the cavity mode with azimuthal index m was calculated from the roots of the m^{th} Bessel function $I_m\left(\frac{2\pi n_{\text{eff}}(\lambda)}{\lambda_{\text{res}}}a\right)$. The optical field was plotted at the resonant wavelength to obtain the corresponding radial number of nodes, n , along the disk radius (a). To account for the modal dispersion of vertically confined modes, the

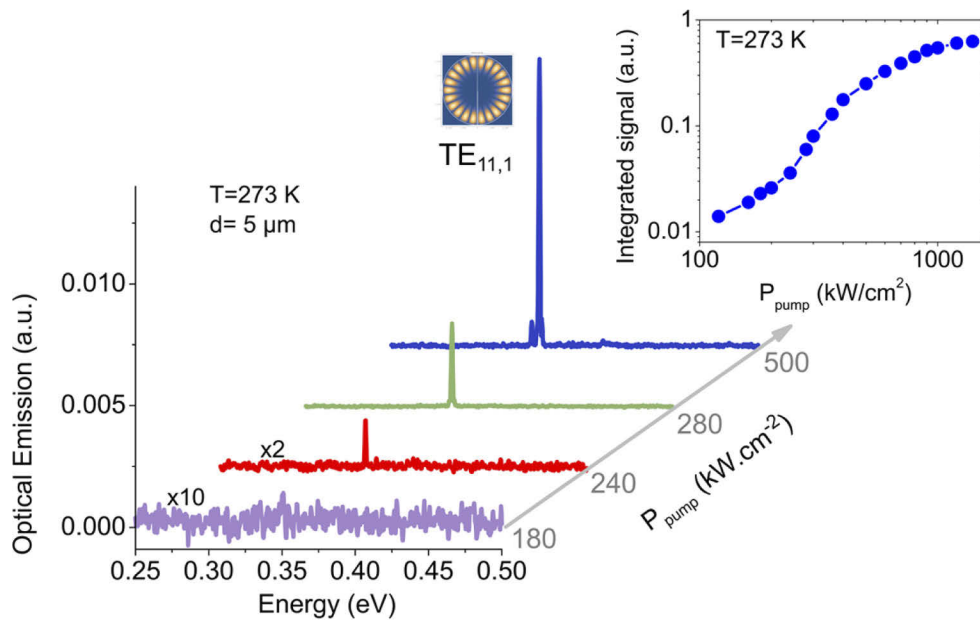


Fig. 3. Emission spectra at 273 K under different excitation densities, up to $500 \text{ kW}\cdot\text{cm}^{-2}$, of a GeSnOI microdisk mesa with a $5 \mu\text{m}$ diameter. The $\text{TE}_{11,1}$ lasing whispering gallery mode profile is shown in the graph. The right inset shows the Light in-Light out curve (Log-Log scale).

effective index $n_{\text{eff}}(\lambda)$ was obtained from 1D slab modeling of TE-polarized waves propagating in the GeSn layer. This 2D analytical model perfectly reproduced the WGM resonances obtained with the aperiodic Fourier modal method, as detailed in Ref. [14].

The lasing spectra under excitation higher than $500 \text{ kW}\cdot\text{cm}^{-2}$, as shown later on, become multimode due to the optical gain spectral and spatial broadenings. A similar behavior was reported in Ref. [6]. While this feature is generally explained in terms of homogeneous or inhomogeneous broadenings, we emphasize that the spectral range with net positive gain is spectrally narrow at high temperature, resulting in a drastic mode selection as shown thereafter.

Figure 4(a) shows the emission spectra of the $5 \mu\text{m}$ diameter microdisk mesa when the temperature increases, starting from 273 K under a fixed pump power of $880 \text{ kW}\cdot\text{cm}^{-2}$. At this pump density, the lasing spectra are multimode between 273 K and 285 K. Above 290 K, lasing occurs preferentially with the $\text{TE}_{11,1}$ mode, i.e. the mode associated with the onset of lasing at 273 K. Lasing is maintained up to 300 K and quenched at 303 K. This represents a major achievement since room temperature lasing is demonstrated here. Figure 4(b) shows the emission spectra as a function of pump power density at fixed heating temperature of 298 K. The corresponding Light-in Light-out (L-L) curve of the integrated signal is shown in the inset. As already observed at 273 K, a clear laser transition is observed at a threshold density of $400 \text{ kW}\cdot\text{cm}^{-2}$, as also shown by the S-shape of the L-L curve plotted on a Log-Log scale. Above the lasing threshold, the peak linewidth is $\sim 1 \text{ meV}$ only. It is comparable to the lasing peak linewidth of 0.5 meV for GeSnOI microdisk mesa at much lower temperatures, i.e. 74 K under similar pumping excitations [9]. Furthermore, there is a clear linewidth narrowing of the lasing peak by a factor close to two, as shown in the inset of Fig. 4(b). According to the Schawlow-Townes theory, a linewidth reduction by a factor of 2 is a signature of the transition from spontaneous emission to coherent emission.

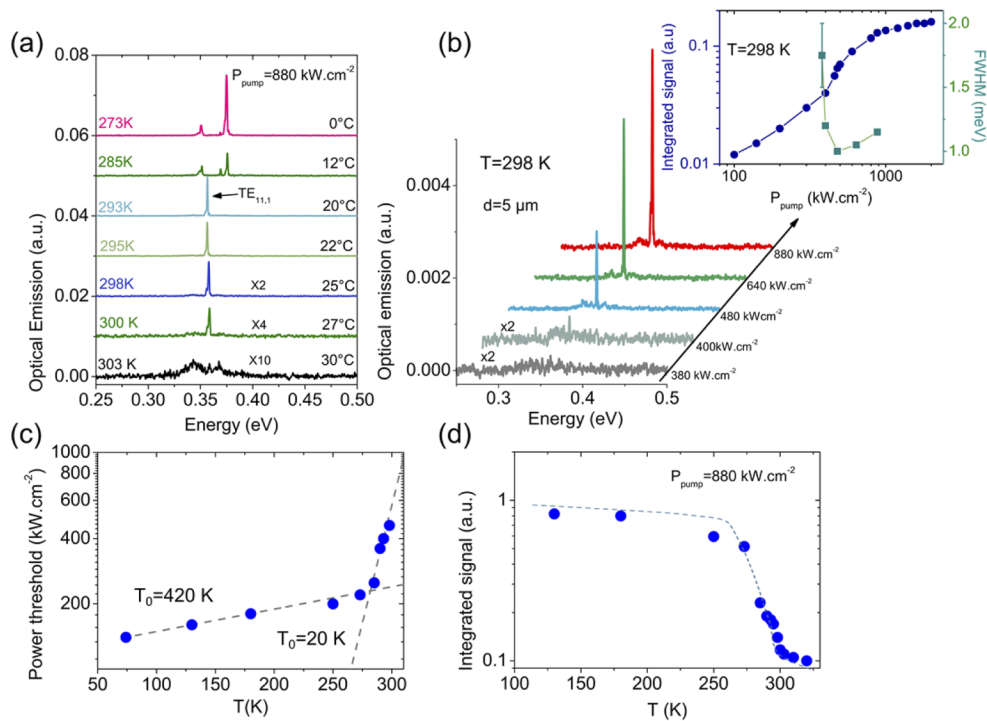


Fig. 4. (a) Temperature dependence, from 273 K up to 303 K, of the optical emission spectra under 880 kW cm^{-2} optical excitation. Lasing is maintained up to 300 K and quenched at 303 K (b) Emission spectra for different excitation densities at a fixed cooling temperature of 298 K. The right inset shows the integrated signal Light in-Light out curve (Log-Log scale) together with the lasing mode linewidths extracted from emission spectra at different pumping powers. The error bar accounts for the lower signal-to-noise ratio below threshold. (c) Lasing threshold as a function of temperature. Dashed lines are exponential fits with T_0 characteristic temperatures of 420 K and 20 K, respectively. (d) Integrated signal as a function of temperature for a fixed pump power density of 880 kW cm^{-2} .

We studied the lasing threshold as a function of temperature over a wider range of temperature as shown in Fig. 4(c). From 75 K up to 273 K, lasing characteristics are stable and the threshold increases only by a factor of two. In that temperature range, the threshold increase is well accounted by an exponential law with a characteristic T_0 temperature as high as 420 K, i.e. 1.4 times T_{room} with a room temperature of 293 K. Such a characteristic shows that the optical gain should potentially be maintained above room temperature. However, above 273 K, the slope abruptly changes and the threshold increases much more rapidly, with a T_0 of 20 K only, then. The slope change above 273 K occurs simultaneously with the onset of a laser signal decrease, as shown in Fig. 4(d). This steep decrease of the signal and the abrupt threshold increase suggest that thermal activation of extra losses occurs in the gain region of the cavity. The laser quenching may be due to carrier losses because of thermal activation of non-radiative processes, for instance on the microdisk mesa sidewalls through photo-induced desorption or adsorption of contaminants, as shown in Ref. [15]. Indeed, lasing whispering gallery modes are close to the microdisk etched sidewalls and should be sensitive to surface contamination there. It should be noted that the $\text{TE}_{11,1}$ mode has the lowest lasing threshold at 273 K and thus the best combination of Q-factor, spectral and spatial overlap with optical gain, enabling it to still lase at higher temperatures. Other studies, beyond the scope of this work, would be

helpful to better assess the role of surface contamination on lasing characteristics above 273 K. Effective surface passivation of GeSn as proposed in Ref. [16] would be helpful in the future to optimize the device performance robustness against temperature. Beyond the detrimental impact of non-radiative surface recombination, the material could also present bulk defects, like p-type vacancies as evidenced in Ref. [17], that may contribute to the fast laser quenching with temperature above 300 K. In view of multiple unknown parameters related to material growth conditions and processing, the fine modeling of optical gain in GeSn as a function of temperature will require further experimental analysis to build a robust model.

4. Discussion

Since lasing is a highly non-linear process involving optical gain and carrier recombination dynamics, a slight change of conditions can have a strong impact, explaining its abrupt quenching with temperature. Additional heating from the optical pump, that has to be increased to reach higher thresholds, contributes to this quenching. We can assume that the use of heterostructures, with for instance SiGeSn ternary alloys as barriers [18,19,20] would be helpful to reduce surface recombination and maintain lasing at higher temperatures with a reduced threshold. With the GeSnOI approach, there is indeed no need to suspend the layer as in [20] [21] under-etched microdisks, resulting in a better thermal management. The interest of the GeSnOI approach was also proven in [22] by bonding GeSn microdisks on SiO₂ layers (with Al₂O₃ intermediate layers and no residual compressive strain, afterwards). Another advantage of the GeSnOI platform that is thoroughly discussed in [22] is the removal of interfacial defects between the GeSn active layer and the Ge strain buffer layer underneath, significantly improving the laser thresholds characteristics in Refs. [9] and [6]. The low-temperature thresholds of the structures investigated here are larger than those reported in Refs. [6] and [9]. The later used lower tin content as gain media and lasing occurred at shorter wavelength, i.e. smaller than 2.4 μm against 3.54 μm here, with then lower free carrier absorption losses. However, the robustness versus temperature is much stronger here because of a significantly higher Sn content, and higher directness of the band structure, a better thermal management and the use of shorter optical pulses.

We have shown that the room temperature hurdle for lasing with GeSn alloys can be overcome. Our GeSnOI approach enabled to fabricate smaller micro-resonators than in [7] and [8], potentially enabling their dense integration on a semiconductor-on-insulator photonic platform as shown in [23]. Further optimizations of the GeSn structural quality, with for example a step graded increase of the Sn content during growth, as in [7] or [24], and the right surface passivation strategy should result in even better performances.

In the near future, one of the main challenges will be to fabricate electrically-pumped devices taking full advantage of the GeSnOI technology. Pin GeSn diodes will then have to be grown and bonded with the process flow shown here. The design of the laser cavity will have to be adapted in order to minimize losses due to the use of metallic electrodes while having the best possible carrier injection in the gain region. We have used here a cavity design, but many other designs, like conventional Fabry-Perot ridge cavities, could be thought of. Our strategy is indeed compatible with complex heterostructures and electronic band engineering, as in Ref. [2] with 100 K electrically pumped lasers.

5. Conclusion

To conclude, we have shown here that room temperature lasing can be obtained with thick GeSn alloys with a tin content of 17% thanks to the use of a GeSnOI specific technology with interfacial misfit dislocations removal, strain engineering, improved optical confinement and thermal management. In numerous previous works with the same tin content alloys and lasers fabricated from as-grown GeSn/Ge-SRB/Si, room temperature lasing was not reached despite

advanced SiGeSn/GeSn heterostructures engineering [7–8,24–26]. The current study emphasizes the potential of the GeSnOI technology.

Funding. Agence Nationale de la Recherche (ANR-17-CE24-0015).

Disclosures. The authors declare that there are no conflicts of interest related to this article.

Data availability. Data underlying the results presented in this paper are not publicly available at this time but may be obtained from the authors upon reasonable request.

References

1. S. Wirths, R. Geiger, N. von den Driesch, G. Mussler, T. Stoica, S. Mantl, Z. Ikonic, M. Luysberg, S. Chiussi, J. M. Hartmann, H. Sigg, J. Faist, D. Buca, and D. Grützmacher, “Lasing in direct-bandgap GeSn alloy grown on Si,” *Nat. Photonics* **9**(2), 88–92 (2015).
2. Y. Zhou, Y. Miao, S. Ojo, H. Tran, G. Abernathy, J. M. Grant, S. Amoah, G. Salamo, W. Du, J. Liu, J. Margetis, J. Tolle, Y. Zhang, G. Sun, R. A. Soref, B. Li, and S.-Q. Yu, “Electrically injected GeSn lasers on Si operating up to 100 K,” *Optica* **7**(8), 924–928 (2020).
3. A. Elbaz, D. Buca, N. von den Driesch, K. Pantzas, G. Patriarche, N. Zerounian, E. Herth, X. Checoury, S. Sauvage, I. Sagnes, A. Foti, R. Ossikovski, J.-M. Hartmann, F. Boeuf, Z. Ikonic, P. Boucaud, D. Grützmacher, and M. El Kurdi, “Ultra-low-threshold continuous-wave and pulsed lasing in tensile-strained GeSn alloys,” *Nat. Photonics* **14**(6), 375–382 (2020).
4. D. Rainko, Z. Ikonic, A. Elbaz, N. von den Driesch, D. Stange, E. Herth, P. Boucaud, M. El Kurdi, D. Grützmacher, and D. Buca, “Impact of tensile strain on low Sn content GeSn lasing,” *Sci. Rep.* **9**(1), 259 (2019).
5. S. Al-Kabi, S. A. Ghetmiri, J. Margetis, T. Pham, Y. Zhou, W. Dou, B. Collier, R. Quinde, W. Du, A. Mosleh, J. Liu, G. Sun, R. A. Soref, J. Tolle, B. Li, M. Mortazavi, H. A. Naseem, and S.-Q. Yu, “An optically pumped 2.5 μm GeSn laser on Si operating at 110 K,” *Appl. Phys. Lett.* **109**(17), 171105 (2016).
6. A. Elbaz, R. Arefin, E. Sakat, B. Wang, E. Herth, G. Patriarche, A. Foti, R. Ossikovski, S. Sauvage, X. Checoury, K. Pantzas, I. Sagnes, J. Chrétien, L. Casiez, M. Bertrand, V. Calvo, N. Pauc, A. Chelnokov, P. Boucaud, F. Boeuf, V. Reboud, J.-M. Hartmann, and M. El Kurdi, “Reduced Lasing Thresholds in GeSn Microdisk Cavities with Defect Management of the Optically Active Region,” *ACS Photonics* **7**(10), 2713–2722 (2020).
7. J. Chrétien, N. Pauc, F. Armand Pilon, M. Bertrand, Q.-M. Thai, L. Casiez, N. Bernier, H. Dansas, P. Gergaud, E. Delamadeleine, R. Khazaka, H. Sigg, J. Faist, A. Chelnokov, V. Reboud, J.-M. Hartmann, and V. Calvo, “GeSn Lasers Covering a Wide Wavelength Range Thanks to Uniaxial Tensile Strain,” *ACS Photonics* **6**(10), 2462–2469 (2019).
8. Y. Zhou, W. Dou, W. Du, S. Ojo, H. Tran, S. A. Ghetmiri, J. Liu, G. Sun, R. Soref, J. Margetis, J. Tolle, B. Li, Z. Chen, M. Mortazavi, and S.-Q. Yu, “Optically Pumped GeSn Lasers Operating at 270 K with Broad Waveguide Structures on Si,” *ACS Photonics* **6**(6), 1434–1441 (2019).
9. B. Wang, E. Sakat, E. Herth, M. Gromovyi, A. Bjelajac, J. Chaste, G. Patriarche, P. Boucaud, F. Boeuf, N. Pauc, V. Calvo, J. Chrétien, M. Frauenrath, A. Chelnokov, V. Reboud, J.-M. Hartmann, and M. El Kurdi, “GeSnOI mid-infrared laser technology,” *Light: Sci. Appl.* **10**(1), 232 (2021).
10. A. Elbaz, M. El Kurdi, A. Aassime, S. Sauvage, X. Checoury, I. Sagnes, F. Boeuf, and P. Boucaud, “Solving thermal issues in tensile-strained Ge microdisks,” *Opt. Express* **26**(22), 28376–28384 (2018).
11. J. Aubin, J. M. Hartmann, A. Gassenq, L. Milord, N. Pauc, V. Reboud, and V. Calvo, “Impact of thickness on the structural properties of high tin content GeSn layers,” *J. Cryst. Growth* **473**, 20–27 (2017).
12. J. M. Hartmann, A. M. Papon, V. Destefanis, and T. Billon, “Reduced pressure chemical vapor deposition of Ge thick layers on Si(001), Si(011) and Si(111),” *J. Cryst. Growth* **310**(24), 5287–5296 (2008).
13. P. Zaumseil, Y. Hou, M. A. Schubert, N. von den Driesch, D. Stange, D. Rainko, M. Virgilio, D. Buca, and G. Capellini, “The thermal stability of epitaxial GeSn layers,” *APL Materials* **6**, 076108 (2018).
14. F. Bigourdan, J.-P. Hugonin, and P. Lalanne, “Aperiodic-Fourier modal method for analysis of body-of-revolution photonic structures,” *J. Opt. Soc. Am. A* **31**(6), 1303–1311 (2014).
15. I. Rousseau, G. Callsen, G. Jacopin, J.-F. Carlin, R. Butté, and N. Grandjean, “Optical absorption and oxygen passivation of surface states in III-nitride photonic devices,” *J. Appl. Phys.* **123**(11), 113103 (2018).
16. L. Groell, A. Attiaoui, S. Assali, and O. Moutanabbir, “Combined Iodine- and Sulfur-Based Treatments for an Effective Passivation of GeSn Surface,” *J. Phys. Chem. C* **125**(17), 9516–9525 (2021).
17. S. Assali, M. Elsayed, J. Nicolas, M. O. Liedke, A. Wagner, M. Butterling, R. Krause-Rehberg, and O. Moutanabbir, “Vacancy complexes in nonequilibrium germanium-tin semiconductors,” *Appl. Phys. Lett.* **114**(25), 251907 (2019).
18. D. Stange, N. von den Driesch, D. Rainko, S. Roesgaard, I. Povstugar, J.-M. Hartmann, T. Stoica, Z. Ikonic, S. Mantl, D. Grützmacher, and D. Buca, “Short-wave infrared LEDs from GeSn/SiGeSn multiple quantum wells,” *Optica* **4**(2), 185–188 (2017).
19. D. Stange, N. von den Driesch, T. Zabel, F. Armand-Pilon, D. Rainko, B. Marzban, P. Zaumseil, J.-M. Hartmann, Z. Ikonic, G. Capellini, S. Mantl, H. Sigg, J. Witzens, D. Grützmacher, and D. Buca, “GeSn/SiGeSn Heterostructure and Multi Quantum Well Lasers,” *ACS Photonics* **5**(11), 4628–4636 (2018).
20. Q. M. Thai, N. Pauc, J. Aubin, M. Bertrand, J. Chrétien, V. Delaye, A. Chelnokov, J.-M. Hartmann, V. Reboud, and V. Calvo, “GeSn heterostructure micro-disk laser operating at 230 K,” *Opt. Express* **26**(25), 32500–32508 (2018).

21. D. Stange, S. Wirths, R. Geiger, C. Schulte-Braucks, B. Marzban, N. von den Driesch, G. Mussler, T. Zabel, T. Stoica, J.-M. Hartmann, S. Mantl, Z. Ikonic, D. Grützmacher, H. Sigg, J. Witzens, and D. Buca, "Optically Pumped GeSn Microdisk Lasers on Si," *ACS Photonics* **3**(7), 1279–1285 (2016).
22. D. Burt, H.-J. Joo, Y. Jung, Y. Kim, M. Chen, Y.-C. Huang, and D. Nam, "Strain-relaxed GeSn-on-insulator (GeSnOI) microdisks," *Opt. Express* **29**(18), 28959–28967 (2021).
23. H.-J. Joo, Y. Kim, D. Burt, Y. Jung, L. Zhang, M. Chen, S. J. Parluhutan, D.-H. Kang, C. Lee, S. Assali, Z. Ikonic, O. Moutanabbir, Y.-H. Cho, C. S. Tan, and D. Nam, "1D photonic crystal direct bandgap GeSn-on-insulator laser," *Appl. Phys. Lett.* **119**(20), 201101 (2021).
24. J. Margetis, S. Al-Kabi, W. Du, W. Dou, Y. Zhou, T. Pham, P. Grant, S. Ghetmiri, A. Mosleh, B. Li, J. Liu, G. Sun, R. Soref, J. Tolle, M. Mortazavi, and S.-Q. Yu, "Si-Based GeSn Lasers with Wavelength Coverage of 827–833 μm and Operating Temperatures up to 180 K," *ACS Photonics* **5**(3), 827–833 (2018).
25. V. Reboud, A. Gassenq, N. Pauc, J. Aubin, L. Milord, Q. M. Thai, M. Bertrand, K. Guillo, D. Rouchon, J. Rothman, T. Zabel, F. Armand Pilon, H. Sigg, A. Chelnokov, J. M. Hartmann, and V. Calvo, "Optically pumped GeSn micro-disks with 16% Sn lasing at 3.1 μm up to 180 K," *Appl. Phys. Lett.* **111**(9), 092101 (2017).
26. W. Du, Q. M. Thai, J. Chrétien, M. Bertrand, L. Casiez, Y. Zhou, J. Margetis, N. Pauc, A. Chelnokov, V. Reboud, V. Calvo, J. Tolle, B. Li, and S.-Q. Yu, "Study of Si-Based GeSn Optically Pumped Lasers With Micro-Disk and Ridge Waveguide Structures," *Front. Phys.* **7**, 147 (2019).

Valorization

Valorization

Publications

1. **M. Frauenrath, J.-M. Hartmann and E. Nolot**, *Boron and Phosphorous Doping of GeSn for Photodetectors and Light Emitting Diodes*, ECS Trans. 98 (5) (2020) 325.
2. **M. Frauenrath, V. Kiyek, N. von den Driesch, M. Veillerot, E. Nolot, D. Buca and J.-M. Hartmann**, *An In-Depth Study of the Boron and Phosphorous Doping of GeSn*, ECS J. Solid State Sci. 10 (2021) 085006.
3. **M. Frauenrath, L. Casiez, O. Concepción, N. Coudurier, N. Gauthier, S.M. N'hari, E. Nolot, P. Rodriguez, D. Buca, N. Pauc, V. Reboud and J.-M. Hartmann**, *Advances in In-situ Boron and Phosphorous Doping of SiGeSn*, ECS Trans. *To be published*.
4. **M. Frauenrath, P. Acosta Alba, A.-M. Papon and J.-M. Hartmann**, *Nanosecond Laser Annealing of in-situ boron-doped Ge layers for dopant activation*, ECS Trans. *To be published*.
5. **M. Frauenrath, P. Acosta Alba, O. Concepción, J.-H. Bae, N. Gauthier, E. Nolot, M. Veillerot, N. Bernier, D Buca and J.-M. Hartmann** *Nanosecond Laser Annealing of pseudomorphic GeSn layers: Impact of Sn content*, J. Appl. Phys. *Submitted*.
6. **M. Frauenrath, P. Acosta Alba, N. Gauthier, E. Nolot, N. Bernier and J.-M. Hartmann** *Pseudomorphic GeSn layers submitted to Multipulse Nanosecond Laser Annealing – Impact of the GeSn/Ge SRB interface*, *To be submitted*.
7. **J.-M. Hartmann, M. Frauenrath, J. Richy and M. Veillerot** *Ultra-high boron doping of Si and Ge for nanoelectronics and photonics*, ECS Trans. 98 (5) (2020) 203.
8. **J.-M. Hartmann, M. Frauenrath and J. Richy** *Epitaxy of pseudomorphic GeSn layers with germane or digermane as Ge precursors and tin tetrachloride as Sn precursor*, ECS Trans. 98 (5) (2020) 225.
9. **J. Chrétien, N. Pauc, Q. M. Thai, F. Armand Pilon, L. Casiez, M. Frauenrath, R. Khazaka, D. Rouchon, J. Faist, H. Sigg, A. Chelnokov, V. Reboud, S. Tardif, J.-M. Hartmann and V. Calvo** *Correlation between strain and maximum lasing temperature in GeSn microbridges*, 2020 IEEE Photonics Conference (IPC).
10. **L. Casiez, M. Bertrand, J. Chrétien, A. Quintero, Q. M. Thai, M. Frauenrath, O. Lartigue, P. Barritault, N. Bernier, P. Rodriguez, A. Chelnokov, J.-M. Hartmann, N. Pauc, V. Calvo and V. Reboud** *GeSn heterostructures LEDs for gas detection*, 2020 IEEE Photonics Conference (IPC).
11. **B. Wang, E. Sakat, E. Herth, M. Gromovji, A. Bjelajac, G. Patriarce, P. Boucaud, F. Boeuf, N. Pauc, V. Calvo, J. Chrétien, M. Frauenrath, A. Chelnokov, V. Reboud, J.-M. Hartmann and M. El Kurdi** *GeSnOI mid-infrared laser technology*, Light Sci. Appl. 10 (2021) 232.
12. **V. Bonino, N. Pauc, V. Calvo, M. Frauenrath, J.-M. Hartmann, A. Chelnokov, V. Reboud, M. Rosenthal and J. Segura-Ruiz** *Microstructuring to Improve the Thermal Stability of GeSn Layers*, ACS Appl. Mater. Interfaces 14 (2022) 22270.
13. **C. Cardoux, L. Casiez, N. Pauc, V. Calvo, N. Courdurier, P. Rodriguez, J. Richy, P. Barritault, O. Lartigue, C. Constancias, M. Frauenrath, J.-M. Hartmann, A**

- Chelnokov, O. Gravrand and V. Reboud** *Room temperature spectral characterization of direct band gap $Ge_{0.85}Sn_{0.15}$ LEDs and photodiodes*, SPIE Silicon Photonics XVII (2022) 12006
14. **Y. Junk, M. Liu, M. Frauenrath, J.-M. Hartmann, D. Grützmacher, D. Buca and Q.-T. Zhao** *Vertical GeSn/Ge Heterostructure Gate-All-Around Nanowire p-MOSFETs*, ECS. Trans. 108 (5) (2022) 83.
 15. **A. Bjelajac, M. Gromovyi, E. Sakat, B. Wang, G. Patriarche, N. Pauc, V. Calvo, P. Boucaud, F. Boeuf, A. Chelnokov, V. Reboud, M. Frauenrath, J.-M. Hartmann, and M. El Kurdi** *Up to 300 K lasing with GeSn-On-Insulator microdisk resonators*, 30 (3) (2022) 3954.
 16. **J. Chrétien, Q. M. Thai, M. Frauenrath, L. Casiez, A. Chelnokov, V. Reboud, J. M. Hartmann, M. El Kurdi, N. Pauc, and V. Calvo** *Room temperature optically pumped GeSn microdisk lasers*, Appl. Phys. Lett. 120 (2022) 051107.
 17. **L. Casiez, N. Bernier, J. Chrétien, J. Richy, D. Rouchon, M. Bertrand, F. Mazen, M. Frauenrath, A. Chelnokov, J.-M. Hartmann, V. Calvo, N. Pauc, V. Reboud, and P. Acosta Alba** *Recrystallization of thick implanted GeSn layers with nanosecond laser annealing*, J. Appl. Phys. 131 (2022) 153103.

Presentations at International Conferences

1. *Boron and Phosphorous Doping of GeSn for Photodetectors and Light Emitting Diodes*, **M. Frauenrath, J.-M. Hartmann and E. Nolot**, Electrochemical Society (ECS) Honolulu (United States of America) 2020.
2. *Epitaxy of pseudomorphic GeSn layers with GeH_4 or Ge_2H_6 as Ge precursor*, **J.-M. Hartmann, M. Frauenrath and J. Richy**, Electrochemical Society (ECS) Honolulu (United States of America) 2020.
3. *Ultra-high boron doping of Si and Ge for nanoelectronics and photonics*, **J.-M. Hartmann, M. Frauenrath, M. Veillerot and J. Richy**, Electrochemical Society (ECS) Honolulu (United States of America) 2020.
4. *Nanosecond Laser Annealing of in-situ boron-doped Ge*, **M. Frauenrath, P. Acosta Alba, M. Veillerot, A.-M. Papon and J.-M. Hartmann**, European – Material Research Society 2021 Spring Meeting, Strasbourg (France) 2021.
5. *Boron and Phosphorous Doping of SiGeSn for Photodetectors and Light Emitting Diodes*, **M. Frauenrath, O. Concepción, E. Nolot, D. Buca and J.-M. Hartmann**, European – Material Research Society 2021 Fall Meeting, Warsaw (Poland) 2021.
6. *Nanosecond Laser Annealing of Pseudomorphic GeSn Layers with Different Sn Contents*, **M. Frauenrath, P. Acosta Alba and J.-M. Hartmann**, European – Material Research Society 2021 Fall Meeting, Warsaw (Poland) 2021.
7. *Pulsed Nanosecond Laser Annealing of intrinsic and phosphorous implanted GeSn layers*, **M. Frauenrath, P. Acosta Alba, N. Gauthier, E. Nolot, N. Bernier and J.-M. Hartmann**, European – Material Research Society 2022 Fall Meeting, Warsaw (Poland) 2022.
8. *(Invited) Advances in In-situ Boron and Phosphorous Doping of SiGeSn*, **M. Frauenrath, L. Casiez, O. Concepción, N. Coudurier, N. Gauthier, S.M. N'hari, E. Nolot, P. Rodriguez, D. Buca, N. Pauc, V. Reboud and J.-M. Hartmann**, Electrochemical Society (ECS) Atlanta (United States of America) 2022.

9. *Nanosecond Laser Annealing of in-situ boron-doped Ge layers for dopant activation*, **M. Frauenrath**, **P. Acosta Alba**, **A.-M. Papon** and **J.-M. Hartmann**, Electrochemical Society (ECS) Atlanta (United States of America) 2022.

Epitaxial growth and nanosecond laser annealing of GeSn/SiGeSn heterostructures

To extend Si integrated photonics from the Near to the Mid-Infrared, new light sources are required. Direct band gap GeSn with a Sn concentration above 8% is a promising candidate to fulfill such a task. Two doping strategies were investigated in order to enhance the performance of electrically pumped (Si)GeSn lasers and achieve room temperature lasing: in-situ doped epitaxy and ion implantation together with Nanosecond Laser Anneal (NLA). Electrically active dopant concentrations of at most $2.8 \times 10^{19} \text{ cm}^{-3}$ were obtained in in-situ boron-doped GeSn layers. Meanwhile, in-situ phosphorous doping of GeSn, with electrically active dopant concentrations of at most $6.9 \times 10^{19} \text{ cm}^{-3}$, was most likely limited by the formation of $\text{Sn}_m\text{P}_n\text{V}$ nanoclusters. Limitations were overcome by switching over to in-situ doped SiGeSn. Indeed, electrically active dopant concentrations of at most $2.0 \times 10^{20} \text{ cm}^{-3}$ (SiGeSn:B) and $2.7 \times 10^{20} \text{ cm}^{-3}$ (SiGeSn:P) were then obtained. High Si/Sn ratios of 3.5 with Si contents of 25% were otherwise obtained, which should be beneficial for electrical carrier confinement. NLA on pseudomorphic GeSn with various Sn contents otherwise resulted in the formation of high crystalline quality GeSn layers with at most 6.3% of Sn in substitutional sites after annealing, something not achievable with standard annealing techniques. Multi pulse NLA highlighted the importance of a smooth liquid/solid interface for the formation of a smooth surface. Furthermore, it was shown that surface structures formed during laser annealing were Sn rich. When laser annealing phosphorous implanted GeSn 6%, electrical activation of phosphorous was otherwise achieved, resulting in a sheet resistance reduction. The knowledge gained during this PhD thesis was used to fabricate the first optically pumped GeSn lasers operating at room temperature.

Keywords: Epitaxy, GeSn alloys, Reduced Pressure Chemical Vapor Deposition, GeSn laser, Nanosecond Laser Annealing, Doping

Croissance épitaxiale et recuit laser nanosecondes d'hétérostructures GeSn/SiGeSn

Une nouvelle source de lumière est indispensable afin d'élargir les domaines d'application de la photonique intégrée sur silicium du proche au moyen infra-rouge. Le GeSn, avec une structure de bande interdite de type directe pour des concentrations en étain supérieures à 8%, est un candidat prometteur pour répondre à cette demande. Deux stratégies de dopage ont été étudiées pour améliorer la performance de lasers (Si)GeSn pompés électriquement et pouvant opérer à température ambiante: la croissance épitaxiale, avec un dopage in-situ, et l'implantation ionique combinée avec des recuits laser nanosecondes (NLA). Des concentrations en ions B au maximum de $2.8 \times 10^{19} \text{ cm}^{-3}$ ont été obtenues dans des couches de GeSn dopées in-situ en bore. Le dopage in-situ phosphore du GeSn, avec des concentrations électriquement actives au maximum de $6.9 \times 10^{19} \text{ cm}^{-3}$, a probablement été limitée par la formation d'amas $\text{Sn}_m\text{P}_n\text{V}$ de taille nanométrique. Ces limitations ont été surmontées en passant au SiGeSn dopé in-situ, avec des concentrations maximales en dopants électriquement actifs de $2.0 \times 10^{20} \text{ cm}^{-3}$ (SiGeSn:B) et $2.7 \times 10^{20} \text{ cm}^{-3}$ (SiGeSn:P). Un rapport élevé entre le silicium et l'étain, de 3.5, avec une concentration maximale en Si de 25% a été obtenu, ce qui devrait être avantageux pour le confinement électriquement des porteurs de charge. Les recuits laser nanoseconde de couches de GeSn pseudomorphes avec différentes concentrations d'étain ont conduit à la formation de couches GeSn de haute qualité cristalline avec au maximum 6.3% d'étain en substitution après recuit, ce qui n'est pas faisable avec des techniques de recuit standards. Le NLA avec des impulsions laser multiples a souligné l'importance de la rugosité de l'interface liquide/solide pour la formation d'une surface lisse. De plus, il a été montré que les structures de surface formées durant le procédé de recuit laser sont riches en Sn. Lors du recuit laser du GeSn 6% implanté phosphore, l'activation électriquement des atomes de phosphore a été réussi, avec une réduction de la résistance carrée. Le savoir accumulé lors de cette thèse a été utilisé pour fabriquer les premiers lasers GeSn pompés optiquement montrant un effet laser à température ambiante.

Mots Clés: Epitaxie, alliages GeSn, Dépôt Chimique en Phase Vapeur à Pression Réduite, laser GeSn, Recuit Laser Nanosecondes, Dopage